3

EDITORIAL BOARD

AIMS AND SCOPE

PUBLISHING GOAL

3Ciencias wants to transmit to society innovative projects and ideas. This goal is reached thought the publication of original articles which are subdue to peer review or thorough the publication of scientific books.

TEMATIC COVERAGE

3C Empresa is a scientific - social journal, where original works are spread, written in English, for dissemination with empirical and theoretical analyzes on financial markets, leadership, human resources, market microestructure, public accounting and bussines management.

OUR TARGET

- Research staff.
- PhD students.
- Professors.
- Research Results Transfer Office.
- Companies that develop research and want to publish some of their works.

SUBMISSION GUIDELINES

3C Empresa is an arbitrated journal that uses the double-blind peer review system, where external experts in the field on which a paper deals evaluate it, always maintaining the anonymity of both the authors and of the reviewers. The journal follows the standards of publication of the APA (American Psychological Association) for indexing in the main international databases.

Each issue of the journal is published in electronic version (e-ISSN: 2254-3376), each work being identified with its respective DOI (Digital Object Identifier System) code.

STRUCTURE

The original works will tend to respect the following structure: introduction, methods, results, discussion/ conclusions, notes, acknowledgments and bibliographical references.
The inclusion of references is mandatory, while notes and acknowledgments are optional. The correct citation will be assessed according to the 7th edition of the APA standards.

PRESENTATION WORK

All the information, as well as the templates to which the works must adhere, can be found at:

https://www.3ciencias.com/en/journals/infromation-for-authors/

https://www.3ciencias.com/en/regulations/templates/

ETHICAL RESPONSIBILITIES

Previously published material is not accepted (they must be unpublished works). The list of signatory authors should include only and exclusively those who have contributed intellectually (authorship), with a maximum of 4 authors per work. Articles that do not strictly comply with the standards are not accepted.

STATISTICAL INFORMATION ON ACCEPTANCE AND INTERNATIONALIZATION FEES

- Number of accepted papers published: 8.
- Level of acceptance of manuscripts in this number: 66,7%.
- Level of rejection of manuscripts: 33,3%.
- Internationalization of authors: 3 countries (India, Spain, China).

Guidelines for authors: https://www.3ciencias.com/en/regulations/instructions/

INDEXATIONS

INDEXATIONS

Dialnet

CSIC
Consejo Superior de Investigaciones Científicas

ÍnDICEs
CSIC

DOAJ DIRECTORY OF OPEN ACCESS JOURNALS

GENAMICS
...research from your desktop
Genamics JournalSeek

WorldCat®

SHERPA/RoMEO

Crossref

ERIHPLUS
EUROPEAN REFERENCE INDEX FOR THE HUMANITIES AND SOCIAL SCIENCES

EuroPub
Directory of Academic and Scientific Journals

ICI WORLD of JOURNALS

/SUMMARY/

3C Tecnología. Glosas de innovación aplicadas a la pyme. ISSN: 2254-4143

Ed.43 | Iss.12 | N.1 January - March 2023

/01/

3C Tecnología. Glosas de innovación aplicadas a la pyme. ISSN: 2254-4143

Ed.43 | Iss.12 | N.1 January - March 2023

USING CLIMATE MODELS TO PREDICT EXTREME RAINFALL TREND IN YANHE RIVERBASIN, CHINA

Saiyu Yang*

College of Humanities and music, Hunan Vocational College of Science And Technology, Changsha, Hunan, 410013, China

glorious_cs1@163.com

Peng Dai

Brilliance Technology Co., Ltd, Chengdu Branch, Chengdu, Sichuan, 610213, China

ABSTRACT

Climate model is an effective medium to study climate system and climate change. Its simulation results are essentially a crucial data basis for climate prediction and climate change risk assessment. With the acceleration of global warming, the surface ecological environment, hydrological dynamic cycle process, social and economic development are all affected thereupon, resulting in certain influence on the production and life of human beings. In this regard, this paper conducts a study on extreme precipitation events of different climate models with Yanhe River Basin as the study area. The results show that: 1. Yanhe River Basin is a sensitive area to climate change. In the future, the precipitation in this area, for a long time will not increase obviously, but fluctuate greatly; 2. The temporal and spatial difference of extreme precipitation events in the study area is significant. From 2000 to 2050, the interdecadal fluctuation of extreme precipitation events in the study area is significant. In the future, the area with the largest volume of precipitation above 12mm will be concentrated in the southeast part of the study area, followed by the western boundary area; 3. There are few areas with precipitation above 50mm in the Yanhe River Basin, and the occurrence frequency has decreased significantly; 4. The simulation results of different climate models are different. Alao, pursuant to the data analysis results, different models have certain differences in the spatial simulation of extreme precipitation. It is speculated that the terrain factors and Monsoon Simulation factors may affect the simulation results of extreme precipitation events.

KEYWORDS

PAPER INDEX

1. INTRODUCTION

Most cities in my country are located on the banks of rivers, lakes and seas, and are threatened by river floods to varying degrees. In the context of global warming, with the acceleration of urbanization, urban torrential rain events frequently occur, extreme flooding events increase, and the resulting disaster losses are also increasing. However, at present, the capacity of urban flood control in my country is generally low, and urban drainage standards are backward. In the event of upstream floods and urban torrential rains, supported by the long-term high water level of external river floods, it is difficult to discharge or even limit the discharge of internal waterlogging, which can easily cause serious flood disasters to the city.

The increase of extreme weather caused by climate change has had an important impact on the ecological environment, economic development and personal and property safety of countries all over the world [1], especially in the Loess Plateau of China, where geological disasters are seriously developed, the use of climate models to study future climate change can effectively deal with the risk of geological disasters caused by climate change. Climate model is a set of mathematical and physical equations that describe the behavior of climate system based on basic physical and chemical laws [2]. The data involved in this program are widely used to predict the characteristics of future climate change and analyze the trend of climate change. The research results of climate prediction based on climate models are an important basis for the government's Special Committee on Climate Change (IPCC) to assess future climate change [3]. At the same time, Representative Concentration Pathways (RCPs) scenarios fully consider the impact of future greenhouse gas emissions on climate change. Among them, RCP 2.6 scenario refers to that the radiation forcing reaches the peak before 2100 and drops to 2.6w/m2 by 2100, and the global average temperature rise is limited to 2.0 °C [4-5]. It can well simulate the average characteristics of large-scale and seasonal climate, but the PCPs spatial resolution (100~500km) is difficult to directly respond to the model to assess the impact of climate change or site scale environmental factors [6]. Therefore, improving the reliability of climate prediction is one of the important issues in the study of Watershed climate models [7].

In order to effectively improve the reliability of climate prediction, this paper introduces the climate model into the analysis of extreme rainfall trends along the river basin. The correction value and the daily precipitation data of future climate change are calculated, and the analysis of the extreme rainfall trend along the river basin in the future is finally completed.

2. CASE STUDIES AND DATA SOURCES

2.1. REGIONAL OVERVIEW AND SITE

Yanhe River Basin is the first-class tributary of the middle reaches of the Yellow River, between 36 ° 23 ′~37 ° 17 ′ N and 108 ° 45 ′~110 ° 28 ′ E. Yanhe River Basin is

one of the serious soil and water loss areas in the Loess Hilly and gully region. It belongs to the warm temperate continental semi-arid climate zone [8-9]. The north is Qingjian River Basin, the southwest is Beiluo River Basin, and the south is connected with Yunyan River Basin [10]. The geographical location of the Yanhe River Basin is shown in Fig 1.
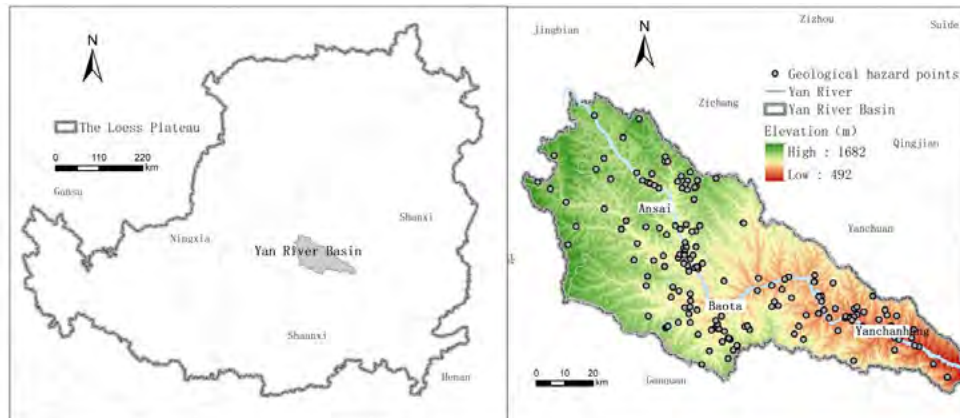
Figure.1. Geographical location of Yanhe River Basin

As shown in Figure 1,the main tributaries of Yanhe River include Xichuan, Xingzi River, Nanchuan and Panlong River, with a total length of 286.9 kilometers, an altitude of 958-1731m and an area of about 7725km2. The basin covers 6 counties and districts including Baota, Ansai and Yanchang, a total of 53 towns and townships, about 1027 administrative villages, with a total population of 990000 [11-12].

2.2. DATA SOURCES

Historical observational meteorological data of Yanhe River Basin is derived from the data of 154 surface meteorological stations covering Shaanxi Province from 1981 to 2013 and interpolated to 0.25 ° by thin disk spline × 0.25 ° horizontal resolution grid, generating multi-year daily precipitation data from China National Meteorological Information Center [13-14]. The global climate model is derived from the coupled multimodal global climate model prediction data set cmip5 in the nex-gddp project in the United States [15]. This data set is the main tool used by IPCC to predict future climate change by simulating earth systems such as atmosphere, ocean, land surface and vegetation, sea ice, etc [16]. Some studies show that cmip5 model has greatly improved the spatial resolution compared with the previous model, and significantly improved the simulation effect of extreme precipitation. Three GCMS in cmip5 are selected to predict future extreme precipitation changes, including the climate system model BCC of Beijing Climate Center_ CCSM, the multidisciplinary climate research model miroc5 jointly developed by the climate system research center of the University of Tokyo, Japan, the Japan Institute of environment and the Japan earth environment research center. It summarizes the earth system, spatial resolution and other parameters of the three climate model data. The model has been used to predict climate change and related extreme events in the Yangtze River Basin, and the model simulation results are good and close to the observed data [17-18]. Spatial resolution of mode data 0.25 ° × 0.25 °, the time resolution is day by day, and the time span is

1981-2060. The typical concentration emission scenario rcp4.5, that is, the emission scenario is set to maintain the current level of population, economic and technological development. By 2100, the radiation forcing will be stable at 4.5w/m2, and the change of greenhouse gas emissions will increase first and then tend to be stable [19].

3.   METHODOLOGY

3.1. ANUSPLIN METEOROLOGICAL INTERPOLATION

Meteorological element data is the basis of a variety of geoscience models and climatology models. Accurate climate element data can be obtained by establishing high-density meteorological observation sites. However, due to the limitations of economic level, technical means and terrain conditions, meteorological data in many places It is more difficult to obtain. In order to obtain meteorological data in areas outside meteorological observation sites, researchers usually combine statistical methods with geographic information systems to estimate based on the observed values of existing meteorological observation sites, that is, spatial interpolation of meteorological element data.

ANUSPLIN software is a classic meteorological interpolation software, based on thin disk spline function, suitable for interpolation of various natural station data. The accuracy is high, and the elevation can be considered as a covariate for difference [20-21]. The model formula is as follows:

$$z_i = f(x_i) + b^T y_i + e_i \quad (i = 1, \cdots, N) \qquad (3. \text{ AUTONUM } \backslash* \text{ Arabic })$$

Where, Z is the dependent variable at point I, f (XI) is the unknown smooth function to be estimated about Xi, Xi is the d-dimensional independent variable, BT is the p-dimensional coefficient about Yi, Yi is the p-dimensional independent covariate, EI is the random error, and N is the number of observations [22].

Where: function f and coefficient b are determined by least square estimation:

$$\sum_{i=1}^{N} \left[\frac{z_i - f(x_i) - b^T y_i}{w_i} \right]^2 + \rho J_m(f) \qquad (3. \text{ AUTONUM } \backslash* \text{ Arabic })$$

Where JM (f) is the roughness measure function of function f (x), which is defined as the m-order partial derivative of function f; ρ is a positive smoothing parameter.

3.2. STATISTICAL DOWNSCALING METHOD

The regional climate model is the result of the comprehensive action of the driving forces of the multi-scale general circulation model, such as latitude, sea land distribution, terrain and underlying surface conditions [23]. The assumptions for using statistical downscaling include: the climate state at different scales is stable and the statistical relationship is significant, and the large-scale climate model simulation is effective and the statistical relationship established is effective. Considering the

complex terrain of the study area, in order to reduce the boundary impact, the north of Hengduan Mountain where the study area is located is taken as the prediction area.

Statistical downscaling adopts a numerical deviation correction method combining statistics and dynamics [24]. The method considers that the climate model of any scale is composed of stable long-term climate state and short-term weather fluctuation. The specific expression is as follows:

$$\alpha(t) = \bar{\alpha} + \alpha'(t) \qquad \left(3.\ \text{AUTONUM } \backslash^* \text{ Arabic } \right)$$

Where, $\alpha(t)$ represents the meteorological condition at any time, α represents the climate state corresponding to the scale where the meteorological condition is located, $\alpha'(t)$ represents the climate anomaly of the scale relative to the secondary scale, and $\bar{\alpha}$ indicates the average climate state [25]. The observation data and climate reanalysis data are divided in this way. For climate models with different spatial scales (such as global and regional), the expression of the linear correction value of the climate anomaly model of the cumulative distribution function is:

$$\frac{\partial \alpha_{LC}}{\partial c} - \frac{\partial \alpha_{\bar{R}A}}{\partial c} = \frac{\partial \alpha'_{GCM}}{\partial c} = k\left(\beta_{RA}^- + \beta'_{GCM} \right) = k\beta_{LC} \qquad \left(3.\ \text{AUTONUM } \backslash^* \text{ Arabic } \right)$$

Where, K is a constant, ∂ is the horizontal and vertical correlation distance, β_{RA}^- is the climate state corresponding to the ground observation data at this spatial scale, and β'_{GCM} is the climate anomaly of the spatial scale corresponding to the global climate model relative to the spatial scale corresponding to the ground observation data. The equation is also applicable to global and regional climate models [26-27]. The equation is valid only when n>1 and $\bar{\alpha}^n = \bar{\alpha}^n$. Therefore, the deviation correction expression of daily precipitation data of future climate change is as follows:

$$Pr_d = \bar{M}_{st_d} + \bar{M}_{prj_d} - M_{st_d} \qquad \left(3.\ \text{AUTONUM } \backslash^* \text{ Arabic } \right)$$

In the formula, Pr_d represents the daily precipitation value after correction, D is 1-365, $\bar{M}_{st\_d}$ and M_{prj_d} are the average value of historical daily climate data and climate change precipitation estimates. M_{st_d} represents the estimated precipitation of climate change [28]. The prediction of extreme rainfall trends along the river basin is realized by the revised daily precipitation value, the average value of historical daily climate data, the average value of climate change precipitation estimates, and the estimated precipitation amount of climate change.

4. 4 RESULT ANALYSIS

4.1. ANALYSIS ON OVERALL CHANGE TREND OF PRECIPITATION

Under the rcp4.5 emission scenario, during the 50 years from 2006 to 2056, the regional average precipitation of extreme precipitation in the study area is shown in Fig 2.
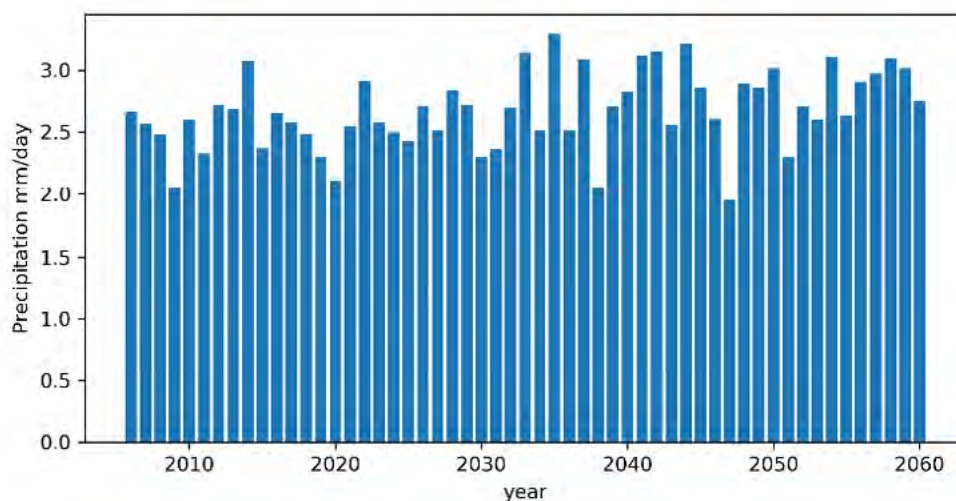
(a) Regional average precipitation.
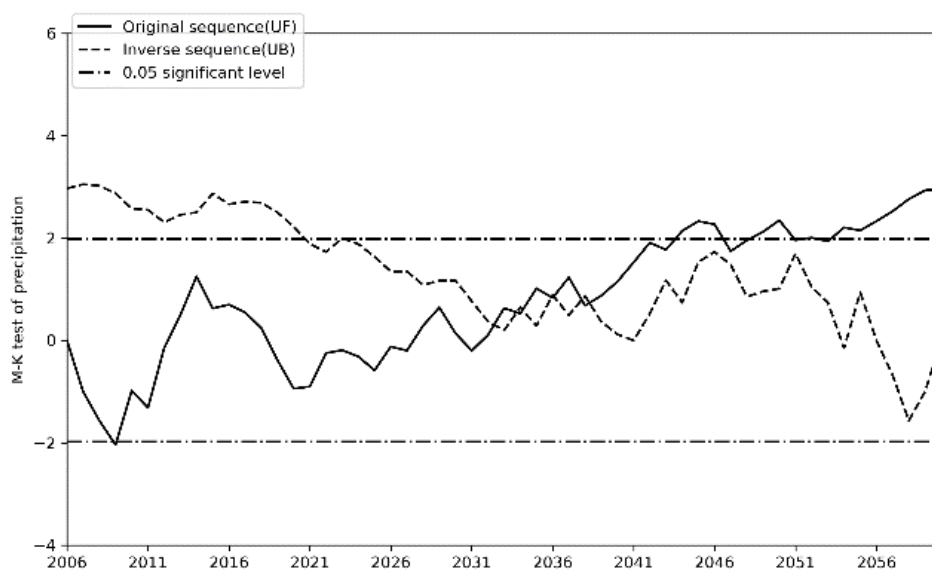
(b) Precipitation Mann-Kendall test.
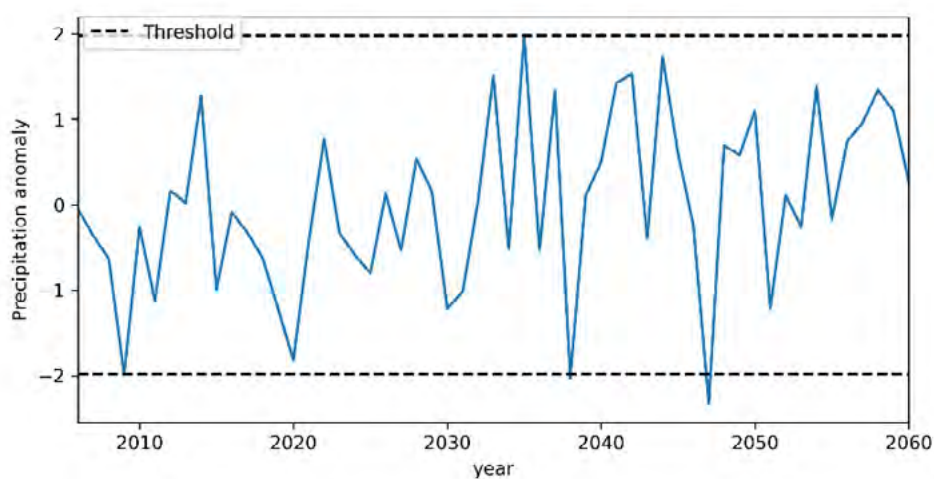
(c) Precipitation anomaly.

Figure 2. Inter-annual departure of extreme precipitation in study area.

Fig 2(a) shows that the annual average daily precipitation in the study area fluctuates around 2.5 mm, with no obvious increase or decrease. Based on the Mann Kendall method, this paper conducted a test and analysis of the precipitation in the study area from 2000 to 2050, and found that the precipitation in the study area fluctuated greatly in the past 50 years. In Fig 2(b), the interannual fluctuations are relatively large around 2036, and the main mutation year in this region is around 2016. During the 50 years from 2000 to 2050, there were more abrupt changes, indicating the possibility of extreme climate events. In addition to the Mann Kendall rainfall test, precipitation anomalies are also analyzed in Fig2(c). The results show that the precipitation anomaly analysis results show a similar trend to the Mann Kendall test results, which more strongly indicate that under the background of future climate change, the rainfall in the study area will change greatly, and extreme precipitation events are more likely to occur [29].

4.2. SPATIAL AND TEMPORAL PATTERN AND ANALYSIS OF EXTREME PRECIPITATION INDEX

In this paper, absolute quantity index, intensity index and frequency index are selected to analyze the spatial and temporal distribution characteristics of extreme precipitation. The results show that there are significant differences in the frequency and distribution pattern of extreme precipitation in the study area. The absolute quantity index analysis results show that in the next 50 years, the precipitation in most parts of the study area may exceed 12mm, especially in the eastern and western parts of the study area. The spatial distribution of absolute indicators is shown in Fig 3.
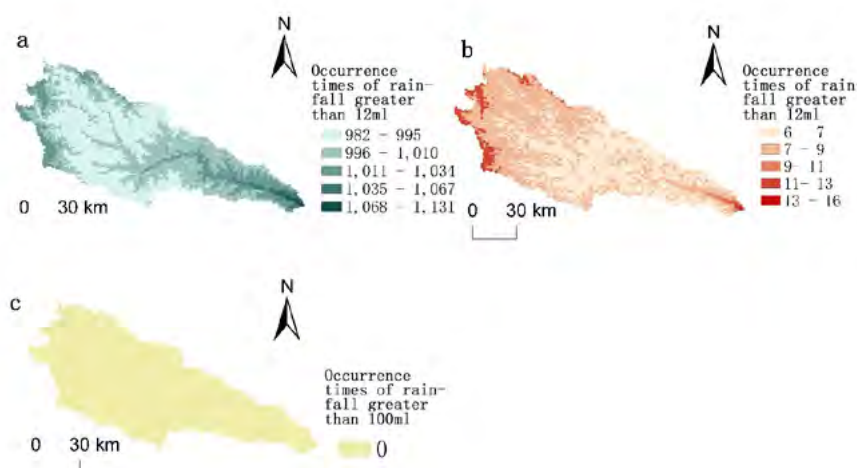
Figure 3. Spatial distribution of otherthe absolute indices: (a) Daily precipitation over 12 (mm); (b) Daily precipitation over 50 (mm); (c) Daily precipitation over 100 (mm).

In a of Fig 3, the number of days with precipitation exceeding 12 mm in some areas may exceed 1000 days, that is, more than 20 times a year. In the future, the areas with the most precipitation above 12 mm will be concentrated in the southeast of the

study area, followed by the western border area. These areas will receive more than 21 times of precipitation above 12mm per year. The central region has the least precipitation, at least 19 times a year. Compared with the areas with precipitation greater than 12mm, there are fewer areas with precipitation greater than 50mm in b of Fig 3, and the frequency of occurrence is significantly lower. The high-value areas are distributed in the southeast border area and the northwest border area. Fig 3 c. For precipitation above 100mm, the study area will not appear. From the temporal and spatial distribution pattern of absolute precipitation index, it can be seen that the erosive precipitation in the study area is widely distributed, and the distribution of heavy rain precipitation is obviously localized, mainly in the junction of the northeast and southwest of the study area [30].

For the case where the daily precipitation of c in Fig 3 exceeds 100mm, the spatial distribution of the intensity index is analyzed, as shown in Fig 4.
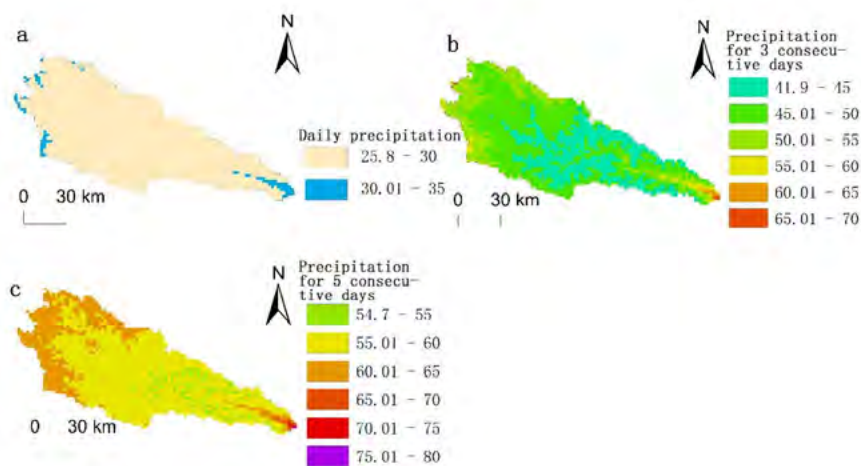
Figure 4. Spatial distribution of the intensity indices: (a) Daily precipitation; (b) Cumulative precipitation in 3 days; (c) Cumulative precipitation in 5 days.

Fig 4 shows that the analysis results of the intensity index show that single precipitation or continuous precipitation of more than 50 mm may occur in most areas, and more precautions should be taken against the risk of extreme rainstorms. In Fig 4a, it can be seen that the areas with daily precipitation rx1 higher than 30mm are only distributed in the southeast and northwest border areas of the study area[31-32]. The terrain in the southeast is lower. The daily precipitation in most areas of the study area is between 25 and 30 mm;

From (b) and (c) in Fig 4, we can see from the spatial distribution of RX3 and rx5 that the areas with precipitation exceeding 55mm for three consecutive days are mainly distributed in the southeast and northwest of the study area with precipitation exceeding 55mm for five consecutive days of the entire study area. In terms of precipitation, the accumulated precipitation in most parts of the study area may exceed 55mm, while the precipitation in the northwest and southeast of the study area may exceed 70mm.

The comparative analysis of the intensity indicators of different indicators shows that under the background of future climate change, extreme short-term sustained

high-intensity precipitation is very likely to occur in most areas of the study area, and the risk of mountain disasters cannot be reduced.

In order to reduce the uncertainty of climate change prediction and the possible model error of predicting a single precipitation, the frequency of extreme precipitation in the study area was analyzed for multiple consecutive days.
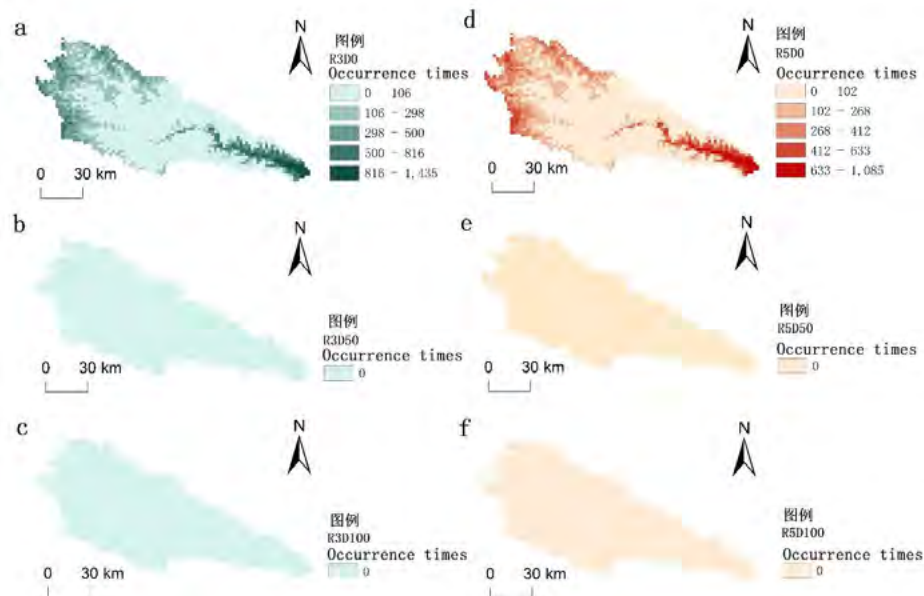
Figure 5. Spatial distribution of the duration indices: (a) The number of over 50 (mm) cumulative precipitation in 3 days; (b) The number of over 100 (mm) cumulative precipitation in 3 days; (c) The number of over 50 (mm) cumulative precipitation in 5 days; (d) The number of over 100 (mm) cumulative precipitation in 5 days.

From (a) and (b) in Fig 5, we can see that precipitation events may occur continuously for 3 days and 5 days in the study area, and the frequency of occurrence is higher in the southeast and northwest of the study area, and the prediction results of the spatial distribution of the intensity index. In addition, it can be seen from c in Fig 5 that due to being in a semi-arid area, the study area did not have extreme precipitation events with precipitation exceeding 50 mm and 100 mm for three consecutive days and five consecutive days, respectively.

4.3. COMPARISON OF DIFFERENT GCM MODELS OF EXTREME PRECIPITATION

Prediction of extreme precipitation events from a single climate model is uncertain. Therefore, this paper selects several representative extreme precipitation indicators for model comparison to reduce the uncertainty of a single climate model. The distribution of extreme precipitation under future climate change is shown in Fig 6.
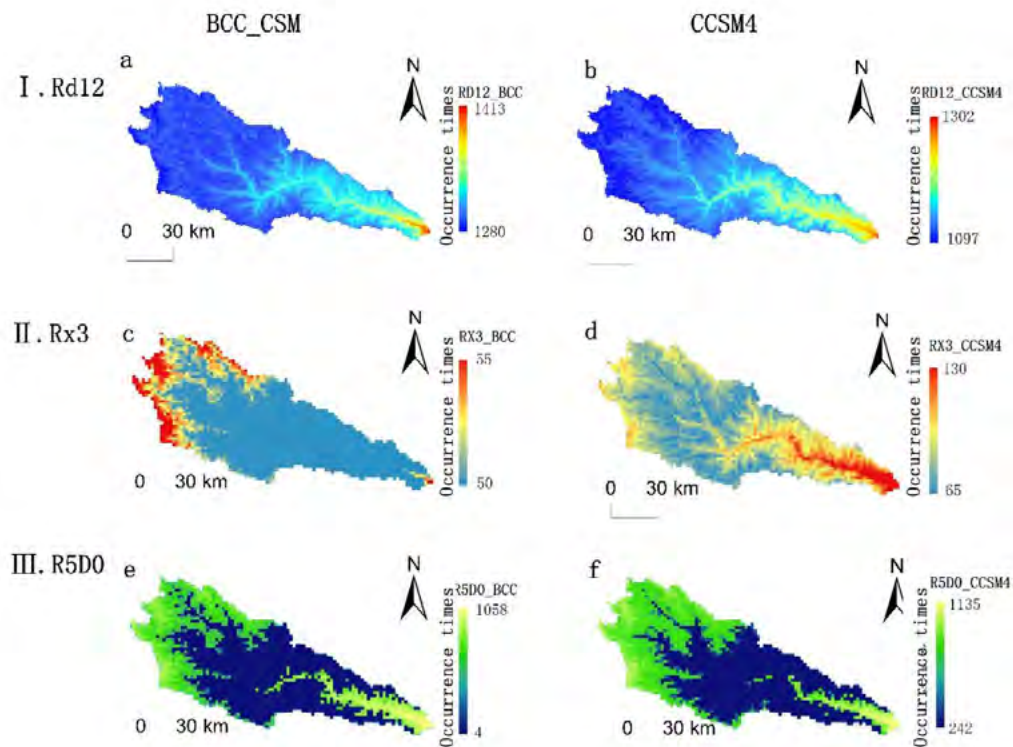
Figure 6. The distributions of extreme precipitation under climate change in the future

According to the data analysis results in Fig 6, there are certain differences in different spatial simulations of extreme precipitation. It is speculated that topographic factors and monsoon simulation factors may affect the simulation results of extreme precipitation events. According to the analysis of extreme precipitation index under different models, as shown in a and b in Fig. 6, the simulation results of absolute quantity index are not very different, while in the BCC_CS model and the miroc5 model, the two models are generally spatially consistent. The number of annual occurrences of absolute precipitation exceeding 12mm is higher than 21. In the BCC_CS mode, the annual occurrence of absolute precipitation exceeding 12mm can reach 28 times. The areas with more occurrences are mainly located in the southeastern part of the study, and the annual occurrence of absolute precipitation exceeding 12 mm in the western part of the study area is less frequent; as shown in c and d in Fig. 6, the precipitation is predicted and evaluated for three consecutive days under the BCC_CS model and the miroc5 model. . There is a certain difference in the amount of precipitation for three consecutive days under these two modes. The maximum precipitation for three consecutive days in the miroc5 mode can reach 130 mm, which is located in the southeastern part of the study area; the frequencies of precipitation events in the BCC_CS mode and the miroc5 mode for 5 consecutive days are shown in e and f in Fig 6. From the results, the precipitation frequency index shows that the average frequency of precipitation events for 5 consecutive days in the study area can reach 22 per year. The simulation results of these two modes also have certain continuity and spatial consistency.

5. DISCUSSION

(1) The climate model with statistical downscaling can effectively reduce the model uncertainty. The terrain of the study area is complex, so it is more practical to select rcp4.5 to maintain the current greenhouse gas emission scenario. First, the simulation effect of different models of IPCC cmip5 on Precipitation in China decreases from the southeast coast to the northwest inland (Sun Jian, 2016). In terms of the simulation effect of average daily precipitation, the simulation effect may be better in some areas, but the overall simulation ability is weak. Therefore, based on the rcp4.5 emission scenario with high stability, statistical downscaling using the meteorological data of regional ground stations can eliminate the uncertainty of the climate model to a certain extent. In small areas with complex terrain, statistical downscaling technology is better than dynamic downscaling in rainfall prediction, because in small areas with complex terrain, extreme precipitation is not only affected by large-scale circulation factors such as monsoon and terrain, but also affected by small-scale climate and weather systems such as surface radiation and cloud, and is easily disturbed by human activities. The numerical deviation correction method combining statistics and dynamics can simulate single day precipitation to a certain extent and improve the accuracy of GCM data, but its long-term trend and extreme precipitation simulation effect need to be further tested in combination with ground data.

(2) The above results show that the frequency and distribution pattern of extreme precipitation in the Yanhe River Basin will be significantly different in the future. In terms of absolute quantity index, most areas in the study area may have more than 12mm of precipitation, and the number of 12mm of daily precipitation in some areas may exceed 20 times a year, mainly concentrated in the southeast, followed by the western region, and less in the central region. The results of intensity index show that most areas in the study area may have single precipitation or continuous precipitation with a daily precipitation of more than 50mm. Areas with a daily precipitation of more than 55mm for three consecutive days are mainly distributed in the southeast and northwest of the study area. Areas with a daily precipitation of more than 55mm for five consecutive days basically cover the whole study area. Precipitation events are likely to occur in the study area for 3 and 5 consecutive days, with more occurrences in the southeast and northwest regions, which is consistent with the predicted results of the spatial distribution of the intensity index. The comparison and analysis of different indexes show that the spatial and temporal distribution of extreme precipitation in the study area is closely related to the terrain, which may be the result of the joint action of regional terrain and climate change.

(3) Rainstorm and continuous precipitation are the main factors inducing geological disasters, and the disaster risk in the study area may be intensified in the future.Geological disasters in mountainous areas are the result of the joint action of extreme weather and disaster pregnant environment. The above analysis shows that under the background of future climate change, the intensity of extreme precipitation in most regions in the study area will increase, the number of precipitation days will increase, and the continuous precipitation for 3 or 5 consecutive days may be large, and the cumulative precipitation can reach 80 mm. The occurrence of continuous

precipitation may not only reduce the threshold of extreme precipitation, but also accelerate the development of disaster pregnant environment such as geological disasters. From the perspective of terrain, steep terrain areas are often prone to geological disasters. Especially in the southeast region where there may be multiple high-intensity extreme precipitation, it is necessary to formulate targeted geological disaster response strategies to adapt to climate change.

6. CONCLUSION

1. Yanhe River Basin is a sensitive area to climate change. In the future, the precipitation in this area will not increase significantly for a long time, but it will fluctuate greatly.

2. From 2000 to 2050, the interdecadal fluctuation of extreme precipitation events in the study area is significant. In the future, the area with the most precipitation above 12 mm will be concentrated in the southeast of the study area, followed by the western boundary area. Compared with the area with precipitation above 12 mm, the area with precipitation above 50 mm will be less, and the occurrence frequency will decrease significantly. According to the results of intensity index, single precipitation or continuous precipitation of more than 50mm may occur in most areas.

3. Different climate models have different simulation effects. According to the data analysis results, different models have certain differences in the spatial simulation of extreme precipitation. It is speculated that the terrain factors and Monsoon Simulation factors may affect the simulation results of extreme precipitation events. When simulating absolute index and continuous precipitation index, BCC_ CSM simulation results are on the high side; When simulating the intensity index for three consecutive days, the simulation result of ccsm4 is higher and is similar to that of BCC_ CSM simulation results have significant differences.

7. DATA AVAILABILITY STATEMENT

The original contributions presented in the study are included in the article/ supplementary material, further in quiries can be directed to the corresponding author.

REFERENCES

(1)   Compilation Committee of the second national assessment report on climate change. (2011). **The second national assessment report on climate change [m]**. *Beijing: Science Press.*

(2)   Zeng Qingcun, zhangxuehong. (1989). **The concept, methods and current situation of climate models [j]**. *Advances in Geoscience*, 4 (3), 1-26.

(3)   Cheng aifang, Feng Qi, Zhang Jiankai. (2015). **Review of research on the response process of climate change under future climate scenarios [j]**. *Geographic science*, 35(1), 84-90.

(4) Moss RH, Edmonds JA, hibbard KA. (2010). **The next generation of Scenarios for climate change research and assessment[J]**. *Nature*, 463(7282), 747.

(5) Flato G. (2017). **Evaluation of climate modes [g] climate change 2013.the physical science basis**. *Working group1 contribution to the fifth asassessment report of the intergovernmental panel on climate change.*

(6) R ISBEY J S, STONE P H. (1996). **A case study of the adequacy of GCM simulations for input to regional climate change assessments[J].** *Journal of Climate*, 9(7), 1441-1467.

(7) LIU Y H, GUO W D, FENG J M. (2011). **A summary of methods for statistical down scaling of meteorological data[J]** *Advances in Earth Science*, 26(8), 837-847.

(8) Zhu Qing, Zhou Zixiang, Liu Ting, Bai Jizhou. (2021). **Study on Some Random Place Somewhere vegetation restoration and ecosystem soil conservation service value gain: a case study of Yanhe Basin[J]**. *Journal of Ecology*, 41(07), 2557-2570.

(9) Wang Shuxia, Zhang Liping, Li Yi, she dunxian. (2019). **Extreme flood events in the Lancang River Basin under Climate Change Scenarios[J]**. *Progress in climate change research*, 15(01), 23-32.

(10) SCHMIDLI J, F R EI C, VIDALE P L. (2006). **Downscaling from GCM precipitation: a benchmark for dynamical and statistical downscaling methods[J]**. *International Journal of Climatology,* 26(5), 679-689

(11) NGAI S T, TANGANG F, JUNENG L. (2017). **Bias correction of global and regional simulated daily precipitation and surface mean temperature over Southeast Asia using quantile mapping method** ［J］. *Global and Planetary Change,* 149, 79-90.

(12) Sarita, Gajbhiye, Chandrashekhar. (2016). **Trend analysis of rainfall time series for Sindh river basin in India[J]**. *Theoretical & Applied Climatology.*

(13) Pawar P S, Rawat U, Yadav A, (2020). **Long Term Trend Analysis of Rainfall, Rainy Days and Drought for Sindh River Basin, Madhya Pradesh, India[J].** *International Journal of Current Microbiology and Applied Sciences,* 9(12), 2738-2749.

(14) Bera S. (2017). **Trend Analysis of Rainfall in Ganga Basin, India during 1901-2000[J].** *American Journal of Climate Change*, 116-131.

(15) [15]Kebede, Asfaw, Zeleke. 2017. **Analysis of rainfall trend and variability for agricultural water management in Awash River Basin, Ethiopia[J]**. *Journal of water and climate change*, 8(1), 127-141.

(16) Jiao P, Wei W, Bao H. (2020). **V**ariation and Trend Analysis of Rainfall in **Qingshui River Basin of Ningxia in China[J]**. *IOP Conference Series Earth and Environmental Science*, 526, 012040.

(17) Shah S A, Kiran M. (2021). **Mann-Kendall Test: Trend Analysis Of Temperature, Rainfall And Discharge Of Ghotki Feeder Canal In District Ghotki, Sindh, Pakistan[J]**. *Environment & Ecosystem Science (EES)*, 5.

(18) Gao S, Wang H W, Sang X L. (2019). **Analyzing the Correlation of Time Series of Rainfall-runoff in Yuanjiang-Red River Basin[J]**. *Systems Engineering.*

(19) Doumouya F, Traore V, Sadio M. (2019). **Rainfall Variability in Sine Saloum River Basin in a Context of Climate Change and Variability[J]**. *Advances in Research*, 6(6), 1-12.

(20) Sinam R. (2019). **RAINFALL TREND ANALYSIS OF BAITARANI RIVER SUB-BASIN, ODISHA.[J]**. *International Journal of Advanced Research,* 7(10), 569-575.

(21) Shimola K, Krishnaveni M. (2018). **Statistical analysis of trend and change point in climate series for a semi-arid basin, Tamil Nadu, India[J]**. *Disaster Advances*, 11(10), 8-15.

(22) Bekele D, Alamirew T, Kebede A. (2018). **Analysis of rainfall trend and variability for agricultural water management in Awash River Basin, Ethiopia[J]**. *Journal of Water & Climate Change*, 8(1), 127-141.

(23) Noreen D N., Khan F., Dil S. (2020). **Trend Analysis of exponential increase of Covid-19 cases in Pakistan (Preprint).**

(24) Kiros G, Shetty A, Nandagiri L. (2017). **Trend Analysis of Temperature Time Series in Geba River Basin, Northern Ethiopia[C].** *HYDRO 2015 INTERNATIONAL 20th International Conference on Hydraulics, Water Resources and River Engineering, IIT Roorkee, India*, December 17-19.

(25) Singh G. (2018). **Analysis of Trend and Variability of Rainfall in the Mid-Mahanadi River Basin of Eastern India.**

(26) Kumar S, Santosh. (2019). **Non-Parametric and Parametric Analysis of Runoff in Satluj River Basin, Himachal Pradesh, India[J]**. *SciPress Ltd*.

(27) She D, Xia J, Zhang Y. (2018). **The trend analysis and statistical distribution of extreme rainfall events in the Huaihe river basin in the past 50 years[J]**. *Acta Geographica Sinica*.

(28) Thakural L N. (2018). **Trend Analysis of Rainfall for the Chaliyar Basin, South India.**

(29) Fernando S, AX Júnior, Stosic T. (2018). **A Brief multifractal analysis of rainfall dynamics in Piracicaba, So Paulo, Brazil[J]**. *Acta Scientiarum Technology*, 40(1).

(30) Tao D U, Xiong L H, Jiang C. (2018). **Nonstationary frequency analysis of rainfall time series in Weihe River Basin[J]**. *Arid Land Geography.*

(31) Singh, A. K., and Sora, M. (2021). **An optimized deep neural network-based financial statement fraud detection in text mining**. *3C Empresa. Investigación y pensamiento crítico*, 10(4), 77-105. https://doi.org/10.17993/3cemp.2021.100448.77-105

(32) Liu Yanwu. (2021). **Analysis and Prediction of College Students' Mental Health Based on K-means Clustering Algorithm**. *Applied Mathematics and Nonlinear Sciences, 7*(1), 501-512. https://doi.org/10.2478/AMNS.2021.1.00099.

CONFLICT OF INTEREST

The authors declare that the research was conducted in the absence of any commercial or financial relationships that could be construed as a potential conflict of interest.

3C Tecnología. Glosas de innovación aplicadas a la pyme. ISSN: 2254-4143

Ed.43 | Iss.12 | N.1 January - March 2023

/02/

3C Tecnología. Glosas de innovación aplicadas a la pyme. ISSN: 2254-4143

Ed.43 | Iss.12 | N.1 January - March 2023

32

APPLYING THE STRENGTH REDUCTION METHOD TO STUDY OF STABILITY OF RESIDUAL MOUNTAINS: A PARTICULAR APPLICATION

Xin Jin*

College of Art and Design, Shaanxi University of Science and Technology, Xi'an, Shaanxi, 710021, China

wyjinxin@sust.edu.cn

Yucheng Hua

College of Art and Design, Shaanxi University of Science and Technology, Xi'an, Shaanxi, 710021, China

Qiao Tang

College of Art and Design, Shaanxi University of Science and Technology, Xi'an, Shaanxi, 710021, China

https://doi.org/10.17993/3ctecno.2023.v12n1e43.33-52

ABSTRACT

Due to huge disaster-caused force, seismic geological disasters primarily induce residual landslide, collapse and debris flow disasters with far higher hazard extent than that of earthquake disasters. Wherefore, this paper, with various vibration slopes caused by the most representative Wenchuan earthquake as research objects, introduces the strength reduction method to the stability study of residual mountains in a certain area, puts forward dynamic stability slope evaluation method based on dynamic and overall strength reduction method to obtain the mountain slope stability situation in the process of gradual instability, searches out the sliding surface of progressive expansion making use of dynamic strength reduction method and calculates dynamic safety index in the process of gradual slope instability pursuant to the calculation advantages of dynamic strength reduction method, so as to realize the analysis and regulation of the whole process of slope instability. The results show that in the stability analysis of a homogeneous slope, the safety index of slope stability calculated by strength reduction method is 6.7%, 8.8% and 10.5% higher than that calculated by finite element limit equilibrium method, Bishop method and Janbu method respectively. In the stability analysis of a multi-layer soil slope, the safety index of slope stability calculated by strength reduction method is 4.8%, 4.3% and 9.4% higher than that calculated by other three algorithms. While in the stability analysis of soft interlining slope, the safety indexes of slope stability calculated by the method proposed in this paper are increased by 26.10%, 29.11% and 26.46% respectively compared with other three algorithms, indicating that the stability of landslide residual mountains calculated by strength reduction method proposed in this paper is the highest.

KEYWORDS

Strength reduction method; Landslide residual mountain; Stability study; Safety index; Sliding surface

PAPER INDEX

1.   INTRODUCTION

In mountainous and hilly areas, landslides are more common, and similar to earthquakes, mudslides and other disasters, generally have relatively large hazard extent. In the vast land area of China, the geographical conditions are relatively complex, and the landslide areas are widely distributed, especially in the mountainous areas of southwest, northwest, and east China [1-2]. When a landslide occurs, partial or whole pieces of land will appear one after another in a relatively slow speed and a relatively long cycle, and will intermittently slide. [3-4].

Landslides are extremely harmful, especially that large-scale landslides can destroy entire villages, cut off rivers, destroy farmland and forests, and even damage the safety of life and property of people and countries to a large extent, seriously hindering and destroying the construction process of countries [5]. Landslides in China have the characteristics of various types, large scale, wide distribution, strong concealment and strong destructiveness, and most landslides are sudden and unpredictable, which brings serious harms to the society [6].

In this regard, it is of great significance to implement monitoring and early warning of landslides. Landslide movement is highly complex and is affected by many factors. At present, it is difficult to thoroughly understand the internal characteristics of each landslide, and to accurately predict each landslide [7-9]. However, landslide monitoring helps to master and analyze the evolution and characteristics of landslide mass. With the continuous progress of landslide monitoring technology, in order to obtain more detailed landslide data, a more in-depth understanding of landslides can be obtained [10-12].

In recent years, many foreign researchers have carried out research on rock mechanics algorithms. For example, the literature [13] introduced the concept of damage mechanics in the metal creep fracture research and rock mechanics research for the first time. The literature [14] used the concept of fracture surface to theoretically discuss the continuous damage behavior of rock and concrete. Since then, people have established various damage theories based on different damage mechanisms and basic theories, and applied them to the study of nonlinear, plastic, and viscoplastic damage of rock materials. The literature [15] first applied the damage theory to establish damage mechanics model of rock-concrete continuum. The literature [16] established corresponding models and theories based on the structural characteristics of the rock itself. The literature [17] proposed the famous "strain equivalence hypothesis", which laid the foundation for the study of damage theory. The literature [18] proposed a new elastic-plastic damage model based on irreversible thermodynamics and damage mechanics, which comprehensively considered plastic friction deformation and plastic pore deformation, and adopted damage variables to describe the development of microscopic defects. The literature[19] defined a damage variable as the second-order tensor of fracture density, took into account the damage evolution of this damage variable pursuant to fracture propagation, and thereby established a corresponding damage model. Based on the homogenization theory, whereafter, a thermodynamic framework for the meso-mechanical damage model was built. Zhu Qizhi et al. reckoned that the rock was a heterogeneous material composed

of an elastic solid matrix and fractures, and proposed a corresponding meso-mechanical damage model. The literature [20], on the basis of considering the dynamic propagation of micro-fractures, proposed a corresponding meso-mechanical model of rock damages, believing that the stress-strain curve, failure strength and damage development rate of rocks were closely related to the friction index, initial fracture length and loading rate. The literature [21] came up with a micro-fracture damage model of brittle rock under uniaxial compression load as well as theories of micro-fracture fracture mechanics and rock damage mechanics based on the assumption of random distribution of micro-fractures. To be concrete, the mechanical properties under the load were analyzed, that is, when the external load reached a certain level, the micro-fractures began to expand,, the mechanical properties of the rock changed, and until the macro-fracture of the rock occurred, the fracture growth rate increased with the external load.

With the in-depth research aiming at foreign researchers, domestic scholars have also carried out research on the stability of rock and soil slopes. For instance, based on the principle of object balance, the literature [22] proposed a finite sliding displacement evaluation method of slope stability according to slope potential deformation, in which the force exceeding the yield resistance of the sliding body is used as the calculation standard for the occurrence of the slope and landslide. The literature [23] used the FLAC valuation method of slope stability according to slope potential deformation, and carried out the research of seismic slope failure mechanism combined with the seismic slope numerical simulation software with both tensile and shear failure functions. Through analysis, it was concluded that the failure of the seismic slope was composed of the upper tensile failure and the lower shear failure of the potential rupture zone, and the method for determining the location of the rupture surface of the earthquake slope was given through various means. The literature [24] performed a large number of on-site investigations. Precisely, on the basis of aforementioned above, the special instability phenomena such as vibration collapse and high-speed ejection of the slope under the strong earthquake load were studied, and the genesis mechanism of earthquake-triggered collapse and landslide was classified according to the specific slope structure. Moreover, a calculation program for the safety index of a landslide numerical simulation software with both tensile was proposed to study the stability of slopes under the condition of known sliding surfaces, and a comparative discussion between the traditional seismic slopes was carried out via FLAC 3D displacement evaluation method. From a mesoscopic approach, the literature [26] studied the instability mode of slopes via a strength reduction calculation module in the RFPA software. The literature [27] discussed the strength reduction method and proposed a more reasonable reduction calculation method, which promoted actual use numerical simulation software with both tensile. With the deepening of research, there are more and more improved algorithms for strength reduction. However, numerous studies have found that in order to study the stability of residual mountains, it urgently requires to take into account the shear-tensile composite yield criterion of mountains, as well as single static safety index, principal stress and cohesion of mountain slopes. For this, numerical simulation software with both tensile did calculate damaged area of the mountain slope [28-30],

but did not consider the soil layer of the mountain slope. Not all the soil layers of the mountains are homogeneous, and some soil layers are multi-layer soil or contain weak inter-layers, so it is very necessary to study the stability of the residual mountain according to the conditions of different soil layers.

Pursuant to the fact that the general algorithm does not take into account the pull fracture and further study landslide residual mountains, in this paper, the shape change and structural damage characteristics of the residual slopes on the rear wall of the landslide is analyzed, and the sliding surface searching of progressive expansion is implemented making use of dynamic strength reduction method. At the same time, the residual slope of the rear wall of a landslide in a certain area is also a typical representative and epitome of the many shaking slopes of the "5.12" Wenchuan earthquake. It can be predicted that in the next 3 to 5 years, it will be a period of high incidence of collapse, landslides and debris flows in earthquake-stricken areas. The research ideas, methods and understanding of its post-earthquake stability will also provide guidance and reference for the evaluation of similar slopes in earthquake-stricken areas.

2. FAILURE CHARACTERISTICS OF MOUNTAIN SLOPES AND IMPROVEMENT OF STRENGTH REDUCTION METHOD

2.1. DEFORMATION AND FAILURE CHARACTERISTICS OF RESIDUAL SLOPE AFTER LANDSLIDE

According to the interpretation of low-altitude aerial photography near the residual mountain on the rear wall of a landslide in a certain area by helicopter, and combined with on-site geological mapping, it shows that after the "5.12" earthquake, there are mainly three groups of fractures on the surface of the entire back-edge mountains[31]. And the distribution of residual mountains and fractures on the rear wall of the landslide is primarily: (1) N40°～50°E and N70°E～EW direction, this group of fractures is mainly consistent with the boundary of the rear wall of a landslide in a certain area, with an extension length of about 20～200m and; (2) N10°W ~ near SN direction ~ N10°E, this group of fractures is the same as the main direction of the Dashuigou and Xiaoshuigou valleys, with an extension length of about 50 ~ 400m, and showing that unloading and tension are towards the free surface of the big and small ditches, but the scale of the side of the small ditch is obviously small; (3) N70°W direction, this group of fractures are distributed on the ridge line of the highest watershed and are consistent with the trend of the ridge line, with an extension length of about about 1000m and belonging to the earthquake-vibration fractures on the steep slope of the ridge [32].

The above-mentioned fractures are all extensional, with an opening width of 10-50 cm. Since the penetration depth of each fracture cannot be measured, according to the earthquake in the core area (such as Dujiangyan, Yingxiu, Wolong, Beichuan,

Qingchuan, etc.), the characteristics of the slope seismic effect (that is, the slope slump effect caused by the earthquake on the thin ridge with a slope gradient of obviously more than 50° and without deep tensile fracture) are adopted to predict the distribution of the residual mountain mass on the rear wall of the landslide in a certain area. The depth of the pull fracture is generally between 10 and 50m. Except for the N40°-50° E group fractures near the front edge of the mountain, which has penetrated into the weakly weathered rock body, the rest of the fractures near the ridge line are expected to be a deep location within the strongly weathered rock body. [33].

Judging from the distribution of the above-mentioned three groups of fractures with different extension directions and scales, the shallow surface layer of the entire residual mountain has basically been disturbed as a whole. Instead, collapse, slide and pull fractures also occur in the direction of large and small ditches, but the former has more advantages. Although the superficial integrity of the residual mountain has been basically completely destroyed, the integrity of the underlying weakly weathered rock mass has remained basically intact.

2.2. ACTUAL FAILURE PROCESS OF MOUNTAIN SLOPE

The slope instability is a gradual process that evolves from part to the whole, rather than an instant process. Because of existence of weak surface, the mechanical index of mountain slope decreases due to rainfall, the load dustribution is unbalanced and local stress concentration occurs, thereby resulting in some elements are damaged first [34]. Slowly, the principal stress will continue to extend and adjust its own concentration after the internal components is damaged, regrouping into a stress region. At this time, the damage area of the mountain structure increases and converges, and finally becomes a complete mass through sliding surface. Figure 1 shows the whole process of slope damage.
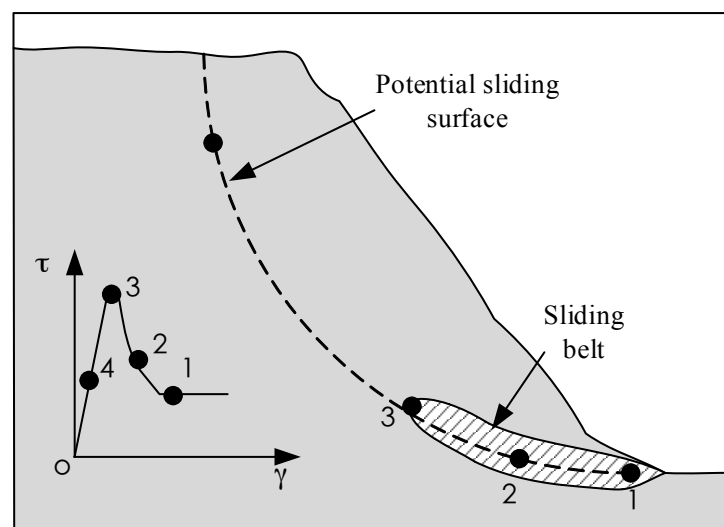
Figure 1. Schematic diagram of progressive failure of mountain slope

In Figure 1, at points 1 and 2, if the shear force is greater than that of the peak point, the mechanical index will decrease due to rainfall,. At this time, it can be

regarded as that the shear stress at point 3 has just peaked, and the shear stress at point 4 is well below the peak value. Moreover, since the sliding belt will continue to expand, the stress will be completed at point 4, the highest point will be completed at point 4, and at the same time, a complete sliding surface will be formed. Obviously, when the sliding zone is produced, its strength value will change from the highest point to the lowest point. In this way, the whole process can improve the characteristics of the formation of the Osian sliding zone.

The damage of slope structure and the process of landslide are not sudden, but gradual. Also, the slope instability is a gradual unsuccessful process, so it is necessary to reflect the whole gradual process of slope stability for evaluation [35]. If the strength value of the slope instability is wanted to decrease, strength reduction calculation will cause the final plastic zone to be too large.

2.3. SLIDING SURFACE SEARCH BASED ON DYNAMIC STRENGTH REDUCTION

The whole process deformation characteristics of geotechnical materials are mainly classified into two types, namely "hardening" and "softening". Regarding the shape change and mechanism damage characteristics of the sliding belt in the unsafe process of mountain slope, relevant researchers have verified via theory and experiments that the sliding belt of the slope has softening characteristics. Thus, the slope stability analysis must take into account the strain softening characteristics of geotechnical materials [36].

Based on referred strength reduction criteria and softening characteristics of the sliding belt, some scholars first proposed a calculation method and then obtained the parameters for reducing the local slope strength cohesion and internal friction angle, as shown in Figure 2
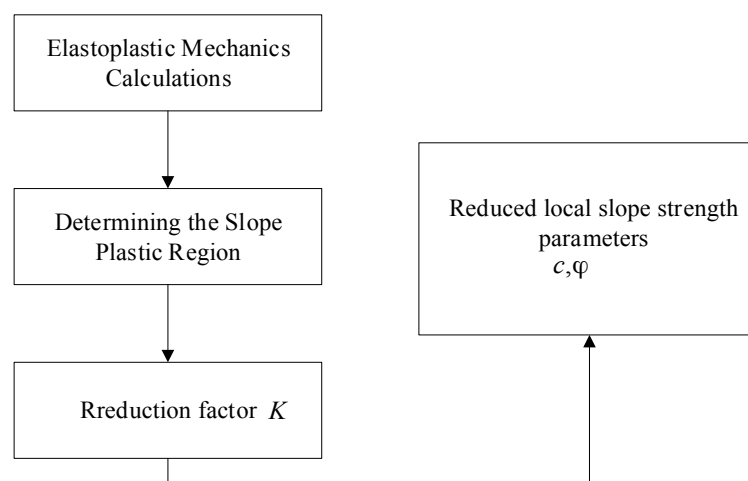
Figure 2. Strength reduction calculation process

Figure 2 shows the strength reduction process in detail, in which the minimum value of principal stress calculated is the same as the value of tensile failure strength. Concretely, it is first to destroy the reduction element index, and then obtain the

parameters for reducing the local slope strength cohesion and internal friction angle, so as to perform mechanical calculation aiming at the slope plastic region. Assuming that the deformation strength characteristics of the sliding zone geotechnical materials conform to the ideal elastic-plastic softening model, by calculating the damaged area of the mountain slope according to the elastic-plastic criterion, it is found that the area of slope increases slowly, which stops when the slope state reaches the limit equilibrium [37].

Tensile failure often occurs in a certain range of landslide crest, so after determining mechanical strength parameters of the sliding belt shear yielding, it is very necessary to integrate the Mohr Coulomb tensile failure model into the numerical study, that is, if the minimum value of principal stress is the same as the value of tensile failure strength, the rock and soil mass will suffer unsafe state process. Tensile composite yield criterion can be expressed as:

$$F^t = \sigma_3 - \sigma_t = 0 \qquad (1)$$

A single static safety index can be expressed as:

$$F^s = \sigma_1 - \frac{1+\sin\varphi}{1-\sin\varphi}\sigma_3 + \frac{2c\cos\varphi}{1-\sin\varphi} = 0 \qquad (2)$$

In the above formulas, σ_1 and σ_3 are the maximum and minimum principal stresses, respectively; c is the cohesion force; φ is the internal friction angle; and σ_t is the tensile strength.

The tensile strength of the slope is basically unchanged, so the tensile strength is not reduced in the strength reduction method [38-39]. Only under the conditions that earthquake and other basic factors work, the tensile strength of the slope will be and needs to be reduced. When calculating the damaged area of the slope according to the elastic-plastic criterion, the mechanical strength parameter of the sliding belt is narrowed by the reduction factor K, that is:

$$\left\{ \begin{array}{l} c_{loc} = \dfrac{c}{K} \\[2ex] \varphi_{loc} = \arctan\dfrac{\tan\varphi}{K} \end{array} \right\} \qquad (3)$$

In the above formula, c_{loc} and φ_{loc} are the cohesion force and the internal friction angle of the local damaged area, respectively

3. DYNAMIC STABILITY ANALYSIS OF MOUNTAIN SLOPE BASED ON STRENGTH REDUCTION METHOD

From the above data research and actual operation, it is obvious that whether the slope is safe and stable as time goes by, the whole process of the slope from local

failure and gradual development to overall instability will change dynamically, experiencing stable, less stable and unstable evolutionary processes.

The steps for evaluating the dynamic stability of mountain slopes are shown in Figure 3.
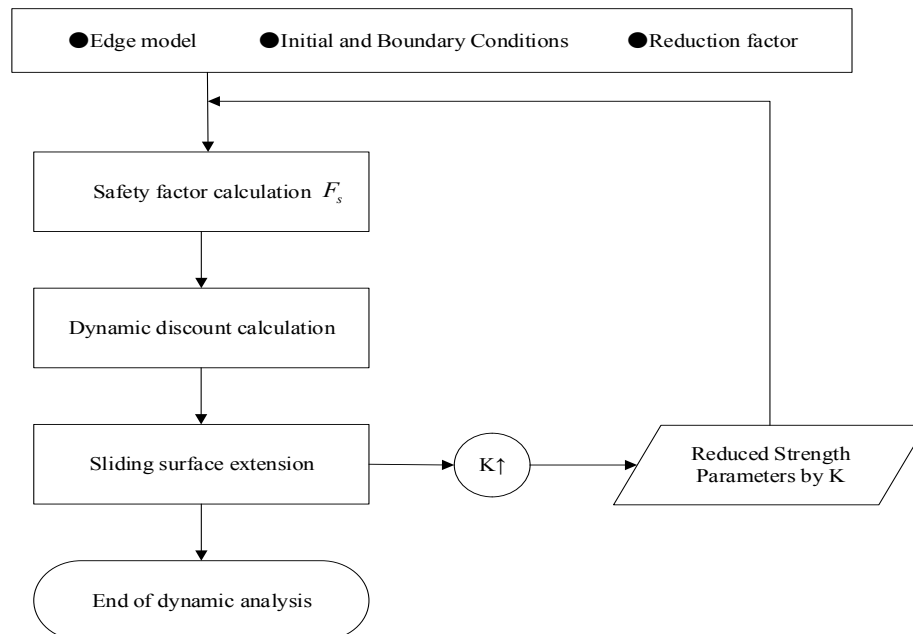
Figure 3. Dynamic evaluation process of mountain slope stability

In the traditional slope stability evaluation method, a single static safety index F_s is used to evaluate the slope stability, but the static safety index F_s is not conducive to the stability analysis and regulation of landslide disasters. Therefore, this paper proposes that the safety index F_s is a dynamic stability evaluation index.

(1) When the plastic zone appears in the local element of the mountain slope, the mechanical parameters of the element in the plastic zone are reduced to indicate that the strength of the local element softens and decreases.

(2) The overall strength reduction method and formula (4) are adopted to reduce the strength parameters c and φ, of the entire slope. The reduction range includes not only the softened plastic zone, but also the unyielding slope. For the plastic zone in step (1), the softened parameter value is reduced. When the reduction reaches a sudden change in the slope displacement, the safety index F_s in the current state is obtained.

(3) According to Figure 3, after the strength parameters c and φ are reduced, the elastoplastic mechanical balance calculation is carried out. Since the elements around the plastic zone of stress concentration will generate a new plastic zone, the plastic zone elements will increase.

(4) The increase of plastic zone elements indicates the expansion of the slope sliding surface. At this time, the mechanical parameters of the newly formed sliding surface are reduced according to steps (1) and (3).

(5) According to step (2), the slope safety index F_s is obtained after sliding surface expansion.

(6) The dynamic and overall strength reduction method is used to repeat the above steps to obtain a series of dynamic safety indexes, stop the reduction after the sliding surface is penetrated, and finish dynamic security and stability evaluation of the slope.

In order to track the evolution law of the slope safety index F_s in the whole process, this paper, combined with the advantages of dynamic strength reduction method, selects a representative section to study how to bring the strength reduction calculation method into the analysis of slope dynamic safety and stability state, in which the possibility of overall landslide occurrence is small in the gradual failure process of the slope, but the reduction index K obtained by the dynamic strength reduction method does not represent the safety index of the slope (as K in equation (3)), only representing the degree of reduction. Therefore, the dynamic and overall strength reduction calculation methods are combined to analyze the slope stability, and slowly enter the unsafe state process, thereby obtaining the safety index via calculation, and obtaining the stability state of the slope on the basis of the safety index.

Concretely, the fractures at an overall back-edge mountain are dislocated to reduce and a representative section is selected as the entire slope, so as to obtain the safety index F under the limit state, that is:

$$\begin{cases} c' = \dfrac{c}{F} \\ \varphi' = \arctan \dfrac{\tan \varphi}{F} \end{cases} \tag{4}$$

In the formula, c' and φ' are the reduced cohesion force and the internal friction angle, respectively.

4. RESULTS AND ANALYSIS

4.1. LANDSLIDE RESIDUAL MOUNTAIN CONDITIONS IN A CERTAIN AREA

In a certain area, there is still a mountain with a vertical length of 460-500m and a horizontal width (between the big water ditch and the small water ditch) of 460-640 m at the rear wall of the landslide, which is characterized by a steep front edge and a gentle back edge. The slope of the front edge (that is, the rear wall of the landslide in a certain area) is about 45°, and the back edge is the original slope with a gentle slope of 10° to 15°. It can be seen via qualitative analysis that the residual mountain mass on the rear wall of a landslide in a certain area will be dominated by local sporadic collapse and slump in the superficial part, and the possibility of overall landslide occurrence is small. Therefore, in the quantitative calculation of stability, the

possible sliding surface is formed based on the most unfavorable residual mountain slope structure and its various structural surfaces, which is regarded as the controlling boundaries for quantitative calculations of stability. At the same time, the various residual mountain slopes and superficial residual mountain slopes formed due to the earthquake will obviously serve as the boundary of the back edge tensile fracture.

Based on comprehensive analysis, it can be inferred that the residual mountain may have a large-scale failure mode: the back edge through fractures are dislocated → the middle layer slides → the front edge shear failure occurs, so it can also be attributed to a three-stage mechanism of tension cracking-sliding-shearing. Among them, the front edge of the slope crest is most likely to collapse.

4.2. EXPERIMENT PARAMETERS OF MOUNTAIN SLOPE IN A CERTAIN AREA

According to the geological prototype, geometric mode of right bank is built, and to perform stability calculation, a representative section is selected. Specifically, the section model of the computational mesh model is set to be 478m long and 470m high, and the total number of elements and nodes is 44695 and 71396 respectively. The rock-material constitutive model adopts the Mohr Coulomb rule for the most suitable elastic-plastic model criterion. The mechanical parameters of the three kinds of rock dikes in the corresponding stratum distribution on the vertical surfaces on the left and right sides, and fixed constraints on the bottom boundary are determined respectively.

Combined with the exposed shape of the section, the slope mass is generalized as $V2$, $V1$, IV, $III2$, $III1$ and II rock-soil mass and concrete after support (C25 strength grade), and the mechanical parameters of the three kinds of rock dikes in the corresponding stratum distribution are the same as IV-type rock mass. The natural bulk density, elastic model and Poisson's ratio appearing in this experiment are all measured by measuring instruments before the experiment. The layer parameter values are shown in Table 1.

Table 1. Parameters of the calculation model for the slope on the right side of the residual mountain.

Medium	Natural test weight / （kN•m^{-3}）	Elastic Modulus /Gpa	Poisson's ratio	Cohesion /Mpa	Internal friction angle /（°）
f231	25.8	2.0	0.28	0.9	22.8
Deep unloading fracture	26.2	2.0	0.28	2.0	36.0
V2 class	22.1	2.0	0.27	1.8	21.8
V1 class	24.5	4.0	0.27	2.0	26.5
IV class	25.8	6.0	0.26	7.0	38.6

III1 class	26.2	8.0	0.24	15.0	50.2
III2 class	26.2	7.5	0.23	17.5	51.3
III class	26.5	9.0	0.22	20.0	52.5

In Table 1, a total of 87 groups of physical and mechanical tests of rock blocks have been completed on the residual mountain. The values of mechanical parameters are comprehensively determined on the basis of indoor and outdoor tests, combined with engineering analogy and parameter inversion.

For a homogeneous slope in mountains at a certain area, its geometric model is shown in Figure 4, and its material property parameters are shown in Table 2.
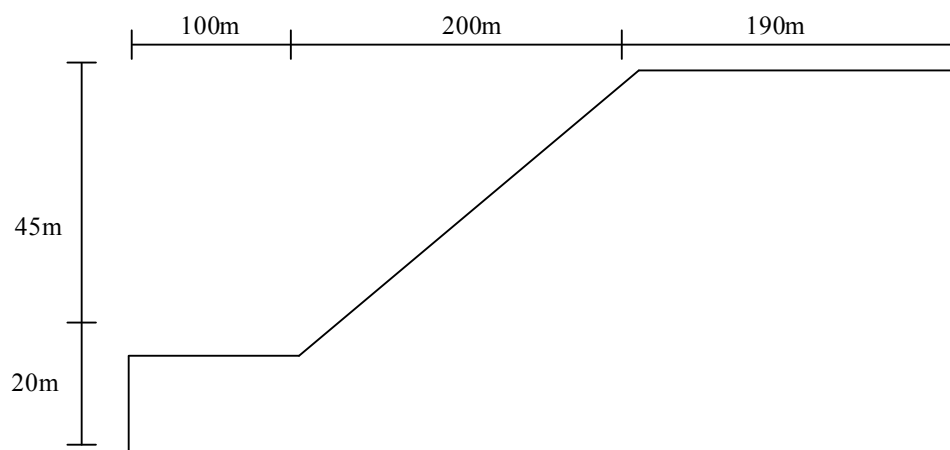
Figure 4. Geometric model of the homogeneous slope of the mountain

Table 2. Soil parameters of mountain homogeneous slope

c/kPa	φ/(°)	γ/（kN/m³）	E/Mpa	υ
3	19.6	20	10	0.25

Midas GTS NX is a kind of software that can analyze soil layers and tunnel structures, which can carry out various analysis of related mountains, strata, soil layers and tunnels, such as the mechanical parameter analysis of the three kinds of rock dikes in the corresponding stratum distribution, as well as solid structure and type analysis, with fast analysis speed, excellent graphics and output capabilities. Therefore, in this study, Midas GTS NX software is adopted to analyze the stability of three kinds of residual mountain slopes using the finite element limit equilibrium method, Bishop method, Janbu method and the mountain slope calculation model designed herein based on the strength reduction method in order.

The geometric model and material property parameters of a multi-layer soil slope on a mountain in a certain area are shown in Figure 5, and Table 3 respectively.
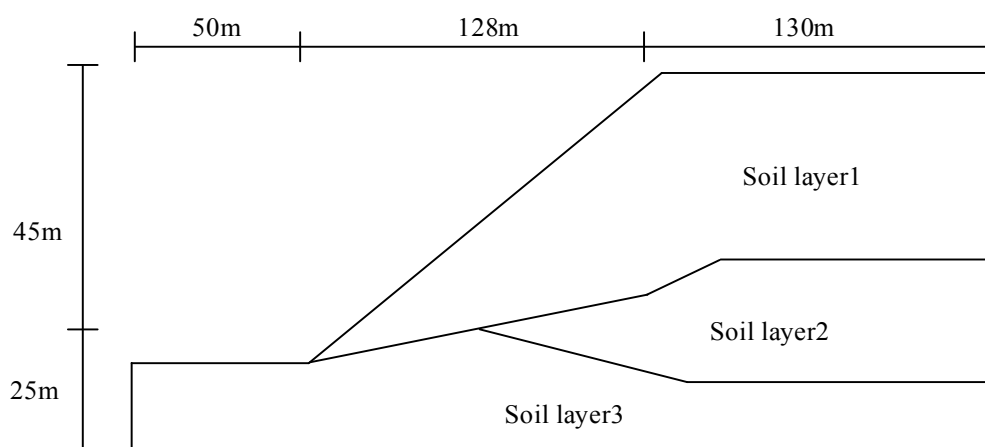
Figure 5. Geometric model of a multi-layer soil slope in mountain

Table 3. Soil parameters of a multi-layer soil slope in mountain

Soil layer	c/kPa	φ/(°)	γ/ (kN/m³)	E/Mpa	υ
1	0	38.0	19.5	10	0.25
2	5.3	23.0	19.5	10	0.25
3	7.2	20.0	19.5	10	0.25

The geometric model and material property parameters of a soft interlining slope in a certain area are shown in Figure 6, and Table 4 respectively.
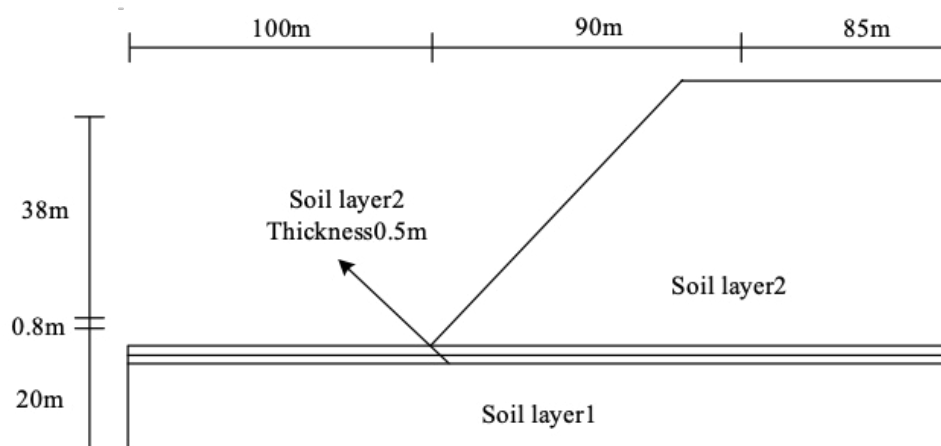
Figure 6. Geometric model of a weak interlining slope in mountain

Table 4. Soil parameters of a weak interlining slope in mountain

Soil layer	c/kPa	φ/(°)	γ/ (kN/m³)	E/Mpa	υ
1	28.5	20.0	18.84	60	0.25
2	0	10.0	18.84	20	0.25

4.3. COMPARE WITH THE RESULTS OF DIFFERENT ALGORITHMS

The calculation results of slope stability are shown in Figure 7 in detail.

After the stability of a homogeneous slope in a certain area is calculated by the finite element limit equilibrium method, the Bishop method, the Janbu method and the mountain slope calculation model designed in this paper according to the mechanical parameters of the three kinds of rock dikes in the corresponding stratum distribution, it is obvious from Figure 7 (a) that, in a certain area, the maximum safety index calculated via mountain slope calculation model designed in this paper is 1.081, while the maximum safety index calculated by the finite element limit equilibrium method is 1.013, the maximum safety index calculated by the Bishop method is 0.993, and the maximum safety index calculated by the Janbu method is 0.978, indicating that the slope stability safety index of a homogeneous slope in a certain area calculated by mountain slope calculation model is increased by 6.7%, 8.8% and 10.5% compared with that calculated by finite element limit equilibrium method, Bishop method and Janbu method respectively.

Similarly, in the stability analysis of a multi-layer soil slope, the maximum safety index calculated by mountain slope calculation model designed in this paper is 1.450, while the maximum safety index calculated by the finite element limit equilibrium method, Bishop method and Janbu method is 1.390, 1.383, and 1.325 successively, indicating that the slope stability safety index of a multi-layer soil slope calculated by strength reduction method is 6.7%, 8.8% and 10.5%. higher than that calculated by finite element limit equilibrium method, Bishop method and Janbu method. The concrete results is as shown in Figure 7(b)

Again, as can be seen from Figure 7(c), in the stability analysis of a weak interlining slope, the safety index calculated by the finite element limit equilibrium method is 1.027, the safety index calculated by the the Bishop method is 1.003., and the safety index calculated by the Janbu method is 1.024. Compared with other three algorithms, the safety index of slope stability calculated by strength reduction method is increased by 26.46%,, 29.11% and 26.10% respectively.
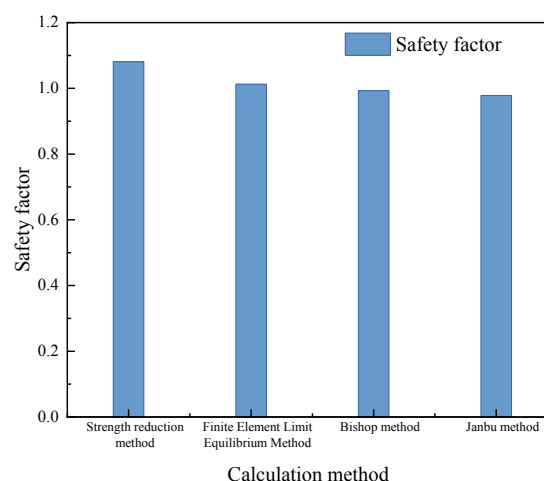
(a) Calculation results of the stability of the homogeneous slope of the mountain
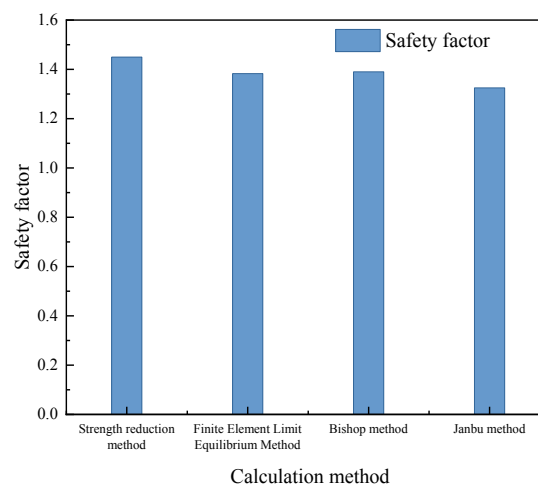
(b) Calculation results of the stability of the multi-layer soil slope in the mountain
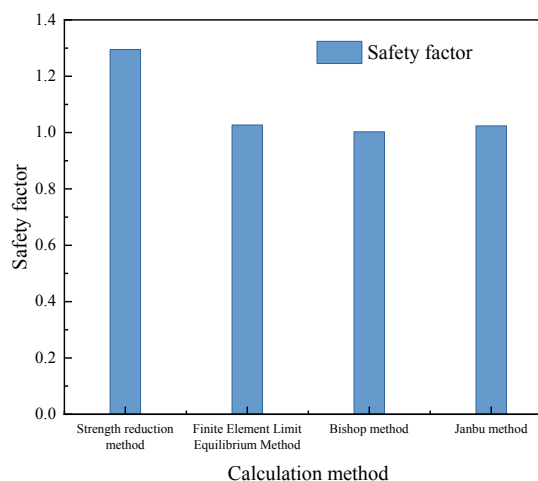
(c) Calculation results of stability of mountain slope with weak interlayer

Figure 7. The results of the mountain stability experiment

All the above data suggests that based on strength reduction method, the mountain slope calculation model designed in this paper has an optimal stability analysis effect for the three kinds of slope types in mountains, and the weak interlining slopes in mountain have the best stability.

5. DISCUSSION

Through the research of this paper, the author thinks that it is necessary to further bring the strength reduction method into the actual use of reinforced concrete in the calculation of the stability safety index of mountain slopes, and maybe the seepage field can be simulated by the function of simulating the temperature field. Also, the author reckons that there are still several deficiencies in the case analysis of this paper. For instance, the influence of groundwater has not been considered and the

application of the various residual mountain slopes in the rock slopes is not studied, where only the shear damage of rock and soil structure is analyzed. In this regard, future research may create a subject aiming at the influence of groundwater on slope stability, and focus on the practical application of strength reduction calculation method in rock slopes on the basis of the tensile failure of rock and soil, the practical application of strength reduction calculation method in the safe and stable state analysis of foundations and underground caverns, and other practical applications from all walks of life. Moreover. how to use the strength reduction method to design the support structure in the foundation, cavern and slope is a also topic worthy of further study.

6.   CONCLUSION

China is a mountainous country, where geological disasters such as landslides occur frequently every year, and losses caused thereupon are vitally massive. When carrying out landslide disaster management, it is the top priority of current mountain stability research to reasonably introduce relevant algorithms into the research on the stability of combined residual mountain slopes. Therefore, this paper proposes a strength reduction calculation model in the study of the stability of the residual mountains. And the following conclusions are drawn from the study:

1. The deformation and failure characteristics of the residual slope on the rear wall of a landslide in a certain area is analyzed. To be precise, from the distribution of three groups of fractures with different extension directions and scales formed on the surface of the residual mountain in a certain area, the vibration unloading effect is not only in the direction of the mouth of the river, but also in the direction of the big water ditch and the small water ditch. Collapse, sliding and cracking also occur, but the former has more advantages. Moreover, although the shallow surface layer of the residual mountain slope in a certain area is disturbed by the earthquake, the integrity of the underlying weakly weathered rock mass remains basically intact.

2. The stability of a multi-layer soil slope in a certain area in residual mountains via the method proposed in this paper, finite element limit equilibrium method, Bishop method and Janbu method is analyzed. It is found that the safety index obtained by the method proposed in this paper is 6.7%, 8.8%, and 10.5% higher than that calculated byother three methods in order.

3. The stability of a homogeneous slope in a certain area in residual mountains via the method proposed in this paper, finite element limit equilibrium method, Bishop method and Janbu method is analyzed. It is obvious that compared with other three methods, the safety index obtained by the method in this paper is increase by 4.8%, 4.3%, and 9.4% respectively. Similarly, in a weak interlining slope the safety index obtained by this method is 26.10%, 29.11%, and 26.46% higher than the other three methods successively, indicating that the stability of the landslide residual mountain calculated by the strength reduction method in this paper is the highest.

7.   DATA AVAILABILITY STATEMENT

The original contributions presented in the study are included in the article/ supplementary material, further inquiries can be directed to the corresponding author.

REFERENCES

(1)   Wei W B, Cheng Y M. (2019). **Stability analysis of slope with water flow by strength reduction method[j]**. *Soils & Foundations*, 50(1), 83-92.

(2)   Chen J F, Liu J X, Xue J F. (2017). **Stability analyses of a reinforced soil wall on soft soils using strength reduction method[J]**. *Engineering Geology.*

(3)   Wang L Y, Chen W Z, Tan X Y. (2019). **Evaluation of mountain slope stability considering the impact of geological interfaces using discrete fractures model[J]**. *Journal of Mountain Science*, 16(9), 2184-2202.

(4)   Wang Y, Jiang W, Li B. (2021). **Deformation Monitoring and Evaluation of Mountain Slope Stability Combined With Ground-based Radar and Spaceborne InSAR Methods.**

(5)   Xin Z, Han J, Zhuoyang L I. (2020). **Viability of high-density resistivity method for evaluating mountain slope stability in Erdaojiang District, Tonghua City, China[J]**. *World Geology: English Edition.*

(6)   Pingkang Wang, Youhai Zhu, Zhenquan Lu, Xia Huang, Shouji Pang and Shuai Zhang. (2017). **Gas hydrate stability zone migration occurred in the Qilian mountain permafrost, Qinghai, Northwest China: Evidences from pyrite morphology and pyrite sulfur isotope[J]**. *Cold Regions Science and Technology.*

(7)   Wang L Y, Chen W Z, Tan X Y. (2019). **Evaluation of mountain slope stability considering the impact of geological interfaces using discrete fractures model[J]**. *Journal of Mountain Science: English Edition*, 16(9), 19.

(8)   Xue F, Wang X. (2018). **Study on stability of the Santai Mountain landslide based on FLAC~(3D) numerical simulation[C]**. *2018 International Conference on Computational Science and Engineering.*

(9)   Liu W. (2018). **Study on foundation stability of a mountain project in Tianjin Binhai district[J]**. *IOP Conference Series Materials Science and Engineering*, 452(3), 032060.

(10) Jian H, Zuo D, Xiao J. (2018). **Fast Evaluation and Application Study for Road Slope Stability in Mountain Area Based on Android Platform[J]**. *Safety and Environmental Engineering.*

(11) Wang H. (2017). **Study on stability of high and steep slope in mountain reservoir[J]**. *Building Structure.*

(12) Dong T W, Zheng Y R, Huang L Z. (2018). **Study of Ultimately Loading of Pile Foundation by Strength Reduction Method of No-Linear Limit Analysis of FEM[J]**. *Advanced Materials Research*, 168-170, 2537-2542.

(13) Simatupang P T, Ohtsuka S. (2018). **Static and Seismic Slope Stability Analyses Based on Strength Reduction Method[J]**. *Doboku Gakkai Ronbunshuu A*, 3, 235-246.

(14) Chen L, Jin X. (2019). **Study on the applicability of three criteria for slope instability using finite element strength reduction method[J]**. *China Civil Engineering Journal*, 45(9), 136-146.

(15) Ying K, Chen P, Yu H. **Analysis of Rock High-Slope Stability Based on a Particle Flow Code Strength Reduction Method[J]**. *Electronic Journal of Geotechnical Engineering*, 20(28), 13421-13430.

(16) Abbas F, Zhu Z, An S. (2021). **Evaluating aggregate stability of soils under different plant species in Ziwuling Mountain area using three renowned methods[J]**. *Catena*, 207(15), 105616.

(17) Wang S, Li X C, Shi L. (2017). **Material point strength reduction method and its application to slope engineering[J]**. *Rock and Soil Mechanics.*

(18) Chen G Q, Huang R Q, Zhou H. (2017). **Research on progressive failure for slope using dynamic strength reduction method[J]**. *Yantu Lixue/Rock and Soil Mechanics*.

(19) Sheng-Dong X U, Zhang X, Zhang J. (2017). **Stability analysis of multi-step slope based on strength reduction method[j].** *Journal of Geological Hazards and Environment Preservation*.

(20) Schneider-Muntau, Barbara, Medicus. (2018). **Strength reduction method in Barodesy[J]**. *Computers & Geotechnics.*

(21) Sun Y, Duan X R, Xu P H. (2021). **Reliability analysis of karst roof stability based on strength reduction method[J]**. *IOP Conference Series: Earth and Environmental Science*, 861(7), 072118(8).

(22) Yunjin H U, Zhong Z, Gao H. (2021). **Three-parameter strength reduction method for slope stability evaluation.**

(23) Zhang Zhewen, Gao Huaxi. (2019). **Effect of repressive layer on stability of seawall based on strength reduction method[J]**. *Water Transport Engineering*, 000(006), 180-185.

(24) Shan, Shan, LU. (2018). **Dynamic Stability Analysis of Arch Dam Abutment Based on Strength Reduction Method[C]**.

(25) Ying K, Chen P, Yu H. (2018). **Analysis of Rock High-Slope Stability Based on a Particle Flow Code Strength Reduction Method[J]**. *Electronic Journal of Geotechnical Engineering*, 20(28), 13421-13430.

(26) Tulu I B, Esterhuizen G S, Klemetti T. (2016). **A case study of multi-seam coal mine entry stability analysis with strength reduction method[J]**. *International Journal of Mining Science and Technology*.

(27) Bai B, Yuan W, Shi L. (2017). **Comparing a new double reduction method to classic strength reduction method for slope stability analysis[J]**. *Rock and Soil Mechanics*, 36(5), 1275-1281.

(28) Y Zhou, T Chen, J Deng. (2019). **Three-dimensional stability analysis of slope regions based on strength reduction method**.

(29) Yang Y, Wang Y, Wu Y. (2017). **The effect of variable modulus elastoplastic strength reduction method on slope stability[J]**. *Electronic Journal of Geotechnical Engineering,* 20(1), 1-10.

(30) Tu Y, Liu X, Zhong Z (2018). **New criteria for defining slope failure using the strength reduction method[J]**. *Engineering Geology*, 212, 63-71.

(31) Schneider-Muntau B, Medicus G, Fellin W. (2017). **Strength reduction method in Barodesy[J]**. *Computers and Geotechnics*, 95, 57-67.

(32) Tulu I B, Esterhuizen G S, Klemetti T. (2018). **A case study of multi-seam coal mine entry stability analysis with strength reduction method[J].** *International Journal of Mining Science and Technology*.

(33) Nie Z B, Zheng H, Zhang T. (2017). **Determination of slope critical slip surfaces using strength reduction method and wavelet transform[J]**. *Rock and Soil Mechanics.*

(34) Hou W, University L. (2018). **Stability Analysis of Inhomogeneous and Multi-step Slope Based on Strength Reduction Method[J]**. *Subgrade Engineering.*

(35) Wei Y, Xiao-Tian H, Xiao-Chun L I. (2017). **A strength reduction method considering reduction of strength parameters coordinating with deformation parameters[J]**. *Rock and Soil Mechanics.*

(36) Yan C, Liu S Y, Xiao-Lei J I. (2018). **Research on a secondary sliding surface analysis approach based on strength reduction method[J]**. *Rock and Soil Mechanics.*

(37) Maqache, N., y Swart, A., J. (2021). **Remotely measuring and controlling specific parameters of a PV module via an RF link**. *3C Tecnología. Glosas de innovación aplicadas a la pyme*, 10(4), 103-129. https://doi.org/10.17993/3ctecno/2021.v10n4e40.103-129

(38) Shen Siqi. (2021). **Multi-attribute decision-making methods based on normal random variables in supply chain risk management**. *Applied Mathematics and Nonlinear Sciences,* 7(1), 719-728. https://doi.org/10.2478/AMNS.2021.2.00147.

CONFLICT OF INTEREST

The authors declare that the research was conducted in the absence of any commercial or financial relationships that could be construed as a potential conflict of interest.

/03/

APPLICATION OF DEEP NN OPTIMIZED BY MULTI-PARAMETER FUSION IN IDEOLOGICAL AND POLITICAL CONSTRUCTION OF PROFESSIONAL COURSES IN COLLEGES AND UNIVERSITIES

Rui Ma*

School of Financial Technology, Suzhou Industrial Park Institute of Service Outsourcing, Suzhou, Jiangsu, 215123, China

mar489@126.com

ABSTRACT

Curriculum ideology and politics is an inherent requirement to achieve the goal of "cultivating morality and cultivating people" in colleges and universities, and it is a beneficial exploration to realize the three-round education. The ideological and political construction of professional courses in colleges and universities not only teaches students knowledge and skills, but also helps students form correct values. Aiming at how to build ideological and political courses in colleges and universities, a design method based on multi-parameter fusion to gradually optimize deep NN is proposed. Firstly, the initial NN model without hidden layer is determined by analyzing the samples and categories, and then the hidden layer is gradually added on the basis of the initial NN to construct a deep NN with multi-parameter fusion optimization. Based on the TensorFlow framework, taking handwritten digit recognition as an example, a deep NN model is gradually designed. During the whole experiment, the network structure, activation function, loss function, optimizer, learning rate and sample batch size are continuously adjusted, and finally a multi-parameter design is designed. The fusion optimized deep NN model with high accuracy provides an effective idea for building a NN. As the learning rate increases, the performance of the NN gradually improves. In the training set and test set, the accuracy rate is almost the highest when the learning rate is 0.3, and the accuracy rate is 93.30% and 92.58% respectively when the number of iterations is 30, which shows that The NN optimized by multi-parameter fusion can be well applied to the ideological and political construction of professional courses in colleges and universities, and has strong application prospects.

KEYWORDS

Deep NN; TensorFlow; Activation function; Learning rate; Loss function

PAPER INDEX

1.   INTRODUCTION

"Course Ideological and Political" is a new education and teaching concept, which is different from the traditional ideological and political course education method, and runs through various professional courses in a hidden education way[1]. Curriculum ideology and professional knowledge education and teaching go in the opposite direction. While teachers disseminate professional knowledge, they also focus on leading students to establish a correct value orientation[2]. Curriculum ideology and politics take professional courses as the carrier, shoulder the important task of value leadership, and make it play the overall effect of "1+1>2". In its construction, teachers and students jointly establish a correct world outlook, outlook on life and values. Although the school has an independent ideological and political curriculum, it is not integrated with the major, so it may lead to the phenomenon that students have a weak sense of social responsibility and professional ethics in the future[3]. The close connection of the three has higher requirements for college students to have correct value orientation and firm ideals and beliefs.

In foreign education and teaching, "ideological and political education" and "ideological and political theory courses" are not clearly used to define the content of their courses, but implicit education is embedded in the teaching of various disciplines. Moral quality and values[4]. The social action model of moral education proposed by American educator Fred Newman. He believes that a virtuous member of society should have material competence, interpersonal competence, and civic competence[5]. Thomas Ricorner's moral education model of perfect personality believes that perfect personality includes three aspects: moral cognition, moral emotion and moral behavior. Section[6]. In 1916, American educator John Dewey pointed out in "Principles of Morality in Education" that "Students are accompanied by ideals, attitudes, moral habits and other learning that are different from the formal curriculum in addition to the learning of the formal curriculum, that is, 'incidental learning'. It is proposed that education must pay attention to the influence of various factors outside the formal curriculum on students" [7]. Fred Newman believes that students can acquire the environmental competencies necessary for meaningful moral discourse only through the study of civic action courses[8]. Sukhomlinsky emphasized that moral education must adhere to the unity of theory and practice, and must run through all aspects of school teaching and education. Teachers must teach and educate people, so that teaching and education are organically unified. In 1991, American educator Thomas Rickner proposed that "'character education' should carry out implicit education, create a campus moral culture atmosphere, fruitful education, democratic classroom life, story discussion method and role simulation training and other moral development[9]. Herbert Heyman made relevant research on political education in his book "Political Socialization: A Study of the Psychology of Political Behavior", studying how individuals receive political education and then disseminate political ideas., and eventually formed a political concept[10]. Dewey pointed out in "Principles of Moral Education" that "the conscious moral teaching in the classroom is not as good as it used to be, and it has committed the error of equating the teaching of ethics with the manipulation and instillation of moral precepts.", put forward that

moral education should focus on practicality[11]. In "Education and Democracy in the 21st Century", Neil Noddings explained the true connotation of democracy in education, and mentioned about patriotism, global citizenship, sublime School education in terms of moral feelings[12]. These all point to the practical significance of curriculum ideological and political construction.

The NN originated from McCulloch-Pitts (MCP) model, which is the earliest prototype of the artificial neural model[13]. In 1985, the perceptron algorithm was proposed, which enabled the MCP model to perform binary processing on multi-dimensional data, and then the back-propagation algorithm was proposed for the rapid development of modern NNs. Opened the door. In the 1980s, inspired convolutional NNs[14] and recurrent NNs[15] were successively proposed, and in the 1990s, LeNet[16] was applied to digit recognition and achieved good results. 2006 In 2009, due to the initial successful application of deep NN theory in machine learning, Hinton et al. proposed the concept of deep learning[17], which attracted people's attention. After years of development, it has gradually developed from a single-layer network to a multi-layer network. The multi-layer NN may contain hundreds of layers and hundreds of megabytes of training parameters. AlexNet, a deep learning architecture proposed in 2012, won the 2012 ILSVRC (image Net large-scale visual recognition challenge) crown, the error rate of Top-5 is reduced to 15.3%[18], and its effect is significantly ahead of traditional methods. In the following years, the recognition error rate has been continuously refreshed by new and deeper convolutional NNs. In 2014, VGGNet Obtained an average correct rate of 89.3%[19], and ResNet proposed by He et al. in 2016 reduced the classification error rate to 3.57%[20], while the SENet error recognition rate proposed by Hu Jie et al. in 2017 is only 2.25%. The introduction of various deep NN models has promoted the development of deep learning.

The rapid development of deep learning is inseparable from the design of better deep learning models, and people have gradually realized that the structure of deep learning models is the top priority of deep learning research[21]. The essence of deep learning is to build an artificial NN model with multiple hidden layers. The structure of artificial NN, whether shallow or deep, is mainly designed based on experiments and experience, but there is no set of specific theories to follow[22]. Based on the TensorFlow framework, this paper adopts a NN design method that is simple and then complex, and multi-parameter fusion is gradually optimized to optimize the ideological and political construction of professional courses in colleges and universities.

2. PRINCIPLES OF DEEP LEARNING MODELS

2.1. INTRODUCTION TO TENSORFLOW

Google has excellent performance in many fields related to computers, and the field of artificial intelligence is no exception[23]. TensforFlow is an excellent open source deep learning framework based on DistBelief developed by Google in 2015. The design of NN structure code is concise, and it is favored by more and more

developers. Not all tensFlow is written in Python, but many underlying codes are written in C++ or CUDA. It provides programming interfaces of Python and C++, and basic operations on threads and queues can be implemented from the bottom layer, and it can also be more convenient to call hardware resources. With the flexible architecture of TensorFlow, users can deploy to multiple platforms (CPU, GPU, TPU) for distributed computing and provide support for big data analysis. TensorFlow is also cross-platform and works on various devices (desktop devices, server clusters, mobile devices, edge devices).

2.2. DEEP NN MODEL DESIGN

2.2.1. DATA PREPROCESSING

In order to more easily extract the relevant information of the data during training, the data needs to be pre-processed. Data preprocessing includes normalization techniques, nonlinear transformations, feature extraction, discrete input, target coding, processing of missing data, and division of datasets, etc. [24]. The partition of the dataset is divided according to the evaluation model method validation and cross-validation. When the model method is validation, after selecting the data set, the data is generally divided into three subsets: training set, validation set and test set[25]. The size of the training set accounts for about 70% of the entire data set. T.

Choose the MNIST dataset, which is a well-known machine vision dataset for handwritten digits. There are two ways to obtain the MNIST dataset, one is to download it from Prof. Yann LeCun's official website, and the other is to use the official case of TensorFlow, and the MNIST dataset is included in TensorFlow[26]. The MNIST data set has 60,000 samples, of which 55,000 samples are training sets, and the other 5,000 samples are part of the validation set. The division of the entire dataset is shown in Table 1.

Table 1. Division of the MNIST dataset

Data set	Number of samples	Sample tensor
Training set	55000	55000×84
Test set	10000	10000×784
Validation set	10000	10000×784

In the data set MNIST, each sample contains the gray value information and the corresponding label of the sample. Each image sample is composed of handwritten digits of 28×28 pixels. In order to simplify the model, through dimensionality reduction processing, the two-dimensional 28× 28 images are converted into a one-dimensional vector with 784 features, then the feature of the training set is a [55000,784] tensor, and the features of the test set are [10000,784] and [10000,784] respectively. tensor. The label corresponding to the training data set is a [55000, 10] tensor, where the 55000th means that there are 55,000 sample images in the training set, and 10

means that the label of each image sample in the training set is a hot encoding containing 10 types of numbers[27].

2.2.2. BUILD A PRELIMINARY MODEL THAT MEETS THE REQUIREMENTS

The samples in the MNIST data set are 28×28 two-dimensional, and the one-dimensional vector has 784 gray values, which determines that the number of neurons in the input layer of the NN model is 784. The MNIST dataset is a total of 10 categories of handwritten digits from 0 to 9, so output layer is 10. First design a simple NN without hidden layers.

The simple NN with multi-parameter fusion is optimized through experiments, and then the hidden layer is gradually increased on the basis of the NN without hidden layer.

2.2.3. CHOOSE ACTIVATION FUNCTION, LOSS FUNCTION AND OPTIMIZER

1. Activation function

The activation function enables the NN to have the ability of hierarchical nonlinear mapping learning, which can approximate any function and solve more complex problems. The relu function has been applied in the deep learning network. How to choose the activation function, there is no definite method, mainly based on some experience[28]. Several commonly used activation functions are as follows:

(1) sigmoid function. sigmoid is a commonly used nonlinear activation function, and its definition is shown in formula (1):

$$f(z) = 1 / \left(1 + e^{\wedge}(-z)\right) \tag{1}$$

The input z is mapped to the range between 0 and 1, but the sigmoid activation function in the DNN will origin the problem of incline explosion and gradient disappearance. The meeting is slow, and the sigmoid function has the disadvantages of exponentiation, which is time-consuming.

(2) tanh function. The problems of gradient disappearance and exponentiation still exist in the deep NN with tanh as the activation function. The analytical expression of the tanh function is shown in formula (2).

$$f(x) = \left(e^{\wedge}x - e^{\wedge}(-x)\right) / \left(e^{\wedge}x + e^{\wedge}(-x)\right) \tag{2}$$

(3) relu function. The analytical appearance of the relu function is revealed in formula (3).

$$relu(x) = \max(0, x) \tag{3}$$

relu is a function that takes the maximum value between partitions. It is not derivable in the entire interval. It only determines the size of the input x and 0.

2. Loss function

The loss function is to estimate the difference between the predicted value ypre = f(x) of the designed NN model and the real value yhat. Usually Loss(yhat, ypre) is used to represent the loss function. Common loss functions are as follows:

(1) 0-1 loss function. The definition of the 0-1 loss function is shown in Equation (4).

$$\text{Loss (yhat , ypre)} = \begin{cases} 1, & \text{yhat} \neq y \text{ pre} \\ 0, & \text{yhat} = \text{ypre} \end{cases} \tag{4}$$

The 0-1 loss function does not consider the difference between the predicted value and the true value. If the prediction is correct, the value of the loss function is 0, otherwise the value of the loss function is 1.

(2) Squared loss function. The definition of the squared loss function is shown in formula (5) and (6).

$$Loss\left(yhat, ypre\right) = \left(yhat - ypre\right)^2 \tag{5}$$

$$H(p,q) = -\sum_x p(x)\log q(x) \tag{6}$$

2.2.4. TRAIN THE MODEL AND EVALUATE THE MODEL

The parameters of the NN model are weight (weight) and bias (threshold). The training model is to repeatedly adjust the weight and bias model parameter values through training samples and learning algorithms, so that the error between the actual output and the ideal output is less, and finally the NN is solved. parameters required by the problem. Among the learning algorithms for training models, the most representative one is the error backpropagation (BP) algorithm, which is widely used in multi-layer feedforward NNs. The methods of evaluating the model include validation and cross-validation, and different evaluation methods also determine the division of the dataset. Common model evaluation indicators for classification problems include confusion matrix, accuracy, precision, recall, specificity, etc., as shown in Table 2(Ying et al.).

Table 2. Model evaluation indicators

Confusion Matrix		Goal		
		True Positives True Negatives	True Positives True Negatives	
Model	predicts positive samples	True Positive（TP）	False Positive（FP）	Positive predictive value or precision =TP/（TP+FP）

Predict Negative Samples	False Negative（FN）	True Negative（TN）	阴性预测值 ＝ （TN）（/ TN + FN）
	Recall =TP/（TP+FN）	Specificity=TN/ （TN+FP）	Precision = （TP+TN）（/ TP+FP+FN+TN）

3. EXPERIMENTAL RESULTS AND ANALYSIS

Experiments were tested using TensorFlow on a Windows 10 system with Intel(R) Core(TM) i7- 6700HQ CPU@2.6 GHz 2.59 GHz, 8 GB RAM.

The sample image in the MNIST dataset is converted into a one-dimensional vector with 784 elements, and neurons number in the input layer is strongminded to be 784, and there are 10 categories of handwritten digits. A simple NN without a hidden layer has only an input layer [29].

(1) Comparison of loss functions. The learning rate is set to 0.1, the training model sample batch size is 100, and the number of iterations is 30. The optimizer uses the gradient descent method to compare the recognition accuracy of the cross entropy and the squared loss function on the simple NN.

Figure 1(a) is the curve relationship between the training model and the accuracy. The upper two curves are a group, which is the accuracy curve when the loss function is cross entropy [30-31]. The lower two curves are Accuracy curves for training and test sets when the loss function is a squared loss function. It could be gotten from Figure 1(a) that at iterations number, the training accuracy set is greater than that of the training set and test set when the loss function is the squared loss function. In Figure 1(b), the group with high loss value is the loss value curve of the training set and the test set when the loss function is a squared loss function. The group is the test set when the loss function is cross entropy. Figure 1(b) shows that the convergence speed is fast when the loss function is irritated information. From the comparison of the accuracy and loss value of cross entropy and squared loss function in Figure 1, it can be seen that irritated information is selected as the loss purpose of simple NN.
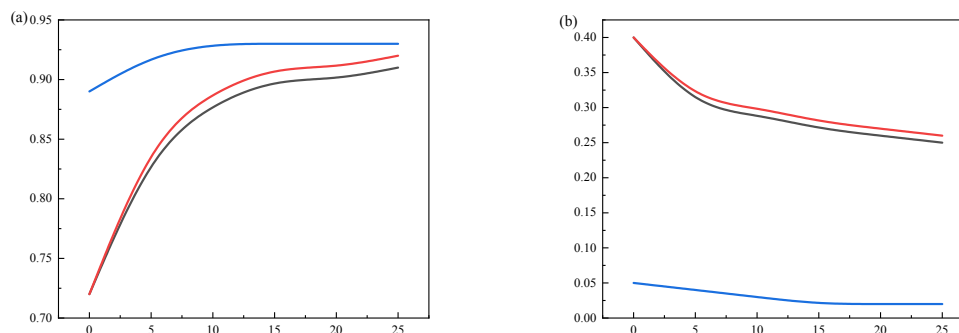
Figure 1. Comparison of cross entropy and square loss function, (a) Curve relationship between iteration times and accuracy; (b) Curve relationship between iteration times and loss value.

(2) Different learning rates. The training model sample batch scope is 100, the iterations number is 30, the optimizer adopts the incline ancestry method, and the damage function is cross entropy. Figure 2 shows the contrast of correctness created on different learning rates. The upper row is the test result, and the lower row is the test result of the test set.

Figure 2(a) shows three curves of the accuracy as a function when the learning rates are 0.1, 0.2 and 0.3, respectively. The untried consequences presented with the increase of the learning rate, the performance of the NN gradually improves. In the training set and the test set, when the learning rate is 0.3, the accuracy is almost the highest, and the number of iterations is 30. The accuracy is 93.30% and 92.58, respectively. %. Figure 2(b) is the curve of the accuracy as a function of the number of iterations when the learning rate is 0.4, 0.5 and 0.6, respectively. The experimental results show that the accuracy fluctuates greatly when the learning rate is 0.5 and 0.6 in the training set, especially when the learning rate is 0.5, the accuracy is unstable. When the number of iterations is 30, the training set with a learning rate of 0.6 has the highest accuracy, and a learning rate of 0.5 has the highest accuracy on the test set. Figure 2(c) is the curve of the accuracy versus the number of iterations when the learning rates are 0.3, 0.5 and 0.6, respectively. The experimental results show that the accuracy of different learning rates is not much different whether it is the training set or the test set. The accuracy of the learning rate of 0.5 and 0.6 is slightly higher than that of the learning rate of 0.3, but the accuracy of the learning rate of 0.5 and 0.6 in the training set is slightly higher. The rate fluctuates greatly. It can be seen from the analysis in Figure 2 that the learning rate is between 0.3 and 0.4, so the learning rate is 0.3.
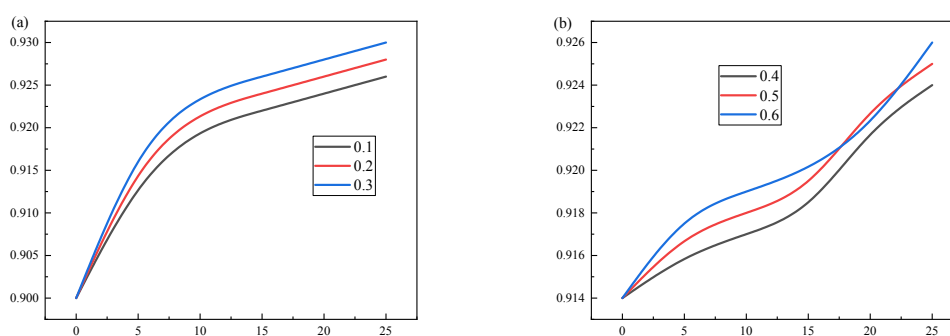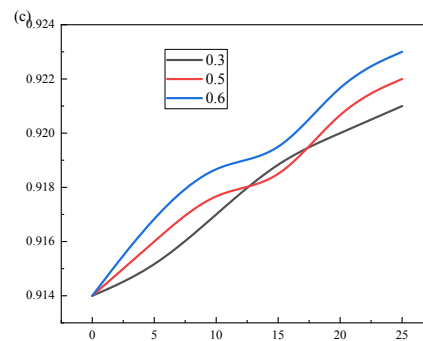
Figure 2. Effect of different learning rates on the accuracy of NN, (a) The learning rates were 0.1, 0.2 and 0.3; (b) The learning rates were 0.4, 0.5 and 0.6; (c) The learning rates were 0.3, 0.5 and 0.6.

(3) Batch size. The learning rate is 0.3, the number of iterations is 30, the optimizer uses gradient descent, and the loss function is cross-entropy to compare the effects of different batch sizes (50, 100, 150, 200, 250, 300) on the NN model. Figure 3 shows the comparison of the accuracy of different batch sizes. The upper row is the test results of the training set with different batch sizes, and the lower row is the test results of the test set with different batch sizes. Figure 3(a) are three plots of accuracy versus number of iterations for batch sizes of 50, 100, and 150. The experimental results show that in the training set, the accuracy rate of batch size 50 is higher than that of batch size 100 and 150, while the accuracy rate of batch size 100 in the test set is higher than that of batch size 50 and 150. Accuracy. Figure 3(b) shows the curve relationship between the accuracy rate and the number of iterations when the batch size is 200, 250 and 300 respectively. In the training set, when the number of iterations is 30 and the batch size is 200, the accuracy rate is 93.03%, which is higher than the batch size of 250 and 200. The accuracy rates corresponding to 300 are 92.89% and 92.85%, and the accuracy is also the highest when the number of iterations in the test set is 30 and the batch size is 200. Figure 3(c) shows the curve relationship of the accuracy rate with the number of iterations when the batch size is 100, 200 and 300 respectively. Whether it is the training set or the test set, the accuracy rate is the highest when the batch size is 100. It can be seen from the analysis in Figure 3 that the model with a batch size of 100 has the best performance.
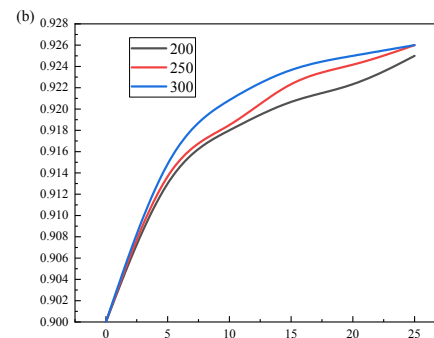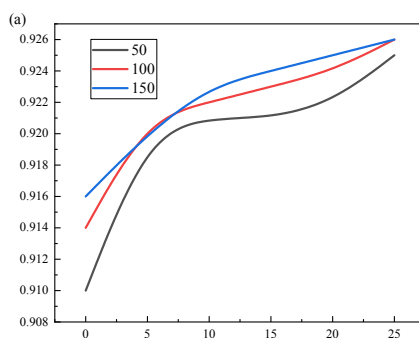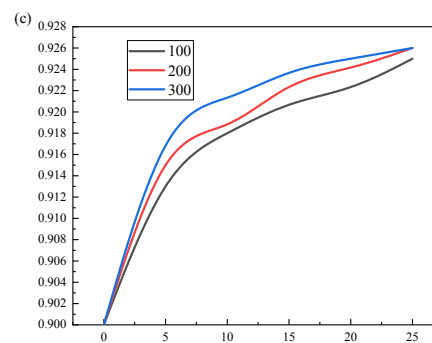
Figure 3. Effect of different batch sizes on the accuracy of NN, (a) Batch sizes 50, 100 and 150; (b) batch sizes 200, 250 and 300; (c) batch sizes 100, 200 and 300.

On the basis of the single hidden layer NN optimized by multi-parameter fusion, a hidden layer is added to continue to optimize the NN model. The sample batch size is 100, the number of iterations is 30, the loss function is cross entropy, the optimizer is the AdaGrad algorithm, there are two hidden layers, the number of neurons in the hidden layer is 500 and 300, and the activation function of the hidden layer is relu, and compare the effects of different learning rates (0.1, 0.15, 0.2, 0.25, 0.3, 0.35, 0.4, 0.45, 0.5, 0.55, 0.6, 0.65, 0.7) on the NN model in the test set. It can be seen from Table 5 that the accuracy of learning rates of 0.1, 0.15, 0.2, 0.25, 0.3, 0.35, 0.4, and 0.45 is higher than that of learning rates of 0.5, 0.55, 0.6, 0.65, and 0.7. The learning rates of 0.1, 0.15, 0.2, 0.25, 0.3, 0.35, and 0.4 have little difference in accuracy, and their accuracy curves with the number of iterations almost overlap each other, with learning rates of 0.2 and 0.25 having the best performance. The experimental results show that the learning rate of the multi-layer hidden layer NN is set to 0.2. The sample batch size is 100, the number of iterations is 30, the loss function is cross entropy, the learning rate is 0.2, the optimizer is the AdaGrad algorithm, two hidden layers, and the number of neurons in the hidden layer is 500 and 300, respectively, in the test set Compare the effect of different activation functions (sigmoid, relu, selu, and tanh) of the hidden layer on the NN model.

Table 3. Different learning rates in the test set

Number	Accuracy of different learning rates (%)										
	0.10	0.15	0.2	0.25	0.3	0.35	0.4	0.45	0.5	0.55	0.60
1	0.964	0.965	0.965	0.967	0.963	0.960	0.954	0.926	0.234	0.402	0.295
2	0.975	0.974	0.974	0.974	0.973	0.967	0.963	0.950	0.911	0.910	0.906
3	0.977	0.978	0.978	0.976	0.972	0.971	0.968	0.959	0.945	0.944	0.941
5	0.978	0.981	0.981	0.979	0.976	0.976	0.972	0.966	0.961	0.956	0.952
10	0.983	0.983	0.983	0.983	0.980	0.975	0.976	0.970	0.970	0.964	0.957
15	0.983	0.985	0.985	0.985	0.983	0.983	0.977	0.972	0.967	0.968	0.964
20	0.984	0.986	0.986	0.987	0.985	0.984	0.982	0.973	0.975	0.971	0.964
25	0.985	0.987	0.987	0.989	0.988	0.986	0.984	0.977	0.976	0.969	0.966
30	0.986	0.988	0.988	0.990	0.989	0.988	0.986	0.980	0.977	0.971	0.967

4. CONCLUSION

Curriculum ideology and politics is an inherent requirement to achieve the goal of "cultivating morality and cultivating people" in colleges and universities, and it is a beneficial exploration to realize the three-round education. In this study, a deep NN model with multi-parameter fusion optimization was constructed and applied to the ideological construction of college professional courses. The following conclusions were drawn: (1) At any number of iterations, when the loss function is cross entropy, the training set and the test set the accuracy of the NN is greater than that of the training set and the test set when the loss function is a squared loss function; (2) With the increase of the learning rate, the performance of the NN gradually improves. In the training set and the test set, when the learning rate is 0.3 The accuracy rates are almost all the highest. The iteration times are 30, and the accuracy rates are 93.30% and 92.58%, respectively. When the iteration times are 30, the training set with a learning rate of 0.6 has the highest accuracy, and a learning rate of 0.5. The test set has the highest accuracy; (3) batch The curve relationship between the accuracy rate and the number of iterations when the number of times is 200, 250 and 300 respectively. In the training set, the number of iterations is 30 and the accuracy rate is 93.03% when the batch size is 200, which is higher than the accuracy rate of 92.89% corresponding to the batch size of 250 and 300. and 92.85%, and the accuracy rate is also the highest when the number of iterations in the test set is 30 and the batch size is 200, and the model with a batch size of 100 has the best performance.

5. CONFLICT OF INTEREST

The authors declared that there is no conflict of interest.

REFERENCES

(1)   Min, W. U. (2020). **Research on the Integration of Curriculum Thought and Politics into the Teaching Practice of Business Etiquette in Higher Vocational Education[J]**. *Journal of International Education and Development,* 4(9), 20-24. https://doi.org/10.47297/wspiedWSP2516-250004.20200409

(2)   Vickers, E. (2009). **Selling 'Socialism with Chinese Characteristics' 'Thought and Politics' and the legitimisation of China's developmental strategy**. *International Journal of Educational Development*, 29(5), 523-531. https://doi.org/10.1016/j.ijedudev.2009.04.012

(3)   Madeleine, Arnot, Jo-Anne, & Dillabough. (1999). **Feminist Politics and Democratic Values in Education. Curriculum Inquiry**. *Special Series on Girls and Women in Education, 29(2), 159-189,* https://doi.org/10.1111/0362-6784.00120

(4)   Cakal, H., Hewstone, M., Schw?R, G., & Heath, A. (2011). **An investigation of the social identity model of collective action and the 'sedative' effect of intergroup contact among Black and White students in South Africa**. *British Journal of Social Psychology*, 50(4), 606-627. https://doi.org/10.1111/j.2044-8309.2011.02075.x

(5) Shi, J., Hao, Z., Saeri, A. K., & Cui, L. (2015). **The dual-pathway model of collective action: Impacts of types of collective action and social identity**. *Group Processes & Intergroup Relations*, 18(1), 45-65. https://doi.org/10.1177/1368430214524288

(6) Park, H. S., Gonsier-Gerdin, J., Hoffman, S., Whaley, S., & Yount, M. (1998). **Applying the Participatory Action Research Model to the Study of Social Inclusion at Worksites**. *Journal of the Association for Persons with Severe Handicaps*, 23(3), 189-202. https://doi.org/10.2511/rpsd.23.3.189

(7) Oel, P. V., Mulatu, D. W., Odongo, V. O., Willy, D. K., & Van, D. (2019). **Using Data on Social Influence and Collective Action for Parameterizing a Geographically-Explicit Agent-Based Model for the Diffusion of Soil Conservation Efforts**. *Environmental Modeling & Assessment, (1)*. https://doi.org/10.1007/S10666-018-9638-Y

(8) Zarpour, M. T. (2013). **Discourse and Dissent in the Diaspora: Civic and Political Lives of Iranian Americans**. http://hdl.handle.net/1903/14216

(9) Lickona, T. (1993). **The Return of Character Education**. *Educational Leadership Journal of the Department of Supervision & Curriculum Development N.e.a*, 51(3), 6-11. https://doi.org/10.1177/0013161X93029004010

(10) Hyman, H. (1971). **Political Socialization**. *International Journal of Psychology*, 6. https://doi.org/10.1080/00207597108246696

(11) Robin, A., & Hodgkin. (2006). **Where Law and Order Start: The Genesis of Boundaries and Norms**. *Journal of Moral Education*. https://doi.org/10.1080/0305724820110205

(12) Olssen, M., Codd, J., & O'Neill, A. M. (2004). **Education Policy: Globalization, Citizenship and Democracy**. *SAGE Publications*, https://doi.org/10.4135/9781446221501

(13) Pospíchal, J., & Kvasnička, V. (2015). **70th Anniversary of Publication: Warren McCulloch & Walter Pitts - A Logical Calculus of the Ideas Immanent in Nervous Activity**. *Springer International Publishing*. https://doi.org/10.1007/978-3-319-10783-7_1

(14) Fukushima, K., Miyake, S., & Ito, T. (1988). **Neocognitron: A Self-Organizing Neural Network Model for a Mechanism of Visual Pattern Recognition**. *IEEE Transactions on Systems Man and Cybernetics*, SMC-13(5), 826-834. https://doi.org/10.1007/978-3-642-46466-9_18

(15) Hu, C., Yan, Z., Jiang, J., Zhang, S., & Gu, T. (2022). **Traditional Chinese Medicine Information Analysis Based on Multi-task Joint Learning Model**. https://doi.org/10.1007/978-981-16-6963-7_25

(16) Lecun, Y., & Bottou, L. (1998). **Gradient-based learning applied to document recognition**. *Proceedings of the IEEE*, 86(11), 2278-2324. https://doi.org/10.1109/5.726791

(17) Hinton, G. E., Osindero, S., & Teh, Y. W. (2006). **A Fast Learning Algorithm for Deep Belief Nets**. *Neural Computation*, 18(7), 1527-1554. https://doi.org/10.1162/neco.2006.18.7.1527

(18) Lawrence, S., Burns, I., Back, A., Tsoi, A. C., & Giles, C. L. (2012). **Neural Network Classification and Prior Class Probabilities**. https://doi.org/10.1007/978-3-642-35289-8_19

(19) Zhang, P., Wei, L., Wang, H., Lei, Y., & Lu, H. (2018). **Deep Gated Attention Networks for Large-scale Street-level Scene Segmentation**. *Pattern Recognition*, 88. https://doi.org/10.1016/j.patcog.2018.12.021

(20) He, K., Zhang, X., Ren, S., & Sun, J. (2016). **Deep Residual Learning for Image Recognition**. *IEEE*. https://doi.org/10.1109/CVPR.2016.90

(21) Yi, S., Wang, X., & Tang, X. (2014). **Deep Learning Face Representation by Joint Identification-Verification.** *Advances in neural information processing systems*, 27. https://doi.org/10.48550/arXiv.1406.4773

(22) Zhang, S., He, Y., Wei, J., Mei, S., & Chen, K. (2019). **Person Re-identification with Joint Verification and Identification of Identity-Attribute Labels**. *IEEE Access*, 7, 126116-126126. https://doi.org/10.1109/ACCESS.2019.2939071

(23) González-Muñoz, M., Bastida, S., & Sánchez-Muniz, F. (2003). **Short-term in vivo digestibility assessment of a highly oxidized and polymerized sunflower oil**. *Journal of the Science of Food and Agriculture*, 83(5), 413-418. https://doi.org/10.1002/jsfa.1383

(24) Canziani, A., Paszke, A., & Culurciello, E. (2016). **An Analysis of Deep Neural Network Models for Practical Applications**. https://doi.org/10.48550/arXiv.1605.07678

(25) A, C. W., A, X. W., Jz, A., Liang, Z. A., Xiao, B. A., Xin, N. B., Ehd, A. (2021). **Uncertainty Estimation for Stereo Matching Based on Evidential Deep Learning**. https://doi.org/10.1016/j.patcog.2021.108498

(26) Cai, W., Zhai, B., Liu, Y., Liu, R., & Ning, X. (2021). **Quadratic polynomial guided fuzzy C-means and dual attention mechanism for medical image segmentation**. *Displays*, 70, 102106. https://doi.org/10.1016/j.displa.2021.102106

(27) Miao, J., Wang, Z., Ning, X., Xiao, N., Cai, W., & Liu, R. (2022). **Practical and secure multifactor authentication protocol for autonomous vehicles in 5G**. *Software: Practice and Experience*. https://doi.org/10.1002/SPE.3087

(28) Ning, X., Gong, K., Li, W., & Zhang, L. (2021). **JWSAA: joint weak saliency and attention aware for person re-identification**. *Neurocomputing*, 453, 801-811. https://doi.org/10.1016/j.neucom.2020.05.106

(29) Yu, Z., Li, S., Sun, L. N. U., Liu, L., & Haining, W. **Multi-distribution noise quantisation: an extreme compression scheme for transformer according to parameter distribution**. https://doi.org/10.1080/09540091.2021.2024510

(30) Medina, R., Breña, J. L., y Esenarro, D. (2021). **Efficient and sustainable improvement of a system of production and commercialization of Essential Molle Oil (Schinus Molle)**. *3C Empresa. Investigación y pensamiento crítico*, 10(4), 43-75. https://doi.org/10.17993/3cemp.2021.100448.43-75

(31) Xiong Xiaokun. (2022). **Research on tourism income index based on ordinary differential mathematical equation**. *Applied Mathematics and Nonlinear Sciences, 7(1), 653-660*. https://doi.org/10.2478/AMNS.2021.2.00113.

3C Tecnología. Glosas de innovación aplicadas a la pyme. ISSN: 2254-4143

Ed.43 | Iss.12 | N.1 January - March 2023

/04/

3C Tecnología. Glosas de innovación aplicadas a la pyme. ISSN: 2254-4143

Ed.43 | Iss.12 | N.1 January - March 2023

69

BASIC DIRECTION AND REALIZATION PATH OF PE TEACHING INNOVATION IN PSS BASED ON DEEP LEARNING MODEL

Huiming Ke

College of Fine Arts, Guangdong Polytechnic Normal University, Guangzhou Guangdong, 510665, China

yangwang_320@sina.com

Yang Wang

School of Materials Design and Engineering, Beijing institute of fashion technology, Beijing, 100029, China

ABSTRACT

At present, the traditional model of PE in PSS (PSS)has seriously affected the quality of PE teaching in PSS and the perception of PE among primary and secondary school students. Because of the urgent need for innovation in PE in PSS, this study proposes the LSTM model to achieve an accurate prediction of the innovation direction of PE in PSS. Based on the LSTM model, the user behavior is classified by extracting the important features of the innovation direction. Expression to achieve accurate prediction of the future development direction of PE. Using the data confusion matrix to estimate the prediction accuracy of the LSTM model, the four evaluation indicators of Accuracy, Precision, F1, and AUC are 0.0532~0.2323 higher than the baseline model. The prediction results of PE teaching innovation in PSS from three aspects of teaching thought, teaching content, teaching objectives and essence are output, which has obvious guiding significance for the overall optimization of PE classrooms in PSS. This result shows that the LSTM prediction model has important practical value.

KEYWORDS

PAPER INDEX

1. INTRODUCTION

Ball games, track and field, and some sports have converted the governments of PE in PSS. Methods such as explanation and demonstration have greatly affected teachers' teaching quality and students' cognition of PE[1]. Such as demonstration and explanation, teaching students to start, long jump, and pull up. Make students directly participate in imitation, resulting in a poor experience and poor effect[2-3]. Therefore, PE teachers need to enrich their teaching methods, improve their teaching ability, make teaching innovations, and flexibly use their innovative methods to teach students, so that students can enjoy high-quality PE courses[4]. Therefore, the reform of PE in schools is domineering.

At present, a considerable part of the exploration of sports innovative education focuses on the innovation of teaching methods[5]. However, if we only innovate in teaching methods all the time, it is difficult for PE to have a leap-forward development. Therefore, the overall reform of PE teaching is highly praised by researchers[6]. To cultivate students' comprehensive sports ability and innovative sports consciousness, researchers propose that PE should become a kind of lifelong education, and the teaching model at this stage must be reformed[7]. According to the characteristics and differences between modern sports and traditional sports, some researchers have made a comparison from the aspects of innovative teaching environment, inducing students' original interest, teachers' innovative teaching technology, teaching evaluation, and extracurricular activities[8-9]. This paper expounds on the design of an innovative education model in PE from four aspects. In addition, some scholars pointed out that in the long-term PE teaching, it is necessary to reform the "systematic learning" mode (traditional teaching mode). Only by combining organically in PE teaching can we innovate. Some researchers also believe that cultivating students' innovative spirit, improving the interest of monks, and resonating through students' innovation, to build a set of general and innovative PE innovation modes in the new era with innovative function and positive thinking[10].

Based on the development of the deep learning model[11], relevant grounds have developed explosively[12-13], and these developments have promoted the innovative development of other industries and other fields. Among them, LSTM is mainly used for the processing of time series. It can accurately predict the most suitable behavior mode for users according to the characteristic data with obvious time input by model users. If the user selects other options, it can make a selection based on the current prediction[14-15]. However, when choosing an innovation direction, it is often related to the existing direction, that is, there is a certain opportunity. According to this characteristic, this study applies the LSTM network to predict the innovation direction of PE teaching in schools of primary and secondary and determines the implementation content and path according to the prediction direction.

2. RELATED WORKS

2.1. RECOMMENDATION ALGORITHM BASED ON DEEP LEARNING AND ITS APPLICATION

Deep learning technology models can accurately capture attributes or features and promote them to a higher level of representation[16]. Early such technologies were limited by the Boltzmann machine (RBM)[17-18]. Hinton et al. Used the Boltzmann machine for modeling according to the data and optimized the fitting efficiency of the Boltzmann machine by using the contrast divergence algorithm[19]. The results showed that the optimized method can be well applied to Netflix. Song et al. proposed to use the NNM of DNN to extract Netflix user information, which is based on a recommendation model[20-21].

RNN is commonly used to process sequence data. Hidari[22] uses the neural network system to take the sequence data of the user's click items in the session record as the input data of RNN. If the quantity of data is large and concentrated, the prediction effect of RNN is very accurate. According to the above research, some researchers[23-24] took the historical behavior of news users as input and used RNN for a recommendation. The research found that it has good results. Liu et al.[25-26] used nearly 15 different RNN algorithms to process user information. On this basis, they found a new deep learning algorithm, which has a two-way RNN structure.

2.2. RECOMMENDATION ALGORITHM AND APPLICATION BASED ON LSTM

LSTM network is improved based on RNN hidden layer unit and has long-term memory function. Generally speaking, the problem that RNN can solve is the problem that LSTM can handle and perform well. At present, the LSTM network is mainly used for natural language processing, speech recognition, and image understanding. Graves[27] et al. Took the lead in applying the LSTM network to word prediction. After training in English and French databases, the accuracy of word prediction is 8% higher than that of standard RNN. Li et al. [28] proposed a Twitter tag recommendation system based on the LSTM network. The system first uses the skip-gram model to generate vocabulary, then uses CNN to generate each sentence in the article into a sentence vector, and finally uses this sentence vector to train the LSTM network. The experimental consequences show that the recommendation based on LSTM achieves better results than the recommendation model of standard RNN and Gru. A large number of research results show that LSTM network is suitable for time series information flow modeling.

3. RELATED CONCEPTS

3.1. RNN NETWORK STRUCTURE

RNN is a kind of time recurrent network, which is considered to be the result of repeated and alternating on the same timeline in a neural network architecture. The

structural characteristics of RNN determine that it is more conducive to processing time-series. RNN structure is shown in Fig.1, where a is the processing unit of the RNN hidden layer, X^T is the input value of the current time, and H^T is the output value of the current time hidden layer. As can be seen from Fig.1, H^T is determined by the current input value X^T and the output value H^{T-1} of the previous time. H^T will affect the output the next time, that is, each output difference is not only related to the current input value. It is also related to the output difference of the previous time. Theoretically, RNN can process any length of time series data. Pascanu[29] and others used detailed digital reasoning to explain the causes of these phenomena, that is, the traditional RNN mode usually changes according to the correct direction of the weight at the end of the time series in the training environment. However, the longer the input time interval, the smaller the impact on the correct change of connection weight. Therefore, the network system is more inclined to input new data and does not have the function of long-term memory.
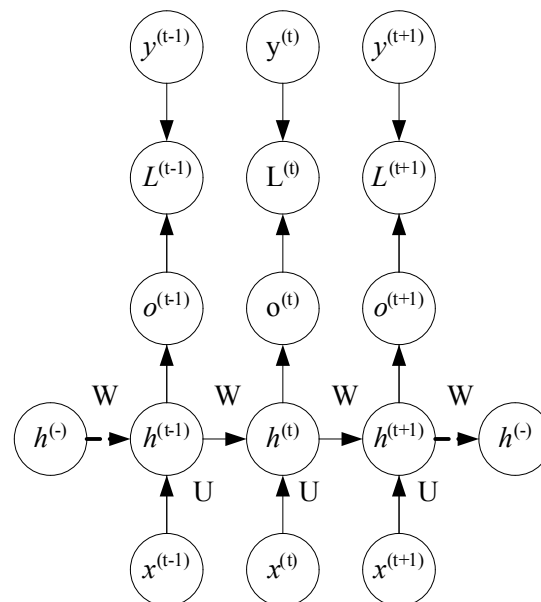
Figure 1. RNN network structure

3.2. LSTM NETWORK STRUCTURE

LSTM completes the problem of gradient disappearance and gradient explosion of the RNN model and retains information for a long time. LSTM and RNN have similar network structures, but the structure of the hidden layer is more complex, as exposed in Fig.2
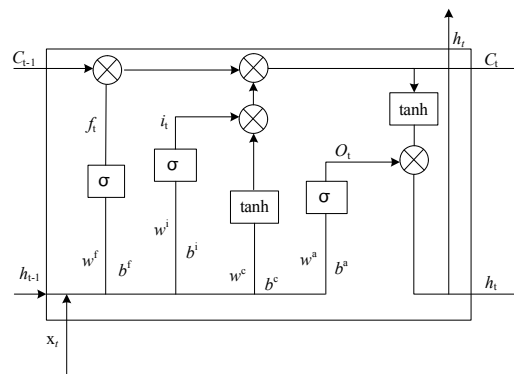
Figure 2. LSTM Structure neurons

There are three control doors inside the LTSM, which are input gate i_t, output gate o_t and forgetting gate f_t. The input x_t at each moment and the output H_{t-1} at the previous moment jointly determine that the state value of each gate unit at the current time has been the intermediate unit C_t. At time t, the update formula of each door is as follows [30].

$$f_t = \sigma\left(w^f \cdot \left[h_{t-1}, x_t\right] + b^f\right) \tag{1}$$

$$i_t = \sigma\left(w^i \cdot \left[h_{t-1}, x_t\right] + b^i\right) \tag{2}$$

$$\tilde{C}_i = tanh(w^c \cdot [h_{t-1}, x_t] + \tag{3}$$

$$C_t = f_t * C_{t-1} + i_t * \tilde{C}_t \tag{4}$$

$$o_t = \sigma\left(w^o \cdot \left[h_{t-1}, x_t\right] + b^o\right) \tag{5}$$

$$h_t = o_t * \tanh\left(C_t\right) \tag{6}$$

3.3. PREDICTION RESULT OUTPUT LAYER

The output layer of the prediction results is a two-layer full connection layer: each node of the first layer is connected to all the data features output by the LSTM unit to realize the integration of local features; Each node of the second layer is connected to the second layer, and each node is fully connected. The integration feature is calculated and the predicted value is output. The calculation is shown in formula (7).

$$y_t = w_t \times h_t \tag{7}$$

4. INNOVATION DIRECTION MODEL BASED ON LSTM MODEL

The recommendation mode can be divided into input part, processing part, and output part according to function. The input part converts the user's original education

method into the numerical form required for calculation through the LSTM network, and the education vector representation used by each user is shown in Fig.3. The processing part processes the input data through the LSTM network to obtain the output result. The structure of the LSTM network needs to be determined, including the number of network layers, time step, and connection settings between layers. We used the educational method as the number of eigenvalues, defines the dimensions of input and output data, and determines the structure of the whole LSTM network model. The softmax layer maps the value of the output vector of the LSTM processing layer to the (0,1) region. The output part takes the last dimension of the processing results of the softmax layer to get the final development direction.
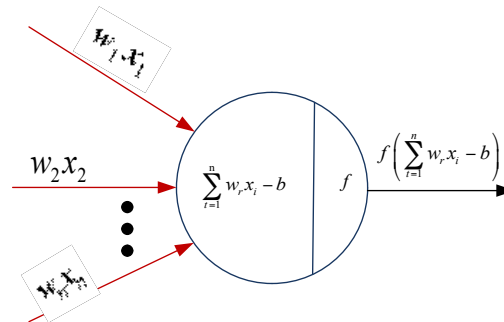
Figure 3. Output model

This study constructs an LSTM classification model. It can be used to identify the index categories of three main sports innovation methods and provide information for the construction of sports innovation development direction. In this paper, the LSTM model adopts a three-tier structure. The number of the intermediate network are 70, 50, and 25 respectively. The "CNN" algorithm is used for gradient training and optimization of network functions. Maxepochs is 70, minibacksize is 30, and the learning rate is 0.001. For each type of sports innovation direction, 70% of data are randomly selected as the data of the training set and 30% as data for testing. An LSTM model is constructed on the MATLAB software platform, and the model is established and trained by using the deep learning function package. The NVI 7732 processor and NVI 7790 processor equipped with Intel are one set of experiment environments.

5. MODEL EVALUATION

Compare the predicted classification results of the LSTM model with the actual labeling results[31] to estimate the presence of the LSTM model. For the model, the binary classification confusion matrix is calculated[32]. The category recognition model uses a one-to-many method to define the confusion matrix[33]. Table 1 lists the "one to many" method of binary classification based on the classical matrix.

Table 1. Confusion matrix of training data set

Class I	On class I
Correct prediction as a positive example (TP_I)	Incorrectly predicted as a counterexample (FN_I)
Incorrectly predicted as positive (FP_I)	Correctly predicted as a counterexample (TN_I)

TP_I is the class I positive sample correctly classified by the model; FN_I is the first type of positive sample of model misclassification; FP_I is another class i samples of model misclassification; TN_I is the class i other samples correctly classified by the model. The average accuracy, average accuracy, average recall, average Kappa coefficient, F_1, and area AUC are calculated to appraise the classification performance of the two BILSTM models[34], as follows:

$$AA = \left(\sum_{i=1}^{k} \frac{TP_i + TN_i}{TP_i + TN_i + FP_i + FN_i} \right) / k \tag{8}$$

$$AP = \left(\sum_{i=1}^{k} \frac{TP_i}{TP_i + FP_i} \right) / k \tag{9}$$

$$AR = \left(\sum_{i=1}^{k} \frac{TP_i}{TP_i + FN_i} \right) / k \tag{10}$$

$$F_1 \text{ score } = \frac{2 AP \cdot AR}{AP + AR} \tag{11}$$

$$AUC = \frac{1}{2} \left(\sum_{i=1}^{k} \frac{TP_i}{TP_i + FN_i} / k + \sum_{i=1}^{k} \frac{TN_i}{TN_i + FP_i} / k \right) \tag{12}$$

$$Kappa = \left(\sum_{i=1}^{k} \frac{p0_i - pe_i}{1 - pe_i} \right) / k \tag{13}$$

Where $p0_i$ is the accuracy and N is the total number of records.

The individual leveling rate index is not very accurate. F_1 score represents the effectiveness of classifier recognition positive classification[35]. Kappa coefficient is an index for conformance testing[36-37].

$$macro - P = \frac{1}{n} \sum_{i=1}^{n} P_i \tag{14}$$

$$macro - R = \frac{1}{n} \sum_{i=1}^{n} R_i \tag{15}$$

$$macro - F_1 = \frac{2 \times macro - P \times marco - R}{macro - P + marco - R} \tag{16}$$

$$E_{accuracy} = \frac{N_T}{N} \tag{17}$$

$$E_{\mathrm{RMSE}} = \sqrt{\frac{\sum_{i=1}^{N}(g_i - p_i)^2}{N}} \qquad (18)$$

Where N_T is the number of environments, N is the total index, g_i is the classification result, and p_i is the classification result predicted by the model[38-39].

6. RESULT ANALYSIS

6.1. BASELINE MODEL PARAMETER SETTING

To prove the efficiency of the projected model, we choose some machine learning methods based on artificial feature engineering to extract features. These methods are often used in decision prediction, Including DT, NB, LDA, LR, SVM, GBDT, and RF. In addition, we also selected two prediction models based on deep learning CNN and CNN RNN as comparison methods. The settings of some baseline model parameters are shown in Table 2, and the other model parameters without initial values are the default values.

Table 2. Setting of baseline model parameters

Baseline method	Baseline parameters	Value
SVM	C, y	C=1,y=1/210
DT	criterion	gini'
GBDT	n_estimator	500
RF	n_estimator	500

We could see from Table 3 that the model proposed in this study is 0.0532 ~ 0.2323 higher than the baseline model in terms of accuracy, precision, F_1, and AUC, and 0.0422 higher than the most competitive CNN-RNN on average. Among the traditional machine learning algorithms, GBDT and RF have the best average performance on the five evaluation indexes, because GBDT and RF are classifiers based on the idea of decision tree integration, and the final result is determined by multiple trees. Better prediction. In the application model of deep learning, CNN-RNN has better performance than CNN, because the CNN-RNN model can not only obtain the locally relevant information between learning behaviors but also capture the time relationship between learning behaviors. To a great extent, it captures potentially important information and improves prediction accuracy. Compared with the deep learning models CNN-RNN and CNN, our CLNN model performs better in the prediction of sports innovation direction. This is mainly because the LSTM model can effectively solve long-standing problems. The simple recurrent neural network (RNN) can make the error transfer through the time and layer gate mechanism when the level is more constant, allowing the periodic network to learn multiple time steps, establish the long-term cause-effect relationship, and expand the prediction presentation of the model.

Table 3. Performance of different models on different evaluation indicators

Method	Accuracy	Precision	Recall	F1	AUC
DT	0.8394	0.8506	0.9666	0.9049	0.6636
NB	0.8388	0.8800	0.9217	0.9004	0.7241
GBDT	0.8792	0.8887	0.9615	0.9237	0.7694
LR	0.8542	0.8583	0.9768	0.9137	0.6848
RF	0.8622	0.8727	0.9668	0.9172	0.7174
SVM	0.8620	0.8977	0.9422	0.9194	0.7689
CNN	0.8724	0.8717	0.9678	0.9224	0.7156
CNN-RNN	0.8562	0.8932	0.9528	0.9241	0.7601
CLNN	0.9363	0.8862	0.9624	0.9602	0.8870

6.2. INNOVATIVE DEVELOPMENT DIRECTION OF PE

Through the performance of different models on different evaluation indicators, it is found that CNN has better accuracy than other models, but its decision-making accuracy is low. Therefore, CNN-LSTM used in this study is the CLNN model. CNN-RNN is optimized to improve the accuracy of prediction and decision-making. This study selects five systems, including the teaching thought system, teaching process nature, and main goal system, teaching content system, teaching evaluation system, and sports text introduction system. According to the parameter comparison of model evaluation indicators in Section 6.1, CNN-LSTM is selected for prediction, and finally, three innovative development directions are determined: innovative teaching concept, innovative nature and main objectives of PE teaching process, and innovative teaching content system.

6.2.1. INNOVATION OF TEACHING IDEAS

Establish the educational thought of "seeking knowledge and innovation" and "health first" facing the future. The thought of "health first" emphasizes the content and methodology of the combination of PE and health education, closely combines the thought of "health first" with the construction of PE discipline and expands the benefits of maintaining and promoting health. In the field of lifelong PE, we should clarify the special role of PE in quality service education and give new directions to the teaching content. PE in PSS should comprehensively promote quality education, and establish the guiding ideology of PE teaching of "seeking knowledge and innovation" and "health first" so that students can master basic physical skills and form a good habit of adhering to physical exercise. physical exercise. PE reform has also changed our thinking set of taking PE as the educational carrier and education as the goal, re-understand the goal, function, content, means, and methods of PE, and building a new PE teaching system for PSS in the 21st century.

6.2.2. ESSENCE OF PE TEACHING PROCESS AND INNOVATION OF MAIN OBJECTIVES

PE is not equal to physical exercise. PE is not fitness. PE alone cannot solve the problem of strengthening the physique. At present, we should combine imparting knowledge and skills with cultivating consciousness, skills, and habits, and pay attention to cultivating students' self-learning and self-habit consciousness, to make students make achievements in PE and lay the foundation of lifelong PE. At the same time, PE should recognize the transformation from "the main purpose of PE is to improve physique" to "health first", and establish the main objectives of PE in PSS: (1) make students have a basic understanding and positive attitude towards PE, understand the original intention of physical exercise, and establish a healthy concept of physical exercise; (2) Master knowledge and correct methods of fitness, and be able to exercise regularly by using a variety of basic sports skills and fitness methods; (3) Exercise independence and the habit of peaceful coexistence.

6.2.3. INNOVATION OF TEACHING CONTENT SYSTEM

Establish the educational content and curriculum system of PSS in China in the 21st century, and strive to form a diversified and comprehensive PE content system. It includes: (1) the combination of PE thought education and physical exercise education; (2) The innovation of primary and secondary school teachers in the teaching methods and contents of PE and the innovation of the PE system; (3) The innovative evaluation system of primary and secondary school sports is constantly changing with the development of the times.

7.   CONCLUSION

This deep learning technology can extract the attributes or features of the data and abstract them into higher-level representations, and use them to predict the direction of PE innovation, which has long-term guiding significance. This research predicts the direction of PE teaching in PSS based on the LSTM model. First, it analyzes and identifies the innovation direction data set, and then uses the LSTM model to extract text context features from both forward and backward directions to predict the innovation direction and implementation path of PE. Finally, the basic direction of the innovation and development of PE is determined, the research is carried out and the following conclusions are drawn: (1) The LSTM model proposed in this study is 0.0532 higher than the baseline model in the four evaluation indicators of Accuracy, Precision, F1, and AUC. ~0.2323, indicating that the LSTM model has excellent prediction accuracy and effect; (2) The PE system is first of all completely dynamic, and the development direction of PE innovation is essentially the direction jointly selected by teachers, students, and schools. PE teaching innovation in PSS should be carried out from three aspects: teaching thought, teaching content, teaching goal, and essence.

8. CONFLICT OF INTEREST

The authors declared that there is no conflict of interest.

REFERENCES

(1) Al-Hazzaa, H. M., Abahussain, N. A., Al-Sobayel, H. I., Qahwaji, D. M., & Musaiger, A. O. (2011). **Physical activity, sedentary behaviors and dietary habits among Saudi adolescents relative to age, gender and region**. *The International Journal of Behavioral Nutrition and Physical Activity*, 8. https://doi.org/10.1186/1479-5868-8-140.

(2) A, C. W., A, X. W., Jz, A., Liang, Z. A., Xiao, B. A., Xin, N. B.,... Ehd, A. (2021). **Uncertainty Estimation for Stereo Matching Based on Evidential Deep Learning**. https://doi.org/10.1016/j.patcog.2021.108498

(3) Aubert, S. (2020). **Active Healthy Kids Global Alliance "Global Matrix" Initiative: Process, Results, Impact and Evaluation**. https://doi.org/10.20381/ruor-24426.

(4) Anthamatten, P., Brink, L., Lampe, S., Greenwood, E., Kingston, B., & Nigg, C. (2011). **An assessment of schoolyard renovation strategies to encourage children's physical activity**. *International Journal of Behavioral Nutrition & Physical Activity*, 8(1), 27. https://doi.org/10.1186/1479-5868-8-27.

(5) Aguilar-Farias, N., Cortinez-O'Ryan, A., Sadarangani, K. P., Oetinger, A. V., & Cristi-Montero, C. (2016). **Results From Chile's 2016 Report Card on Physical Activity for Children and Youth**. *Journal of Physical Activity and Health*, 13(2), S117-S123. https://doi.org/10.1123/jpah.2016-0314.

(6) Russell, R. D. (1975). **Health Education**. *Project of Joint Committee on Health Problems in Education of the National Education Association and the American Medical Association. communication quarterly*.

(7) Miao, J., Wang, Z., Ning, X., Xiao, N., Cai, W., & Liu, R. (2022). **Practical and secure multifactor authentication protocol for autonomous vehicles in 5G**. *Software: Practice and Experience*. https://doi.org//10.1002/SPE.3087

(8) Ayers, W. (2018). **The Shifting Ground of Curriculum Thought and Everyday Practice: Thinking About Schools**.

(9) Ning, X., Gong, K., Li, W., & Zhang, L. (2021). **JWSAA: joint weak saliency and attention aware for person re-identification**. *Neurocomputing*, 453, 801-811. https://doi.org/10.1016/j.neucom.2020.05.106

(10) Heyneman, S. P., & Lee, B. (2016). **International organizations and the future of education assistance**. *International Journal of Educational Development*, 48(3), 9-22. https://doi.org/10.1016/j.ijedudev.2015.11.009.

(11) Hao, X., Zhang, G., & Ma, S. (2016). **Deep Learning**. *International Journal of Semantic Computing*, 10(03), 417-439. https://doi.org/10.1142/S1793351X16500045

(12) Qiu, L., Liu, Y., Hu, Q., & Liu, Y. (2018). **Student dropout prediction in massive open online courses by convolutional neural networks**. *Soft Computing*, 23. https://doi.org/10.1007/s00500-018-3581-3

(13) Yang, B., Lei, Y., Liu, J., & Li, W. (2016). **Social Collaborative Filtering by Trust**. *IEEE Transactions on Pattern Analysis and Machine Intelligence*, 1-1. https://doi.org/10.1109/tpami.2016.2605085

(14) Naeen, H. M., & Jalali, M. (2019). **A decentralized trust-aware collaborative filtering recommender system based on weighted items for social tagging systems**. https://doi.org/10.48550/arXiv.1906.05143

(15) Yan, C., Pang, G., Bai, X., Liu, C., Xin, N., Gu, L., & Zhou, J. (2021). **Beyond triplet loss: person re-identification with fine-grained difference-aware pairwise loss**. I*EEE Transactions on Multimedia*. https://doi.org/10.1109/TMM.2021.3069562

(16) Khatun, A., Denman, S., Sridharan, S., & Fookes, C. (2020). **Joint identification-verification for person re-identification: A four stream deep learning approach with improved quartet loss function**. *Computer Vision and Image Understanding,* 197-198, 102989. https://doi.org/10.1016/j.cviu.2020.102989

(17) Cai, W., Zhai, B., Liu, Y., Liu, R., & Ning, X. (2021). **Quadratic polynomial guided fuzzy C-means and dual attention mechanism for medical image segmentation**. *Displays*, 70, 102106. https://doi.org/10.1016/j.displa.2021.102106

(18) Roch, S. (2011). **Phase Transition in Distance-Based Phylogeny Reconstruction**. *Computer Science*. https://doi.org/10.48550/arXiv.1108.5781

(19) RUMELHART, D. E., Hinton, G. E., & Williams, R. J. (1988). **Learning Internal Representations by Error Propagation: Readings in Cognitive ence**. https://doi.org/10.1007/978-0-387-39940-9_3246

(20) Theodoros K. Dikaliotis, Tracey Ho, Sidharth Jaggi, Svitlana Vyetrenko, Hongyi Yao, Michelle Effros, Jörg Kliewer, Elona Erez. (2010). **Multiple-access Network Information-flow and Correction Codes**. *IEEE Transactions on Information Theory*, 57(2), 1067-1079, https://doi.org/10.1109/TIT.2010.2095130.

(21) Ning, X., Duan, P., Li, W., & Zhang, S. (2020). **Real-time 3D face alignment using an encoder-decoder network with an efficient deconvolution layer**. *IEEE Signal Processing Letters*, 27, 1944-1948. https://doi.org/10.1109/LSP.2020.3032277

(22) Hidasi, B., Karatzoglou, A., Baltrunas, L., & Tikk, D. (2015). **Session-based Recommendations with Recurrent Neural Networks**. *Computer ence*. https://doi.org/10.48550/arXiv.1511.06939

(23) Haruki Okamura, Hiroko Tsutsui, Toshinori Komatsu, Masuo Yutsudo, Akira Hakura, Tadao Tanimoto, Kakuji Torigoe, Takanori Okura, Yoshiyuki Nukada, Kazuko Hattori, Kenji Akita, Motoshi Namba, Fujimi Tanabe, Kaori Konishi, Shigeharu Fukuda & Masashi Kurimoto. (1995). **Cloning of a new cytokine that induces IFN-gamma production by T cells**. *Nature*, 378(6552), 88. https://doi.org/10.1038/378088a0

(24) Shan, W. (2022). **Digital streaming media distribution and transmission process optimisation based on adaptive recurrent neural network. Connection Science**, 34(1), 1169-1180. https://doi.org/10.1080/09540091.2022.2052264

(25)   Szegedy, C., Liu, W., Jia, Y., Sermanet, P., & Rabinovich, A. (2014). **Going Deeper with Convolutions**. *IEEE Computer Society*. https://doi.org/10.1109/CVPR.2015.7298594

(26)   Ying, L., Nan, Z. Q., Ping, W. F., Kiang, C. T., Pang, L. K., Chang, Z. H.,... Nam, L. **Adaptive weights learning in CNN feature fusion for crime scene investigation image classification**. *Connection Science*. https://doi.org/10.1080/09540091.2021.1875987

(27)   Graves, A. (2012). **Long Short-Term Memory**. *Springer Berlin Heidelberg*. https://doi.org/10.1007/978-3-642-24797-2_4

(28)   Li, W., & Abiad, V. (1990). **Institutions, Institutional Change and Economic Performance**. *Social Science Electronic Publishing*, 18(1), 142-144. https://doi.org/10.1017/CBO9780511808678

(29)   Pascanu, R., Mikolov, T., & Bengio, Y. (2012). **On the difficulty of training Recurrent Neural Networks**. *JMLR.org*. https://doi.org/10.1007/s12088-011-0245-8

(30)   Le, Q. V., & Mikolov, T. (2014). **Distributed Representations of Sentences and Documents. arXiv e-prints**.

(31)   Zhou, Y., Daamen, W., Vellinga, T., & Hoogendoorn, S. P. (2019). **Ship classification based on ship behavior clustering from AIS data**. *Ocean Engineering*, 175(MAR.1), 176-187. https://doi.org/10.1016/j.oceaneng.2019.02.005.

(32)   Meng, W., Wei, Y., Liu, P., Zhu, Z., & Yin, H. (2019). **Aspect Based Sentiment Analysis With Feature Enhanced Attention CNN-BiLSTM**. *IEEE Access*, 7, 167240-167249. https://doi.org/10.1109/ACCESS.2019.2952888.

(33)   Yu, S., Liu, D., Zhu, W., Zhang, Y., & Zhao, S. (2020). **Attention-based LSTM, GRU and CNN for short text classification**. *Journal of Intelligent and Fuzzy Systems*, 39(1), 1-8. https://doi.org/10.3233/JIFS-191171.

(34)   Ma, J., Jia, C., Yang, X., Cheng, X., & Zhang, C. (2020). **A Data-Driven Approach for Collision Risk Early Warning in Vessel Encounter Situations Using Attention-BiLSTM**. *IEEE Access*, 8, 188771-188783. https://doi.org/10.1109/ACCESS.2020.3031722.

(35)   Ma, X., & Hovy, E. (2016). **End-to-end Sequence Labeling via Bi-directional LSTM-CNNs-CRF.** *Paper presented at the Proceedings of the 54th Annual Meeting of the Association for Computational Linguistics, 1*. https://doi.org/10.13140/RG.2.1.2182.5685.

(36)   Chen, G., Lin, H., Hu, H., Yan, Y., Wan, Y., Xiao, T., & Peng, Y. (2022). **Research on the Measurement of Ship's Tank Capacity Based on the Monte Carlo Method**. *Chemistry and Technology of Fuels and Oils*, 58(1), 232-236. https://doi.org/10.1007/s10553-022-01371-x.

(37)   Sheng, K., Liu, Z., Zhou, D., He, A., & Feng, C. (2017). **Research on Ship Classification Based on Trajectory Features**. *Journal of Navigation*, 1-17. https://doi.org/10.1017/S0373463317000546.

(38)   Dewani, A., Memon, M. A., y Bhatti, S. (2021). **Development of computational linguistic resources for automated detection of textual cyberbullying threats in Roman Urdu language**. *3C TIC. Cuadernos de desarrollo aplicados a las TIC*, 10(2), 101-121. https://doi.org/10.17993/3ctic.2021.102.101-121

(39) Hong Chen,Xuefei Peng & Caiyun Chen. (2022). **Corporate social responsibility fulfilment, product-market competition and debt risk: Evidence from China**. *Applied Mathematics and Nonlinear Sciences, 7(2), 757-772.* https://doi.org/10.2478/AMNS.2021.2.00163.

/05/

DEEP LEARNING NETWORK-BASED EVALUATION METHOD OF ONLINE TEACHING QUALITY OF INTERNATIONAL CHINESE EDUCATION

Wenling Lai*

Tongshi College of Quality Education, Wuchang University of Technology, Wuhan, Hubei, 430223, China

lwl001325@126.com

ABSTRACT

The development of vocational education in the information age requires us to think about the path and strategy of active change. Course teaching quality evaluation should also shift from passive evaluation of online teaching development to active construction of a mixed teaching quality evaluation system. In the information age, the development of teaching resources is dizzying. From paper to digital, from single to diverse, from offline to online, from scarcity to mass—various changes impact the traditional teaching model. Aiming at the online teaching quality evaluation of international Chinese education on the Internet, this paper proposes a method based on deep learning. Firstly, this paper proposes an index system construction and evaluation index weighting for online teaching of international Chinese education, and collects online data as a corpus at the same time. Then construct the CNN_BiLSTM_Att model, which is composed of the CNN module, the BiLSTM module and the Att module. Finally, compare with other model experiments. The experimental results show that CNN_BiLSTM_Att has achieved the best results in the evaluation index results, with P and F1 reaching 97.89% and 97.85%. Compared with other models, the overall effect is improved by 2%~5%. From this, the superiority of the model in the online teaching quality evaluation standard task of this paper can be obtained.

KEYWORDS

Deep learning technology; teaching evaluation; international Chinese education; online teaching

PAPER INDEX

1.   INTRODUCTION

Data in the teaching and learning process, deep learning technology has an impact on various elements of the education system in the analysis stage, strategy selection stage and evaluation stage of instructional design. Meet the teaching needs of teachers who need a lot of investigation and not enough experience guidance, and provide guidance for "learner-centered" instructional design [1-3].

(1) The analysis phase of instructional design: Conduct a learning needs analysis. Through the deep learning technology to analyze the student's online learning behavior, it is possible to accurately grasp the students' mastery of knowledge. Learner characteristic analysis, the application of deep learning can help teachers determine the cognitive development level of learners and analyze the starting ability of learners[4].

(2) Strategy selection phase: Deep learning technology has changed the traditional teaching environment of teachers and courseware, and formed an intelligent teaching and learning environment that can analyze intelligently and assist students' personalized learning [5-7].

(3) Teaching evaluation stage: Teacher and student evaluation, based on deep learning data analysis technology, makes the evaluation of students' learning results more scientific and accurate, reduces the difficulty of analysis, shortens the feedback cycle, and enables teachers to have a more accurate grasp of students' learning status. The artificial intelligence technology based on deep learning assists teachers in supervising and evaluating students' learning behavior, reducing the burden of teachers' teaching management, and the intelligent marking system helps teachers reduce repetitive work [8].

International Chinese education is not only a discipline, but also a "national and national cause", with the dual attributes of discipline and career. As a discipline, since its inception, international Chinese education has been "growing up with the progress of the Republic" [9]. Encourage teaching institutions, teachers, students and resource builders to adjust, change and innovate accordingly. Especially the sudden epidemic has exacerbated this change. How to effectively construct resources to deal with the new online teaching quality evaluation method is a problem we need to solve.

Online Chinese teaching for international students provides conditions for liberating teachers, innovating the research of international Chinese education, solving old problems, discovering new problems, exploring new laws, and enriching the content of subject research. It is necessary to make full use of the opportunity of international Chinese online teaching, data, and teachers' division of labor and cooperation models brought by online teaching. On the other hand, it is necessary to start from promoting the upgrading of international Chinese education and international Chinese education, improve online Chinese teaching from the aspects of system, model, platform construction, etc., and lead the development of online Chinese teaching [10-11].

Under traditional conditions [12], the evaluation data is obtained by means of a questionnaire survey, and then the results are finally obtained through tedious sorting

work. This method requires a lot of time and material resources, and there are problems such as inaccurate data collected in special questionnaires. Using intelligent technical means to obtain real-time online course evaluation data and analyze it, the results obtained by using deep neural network learning technology have high accuracy, and the feedback results are used as the basis for teachers to change their learning methods.

Therefore, this paper proposes a method based on deep learning. The main work is highlighted as follows:

(1) The evaluation standard system is constructed for the online teaching quality evaluation method of international Chinese education on the Internet.

(2) Design a set of analytical methods to weight the evaluation indicators.

(3) The CNN_BiLSTM_Att network framework is built to realize the online teaching quality evaluation of international Chinese education [13-14].

2. METHODOLOGY

2.1. CONSTRUCTION OF ONLINE TEACHING QUALITY EVALUATION INDEX SYSTEM

Online teaching quality evaluation system is an important foundation and guarantee for online teaching quality, is shown in Fig 1. In order to ensure that the online teaching quality evaluation index system plays the functions of supervision and incentives, it is required to follow the objectivity, purpose, consistency, comprehensiveness and operability of the indicators [15].

(1) The principle of objectivity is important guarantee for the effectiveness and credibility of online teaching quality evaluation results, and requires scientific formulation. The process of evaluation criteria should be open and transparent, and the evaluation results should be collected to ensure the reliability of online teaching quality evaluation data.

(2) This paper is to improve the level of teaching evaluation quality, stimulate teachers' enthusiasm for teaching.
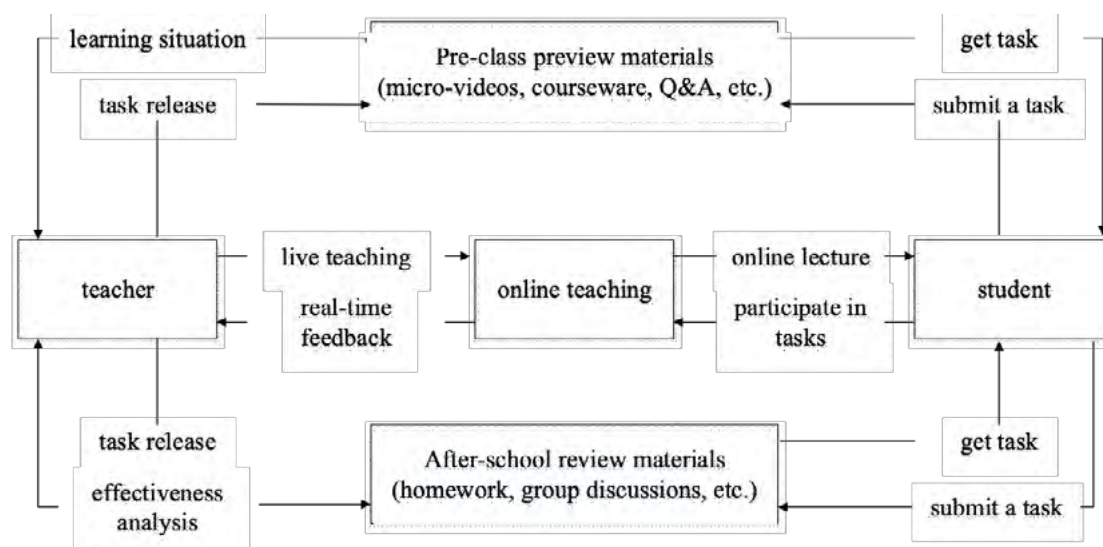
Figure 1. Online teaching quality evaluation index system

(3) The principle of consistency refers to scientific, standardized and systematic selection of online quality evaluation indicators, requires evaluation indicators to be based on the laws of online teaching at different ages.

(4) The principle of comprehensiveness requires that online teaching quality evaluation indicators should cover various cannot be limited to certain aspects and certain indicators.

(5) The principle of operability requires system is practical and feasible, and can be carried out continuously and effectively on a large scale.

2.2. WEIGHTING OF EVALUATION INDICATORS BASED ON ANALYTIC HIERARCHY PROCESS

Online teaching quality evaluation index system based on the questionnaire survey method and the expert online consultation method based on the analytic hierarchy process. Colleges and universities at different levels need to consider many factors such as online course settings, teaching methods, and student source quality when building an online teaching quality evaluation system [16-18].

Table 1. Weights of online teaching quality evaluation indicators

Evaluation subject	Weights	Evaluation indicators	Weights	Weights ratio
Teaching management department	21. 61%	teacher behavior	50%	10. 805%
		student behavior	50%	10. 805%
Teaching supervision	18. 31%	teaching process	48. 5%	8. 88%
		teaching effect	26. 67%	4. 88%
		instructional Design	15. 27%	2. 8%
		education resources	9. 56%	1. 75%
Student	34.82%	teaching method	45. 35%	15. 79%
		teaching content	24. 2%	8. 43%
		teaching effect	19. 72%	6. 87%
		teaching attitude	10. 72%	3. 73%
Ministry of international Chinese education	14. 32%	teaching materials	61. 44%	8. 88%
		assessment link	26. 84%	3. 84%
		teaching routine	11. 72%	1. 68%
Chinese teacher	10. 95%	teaching readiness	60%	6. 57%
		teaching implementation	20%	2. 19%
		teaching feedback	20%	2. 19%

(1) According to the index system of online quality evaluation, target evaluation layer online teaching quality evaluation, and the criterion evaluation layer includes the teaching management department, the evaluation of teaching supervision, and students, the evaluation of the ministry of international Chinese education and the self-evaluation of Chinese teachers. The scheme evaluation layer is the evaluation index of each evaluation subject, and a hierarchical structure evaluation model is constructed.

(2) Constructing a comparative judgment matrix by conducting online special consultation and analysis on the relative importance of the pairwise comparison between the evaluation subjects and the evaluation indicators to 10 experts;

(3) Carry out the consistency test, the results show that each judgment matrix CR < 0.1, all passed the test;

(4) The weight of the quality evaluation index, calculation results is shown in Table 1.

2.3. CNN_BILSTM MODEL

Online teaching quality evaluation model for international Chinese education is constructed convolutional neural network (CNN) and bidirectional long short-term memory network (BiLSTM)-based. The attention mechanism is introduced on the basis of BiLSTM and CNN, and structure is shown in Fig 2.
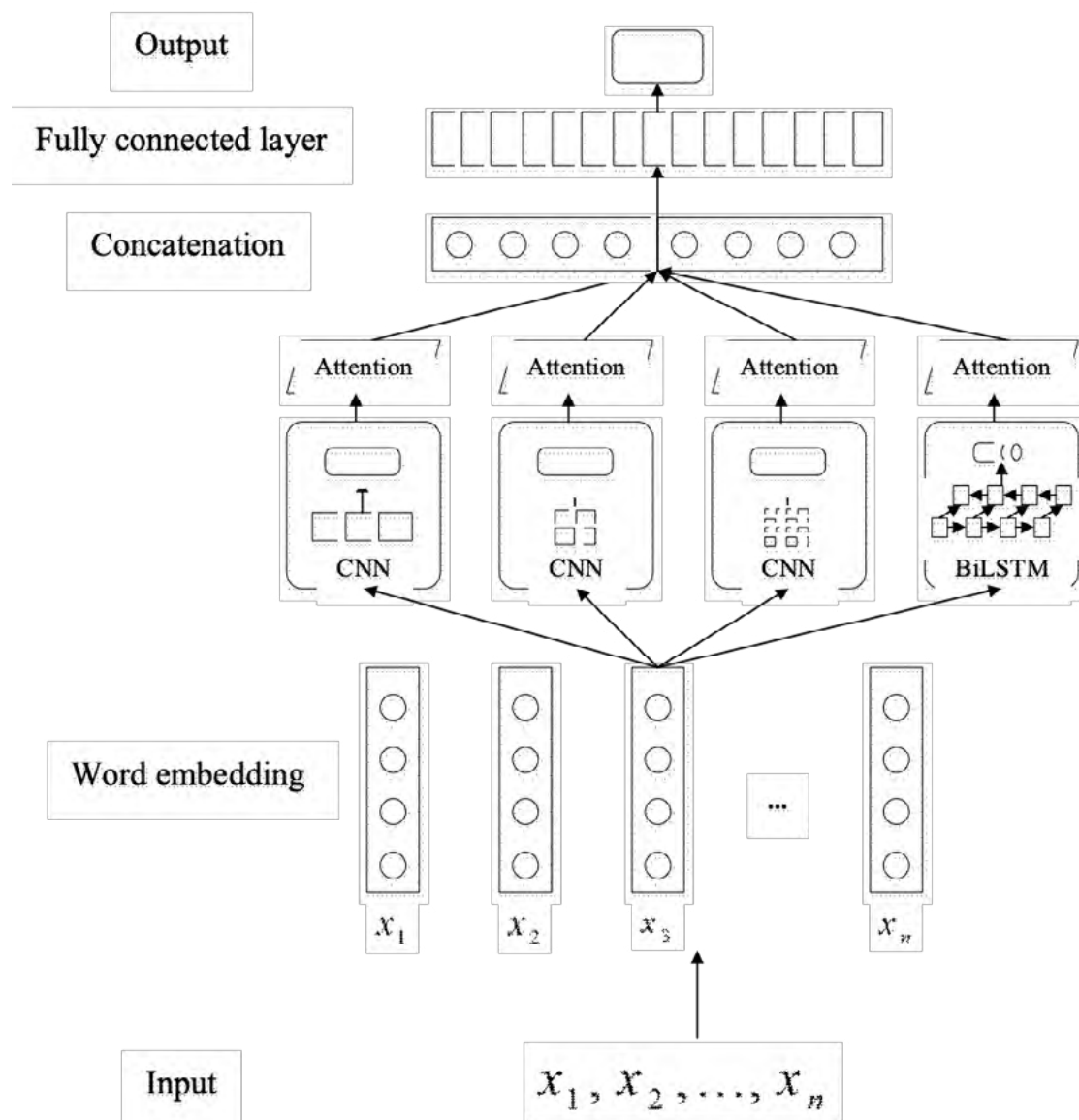
Figure 2. CNN_BiLSTM model

2.4. WORD VECTOR REPRESENTATION LAYER

After the text data is preprocessed, it is vectorized and then input into the online teaching quality evaluation model for the next step [19]. The corpus data size is about 6.3GB, and the Word2Vec tool is used for large-scale text training to convert the text into a low-density vector space. This paper selects the Word2Vec tool skip-gram model to training word-vectors. The skip-gram model takes all the words in the corpus as the central word, and predicts the lexical information of its context through the conditional probability distribution of the correspondence between the central word and the context. The expression formula is as follows:

$$P(W_i \mid W_t) = \frac{P(W_i \mid W_t)}{P(W_t)} P(W_i) \qquad (1)$$

where $i = t - 1, t - 2, t + 1, t + 2$, W_i is the context, that is, the representation vector of the surrounding words; W_t is the center word; word-vectors obtained by

training as $[W_1, W_2, \ldots, W_n]$, where n is the total number of text words. The word embedding layer converts words into $[x_1, x_2, \ldots, x_n]$. The training parameters of the Word2Vec is shown in Table 2.

Table 2. Word2Vec model parameters

parameter	value	Parameter meaning
sg	1	training model selection Skip-gram
window	5	window size
min_count	3	Minimum number of occurrences of a word
vector_size	350	vector dimension
epoch	8	number of iterations
hs	0	negative sampling
negative	6	number of negative samples

2.5. CNN NETWORK

As a special type of forward neural network, CNN is used in the field of natural language processing (NLP) in recent years [20]. The basic structure is divided into three parts, input layer, convolutional layer and pooling layer, and fully connected layer, as shown in Fig 3. The features extracted by the convolution layer first represent the text in the form of word vector matrix, and then scan the matrix through convolution kernels of different sizes. During the scanning process, the parameter values of the filters composed of the convolution kernels are fixed. After filtering new feature map is mapped, and all elements on the feature map come from filters with consistent parameters.

(1) Enter the evaluation index text input sequence $S = \{x_1, x_2, \ldots, x_n\}$, the pre-trained word vector is R^d. The convolution formula for the number of words h in each window is:

$$c_i = ReLU(\omega w_{i:i+h-1}) + b \tag{2}$$

where, c_i is the convolution result; ReLU is the nonlinear activation function; i is the number of words taken per convolution.

(2) The text sequence is n, and the window length is n-h+1. Result formula is:

$$C = [C_1, C_2, \ldots, C_{n-h+1}] \tag{3}$$

(3) Then, the pooling operation is performed on the result of the convolutional layer according to the pooling layer, and the output sequence features the parameters and calculation next layer to prevent over-fitting.

(4) Finally, the CNN model convolves the contextual semantic content of the word window to better represent the local features of the text sequence.
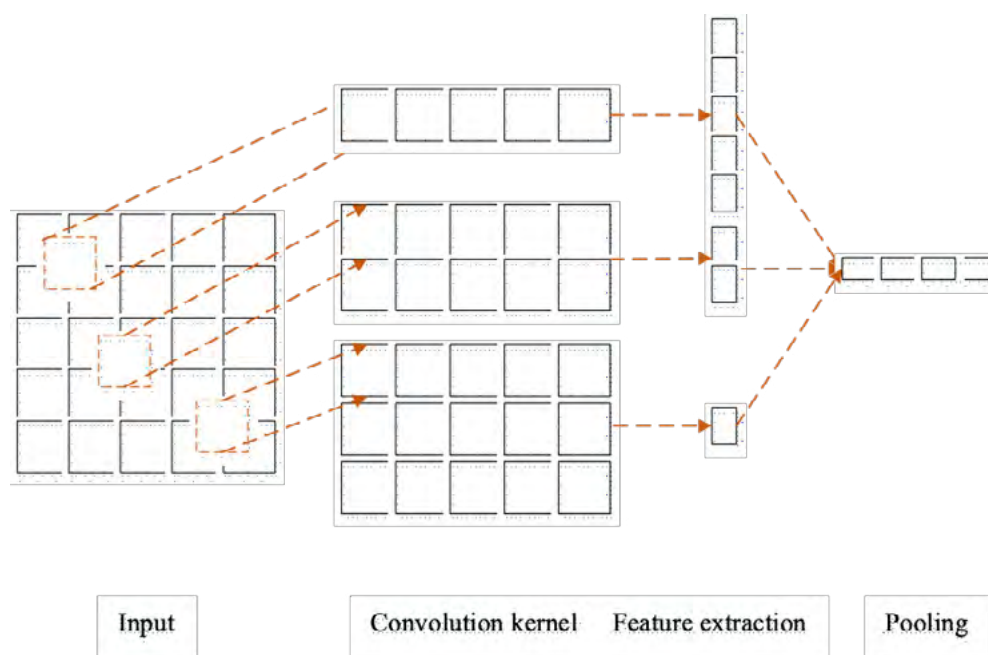
Figure 3. CNN network structure example

2.6. BILSTM NEURAL NETWORK LAYERS

LSTM is a special recurrent neural network (RNN) composed of one cell unit and three gates, is shown in Fig 4. The cell unit is the core computing power and records the current computing state. Forget gates, input gates, and output gates regulate the flow of information to and from memory cells. The forget gate clears the memory cells of useless information. The input gate selects the input information of the current memory cell. The output gate determines the final output of the information, so that the storage unit can effectively store the semantic information of a longer sequence.
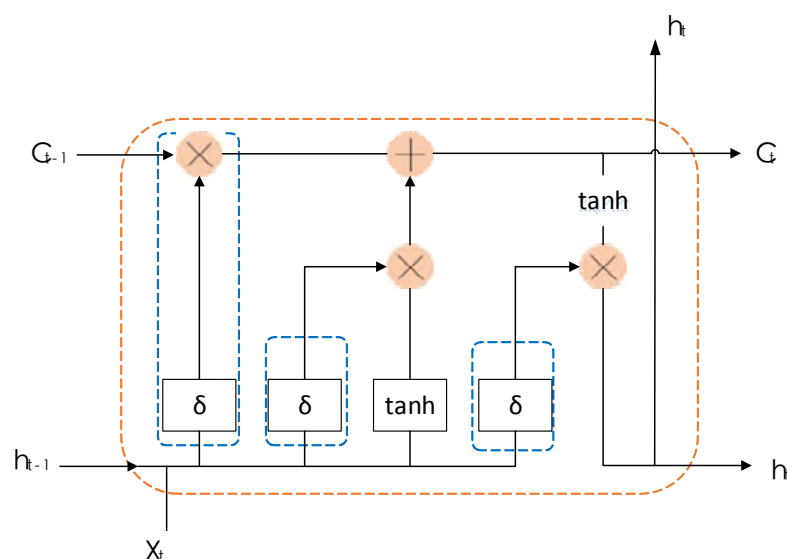
Figure 4. LSTM network structure example

(1) The LSTM unit calculation process is as follows:

$$i_t = \delta(W_i x_t + U_i h_{t-1} + b_i) \tag{4}$$

$$o_t = \delta(W_o x_t + U_o h_{t-1} + b_o) \tag{5}$$

$$f_t = \delta(W_f x_t + U_f h_{t-1} + b_f) \tag{6}$$

where x_t is the input text vector; δ is the sigmoid function and tanh is the activation function; $i_t,\ o_t, f_t$ are the input gate, output gate and forget gate, respectively.

(2) The information unit stored at time t is c_t, where the input gate and forget gate are not used to adjust the information unit.

$$c_t = \tanh(W_c x_t + U_c h_{t-1} + b_c) \tag{7}$$

where, $W_i, W_o, W_f\ and\ W_c$ are the weights of different gate control mechanisms on the input text vector x_t; $U_i,\ U_o,\ U_f\ and\ U_c$ are the weights of different gate control mechanisms on the hidden layer vector h_{t-1}; $b_i,\ b_o,\ b_f\ and\ b_c$ are bias vectors.

(3) Then, the unit information input gate at the previous moment is stored in c_t.

$$c_t = f_t c_{t-1} + i_t \widetilde{c}_t \tag{8}$$

$$h_t = o_t \tanh(c_t) \tag{9}$$

where, the hidden-layer h_t is the output gate and the storage gate c_t.

(4) Finally, the forward and backward outputs of the LSTM unit at time t are concatenated by using and building the BiLSTM network layer is shown in Fig 5.

$$h_t = [\overrightarrow{h_t}, \overleftarrow{h_t}] \in R^n \tag{10}$$

where n represents the vector set.
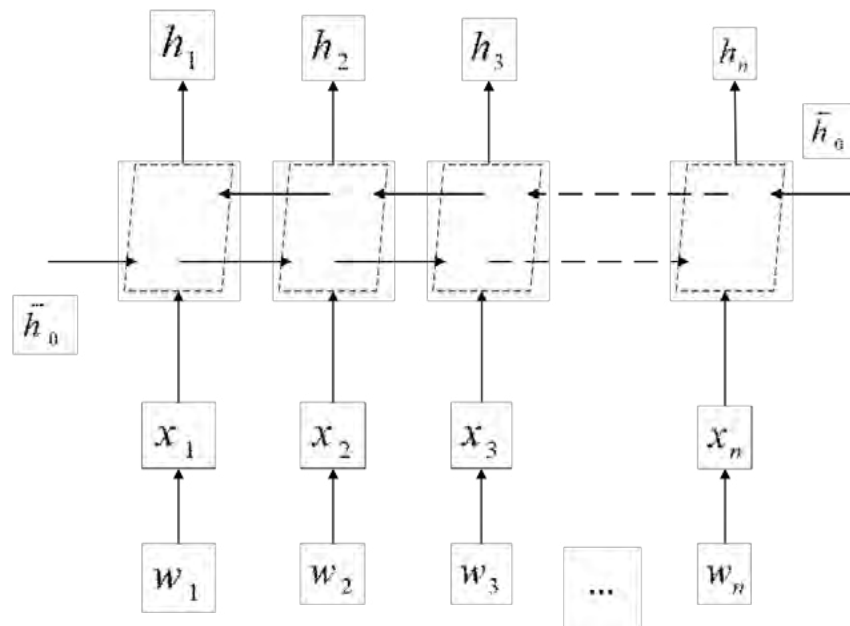
Figure 5. BiLSTM network structure example

2.7. ATTENTION MECHANISM

Although BiLSTM neural network can establish context-related semantic vector information, it does not highlight the relevance of current semantic information and context [21-22]. Introducing the attention mechanism at the output of the BiLSTM layer can effectively emphasize the importance in the contextual information, and enhance the feature expression of semantic information. The attention mechanism is shown in Fig 6.
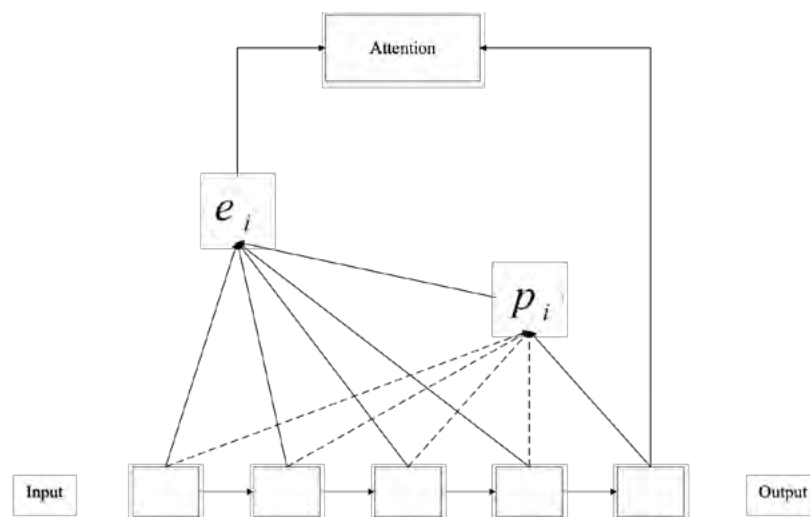
Figure 6. attention mechanism structure

(1) First, calculate the weight score e_i as shown in the formula:

$$e_i = \tanh(W_i h_t + b_i) \qquad (11)$$

where, W_i is the weight matrix; h_t is the BiLSTM output vector; b_i is the bias vector.

(2) Then, adopt the softmax function to calculate the attention mechanism weight score.

$$P_i = \frac{\exp(e_i)}{\sum_{i=1}^{n} \exp(e_i)} \quad (12)$$

(3) Finally, the point multiplication and accumulation operations are performed on the output vector h_t of the BiLSTM layer and the weight vector P_i to obtain the output Attention of the attention layer.

$$\text{Attention} = \sum_{i=1}^{n} P_i h_t \quad (13)$$

2.8. OUTPUT LAYER AND LOSS FUNCTION

A fully connected layer is introduced after the attention layer [23]. First, the weighted vector of text features is mapped into the label space of evaluation categories. Then the Dropout mechanism is introduced after the fully connected layer to avoid the weight update only relying on some features and model overfitting. Finally, the softmax classifier is evaluation category to which the text belongs, and the model prediction result is directly output.

Among them, set the softmax classifier loss function as the overall training of the model:

$$\text{Loss}\left(y, \hat{y}\right) = -\sum_{i=1}^{k} y_i \ln \hat{y}_i \quad (12)$$

where, $\hat{y}$ is the label normalization probability; y is the true label probability; the Adam optimizer is set to continuously update the model parameters and continuously reduce the loss function value of the model.

3. ACTUAL CASE ANALYSIS AND VERIFICATION

3.1. DATA DESCRIPTION

In the 2019-2021 online storage data of International Chinese Education Online Teaching Quality Evaluation, text is randomly selected as the corpus. The experiment is carried out by means of cross-validation, and the training set 80%, validation set 10% and test set 10%.

The development environment is Linux system, GPU uses NVIDIA GeForce RTX 2080Ti (11GB), Python version 3.6.5, framework uses pytorch1.7 and tensorflow1.15 version, CUDA uses version 10.1.

The experiment adopts a 3-layer CNN model architecture[24-25]. The word vector convolution windows are set to 3, 4, and 5 respectively. After the pooling operation, the outputs of each layer are fused to enrich the local features of the context. Set the number of LSTM units to 128 and the dropout ratio to 0.5. A multi-class cross-entropy loss function is used. Set the batch sample size to 32, the number of training rounds to 20, optimizer Adam, and cross-validation to evaluate the prediction performance, where models hyperparameter settings are shown in Table 3.

Table 3. Setting of experimental parameters

parameter	value	parameter	value
vee_win	100	activation	relu
vec_dim	4	lstm_untis	128
lr	0.001	dropout	0.5
max_len	100	optimizer	Adam
mum_filters	128	batch_size	32
kernel_size	3、4、5	epochs	20

3.2. MODEL PREDICTION AND EVALUATION INDEX

The experimental evaluation system includes recall rate (R), precision rate (P) and F_1 (F-measure) as indicators for evaluating model performance. The specific formulas of each standard are as follows:

$$R = \frac{TP}{TP + FN} \tag{14}$$

$$P = \frac{TP}{TP + FP} \tag{15}$$

$$F_1 = \frac{2PR}{P + R} \tag{16}$$

where, TP is the correct number of correct text predictions; FP is the correct number of incorrect text predictions; FN is the correct number of correct text predictions; F_1 is the harmonic mean of precision and recall.

3.3. COMPARISON OF PREDICTION RESULTS BETWEEN DIFFERENT MODELS

Mechanism of CNN neural network, LSTM and Attention mechanism in model fusion is also discussed. Ten groups of comparative experiments are set up, and the input is word2vec pre-trained word vector. To verify the influence of various models on the expression and extraction of text features when processing text sequences. The comparative experiment is constructed as follows.

(1) CNN model: CNN performs convolution, pooling, and Flatten operations on word vectors. The input extracts the local features, and uses the fully connected layer to reduce the dimension. Finally, the softmax classifier is used to output the prediction result.

(2) TextCNN model: Set 3 convolution kernel windows of different sizes. Convolutional layer and pooling layer with the same parameters, splicing the output vector of the pooling layer by line, enriching the semantic expression of local features of the text.

(3) LSTM model: The input sequence is used for backward semantic modeling, the high-level features of the text are extracted, the two fully connected layers are connected to reduce the dimension, and the prediction result is directly output.

(4) CNN_LSTM model: First use CNN to extract the local features, and then use LSTM to extract the backward semantic information output by CNN.

(5) LSTM_CNN model: first use LSTM for backward semantic modeling, and then use CNN to extract local features from the output of LSTM.

(6) CNN-BiLSTM model: First use CNN to extract the local features and then use BiLSTM to extract the forward and backward semantic information output by CNN, and further construct the feature expression of the text.

(7) BiLSTM model: Forward and backward semantic modeling is performed on the input sequence, high-level features of the text are extracted, two fully connected layers are connected to reduce the dimension, and the prediction result is directly output.

(8) CNN_Att model: CNN extracts the local features of the input sequence, and the Attention mechanism weights the text features to reduce the impact of noise features on the classification effect.

(9) BiLSTM_Att model: BiLSTM constructs the contextual semantic information of the input sequence, extracts the high-level features of the text, and the Attention mechanism weights the text features to reduce the impact of noise features on the classification effect.

(10) CNN_BiLSTM_Att model: CNN extracts the local features of the input sequence, and then uses BiLSTM to extract the forward and backward semantic information output by the CNN, and further constructs the feature expression of the text. The Attention mechanism weights the text features to reduce the influence of noise features on the classification effect.

Table 4. Results of different models.

Model	P/%	R/%	F_1/%
CNN	86.93	87.23	86.31
TextCNN	88.31	87.62	89.64
LSTM	89.20	90.31	91.24
CNN_LSTM	90.98	91.98	90.31
LSTM_CNN	92.35	93.09	93.02
CNN-BiLSTM	94.13	93.92	93.97
BiLSTM	93.16	94.36	92.49
CNN_Att	96.20	96.08	93.52
BiLSTM_Att	94.12	93.92	93.49
CNN_BiLSTM_Att	97.89	97.76	97.85
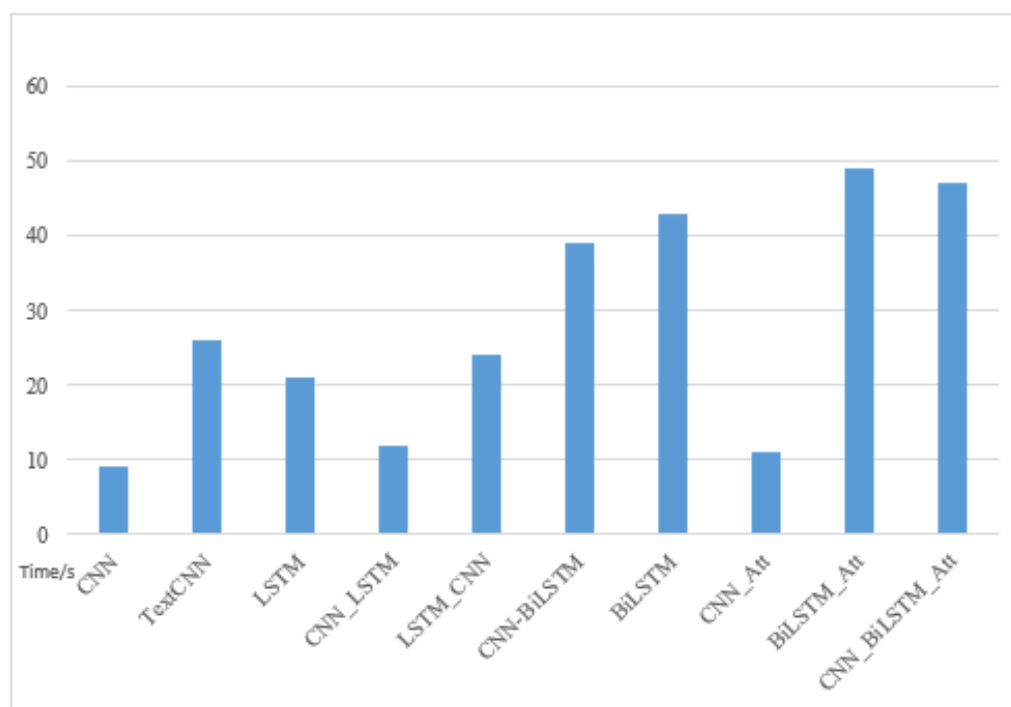
Figure 7. Execution time of models
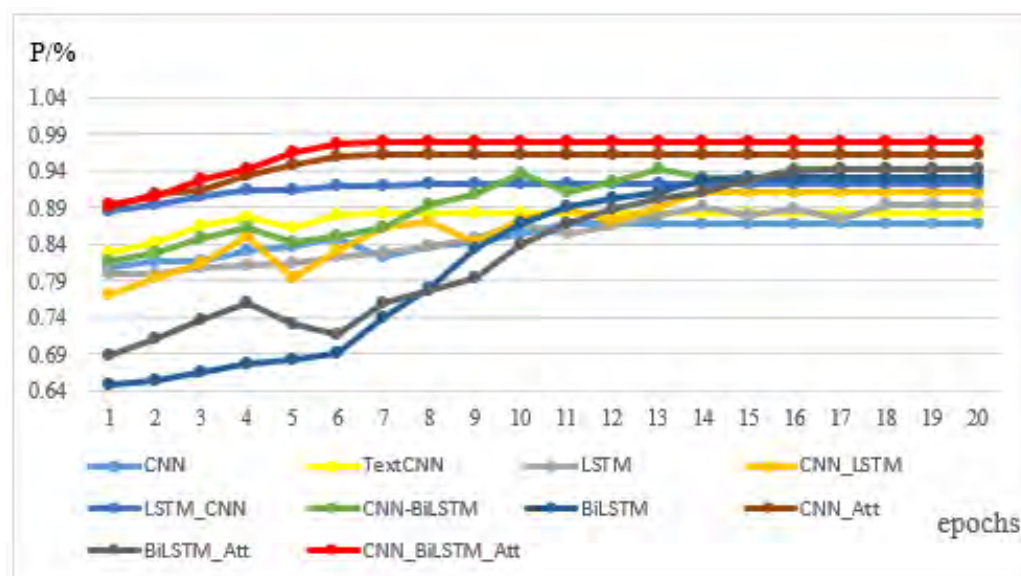
Figure 8. Precision trend of validation set of models

After multiple rounds of experiments and cross-validation of the experimental results, the evaluation results of various baseline models and fusion models are shown in Table 4, and the model execution time is shown in Fig 7. Visually demonstrate the superiority of the CNN_BiLSTM_Att model, the training process of each model is analyzed, and the accuracy change process of the validation set for each model training process is shown in Fig 8.

From the experimental results in Table 4, CNN_BiLSTM_Att model proposed in this paper has achieved the results in the evaluation index results, with F1 reaching 97.85%. Compared with other models, the overall effect is improved by 2%~5%. The superiority of this model can be obtained. According to the change trend of the accuracy rate of the validation set of various algorithm models during the training process, due to the characteristics of the corpus, the various models with CNN as the baseline basically reach the convergence state after 10 epochs, and the accuracy rate is high. The model with LSTM as the baseline has a turbulent trend as a whole, and it basically reaches convergence after 18 epochs. The variation trend of the accuracy rate of the validation set of the model in this paper is the best, reaching a state of convergence after 7 epochs, and the accuracy rate converges at 97.89%, which is significantly higher than other models in the comparison experiments, which further verifies the effectiveness and robustness of the model in this paper.

4. CONCLUSION

Aiming at the characteristics of online teaching quality evaluation of international Chinese education on the Internet, this paper first proposes the online teaching quality evaluation method of international Chinese education on the Internet to construct the evaluation standard system and to give weights to the evaluation indicators. Then, combined with the characteristics of CNN, LSTM and Attention mechanism, CNN_BiLSTM_Att-based Chinese education online teaching quality evaluation.

(1) The model extracts text local features within word windows through a multi-layer CNN structure. At the same time, the local feature representation of the concatenated text is used as the input of BiLSTM.

(2) BiLSTM performs forward and backward text semantic modeling to obtain high-level feature representations of text sequences.

(3) The Attention mechanism performs feature weighting to reduce the influence of noise features.

The experimental results show that the execution efficiency and accuracy of the CNN_BiLSTM_Att model have achieved excellent results in various model comparison experiments, which are suitable for online teaching quality evaluation of international Chinese education. In the following research, we will focus on further analysis from the aspects of word vector encoding, attention mechanism algorithm, overall model structure and model hyperparameter settings to improve the overall efficiency of the model.

CONFLICT OF INTEREST

The authors declared that there is no conflict of interest

REFERENCES

(1)   Wu, Y., & Wang, J. (2022). **Three-stage blended Chinese teaching online and offline for international students: a case study on Chinese teaching for international students in s university**. *Journal of Higher Education Research*, 3(2), 207-211.

(2)   Yang, H., Chen, J., & Zhan, X. (2022). **"Integrated" Ideological and Political Education System for TCSOL Major**. *The International Conference on Artificial Intelligence and Logistics Engineering. Springer, Cham.*

(3)   Kong, L., Woods, O., & Zhu, H. (2022). **The (de) territorialized appeal of international schools in china: forging brands, boundaries and inter-belonging in segregated urban space**. *Urban Studies*, 59.

(4)   Owens, L. M. D., & Kadakia, C. (2022). **Instructional Design in a Digital Age: A New Model Is Taking Hold**. *The Learning Ideas Conference. Springer, Cham.*

(5)   Yan, Y. (2021). **Analysis on the strategies of information technology to improve autonomous learning in higher vocational english teaching.**

(6)   Liu, L., & Tsai, S. B. (2021). **Intelligent recognition and teaching of english fuzzy texts based on fuzzy computing and big data.** *Wireless Communications and Mobile Computing*, 2021(1), 1-10.

(7)   Kaire, U., Mari, K., & Liisa, P. (2018). **Relations between students' perceptions of the teaching-learning environment and teachers' approaches to teaching: a qualitative study**. *Journal of Further & Higher Education*, 1-20.

(8)   Mishra, A. R., Chandel, A., & Saeidi, P. (2022). **Low-carbon tourism strategy evaluation and selection using interval-valued intuitionistic fuzzy additive**

ratio assessment approach based on similarity measures. *Environment, Development and Sustainability: A Multidisciplinary Approach to the Theory and Practice of Sustainable Development*, 24.

(9) Sang, G., Valcke, M., Braak, J. V., Tondeur, J., & Chang, Z. (2011). **Predicting ict integration into classroom teaching in chinese primary schools: exploring the complex interplay of teacher-related variables**. *Journal of Computer Assisted Learning*, 27(2), 160-172.

(10) Chen, Z. F., Zhi-Gang, Y. U., Liu, S., & Li-ping. (2010). **Research on software engineering one frame with four aspects in practical teaching system**. *Computer Education* (9), 136-139.

(11) Hong, TAN, College, of, International, & Studies, et al. (2014). **The problems in rural english teaching and the optimization path: a study based on the chinese general social survey data**. *Asian Agricultural Research* (8), 4.

(12) Vandebroek, I., Thomas, E., Sanca, S., Damme, P. V., & Kimpe, N. D. (2008). **Comparison of health conditions treated with traditional and biomedical health care in a quechua community in rural bolivia**. *Journal of Ethnobiology and Ethnomedicine*, 4(1), 1.

(13) Chen, W., Ye, S., Xu, G., & Yang, L. (2022). **Futures Trend Forecasting Based onAttention Hybrid Neural Network**. *The International Conference on Natural Computation, Fuzzy Systems and Knowledge Discovery. Springer, Cham.*

(14) Ying L, Qian Nan Z, Fu Ping W, et al. (2021). **Adaptive weights learning in CNN feature fusion for crime scene investigation image classification[J]**. Connection Science, 33(3), 719-734.

(15) Zhao, P., & Peng, J. (2001). **High efficient and intensified use of urban land and its evaluation index system**. *Resources Science.*

(16) Liu, F., & Hai, H. L. (2005). T**he voting analytic hierarchy process method for selecting supplier**. *International Journal of Production Economics*, 97(3), 308-317.

(17) Nydick, R. L., & Hill, R. P. (1992). **Using the analytic hierarchy process to structure the supplier selection procedure**. *International Journal of Purchasing & Materials Management*, 28(2), 31-36.

(18) Mei, & Liang. (2011). **Research of index weighting on evaluation index system of partner selection in technical standard alliance by using fuzzy analytic hierarchy process**. *Energy Procedia*, 13, 9922-9929.

(19) Sadr, H., & Soleimandarabi, M. N. (2022). **Acnn-tl: attention-based convolutional neural network coupling with transfer learning and contextualized word representation for enhancing the performance of sentiment classification**. *The Journal of Supercomputing*, 78(7), 10149-10175.

(20) Shan W. (2022). **Digital streaming media distribution and transmission process optimisation based on adaptive recurrent neural network[J]**. *Connection Science*, 34(1), 1169-1180.

(21) Wang, Xuan, Xu, Ruifeng, He, & Yulan, et al. (2017). **Improving sentiment analysis via sentence type classification using bilstm-crf and cnn**. *Expert Systems with Application.*

(22) X. Ning, K. Gong, W. Li, and L. Zhang. (2021). **JWSAA: Joint Weak Saliency and Attention Aware for person re-identification**, *Neurocomputing*, 453, 801-811. https://doi.org/10.1016/j.neucom.2020.05.106.

(23) W Cai, B Zhai, Y Liu. (2021). **Quadratic polynomial guided fuzzy C-means and dual attention mechanism for medical image segmentation**. *Displays*, 70, 102106. https://doi.org/10.1016/j.displa.2021.102106.

(24) Kaseng, F., Lezama, P., Inquilla, R., y Rodriguez, C. (2020). **Evolution and advance usage of Internet in Peru**. *3C TIC. Cuadernos de desarrollo aplicados a las TIC*, 9(4), 113-127. https://doi.org/10.17993/3ctic.2020.94.113-127

(25) Yan Kang,Jinling Song,Mingming Bian,Haipeng Feng & Salama Mohamed. (2022). **Red tide monitoring method in coastal waters of Hebei Province based on decision tree classification**. *Applied Mathematics and Nonlinear Sciences, 7(1), 43-60.* https://doi.org/10.2478/AMNS.2022.1.00051.

/06/

3C Tecnología. Glosas de innovación aplicadas a la pyme. ISSN: 2254-4143

Ed.43 | Iss.12 | N.1 January - March 2023

RESEARCH ON INNOVATION OF DAILY IDEOLOGICAL AND POLITICAL EDUCATION FOR COLLEGE STUDENTS BASED ON DEEP LEARNING MODEL

Xianwei Zhang*

College of Economics, Shenzhen Polytechnic, Shenzhen, Guangdong, 518055, China

zxw5460@126.com

Yueyan Zhang

Department of Pharmacy, The Second People's Hospital of Longgang District of Shenzhen, Shenzhen, Guangdong, 518112, China

ABSTRACT

Various network information is mixed, which has a great impact education, with continuous development informatization. However, development of informatization has provided convenience for the daily ideological political education, effectively solved time and space limitation daily ideological, and sustainable development. Therefore, positively influence formation of college students' noble morality. The informatization education resources can be effectively integrated, and the utilization rate resources improved. Information resources of ideological and political education, we propose a complete block diagram of the daily ideological system of college students. First, design a complete interactive analysis questionnaire for college student's role of daily ideological and political education. Through questionnaire survey method, the survey and statistical weight scores were conducted to analyze the proportion of each indicator. Then, the framework of education in the network environment is adopted, which includes, class tutoring learning, class interactive learning, class in-depth study, process evaluation and feedback evaluation. Learn through a period of ideological and political education. Collect data as our training corpus. Finally, the training prediction model BERT-BiLSTM-CRF-based trained. Prediction of F1 BERT-BiLSTM-CRF -based can reach 91.09%.

KEYWORDS

PAPER INDEX

1.   INTRODUCTION

Daily ideological, political education refers to political education activities that characterized by practicality, pertinence, and interactivity in addition to ideological and political theory courses [1-3]. Thematic education, campus culture, community activities, mental health education, social practice, financial aid education.

With development social informatization, daily ideological political education of college students has always been focus attention [4-6]. Exchanges and social information are numerous and complex [7]. The circulation of some information affects the formation of college students' ideological character. Today's daily ideological education guide cultivation morality through teachers' reasoning as in the past. Corresponding innovations and changes, which can positively affect the formation noble morality information resources [8]. Through the mining and utilization of new and modern network information resources in informatization, the informatization education resources can be effectively integrated [9].

At present, informatization and data, and various fields have begun to the industry [10-12]. Innovation work of college students, how times and develop scientifically data technology, deep learning technology to important issue faced [13-15]. Promote development of ideological and political education, so that content of daily ideological and political education is increasingly enriched and the means are increasingly perfected. Online resources for teaching have the following effects:

(1) The concept of mining resources, rejects information technology methods such as multimedia courseware for teaching [16].

(2) The information-based educational resources the information-based resources are simply applied to the daily ideological, and have not exerted the greatest effect [17].

(3) Information platforms are flooded complex information, and some unhealthy resources are also invisibly absorbed by students, which directly affects healthy development of college students' political education [18].

Data mining utilization of information resources high-quality information education resources play the growth [19]. Correct data helps to promote the cultivation of high morality and correct outlook on life and values for college students. It is required deep understanding of the importance of information resource mining and to carry out effective mining and utilization healthy education [20]. Through deep learning technology recommendation and prediction ultimately improve daily training program for college students.

Neural network gradually develops and matures [21-23]. Emergence word vectors can solve problem of data sparseness in high-dimensional space, and can also add more features. The classification and recognition method Bi-directional Long Short-Term Memory (BiLSTM)-based has improved accuracy compared with traditional methods [24]. In addition, many pre-training models such as Bidirectional Encoder Representations from Transformers (BERT), Long Short-Term Memory (LSTM) networks, Transformer, etc. have recently been used, combined with self-attention

mechanism, transfer learning, etc. to improve classification accuracy methods [25]. BERT-BiLSTM-CRF classification method based on BERT and BERT-BiLSTM is compared with CRF, Convolutional Neural Network (CNN), LSTM and other methods, and obtained. Higher classification accuracy [26].

Therefore, we propose a training plan based on improving the recommendation and prediction through deep learning technology, ultimately. Among them, the main work is highlighted as follows:

(1) Design a complete set of interactive analysis questionnaires. Through the questionnaire survey method, the survey and statistical weight scores were conducted to analyze the proportion of each indicator.

(2) Adopt the framework in the network environment, which includes five aspects: class tutoring learning, class interactive learning, class in-depth study, process evaluation and feedback evaluation. Learn through a period of ideological and political education. Collect data as our training corpus.

(3) Design and propose CNN、CNN-CRF、LSTM、LSTM-CRF、BiLSTM、BiLSTM-CRF and BERT-BiLSTM-CRF. The experimental results are analyzed and discussed.

2.   METHODOLOGY

2.1. INTERACTION ANALYSIS METHOD OF IDEOLOGICAL AND POLITICAL EDUCATION

Research application of new methods of data in ideological and political education. Deep learning analysis data method can predict and analyze the students' network thinking and behavior. Through mining and data to establish a deep learning model, it can realize the whole-process and full-sample analysis of individual students or groups, and realize personalized recommendation for innovation and reform[27-28]. We conduct online questionnaire surveys and statistical analysis through the following five aspects, is shown Table 1.

Table 1. Questionnaire

Student Group Category\Evaluation Proportion		Proportion of evaluation grades (%)					
		0	1	2	3	4	Weights
Different types of students	"985" college students	6.0	5.1	28.6	36.0	24.3	
	Non-"985" college students	3.1	6.0	27.4	38.1	25.4	
Students of different disciplines	Humanities	3.8	7.2	25.4	37.0	26.6	
	Social studies	3.8	6.0	28.7	34.7	25.8	
	Science and Engineering	1.9	7.9	25.4	40.0	24.8	
	Agricultural disciplines	2.9	6.1	41.2	25.8	23.0	
	Medical disciplines	1.8	4.5	29.7	37.9	26.1	

	Undergraduate (freshman)	4.0	7.1	28.3	36.6	24.0
	Undergraduate (Sophomore)	4.2	6.9	29.1	20.8	29.2
Students of different ages	Undergraduate (Junior)	4.2	4.9	25.7	35.2	30
	Undergraduate (senior year)	2.9	13.8	23.3	23.9	36.1
	Postgraduate	3.0	6.9	27.7	38.1	23.4
	PhD student	2.5	4.8	27.5	36.3	29.8
Students with cadre experience (yes/no)	Officer experience (yes)	3.0	8.2	26.4	38.7	23.7
	Cadre Experience (No)	2.7	6.4	27.1	38.1	25.7
Political status	Party member (yes)	3.1	6.7	26.6	38.1	25.5
	Party member (no)	4.2	7.9	35.1	32.8	20.0

(1) College students' overall evaluation of campus cultural activities.

(2) The situation of the Party and Youth League organizations where different groups of college students are located to carry out organizational life. College students of different age groups, disciplines, and political outlooks have significant differences in the conditions of their party and youth organizations to carry out organizational life.

(3) The satisfaction evaluation of college students on the activities of the Party and Youth League.

(4) The development status education for college students.

(5) Participating in student associations and the satisfaction evaluation of student association activities.

2.2. FRAMEWORK OF IDEOLOGICAL AND POLITICAL EDUCATION IN THE NETWORK ENVIRONMENT

Effective use of network resources ideological and political educator. Improve work effectiveness is urgent. We build a set of ideological education work framework in the network environment, Fig 1.
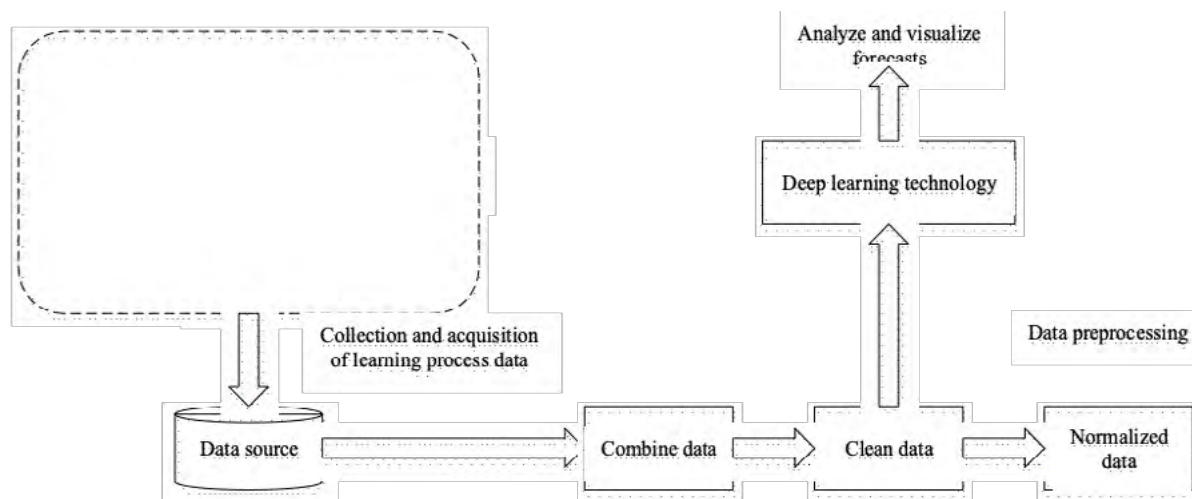
Figure 1. Network Environment

(1) Pre-class tutoring: Pre-class tutoring is the preparatory work for classroom teaching. The key point of tutoring learning is to use the ideological education and teaching materials provided by teachers to allow students to independently find out the ideological tasks and difficulties of the study unit, so that classroom listening is more targeted. The method is to use the "online ideological and political education" or "Communist Youth League ideological education" video function module of the network to issue the pre-class autonomous learning content (the content can be discussion or divergent thinking, etc.) to each student or each group.

(2) Interactive learning in class: Questionnaires about students' difficult points, and then use the questionnaire survey module to interact with students. At the same time, teach knowledge points by watching and other methods.

(3) In-depth study after class: In-depth study after class refers to an important process in which teachers use question answering discussions or tests to conduct complementary learning with students after class teaching. Through this stage, consolidate achieve the teaching purpose of in-depth understanding and further improvement.

(4) Process assessment and evaluation: Assessment and evaluation refers to the process in which teachers need to evaluate the teaching link in a timely manner, which can be carried out by using the assessment question bank (note that this process is the data automatically generated by the system). Teachers only need to give praise to students with outstanding performance and good learning effect motivate other students.

(5) Feedback or evaluation: Students give feedback on the pre-class, after-class, and assessment. Final calculation ratio is converted into a score, in which we divide the percentile system into four grades, 0~20, 20~40, 40~60, 60~80 and 80~100, and collect the information in Table 1 and the selected courses. Information such as name and viewing time are used as a corpus.

2.3. BERT-BILSTM-CRF CONSTRUCTION

Language preprocessing, a language task for classification, has been a hot research topic. Compared with traditional language models, it is more conducive to classification for classification tasks. Collected in this paper contains text and scores. For the mixed text of text and scores, corresponding features are extracted in the first layer. BERT-BiLSTM-CRF framework is shown in Fig 2. Divided into 4 layers:

(1) BERT and normalization layer. BERT can represent polysemy, and the corpus is pre-trained by BERT, as shown in Fig 3. At the same time, normalization is performed for the score features, and the value range of all features is between [0, 1].

(2) Second layer: BiLSTM layer. BiLSTM uses forward-LSTM and backward -LSTM to capture the contextual features of the text.

(3) Third layer: Attention layer, which different levels of contextual information, assigns different weights to it, and captures the latent semantic features between texts.

(4) Fourth layer: CRF to ensure the predicted labels. CRF to decode and label the output results, and extract and classify entities.
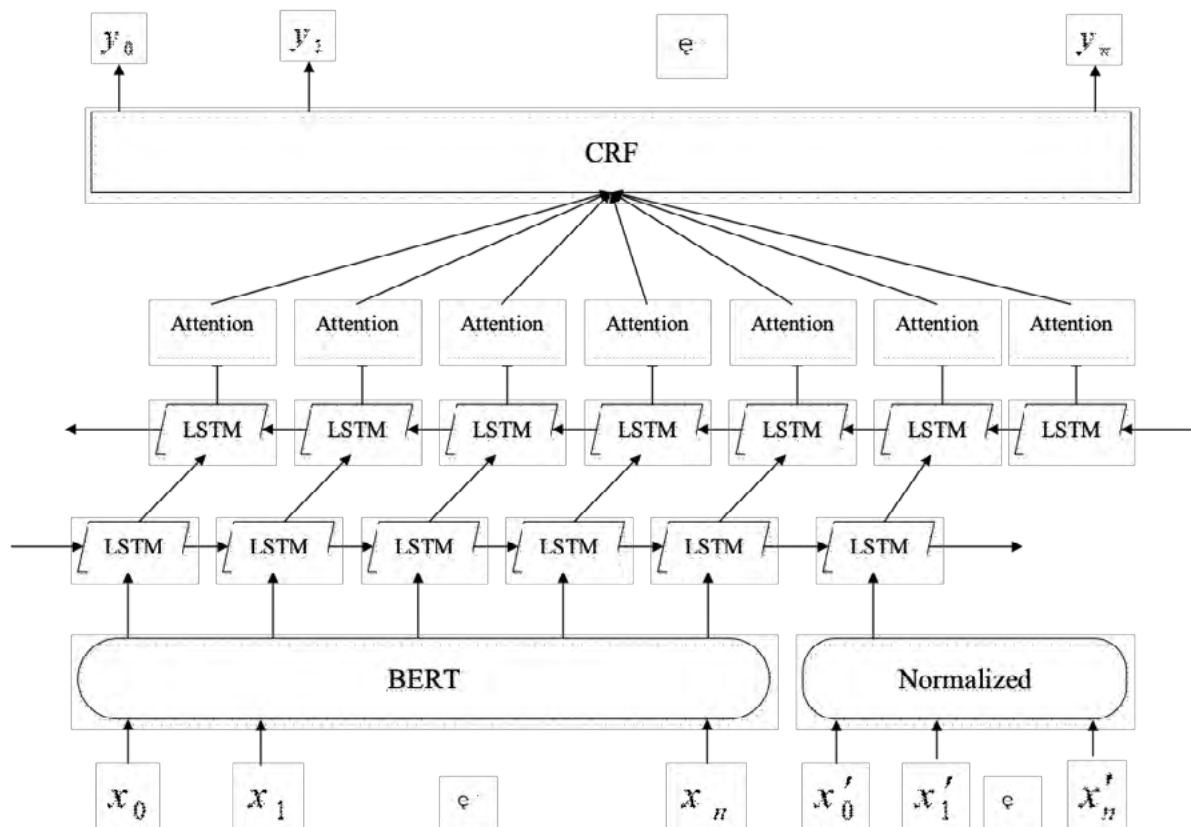
Figure 2. BERT-BiLSTM-CRF framework
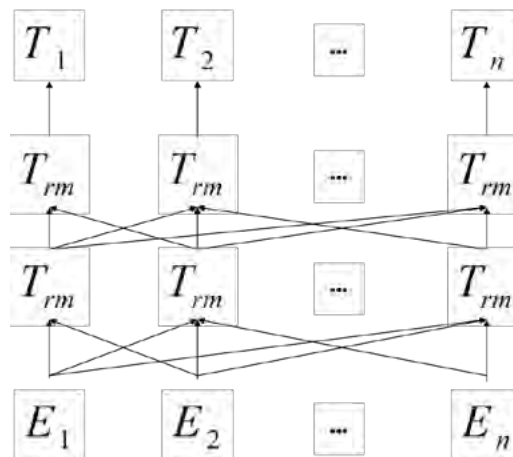
Figure 3. BERT's network structure

2.3.1. BERT AND NORMALIZATION

Language models through one-hot, Word2Vec, ELMO, GPT to BERT. However, module adopted in this paper performs pre-processing on sentences, according to the characteristics of Chinese word segmentation, the method of whole word Mask is applied to Chinese. In the whole word Mask.

Deep network based on "self-attention mechanism", and its encoder structure is shown in Fig 4. Do not have the ability to obtain the sequence of the entire sentence

like RNN, so to solve this problem, Transformer adds position encoding before data preprocessing, and sums it with the input vector data to get the relative position.
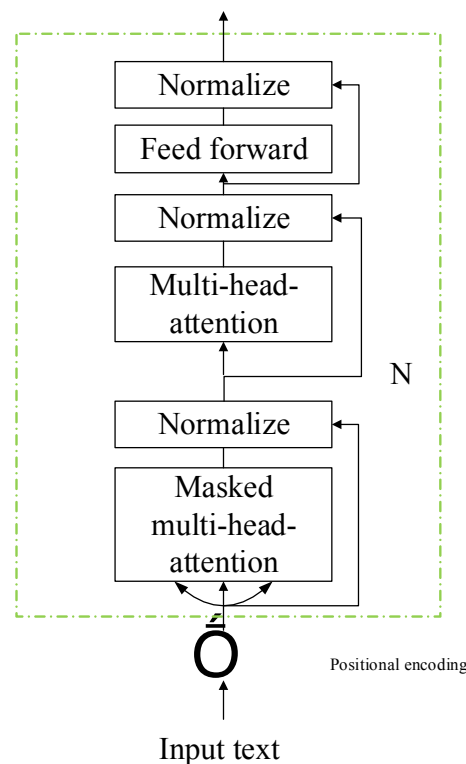
Figure 4. Transformer

First, word segmentation text sequence is obtained through word segmentation processing. Part of the word segmentation sequence is used for whole word Mask, in which a special mark [CLS] is added at the beginning of the sequence, and the sentences are separated by a mark [SEP].

For score value, we use normalization processing. First, the distance digital feature (column) is regarded as the unit 1, and then we look at the ratio of the distance between x and the minimum value to the total distance. The final output is a percentage between [0,1].

$$\frac{X - Min}{Max - Min} \tag{1}$$

where Min and Max are the minimum and maximum values of the property, respectively.

$$\text{Attention}(Q, K, V) = Softmax(\frac{QK^T}{\sqrt{d_k}})V \tag{2}$$

where, Q, K, V are word vector matrices, and d_k is the Embedding dimension.

The multi-head attention mechanism is projected through multiple different linear transformation pairs:

$$\text{MultiHead}(Q, K, V) = Concat(head_1, head_2, ..., head_n)W^0 \qquad (3)$$

$$head_1 = Attention(QW_i^Q, KW_i^K, VW_i^V) \qquad (4)$$

where W is the weight matrix. Location information in different spaces.

ReLU and linear activation function form a fully connected feedforward network (FFN).

$$\text{FNN(Z)} = \max\left(0, ZW_1 + b_1\right)W_2 + b_2 \qquad (5)$$

where the output of the multi-head attention mechanism is denoted as Z, and b is the bias vector.

2.3.2. BILSTM

The relevant information of the previous moment cannot be used for the next moment. Recurrent Neural Networks (RNNs) have this capability. However, it is difficult to learn relevant information when the predicted points are far away from the dependent relevant information. LSTM can solve this problem very well and learn long-term dependency information. LSTM addresses the exploding or vanishing gradients that occur during RNN training. Unit structure is shown in Fig 5.
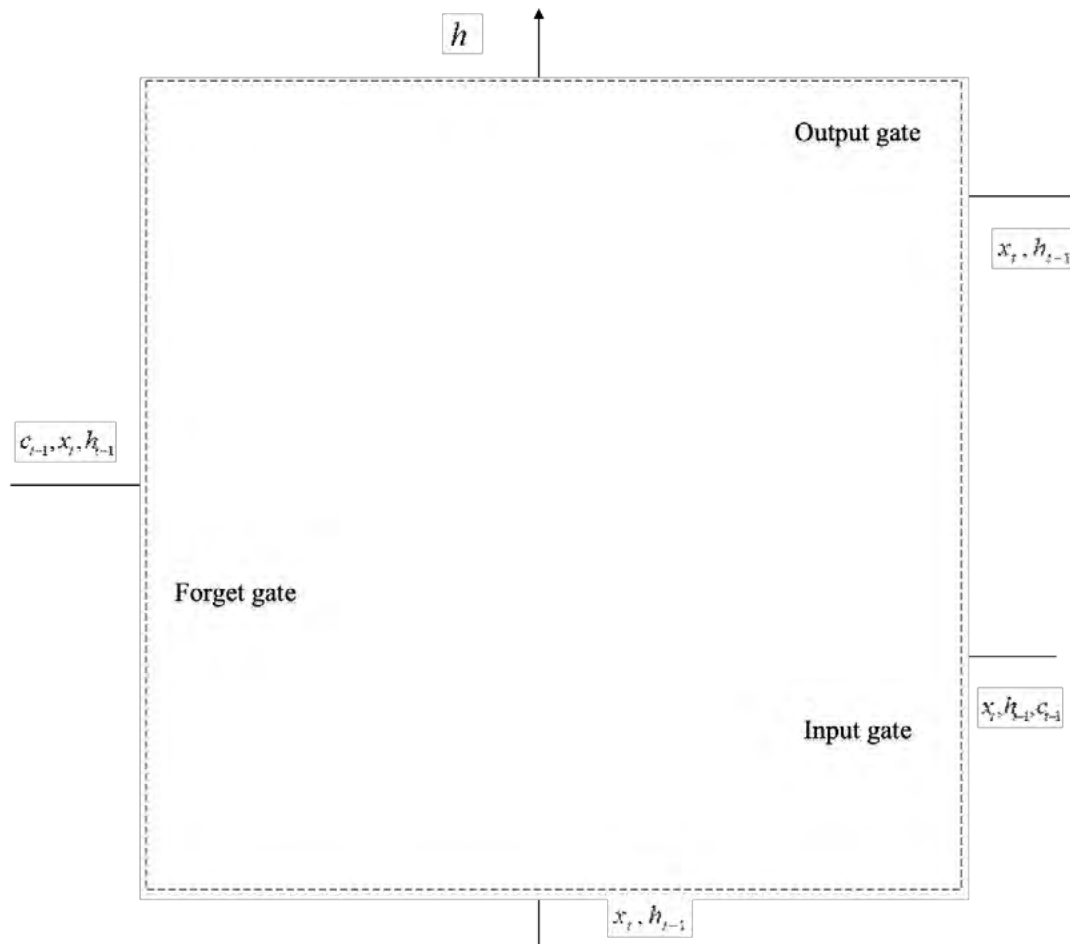
Figure 5. LSTM

The common function of input and forgetting gate is to discard the useless sequence information. For entire structure, the result of multiplying the output gate. Its structure is expressed by the formula as follows:

$$i_t = \delta(W_i x_t + U_i h_{t-1} + b_i) \tag{6}$$

$$o_t = \delta(W_o x_t + U_o h_{t-1} + b_o) \tag{7}$$

$$f_t = \delta(W_f x_t + U_f h_{t-1} + b_f) \tag{8}$$

where x_t is the input text vector; δ is the sigmoid function; tanh is the activation function; i_t, o_t, f_t are the input gate, output gate and forget gate, respectively.

Unit of information stored is $cell_t$, where input gate and forget gate are not used to adjust the information cell.

$$cell_t = \tanh(W_c x_t + U_c h_{t-1} + b_c) \tag{10}$$

where, W_i, W_o, W_f and W_c are the weights of different gate control mechanisms on the input text vector x_t; U_i, U_o, U_f and U_c are the weights of different gate control mechanisms on the hidden layer vector h_{t-1}; b_i, b_o, b_f and b_c are bias vectors.

Unit information of forget gate and previous moment is stored in $cell_t$.

$$cell_t = f_t cell_{t-1} + i_t \tilde{cell}_t \tag{11}$$

$$h_t = o_t \tanh(cell_t) \tag{12}$$

where, the hidden layer h_t is calculated by the output gate and the storage gate $cell_t$.

At the same time, input a word vector B output from the RERT pre-training language model to BiLSTM, X_t represents the input data at time t, $\overrightarrow{h}_t$, $\overleftarrow{h}_t$ and $\overrightarrow{h}_t = (\overrightarrow{h}_0, \overrightarrow{h}_1, \ldots, \overrightarrow{h}_t)$ and $\overleftarrow{h}_t = (\overleftarrow{h}_0, \overleftarrow{h}_1, \ldots, \overleftarrow{h}_t)$.

Finally, the two are combined to obtain the output of BiLSTM at $h_t = [\overrightarrow{h}_t, \overleftarrow{h}_t]$, and the forward and backward outputs of the LSTM unit at time t are spliced. Get a sequence of hidden states t_0, t_1, $\ldots$, t_i.

$$h_t = [\overrightarrow{h}_t, \overleftarrow{h}_t] \in R^n \tag{13}$$

where n represents the vector set.

2.3.3. ATTENTION MECHANISM

BiLSTM can obtain contextual information, but does not highlight the latent semantic correlation between current sequence feature information and contextual

information. Therefore, an attention layer is added after the BiLSTM network to mine the latent semantic features between texts.

First, word vector sequence into BiLSTM to extract contextual features.

$$v_t = \tanh(h_t) \tag{14}$$

where, the attention weight is v_t; h_t is the feature vector output by the BiLSTM layer.

Then, the attention mechanism different weights to the different feature vectors of the text.

$$P_t = \frac{\exp(v_t)}{\sum_{t-1}^{n} \exp(v_t)} \tag{15}$$

attention weight probability vector is P_t.

Finally, contextual features and latent semantic features is generated.

$$\alpha_t = \sum_{t-1}^{n} P_t h_t \tag{16}$$

where, the attention weights are configured as α_t.

2.3.4. CRF

CRF chooses conditional random fields for sequence labeling. Classification task, dependencies between adjacent labels. CRF can obtain an optimal prediction sequence through the relationship between adjacent tags. It can make up for the shortcomings of BiLSTM.

First, input any sequence $X = (x_0, x_1, \ldots, x_n)$.

Then, number n words and the number of k labels. For prediction sequence $Y = (y_0, y_1, \ldots, y_n)$, the score function:

$$S(X, Y) = \sum_{i=0}^{n} A_{y_i, y_{i+1}} + \sum_{i=1}^{n} P_{i, y_i} \tag{17}$$

where, A_{ij} represents score; A represents transfer score matrix; The probability that the Y is generated is:

$$P(Y \mid X) = \frac{e^{s(X,Y)}}{\sum_{Y \in Y_X} s(X, Y)} \tag{18}$$

Finally, decoder the largest score.

$$\text{In}\left(P(Y\,|\,X)\right) = s(X, Y) - \text{In}(\sum_{Y \in Y_X} s(X, Y)) \qquad (19)$$

$$Y^* = argmax\, s(X, Y)_{Y \in Y_X} \qquad (20)$$

where, Y represents real annotation sequence; Y_X represents possible annotation sequences.

3. EXPERIMENTAL RESULTS AND ANALYSIS

3.1. DATASET AND TRAINING ENVIRONMENT CONFIGURATION

The corpus used in this experiment includes student names, place names, course names, and ages. The experimental data mainly comes from the daily ideological education storage data of a college from 2019 to 2022, including 502 electronic feedback questionnaires with a total of 16,465,469 words. The data in the electronic feedback questionnaire was 10% as the test set, 10% as the validation set and 80% as the training set. IData, the marked data will not be changed, and if there are missing features, 0 will be added.

Table 3. Experimental Environment and Hyperparameters

Category	configuration			configuration
Hardware	CPU	GTX 2080Ti	RAM	128GB
	GPU	E5-2650L V3-8	video memory	11GB
	operating system	Ubuntu 18.04		Linux 64
Software	Python	3.6.12	Tensorflow	2.2.0
	CUDA	11.0		
Parameter	Transformer layer	12	Hidden layer dimension	768
	optimizer	Adam	learning rate	0.001

Training process, Adam optimizer is used; learning rate is 0.001. At the same time, LSTM_dim is 200, batch_size is 64, and max_seq_len is 128. In order to prevent the overfitting problem. The specific hyperparameter settings and training environment configuration is shown in Table 3.

3.2. DATASET LABELING AND EVALUATION METRICS

The BIO system, which has 7 labels. In this paper, the recall rate R, precision rate P and F1 value are used to evaluate the performance of the model. The calculation methods of each evaluation index are as follows:

A is the total number of entities, and B is the predicted number.

$$P = \frac{a}{B} \times 100\% \qquad (21)$$

$$R = \frac{a}{A} \times 100\% \qquad (22)$$

$$F_1 = \frac{2PR}{P + R} \times 100\% \qquad (23)$$

3.3. RESULTS AND ANALYSIS

On the dataset, CNN、CNN-CRF、LSTM、LSTM-CRF、BiLSTM、BiLSTM-CRF and BERT-BiLSTM-CRF are used for performance analysis, are shown in Table 5.

(1) CNN model and the LSTM model, it can be seen that LSTM is better than the training dataset in this paper.

(2) CNN, LSTM model and CNN-CRF, LSTM-CRF model, it can be seen that after adding CRF module, the F1 value is improved. This is because CRF can take full advantage of the association of adjacent tags.

(3) LSTM-CRF and the BiLSTM-CRF. BiLSTM performs better than LSTM, because LSTM use the following information.

(4) BiLSTM-CRF and the BERT-BiLSTM-CRF, the F1 value improved, because the BERT deeply extract text semantic information and fully characterize polysemy.

(5) Among them, the attention mechanism makes the model focus more on finding input information more relevant to the current output, strengthens the latent semantic correlation between current information and contextual information, and improves the accuracy of prediction.

Table 5. Comparison of the effects of each model (/%)

Model	P	R	F_1
CNN	80.83	79.52	79.67
LSTM	81.59	82.18	81.37
CNN-CRF	81.16	80.87	80.15
LSTM-CRF	82.68	83.12	82.34
BiLSTM	83.48	83.12	83.02
BiLSTM-CRF	85.87	85.45	85.09
BERT-BiLSTM-CRF	91.63	90.56	91.09

At the same time, the time required for each model training round is also compared, as shown in Table 6. Traditional model is about 15 times that of the BERT-BiLSTM-CRF. Training time of the BERT-BiLSTM-CRF is the least among all models, indicating that the BERT of the whole word Mask has higher training efficiency. Compares and analyzes the update of the F_1 value in the first 25 rounds, as shown in Fig 6.

Table 6. Training time (/s)

Model	Time
CNN	1089
LSTM	1834
CNN-CRF	227
LSTM-CRF	392
BiLSTM	452
BiLSTM-CRF	351
BERT-BiLSTM-CRF	120
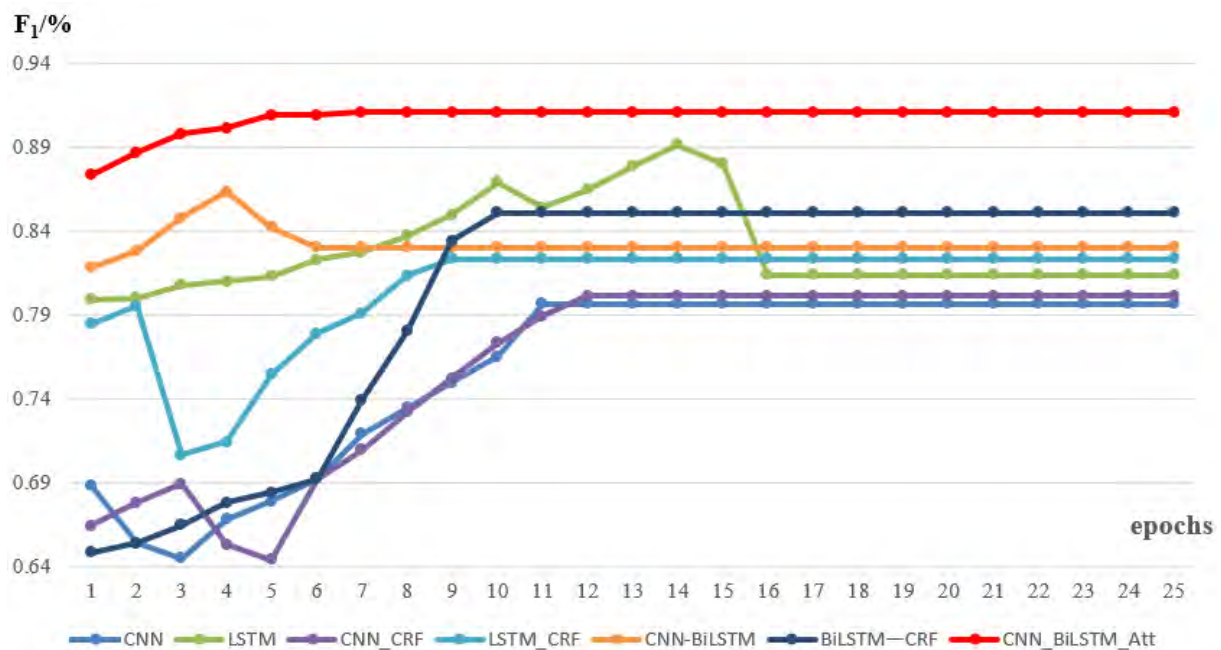
Figure 6. Experimental results

CONCLUSION

In this paper, information resources are used to positively influence the formation of college students' noble morality. Informatization education resources can be effectively integrated, and the utilization rate of the ideological and political education resources can be improved. (1) Design complete interactive analysis questionnaires for college students to evaluate the role of daily ideological and political education. Through questionnaire survey method, survey and statistical weight scores were conducted to analyze the proportion of each indicator.

(2) Adopt the ideological political education work framework, which includes five aspects: class tutoring, class interactive learning, class in-depth study, process evaluation and feedback evaluation. Learn through a period of ideological and political education. Collect data as our training corpus.

(3) Design and propose CNN、CNN-CRF、LSTM、LSTM-CRF、BiLSTM、BiLSTM-CRF and BERT-BiLSTM-CRF. Experimental results are analyzed and discussed.

Finally, the training prediction model based on the BERT-BiLSTM-CRF model is trained and compared with other models. Experimental results show prediction accuracy based on the BERT-BiLSTM-CRF is the best. Deep learning prediction is only a reference direction, and practical application.

CONFLICT OF INTEREST

The authors declared that there is no conflict of interest

REFERENCES

(1)   Wang, D. (2005). **Construct of the content system of ideological and political education in human concern**. *Teaching & Research.*

(2)   Shi, Y. (2006). **On the teaching students in accordance with their aptitude in the ideological and political education of students in vocational colleges.** *Vocational Education & Economic Research(Journal of Loudi Vocational & Technical College)*, 14(5), 679-691.

(3)   Jia, C., & Dan, L. (2016). **On ways to infiltrate ecological civilization education into ideological and political education of higher vocational colleges**. *Science education article collects*, 56(4), 337-341.

(4)   Geng, S., & Kang, Y. (2012). **The innovation of the subject in ideological and political education from the prospective of social interconstitutive theory**. *Social Sciences Journal of Universities in Shanxi,* 441(1), 99-104.

(5)   Zhang, T. C., & Xiao, F. S. (2010). **The red resources and ideological and political education of university students**. *Teaching and Research.*

(6)   Li, J., & Zhang, T. (2011). **Three smart combinations of ideological and political education in colleges and universities**. *Social Sciences Journal of Universities in Shanxi*, 22(2003), 4038-4046.

(7)   Yan, L. I., Zeng, W. L., & Hai-Tao, H. E. (2010). **An analysis of the college students' ideological and political education vector under the new media environment**. *Journal of Chongqing University of Posts and Telecommunications (Social Science Edition).*

(8)   Chen, W. B. (2001). **A further study on the regularity in the process of ideological and political education**. *Journal of Central China Normal University (Humanities and Social Sciences).*

(9)   Pan, Y., & Tu, K. (2011). **Method innovation of undergraduate ideological and political education based on network environment**. *Procedia Engineering*, 15(1), 2752-2756.

(10) Yang, H., Chen, J., & Zhan, X. (2022). **"Integrated" Ideological and Political Education System for TCSOL Major**. *The International Conference on Artificial Intelligence and Logistics Engineering. Springer, Cham.*

(11) Si, Y. (2022). **On the influence of party history education on ideological and political education for medical students**. *Journal of Higher Education Research*, 3(2), 141-145.

(12) Tao, T., & Lv, X. (2022). **Construction of ideological and political education in colleges and universities based on the carrier of smartphone**. *Security and Communication Networks.*

(13) Yu, L., Chen, Y., & Wang, L. (2021). **Bibliometric analysis of research literature on ideological and political education by curriculum based on sati**. *Journal of Physics: Conference Series*, 1852(4), 042072.

(14) Li, X., Dong, Y., Jiang, Y., & Ogunmola, G. A. (2021). **Analysis of the teaching quality of college ideological and political education based on deep learning**. *Journal of Interconnection Networks.*

(15) Sun, J., & University, N. N. (2020). **Classical marxist writers' discussions on the subject of ideological and political education**. *Journal of Northwest Normal University(Social Sciences).*

(16) Yu, C. (2019). **Kuram ve uygulamada etm blmler educational sciences: theory & practice 2989 innovative methods of ideological and political education for college students based on ideological cognition science.**

(17) Cheng, P., Yang, L., Niu, T., & Li, B. (2022). **On the ideological and political education of material specialty courses under the background of the internet.** *Journal of Higher Education Research*, 3(1), 79-82.

(18) Zhou, Y. (2022). **The application of curriculum ideology and politics in the training of judicial vocational education talents**. *Journal of Higher Education Research*, 3(2), 155-159.

(19) Wu, X. (2022). **Research on the reform of ideological and political teaching evaluation method of college english course based on "online and offline" teaching**. *Journal of Higher Education Research*, 3(1), 87-90.

(20) Chen, B., & Pan, X. (2022). **Practice and exploration of integrating curriculum ideology and politics into digital logic circuit course**. *Open Journal of Social Sciences*, 10(4), 8.

(21) Bai X, Wang X, Liu X. (2021). **Explainable Deep Learning for Efficient and Robust Pattern Recognition: A Survey of Recent Developments**. *Pattern Recognition*, 108102.

(22) Shafay, M., Ahmad, R. W., Salah, K., Yaqoob, I., Jayaraman, R., & Omar, M. (2022). **Blockchain for deep learning: review and open challenges**. *Cluster Computing*, 1-25.

(23) Wang C, Zhou J, Xiao B. (2021). **Uncertainty Estimation for Stereo Matching Based on Evidential Deep Learning**. *Pattern Recognition*, 1. https://doi.org/10.1016/j.patcog.2021.108498

(24) W. Cai, D. Liu, X. Ning. (2021). **Voxel-based Three-view Hybrid Parallel Network for 3D Object Classification.** *Displays,* 69(1).

(25) Shan W. (2022). **Digital streaming media distribution and transmission process optimisation based on adaptive recurrent neural network[J]**. *Connection Science*, 34(1), 1169-1180.

(26) Ying L, Qian Nan Z, Fu Ping W. (2021). **Adaptive weights learning in CNN feature fusion for crime scene investigation image classification[J]**. *Connection Science*, 33(3), 719-734.

(27) Kaseng, F., Lezama, P., Inquilla, R., y Rodriguez, C. (2020). **Evolution and advance usage of Internet in Peru**. *3C TIC. Cuadernos de desarrollo aplicados a las TIC*, 9(4), 113-127. https://doi.org/10.17993/3ctic.2020.94.113-127

(28) Guan Fuyu,Cao Jie,Ren Jie & Song Wenli. (2021). **The teaching of sports science of track and field-based on nonlinear mathematical equations**. *Applied Mathematics and Nonlinear Sciences,* 7(1), 191-198. https://doi.org/10.2478/amns.2021.2.00155

3C Tecnología. Glosas de innovación aplicadas a la pyme. ISSN: 2254-4143

Ed.43 | Iss.12 | N.1 January - March 2023

/07/

3C Tecnología. Glosas de innovación aplicadas a la pyme. ISSN: 2254-4143

Ed.43 | Iss.12 | N.1 January - March 2023

126

RESEARCH ON PHYSICAL FITNESS TRAINING OF FOOTBALL PLAYERS BASED ON IMPROVED LSTM NEURAL NETWORK TO IMPROVE PHYSICAL ENERGY SAVING AND HEALTH

Nengchao Pan*

Department of Basic Studies, Beihai Vocational College, Beihai, Guangxi, 536000, China

bhzypnc@163.com

ABSTRACT

In order to ensure that the physical function of football players adapts to the development of modern football level, and avoid the phenomenon of inability to adapt to the intensity of modern football games due to lack of physical fitness. Aiming at the physical training of football players, this paper proposes an improved long-short-term memory network (W-LSTM) model for the optimization and prediction of physical training. The model effectively combines the global feature extraction ability of LSTM for time series data and the preprocessing ability of the extracted data, which reduces the loss of feature information and achieves high prediction accuracy. The front door is added on the basis of LSTM, which combines training and physical function to reduce the impact of fluctuations in data outliers on the prediction results, effectively improving the accuracy of physical training optimization and prediction, and using body shape, exercise tolerance, exercise intensity and fitness level as input values to conduct comparative experiments on the three models of W-LSTM, LM-BP and ARIMA. The study found that W-LSTM has a lower mean square error (0.011) and a higher correlation coefficient (0.985), indicating that the model proposed in this paper is significantly better than other existing comparison models in terms of the accuracy of prediction results.

KEYWORDS

W-LSTM; Football; Athlete; Physical fitness; Prediction model

PAPER INDEX

3C Tecnología. Glosas de innovación aplicadas a la pyme. ISSN: 2254-4143

Ed.43 | Iss.12 | N.1 January - March 2023

1. INTRODUCTION

With the increasing level of football around the world, the competition is intensifying, and the level of scientific training is also increasing. The daily training experience of football players around the world shows that athletes in different periods and regions follow some almost the same training principles in terms of training content and training methods, and have some similar or even common characteristics [1]. However, with the diversification of the world football level and training process, this lack of training content and training methods for individual characteristics has been unable to adapt to the inevitable laws of football development, and will inevitably hinder the improvement of athletes' competitive ability and regional football level [2]. Therefore, while we carry out the overall general training of football players, it is absolutely necessary to carry out individualized training for players, and it is also in line with the general law of the development of world football.

The physical training of football players is a time series problem for improving physical energy and health. For the prediction problem of time series, long-short term memory neural network [3] (long-short term memory, LSTM) has been widely used in speech recognition [4], network Flow prediction [5], pre-drilling logging curve prediction[6], power and image prediction [7-8], toxic gas law prediction[9] and other fields. Mao et al. proposed an LSTM model for image caption generation as early as 2015, pioneering the application of this research field in image caption generation. Peng et al. [10] used LSTM for the prediction of generated sentences, using dual LSTM layers to tune the parameters to improve the accuracy of sentence generation. In 2017, some scholars proposed a new time-varying parallel recurrent neural network for the generation of sports health image captions, which can obtain dynamic visual and textual representations at each time step, thus solving existing methods. The problem that currently generated words do not match the obtained image features in [11]. In addition, some scholars have applied the attention mechanism to the prediction of physical education innovation indicators, and found that the attention model can effectively improve the prediction accuracy of the innovation direction of physical education [12]. Kyunghyun et al. [13-14] proposed another gating mechanism of Gated Recurrent Unit (GRU), which is different from LSTM. The goal is to make each recurrent unit adaptively capture the dependencies of different time scales. Chung et al. [15] also conducted a specific study on GRU. However, this idea is also difficult to process data in combination with abnormal fluctuations and large fluctuations of data.

Physical fitness is one of the five basic elements of football players' competitive ability, and it is the physical ability necessary for football players to perform their technical and tactical skills normally and achieve excellent sports performance [16]. Physical fitness plays a pivotal role in a competitive football game. However, each athlete's upper limit of physical fitness and reserves are not the same, so it is difficult to excavate the limit of each athlete if the traditional unified training method is used [17]. In this regard, this study addresses the importance of physical fitness training using the LSTM model. However, the traditional long-term memory neural network model has the problem of premature saturation. Therefore, considering the

improvement of the standard LSTM model, a new W-LSTM model is proposed to input physical fitness data and physical function data to train the model to reduce the number of different athletes. The influence of physical fitness and physical fitness on the prediction results, so as to provide a suitable numerical basis for the training of different athletes.

2. W-LSTM RELATED MODEL THEORY

2.1. DATA PREPROCESSING

Since the athlete's physique is affected by training and physical function, the following definitions are made: define t as the number of training days: xi represents the physical fitness data of the i-th day, then the input data is $Xi = \{x1, \ x2......xt\}, \ \ X2 = \{x2, \ x3......xt + 1\}$, and so on, until the last day; the physical energy fluctuation is calculated using the formula $\Delta pi = pi - pi - 1$, when i = 1, assuming that the data of the previous day is 0, then $\Delta w1 = w1$, the input format for physical fitness is $\Delta Pi = \{\Delta p1, \ \Delta p2......\Delta pt\}, \ \Delta P2 = \{\Delta p2, \ \Delta p3, \ ......\Delta pt + 1\}$, and so on until the last day.

2.2. DEFINITION OF THE MODEL

The input to the LSTM model consists of trained and physical performance data, i.e. using the data from the previous t days as input to predict physical performance on day t + 1 [18]. LSTM is a special RNN structure, which was proposed by Hochreiter et al. [19] in 1997 to decide when and how to update the hidden state of RNN. Due to its unique design structure, LSTM can solve the gradient very well. Disappearance problem, it is especially suitable for dealing with timing problems. Standard LSTM units include forget, input, and output gates [20]. On the basis of LSTM, W-LSTM processes its input information accordingly, and takes training and physical function data as data input, and it also includes pre-gate, forget gate and output gate [21] (Fig. 1), therefore, it can process more information than a standard LSTM, and its input in this study contains training and physical performance information.
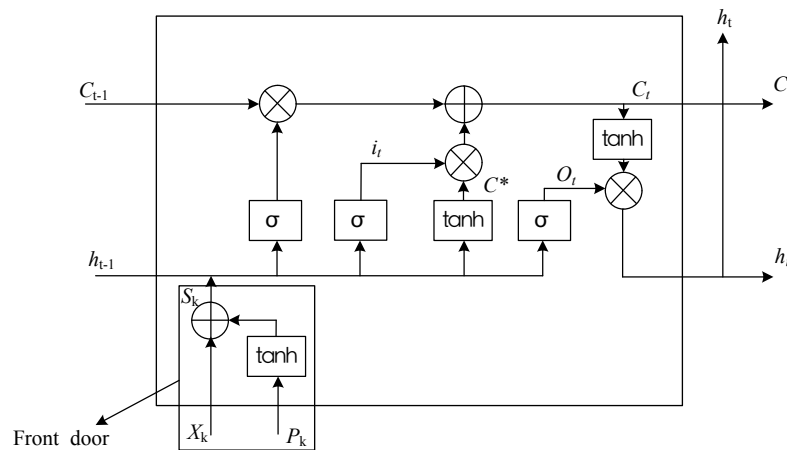
Figure 1. W-LSTM structure

Front gate, which combines body function information and function change information to form combined information:

$$s_k = W_x \times X_i + b_x + \tanh(\ _P \times P_i \quad _p \tag{1}$$

Among them, X_i is the body function used to analyze the law of physical changes, P_i is the function fluctuation information extracted from the physical energy information as input alone to strengthen the model's processing of physical energy fluctuations, $\{Wx, Wp, bx, bp\}$ are network parameters [22]. The output result of the tanh activation function is between [-1, 1]. The closer the output value is to -1, the greater the negative fluctuation; the closer the output value is to 1, the greater the positive fluctuation. The larger the data fluctuation, the greater the impact on the training of the W-LSTM model. On the contrary, when the fluctuation is 0, the input fluctuation data has no effect on the training of the model. At this time, the W-LSTM model is equivalent to the standard LSTM [23].

Forget gate is the historical state information that controls whether to "forget" [24].

$$f_f = \sigma \quad \times h_{t-} + \ _f \times s_k + \ _f \tag{2}$$

Among them, h_{t-1} is the hidden state of the previous sequence, and S_k is the input sequence of this time. Define W_f as the weighted matrix of h_{t-1}, U_f as the weighted matrix of S_k, and b_f as the bias.

The Input gate is responsible for supplementing the current input to the latest "memory". It consists of two parts: first, the Sigmoid layer outputs it; second, a Tanh layer creates a new candidate value vector, which will be added into the state. Define {Wt,Ut,bt}{Wa,Ua,ba} as the network parameters of the input gate, then

$$i_t = \sigma(w_t \times h_{t-1} + U_i \times s_i + b_t) \tag{3}$$

$$C^* = \tanh(w_a \times h_{t-1} + U_a \times s_k + b_a) \tag{4}$$

Then update the cell state:

$$C_t = C_{t-1} \times f_t + i_i \times C^* \tag{5}$$

The output gate controls how much "memory" can be used in the update of the next layer of the network. Define $\{Wo, Uo, bo\}$ as the network parameters of the output gate, and the calculation of the output gate can be expressed by formula 6:

$$O_t = \sigma(w_o \times s_k + U_o \times h_{t-1} + b_o) \tag{6}$$

After calculating O_t, it is necessary to use the Tanh function to suppress the memory value to [-1, 1], so the output formula of the final output gate is:

$$h_t = O_t \times \tanh(C_t) \tag{7}$$

The historical information output by the last W-LSTM layer passes through a prediction layer and outputs the result y:

$$y = W \times h_t + b \tag{8}$$

2.3. TRAINING PROCESS

The training process of W-LSTM is as follows: Calculate the output value of the W-LSTM cell according to the forward calculation formulas (1) ~ (8) [25]; Backpropagate in two directions according to time and network level to calculate the error term; according to the corresponding, calculate the gradient of each weight, and update the weight; repeat (1) to (3) to obtain a set of optimal parameters and keep them. To prevent overfitting during training, this study uses the Dropout regularization technique [26], which was proposed by Prof. Hinton's team in 2014. Dropout provides a clever way to increase the generalization ability of a network model by reducing weight connections.

3. TEST AND RESULT ANALYSIS

3.1. EXPERIMENT SETUP INSTRUCTIONS

In this section, the proposed W-LSTM model will be evaluated experimentally. The experimental environment is: INTEL Corei5 CPU, 2.80GHz; 4G memory. The experimental data is the daily training data of a football team in Xi'an from April 2022 to May 2022. Each comparative experiment was run 10 times, and the average value was taken.

Three comparison models are set up:

(1) W-LSTM model, input historical function information and physical fitness fluctuation information to train the model to make predictions.

(2) The BP neural network improved by the LM algorithm only takes the historical functional information as input, and uses the physical fitness information of the previous n days to predict the physical fitness situation of the n+1th day.

(3) The ARIMA model regards the data sequence generated by physical fitness over time as a random sequence, and uses a certain mathematical model to approximately describe this sequence.

At the same time, in order to test the universality of the W-LSTM model, the three models were compared using four data of body shape, exercise tolerance, exercise intensity and fitness level.

3.2. SIMULATION COMPARISON TEST

This summary uses the W-LSTM model, the BP neural network improved by the LM algorithm and the ARIMA model to conduct experiments, and the mean square error (MSE) and the coefficient of determination (R2) are used to determine the accuracy of the prediction results.

$$MSE:$$

$$MSE = \frac{\sum (\text{Y\_actual} - Y\_\text{predict})^2}{n} \tag{9}$$

$$R^2:$$

$$R^2 = 1 - \frac{\sum (\text{Y\_actual} - Y\_\text{predict})^2}{\sum (\text{Y\_actual} - Y\_\text{mean})^2} \tag{10}$$

MSE and R2 are commonly used indicators to evaluate the accuracy of the model. MSE is a measure that reflects the degree of difference between the estimator and the estimated value. The smaller the MSE, the higher the accuracy of the model; the larger the R2, the greater the difference between the independent variable and the dependent variable. The higher the degree of explanation, the higher the percentage of changes caused by independent variables in the total change, and the denser the observation points are near the regression line, which means the higher the model fit. Where n represents the total sample, Y_actual represents the real data, Y_predict represents the prediction result, and Y_mean represents the average value of the real data.
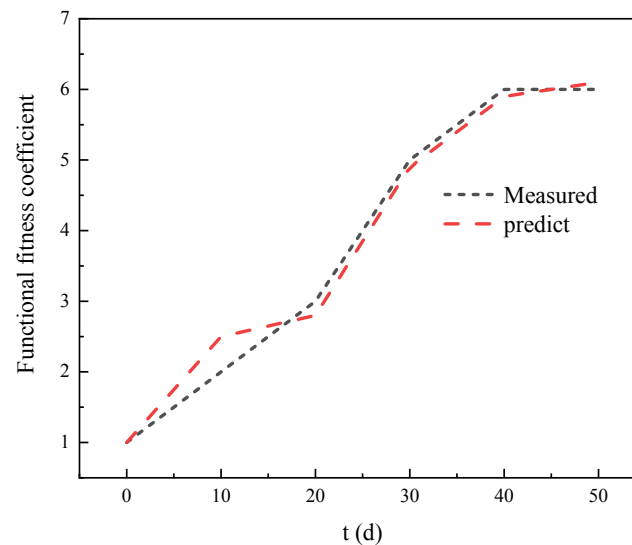
Figure 2. W-LSTM prediction results

By modeling and predicting the physical function sequence, Figures 2 and 3 are the comparison between the prediction results obtained by the W-LSTM model and the ARIMA model and the actual data. Obviously, for the W-LSTM model, the experimental value and the predicted value are extremely coincident and very close, which shows that the W-LSTM model proposed in this study has better prediction results.

By observing the data in Figure 3, it is found that the experimental results of the ARIMA model deviate significantly from other models, the coincidence rate between the experimental values and the predicted values is low, and R2 is even less than 0, which means that the predicted results have nothing to do with the original data. The ARIMA model performs well when dealing with stationary time series. When the data is not stationary, a stationary sequence needs to be obtained through a certain processing method. The physical function data used in this experiment has continuous invariance and mutation, that is, continuous invariance within a period of time. Change, the initial stage gradually increases, this characteristic leads to the loss of too much information when the data is differentiated, resulting in an extremely poor prediction effect of the ARIMA model and a large deviation.
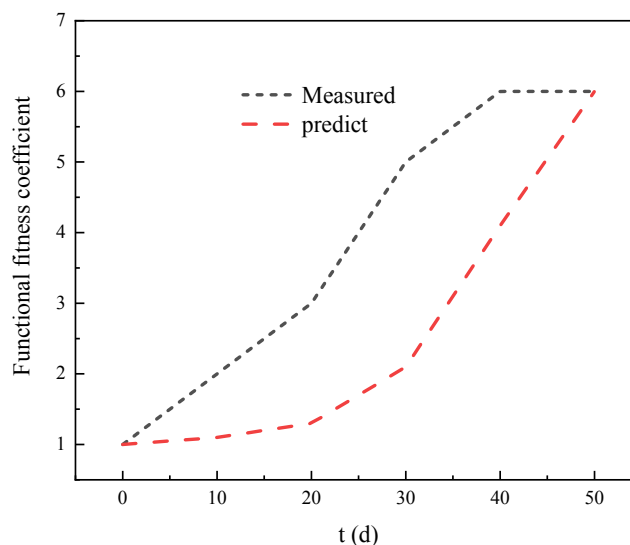
Figure 3. ARIMA model prediction results

After the training, the input data is used for prediction, and the MSE of the W-LSTM model and the BP neural network improved by the LM algorithm changes as the prediction progresses, as shown in Figure 4. The MSE of the W-LSTM model is 0.032, the MSE of the LM-BP model is 0.059, and the MSE of the ARIMA model is 0.923. The MSE of the W-LSTM model is smaller than other models, and the model has the highest accuracy; while R is larger than other models, which means that the fitting degree of the W-LSTM model is higher than that of other models. In general, the MSE trends of the two models are roughly the same, and the MSE of the W-LSTM model is generally smaller than the MSE of the BP neural network improved by the LM algorithm [27].
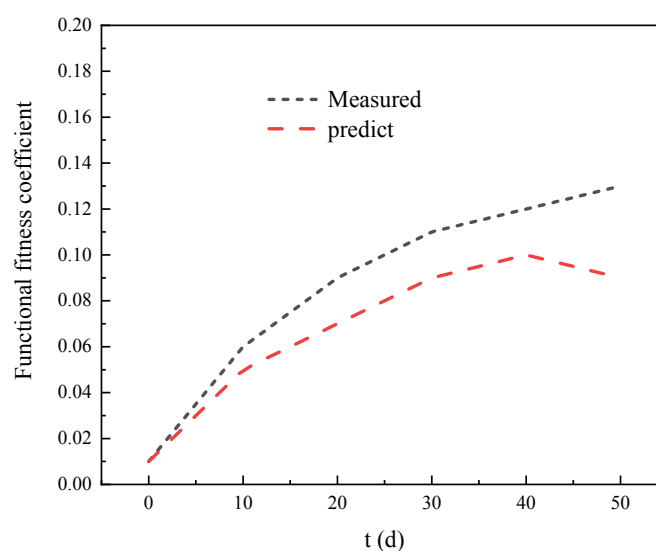
Figure 4. W-LSTM model and BP neural network improved by LM algorithm

Changes in MSE

The input data fluctuates greatly at one-third of the total data, and at this time, the MSE of both models has a short-term increase, while the MSE fluctuation of the W-LSTM model is smaller than that of the BP neural network improved by the LM algorithm. This shows that the W-LSTM model has a better effect on handling large fluctuations in data. In order to verify the universality of the W-LSTM model, four kinds of data of body shape, exercise tolerance, exercise intensity and health level are used as input to carry out comparative experiments on the three models. The experimental results are shown in Table 1. The table shows the evaluation index of the prediction results of the three models on the four factors respectively. It can be seen that W-LSTM has better results than other models, and it shows that the W-LSTM model has good universality [28-29].

Table 1. MSE and R^2 comparison

MSE				
Model	Body shape	Exercise tolerance	Exercise intensity	Fitness level
W-LSTM	0.074	0.031	0.137	0.011
LM-BP	0.163	0.048	0.238	0.017
ARIMA	3.244	-0.891	4.618	0.9048
R^2				
W-LSTM	0.985	0.867	0.904	0.935
LM-BP	0.967	0.793	0.833	0.919
ARIMA	0.317	-2.442	-2.191	-2.771

It can be seen from the above experiments that the W-LSTM model has higher accuracy, better fitting degree and good universality. On the whole, W-LSTM is a good prediction model for the physical fitness prediction problem of football players.

4. CONCLUSION

This paper proposes a physical fitness prediction method for football players based on the W-LSTM network model. The model is mainly constructed by LSTM, which can effectively extract the local and global features of influencing factors. After data analysis and variable reordering based on the maximum information coefficient method, making the data distribution more regular and easy to train. The research compares the prediction results of W-LSTM, LM-BP, and ARIMA models. The experimental results show that: (1) the prediction accuracy of W-LSTM is significantly better than other methods LM-BP and ARIMA models; (2) W-LSTM has lower MSE and higher R2 compared to the other two models, the correlation coefficient of its body shape reaches 0.985; (3) The LSTM is improved to become W-LSTM, and it is of practical value to apply it to the physical fitness prediction of football players.

5. CONFLICT OF INTEREST

The authors declared that there is no conflict of interest.

REFERENCES

(1) Bangsbo, J., Mohr, M., & Krustrup, P. (2006). **Physical and metabolic demands of training and match-play in the elite football player**. *J Sports Sci*, 24(7), 665-674. https://doi.org/10.1080/02640410500482529

(2) Bangsbo, J., Mohr, M., & Krustrup, P. Bangsbo J, Mohr M, Krustrup P. (2006). **Physical and metabolic demands of training and match-play in the elite football player.** *Journal of Sports Sciences,* 24(7), 665-674. https://doi.org/10.1080/02640410500482529

(3) Chen, Y., Wang, L., Hu, J., & Ye, M. (2020). **Vision-Based Fall Event Detection in Complex Background Using Attention Guided Bi-directional LSTM.** https://doi.org/10.1109/ACCESS.2020.3021795

(4) Gao, M., Li, J., Hong, F., & Long, D. (2019). **Day-ahead power forecasting in a large-scale photovoltaic plant based on weather classification using LSTM**. *Energy*, 187, 115838.115831-115838.115812. https://doi.org/10.1016/j.energy.2019.07.168

(5) Li, L., Yang, Y., Yuan, Z., & Chen, Z. (2021). **A spatial-temporal approach for traffic status analysis and prediction based on Bi-LSTM structure**. *Modern Physics Letters B*, 35(31). https://doi.org/10.1142/S0217984921504819

(6) Petridis, S., Li, Z., & Pantic, M. (2017). **End-To-End Visual Speech Recognition With LSTMs**. *IEEE*. https://doi.org/10.1109/ICASSP.2017.7952625

(7) Li, Y., Ye, F., Liu, Z., Wang, Z., & Mao, Y. (2021). **A Short-Term Photovoltaic Power Generation Forecast Method Based on LSTM**. *Mathematical Problems in Engineering.* https://doi.org/10.1155/2021/6613123

(8) Shen, Y., Shao, P., Chen, G., Gu, X., & Zhu, J. (2021). **An identification method of anti-electricity theft load based on long and short-term memory network**. *Procedia Computer Science*, 183(8), 440-447. https://doi.org/10.1016/j.procs.2021.02.082

(9) Ren, Y., Wang, J., Yang, C., Xiao, C., & Li, S. (2021). **Wind and Solar Integrated Power Prediction Method Research Based on DT-CWT and LSTM**. *Journal of Physics Conference Series*, 1754(1), 012008. https://doi.org/10.1088/1742-6596/1754/1/012008

(10) Peng, Y., Liu, X., Wang, W., Zhao, X., & Wei, M. (2019). **Image caption model of double LSTM with scene factors**. *Image and Vision Computing*, 86(JUN.), 38-44. https://doi.org/10.1016/j.imavis.2019.03.003

(11) Qian, F., Chen, L., Li, J., Ding, C., & Wang, J. (2019). **Direct Prediction of the Toxic Gas Diffusion Rule in a Real Environment Based on LSTM**. *International Journal of Environmental Research and Public Health*, 16(12), 2133. https://doi.org/10.3390/ijerph16122133

(12) Zhou, L., & Bian, X. (2019). **Improved text sentiment classification method based on BiGRU-Attention**. *Journal of Physics: Conference Series*, 1345(3), 032097. https://doi.org/10.1088/1742-6596/1345/3/032097

(13) Tian, X., & Li, J. (2019). **A novel improved fruit fly optimization algorithm for aerodynamic shape design optimization**. *Knowledge Based Systems*, 179(SEP.1), 77-91. https://doi.org/10.1016/j.knosys.2019.05.005.

(14) Zhang, F. (2019). **Research on Improving Prediction Accuracy of Sports Performance by Using Glowworm Algorithm to Optimize Neural Network**. *International Journal of Information and Education Technology*, 9(4), 302-305. https://doi.org/10.18178/ijiet.2019.9.4.1216

(15) Rosenfeld, P. J., Brown, D. M., Heier, J. S., Boyer, D. S., Kaiser, P. K., Chung, C. Y., Group, M. S. (2004). **Ranibizumab for neovascular age-related macular degeneration**. https://doi.org/10.1016/j.ajo.2005.02.003

(16) Krustrup, P., Mohr, M., & Bangsbo, J. (2002). **Activity profile and physiological demands of top-class soccer assistant refereeing in relation to training status**. *J Sports*, 20(11), 861-871. https://doi.org/10.1080/026404102320761778

(17) Dooman, C. S., & Jones, D. (2009). **Down, But Not Out: In-Season Resistance Training for the Injured Collegiate Football Player**. *Strength & Conditioning Journal*, 31(5), 59-68. https://doi.org/10.1519/ssc.0b013e3181b9983e

(18) A, C. W., A, X. W., Jz, A., Liang, Z. A., Xiao, B. A., Xin, N. B., Ehd, A. (2021). **Uncertainty Estimation for Stereo Matching Based on Evidential Deep Learning.** https://doi.org/10.1016/j.patcog.2021.108498

(19) Zohali, H., Naderi, B., & Mohammadi, M. (2019). **The economic lot scheduling problem in limited-buffer flexible flow shops: Mathematical models and a discrete fruit fly algorithm**. *Applied Soft Computing*. https://doi.org/10.1016/j.asoc.2019.03.054

(20) Cai, W., Zhai, B., Liu, Y., Liu, R., & Ning, X. (2021). **Quadratic polynomial guided fuzzy C-means and dual attention mechanism for medical image segmentation**. *Displays*, 70, 102106. https://doi.org/10.1016/j.displa.2021.102106

(21) Miao, J., Wang, Z., Ning, X., Xiao, N., Cai, W., & Liu, R. (2022). **Practical and secure multifactor authentication protocol for autonomous vehicles in 5G**. *Software: Practice and Experience*. https://doi.org/10.1002/SPE.3087

(22) Ning, X., Duan, P., Li, W., & Zhang, S. (2020). **Real-time 3D face alignment using an encoder-decoder network with an efficient deconvolution layer**. *IEEE Signal Processing Letters*, 27, 1944-1948. https://doi.org/doi.org/10.1109/LSP.2020.3032277

(23) Ying, L., Nan, Z. Q., Ping, W. F., Kiang, C. T., Pang, L. K., Chang, Z. H., Nam, L. (2021). **Adaptive weights learning in CNN feature fusion for crime scene investigation image classification**. *Connection Science*. https://doi.org/10.1080/09540091.2021.1875987

(24) Ning, X., Gong, K., Li, W., & Zhang, L. (2021). **JWSAA: joint weak saliency and attention aware for person re-identification**. *Neurocomputing*, 453, 801-811. https://doi.org/10.1016/j.neucom.2020.05.106

(25) Yan, C., Pang, G., Bai, X., Liu, C., Xin, N., Gu, L., & Zhou, J. (2021). **Beyond triplet loss: person re-identification with fine-grained difference-aware**

pairwise loss. *IEEE Transactions on Multimedia*. https://doi.org/10.1109/TMM.2021.3069562

(26) Connor, J. T., Martin, R. D., & Atlas, L. E. (2002). **Recurrent neural networks and robust time series prediction**. *IEEE Transactions on Neural Networks*, 5(2), 240-254. https://doi.org/10.1109/72.279188

(27) Yu, Z., Li, S., Sun, L. N. U., Liu, L., & Haining, W. **Multi-distribution noise quantisation: an extreme compression scheme for transformer according to parameter distribution**. https://doi.org/10.1080/09540091.2021.2024510

(28) Frayssinet, M., Esenarro, D., Juárez, F. F., y Díaz, M. (2021). **Methodology based on the NIST cybersecurity framework as a proposal for cybersecurity management in government organizations**. *3C TIC. Cuadernos de desarrollo aplicados a las TIC*, 10(2), 123-141. https://doi.org/10.17993/3ctic.2021.102.123-141

(29) Zhang Min, Lu Xuewen, Hoffman Ettiene, Kharabsheh Radwan & Xiao Qianghua. (2022). **Radioactive source search problem and optimisation model based on meta-heuristic algorithm**. *Applied Mathematics and Nonlinear Sciences*, 7 (2), 601-630. https://doi.org/10.2478/AMNS.2021.2.00159.

3C Tecnología. Glosas de innovación aplicadas a la pyme. ISSN: 2254-4143

Ed.43 | Iss.12 | N.1 January - March 2023

/08/

3C Tecnología. Glosas de innovación aplicadas a la pyme. ISSN: 2254-4143

Ed.43 | Iss.12 | N.1 January - March 2023

141

THE SIGNIFICANCE OF THE CONVOLUTIONAL DEEP LEARNING MODEL IN THE INTELLIGENT COLLABORATIVE CORRECTION OF ENGLISH WRITING

Hong Wang*

Department of Social Work, Formerly the Ministry of Civil Affairs Management Cadre Institute, Beijing College of Social Administration, Beijing, 102628, China

hongw_200466@163.com

ABSTRACT

To ensure the normal operation of English composition grammar correction and avoid inaccurate detection caused by faults, it is of great significance to detect abnormal working conditions in time and diagnose them accurately. Aiming at the complexity of grammar correction, this paper proposes a PLSTM-CNN model for fault detection in the grammar correction process. The model effectively combines the global feature extraction ability of LSTM for time series data and the ability of the CNN model to extract local features, which reduces the loss of feature information and achieves a higher fault detection rate. A one-dimensional dense CNN is used as the main body of the CNN, and the LSTM network is sensitive to changes in sequence information to avoid model overfitting while building a deeper network. The maximum mutual information coefficient (MMIC) data preprocessing method is adopted to improve the local correlation of the data and improve the efficiency of the PLSTM-CNN model to detect faults from different initial conditions. The research results show that the parallel PLSTM-CNN has better prediction performance than the serial PLSTM-CNN, and its FDR and FPR are 90.5% and 0.051, respectively. It shows that the use of convolutional deep learning models for the prediction of writing grammar correction faults has strong application prospects.

KEYWORDS

PLSTM-CNN; Fault detection; English writing; grammar; Deep learning.

3C Tecnología. Glosas de innovación aplicadas a la pyme. ISSN: 2254-4143

Ed.43 | Iss.12 | N.1 January - March 2023

PAPER INDEX

1.   INTRODUCTION

Writing ability is an important basis for measuring students' English learning and practical ability, and plays an significant role in promoting the overall development of language skills. In recent years, the rapid development of computers and networks has laid the foundation for the reform of college English writing [1]. Due to the limitations of the current technology of the automatic evaluation system, more feedback is given to students at the vocabulary level, but there are still many problems in the evaluation of syntax, text structure, logic, and coherence. Therefore, relying solely on machine correction and feedback is of limited help to students [2]. To solve this problem, manual intervention and feedback are required [3]. Therefore, the need for intelligent collaboration is extremely necessary.

The research on English marking begins with writing feedback. Research on writing feedback began in the 1950s. Before this, writing feedback was conducted by teachers. During this period, some scholars conducted comparative studies on teachers' correction of students' compositions and students' peer evaluation under the guidance of teachers and found that peer feedback was better than teacher feedback [4]. In the following decades, more and more researchers from China and abroad began to pay attention to the application of peer feedback in practical teaching and research, and their research results provided a lot of guidance for our teaching and research [5]. However, some problems and difficulties with peer feedback have also been found in some studies. For example, the correctness, fairness, and effectiveness of feedback are often questioned, and the operability in writing classrooms also needs to be verified. In the 1960s, Professor Ellis Page of Duke University in the United States developed the PEG automatic composition scoring system, and the automatic writing evaluation system (AWES) gradually developed [6]. For decades, especially with the development of artificial intelligence technology, the development of foreign writing automatic evaluation systems has made great progress, such as Criterion, My Access, and Writing Roadmap [7]. Then there is the study of translation. According to the basic principle of deep reinforcement learning algorithm, some researchers designed a neural machine translation model, introduced the evaluation mechanism to the level of the sentence to be translated, predicted the convergence of the translation, and used the deep reinforcement learning algorithm as a guiding strategy for translation. Optimize the word sequence of the translation target, integrate the monolingual corpus into the training of deep reinforcement learning, and alleviate the data-sparse problem of translation sentences. After experimental tests, it is found that this model can improve the overall performance of machine translation. Compared with other translation models, Whether it is Chinese-Korean or Korean-Chinese, the BLEU value has been significantly improved [8], but the performance in other aspects is poor. Considering the problems existing in traditional machine translation, some researchers have designed a neural machine translation model based on the basic principle of quality estimation, and used the quality estimation method to score the pseudo-parallel data generated by reverse translation, and use the data with higher scores as the basis for quality estimation. Design of CNN's English Machine Translation Minor Error Detection System [9]. Some scholars use the input of the

neural network to control the quality of the pseudo-parallel data generated by the reverse translation, and provide a rich training network as the output for the neural network model. After experimental tests, it is found that compared with the traditional model, the model has no effect on the forward translation or reverse translation. For translation, the BLEU value has been improved, but the function cannot meet the design requirements [10].

One-dimensional CNN [11] divides the input data along a single dimension without windowing operation, which is easier to train and has less computational complexity. Although 1D convolution is the current popular deep learning method, it still has some limitations. Although the CNN can extract the local features of the data, its ability to extract the global features of the data is weak. To obtain beneficial features such as global and local use of data at the same time, this paper proposes an LSTM-CNN structure based on a parallel structure, which combines the local features extracted by the CNN and the global features extracted by LSTM to make full use of the data. features to improve the accuracy of the model, thereby reducing the translation accident rate [12].

2.   CORRELATION MODEL THEORY

2.1. 1D-CNN

A CNN is one of the widely studied deep learning algorithms, which has the characteristics of local connection, weight sharing, and downsampling [13]. The difference between 1D-CNN and classical CNN is the dimension of the convolution kernel, which has been widely used in time series feature extraction in recent years [14]. The one-dimensional convolution operation is shown in Figure 1, and its mathematical model is shown in formula (1):

$$H_i = f(H_{i-1} \otimes W_i + b_i) \tag{1}$$

Among them, Hi is the input feature quantity of the ith layer; Wi and bi represent the weight and corresponding bias of the convolution kernel of the ith layer respectively; f represents the activation function, here is the Relu activation function, which has a good nonlinear expression ability.

Pooling layers are also known as subsampling layers. The sub-sampling layer downsamples the feature map according to the rules and reduces the dimension of the convolutional feature to reduce the parameters and calculation amount inside the CNN, and at the same time suppress the network overfitting.

Suppose H^l_t is the jth feature map of the l-th sub-sampling layer, and its sampling process is as shown in formula (2), which represents the next sampling function. Each output feature map corresponds to its own multiplicative bias B^l_j and an additive bias b^l_j [15].

$$H_j^l = f\left(\beta_j^l down\left(H_j^{l-1}\right) + b_j^l\right) \tag{2}$$

2.2. DCNN

To alleviate the gradient explosion problem caused by the network depth, the dense CNN [16] (Dense CNN, DCNN) further connects each sub-layer based on the residual network structure, so that the output of each layer of the network is used as The input of one layer ensures maximum feature reuse, alleviates the gradient disappearance and gradient explosion problems caused by the increase in the number of network layers and makes the network information flow more smoothly.

Assuming that the number of network layers is, the DCNN contains a total of N/(N+1)/2 connections. Through the sequence x_0 passed through the convolutional layer, the input of the nth layer is the feature map of all previous layers, as shown in the following formula (3):

$$x_n = H([x_0, x_1, \cdots, x_{n-1}]) \tag{3}$$

Among them, $[x_0, x_1, \ldots, x_{n-1}]$ represents the feature map in the 0,1...,n-1 layer; Hl( ) represents the normalized linear correction unit, Relu activation function, pooling operation and volume Product equivalence transformation. The output of the convolutional layer and the pooling method formula is as follows:

$$\lambda_{output} = \left\lceil \frac{\lambda_{input}}{S} \right\rceil \tag{9}$$

$$\lambda_{output} = \left\lceil \frac{\lambda_{input} - F + 1}{S} \right\rceil \tag{10}$$

2.3. LSTM LONG SHORT-TERM MEMORY NETWORK

A Long Short-Term Memory Network (LSTM) is a temporal recurrent neural network that is an optimization of a Recurrent Neural Network (RNN). RNN is often used to analyze and predict time series, but it is used for short time series, and it is not suitable for long-distance and long period time series. LSTM perfectly solves the shortcomings of RNN. It significantly improves the model's ability to analyze and predict long sequences by designing hidden layers without changing the original model structure. The operation state of LSTM is almost linear, and the entire operation mode is also chain operation, and there will be no problems such as gradient expansion and disappearance in the RNN training process, which improves the prediction effect and accuracy. The LSTM model is mainly composed of a forgetting gate, input gate, and output gate. After the unit gate enters the forgetting gate, the forgetting gate is responsible for screening out the unit state that can be retained to the current moment at the previous moment, and the input gate is responsible for

screening out a certain number of cells. The input at the current moment is the unit state at the current moment, and the output gate is responsible for the output of the unit state [17].

Information is mainly selected through three gate structures: input gate, forget gate, and output gate. Taking the t-th sample as an example is the input data at the current moment. Equation (13)~(18) is the process performed by the LSTM unit [20]:

$$f_t = \sigma \left(w^f \cdot \left[h_{t-1}, x_t \right] + b^f \right) \tag{11}$$

$$i_t = \sigma \left(w^i \cdot \left[h_{t-1}, x_t \right] + b^i \right) \tag{12}$$

$$\tilde{C}_t = \tanh \left(w^c \cdot \left[h_{t-1}, x_t \right] + b^c \right) \tag{13}$$

Where w_f, w_i, w_c, and w_o are the weights of the corresponding forgetting gate, input gate, and output gate respectively [18].

2.4. MODEL STRUCTURE DIAGRAM

According to the above model theory, a joint prediction and correction model of DCNN and LSTM is established, combined with the advantages of the LSTM algorithm, an LSTM-CNN hybrid model is formed to perform model training on the data set, and the short text of unknown category is predicted by the trained model. As shown in Fig.1 [19], this parallel network structure avoids feature loss to the greatest extent and preserves the global and local information of data features; the residual structure enhances CNN stability and reduces resource occupancy; batch normalization layer (Batch normalization, BN) to speed up network training and suppress network overfitting; the global average pooling layer on the left splices the dimensionality-reduced feature map with the network feature map on the right, and finally sends it to the classification layer [20].
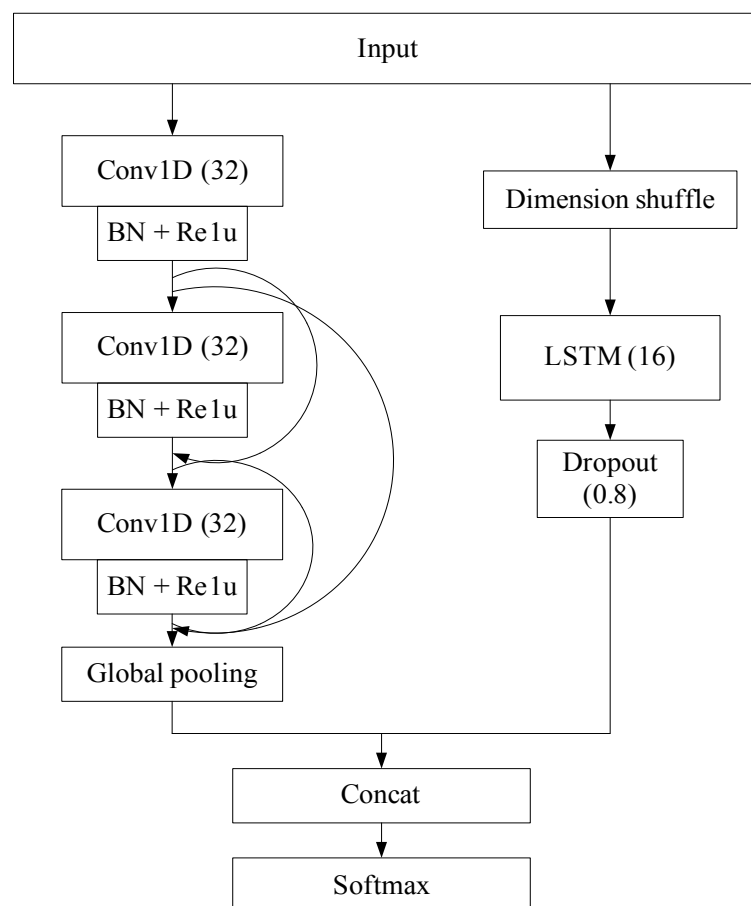
Figure 1. PLSTM-CNN network model

3. EXPERIMENT AND RESULT ANALYSIS

3.1. EVALUATION RESULTS

To show the fault checking results and evaluate the model performance, two metrics, Fault Diagnosis Rate (FDR) and False Positive Rate (FPR), were used to evaluate the model performance. FDR and FPR are defined in [21].

Among them, TP (True Positives) represents the number of instances that are positive classes and are predicted to be positive classes, FN (False Negative) represents the number of positive classes that are predicted to be negative, and FP (False Positives) that instances are negative classes that are predicted to be positive The number of classes, TN (True Negative) represents the number of instances that are predicted to be negative classes.

To verify the performance of the proposed method, the diagnostic results of the test data based on the PLSTM CNN model are compared with the results of the two-dimensional CNN model-based method and the LSTM model-based method on the test data, and the results are shown in the table., the average fault diagnosis rate based on the PLSTM-CNN model in the table is 91.4% [22].

Table 1. The comparison of fault results

Fault type	FDR			FPR		
	2D-CNN	LSTM	PLSTM-CNN	2D-CNN	LSTM	PLSTM-CNN
Normal	0.91	1.0	1.0	0.08	0.03	0
Fault1	1.0	1.0	1.0	0	0	0
Fault2	1.0	1.0	0.81	0	0	0
Fault3	0.48	1.0	0.92	0.24	0.14	0.07
Fault4	1.0	0.81	0.34	0	0	0
Fault5	1.0	0.92	1.0	0	0	0
Fault6	1.0	0.34	1.0	0	0	0
Fault7	1.0	1.0	1.0	0	0	0
Fault8	1.0	1.0	1.0	0.1	0	0
Fault9	1.0	1.0	1.0	0.58	0.21	0.17
Fault10	1.0	1.0	0.37	0.06	0.01	0.02
Fault11	0.81	1.0	0.33	0.03	0.02	0.01
Fault12	0.92	0.48	0.98	0.05	0.04	0.01
Fault13	0.34	1.0	0.92	0.16	0.05	0.04
Fault14	0.82	1.0	0.89	0.15	0.61	0.05
Fault15	0.96	1.0	1.0	0.79	0.61	0.51
Fault16	0.84	1.0	0.98	0.69	0.62	0.48
Fault17	0.09	1.0	1.0	0.05	0.02	0.02
Fault18	0.96	1.0	1.0	0	0	0
Fault19	1.0	0.48	1.0	0	0	0
Fault20	1.0	1.0	1.0	0	0	0
Average	0.86	0.91	0.88	0.14	0.11	0.07

We find that the classification accuracy of different faults varies widely. The detection rate of faults 3 and 9 is less than 90%, and the detection rate of faults 15 and 16 is less than 50%. In addition, the detection rates of the remaining 16 faults are all higher than 90%, of which the detection rate of faults 1, 2, 4, 5, 6, 7, 8, 17, 19, and 20 is 100%. Therefore, PLSTM-CNN can effectively isolate most of the faults, and only a few faults perform poorly. Through the analysis of the data in the table, it is found that the lower accuracy of faults 3, 9, 15, and 16 is due to the higher degree of confusion among them, which is consistent with the previous mutual information calculation results [23]. The PLSTM-CNN model proposed in this paper makes full use of the local and global features of the original data, and the fault detection rate and false-positive rate are better than 2D-CNN and LSTM models in faults 3, 9, 15, and 16 with a high degree of confusion. Because both fault 3 and fault 9 are related to the

change in the initial number of articles, this paper rearranges the variables according to the method of the maximum mutual information coefficient based on the initial number of articles, which further improves the fault detection rate of faults 3 and 9. The degree of confusion of faults 15 and 16 is too high, and there is no effective fault detection method [24].
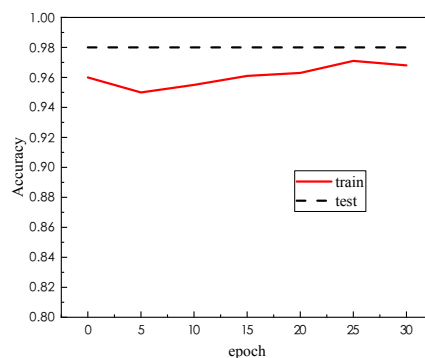
Figure 2. Recognition accuracy of learning rate self-enhancement algorithm

It can be seen from Fig.2 that when the number of iterations is 25, the accuracy rate is the highest, which is 97.3%, which shows that the use of PLSTM-CNN for English composition grammar detection has strong applicability. In addition, it can be seen from Figure 4 that as the iteration continues, the recognition accuracy of the DCNN model continues to rise. After reaching a certain level, the accuracy does not change and the network model converges. Therefore, the DCNN model used in this study has a good effect., it starts to converge after reaching a certain number of iterations. In this study, this algorithm is used to optimize DCNN with a certain preprocessing effect [25-27].

3.2. COMPARATIVE EXPERIMENT

To further illustrate the advantages of the parallel neural network structure, we did the following experiments on average fault detection rate, model training and testing time, and model stability under small sample conditions.

3.2.1. COMPARISON OF AVERAGE FAILURE DETECTION RATES

To further compare the fault detection capabilities of serial and parallel network models, based on the data set above, we designed a traditional serial network structure, as shown in Fig.3. The experimental results are shown in Fig.4. The average F1 scores on the PLSTM-CNN, tandem LSTM-CNN, LSTM, 1D-CNN, and 2D-CNN models are 92.13%, 89.54%, 84.08%, 84.80%, and 85.78%, respectively. This shows that parallel CLSTM-CNN has better fault detection performance than serial LSTM-CNN [28].
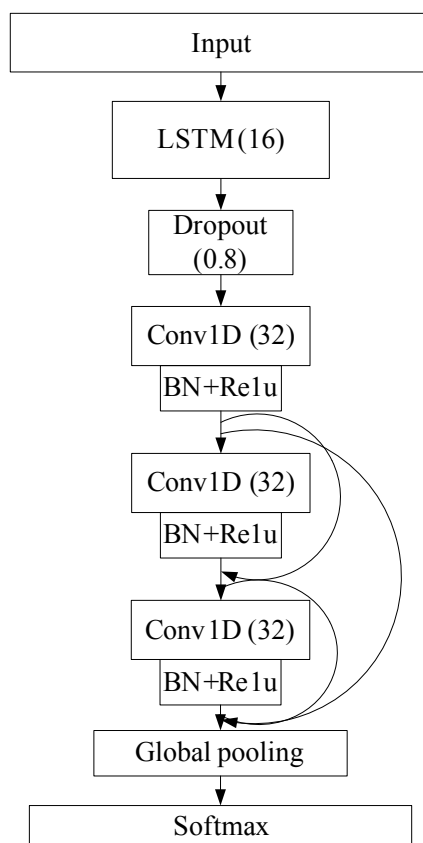
Figure 3. Serial LSTM-CNN network structure

The experimental results are shown in Fig.4. The average F1 scores on the PLSTM-CNN, tandem LSTM-CNN, LSTM, 1D-CNN, and 2D-CNN models are 92.13%, 89.54%, 84.08%, 84.80%, and 85.78%, respectively. This shows that parallel CLSTM-CNN has better fault detection performance than serial LSTM-CNN.
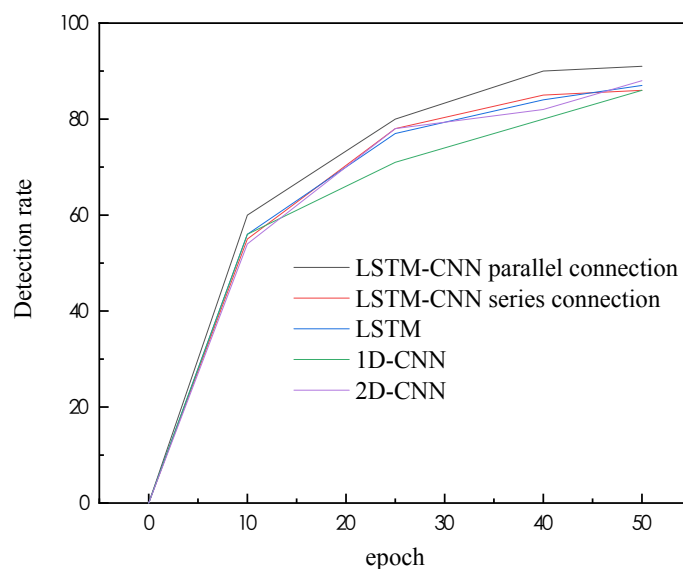
Figure 4. Mean failure detection rate

3.2.2. MODEL INFERENCE AND INFERENCE TIME COMPARISON

The PLSTM-CNN model takes 4.2 seconds to train for each epoch and 7 minutes to train for 100 epochs. The main reasons for its faster training speed are: considering the real-time nature of fault monitoring, the convolution layer in this paper is selected as one-dimensional convolution, which has fewer parameters. Under the conditions of the same network and hyperparameters, the calculation time is shorter, but Some accuracy will be lost.

Meanwhile, training deep 2D convolutional networks usually require special hardware devices, such as cloud computing or GPU acceleration. But 1D-CNN can be implemented on the CPU of ordinary computers, and its low computational requirements and compact structure are very suitable for real-time monitoring and low-cost applications.

Table 2. Comparison of training and inference time

Model	Training time for one epoch (s)	Reasoning time for one epoch (ms)
1D-CNN	2.54	10
2D-CNN	65	200
LSTM	3	12
PC LSTM-CNN	3.8	20
SC-LSTM-CNN	4.2	25

3.2.3. COMPARISON OF AVERAGE FAULT DETECTION RATES FOR SMALL SAMPLES

Considering that the actual English composition grammar detection fault samples are scarce, the experiment will reduce the number of each type of fault sample. Set the sampling time to 3 minutes, run for 10 hours under normal conditions, and collect 2000 normal samples. In the simulation of 20 kinds of faults, the simulator runs normally for 1 hour, then introduces the corresponding faults, and then continues to run for 1 hour. Thus, 1 hour of failure data (200 failure samples) was collected per simulation. The simulations for each failure type were repeated ten times with ten different initial states. The simulation platform collects a total of 4200 sample data, including 2000 normal samples and 2000 samples for each fault. Choose 70% of the data for training, 20% for testing, and 10% for validation. The experimental results are shown in Table 3:

Table 3. Average failure detection rate of small samples

Model	FDR	FPR
1D-CNN	83.4%	0.1
2D-CNN	78.5%	0.08
LSTM	84.6%	0.09
PC LSTM-CNN	84.8%	0.12
SC-LSTM-CNN	90.5%	0.051

The study found that SC-LSTM-CNN has a high FDR and a small value of FPR, which shows that the parallel LSTM-CNN has extremely high prediction accuracy and stability. Although PC-LSTM-CNN has a high FDR, its FPR value is high, indicating that its stability is poor and the prediction accuracy is average. The above results confirm that the parallel LSTM-CNN can still maintain high accuracy on small sample datasets, and its network structure is more stable than the serial network [29]. 2D-CNN requires a large number of training samples to guarantee the accuracy, while 1D-CNN still performs well on small-sample datasets[30-31].

4. CONCLUSION

This paper proposes a grammar writing check fault detection method based on the PLSTM-CNN network model. The model is constructed by LSTM, one-dimensional dense convolutional layer, one-dimensional global pooling layer, and Dropout layer, which can effectively extract the local and Global features; after data analysis and variable reordering based on the maximum information coefficient method, the data distribution is made more regular and easy to train. The study compares the fault detection results of PLSTM-CNN, tandem LSTM-CNN, LSTM, and 2D-CNN. The experimental results show that: (1) the fault detection accuracy and false positive rate of PLSTM-CNN are significantly better than other methods; (2) for the difficult-to-detect faults 3 and 9, the PLSTM-CNN model still performs well; (3) parallel Compared with the serial structure, the PLSTM-CNN structure has better accuracy and stability, and its FDR and FPR are 90.5% and 0.051, respectively.

5. CONFLICT OF INTEREST

The authors declared that there is no conflict of interest. REFERENCES

REFERENCES

(1)   Tao, Y., Shi, H., Song, B., & Tan, S. (2020). **A Novel Dynamic Weight Principal Component Analysis Method and Hierarchical Monitoring Strategy for Process Fault Detection and Diagnosis**. *IEEE Transactions on Industrial Electronics*, (99), 1-1. https://doi.org/10.1109/TIE.2019.2942560

(2) A, C. W., A, X. W., Jz, A., Liang, Z. A., Xiao, B. A., Xin, N. B. Ehd, A. (2021). **Uncertainty Estimation for Stereo Matching Based on Evidential Deep Learning.** https://doi.org/10.1016/j.patcog.2021.108498

(3) Cai, W., Zhai, B., Liu, Y., Liu, R., & Ning, X. (2021). **Quadratic polynomial guided fuzzy C-means and dual attention mechanism for medical image segmentation**. *Displays*, 70, 102106. https://doi.org/10.1016/j.displa.2021.102106

(4) Ning, X., Duan, P., Li, W., & Zhang, S. (2020). **Real-time 3D face alignment using an encoder-decoder network with an efficient deconvolution layer**. *IEEE Signal Processing Letters*, 27, 1944-1948. https://doi.org/10.1109/LSP.2020.3032277

(5) Miao, J., Wang, Z., Ning, X., Xiao, N., Cai, W., & Liu, R. (2022). **Practical and secure multifactor authentication protocol for autonomous vehicles in 5G.** *Software: Practice and Experience*. https://doi.org/10.1002/SPE.3087

(6) Beruvides, G., Casta?O, F., Quiza, R., & Haber, R. E. (2016). **Surface roughness modeling and optimization of tungsten–copper alloys in micro-milling processes**. *Measurement*, 246-252. https://doi.org/10.1016/j.measurement.2016.03.002

(7) Chen, Y., Wang, L., Hu, J., & Ye, M. (2020). **Vision-Based Fall Event Detection in Complex Background Using Attention Guided Bi-directional LSTM**. https://doi.org/10.1109/ACCESS.2020.3021795

(8) Shan, W. (2022). **Digital streaming media distribution and transmission process optimisation based on adaptive recurrent neural network**. *Connection Science*, 34(1), 1169-1180. https://doi.org/10.1080/09540091.2022.2052264

(9) Yan, C., Pang, G., Bai, X., Liu, C., Xin, N., Gu, L., & Zhou, J. (2021). **Beyond triplet loss: person re-identification with fine-grained difference-aware pairwise loss**. *IEEE Transactions on Multimedia*. https://doi.org/10.1109/TMM.2021.3069562

(10) Hu, X., Liu, T., Hao, X., & Lin, C. (2022). **Attention-based Conv-LSTM and Bi-LSTM networks for large-scale traffic speed prediction**. *The Journal of Supercomputing*, 1-24. https://doi.org/10.1007/s11227-022-04386-7

(11) Huang, Z., Wei, X., & Kai, Y. (2015). **Bidirectional LSTM-CRF Models for Sequence Tagging**. *Computer Science*. https://doi.org/10.48550/arXiv.1508.01991

(12) Jin, C., Shi, Z., Li, W., & Guo, Y. (2021). **Bidirectional LSTM-CRF Attention-based Model for Chinese Word Segmentation**. https://doi.org/10.48550/arXiv.2105.09681

(13) Ying, L., Nan, Z. Q., Ping, W. F., Kiang, C. T., Pang, L. K., Chang, Z. H. Nam, L. (2021). **Adaptive weights learning in CNN feature fusion for crime scene investigation image classification**. *Connection Science*. https://doi.org/10.1080/09540091.2021.1875987

(14) Li, D., & Lasenby, J. (2021). **Spatiotemporal Attention-Based Graph Convolution Network for Segment-Level Traffic Prediction**. *IEEE Transactions on Intelligent Transportation Systems*, (99), 1-9. https://doi.org/10.1109/TITS.2021.3078187

(15) Li, M., Liu, X., & Xiong, A. (2002). **Prediction of the mechanical properties of forged TC11 titanium alloy by ANN**. J*ournal of Materials Processing Technology*, 121(1), 1-4. https://doi.org/10.1016/S0924-0136(01)01006-8

(16) Liu, Z., Zhou, W., & Li, H. (2019). **AB-LSTM: Attention-based Bidirectional LSTM Model for Scene Text Detection**. *ACM Transactions on Multimedia Computing Communications and Applications*, 15(4), 1-23. https://doi.org/10.1145/3356728

(17) Olave, M., Sagartzazu, X., Damian, J., & Serna, A. (2010). **Design of Four Contact-Point Slewing Bearing With a New Load Distribution Procedure to Account for Structural Stiffness**. *Journal of Mechanical Design*, 132(2), 021006. https://doi.org/10.1115/1.4000834

(18) Tang, D., Wei, F., Nan, Y., Ming, Z., & Bing, Q. (2014). **Learning Sentiment-Specific Word Embedding for Twitter Sentiment Classification**. *Paper presented at the Proceedings of the 52nd Annual Meeting of the Association for Computational Linguistics,* 1.

(19) Gao, Y., & Yu, D. (2020). **Total variation on horizontal visibility graph and its application to rolling bearing fault diagnosis**. *Mechanism and Machine Theory*, 147, 103768. https://doi.org/10.1016/j.mechmachtheory.2019.103768

(20) Nguyen, T. (2019). **Spatiotemporal Tile-based Attention-guided LSTMs for Traffic Video Prediction**. https://doi.org/10.48550/arXiv.1910.11030

(21) Sagnika, S., Mishra, B., & Meher, S. K. **An attention-based CNN-LSTM model for subjectivity detection in opinion-mining**. *Neural Computing and Applications*, 1-14. https://doi.org/10.1007/s00521-021-06328-5

(22) Shan, X., Wang, Y., Dong, M., & Xia, J. (2021). **Application Research and Analysis of Geographic Information System in Intelligent City Surveying and Mappinge**. *Journal of Physics: Conference Series*, 1881(4), 042071. https://doi.org/10.1088/1742-6596/1881/4/042071

(23) Shi, X., & Wang, B. (2021). **Application of New Surveying and Mapping Technology in the Construction of Smart City.** *E3S Web of Conferences*, 236, 04031. https://doi.org/10.1051/e3sconf/202123604031

(24) Shi, Z. L., Gong, Y., Cao, M., & Xiao, S. (2010). D**iscussion on the Application of Surveying and Mapping Technology in the Internet of Things Times**. *Modern Surveying and Mapping*, 65(4), 503-515. https://doi.org/10.1016/j.neuron.2010.01.035

(25) Andrejic, M., Bojovic, N., & Kilibarda, M. (2016). **A framework for measuring transport efficiency in distribution centers**. *Transport Policy,* 45(JAN.), 99-106. https://doi.org/10.1016/j.tranpol.2015.09.013

(26) Bergstrom, J. C., Braden, J. B., & Kolstad, C. D. (1991). **Measuring the demand for environmental quality**. *American Journal of Agricultural Economics*, 75(1), 244. https://doi.org/10.2307/1242975

(27) Brock, W. A., & Taylor, M. S. (2005). **Economic Growth and The Environment: A Review of Theory and Empirics**. *Handbook of Economic Growth*. https://doi.org/10.1016/S1574-0684(05)01028-2

(28) Wang, M., Zhou, J., Gao, J., Li, Z., & Li, E. (2020). **Milling Tool Wear Prediction Method Based on Deep Learning under Variable Working**

Conditions. *IEEE Access*, 99, 1-1. https://doi.org/10.1109/ACCESS.2020.3010378

(29) Amin, T., Khan, F., Ahmed, S., & Imtiaz, S. (2020). **A novel data-driven methodology for fault detection and dynamic risk assessment**. *The Canadian Journal of Chemical Engineering*. https://doi.org/10.1002/cjce.23760

(30) Horani M. O., Najeeb, M., y Saeed, A. (2021). **Model electric car with wireless charging using solar energy**. *3C Tecnología. Glosas de innovación aplicadas a la pyme*, 10(4), 89-101. https://doi.org/10.17993/3ctecno/2021.v10n4e40.89-101

(31) Chang Jingying,Lan Weibin & Lan Wenhao. (2021). **Higher education innovation and reform model based on hierarchical probit**. *Applied Mathematics and Nonlinear Sciences, 7*(1), 175-182. https://doi.org/10.2478/AMNS.2021.2.00154

/09/

APPLICATION OF SURVEYING AND MAPPING TECHNOLOGY BASED ON DEEP LEARNING MODEL IN PETROLEUM GEOLOGICAL EXPLORATION

Sheng Sun*

School of Modern Service Management, Shandong Youth University of Political Science, Jinan, Shandong, 250103, China

sunsdjn2013@163.com

Ping Shu

School of Philosophy and Social Development, Shandong University, Jinan, Shandong, 250103, China

ABSTRACT

Surveying and mapping technology is one of the key technologies used in petroleum geological exploration and has made significant contributions to geological exploration. However, with the development of science and technology, traditional surveying and mapping technology has low work efficiency and poor information accuracy, which limits its application. This study proposes a surveying and mapping technology based on the 1DCNN-LSTM deep learning model. Through feature selection and feature optimization, the important features extracted by 1DCNN are predicted through LSTM, and the development direction of surveying and mapping technology is optimized and predicted to promote the development of new surveying and mapping technologies. application. By using the orthogonal test to optimize the input factors, determine the relative order of the influence of the factors, and use the 1DCNN-LSTM and BP neural network to train and verify the input factors respectively. The research results show that 1DCNN-LSTM has higher prediction accuracy, and the prediction accuracy is The results show that the 1DCNN-LSTM deep learning model used in the optimization of petroleum geological exploration and mapping technology in this study has strong practical significance.

KEYWORDS

1DCNN-LSTM; Mapping technology; Deep learning model; Neural network; Optimization.

PAPER INDEX

1.   INTRODUCTION

The traditional surveying and mapping technology has low work efficiency and requires a lot of human resources to complete the survey work, but the final information accuracy is poor [1]. Under the rapid development of modern social science and technology, new surveying and mapping technologies with better performance have been developed. Digital surveying and mapping are the main forms, and they have been applied to the fields of hydrogeology, petroleum engineering, and other fields, and played their due role in the field of geological exploration. It greatly promotes the development of the exploration field, especially the geological exploration, and the accuracy requirements of the surveying and mapping technology are increasing day by day [2-3]. Therefore, it is extremely necessary to optimize the surveying and mapping technology.

At present, there is little research on the optimization of surveying and mapping technology, and it is of great significance to use deep learning models to optimize surveying and mapping technology. In recent years, some scholars have done a lot of work. Lu X H [4] established a prediction model of surveying and mapping technology through regression analysis using cutting parameters as independent variables. Beruvides [5] used the vibration signal sent out during the training process to establish the prediction model of surveying and mapping technology by using the adaptive neuro-fuzzy inference system and obtained a higher fitting index and better generalization ability. Some researchers [6] used the improved particle swarm algorithm to optimize the node selection of the hidden layer of the BP network and established the prediction model of the surveying and mapping technology. In addition, some researchers [7] proposed a parameter synchronization optimization algorithm for GA signal feature recognition and mapping prediction, established a GA-WPT-ELM prediction model, and obtained high prediction accuracy. With the development of artificial intelligence, deep learning makes data processing and results in prediction more efficient and accurate [8]. Its long short-term memory (LSTM) neural network algorithm improves the gradient disappearance problem of traditional recurrent neural networks (RNN) and provides a new method for the prediction of sequence data. Prediction problems are applied in the field of new technologies [9]. Wang M W et al. [10] established a long short-term memory model and realized the prediction of the wear of surveying and mapping tools by taking advantage of its advantages of solving the accumulation effect. Some researchers [11] proposed a traditional surveying and mapping stage identification model based on a deep LSTM neural network, which can more accurately reflect the wear state of surveying and mapping compared with traditional machine learning methods. Yu [12] proposed a state recognition method based on LSTM, which has higher recognition accuracy than BP neural network algorithm and SVM algorithm..

Although the LSTM network solves the problem of vanishing gradients, it has poor performance for batch sequence data processing, resulting in lower accuracy of the model in result prediction [13-14]. In this paper, taking petroleum surveying and mapping technology as the research object, a prediction model based on the combination of one-dimensional convolution and long short-term memory (1DCNN-

LSTM) neural network is established to solve the problem of batch sequence data processing, sample key feature learning, and small sample data processing. Mapping technology optimizes precision problems. Through examples and experiments, the effectiveness of the 1DCNN-LSTM prediction model for the prediction of the development of mapping technology is verified.

2. CORRELATION MODEL THEORY

2.1. LONG SHORT TERM MEMORY (LSTM)

Compared with the traditional RNN, the core idea of the LSTM neural network is to introduce "three gates" in each memory unit, use the three gates to interact with the unit state, and change the information borne by the united state. The retention of information is selectively determined within neurons. The most widely used LSTM network structure is shown in Fig.1.
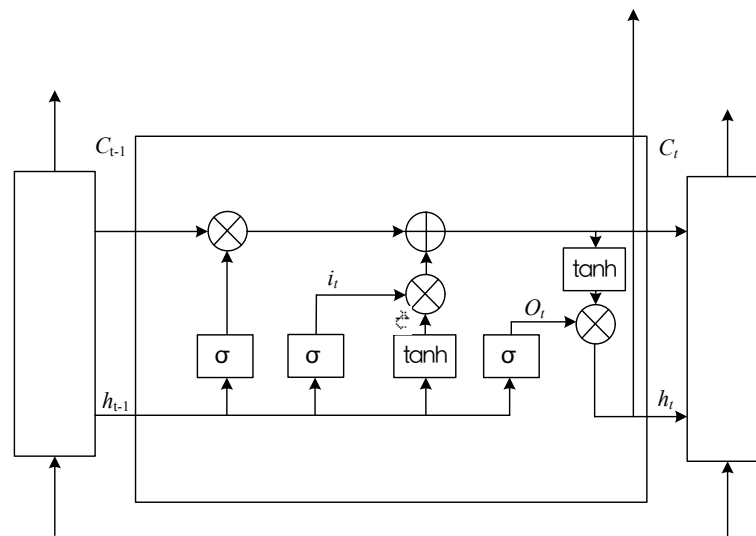
Figure 1. LSTM network structure.

As shown in Figure 1, the "three gates" of the LSTM network are the input gate which determines the retention of new information; the output gate Ot determines the output degree of information; the forgetting gate ft determines the retention of the original information state [15]. Its mathematical expression is as follows:

$$o_t = \sigma \left(w^o \cdot \left[h_{t-1}, x_t \right] + b^o \right) \tag{1}$$

$$h_t = o_t * \tanh \left(C_t \right) \tag{2}$$

In the formula: σ is the sigmoid activation function, the output range is 0~1; h_{t-1} is the input at the previous moment; x_t is the input at the current moment; W and b are the weight coefficients and bias terms corresponding to the three gates, respectively [16].

The LSTM network reduces the number of network layers and the sequence length through three gated structures effectively solves the problem of gradient disappearance and realizes the prediction of sequence data [17]. However, due to the poor processing of batch sequence data in the LSTM network itself, this paper introduces a 1DCNN network structure to make up for this deficiency.

2.2. ONE-DIMENSIONAL CONVOLUTIONAL NEURAL NETWORK (1DCNN)

Convolutional neural network (CNN) is one of the most perfect algorithms in the field of deep learning [18], which is divided into one-dimensional, two-dimensional, and three-dimensional. Among them, 1DCNN is good at processing sequence data, so this paper selects the 1DCNN network for data processing, the structure is shown in Figure 2. As shown in Figure 2, the sequence data is input into 1DCNN for preliminary feature extraction [19], and the sub-sequences composed of high-level features are effectively extracted, and the interference information is removed as the input node of the LSTM layer. At the same time, the network can directly identify local simple patterns in the data and apply them to higher-level networks to form more complex network patterns [20].
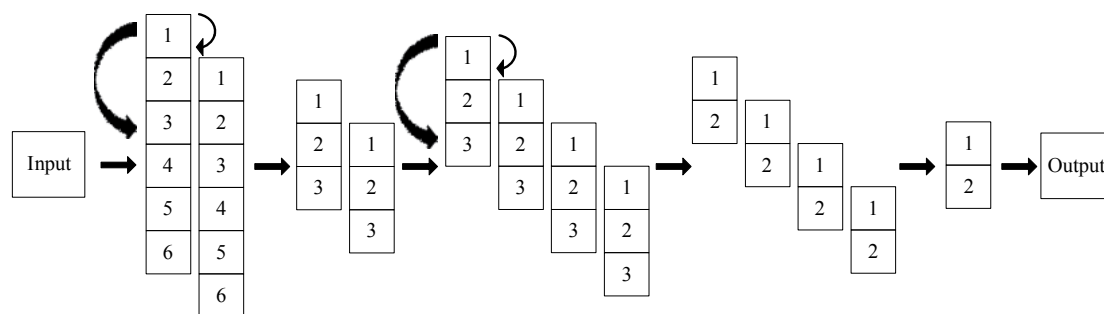
Figure 2. The structure of the 1DCNN convolutional layer.

Let the ith input data of the convolution layer be I_i, the convolution kernels are W_i, each with n pieces, the bias is B_i, the activation function is f, and the downsampling operation is to further reduce the dimension of the features of the convolution output., and input the corresponding output to the fully connected layer, the fully connected layer obtains the classification result of this round after weight transformation and activation, and the corresponding classification error is obtained by comparing with the true value of the classification [21]. Let the input feature of the fully connected layer be T, the corresponding weight is W, the bias is B, and the activation function is f, the output of the convolutional layer and the pooling method formula is as follows [22]:

$$O_t = f(WX + b) \tag{3}$$

$$O_t = ReLU\left[\left(\sum_{i=0}^{\lambda-1} W_i x_{t+i}\right) + b\right] \tag{4}$$

$$P\left(y^i = j \middle| x^i; \theta\right) = \frac{e^{\theta_j T_x i}}{\sum_{K=1}^{K} e^{\theta_j T_x i}} \tag{5}$$

Among them, W is the convolution kernel, $X \in RT \times n$ is the input word vector matrix, and parameter b is the bias term. Commonly used nonlinear activation functions are Sigmoid or ReLU. x is the output vector of the previous neural network [23].

2.3. DCNN-LSTM NETWORK MODEL CONSTRUCTION

2.3.1. MODEL BUILDING

Based on the ability of 1DCNN layer data processing and LSTM layer data prediction, a 1DCNN-LSTM surface roughness prediction model was established [24]. Its structure is shown in Fig.3, including a one-dimensional convolutional layer, a Batch-Normalize layer, an LSTM layer, and a fully connected layer [25]. After the data is input, through the Conv algorithm, the features are identified and then entered into the LSTM layer and the fully connected layer.
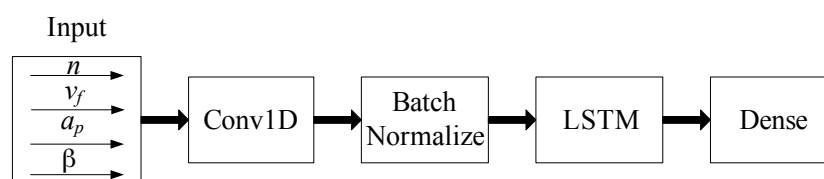
Figure 3. 1DCNN-LSTM prediction model structure.

2.3.2. MODEL PARAMETER DETERMINATION AND DATA PREPROCESSING

There are many influencing factors of surveying and mapping technology, mainly including field surveying and mapping n, network layout vf, dynamic real-time surveying and mapping ap, and geodetic surveying control network point β. There is a complex nonlinear relationship between these four parameters and new surveying and mapping technology. Therefore, based on the establishment of the prediction model framework, the prediction model is optimized through parameter selection [26], and the specific steps are as follows:

(1) Input layer and output layer. The four milling parameters n, vf, ap and β are used as the input node of the prediction model, and the surface roughness Ra is used as the output node of the prediction model.

(2) Hidden layer. The hidden layer plays a key role in the network architecture. The number of filters (filters) of the one-dimensional convolutional layer of the model is 1, the size of the convolution kernel (kernel_size) is 3, and the stride (stride) is 1, and the padding (padding) is 1. The LSTM layer node is 2, and the fully connected layer node is 2.

(3) Learning rate. To adjust the appropriate learning rate parameters and avoid going over the optimal solution or the model falling into the local optimal solution, through continuous testing and adjustment, the Adam algorithm model is used, and the learning rate parameter is finally selected as 0.001.

(4) Data preprocessing. In this dataset, *n*, *vf*, *ap* and *β* of each group of experiments constitute a set of input parameters, the output parameters are the micro-milling surface roughness of each group, and the input parameters and output parameters constitute a set of sample data.

The purpose of preprocessing the sample data is to normalize the data features of each dimension to the same value range so that the model training effect is better and the generalization ability is stronger. For this purpose, all input data are normalized to [0, 1] in this paper, and the normalization formula is:

$$y_i = \frac{x_i - x_{i\min}}{x_{i\max} - x_{i\min}} \tag{15}$$

In the formula: x_i is the original data; x_{min} is the minimum value in the original data; x_{imax} is the maximum value in the original data; y_i is the normalized value, and $y_i \in [0,1]$.

After data preprocessing, the data can be used as an input layer node for Ra prediction.

3. TEST AND RESULT ANALYSIS

3.1. ORTHOGONAL TEST TO OPTIMIZE INPUT FACTORS

In the micro-slot milling experiment, this paper mainly considers the influence of spindle speed n, feed rate vf, milling depth ap, and micro-milling cutter helix angle β on the surface roughness. To fully consider the influence of the above four factors on the surface roughness in a small number of experiments, a four-factor and five-level orthogonal experiment were carried out, and the parameters are shown in Table 1.

Table 1. Orthogonal parameter factor level table.

Level	Field surveying and mapping coefficient	Network speed	Dynamic real-time mapping depth	Geodetic Control Dot Spiral Angle
1	5	1.5	10	25
2	15	3.0	15	30
3	25	4.5	20	35
4	35	6.0	25	40
	45	7.5	30	45

The range analysis method was used to process the experimental results to obtain the relationship between each factor and the surface roughness Ra, as shown in Figure 4.
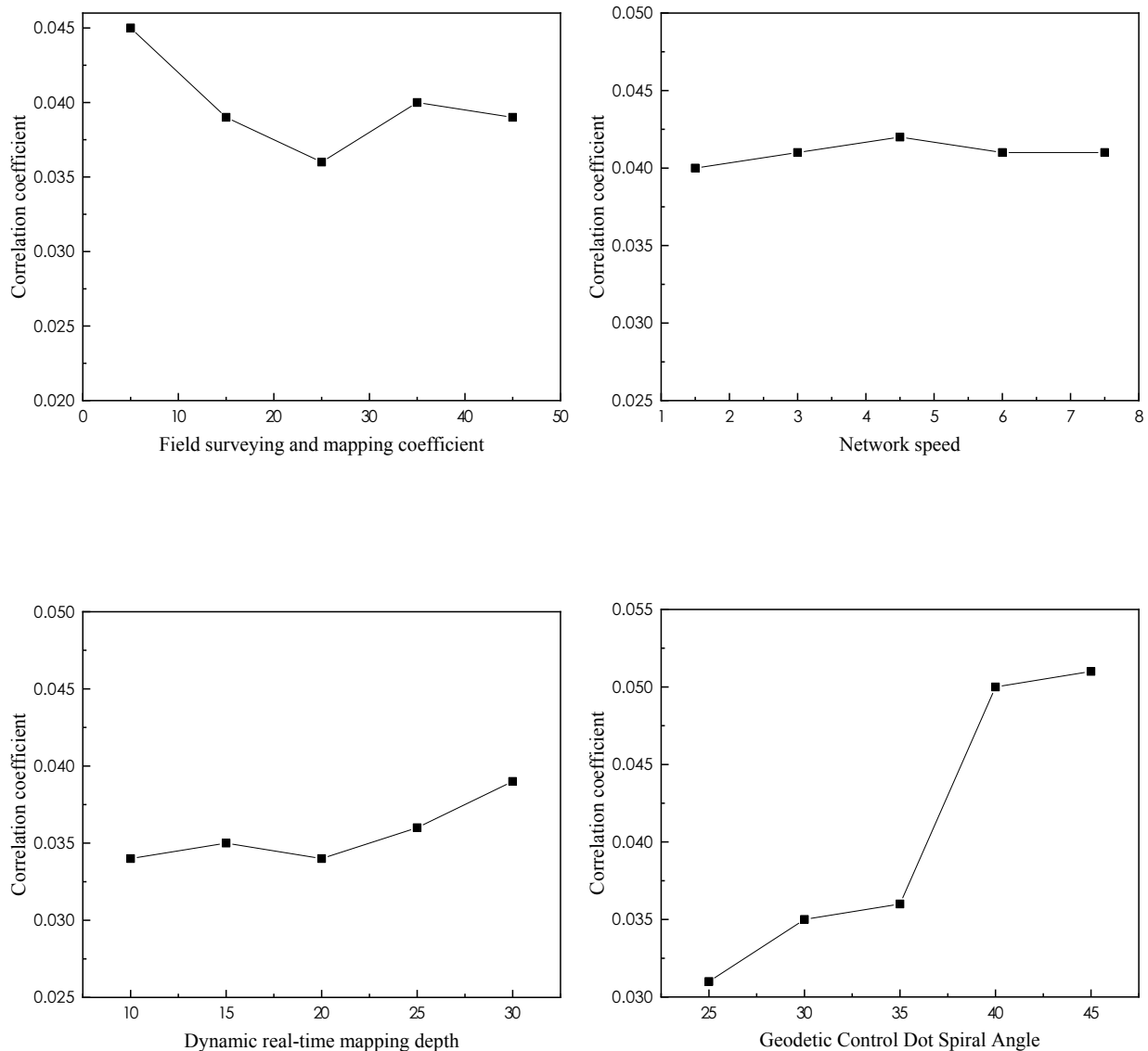
Figure 4. The relationship between the experimental factors and the Ra value of the surveying and mapping technology, a) field surveying and mapping coefficient; b) network speed; c) Dynamic real-time mapping depth d) Geodetic control network point helix angle.

It can be seen from the figure that the dynamic real-time surveying and mapping depth and the geodetic control network point helix angle have similar effects on the surveying and mapping technology, the correlation coefficient increases with the increase of its value, and the geodetic control network point helix angle has the most significant impact on the surveying and mapping technology; surveying and mapping The technical correlation coefficient decreases with the increase of the field surveying and mapping coefficient; however, the influence of the network deployment speed is not significant, so a slightly larger network deployment speed can be adopted to improve the correlation coefficient of the surveying and mapping technology. In addition, for the field surveying and mapping coefficient, with the increase of the abscissa, the correlation coefficient shows a downward trend, while the distribution speed has almost no change. However, for the dynamic real-time mapping depth and

the geodetic control mesh point helix angle, both show an upward trend with increasing depth and angle.

3.2. DCNN-LSTM MODEL PREDICTION AND RESULT ANALYSIS

To obtain accurate and credible batch training data sets, 139 groups of random experiments were performed, and 164 groups of training data sets were obtained. Combined with various influencing factors, the main parameters of the random experiment are shown in Table 2. To make the model training more balanced, the dataset is randomly distributed before training, and then the normalized dataset is input into the model to start training [27]. The epochs are chosen to be 5000 times, during the training process of each epoch, all training datasets will be trained once, and the network automatically calculates the gradient of the batch loss concerning the weights and updates the weights accordingly.

Table 2. Parameter range

Field surveying and mapping coefficient	Network speed	Dynamic real-time mapping depth	Geodetic Control Dot Spiral Angle
5000-75000	1.5-100	6-100	25,30,35,40,45

The 164 datasets are divided into two groups, of which 150 are training sets and the remaining 14 are validation sets. The training process of the 1DCNN-LSTM model is shown in Figure 5. It can be seen from the figure that when the training round reaches 3000 times, the training accuracy has reached about 95%, and the verification accuracy has reached about 91%, indicating that the accuracy is high. Very stable and meets forecast requirements. To verify the accuracy of the 1DCNN-LSTM prediction model, 15 sets of experimental parameters were designed for testing, and the experimental data were normalized and input into the two prediction models of the 1DCNN-LSTM neural network and BP neural network, respectively. prediction results.

Table 3. Prediction results

Number	1DCNN-LSTM Neural Network		BP neural network	
	Ra predicted value	Error percentage	Ra predicted value	Error percentage
1	0.1681	4.2	0.2181	11.09
2	0.0861	3.1	0.2132	12.15
3	0.0192	5.1	0.1055	16.33
4	0.0523	6.4	0.0755	21.36
5	0.0490	0.8	0.0489	18.55
6	0.0207	5.1	0.0230	20.91
7	0.0568	3.2	0.0110	4.64
8	0.0772	2.1	0.0225	9.24

9	0.1191	9.1	0.0762	6.22
10	0.0875	7.8	0.0868	3.81
11	0.0542	6.1	0.0871	25.1
12	0.1121	5.3	0.0940	13.84
13	0.0258	2.2	0.0123	11.2
14	0.1391	10.1	0.1012	13.6
15	0.0913	7.1	0.0847	22.2

As shown in Table 3, to compare the prediction accuracy of the two models, the average relative prediction error is used as the evaluation index, and the formula is as follows:

$$\delta = \frac{\sum_{i=1}^{n}|R_{ai}| - \overline{R_{ai}}}{\sum_{i=1}^{n}\overline{R_{ai}}} \tag{16}$$

In the formula: δ is the average relative prediction error; R_{ai} is the predicted value of each model; R_{ai}^{-} is the measured value of the milling test.
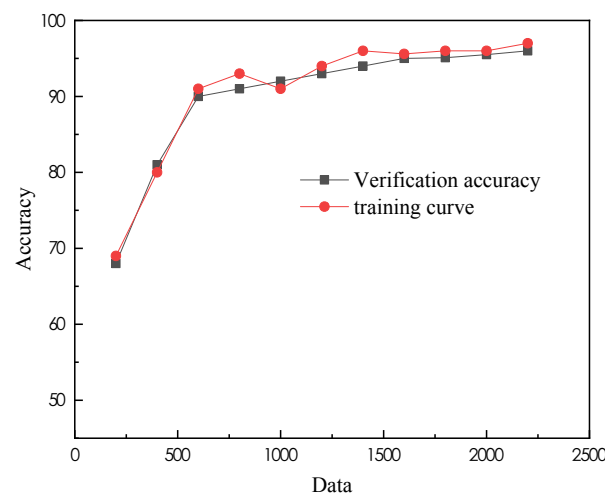
Figure 5. 1DCNN-LSTM prediction model training process

According to the evaluation indicators, the 1DCNN-LSTM model is 5.90%, while the BP model is 14.92%, and the evaluation effect of the 1DCNN-LSTM model is much higher than that of the BP model. It shows that the sample features adaptively extracted by the 1DCNN layer can better reflect the efficient data processing capability of the network layer than the artificial extraction features, and the short sequence samples composed of high-level features can effectively improve the prediction accuracy for the data extraction and analysis of the LSTM layer. Based on this, the prediction model established by the 1DCNN-LSTM network can accurately predict the improvement direction of the mapping technology under different parameters, which fully proves that the prediction model has strong applicability and

high prediction accuracy. According to the above results, it can be concluded that the model meets the requirements of accurate prediction [28].

3.3. APPLICATION OF NEW TECHNOLOGY OF SURVEYING AND MAPPING IN PETROLEUM GEOLOGICAL EXPLORATION

3.3.1. FIELD SURVEYING AND MAPPING

When using new surveying and mapping technology for field surveying and mapping work, it is necessary to select an accurate measurement point to ensure the accuracy of the measurement results[29-30]. Since this measurement point has a decisive impact on the accuracy of the entire measurement Make preparations such as the frame to ensure that the technology can be effectively used.

3.3.2. CLOTH NET

In the work of network layout, it is necessary to use connection points or line connections to achieve it. When performing network layout work for different measurement areas, it is necessary to do a good job of understanding the local terrain and formulate a reasonable network layout strategy according to the situation of the measurement area. For example, in the process of work, two different ways of construction network and information network are formulated according to the needs. At the same time, reasonable network distribution can also ensure the network strength during work, to ensure that the system can make full use of the network for efficient data measurement and storage, and at the same time make the measurement results more accurate.

3.3.3. DYNAMIC REAL-TIME MAPPING

The dynamic real-time surveying and mapping work requires a base station, and at the same time surveying and mapping, it is ensured that each device is used reasonably to improve the accuracy of the surveying and mapping work. In the survey work, it is necessary to use a large number of wireless transmission technology, and the obtained surveying and mapping results are sent to the information receiving station. When observing whether the rover at the scene can receive the information sent from different sending stations, it can also rely on the data transmitted by the base station. to locate. The base station and the mobile station can use the data observed by themselves and the difference value transmitted by themselves to calculate to obtain the relative positions of different stations, to output and store the three-dimensional coordinates.

3.3.4. GEODETIC CONTROL NETWORK

The new surveying and mapping technology in the geodetic control network is to use satellite positioning technology to complete the measurement of the basic control network. Since my country has a very large land area, the distance between each geodetic control network Measuring tool does not perform effective distance measurements. In the measurement of the urban control network, measurement tools need to be used frequently, and the measurement tools need to cover a larger area and have higher accuracy. The new technology of surveying and mapping has the above characteristics, can meet the requirements of related surveying work, and has the advantage of simple operation, which can solve the above surveying problems.

4. CONCLUSION

The traditional surveying and mapping technology has low work efficiency and requires a lot of human resources to complete the survey work, but the final information accuracy is poor. This study, this paper takes petroleum surveying and mapping technology as the research object, and establishes a prediction model based on the combination of one-dimensional convolution and long short-term memory (1DCNN-LSTM) neural network, using orthogonal optimization to optimize input parameters, increase prediction accuracy, and at the same time with BP The accuracy of the neural network is compared, and the following conclusions are obtained: (1) The input parameters of the 1DCNN-LSTM optimized by the orthogonal test optimization method, the results predicted by the model have high prediction accuracy, high prediction effectiveness, and correlation. The influencing factors are the dynamic real-time surveying and mapping depth and the geodetic control network point helix angle, field surveying, and network layout; (2) The prediction accuracy of 1DCNN-LSTM for oil exploration surveying and mapping technology is significantly higher than that of BP neural network, and the errors of the two are the highest, respectively. 10.1% and 25.1%; (3) The sample features adaptively extracted by the DCNN layer can better reflect the efficient data processing capability of the network layer than the artificially extracted features, and the short sequence samples composed of high-level features are for the data of the LSTM layer. Extraction analysis effectively improves prediction accuracy.

5. CONFLICT OF INTEREST

The authors declared that there is no conflict of interest.

REFERENCES

(1)   Lu, W., Zhao, L. J., & Xu, R. (2021). **Remote sensing image processing technology based on mobile augmented reality technology in surveying and mapping engineering**. *Soft Computing,* (4). https://doi.org/10.1007/s00500-021-05650-3

(2)   Shan, X., Wang, Y., Dong, M., & Xia, J. (2021). **Application Research and Analysis of Geographic Information System in Intelligent City Surveying**

and Mappinge. *Journal of Physics: Conference Series*, 1881(4), 042071. https://doi.org/10.1088/1742-6596/1881/4/042071

(3) Xc, A., Bta, B., Yan, L. A., Xx, A., Lei, L. C., Hk, A., & Jl, A. (2019). **Dynamic recrystallization behavior of the Ti–48Al–2Cr–2Nb alloy during isothermal hot deformation**. *Progress in Natural Science: Materials International*, 29(5), 587-594. https://doi.org/10.1016/j.pnsc.2019.08.004

(4) Lu, X., Wang, F. R., Xue, L., Feng, Y., & Liang, S. Y. (2019). **Investigation of material removal rate and surface roughness using multi-objective optimization for micro-milling of inconel 718**. *Industrial Lubrication and Tribology*, 71(6). https://doi.org/10.1108/ILT-07-2018-0259

(5) Beruvides, G., Casta?O, F., Quiza, R., & Haber, R. E. (2016). **Surface roughness modeling and optimization of tungsten–copper alloys in micro-milling processes**. *Measurement*, 246-252. https://doi.org/10.1016/j.measurement.2016.03.002

(6) Shi, Z. L., Gong, Y., Cao, M., & Xiao, S. (2010). **Discussion on the Application of Surveying and Mapping Technology in the Internet of Things Times**. *Modern Surveying and Mapping*, 65(4), 503-515. https://doi.org/10.1016/j.neuron.2010.01.035

(7) Shi, X., & Wang, B. (2021). **Application of New Surveying and Mapping Technology in the Construction of Smart City**. *E3S Web of Conferences*, 236, 04031. https://doi.org/10.1051/e3sconf/202123604031

(8) Wang, J., Ran, R., Song, Z., & Sun, J. (2017). **Short-Term Photovoltaic Power Generation Forecasting Based on Environmental Factors and GA-SVM**. *Journal of Electrical Engineering & Technology*, 12(1), 64-71. https://doi.org/10.5370/JEET.2017.12.1.064

(9) Zhang, X. Y., Deng, C. H., & Chen, T. T. (2011). **Ultra-Short-Term Ahead Generating Power Forecasting for PV System Based on Markov Chain for Error Series**. *Advanced Materials Research*, 347-353, 1498-1505. https://doi.org/10.4028/www.scientific.net/AMR.347-353.1498

(10) Wang, M., Zhou, J., Gao, J., Li, Z., & Li, E. (2020). **Milling Tool Wear Prediction Method Based on Deep Learning under Variable Working Conditions**. *IEEE Access*, 8, 140726-140735. https://doi.org/10.1109/ACCESS.2020.3010378

(11) Yi, S., Wang, X., & Tang, X. (2014). **Deep Learning Face Representation by Joint Identification-Verification**. *Advances in neural information processing systems*, 27. https://doi.org/10.48550/arXiv.1406.4773

(12) Yu, S., Zeng, W., Zhao, Y., Shao, Y., & Zhou, Y. (2012). **Modeling the Correlation of Composition-Processing-Property for TC11 Titanium Alloy Based on Principal Component Analysis and Artificial Neural Network**. *Journal of Materials Engineering & Performance*, 21(11), 2231-2237. https://doi.org/10.1007/s11665-012-0162-y

(13) Huang, Z., Wei, X., & Kai, Y. (2015). **Bidirectional LSTM-CRF Models for Sequence Tagging**. *Computer Science*. https://doi.org/10.48550/arXiv.1508.01991

(14) Li, M., Liu, X., & Xiong, A. (2002). **Prediction of the mechanical properties of forged TC11 titanium alloy by ANN**. *Journal of Materials Processing Technology*, 121(1), 1-4. https://doi.org/10.1016/S0924-0136(01)01006-8

(15) Cai, W., Zhai, B., Liu, Y., Liu, R., & Ning, X. (2021). **Quadratic polynomial guided fuzzy C-means and dual attention mechanism for medical image segmentation**. *Displays*, 70, 102106. https://doi.org/10.1016/j.displa.2021.102106

(16) Miao, J., Wang, Z., Ning, X., Xiao, N., Cai, W., & Liu, R. (2022). **Practical and secure multifactor authentication protocol for autonomous vehicles in 5G**. *Software: Practice and Experience*. https://doi.org/10.1002/SPE.3087

(17) Liu, Z., Zhou, W., & Li, H. (2019). **AB-LSTM: Attention-based Bidirectional LSTM Model for Scene Text Detection**. *ACM Transactions on Multimedia Computing Communications and Applications*, 15(4), 1-23. https://doi.org/10.1145/3356728

(18) Ning, X., Duan, P., Li, W., & Zhang, S. (2020). **Real-time 3D face alignment using an encoder-decoder network with an efficient deconvolution layer**. *IEEE Signal Processing Letters*, 27, 1944-1948. https://doi.org/10.1109/LSP.2020.3032277

(19) Sagnika, S., Mishra, B., & Meher, S. K. **An attention-based CNN-LSTM model for subjectivity detection in opinion-mining**. *Neural Computing and Applications*, 1-14. https://doi.org/10.1007/s00521-021-06328-5

(20) Ning, X., Gong, K., Li, W., & Zhang, L. (2021). **JWSAA: joint weak saliency and attention aware for person re-identification**. *Neurocomputing*, 453, 801-811. https://doi.org/10.1016/j.neucom.2020.05.106

(21) Shan, W. (2022). **Digital streaming media distribution and transmission process optimisation based on adaptive recurrent neural network**. *Connection Science*, 34(1), 1169-1180. https://doi.org/10.1080/09540091.2022.2052264

(22) Chen, Y., Wang, L., Hu, J., & Ye, M. (2020). **Vision-Based Fall Event Detection in Complex Background Using Attention Guided Bi-directional LSTM**. https://doi.org/10.1109/ACCESS.2020.3021795

(23) Qi, F., Gao, C., Lan, W., Yue, Z., Song, T., & Li, Q. (2018). **Spatio-temporal fall event detection in complex scenes using attention guided LSTM**. *Pattern Recognition Letters*, S016786551830504X-. https://doi.org/10.1016/j.patrec.2018.08.031

(24) Yan, C., Pang, G., Bai, X., Liu, C., Xin, N., Gu, L., & Zhou, J. (2021). **Beyond triplet loss: person re-identification with fine-grained difference-aware pairwise loss**. *IEEE Transactions on Multimedia*. https://doi.org/10.1109/TMM.2021.3069562

(25) Nguyen, T. (2019). **Spatiotemporal Tile-based Attention-guided LSTMs for Traffic Video Prediction**. https://doi.org/10.48550/arXiv.1910.11030

(26) Ying, L., Nan, Z. Q., Ping, W. F., Kiang, C. T., Pang, L. K., Chang, Z. H., Nam, L. **Adaptive weights learning in CNN feature fusion for crime scene investigation image classification**. *Connection Science*. https://doi.org/10.1080/09540091.2021.1875987

3C Tecnología. Glosas de innovación aplicadas a la pyme. ISSN: 2254-4143   Ed.43 | Iss.12 | N.1 January - March 2023

(27) Li, D., & Lasenby, J. (2022). **Spatiotemporal Attention-Based Graph Convolution Network for Segment-Level Traffic Prediction**. *IEEE Transactions on Intelligent Transportation Systems*, 23(7), 8337-8345. https://doi.org/10.1109/TITS.2021.3078187

(28) Hu, X., Liu, T., Hao, X., & Lin, C. (2022). Attention-based Conv-LSTM and Bi-LSTM networks for large-scale traffic speed prediction. The Journal of Supercomputing, 1-24. https://doi.org/10.1007/s11227-022-04386-7

(29) Juárez, F. F., Esenarro, D., Díaz, M., y Frayssinet, M. (2021). **Model based on balanced scorecard applied to the strategic plan of a peruvian public entity**. *3C Empresa. Investigación y pensamiento crítico*, 10(4), 127-147. https://doi.org/10.17993/3cemp.2021.100448.127-147

(30) Xu Bo, Wang Ran, Peng Baoying, Alqurashi Fahad Abdullah & Salama Mohamad. (2021). **Automatic parameter selection ZVD shaping algorithm for crane vibration suppression based on particle swarm optimisation**. *Applied Mathematics and Nonlinear Sciences, 7*(1), 73-82. https://doi.org/10.2478/AMNS.2021.1.00075

3C Tecnología. Glosas de innovación aplicadas a la pyme. ISSN: 2254-4143

Ed.43 | Iss.12 | N.1 January - March 2023

/10/

3C Tecnología. Glosas de innovación aplicadas a la pyme. ISSN: 2254-4143

Ed.43 | Iss.12 | N.1 January - March 2023

175

EVALUATION THE WATER QUALITY OF AL-RUSAFA TREATMENT PLANT IN BAGHDAD CITY / AL-RUSAFA SIDE USING SEVERAL WATER QUALITY INDICES

Ahmed Amer Shanoon*

College of Engineer, Al-Nahrain University, Baghdad, Iraq

st.ahmed.amer@ced.nahrainuniv.edu.iq

Prof. Dr. Jabbar H. Al-Baidhani

College of Engineer, Al-Nahrain University, Baghdad, Iraq

https://doi.org/10.17993/3ctecno.2023.v12n1e43.176-189

ABSTRACT

The present study was conducted drinking water treatment plant located in districts which is (Al-Rusafa) in Baghdad city. The study aims to assess the water quality produced from the above plant using various water quality indices. Twelve physical and chemical parameters have been tested which are pH, turbidity, electrical conductivity, calcium, magnesium, chloride, total hardness, alkalinity, sulfate, sodium and total dissolved solids. Five different approaches and methodologies of water quality indices were applied to get the level of pollution during a period of nine months, starting from November 2021 until July 2022.The values WAV WQI for water treatment pant indicate that the water quality was good. Also, the results of the MNE WQI showed that water treatment plant produced clean water, but Al-Rusafa treatment plant in April, the water was very clean. The values of (weighted method) indicated that the water quality for water treatment plant was good. It was found that water treatment plant studied gives excellent quality using based on values of CCME and BCWQI indices. It is found that the values of all chemical and physical parameters are within Iraqi standards. Finally, in the present study, many statistical equation were found for the purpose of calculating the water quality index for water treatment plant studied with a proper coefficient of determinations.

KEYWORDS

Water Quality Indices, WAV WQI, water treatment plants, CCME, BCWQI.

PAPER INDEX

INTRODUCTION

Water is a valuable natural resource that we utilize for drinking and a variety of other reasons in our daily lives. [1]. Safe drinking water is essential for human health around the world; as a universal solvent, water is a primary source of protection against contamination and illness, according to the World Health Organization (WHO) Water-borne diseases account for 80% of all diseases, and drinking water in many countries does not satisfy WHO criteria [2], with 3.1 percent of deaths attributed to the unclean and poor quality of water. [3]. Water pollution occurs when unwanted contaminants enter water, altering its quality and posing a threat to the environment and human health. [4]. Some drinking water supplies have been contaminated with germs, viruses, heavy metals, and salts as a result of insufficient treatment and management of waste industrial outputs. [5] Diseases such as cholera, dysentery, and typhoid are caused by a lack of safe drinking water and proper sanitation measures, and millions of lives are lost each year in impoverished countries [6]. Water is required not only for metabolic systems in the human body, but also for other activities related with human life, such as distilled water for laboratories, medical factories, minerals in drinking water, industries, agricultural, aquatic cultures, and other similar activities [7]. The WQI can be defined as a mathematical tool transforming large quantities of data obtained from physical and chemical properties of water into a single number representing the level of water quality (Bharti and Katyal, 2011) [14]. Water quality is determined by its physical, chemical, and biological characteristics. Before using water for different intended uses, such as potable, agricultural, recreational, and industrial water utilizations, it is vital to determine the water's quality. It's critical to establish water quality metrics in order to assess the condition, quality, and level of contamination of surface water. Processing related data is necessary, and professionals should be shown the outcomes. Using water quality indicators is one of the simplest ways to evaluate current water quality conditions [10]. A need for all living things as a result, "no water, no life" is correct [9]. As a result, the goal of water treatment is to deliver water that is as close to pure as possible. Depending on the source of water, the degree of contamination, and the desired water quality, this treatment may be traditional or advanced. All water treatment plants in Iraq are conventional, and they strive to remove suspended and pathogenic contaminants. Sedimentation and filtering with coagulant assistance are employed to remove suspended and colloidal particles in these traditional plants, and chlorine is used to kill pathogens. After the water had went through the treatment process, multiple tests were carried out to measure its parameters and compare them to standards in order to assess its quality and determine whether it fulfilled the requisite criteria. Physical, chemical, and biological factors are all tested in this water.

The Tigris river is Baghdad's primary source of drinking water; yet, in recent years, there has been a rise in wastewater and direct Tigris river discharge. Furthermore, the presence of antibiotics in drinking water, in addition to other contaminants, was discovered [8], As a result, one of the most important resources is water.The research on green ecological agriculture management is of great significance to the development of ecological agriculture and the solution of various drawbacks and

crises brought by modern agriculture. However, in the current e-commerce sales, the safety and quality of agricultural products cannot be presented to customers. Based on this, in our research, we build an information-based digital management platform, which includes developed languages, frameworks and database. In the digital information management platform, we track and monitor the agricultural product information of green ecological agriculture in Northeast China throughout the whole process, so as to ensure the safety and quality of the agricultural products during the sale of the agricultural products on the e-commerce platform. In addition, we also discussed the economic benefits of this digital information platform for green ecological agriculture.

CONSTRUCTION OF INFORMATION DIGITAL MANAGEMENT PLATFORM

In order to better understand the situation of green ecological agriculture in Northeast China, this chapter mainly introduces the development languages, development frameworks and tools used in the electronic platform of agricultural products, and gives a brief introduction to them according to the situation of green ecological agriculture in Northeast China. The advantages and reasons for selection are analyzed one by one. These theories or tools include: languages, frameworks, and databases.

It is necessary to continually studying the water quality, because it is greatly affects human health. For the purpose of evaluating the level of drinking water quality in the city of Baghdad, more than one water quality index has been used and selected plant on the Rusafa side, which is: AL-Rusafa.

STUDY AREA AND METHODS

The present study was conducted to evaluate the treatment efficiency of water treatment plant in the city of Baghdad on the Rusafa side which is :(AL-Rusafa) using five indices of water quality. The source of raw water of these plant is the Tigris river.

Samples of drinking water were collected from plant studied for the period from November 2021 to July 2022. Twelve parameters were used for calculating the water quality index. These parameters are: pH, turbidity, electrical conductivity, calcium, magnesium, chloride, total hardness, alkalinity, sulfate, sodium and total dissolved solids. The Iraqi recommended Guidelines for drinking water specifications are presented in Table 1.

1.   MEASUREMENT OF WATER QUALITY INDEX

The most general characteristic of the present study is the use of several water quality indices in order to ascertain the level of pollution in sone water treatment plant in the Baghdad city Al- Rusafa side.The water quality indices used in the present study are as follows:

1.1. WEIGH AVERAGE METHOD WAV (WQI)

The WQI index can be determined by the following steps [11]:

1) In this method each parameter has been given a relative weight (Wi).

2) Computing the quality rating scale (qi) for each parameter by using the following equation:

$$qi=(Ci/Si)100 \qquad (1)$$

Where:

qi= quality rating scale

Ci= concentration of each parameter in each water sample in (mg/L).

Si=Iraqi drinking water standards for each chemical parameter.

3) Computing the sub index of each parameter by using the following equation:

$$SIi=Wi×qi \qquad (2)$$

Where

SIi= is the sub index of each parameter

$$WQI = \sum SIi \qquad (3)$$

1.2. THE MINISTRY AND ENVIRONMENT METHOD MNE WQI

The second water quality index is the method which is adopted by Ministry of Nature and Environment (MNE) of Mongolia [12]. In this method the number of parameters has been taken into account and all the parameters have the same weight. The selected parameters included (Ca^{+2}, Mg^{+2}, TH, Cl^-, Na^+, $SO4^{-2}$, Alk, Fe^{+3} and TDS).

$$WQI = \sum(Ci/Si)/n \qquad (4)$$

Where:

n= is the number of parameters

1.3. WATER QUALITY INDEX

In order to calculate the Water Quality Index, the following steps were used:

Weighting: The word weighting implies relative significance of each of the factor in the overall water quality and it depends on the permissible level in drinking water as suggested by Iraqi standard. Factors which have higher permissible limits are less harmful and have low weightings [13].

$$Wi = K/Sn \qquad (1)$$

Wi - Unit weight of chemical factor, K - constant of proportionality and is given as:

$$K=1/(1/Vs1+1/Vs2+ \ldots\ldots+1/Vsn) \qquad (2)$$

Vsi - standard value of ith parameter

Rating scale: Each chemical factor has been assigned a water quality rating to calculate WQI.

$$Qi = 100 [(Va-Vi)/ (Vs-Vi) \qquad (3)$$

Where,

Qi = Water quality for each parameter (i)

Va - average of measured values in the water sample for three months at one place

Vs - Standard value of ith parameter

Vi - ideal value for pure water (0 for all parameters except pH)

The above equation becomes:

$$Qi=100(Va/Vs) \qquad (4)$$

For pH: The ideal value = 7.0; Max. Permissible value = 8.5,

$$QpH = 100 [(Va-7.0)/ (8.5-7.0)]$$

$$WQIi=Qi*Wi \qquad (5)$$

$$Water\ Quality\ Index\ (WQI) = [\Sigma\ QiWi)/\Sigma Wi\ ] \qquad (6)$$

ΣWi = total unit weight of all chemical factors.

1.4. THE CCME WQI INDEX:

In the present study CCME WQI was used to calculate the water quality. This index can be determined as follows:

The F1 is called Scope which represents the percentage of variables that do not meet their objectives at least once during the interval under consideration ("failed variables"), relative to the total number of variables measured:

F1=[(Number of failed variables)/(Total number of variables)]*100

F2 is called Frequency which represents the percentage of failed tests :

F2=[(Number of failed tests)/(Total number of tests)]*100

F3 is called Amplitude, which represents the deviations of the failed tests from their objectives. It is determined as follows:

The term "Excursion" represents the number of times that certain concentration is different from the objective. When the value of the test is less than the objective, Excursion is given by:

Excursion=[(Failed Test value)/Objective]-1

When test value is greater than the objective, Excursion is given by:

Excursion=[Objective/(Failed Test value)]-1

The sum of exertions of individual tests divided by the total number of tests is called normalized sum of excursions (*nse*) and is computed as follows:

$$nse = \left[\frac{\sum_{i=1}^{n} \text{Excursion}}{\text{Failed Test value}} \right] - 1$$

F3 is a function of nse and is given by:

$$F3 = \left[\frac{\text{nse}}{0.01 + 0.01\text{nse}} \right] - 1$$

Finally CCME WQI is calculated as follows:

$$CCMEWQI = 100 - \left[\frac{\sqrt{F_1^2 + F_2^2 + F_3^2}}{1.732} \right]$$

The water quality is ranked according to CCME WQI as stated in Table(Bharti and Katyal, 2011)

1.5. BRITISH COLUMBIA WATER QUALITY INDEX (*BCWQI*).

This index was developed by the Canadian Ministry of Environ-ment as an increasing index. For water quality evaluation, where water quality parameters are measured and their violation is determined by comparison with a predefined limit. The *BCWQI* makes possible the classification on the basis of all existing measurement parameters(15). The formula is expressed as:

$$BCWQI = \left[\frac{F_1^2 + F_2^2}{1.453} \right]^{0.5}$$

Where: *F*1 (scope) = number of the non-succeeded varia-bles to the total number of the variables; *F*2 (frequency) = number of the unsuccessful tests to the total number of tests.

$$F1 = \frac{NF}{TNV} * 100$$

$$F2 = \frac{NFT}{TNT} * 100$$

Where: *NF* = number of the failed variables, *TNV* = total number of variables, *NFT* = number of the failed test; *TNT* = total number of the tests.

In the *BCWQI* formula 1.453 is the constant used to give confidence to the scale index number from 0 to 100. The degree of the confidence in the *BCWQI* depends on the repeated sampling procedure [POONAM 2013].

In order to calculate the *WQI*, the Iraqi drinking water standard values corresponding to the measured parameters were used, as shown in Table 1.

Table 1. Iraqi drinking water standards [17],[18],[19],[20],[21],[22],[23]

parameter	unit	Iraqi standard
pH	-	6.5-8.5
Alkalinity	mg/L	125-200
Total Hardness as CaCO3	mg/L	500
Magnesium (Mg^{+2})	mg/L	100
Calcium (Ca^{+2})	mg/L	150
Sodium (Na^+)	mg/L	200
Chloride ($Cl-$)	mg/L	350
Sulphate $SO4^{-2}$	mg/L	400
Turbidity	NTU	5
Conductivity	µs/cm	2000
TDS	mg/L	1000

Table 2. Water quality classification based on WAV method

WQI value	Water Quality
0-25	Excellent
26-50	Good water
51-75	Poor water
76-100	Very poor water
>100	Water unsuitable for drinking

Table 3. Water quality classification based on MNE method

WQI value	Water Quality
≤0.3	Very clean
0.31-0.89	clean
0.9-2.49	Slightly polluted
2.5-3.99	Moderately polluted
4-5.99	Heavily polluted
≥6.0	Dirty water

Table 4. Water quality index scale

WQI	Description
0-25	Excellent
26-50	Good
51-75	Moderately polluted
76-100	severely polluted
>100	unfit for human consumption

Table 5. The water quality is ranked according to CCME and BCWQI WQI as stated.

CWQI Categories	Ranks
95-100	Excellent
80-94	Good
65-79	Fair
45-64	Marginal

RESULTS AND ANALYSIS

The values of WAV WQI index of water treatment pant are between (29.91-36.98) for treated water, and those results showed that indicators of treated water of water treatment plant studied were good, while the highest value was (36.98) in January due to the high concentration of Cl- and Mg+2. Also, the results showed that the values of the MNE WQI of water treatment plant studied are between (0.298-0.35) for the treated water and all the values indicated that the treated water is clean, but gives very clean according to MNE method classification in June month, while the highest value was (0.35) in January due to the high concentration of Cl- and Mg+2. The values of index of (weighted method) ranged between (33.19-48.44) for the treated water. The results showed that all index values of treated water of water treatment plant studied were good, according to WQI method classification. The highest value found was(48.44) in July, due to the high concentration of TH,Ph and Na. The obtained value of the Canadian index was (99.99) for the treated water for all months studied, and the such value indicates that the treated water is excellent according to CCME method classification. Also, the value of the British index was (100) for the treated water for all months studied, and such value indicates that the treated water is excellent according to BCWQI method classification. The statistical program which is called STATISTICA,version (25) was used concluding statistical equations of water quality index in terms of time for all plant studied. The coefficient of determination (R^2) is calculated to find the degree of credibility of the equations obtained, which is as follows of Al-Rusafa Water Treatment Plant as show in the figer.

In which, WAV is,and t is in(month).The cofficent of determination R^2 is equal to 0.855.

$$WAV=42.45-5.18\, t +0.71\, (t)^2 -0.03\, (t)^3 \qquad (1)$$

In which, MNE is,and t is in(month).The cofficent of determination R^2 is equal to 0.801.

$$MNE=40.08-4.47\, t +0.67\, (t)^2 -0.03\, (t)^3 \qquad (2)$$

In which, WQI is,and t is in(month).The cofficent of determination R^2 is equal to 0.709.

$$WQI=47.8-9.02\, t +2.03\, (t)2 -0.11\, (t)3 \qquad (3)$$
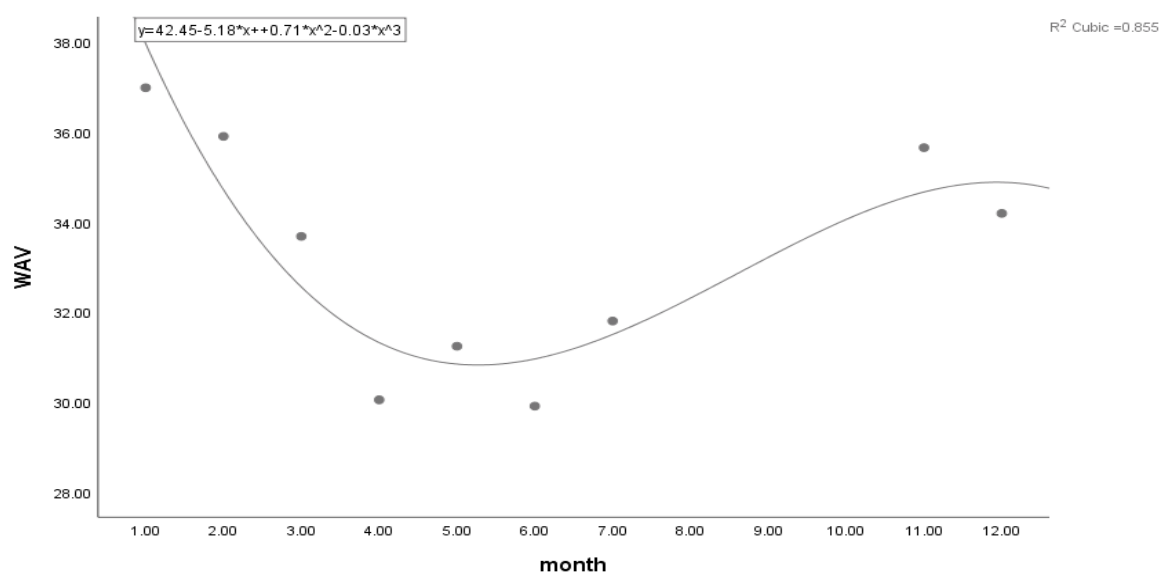
Figure. 1. Statistical Relationship of WAV Index and Time for Al-Rusafa Water Treatment Plant.
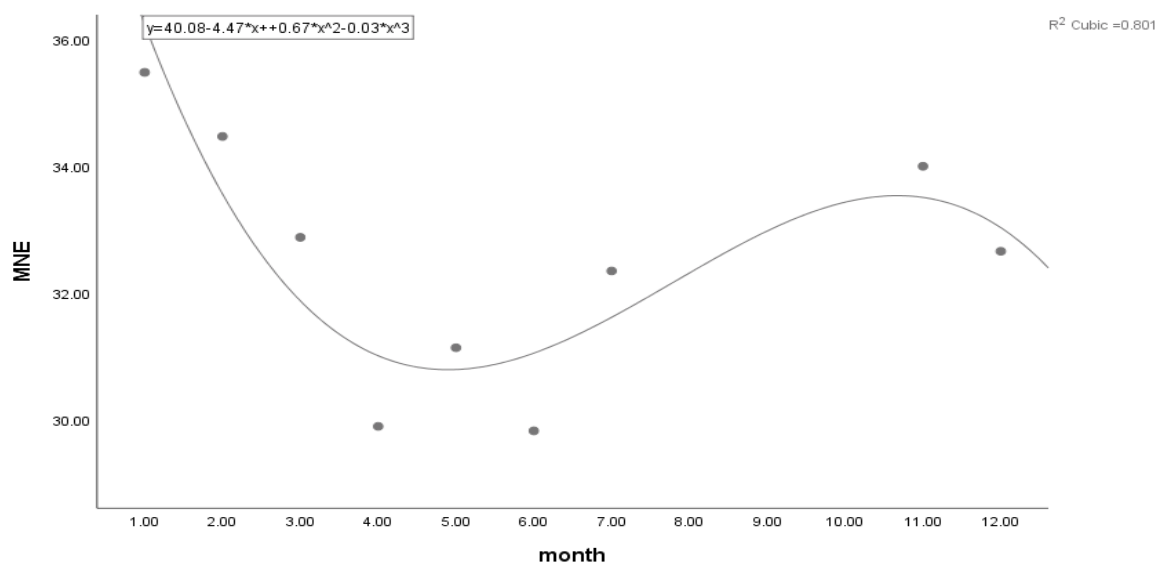
Figure 2. Statistical Relationship of MNE Index and Time for Al-Rusafa Water Treatment Plant.
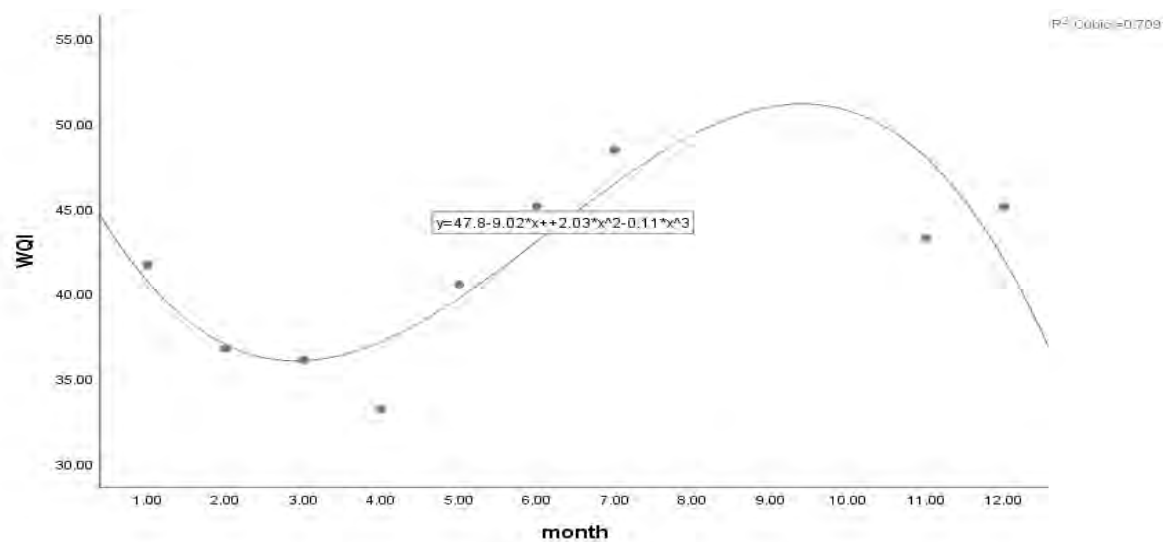
Figure 3. Statistical Relationship of WQI Index and Time for Al-Rusafa Water Treatment Plant.

In which, CCME is,and t is in(month)of all Water Treatment Plant:

$$CCME = 0*t + 99.99 \qquad (4)$$

In which, BCWQI is,and t is in(month)of all Water Treatment Plant:

$$BCWQI = 0*t + 100 \qquad (5)$$
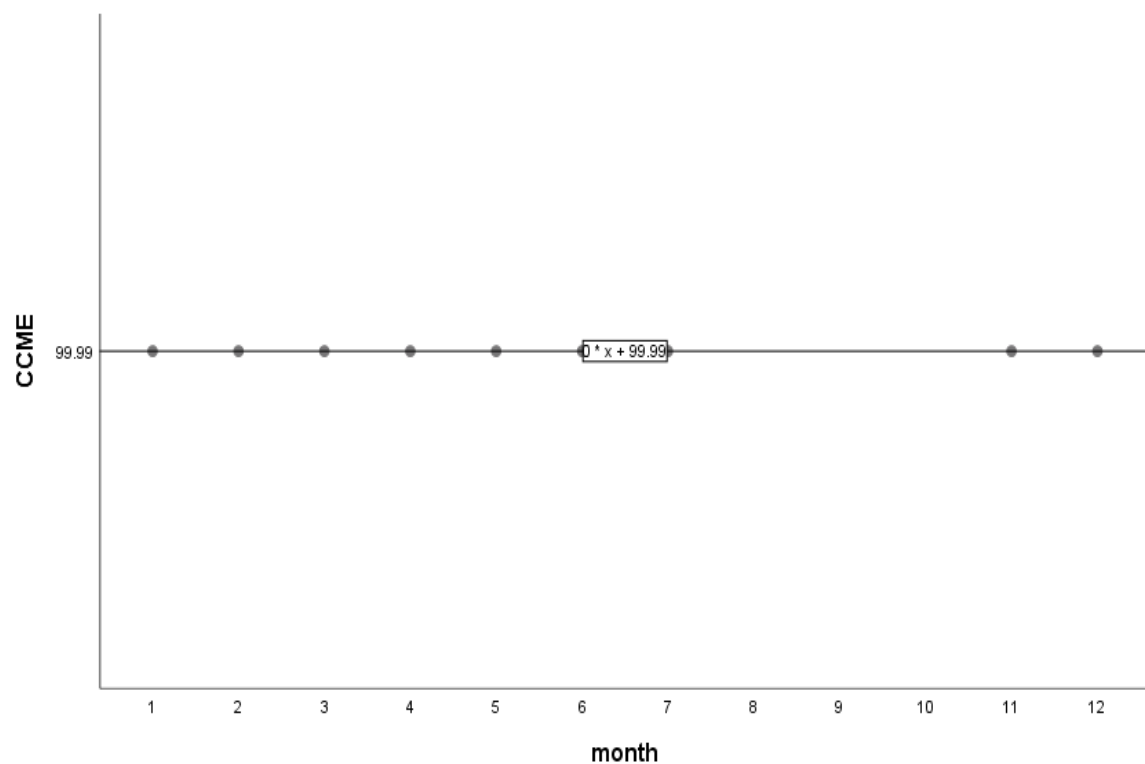
Figure 4. Statistical Relationship of CCME Index and Time for Al-Rusafa Water Treatment Plant
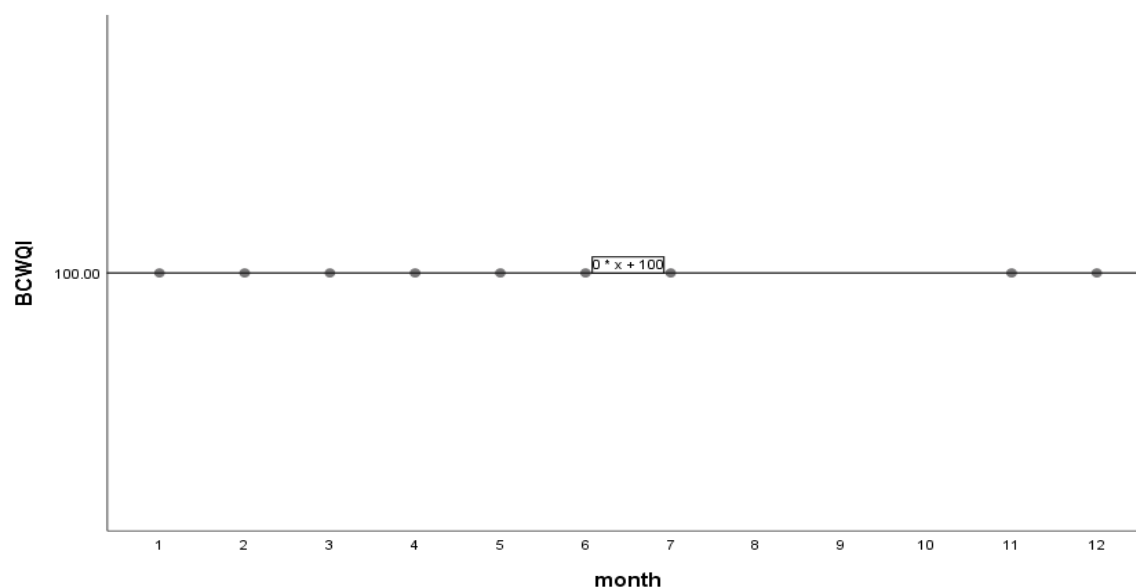
Figure 5. Statistical Relationship of BCWQI Index and Time for Al-Rusafa Water Treatment Plant.

CONCLUSIONS

The results showed that the treated water quality from the water treatment plant studies was good according to the WAV classification. All values of MNE index for treated water from all water treatment plant studied showed that the water is clean but in April, the water quality was very clean according to MNE method classification. All values of WQI for treated water produced from water treatment plant showed that treated water is good water WQI method classification. The results showed that the water quality for treated water was excellent according to the CCME classification. Finally the results showed excellent water quality can be obtained for treated water based on the BCWQI classification.

Table 6. Average monthly test results for treated water produced from Al-Rusafa WTP.(16)

Parameter	unit	Value in test								
		Nov 2021	Dec 2021	Jan 2022	Feb 2022	Mar 2022	Apr 2022	May 2022	Jun 2022	Jul 2022
Turbidity	NTU	2.8	1.9	1.7	1.1	1.1	0.9	1.5	1.8	2.0
TH	mg·dm-3	312	301	331	325	299	258	257	254	264
PH	-	7.88	7.87	7.81	7.9	7.88	7.87	7.89	7.94	7.98
TDS	mg·dm-3	589	558	585	556	516	456	496	458	471
alk	mg·dm-3	144	141	148	153	152	148	139	139	141
Cl-	mg·dm-3	71	68	73	67	61	53	64	55	62
Mg2+	mg·dm-3	31	29	33	32	28	23	22	23	24
Fe2+	mg·dm-3	0.11	0.04	0.04	0.03	0.05	0.04	0.06	0.05	0.07

NO3 -	mg·dm-3	0.42	0.33	0.67	0.43	0.78	0.99	1.16	1.01	1.02
NH3 +	mg·dm-3	0.01	0.01	0.01	0.01	0.01	0.01	0.01	0.01	0.01
Calcium (Ca^{+2})	mg/L	74	73	78	78	74	66	66	64	66
Sodium (Na^{+})	mg/L	70.6	69.2	80	79	93	102	106	104	131
Sulfate (SO_4)	mg/L	195	185	195	188	173	155	168	154	160
EC	µs/cm	879	833	873	830	770	681	741	683	704

Table 7. Water quality indices for Al-Rusafa WTP

WQI	11/2021	12/2021	1/2022	2/2022	3/2022	4/2022	5/2022	6/2022	7/2022
WAV	35.6532	34.1972	36.9857	35.9043	33.6845	30.0593	31.2486	29.9148	31.8064
MNE	0.3400	0.3266	0.3548	0.3447	0.3288	0.2990	0.3114	0.2983	0.3235
wqi	43.246	45.088	41.679	36.753	36.083	33.195	40.525	45.129	48.441
CCME	99.99	99.99	99.99	99.99	99.99	99.99	99.99	99.99	99.99
BCWQI	100	100	100	100	100	100	100	100	100

REFERENCES

(1) Bibi, S., Khan, R. L., Nazir, R., Khan, P., Rehman, H. U., Shakir, S. K. and Jan, R. (2016). **Heavy Metals Analysis in Drinking Water of Lakki Marwat District, KPK, Pakistan**. *World Applied Sciences Journal*, 34(1), 15-19.

(2) Khan, N., Hussain, S. T., Saboor, A., Jamila, N. and Kim, K. S. (2019). **Physicochemical Investigation of The Drinking Water Sources from Mardan, Khyber Pakhtunkhwa, Pakistan**. *Life Science Journal*, 16(3).

(3) Pawari, M. J. and Gawande, S. (2015). **Ground Water Pollution & Its Consequence**. *International Journal of Engineering Research and General Science*, 3(4), 773-776

(4) Alrumman, S., Keshk, S. and El Kott, A. (2016). **Water Pollution: Source & Treatment**. *American Journal of Environmental Engineering*, 88-98.

(5) Rafi, M. K., Rmachar, T. and Umamahesh, M. (2011). **A Study on Chemical Analysis of Drinking Water from Some Communities in Nandyal rural areas of Kurnool district, Andhra pradesh, India**. *International Journal of Civil and Structural Engineering*, 2(1), 351.

(6) Ombaka, O., Gichumbi, J. M. and Kibara, D. (2013). **Evaluation of Ground Water and Tap Water Quality in the villages surrounding Chuka town, Kenya**. *Journal of Chemical, Biological and Physical Sciences (JCBPS)*, 3(2), 1551.

(7) Dkhar, E. N., Dkhar, P. S. and Anal, J. M. H. (2014). **Trace Elements Analysis in Drinking Water of Meghalaya by using Graphite Furnace-Atomic**

Absorption Spectroscopy and in relation to Environmental and Health Issues. *Journal of Chemistry.*

(8)   Hassan, F. M. and Mahmood, A. R. (2018). **Evaluate the Efficiency of Drinking Water Treatment Stations in Baghdad City— Iraq**. *J. Appl. Environ. Microbiol*, 6, 1-9.

(9)   Patel, T., Mahour, P. K., Mahour, R., Lautre, H. K. and Shah, P. (2016). **Physicochemical Analysis of Ground Water Quality of Dhrol**. *Environ Sci Ind J*, 12(12), 127-133.

(10) Gray N. F. (2008). **Drinking Water Quality.** *2nd edition, Cambridge University Press.*

(11) McDuffie B. and Haney J.T. (1973). **A Proposed river pollution index paper presented to American Chem**. *Society, Division of water, Air and waste Engineering*.

(12) Altansukh O. and Davaa G. (2011). **Application of Index Analysis to evaluate the Quality of Tuul River in Mangolia.**

(13) Kalavathy S., SharmaT. R., Sureshkumar P., (2011). **Water Quality Index of River Cauvery in Tiruchirappalli district, Tamilnadu.** *ARCH. ENVIRON. SCI.*, 5, 55-61.

(14) Bharti, N. and D. Katyal. (2011). **Water quality indices used for surface water vulnerability assessment**. *Int. J. Environ. Sci.*, 2(1): 154-173.

(15) POONAM T. (2013). **Estimation of tap water quality in Babylon Governorate/ Iraq**. *International Journal of Advances in Chemistry (IJAC)*. 1(1), 43-45.

(16) **Water treatment plant laboratory in Al-Rusafa, Baghdad Municipality, Baghdad Water Department**.

(17) **The Egyptian Standard for Drinking Water.** No. 108 of 1995.

(18) **Jordanian specification 286 for the year 2008**.

(19) **WHO International Drinking Water Standards 2007 and 2004**.

(20) **Tables comparing drinking water standards in Arab countries with WHO guides (via the internet) for the year 2007**.

(21) **Guidelines for Drinking Water Quality (Second Edition). Part One - Recommendations - About the World Health Organization Global Regional Office for the Middle East (1999)**.

(22) **Enviromental Toxicology & Chemistry**.

(23) **Standarad methods for the examination of water and waste water, edition 20 of 1998**.

3C Tecnología. Glosas de innovación aplicadas a la pyme. ISSN: 2254-4143

Ed.43 | Iss.12 | N.1 January - March 2023

/11/

3C Tecnología. Glosas de innovación aplicadas a la pyme. ISSN: 2254-4143

Ed.43 | Iss.12 | N.1 January - March 2023

190

3C Tecnología. Glosas de innovación aplicadas a la pyme. ISSN: 2254-4143

Ed.43 | Iss.12 | N.1 January - March 2023

STOPPING POWER CALCULATION OF PROTONS AND α–PARTICLES FOR C2H4 AND C6H6 IN ENERGY RANGE 0.01-1000 MEV

Ebtehaj H. Ali*

Department of Physics, College of Education for Girls, University of Kufa, Najaf, Iraq.

ebtehajalsultani2020@gmail.com

Rashid O. Kadhim

Department of Physics, College of Education for Girls, University of Kufa, Najaf, Iraq.

ABSTRACT

In this research, a theoretical study was conducted to calculate the total stopping power of some relativistic heavy ions (protons and alpha particles) during their passage through some media (ethylene and benzene) in the energy range (0.01-1000 MeV). The equations were programmed using MATLAB2021, the curve fitting tool was used, and the calculated results were compared with the experimental data of the P-Star and A-Star programs for the same missiles in those organic compounds.

KEYWORDS

Mass stopping power, Bethe formula, Relativistic heavy ions, MATLAB2021, P-Star, A-Star.

PAPER INDEX

INTRODUCTION

Nuclear and electronic stopping power are two categories of stopping power that measure the energy loss rate per unit distance in a material [1]. The mechanism of energy loss depends on the charge and velocity of the charged particle and the nature of the material medium [2]. When passing in the material medium, As is well known, charged particles lose some of their kinetic energy when colliding with the target matter. The continuous operation on the particle path in the medium causes charged particles to lose kinetic energy until they reach zero, at which point they lose all kinetic energy and reach the using Bethe equations. [3] It is denoted by the symbol -dEdx and is measured in MeV.cm^{-1}. The mass stopping power, -dEdx, is calculated by dividing the stopping power by the density of the material and is measured in MeV cm^2 g^{-1} [4]. Electromagnetic force causes an electron to lose energy in collisions with atomic electrons, resulting in excitation and ionization [5]. In an inelastic collision, atomic orbital electrons collide. This is so-called because it causes middle-atom excitations and ionizations (Collisional Stopping Power). In the case of the inelastic nuclear collisional, "Bremsstrahlung" radiation is produced, with a stopping power equal to (radiative stopping power) [6]. The overall stopping power of target materials is calculated when the product of inelastic collisions and excitation is proportional to the stopping power.Combining the collisional and radiative stopping powers produces the total stopping power:

$$\left(-\frac{dE}{dx}\right)_{tot} = \left(-\frac{dE}{dx}\right)_{col} + \left(-\frac{dE}{dx}\right)_{rad} \qquad (1)$$

THEORY

The stopping power of a medium is defined as the average unit of energy loss suffered by charge particles per unit path length in the medium under consideration, which can be written as (-dE/dx) depending on the projectile charge and the target matter. [5]. Mass collision-stopping power is widely used to reduce reliance on medium density (ρ). These studies were both theoretical and experimental, employing a variety of methods. [6]. For compounds, the Bragg additive rule has been found to be quite effective. According to the rule, The mass-stopping power of a multi-element substance is equal to the weighted sum of the mass-stopping power of its constituent atoms. [7].

$$\left(\frac{-dE}{\rho dx}\right)_{com} = \sum_i \omega_i \left(\frac{-dE}{\rho dx}\right)_i \qquad (2)$$

Where ω_i: the ratio of the weight of the elements in the compound.

$$\omega_i = \frac{n_i A_i}{A_{comp}} \qquad (3)$$

n_i : number of atoms. A_i: atomic mass of elements in medium, A_{comp}: atomic mass of medium, ρ: the density of the medium, $((-dE)/\rho dx)\_com$: Mass stopping power of compound, $((-dE)/\rho dx)_i$: Mass-stopping power for the elements in the compound.

Because the radiative stopping power is efficient, increasing the energy at the incident -particle energies (10^0-10^3) MeV reduces the mass stopping power. [8].

$$-\frac{dE}{dx} = K\frac{Z_2 Z_1^2}{A\beta^2}L_{\text{Bethe}} \tag{4}$$

where,

$$L_{\text{Bethe}} = ln\left[\frac{2m_e c^2\beta^2}{1-\beta^2}\right] - \beta^2 - ln <I> \tag{5}$$

$K = 0.307075\ MeV\cdot cm^2/g$, Z_2 the atomic number of elements, Z_1 the atomic number of ions (projectile), A atomic mass of elements, β ratio of the velocity of a projectile to the speed of light, m_e Mass of electron, c speed of light, and I ionization potential of the medium in eV [9].

The stopping power is calculated by multiplying the stopping power multiplied by the linear attenuation coefficient for a given type of charged particle at a given energy. (, the probability of an electronic collision per unit distance traveled), as well as the average energy loss per collision (Qavg). [10].

$$-\frac{dE}{\rho dx} = \frac{\mu Q_{\text{avg}}}{\rho} = \frac{\mu}{\rho}\int_{Q_{min}}^{Q_{max}} QW(Q)dQ \tag{6}$$

The maximum possible energy transfer (Qmax), or the energy transfer by head-on collision ($2\gamma^2 mv2$), and the minimum possible energy transfer (Qmin), or the medium's mean excitation energy (I). [11].

Because it accounts for all possible atomic ionizations, as well as atomic excitations, an atom's mean The energy of excitation is always greater than the energy of ionization, whereas the atomic ionization energy is the energy required to remove the least bound atomic electron (i.e., valence electron in the outer shell) [12-13].

RESULTS AND DISCUSSION

The mass stopping power was calculated using the Bethe formula for two materials, ethylene C_2H_4 and benzene C_6H_6, with a proton and α-particle energy range from 10^{-2} MeV to 10^3 MeV. Using "MATLAB2021" program.

The table (1) show the stopping power values for protons and α-particle in ethylene and benzene. Figures (1,2,3,4) showed a strong agreement between the current work with P-Star and A-Star at all energies in target materials, as shown in table.3.

Table 1. Mass stopping power for proton and α-particle in ethylene C2H4 and benzene C6H6.

Energy (MeV)	β^2	v (m/sec)	Mass Stopping Power (MeV cm²/g) C_2H_4	Mass Stopping Power (MeV cm²/g) C_6H_6	β^2	v (m/sec)	Mass Stopping Power (MeV cm²/g) C_2H_4	Mass Stopping Power (MeV cm²/g) C_6H_6
		Proton				α-particle		
0.01	0.000021	1384599.00	-7852.4	-8611.1	0.000005	694820.70	-304822.6	-306563.1
0.02	0.000043	1958103.04	-1076.8	-1619.4	0.000011	982622.87	-107151.2	-110612.7
0.03	0.000064	2398157.50	393.282	-32.006	0.000016	1203459.90	-53783.89	-57102.12
0.04	0.000085	2769131.64	886.274	533.449	0.000021	1389633.00	-30945.63	-33972.06
0.05	0.000106	3095958.56	1075.954	772.682	0.000027	1553653.81	-18928.33	-21683.17
0.06	0.000128	3391425.60	1146.474	879.440	0.000032	1701939.05	-11805.29	-14328.20
0.07	0.000149	3663129.05	1163.762	924.506	0.000038	1838300.58	-7242.972	-9570.128
0.08	0.000170	3916018.40	1155.540	938.330	0.000043	1965222.03	-4157.814	-6318.883
0.09	0.000192	4153531.58	1134.760	935.521	0.000048	2084428.54	-1986.755	-4005.564
0.1	0.000213	4378171.74	1107.924	923.647	0.000054	2197176.18	-412.133	-2307.846
0.2	0.000426	6191175.36	839.016	730.547	0.000107	3107213.86	4320.087	3113.057
0.3	0.000639	7582004.78	670.562	591.876	0.000161	3805467.69	4645.263	3739.487
0.4	0.000852	8754245.98	562.137	499.727	0.000215	4394087.21	4423.349	3690.215
0.5	0.001064	9786763.18	486.476	434.440	0.000268	4912640.04	4121.660	3501.760
0.6	0.001277	10720006.14	430.447	385.646	0.000322	5381419.30	3831.700	3292.375
0.7	0.001489	11578005.86	387.120	347.676	0.000375	5812480.28	3572.041	3093.279
0.8	0.001702	12376421.14	352.508	317.204	0.000429	6213677.83	3343.647	2912.233
0.9	0.001914	13126129.51	324.151	292.148	0.000483	6590468.06	3143.163	2749.883
1	0.002127	13835051.47	300.446	271.143	0.000536	6946823.60	2966.558	2604.714
2	0.004247	19550123.42	178.982	162.674	0.001072	9822317.05	1936.584	1729.670
3	0.006360	23924853.58	130.633	119.107	0.001607	12027414.67	1468.118	1320.013
4	0.008467	27604077.67	104.049	95.052	0.002142	13885271.85	1195.475	1078.973
5	0.010566	30837790.82	87.044	79.625	0.002677	15521087.77	1015.060	918.483
6	0.012659	33754316.50	75.153	68.817	0.003211	16999085.82	885.915	803.130
7	0.014746	36429950.03	66.331	60.788	0.003744	18357425.61	788.426	715.791
8	0.016826	38914444.53	59.505	54.569	0.004278	19620975.41	711.953	647.124
9	0.018899	41242388.30	54.055	49.598	0.004810	20807012.35	650.195	591.568
10	0.020966	43438986.55	49.593	45.526	0.005343	21928118.41	599.173	545.599
20	0.041280	60952149.63	28.066	25.835	0.010643	30949015.06	346.153	316.661
30	0.060967	74074752.06	20.126	18.551	0.015900	37829067.08	249.383	228.630
40	0.080055	84881964.82	15.926	14.693	0.021116	43594415.15	197.198	181.032
50	0.098566	94185858.35	13.308	12.285	0.026291	48643452.36	164.229	150.910
60	0.116525	102407122.21	11.512	10.632	0.031425	53180963.13	141.379	130.009
70	0.133952	109798179.81	10.200	9.424	0.036518	57328875.04	124.546	114.596
80	0.150868	116525142.64	9.197	8.500	0.041571	61166812.12	111.594	102.729

90	0.167293	122704532.11	8.406	7.771	0.046584	64750208.80	101.300	93.291
100	0.183247	128422011.09	7.764	7.179	0.051559	68119520.35	92.909	85.593
200	0.320379	169806066.13	4.772	4.418	0.099230	94502418.39	52.924	48.856
300	0.425665	195729016.46	3.734	3.460	0.143396	113602884.92	38.452	35.532
400	0.508253	213875689.79	3.214	2.979	0.184391	128822328.17	30.889	28.562
500	0.574229	227333673.23	2.905	2.694	0.222512	141513629.59	26.219	24.255
600	0.627766	237694985.92	2.705	2.509	0.258022	152387617.68	23.043	21.325
700	0.671805	245891097.08	2.567	2.382	0.291154	161875929.18	20.742	19.201
800	0.708467	252511435.02	2.467	2.290	0.322114	170265367.43	18.998	17.591
900	0.739312	257949799.09	2.394	2.222	0.351090	177758605.24	17.631	16.329
1000	0.765509	262480130.00	2.338	2.170	0.378247	184505413.74	16.532	15.314

Table 2. Rates of elements in ethylene C2H4, and benzene C6H6.

Target	C	H
C_2H_4	0.8563	0.1437
C_6H_6	0.9226	0.0774

Table 3. Correlation coefficient between positive calculations Bethe relative equation and values P-star for the proton and values A-star for α-particle.

Target	Proton	α-particle
C_2H_4	0.9745	0.9711
C_6H_6	0.9877	0.9823
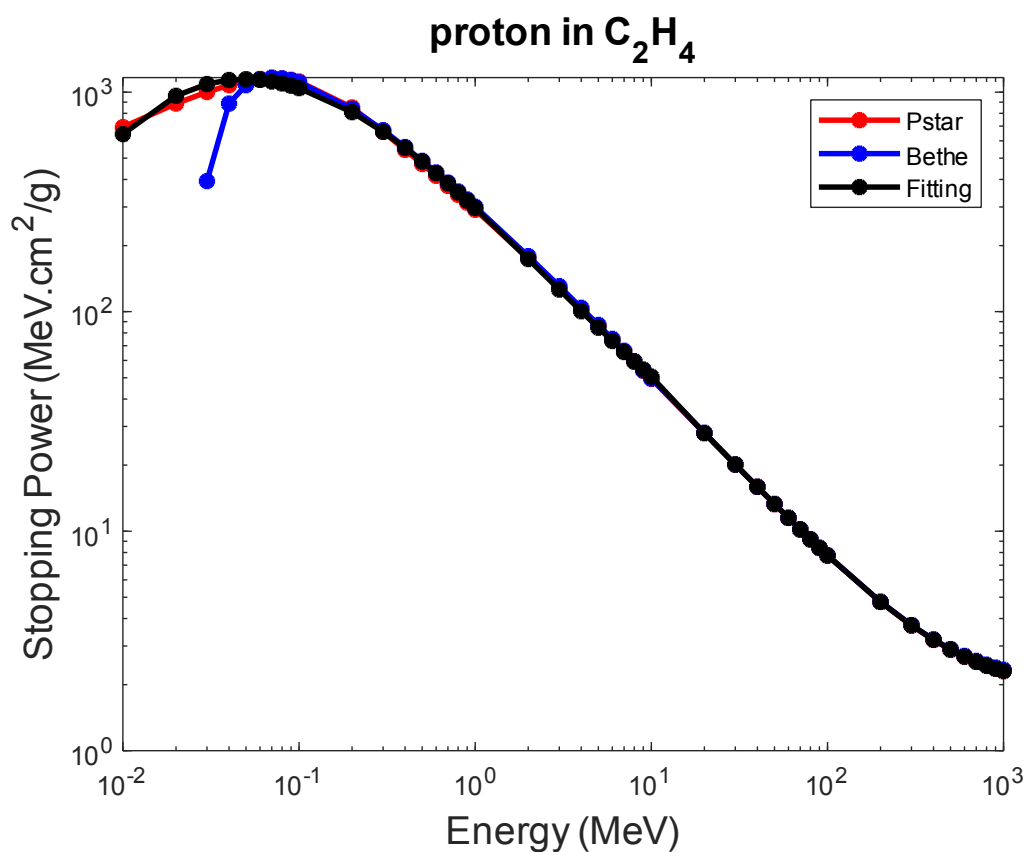
Figure 1. Show the P-Star mass stopping power in C2H4 as a function of proton energies
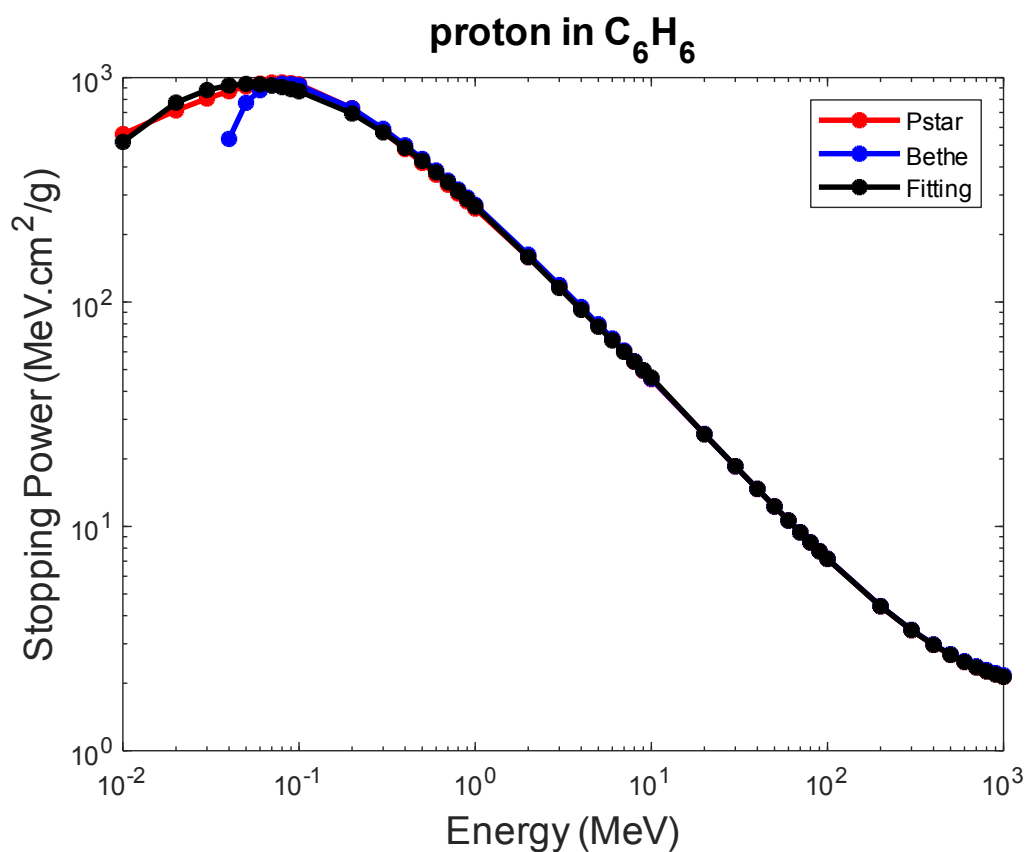
Figure 2. Show the P-Star mass stopping power in C6H6 as a function of proton energies.

He^{+2} in C$_2$H$_4$
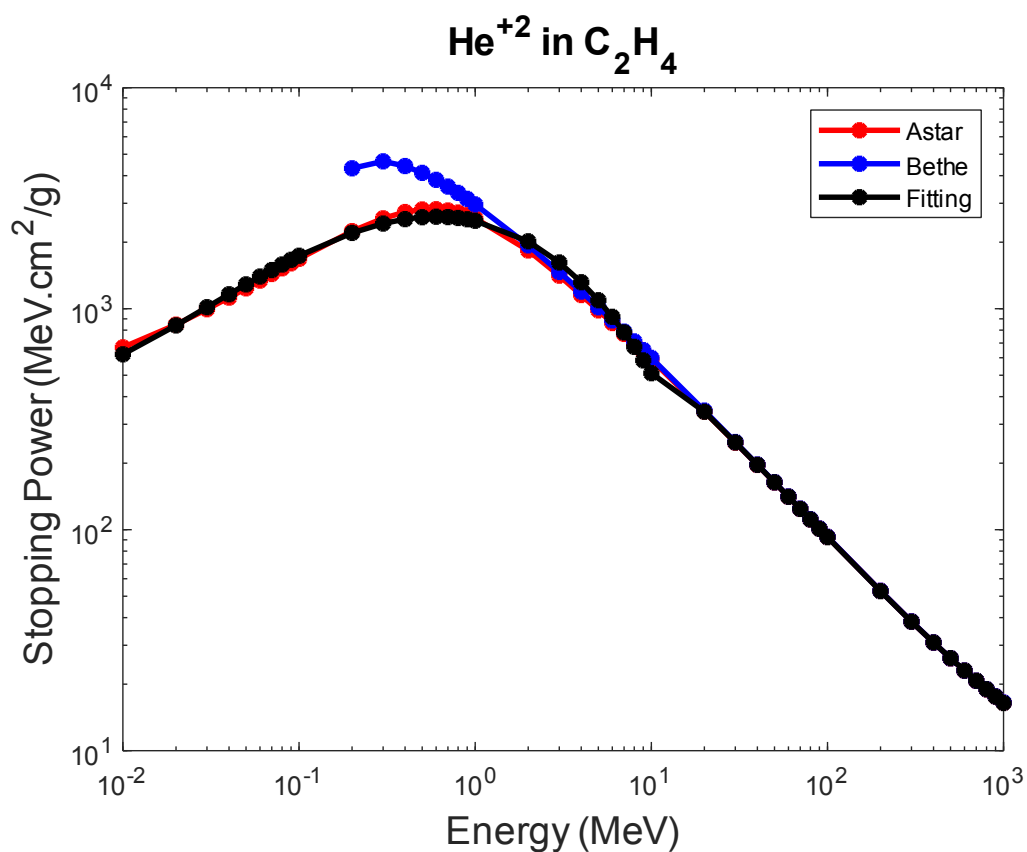

Figure 3. Show the A-Star mass stopping power in C2H4 as a function of -particle energies.
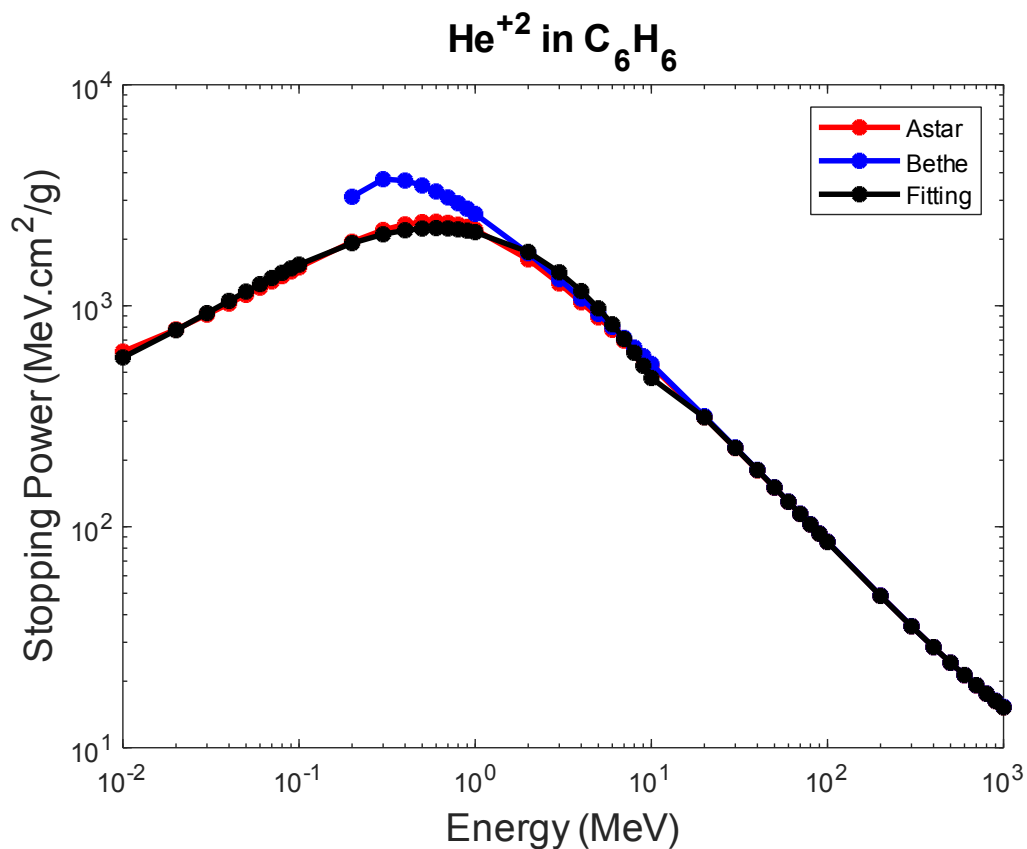
He^{+2} in C$_6$H$_6$

Figure 4. Show the work with A-Star mass stopping power in C6H6 as a function of α-particle energies.

CONCLUSIONS

1. The Bethe formula is adequate for regulating the mass-stopping power of the organic compounds investigated.

2. Calculations show that the mass-stopping power increases with increasing energy at incident proton energies (10^{-1}-10^1) MeV due to the collision-stopping power.

3. Because the radiative stopping power is efficient, the mass stopping power decreases as the energy at the energies of incident particles (10^{-1}-10^3) MeV increases.

4. Calculations show the mass-stopping power increases with increasing energy at incident-particle energies (10^{-2}-10^0) MeV because the collision-stopping power is the result.

5. Because the radiative stopping power is efficient, increasing the energy at the incident-particle energies (10^0-10^3) MeV reduces the mass stopping power.

REFERENCES

(1)   Balashova, L. L., and A. A. Sokolik. (2006). **Alignment dependence of the stopping effective charge of swift excited ions in the degenerate electron gas.** *Nuclear Instruments and Methods in Physics Research Section B: Beam Interactions with Materials and Atoms, 245(*1), 28-31.

(2)   Weng, M. S., Andreas Schinner, A. Sharma, and Peter Sigmund. (2006). **Primary electron spectra from swift heavy-ion impact**. *The European Physical Journal D-Atomic, Molecular, Optical and Plasma Physics,* 39(2), 209-221.

(3)   A. Jablonski‹ S. Tanuma‹ and C. J. Powell. (2006). **New universal expression for the electron stopping power for energies between 200 eV and 30 keV Surf.** *Interface Anal.*

(4)   Campillo, I., J. M. Pitarke, and A. G. Eguiluz. (1998). **Electronic stopping power of aluminum crystal**. *Physical Review B,* 58(16), 10307.

(5)   Tanuma, S., Cedric J. Powell, and David R. Penn. (2008). **Calculations of stopping powers of 100 eV–30 keV electrons in 31 elemental solids**. *Journal of Applied Physics,* 103(6), 063707.

(6)   Babkin, R. Yu, et al. (2009). **Determination of the effective nuclear charge for free ions of transition metals from experimental spectra**. *Optics and Spectroscopy,* 107(1), 9-15.

(7)   Ulmer, W. (2011). **The Role of Electron capture and energy exchange of positively charged particles passing through Matter**. *arXiv preprint arXiv,* 1109.

(8)   Gümüş, Hasan, and Önder Kabadayi. (2010). **Practical calculations of stopping powers for intermediate energy electrons in some elemental solids**. *Vacuum*, 85(2), 245-252.

(9)   Lamarsh, John R., and Anthony John Baratta. (2001). **Introduction to nuclear engineering**. *Vol. 3. Upper Saddle River, NJ: Prentice hall*.

(10) Hovington, Pierre, et al. (1997). **¡CASINO: a new Monte Carlo code in C language for electron beam interactions—part III: stopping power at low energies**. *Scanning,* 19(1), 29-35.

(11) Baily, Norman A., and George C. Brown. (1959). **The relative stopping powers of pure gases to that of air**. Radiation Research, 11(6), 745-753.

(12) Groom, Donald E., Nikolai V. Mokhov, and Sergei I. Striganov. (2001). **Muon stopping power and range tables 10 MeV–100 TeV**. *Atomic Data and Nuclear Data Tables,* 78(2), 183-356.

(13) Toledo, Manuel R. Nevárez, and Verónica Yánez Ortiz. (2018). **Estimación de la incertidumbre en un prototipo experimental basado en hardware libre para la medición de variables físicas que describen el movimiento de una partícula**. *3c Tecnología: glosas de innovación aplicadas a la pyme,* 7(2), 62-81.

/12/

INVESTIGATION OF WASTE COOKING OIL-DIESEL BLEND WITH COPPER OXIDE ADDITIVES AS FUEL FOR DIESEL ENGINE UNDER VARIATIONS IN FUEL INJECTION PRESSURE

Madhuri G. Chatur

Research Scholar, Department of Mechanical Engineering, Sandip University, Nashik (India).

madhurisdeokar@gmail.com - https://orcid.org/0000-0001-8305-1425

Anil Maheshwari

Professor, Department of Mechanical Engineering, Sandip University, Nashik (India).

anil.maheshwari@sandipuniversity.edu.in - https://orcid.org/0000-0001-7746-8531

Srinidhi Campli

Associate Professor, Department of Mechanical Engineering, RSCOE, Pune (India).

srinidhicampli@gmail.com - https://orcid.org/0000-0003-4998-5608
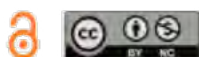
ABSTRACT

Fuel Injection is a significant factor when biodiesel-diesel blends are fired in diesel engines as they have very diverse property when related to diesel. The current work describes unusual experimental study of CI engine fuelled with Waste cooking methyl ester with copper oxide nano additives at varying fuel injection pressures. The Copper oxide nano additives were manufactured using homogenous addition method and were subjected to studies such as XRD and SEM characterization. These synthesized nanoparticles were later added in waste cooking oil biodiesel blend (WCO20) with levels of 10 ppm, 20 ppm, 30 ppm, and 40ppm. The results were noted from a DI-CI VCR engine coupled with an eddy current dynamometer. The addition of CuO particles reduces the ignition delay of WCO20 and raises the thermal efficiency of the engine by an average of 3.9% and limits HC emission by 15.6%.

KEYWORDS

Diesel engine, Performance and emission, NOx emission, nano fuel additives

PAPER INDEX

1. INTRODUCTION

The frequent rise in fuel prices leads to higher inflation rates which create a hard time for the common man to face day-to-day economic challenges [1, 2]. The primary fuel for the transportation sector is diesel and with a high number of diesel engines running today, researchers have been tasked to find alternate fuel for CI engines [3, 4]. Diesel engines when patented, used peanut oil and with their strategy of fuel combustion being compression ignition, thereby denser fuels can be used [5, 6]. Vegetable oils when fuelled in diesel engines in cold environments tend to clog fuel supply due to their clouding effect at lower temperatures [7, 8]. So the usage of straight oils as an alternate fuel is out of the question and hence oils need to be processed to reduce their density and viscosity such that they can be more suitable for diesel engines [9, 10]. Oils when transesterified lead to ester formation and when these esters possess properties proportional when equated to diesel fuel. But still, when the properties of pure esters are compared to conventional diesel fuel they factor out the possibility to be used as an alternative fuel to diesel engines [11, 12]. To address this issue, Esterified oils or Biodiesel are blended with diesel fuel and by doing so, the properties of the Esterified oil-diesel blend have in-line fuel properties [13, 14]. When these blends are combusted in regular diesel engines, the thermal performance is good and emissions like CO and HC are limited [15, 16, 1-3]. But the real problem which restricts the use of Blended Diesel-Oil esters is the fuel consumption rate and levels of NOx [17, 18]. Researchers performed experimentation under varying blends 10, 20 and 30% volumetric concentration with diesel and loading 25%, 50%, 75%, and 100% [19, 20]. They concluded biodiesel lowered the efficiency and enhanced the consumption at all loads. Also, the blends derived from Sterculia foetida biodiesel lowered the HC, CO, and NOx emissions at all loads when related to diesel. Yuvarajan Devarajan [30] performed experimental studies on diesel engine fueled with Ricebrain oil esterified for evaluation of emission and performance physiognomies Experimentations revealed that blends of rice bran biodiesel augmented the thermal efficiency and plummeted the BSFC values of the engine [21-23]. Furthermore, the NOx, Smoke, HC, and CO also recorded a decent fall. Shanmugam et.al [29] conducted experimentation using 1-decanol blend designated as D70L20DEC10 under variational influence of CR (16:1, 17.5:1, and 19:1) and EGR (0%, 10%, and 20%) on diesel engine characteristics. They found that the NOx emission rose with rising CR and condensed with growing EGR rates. Both HC and CO emissions dropped with higher CR values and were augmented with the insertion of EGR. They concluded the CR 19:1 and 10% EGR rate were the best operating CI engine parameters for the ternary blend. Esterified oils or Biodiesel have low calorific value due to which, the combustion of fuel is better but the amount of fuel consumed per power unit is higher [24-27]. Researchers have tried to address this issue by varying the fuel injection pressure and timing of fuel inlet into the combustion chamber [28-30]. Lower Biodiesel-diesel blends have slightly higher density and viscosity due to which the fuel management systems [8-10], have to be changed for better combustion of these denser blends [31]. Increasing the fuel inlet pressure does push the fuel further in the compressed air and thereby enhancing the fuel-air mixing process [31, 32]. But by doing so, the fuel pump and injector need to be changed

[31-35]. Also, denser fuels when injected at higher pressure show higher fuel combustion pockets thereby exhibiting, a higher amount of uncontrolled combustion activity [16, 17]. In recent years, a lot of work is done to challenge this malfunction and one of the ways seems to be the use of nano metal oxides [13-15]. Nano metal oxides have a higher surface area than volume ratio, which tends to absorb the heat of combustion and retard the ignition delay of fuel [12]. Nano fuel additives also increase the amount of fuel combustion activity and also help in the reduction of soot formation. In addition to this, many Nano metal oxide additives also retard the formation of CO and HC emissions which signify cleaner fuel burning [19]. In the current paper, a blend of used cooking oil esters-diesel with copper oxide nano fuel additives is used to power diesel engines with variations in fuel injection pressure. The reason behind using waste cooking is to reduce the amount of wastage of used cooking oil and also the literature on enhancing the emission reduction using WCO and nanoadditives is minimal.

1.1. NOVELTY OF CURRENT STUDY

The paper concentrates on the impact of variation of fuel injection pressure (FIP), as an engine parameter and gradational dosing level of copper oxide nanoparticles WCO20 blend. WCO20 blend was chosen because the current biofuel policy framed by Government of India is the implementation of 20% biodiesel blending in diesel fuel. Also, the properties observed by the 20% blend of WCO and Diesel were in line with diesel fuel. The entire study is performed in 2 stages. In the primary stage, Copper oxide nanoparticles were synthesized using the homogenous addition method and subjected to nanoparticle studies such as XRD, and SEM for significance and morphological study. Collaterally used cooking oil is transesterified using KOH and methanol. And Finally, the synthesized Copper oxide particles are added to the WCO20 blend (80%vol.:20 %vol. diesel-waste / used cooking oil methyl ester) at various dosing levels of 10, 20, 30, and 40ppm to obtain nano fuel blends of WCO20+10ppm CuO, WCO20+20ppm CuO, WCO20+30 CuO, and WCO20+40ppm CuO. These derived four fuel blends were fuelled in a VCR-CI engine with variations in load (25%, 20% 75%, and 100%) and fuel injection pressure variations (180bar, 210Bar, and 240Bar).

2. EXPERIMENTAL PROCEDURES

2.1. NANOPARTICLE BLENDS

Copper Oxide particles were synthesized using a homogenous addition method, where 2.01 gms of potassium hydroxide and 2.87 g of Cuprous Chloride (CuCl2) were taken and mixed in deionized water (solvent). Later, this mixture was filtered filter separation process. The strained matrix was dried and sintered further with a sintering temperature of 600 deg (Celsius scale). The sintered particles were subjected to various characterization techniques to signify the formation of Copper Oxide. X-ray

diffraction was observed on the particles (Figure 1). The observations were noted on the peaks observed in fig.1 which resemble JCPDS No 48-1548. Table 1 provides the necessary data obtained from the XRD spectra analysis. The FESEM imaging of the particles explains the flake type morphology. Figure 2 shows the FESEM images of CuO particles. The average particle size observed under 500nm magnification was around 289 nm.
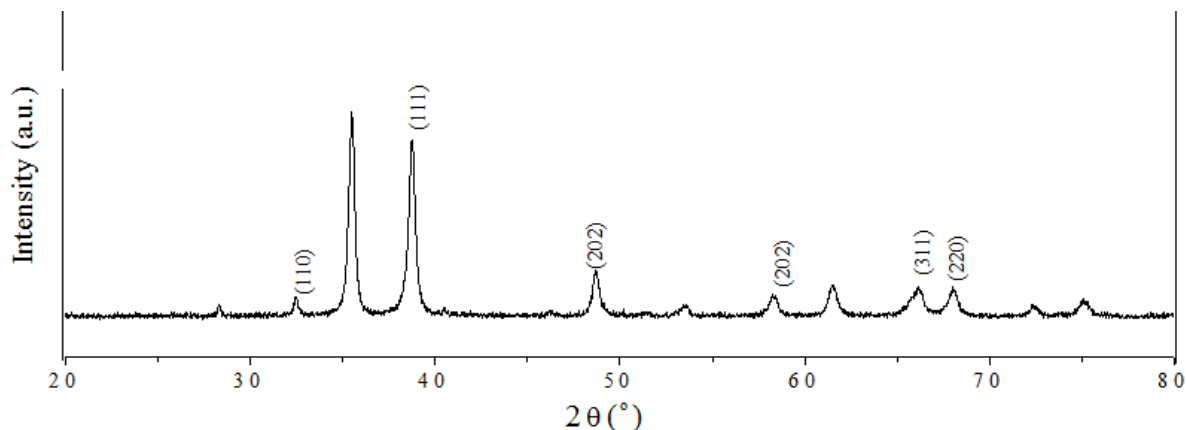
Figure 1. X-ray diffraction of CuO nanoparticles.

Table 1. Characterization of copper oxide nano additives.

Parameters	Size
Lattice constant (c)	4.259
% phase	5.41
Crystalline size	89.35
Theoretical density	37.36 nm
Axial ratio (C/A)	5.95e5 g/cm3
Average particle size	305.59 nm
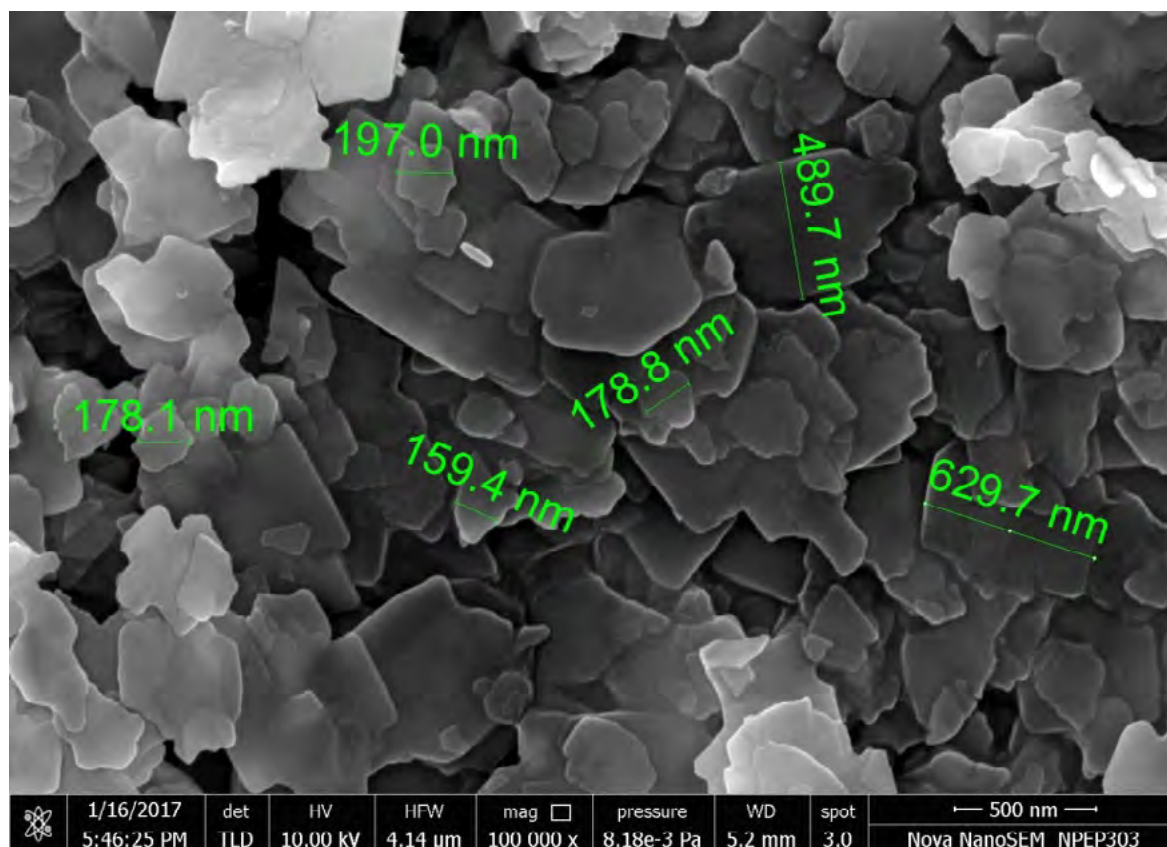
Figure 2. FESEM of CuO nanoparticles.

2.2. BIODIESEL PREPARATION

Used cooking oil was obtained from the local restaurants that used refined rice bran oil for cooking or frying food items. This oil was first sieved for removal of impurities and later transesterified using a known volume of methanol and KOH as reaction catalysts using the soxhlet apparatus [28]. The time for the transesterification reaction was kept at 2hrs and the reaction temperature was maintained at 65 deg. Celsius. Later the obtained esterified mixture was subjected to gravity separation, where the bioester was separated. These derived esters were later washed several times to remove traces of methanol and KOH. The washed used cooking oil methyl esters were later blended with diesel to volumetric proportions of 20%vol. Methyl esters: 80 % vol. Diesel.

2.3. PREPARATION OF TEST FUELS

Four solutions (150 ml) of Isopropyl alcohol were taken and copper Oxide nanoparticles particles were dissolved at various concentration levels of 10, 20, 30, and 40ppm. Later these four nano fuel solutions were added to the Used Cooking oil methyl ester blend WCO20. Later this biodiesel having CuO nano fuel were subjected to ultra sonication at preset rpm. Further, diestrol surfactant was added to bring up better mixing through surface modification. So a total of 04 Biodiesel test fuels were prepared and designated as WCO20+10ppm CuO, WCO20+20ppm CuO,

WCO20+30 CuO, and WCO20+40ppm CuO. The properties of solutions are tabulated in Table 2.

Table 2. Thermo physical properties of test fuels.

Property	Standard	WCO20	WCO20+10 ppm	WCO20+20 ppm	WCO20+30 ppm	WCO20+40 ppm	Diesel
Density, kg/m3	IS 1448 P:16	844	847	851	855	859	825
Calorific value, MJ/kg	IS 1448 P:6	40.52	40.66	40.69	40.72	40.67	42.62
Kinematic Viscosity at 40 0C	IS 1448 P:25	4.25	4.23	4.21	4.15	4.14	2.83
Flash point, 0C	IS 1448 P:20	91	96	95	96	96	69
Cloud point, 0C	IS 1448 P:10	8.9	9.1	9.2	9.2	9.2	6.2
Pour point, 0C	IS 1448 P:10	4.5	4.6	4.6	4.7	4.7	3.4
Cetane index	Calculative Method	51	-	-	-	-	42

3. EXPERIMENTAL SETUP

The experimentation of 04-derived WCO20 blends having CuO particles was tested on a Direct Fuel Injection-VCR test rig. The engine was governor controlled for a preset speed of 1500rpm and the specifications of the engine are tabulated in Table 03. Figure 3 elaborates the line sketch of the test setup. The observation relating to thermal performance and emissions were noted at CR17.5 and injection timing of 23 deg. bTDC. The engine was warmed by using diesel as starting fuel and later changed for the remaining fuels. Also, the engine was allowed to run until stabilization. The readings were noted at incremental loads of 25%, 50%, 75%, and full engine load and at pulsating fuel injection pressures of 180bar, 210bar, and 240 bar pressures. The variation of Injection pressures was done by using calibrated injectors of defined fuel injection pressures of 180bar, 210bar, and 240bar. The specification of the fuel injectors is tabulated in table 04. Uncertainty analysis was performed using all the values of instruments and emission responses. The Overall error of the amount of uncertainty was around ±2.29%. Table 05 displays all the instrument's range and accuracy and level of vagueness.

Table 3. Engine Specifications.

Manufacture	Kirloskar Oil.
SFC	251 g/kWhr.
Rated power	5.4 kW at 1500 RPM
Standard CR	17.5:1
Bore	87.5 mm
Stroke	110 mm
Injection Timing	23 deg before TDC
Inlet valve open bTDC	4.5 deg bTDC
Exhaust valve open	35.5 deg b BDC
Inlet valve close	35.5 deg a BDC
Exhaust valve close	4.5 deg a TDC

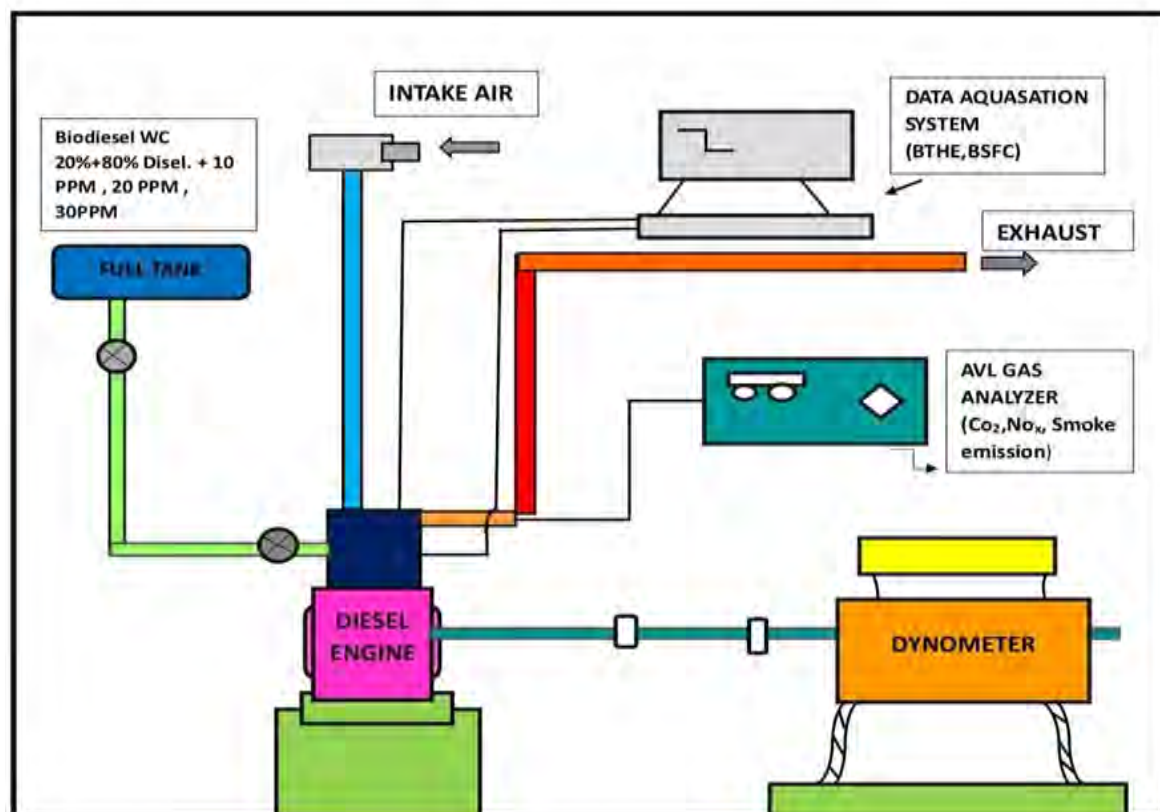
Figure 3. Schematic diagram of experimental engine test setup.

Table 4. Injector specifications.

Injector Make	Bosch
Fuel Injection pressure	180,210, 240bar
Number of Holes	3
Type of Injection	Jerk type
Nozzle Hole diameter(mm)	0.16

Table 5. Device specifications and terminology.

Device specification	Range	Accuracy	Uncertainties
Carbon monoxides (CO)	0-10.00%	±0.01%	±0.1
Carbon Dioxides (CO2)	0-20.00%	±0.01%	±0.15
Oxides of Nitrogen (NOx)	0-5000 ppm	±1 ppm	±0.2
Oxygen (O2)	0-25.00%	±0.01%	±0.1
Hydrocarbons (HC)	1-1500 ppm	±1 ppm	±0.2
Exhaust gas temp. (EGT)	0-5000C	±10C	±0.1
Tachometer	0-10000 rpm	±10 rpm	±0.2
Fuel flow meter	1-30 cc	±0.1 cc	±0.5

4. RESULTS AND DISCUSSION

The results of the engine are categorized into two stages. In the first stage, the performance results of the engine were measured in terms of thermal efficiency, rate of fuel consumption, and the temperature of combusted gases. In the next phase, the emissions studies coming out of the engine are measured by using AVL make gas analyzers and smoke meters. All Performance and emissions responses were noted varying loads with increments of 25% loading and at static Engine Volumetric ratio of 17.5 and Fuel Injection timing of 23 deg. bTDC.

4.1. PERFORMANCE STUDIES

4.1.1. BRAKE THERMAL EFFICIENCY

The derived thermal efficiency of 04 nanoparticle-dosed WCO20 blends, WCO20 blend, and Diesel is portrayed in Figure 4. The observations were noted for 06 fuels in incremental loads of 25%. It could be illustrated from Figure 4 that as the load is incremented the BTHE values also rose. Also, we could so see that the addition of CuO additives does boost the BTHE values. The amount of rise in BTHE for WCO20 with 10ppm, 20ppm, 30ppm, and 40ppm is when compared to base blend (WCO20) and the rise thermal output observed for WCO20+10ppm, WCO20+20ppm,

WCO20+30ppm, and WCO20+40ppm when compared to diesel was. This was due to the phenomenon of secondary atomization and the micro explosion of Cu-Isopropyl alcohol nano fuel emulsion. These emulsified fuels tend to shorten the ignition delay and there increasing the combustion duration due to which the BTHE values were found high. When Nano additive-alcohol solution is exposed to higher pressure and temperature environment, leads to an explosion of alcohol. Later this explosion or combustion further diminishes the ignition delay of the WCO20 fuel. This catalytic combustion activity is responsible for the enhanced thermal efficiency phenomenon. Furthermore, the initiation of higher fuel inlet pressure does provide better mixing of air/fuel and thereby contributing to retarded fuel ignition delay. Also, we could observe the maximum thermal efficiency was observed for WCO20 having 20ppm of CuO at 240bar. The observations found are in line with [21, 22].
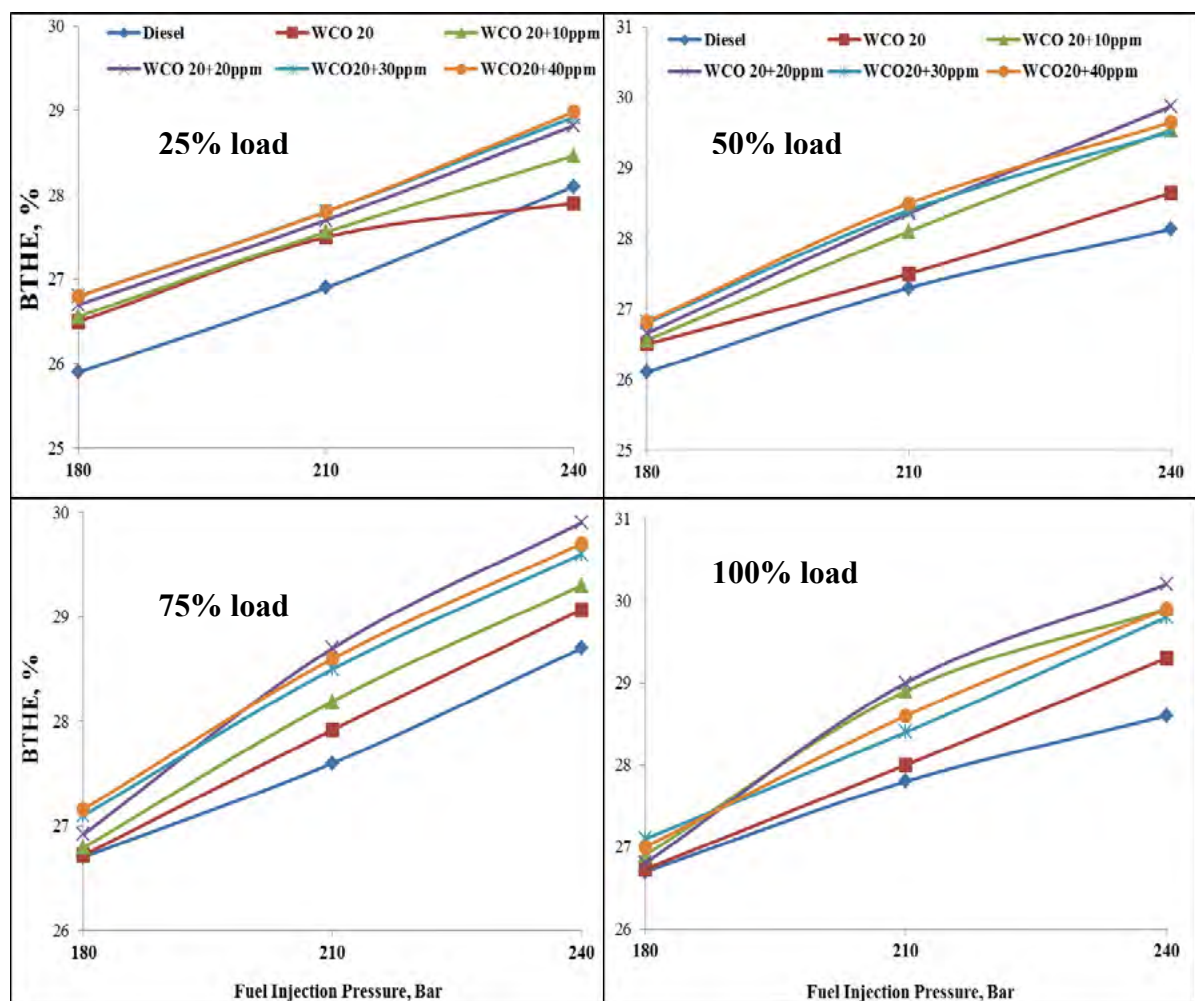
Figure 4. Variation of brake thermal efficiency at varying injection pressures, loads and levels of CuO.

4.1.2. BRAKE SPECIFIC FUEL CONSUMPTION

The main limiting factor why Biodiesel blends are not so extensively used is due to the fuel consumption rates and Figure 5 exhibits the BSFC values for varying FIP(fuel Injection pressure) and load variations. The least BSFC values for loads were shown by diesel and this was due to the higher heating value of diesel which contributes to

attaining higher HRR values [24]. It could be observed that when Copper oxide was added to WCO20 blends the BSFC values does plummet to a small extent. The percentile decline found when WCO20 with 10ppm, 20ppm, 30ppm, and 40ppm of CuO was doped was 1.6%, 4.2%, 3.3%, and 3.2% respectively when compared to the base blend. The addition of these oxide additives in the WCO 20 blend does retard the fuel ignition delay and thereby time allocation for the total amount of fuel combustion per KW of power is more. However, the values of BSFC of WCO20 with CuO were not promising when compared to diesel. Also, it could be noted that at higher FIP and at full load conditions, the BSFC values were least for all test fuels. Biodiesel which is denser and has a higher flash point does require enhanced fuel injection pressure for them to stream into denser compressed air. The amount of decline of BSFC values when injection pressure was changed from 210bar to 240 bar for WCO 20, WCO+10ppm of CuO, WCO+20ppm of CuO, WCO20+30ppm of CuO, and WCO20+40ppm of CuO was 3.4%, 4.6%, 4.3%, and 4.2% respectively.
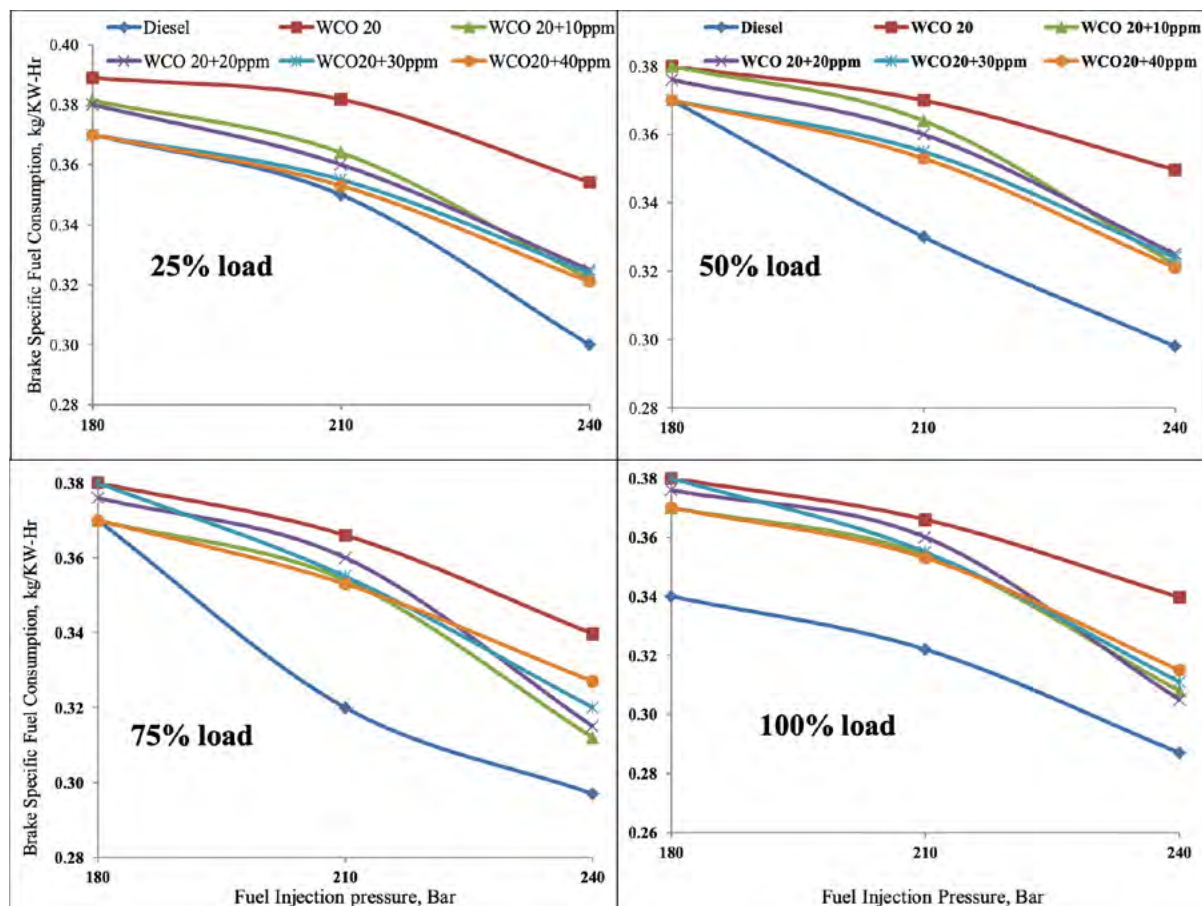
Figure 5. Variation of brake specific fuel consumption at varying injection pressures, loads and levels of CuO.

4.1.3. EXHAUST GAS TEMPERATURES

Exhaust gas temperatures (EGT) of the CI engines play a prominent role in the formation of oxides of nitrogen emissions [18]. Also, higher combustion rates display higher HRR and EGTs. Figure 6 explains the temperatures of exhaust gases formed after combustion at varying Loads and FIP's for all 06 test fuels. WCO20+20ppm displayed Peak EGT values for 240bar pressure and at full load conditions and diesel

displayed the least EGTs for all loads and FIP's. The rise in EGT was found when the FIP was changed from 210bar to 240 bar for WCO 20, WCO+10ppm of CuO, WCO+20ppm of CuO, WCO20+30ppm of CuO, and WCO20+40ppm of CuO was 5.6%, 6.2%, 8.3%, 7.8%, and 7.7% respectively when compared to diesel. Also, the EGT ascent percentile at 240bar for WCO+10ppm of CuO, WCO+20ppm of CuO, WCO20+30ppm of CuO, and WCO20+40ppm of CuO was 3.6%, 4.5%, 3.9%, and 3.7% respectively when compared with Base blend WCO20. This might be due to higher injection pressure and good cetane rating of fuel which tend to control the combustion activity and thereby reduce the fuel ignition delay.
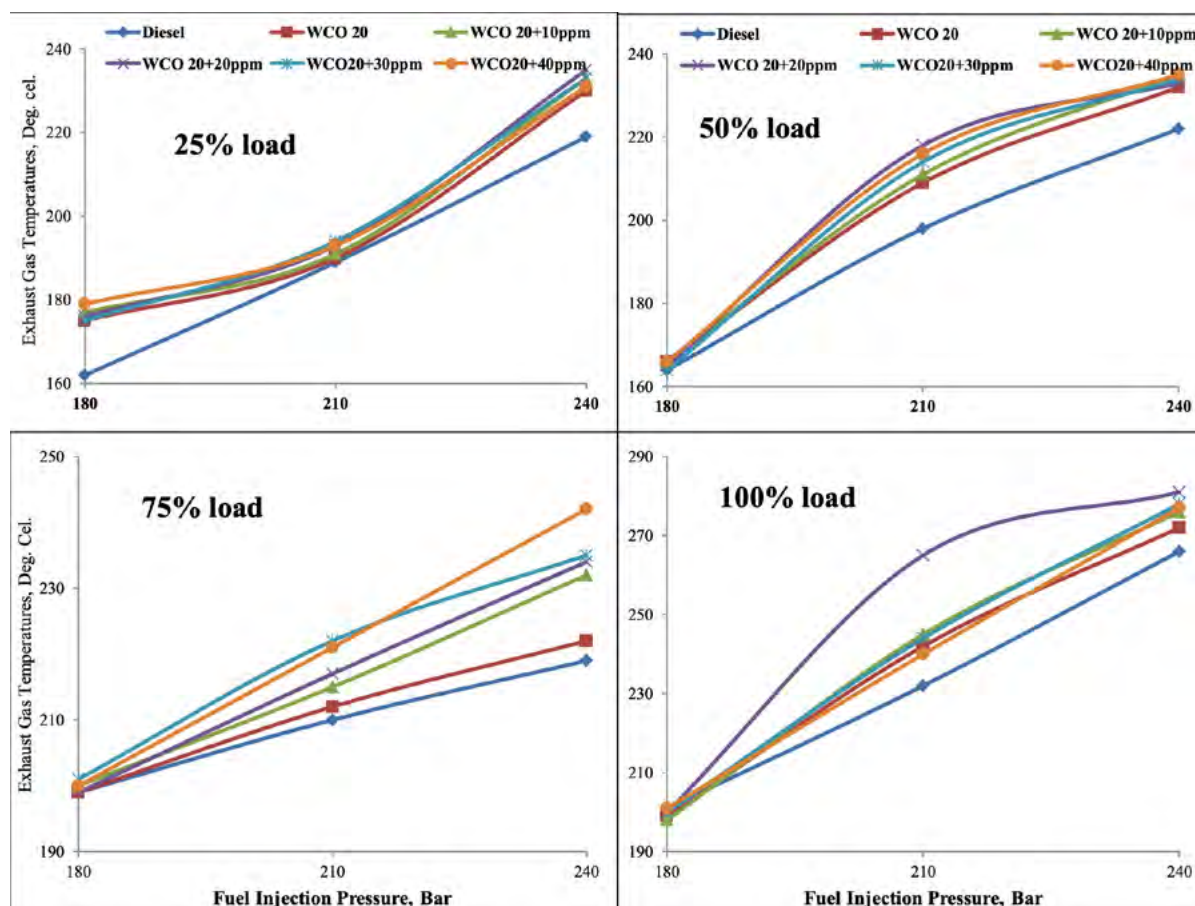
Figure 6. Variation of exhaust gas tempratures at varying injection pressures, loads and levels of CuO.

4.2. EMISSION STUDIES

4.2.1. OXIDES OF CARBON

During the oxidation of fuel, the products do have the presence of carbon dioxide as a result. Furthermore, its conventional wisdom that, the higher the CO_2 levels, the better the combustion of fuel [4, 6]. On the other hand, the presence of CO in the exhaust gases of fuel combustion signifies incomplete combustion. It can be observed from Figure 7 and Figure 8 the percentile presence of CO and CO_2, respectively, for all 6 fuels incremental load and fuel injection pressure. It could be observed that amount of CO_2 increases with increasing load and fuel injection pressure. Diesel

exhibits the least CO2 levels when compared with WCO20. Also, the presence of CuO in WCO20 shoots up the levels of CO2. The percentile rise in CO2 levels when CuO is added in WCO with adulteration levels of 10ppm, 20ppm, 30ppm, and 40ppm is 2.8%, 4.9%. 4.4% and 3.7% when compared with WCO20. Also, with the enhancement in the Injection pressure from 210bar to 240bar, the rise in CO2 levels found were 2.3%, 3.2%, 3.5%, 7.6%, 6.1%, and 6.2% for Diesel, WCO 20, WCO+10ppm of CuO, WCO+20ppm of CuO, WCO+30ppm of CuO, and WCO+40ppm of CuO respectively. Emulsified esters have good cetane number and the presence of nanoadditives does retard the fuel ignition delay and thereby incrementation combustion duration due to which the formation of dioxides are more than CO.
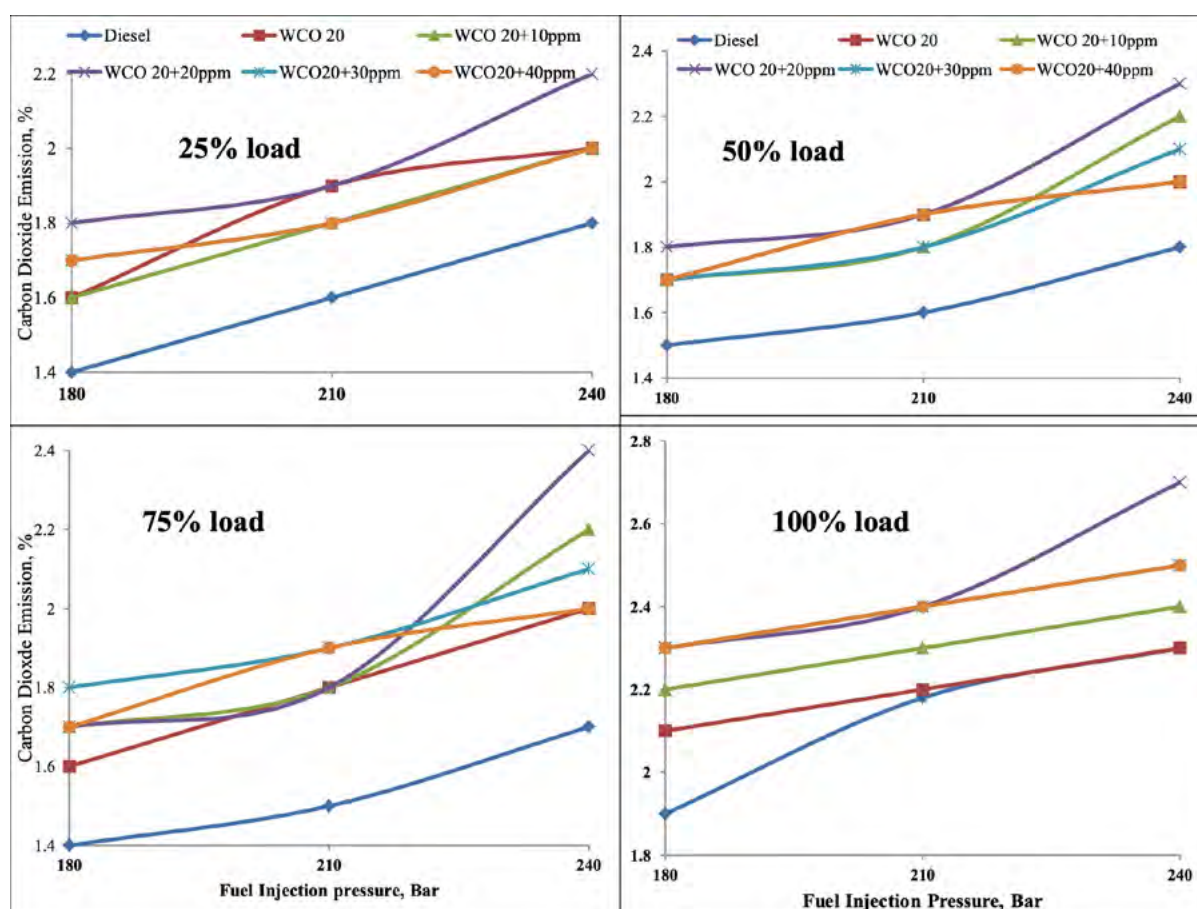
Figure 7. Variation of CO2 emissions at varying injection pressures, loads and levels of CuO.

4.2.2. CARBON MONOXIDE

When the levels of carbon dioxide rise, the levels of CO reduce for test fuels. Figure 8 explains the levels of CO emissions. It could be observed that Diesel fuel combustion provides the highest CO levels when compared to other fuels. The levels of CO declined with a gradual rise in engine loads and fuel injection pressure which are in line with the findings of [7, 11]. Also, the addition of CuO in the base blend further reduces the CO emission. The percentile descent in CO levels when CuO is added in WCO20 with sullying levels of 10ppm, 20ppm, 30ppm, and 40ppm is 1.9%, 3.8%. 3.4% and 3.2% respectively when compared with the base blend. Also, with the enhancement in the Injection pressure from 210bar to 240bar, the rise in CO2 levels

found were 2.3%, 3.2%, 3.5%, 7.6%, 6.1%, and 6.2% for Diesel, WCO 20, WCO+10ppm of CuO, WCO+20ppm of CuO, WCO+30ppm of CuO and WCO+40ppm of CuO respectively.
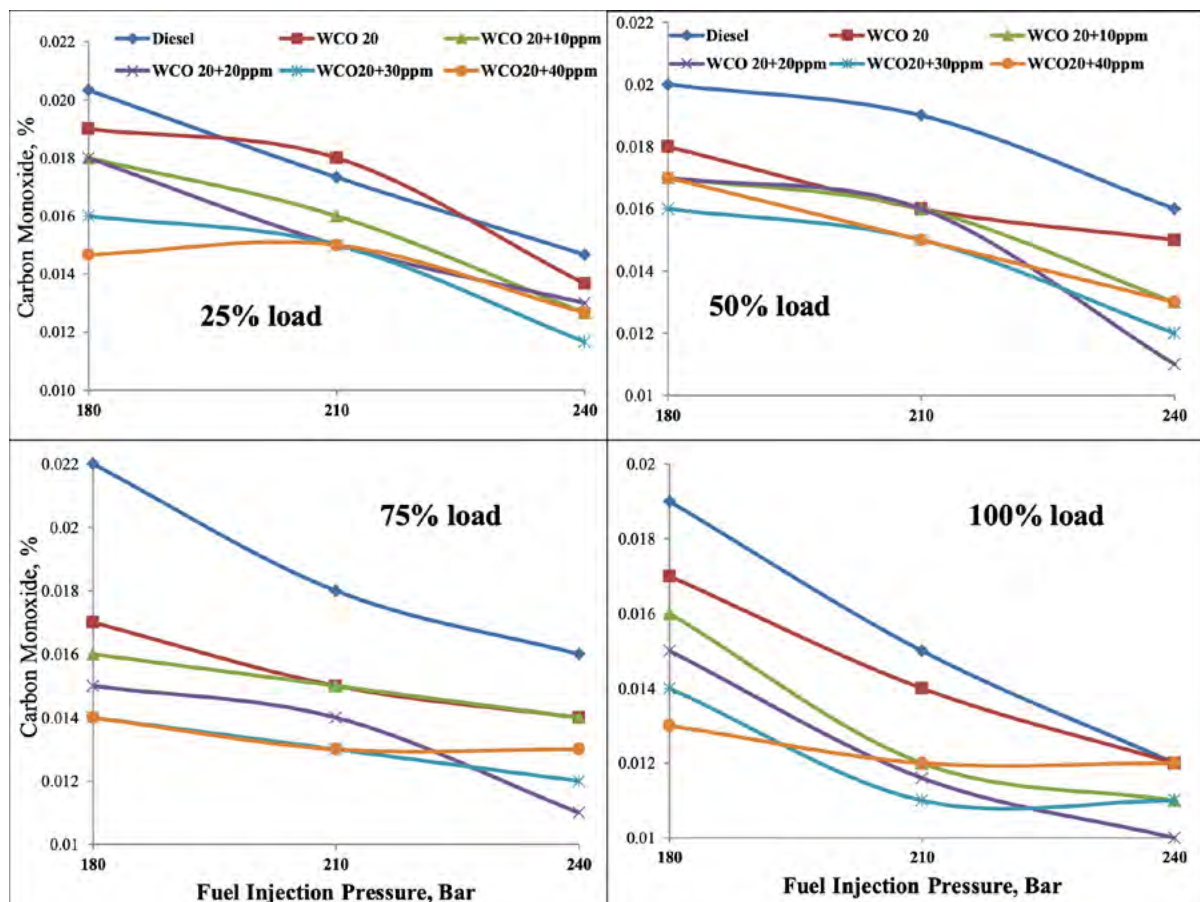
Figure 8. Variation of CO emissions at varying injection pressures, loads and levels of CuO.

4.2.3. HYDROCARBON EMISSION

Hydrocarbon emission is eminent in fuel combustion even though diesel engine operates in Lean air-fuel mixture ratios. Figure 9 shows the obtained ppm levels of HC emission for all test fuels at varying loads and fuel injection pressures. It was observed that with incrementation of engine load and fuel Injection pressure the levels of HC emission reduced. Diesel showed the highest HC emission when compared to the rest test fuels. It could be observed that with a change in fuel injection pressure from 210bar to 240bar, the percentile descent in HC emission for Diesel, WCO 20, WCO+10ppm of CuO, WCO+20ppm of CuO, WCO+30ppm of CuO, and WCO+40ppm of CuO is 5.56%, 11.76%, 12.5%, 20%, 18.75%, and 13.6% respectively. Also the addition of CuO in WCO20, the observed decent in HC emission was 6.67%, 21%, 16.7% and 17.6% for 10ppm, 20ppm, 30ppm and 40ppm respectively. These are in line with the findings [6, 23].
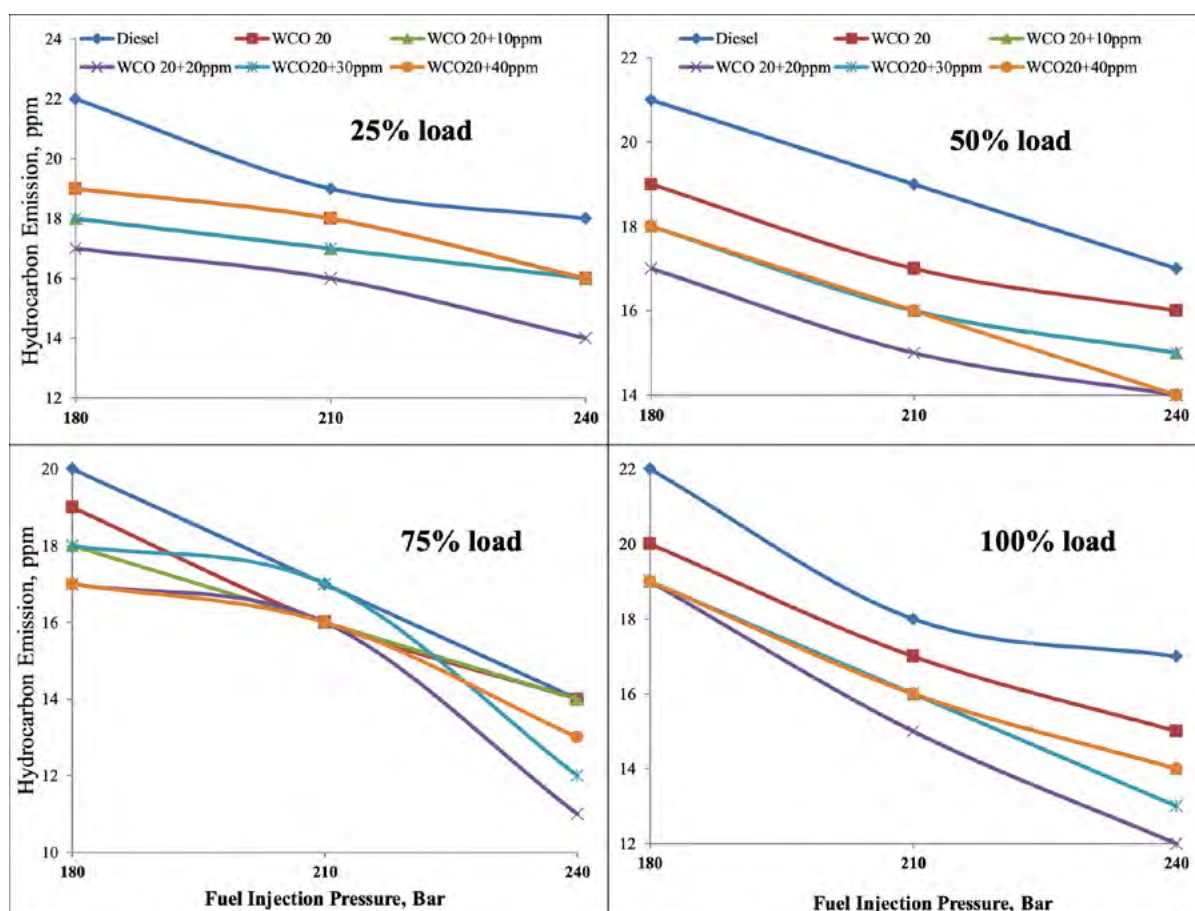
Figure 9. Variation of HC emissions at varying injection pressures, loads and levels of CuO.

4.2.4. NITROGEN OXIDE EMISSION

The development of Nitrogen oxides is inevitable as the combustion of fuel will lead to heat generation and which in turn acts as a catalyst for the formation of NOx [20, 27]. It could be observed from Figure 10 that with incrementation of load and fuel injection pressure leads to rise in levels of NOx [25, 26]. The temperatures of combusted gas play a direct role in signifying the NOx emission as higher EGT leads to higher combustion temperature and higher temperature acts as a catalyst for NOx formation. Most researchers have often discussed the heavy rise in NOx levels with higher volumes of Biodiesel in biodiesel-diesel blends (BDD) which limits the use of higher BDD blends. In the current study, it was found that the addition of CuO in the WCO20 blend ascents the NOx levels but to a small extent. It was observed that higher fuel injection pressure of 240Bar, the ascent found for NOx with 10ppm, 20ppm, 30ppm, and 40ppm addition of CuO in WCO20 was found to be 1.5%, 2.89%, 3.78%, and 4.8% respectively. Similar observations were noted by Keskin et.al.[28] with 8ppm and 16ppm of manganese dioxide nanoparticles in vegetable oil biodiesel blends led to an increased NOx emission.
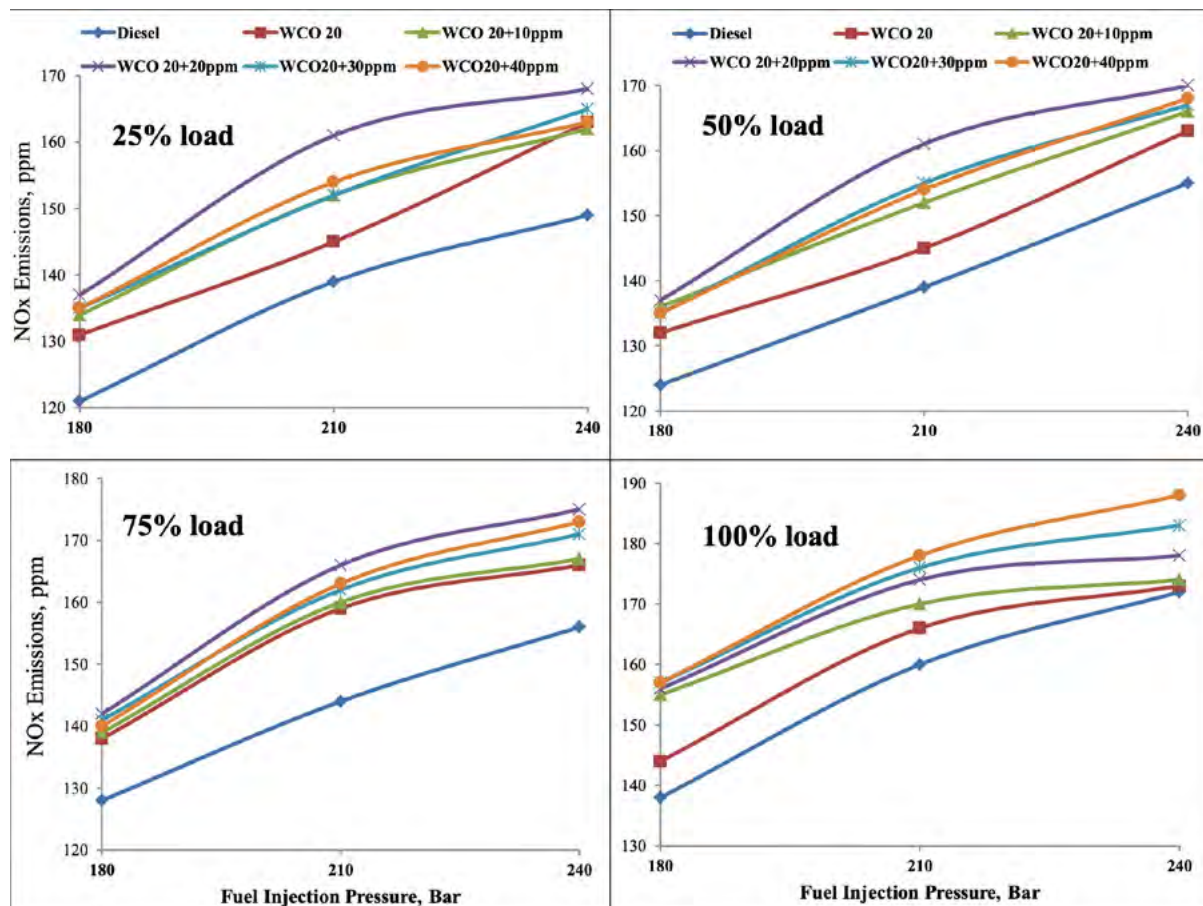
Figure 10. Variation Of NOx emissions at varying injection pressures, loads and levels of CuO.

4.2.5. SMOKE LEVELS

The measured smoke levels for all 6 test fuels could be observed in Figure 11. The Hartrige Smoke Levels diminished with gradual incrementation of fuel injection pressure and engine loads. It could be observed that WCO20 HSU levels were much higher than that of diesel. It could be observed that with IOP 240 bar, the rise in HSU levels when compared to Diesel were 17%, 11.2%, 10.3%,10.2%, and 10.8% respectively for WCO20 having 0, 10ppm, 20ppm, 30ppm and 40ppm of CuO. Also, with the addition of CuO in WCO20 at 240 bar pressure, the descent of HSU found was 1.9%, 6.4%, 4.7%, and 4.3% respectively when compared to the Base blend (WCO20).
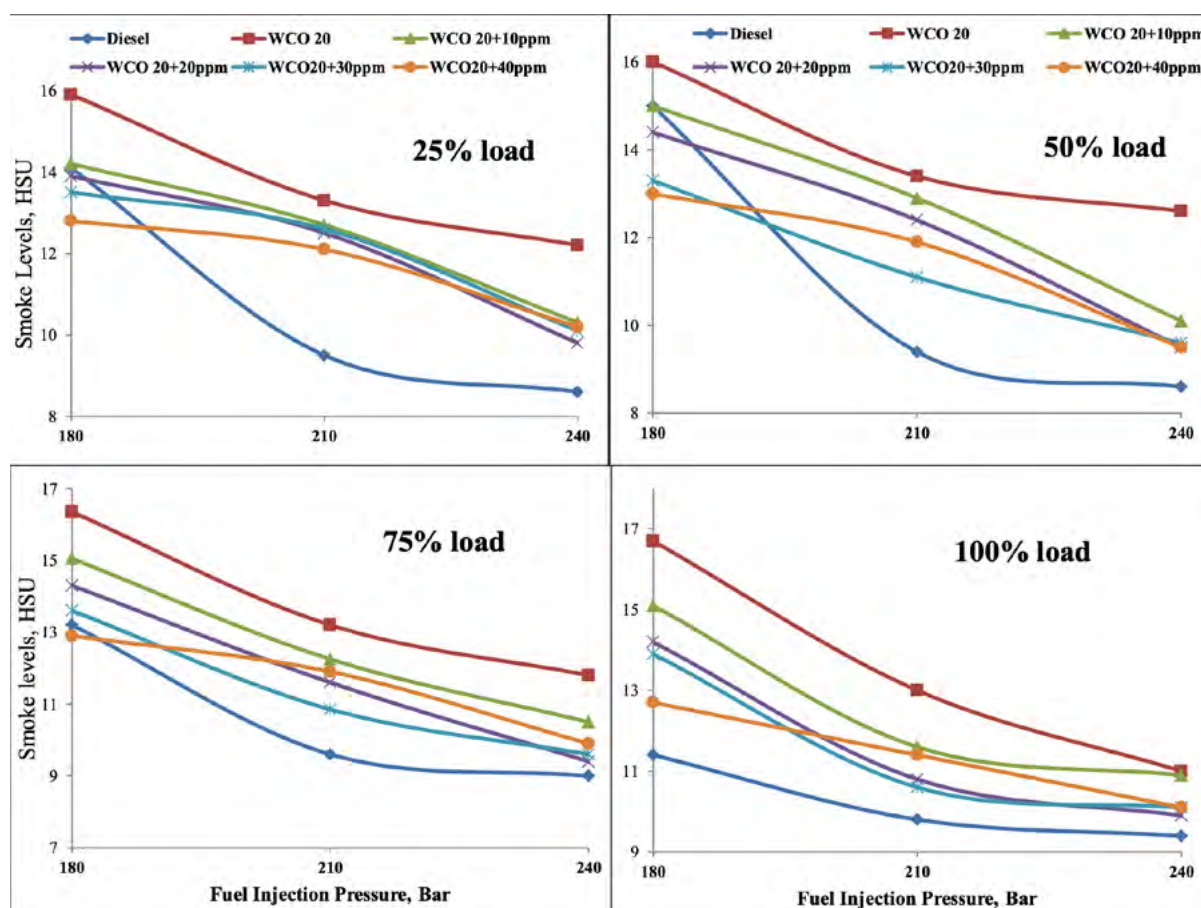
Figure 11. Variation of smoke levels emissions at varying injection pressures, loads and levels of CuO.

5. CONCLUSIONS

The present explains the performance and emission features displayed by engine when fuelled with Waste Cooking oil blend and with addition of copper oxide fuel additives with dosing levels of 10ppm, 20ppm, 30ppm and 40ppm. The engine observations were noted at increasing loads and variations in fuel inlet pressure. Below are some major inferences witnessed.

1. The addition of CuO in WCO20 does retard the Viscosity of fuel and increases the density of fuel.

2. The Presence of Copper oxide Nano-additives in WCO20 blend does contribute in reducing the ignition delay. This reduction helps in obtaining the complete combustion of fuel.

3. Higher Fuel Injection pressure does play a promising role in improvement in Performance and emission features of engine. Also the inculcation of CuO at Higher FIP of 240bar does further promote in constricting the levels of NOx.

4. The BTHE of the engine rose with the addition of CuO in WCO20. Also the BSFC values were limited by the addition of CuO in WCO20.

5. The Levels of HC and CO retarded with the addition of CuO in WCO20 even at higher fuel injection pressures. The average decline found for CO and HC

emission with addition of 20ppm CuO in WCO20 were 2.9% and 12.6% respectively.

REFERENCES

(1)   A Halwe-Pandharikar, SJ Deshmukh, NJ Kanu. (2022). **Numerical investigation and experimental analysis of nanoparticles modified unique waste cooking oil biodiesel fueled C. I. Engine using single zone thermodynamic model for sustainable development**. *AIP Advances,* 12, 095218. https://doi.org/10.1063/5.0103308

(2)   AD Halwe, SJ Deshmukh, NJ Kanu, E Gupta, RB Tale. (2021). **Optimization of the novel hydrodynamic cavitation based waste cooking oil biodiesel production process parameters using integrated L9 Taguchi and RSM approach**. *Materials Today: Proceedings,* 47, 5934-5941. https://doi.org/10.1016/j.matpr.2021.04.484

(3)   Srinidhi, C., A. Madhusudhan, and S. V. Channapattana. (2019). **Parametric studies of CI engine at various injection strategies using biodiesel blended nanoparticles as fuel**. *International Journal of Ambient Energy,* 1-11.

(4)   NJ Kanu, S Guluwadi, V Pandey, S Suyambazhahan. (2021). **Experimental Investigation of Emission Characteristics on Can-Combustor Using Jatropha Based Bio-derived Synthetic Paraffinic Kerosene**. *Smart Science*. https://doi.org/10.1080/23080477.2021.1938503

(5)   Srinidhi, Campli, A. Madhusudhan, S. V. Channapattana, S. V. Gawali, and Kiran Aithal. (2021). **RSM based parameter optimization of CI engine fuelled with nickel oxide dosed Azadirachta indica methyl ester**. *Energy,* 234, 121282.

(6)   Srivastava AK, Soni SL, Sharma D, Jain NL. (2018). **Effect of injection pressure on performance, emission and combustion characteristics of diesel-acetylene-fuelled single cylinder stationary CI engine**. *Environ Sci Pollut Res,* 25(8), 7767-7775. https://doi.org/10.1007/s11356-017-1070-3

(7)   Puhan S, Jegan R, Balasubbramanian K, Nagarajan G. (2009). **Effect of injection pressure on performance, emission and combustion characteristics of high linolenic linseed oil methyl ester in a DI diesel engine**. *Renew Energy,* 34(5), 1227-1233. https://doi.org/10.1016/j.renene.2008.10.001

(8)   Rao G, Kumar GN, Herbert M. (2018). **Effect of injection pressure on the performance and emission characteristics of CI engineusing Vateria indica biodiesel**. *Int J Ambient Energy,* 1-10. https://doi.org/10.1080/01430750.2017.1421575

(9)   Nanthagopal K, Ashok B, Raj RTK. (2016). **Influence of fuel injection pressures on Calophyllum inophyllum methyl ester direct injection diesel engine**. *Energy Convers. Manag,* 116, 165-173. https://doi.org/10.1016/j.enconman.2016.03.002

(10)   Srinidhi, C., A. Madhusudhan, and S. V. Channapattana. (2019). **Effect of NiO nanoparticles on performance and emission characteristics at various injection timings using biodiesel-diesel blends**. *Fuel,* 235, 185-193.

(11) Shehata MS, Attia AMA, Razek SMA. (2015). **Corn and soybean biodiesel blends as alternative fuels for diesel engine at different injection pressures**. *Fuel,* 161, 49-58. https://doi.org/10.1016/j.fuel.2015.08.037

(12) Kannan GR, Karvembu R, Anand R. (2011). **Effect of metal based additive on performance emission and combustion characteristics of diesel engine fuelled with biodiesel**. *Appl Energy*, 88,: 3694-703. https://doi.org/10.1016/j.apenergy.2011.04.043

(13) Campli, Pratik Kshirsagar, Moreshwar Joshi, Anish Kulkarni, S. V. Channapattana, A. Madhusudan, Kiran Aithal, and Shivaji Gawali. (2021). **Effect of fuel injection timing on CI engine fuelled with neem biodiesel blends-a comparative study of experimental and numerical simulation**. *International Journal of Energy and Environmental Engineering,* 2021, 1-12.

(14) Srinidhi C, Madhusudhan A. (2017). **A diesel engine performance investigation fuelled with nickel oxide nano fuel-methyl ester**. *Int J Renew Energy Res,* 7(2), 676-681.

(15) Kannan, K. and Udayakumar, M. (2010). **Experimental study of the effect of fuel injection pressure on diesel engine performance and emission.** *ARPN Journal of Engineering and Applied Sciences*, 5(5), 42-45.

(16) Ong HC, Silitonga AS, Masjuki HH, Mahlia TM, Chong WT, Boosroh MH. (2013). **Production and comparative fuel properties of biodiesel from non-edible oils: Jatropha curcas, Sterculia foetida and Ceiba pentandra**. *Energy Convers Manage,* 73, 245-255.

(17) Chen PC, Wang WC, Roberts WL, Fang T. (2013). **Spray and atomization of diesel fuel and its alternatives from a single-hole injector using a common rail fuel injection system**. *Fuel,* 103, 850-861.

(18) Avinash Kumar Agarwal, Dhananjay Kumar Srivastava, Atul Dhar, Rakesh Kumar Maurya, Pravesh Chandra Shukla, Akhilendra Pratap Singh. (2013). **Effect of fuel injection timing and pressure on combustion, emissions and performance characteristics of a single cylinder diesel engine.** *Fuel*, 111. https://doi.org/10.1016/j.fuel.2013.03.016

(19) Manzoore Elahi M. Soudagar, Nik-Nazri Nik-Ghazali, Md. Abul Kalam, I.A. Badruddin, N.R. Banapurmath, Naveed Akram. (2018). **The effect of nano-additives in diesel-biodiesel fuel blends: A comprehensive review on stability, engine performance and emission characteristics.** *Energy Conversion and Management*, 178, 146-177. https://doi.org/10.1016/j.enconman.2018.10.019

(20) Jaichandar S, Annamalai K. (2013). **Combined impact of injection pressure and combustion chamber geometry on the performance of a biodiesel fueled diesel engine**. *Energy,* 55, 330-339.

(21) Ranjan A, Dawn S, Jayaprabakar J, Nirmala N, Saikiran K, Sriram SS. (2018). **Experimental investigation on effect of MgO nanoparticles on cold flow properties, performance, emission and combustion characteristics of waste cooking oil biodiesel**. *Fuel,* 220, 780-791.

(22) Ahmed I. El-Seesy, Hamdy Hassan, S. Ookawara, (2018). **Effects of graphene nanoplatelet addition to jatropha Biodiesel-Diesel mixture on the performance and emission characteristics of a diesel engine.** *Energy*, 147, 1129-1152. https://doi.org/10.1016/j.energy.2018.01.108

(23) Vellaiyan, S. (2019). **Enhancement in combustion, performance, and emission characteristics of a diesel engine fueled with diesel, biodiesel, and its blends by using nanoadditive.** *Environ Sci Pollut Res.* https://doi.org/10.1007/s11356-019-04356-2

(24) Varatharaju Perumal, M. Ilangkumaran, (2018). **The influence of copper oxide nano particle added pongamia methyl ester biodiesel on the performance, combustion and emission of a diesel engine.** *Fuel*, 232, 791-802. https://doi.org/10.1016/j.fuel.2018.04.129

(25) Senthilraja S, Karthikeyan M, Gangadevi R. (2010). **Nanofluid applications in future automobiles: a comprehensive review of existing data**. *Nano Micro Lett,* 2, 306-310.

(26) Lim Y, Qia YS. (2012). **Combustion of Nanofluid fuels with the addition of boron and iron particles at dilute and dense concentrations**. *Combust Flame,* 159, 1732-1740.

(27) Keskin A, Yaşar A, Yıldızhan Ş, Uludamar E, Emen FM, Külcü N. (2018). **Evaluation of diesel fuel-biodiesel blends with palladium and acetylferrocene based additives in a diesel engine**. *Fuel,* 216, 349-355

(28) Subbiah, Ganesan, Yuvarajan Devarajan, Ruby Mishra, and Jeyaseelan Thangaraja. (2022). **Experimental research on waste and inedible feedstock as a partial alternate fuel: environmental protection and energy-saving initiative**. *Biomass Conversion and Biorefinery,* 1-13.

(29) Shanmugam, Rajasekaran, Damodharan Dillikannan, Gopal Kaliyaperumal, Melvin Victor De Poures, and Rajesh Kumar Babu. (2021). **A comprehensive study on the effects of 1-decanol, compression ratio and exhaust gas recirculation on diesel engine characteristics powered with low density polyethylene oil**. *Energy Sources, Part A: Recovery, Utilization, and Environmental Effects,* 43(23), 3064-3081.

(30) Devarajan, Yuvarajan, Gautam Choubey, and Kulmani Mehar. (2020). **Ignition analysis on neat alcohols and biodiesel blends propelled research compression ignition engine**. *Energy Sources, Part A: Recovery, Utilization, and Environmental Effects,* 42(23), 2911-2922.

(31) Justin Abraham Baby, Sajin, S. Suresh Babu, and Yuvarajan Devarajan. (2021). **Performance study of neat biodiesel-gas fuelled diesel engine**. *International Journal of Ambient Energy,* 42(3), 269-273.

(32) V Pandey, A Bekele, GMS Ahmed, NJ Kanu, GK Singh. (2021). **An application of conjugate gradient technique for determination of thermal conductivity as an inverse engineering problem**. *Materials Today: Proceedings,* 47, 3082-3087. https://doi.org/10.1016/j.matpr.2021.06.073

(33) V Pandey, NJ Kanu, GK Singh, B Gadissa, (2021). **AZ31-alloy, H13-die combination heat transfer characteristics by using inverse heat conduction algorithm**. *Materials Today: Proceedings,* 44, 4762-4766. https://doi.org/10.1016/j.matpr.2020.11.258

(34) Chatur, Madhuri G., Anil Maheshwari, and Srinidhi Campli. (2022). **Investigation of waste cooking oil-diesel blend with copper oxide additives as fuel for diesel engine under variations in compression ratio**. *International Journal of Energy and Environmental Engineering,* 1-12.

(35) Dhiraj S. Patil, Dattatray A. Chopade, Manoj A. Kumbhalkar. (2018). **Experimental investigation of effect of cerium oxide nanoparticles as a fuel additive in cottonseed biodiesel blends.** *MAYFEB Journal of Mechanical Engineering*, 1, 1-12.

3C Tecnología. Glosas de innovación aplicadas a la pyme. ISSN: 2254-4143

Ed.43 | Iss.12 | N.1 January - March 2023

/13/

3C Tecnología. Glosas de innovación aplicadas a la pyme. ISSN: 2254-4143

Ed.43 | Iss.12 | N.1 January - March 2023

224

PREPARATION OF THE ENVIRONMENTALLY FRIENDLY GREEN NANO INSECTICIDE USING COPPER SALTS

H. M. AL-HAMDANI*

Market Research & Consumer protection Center/Univ. of Baghdad / Iraq

cioffi16@yahoo.com

R. S. HAMEED

Biological Department, Al-Mustansiriya University, Baghdad/Iraq

https://doi.org/10.17993/3ctecno.2023.v12n1e43.225-241

ABSTRACT

The nanoparticle was prepared using aqueous extract of naringin Citrus aurantium and copper salts, which are 100% local materials to combat the white fly Bemisia tabaci, which have the ability to transmit and spread plant diseases at a very high rate and pose a great threat to global food production. In tropical and subtropical regions, the insect problem used in the study has become one of the most serious problems facing crop protection. The economic losses are estimated in the hundreds of millions of dollars. The prepared nanoparticles were characterized by the following assays:UV-visible spectrophotometry, SEM, AFM and FTIR. The results of the study showed that the nanoparticles of copper salts were more effective in the mortality rates of nymphs, eggs, and whole insects of the whitefly at concentrations of 100, 200 and 300 ppm, in addition to that the effectiveness of the nanocide led to higher mortality rates for the third, fourth and virginal stages of whitefly at 300 ppm concentrations compared to the results Aqueous extract of Citrus aurantium and copper salts.

KEYWORDS

Nanoparticles, Bemisia tabaci, SEM, AFM, FTIR, and UV-Visible.

PAPER INDEX

1.   INTRODUCTION

In Iraq, orchids have recently been exposed to infestation with a large number of different insect pests, which led to various damages in severity and size depending on the elements of the prevailing climate and among these insect species are the Aleuroclava Jasmine fly and the jasmine fly on citrus trees. In addition to the white fruit fly (Mediterranean fly), spiders and powdery mildew insects of citrus trees are widely spread in the central regions of Iraq's governorates such as Diyala, Baghdad, Salah al-Din, Karbala, Babil and Wasit, which has exacerbated the damage and the deterioration of trees and their total production[1,2].Thus the use of chemical pesticides is one of the most important applied methods for its rapid effect in reducing high population density and reducing its damage to agricultural crops. It was pointed out the importance of using a pesticide to control white flies on citrus fruits in Iraq and the midacloprid, carbosufan and methyl pesticides were also given the highest rates to kill the whitefly[3, 4].The second half of the twentieth century witnessed an increase in the use of chemical pesticides in controlling various agricultural pests, and it was later found that many pesticides have high toxicity and affect human and animal health as well as negative effects on the entire ecosystem. Likewise, the discovery and use of techniques such as encapsulation and controlled release led to a radical change in the use of pesticides, as many pesticide companies produced products containing nanoparticles with sizes ranging from 100 to 250 nanometers that could dissolve in water more than it is in current pesticides [5,6].In addition, the nanoparticles have a role in treating pollution from chlorine solvents, organic chlorine pesticides, organic dyes and many inorganic compounds [7].The amount of agricultural pesticides used in Iraq is frightening and requires a serious pause to limit its use or the use of advanced modern pesticides because it causes many serious diseases, including kidney failure, cancers of all kinds, congenital and reproductive malformations and neurological diseases[2,8].Also, farmers' failure to use the recommended concentrations and relying on their personal experiences in using these preventive and professional pesticides led to a reduction in safety methods, and the occurrence of injuries and poisoning for farmers [1,2, 9].Previous experiments demonstrated the possibility of synthesizing copper oxide nanoparticles using plant extracts and testing their efficacy as a preservative for wood by using extracts from neem leaves (Azadirachta indica, Pongamia pinnata, Lantana camara and Citrus reticulata) this is for the synthesis of copper [10].While another study showed by summarizing the data of plants used to synthesize CuNPs nanoparticles and opening a new path for researchers to explore those plants that had not been used in the past [11].Also another study showed the development of a non-toxic and cost-effective biological method for the synthesis of CuNPs, which is a green method for the synthesis of copper nanoparticles within 15-20 minutes and its high effectiveness against many pathogenic microbes [12,13,14]. Therefore, this study aimed to arrive at a preparation of an environmentally friendly insecticide using copper nanoparticles and to replace the chemicals in preparing copper nanoparticles using the active ingredients of naringin (Citrus aurantium) extract to control the whitefly.

2.   MATERIAL AND METHODS

2.1. PREPARATION OF AQUEOUS EXTRACTS

Naringin (Citrus aurantium) leaves was prepared by taking 20 grams of previously washed leaves and cutting them into very small pieces and placed in a volumetric flask of 250 ml and adding 100 ml of distilled water to them and the mixture was boiled for 10-12 minutes, then it was filtered and stored in the refrigerator on 4 o C until experiment and chemical analyzes are performed.

2.1.1.   PHYTOCHEMICAL ANALYSIS

The extract of alcoholic naringin prepared for phytochemical detection to reveal the various biological components of the plant such Tannins, Carbohydrates, Glycosides, Phenols, Resins, Flavonoids, Saponins, Alkaloids, Protein, Comarins, Turbines and Steroid was done using standard protocols [11].

2.1.2. PREPARATION OF NANOPARTICLES

It was taken 60 ml of 0.1 M of Cuso4 copper sulfate and added to 10 ml of aqueous extract of naringin Citrus aurantium gradually with constant stirring, after which a few drops of 1 M of NaOH were added and the pH was adjusted to 8 of the solution. Continue magnetic stirring at room temperature for 1 period/ 4 hour until the color changes to a dark black color, which indicates the occurrence of the reaction and the creation of nanoparticles, as in Figure 1, [4,15]

Figure 1. Preparation of CuSo4 nanoparticle

2.2. CHARACTERIZE THE NANOPARTICLES

The nanoparticles were detected at the Nanotechnology Center / University of Technology/Baghdad by using:

2.2.1. UV-VISIBLE SPECTROMETRY

The ultraviolet rays were used to study the optical properties with a UV-Visible spectrometry (meter teeh sp 8001) in the range of 300-800 nm [16]

2.2.2. XRD ANALYSIS

It was used X-ray (XRD- 700 Shimadza maxima –a) X-Ray diffract meter to determine the crystal phases and estimate the size of the crystals, and that with an electric voltage of 40KV and a current of 30 MA and with a scan range of 100,000) (-20,000 degrees. Also, XRD patterns were recorded within 0.12. Seconds of scanning speed and using Cu tubes with copper wavelength 1.54 Ao. [17,18]

2.2.3. FTIR SPECTROSCOPY

An infrared analysis of copper Nano forms was performed with FTIR - 8400S, SHIMAZW-FTIR spectroscopy with a wavelength ranging between (500 - 4000) cm -1[19, 20].

2.2.4. SCANNING ELECTRON MICROSCOPE (SEM)

The scanning electron microscope is of the type (TESCAN-VEGA / USA) where the Nano scale particles are scanned with 3 nm beams and 30kv electric voltage knowing that the device is connected and programmed with computer programs to analyze the average particle size in the sample [21].

2.2.5. PARTICLE SIZE DISTRIBUTION ANALYSIS

This device is important for determining fast and accurate size distributions of copper nanoparticles (vision 5.34) with a range ranging from (6- 2 µm nm), and the dynamic light scattering at 90 degrees, at temperatures from (-110-5) m using high power (35 mW) for a laser diode.

2.2.6. AFM EXAMINATION

A three-dimensional image was taken showing the copper sulphate nanoparticles using the deposition method as shown in figure 1.

2.3. BREEDING WHITEFLY BEMISIA TABACI

Five eggplant seedlings were purchased in pots and placed inside breeding houses covered from the outside with a dull cloth. Seven pairs of whitefly's adults were released into each cage for the insect brought from greenhouses and from both sexes and after 24 hours of laying eggs, the eggs were isolated for each seedling, with the same the method for nymphs, replicates (eggs, nymphs) were treated, duplicates were treated with the prepared pesticide by sprinkler, and the killing numbers readings were taken and recorded after 24, 48, and 72 hours, and the percentage of pesticide efficacy was calculated using the percentage killing percentage according to Abbot's formula [6], after which the percentage of the killed percentage was converted into proportions Angle according to and then subjected to statistical analysis [22]

$$Fatalities\% = \frac{Number\,of\,pest\,before\,treatment\,x\,Number\,of\,pest\,after\,treatment}{Number\,of\,pest\,before\,treatment\,x\,Number\,of\,pest\,after\,treatment} \times 100 (1)$$

2.4. FIELD EVALUATION OF THE EFFECTIVENESS OF NANOPARTICLES ON WHITEFLY

The experiment was carried out on eggplant plants in the greenhouse at the Zaafaraniya farm in Baghdad city, with three replicates (a plastic house) for the pesticide under test, and three replicates of the another standard pesticide (deltamethrine) for good comparison between treatments. The population density of whitefly Bemisia tabaci was calculated before the control process was carried out by randomly selecting ten plants for each replicate, in which the numbers of adults were calculated on the plant leaf in three locations for each plant, which are the top, middle and bottom (30 leave). Then the plants were sprayed with Nano pesticide by holder, then the results of killing % were taken after 24, 48 and 72 hours in the same way mentioned above.

2.5. FIELD EXPERIMENT

For each treatment, the numbers of live eggs, nymphs, and adults were estimated before treatment and after spraying one day, three days and one week after the start of the treatment, as the adults were calculated by direct counting method, and the live numbers of adult adults were counted in the statistical analysis in order to take into account the accuracy of the experiment in order to not remain dead adult's adherent to the surface of the leaf.

Figure 2. life stages of the whitefly Bemisia tabaci

2.6. STATISTICAL ANALYSIS

The killing percentage was corrected according to Abbott's equation to angle ratios [23]. It was subjected to statistical analysis to find out the effect of different factors on the studied traits. The significant differences between the averages were compared with the lowest significant difference test [10].

3.   RESULTS AND DISCUSSION

3.1. PHYTOCHEMICAL SCREENING

It was presented the active ingredients in the aqueous extract of naringin Citrus aurantium such as phenols, flavonoids, alkaloids, terpenoid, tannin, protein, charbohydrates, steroids and saponins in Table 1. Results of this study showed a highest content of total phenole, alkaloids and protein, then terpenoid, tannin, charbohydrates and steroides with medium content as in Table 1. Those active ingredients which are a byproduct of the metabolism in all kinds of fruits and vegetables act as a great role in protecting the cell from deterioration and stress and acting as antioxidants to reduce the toxic effects for free radicals [24].

Table 1. The active ingredients in the Citrus Naring aqueous extraction.

Phytochemical test	Results
Total phenol	++++
Alkaloids	+++
Terpenoids	++
Tannin	++
Protein	+++
Carbohydrates	++

| Steroids | ++ |
| Saponin | ++ |

Heavy content, ++=medium content=+++

3.2. NANOPARTICLES CHARACTERIZATION

The nanoparticles were described in the Nanotechnology Center / University of Technology / Baghdad followed different ways.

3.2.1. UV-VISIBLE SPECTROMETRY

The ultraviolet rays were used to study the optical properties with a UV-Visible spectrometry (meter teeh sp 8001) in the range of 300-800 nm [25, 26].
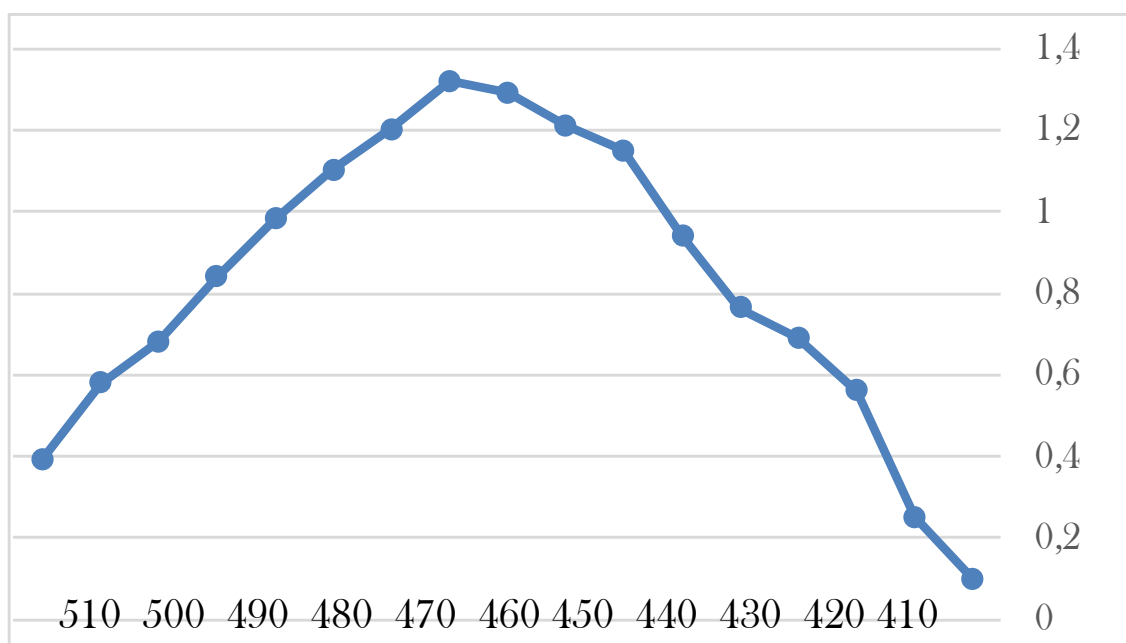
Figure 3. The synthesis of copper nanoparticles using UV-Visible radiation.

3.3. X-RAY DIFFRACTION XRD ANALYSIS

It was used X-ray (XRD- 700 Shimadza maxima –a) X-Ray diffract meter to determine the crystal phases and estimate the size of the crystals with an electric voltage of 40KV and a current of 30 MA and with a scan range between 100,000) (-20,000 degrees. Then, XRD patterns were recorded within 0.12 degrees, seconds of scanning speed and using Cu tubes with copper wavelength of 1.54 Ao. [27, 28].
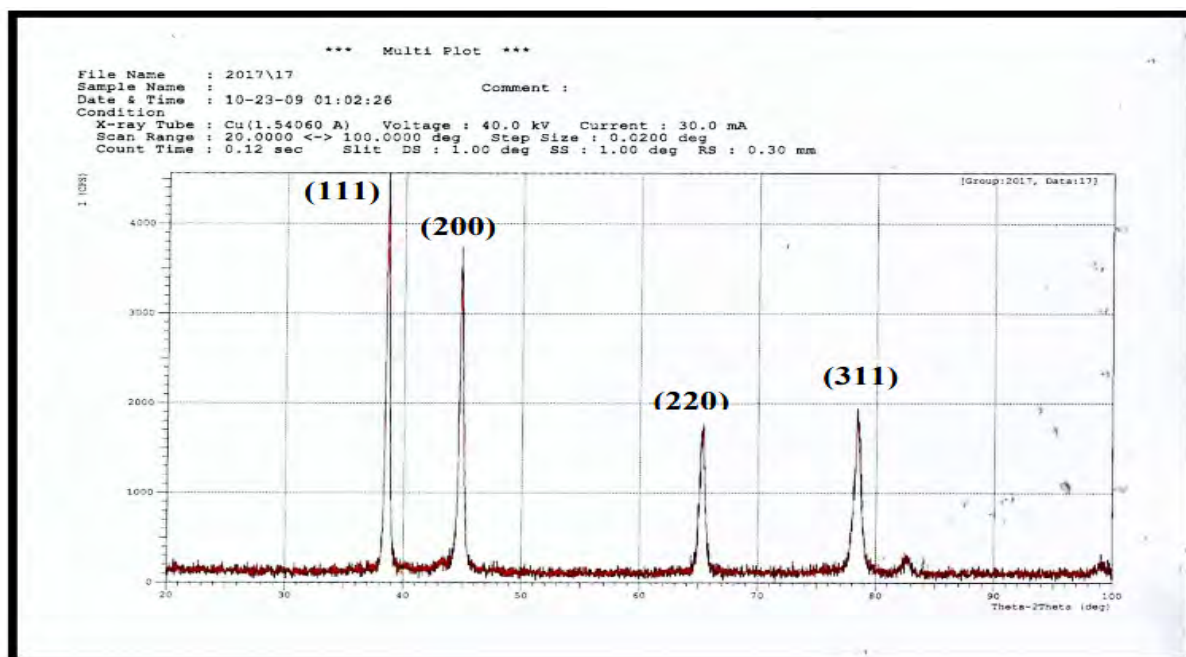
Figure 4. The XRD diffraction of copper nanoparticles

3.4. FTIR- SPECTROSCOPY

An infrared analysis of iron Nano forms was performed with FTIR-8400S, SHIMAZW-FTIR spectroscopy with a wavelength ranging between (500 - 4000) cm -1 (Huang, et al., 2018). The use of FT-IR is to find the particles and their functional groups present in the prepared copper nanoparticles. The peaks that appeared are: 3387, 3377.39, 2922, 1645, 15237, 1377, 1246, 1153, 1028, 1028, 9335, 852, 761, 659, 574, 659, 574, 437, 395, 375, that refers to: Alcohol (OH, Alkane (C-H), Alkene (= C-H), Amine (C-N), Nitro compounds (N-O), Stretch-Acid (OH) and Ester (C=C) [28,29].
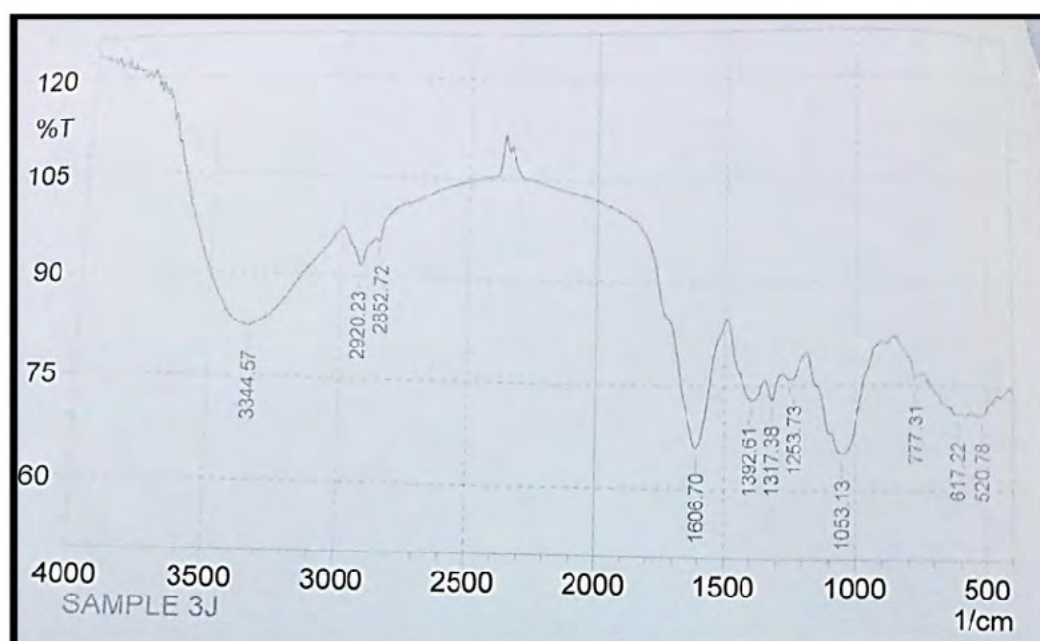
Figure 5. shows the results of the FT-IR examination.

3.5. SCANNING ELECTRON MICROSCOPE (SEM)

The scanning electron microscope is of the type (TESCAN-VEGA / USA), in which the nanoparticles are scanned with 3 nm beams and 30 kv electric voltage knowing that the device is connected and programmed with computer programs to analyze the average particle size in the sample [21].
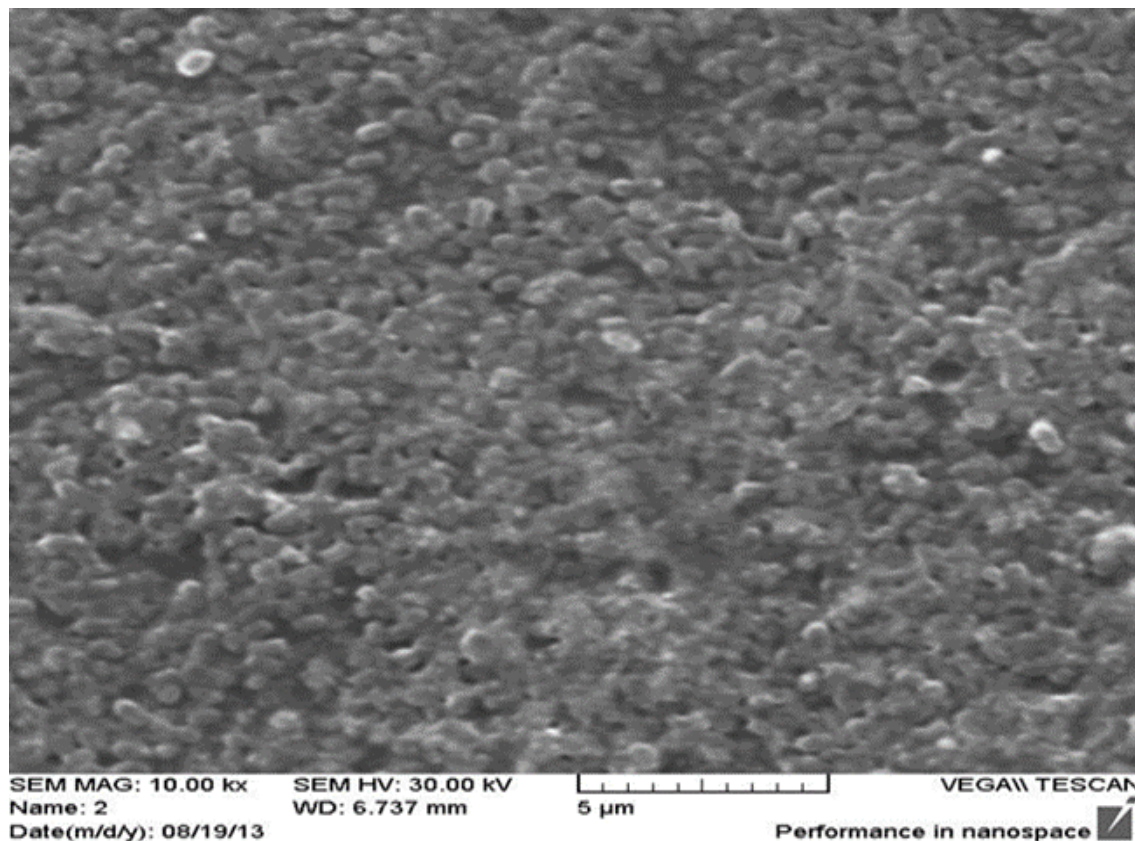
Figure 6. Image of CuSo4 nanoparticles using a scanning electron microscope SEM

3.6. PARTICLE SIZE DISTRIBUTION ANALYSIS

This device is important for determining fast and accurate size distributions of iron nanoparticles (vesion 5.34) with a range ranging from (6- 2 µm nm), and the dynamic light scattering at 90 degrees, at temperatures from (-110-5) m using high power (35 mW) for a laser diode.
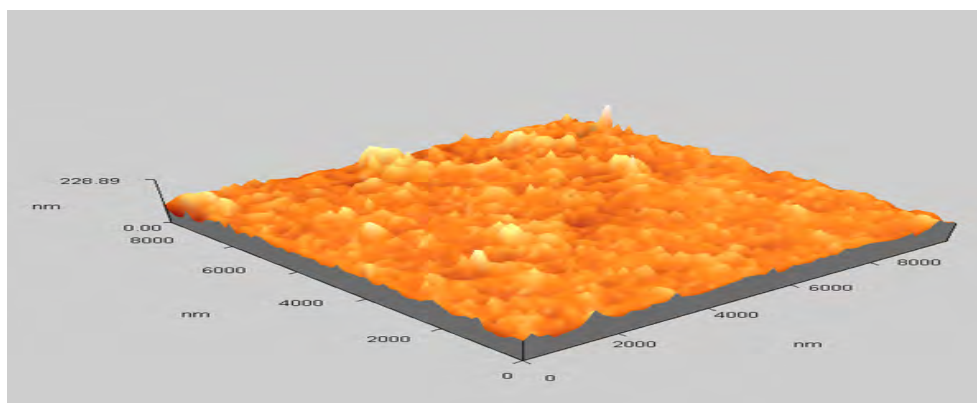
Figure 7a. FAM of synthesized Copper nanoparticles with naringin leaf broth.
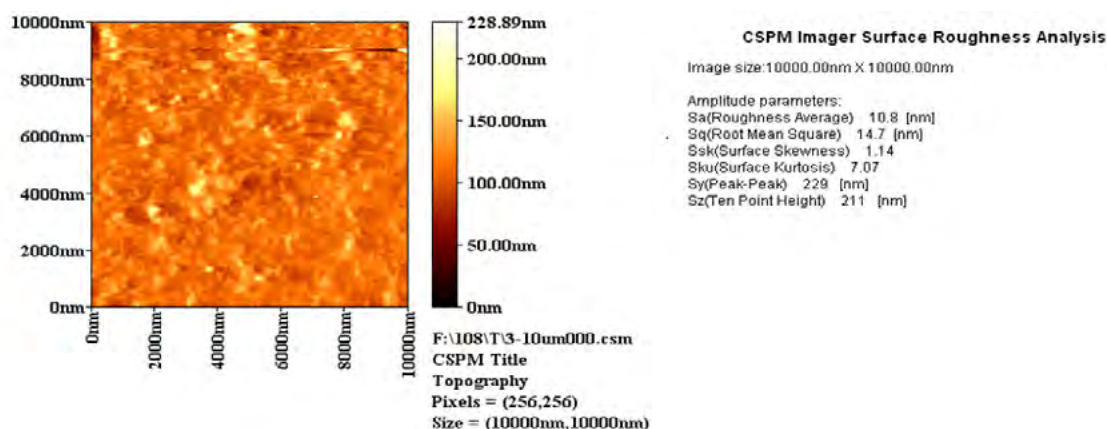
Figure 7b. AFM of synthesized Copper nanoparticles with naringin leaf extract

3.7. EFFECT OF NARINGIN (CITRUS AURANTIUM) EXTRACT ON WHITEFLY STAGES)

Results of this study presented the effect of naringin leaf extract on the mortality percent of whitefly's eggs and nymphs in Table 2. Results of this study were showed by increased the concentrations of extract from 100, 200 to 300 ppm showed a high (P≤0.05) significant effect on whitefly's eggs were 7.6, 18.8 and 26.8 respectively. Also showed a high significant effect (P≤0.05) on whitefly's nymphs were 9.8, 33.5 and 44.8 for 100, 200 and 300 ppm of the copper nanoparticles extract respectively as in Table 2. [28,30].

Table 2. Effect of citruses Naringin leaves extract on whitefly eggs and nymphs.

Extract concentration (ppm)	Mortality %	
	Whitefly eggs	Whitefly nymphs
100 ppm	8.0	9
200 ppm	15.0	27
300 ppm	27.0	44
Average	16.6	27
LSD	4.726 *	6.033 *

* (P≤0.05).

3.8. EFFECT OF COPPER SALT EXTRACT ON WHITEFLY STAGES

Results of this study presented the effect of copper salt extract on the mortality percent of whitefly's eggs and nymphs in Table 3. Results of this study were showed by increased the concentrations of extract from 100, 200 to 300 ppm showed a high (P≤0.05) significant effect on whitefly's eggs were 0.8, 1.8 and 4.8 respectively. Also showed a high significant effect (P≤0.05) on whitefly's nymphs were 2.4, 7.4 and 11.8 for 100, 200 and 300 ppm of the copper salt extract respectively as in Table 3, [1, 28].

Table 3. Effect of copper salts on whitefly eggs and nymphs.

Extract concentration (ppm)	Mortality %	
	Whitefly eggs	Whitefly nymphs
100 ppm	0.8	2.4
200 ppm	1.8	7.4
300 ppm	4.8	11.8
Average	2.5	7.2
LSD	1.152 *	2.894 *
* (P≤0.05).		

3.9. EFFECT NANOPARTICLES CITRUS WITH NARINGIN EXTRACT ON WHITEFLY STAGES

Results of this study presented the effect of nanoparticles citrus with naringin extract on the mortality percent of whitefly's eggs and nymphs in Table 4. Results of this study were showed by increased the concentrations of extract from 100, 200 to 300 ppm showed a high (P≤0.05) significant effect on whitefly's eggs were 2.3, 7.8 and 11.8 respectively. Also showed a high significant effect (P≤0.05) on whitefly's nymphs were 72, 88 and 98 for 100, 200 and 300 ppm of the nanoparticles citrus with naringin extract respectively as in Table 4. Also, it was showed that the average rate of nymphs' mortality was significantly higher 86, compared to average rate of whitefly's egg 7.3. [20, 31-32].

Table 4. Effect of synthesized nanoparticles on whitefly's egg and nymphs.

Extract concentration (ppm)	Mortality %	
	Whitefly eggs	Whitefly nymphs
100 ppm	2.3	72
200 ppm	7.8	88
300 ppm	11.8	98
Average	7.3	86
LSD	2.637 *	7.905 *
* (P≤0.05).		

3.10. NANOPARTICLE EFFICIENCY

The results of nanoparticle efficiency on whiteflies (Bemisia tabaci) tabulated as in Table 5. It was founded, the relative efficiency of the copper nanoparticles of Citrus aurantium leaf extract in controlling white flies in the field was marked highly significant difference (P≤0.05) 96.8%, 97.6% and 100% after 24, 48 and 72 hours, respectively compare with relative efficiency of the standard pesticide Decis on

Bemisia tabaci which reached 59,0, 48. 5 and 40.2 %, respectively. Note that the recorded fact distinguishes whiteflies as their tolerance and resistance to many chemical pesticides, so the Nanopesticide can be considered very effective and it is recommended to use it to combat this pest. This results identical to [6][3] were founded whiteflies have the ability to develop resistance to both conventional and nonconventional insecticides. Through the results obtained, the nanoparticles from the aqueous extract of naringin (Citrus aurantium) showed a very high significant effect in the mortality rate of the mosquitoes of the third and fourth stages and the virgin in vitro; in addition to its significant effect on the mortality rates of the white fly stages in the laboratory and in the field. These results came close to what he found [28]

Table 5. The relative efficacy of the nanoparticles of citruses naringin leaf extract on adult phase of Bemisia tabaci whiteflies compared to Deltamethrine 2.5% EC.

Examination times (Hours)	Relative efficiency of 2.5% of Deltamethrine pesticide	Relative efficiency of Citrus *aurantium* leaf nanoparticles
24 hr.	59.0	96.8
48 hr.	48.5	97.6
72 hr.	40.2	100
LSD	5.482 *	5.077 NS

* (P≤0.05).

4. CONCLUSION

The results of the study showed the possibility and ease of preparing environmentally friendly nanoparticles synthesis using aqueous extract of naringin (Citrus aurantium) with copper salts. Moreover, the prepared nanoparticles are fixed and unchanging, that is, when the nanoparticles are formed, the color of the extract changes from light green to black and remains constant. Also, the raw materials used to prepare nanoparticles are inexpensive. Also, the nanoparticles do not generate generations of insect resistance as is the case with chemical pesticides. So this idea can be used in the Ministry of Agriculture, and for the benefit of citrus orchard farmers, which are widespread in most governorates of the country, especially central, southern and northern Iraq, in addition to the fact that most of Iraq's lands are suitable for growing fruits, especially citrus fruits. But there are political factors, administrative and economic corruption, mismanagement of the water of the Tigris and Euphrates rivers, the spread of various plant diseases, including powdery mildew and the spread of the white fruit fly, as well as high temperatures and drought in the long summer, which led to the reluctance of farmers to abandon most orchards. Therefore, this study proved the possibility of finding an alternative to traditional chemical insecticides by using green nanotechnology as an environmentally friendly and safe insecticide that would not be used in Iraq beforehand.

ACKNOWLEDGMENTS

REFERENCES

(1)   Al-Myah A. R., Al-Mansour A., Al-Dhahirm A. (2011). **Effect of Some Plants Extracts on the Mortality of the Larval Mosquitoes Culex pipiens molestus Forskål [Arabic].** *Basra Journal of Science,* 29(1), 47-61.

(2)   Al-Kenani E. (2016). **The Role of geographical factors in the cultiration of fruit trees in husseiniya. MS.c.** *Karbala Governorate. University of Karbala, Iraq,* 265.

(3)   Athanassiou C., Kavallieratos N., Benelli G., Losic D., Rani P. and Desneux N. (2018). **Nanoparticles for pest control: current status and future perspectives.** *Journal of Pest Science,* 91(1), 1-15. - https://doi.org/10.1007/s10340-017-0898-0

(4)   Azwanida N.N. (2015). **A review on the extraction methods use in medicinal plants, principle, strength and limitation.** *Medicinal and Aromatic Plants,* 4(3), 1-6. https://doi.org/10.4172/2167-0412.1000196

(5)   Addadi L. Weiner S. (1992). **Control and Design Principles in Biological Mineralization.** *Angewandte Chemie International Edition,* 31(2), 153-169.

(6)   Zannat R., Rahman M., Afroz M. (2022). **Application of Nanotechnology in Insect Pest Management: A Review.** *SAARC Journal of Agriculture,* 2022, 19(2), 1-11. https://doi.org/10.3329/sja.v19i2.57668

(7)   Krishnaraj C., Jagan E.G., Rajasekar S., Selvakumar P., Kalaichelvan P.T. Mohan, N. (2010). **Synthesis of silver nanoparticles using Acalypha indica leaf extracts and its antibacterial activity against water borne pathogens.** *Colloids and Surfaces B: Biointerfaces,* 76(1), 50-56. https://doi.org/10.1016/j.colsurfb.2009.10.008

(8)   Beets-Tan J., Van Engelshoven J.M.A., Greve J.W.M. (1998). **Hepatic Adenoma and Focal Nodular Hyper- plasia: MR Findings with Superparamagnetic Iron Oxide- enhanced MRI.** *Clinical Imaging,* 22(3), 211-215.

(9)   Salamanca-Buentello F., Persad D.L., Court E.B., Martin D.K., Daar A.S., Singer P.A. (2005). **Nanotechnology and the developing world.** *PLoS Medicine, 2(5),* e97. -https://doi.org/10.1371/journal.pmed.0020097

(10)   Narayanan K.B., Sakthivel N. (2011). **Green synthesis of biogenic metal nanoparticles by terrestrial and aquatic phototrophic and heterotrophic eukaryotes and biocompatible agents.** *Advances in Colloid and Interface Science,* 169(2), 59-79. https://doi.org/10.1016/j.cis.2011.08.004

(11)   Jain S., Jain A. DevraV. (2016). **Copper nanoparticles catalyzed oxidation of threonine by peroxomonosulfate.** *Journal of Saudi Chemical Society, 21(7),* 803-810. https://doi.org/10.1016/j.jscs.2015.12.004

(12) Iida H.,Takayanagi K.,Nakanishi T. Osaka,T. (2016). **Synthesis of Fe3O4 Nanoparticles with Various Sizes and Magnetic Properties by Controlled Hydrolysis.** *Journal of Colloid and Interface Science,* 314(1), 21-30. https://doi.org/10.1016/j.jcis.2007.05.047

(13) Matei A., Cernica I., Cadar O., Roman C. SchiopuV. (2008). **Synthesis and characterization of ZnO-polymer nanocomposites.** *The International Journal of Material Forming,* 1, 767-770.

(14) Castillo-Henríquez L., Alfaro-Aguilar K., Ugalde-Álvarez J., Vega-Fernández L., de Oca Vásquez G. M., Vega-Baudrit J.R. (2020). **Green Synthesis of Gold and Silver Nanoparticles from Plant Extracts and Their Possible Applications as Antimicrobial Agents in the Agricultural Area.** *Nanomaterials,* 10(9), 1763. https://doi.org/10.3390/nano10091763

(15) Mondal P., Anweshan A., Purkait, M.K. (2020). **Green synthesis and environmental application of iron-based nanomaterials and nanocomposite: A review.** *Chemosphere,* 259, 127509. https://doi.org/10.1016/j.chemosphere.2020.127509

(16) Gupta A.K., Gupta M. (2015). **Synthesis and Surface Engi-neering of Iron Oxide Nanoparticles for Biomedical Applications.** *Biomaterials*. 26(18), 3995-4021. https://doi.org/10.1016/j.biomaterials.2004.10.012

(17) Capinera J.L.(2002). **Cabbage Looper, Trichoplusia ni (Hübner) (Insecta:Lepidoptera: Noctuidae). series of Featured Creatures from the Entomology and Nematology Department, Florida Cooperative Extension Service.** *Institute of Food and Agricultural Sciences, University of Florida,* 2002(7). https://doi.org/10.32473/edis-in273-1999

(18) Okonkwo C.C., Edoziunob F.O., Orakwea L.C. (2020). **Environmental Nano-remediation in Nigeria: A Review of its potentials.** *Algerian Journal of Engineering and Technology,* 1-15. https://doi.org/10.5281/zenodo.4091801

(19) Dang T.M.D., Le T.T.T., Fribourg-Blanc E. Dang M.C. (2011). **The Influence of Solvents and Surfactants on the Preparation of Copper Nanoparticles by a Chemical Reduction Method.** Advances in Natural Sciences: *Nanoscience and Nanotechnology, 2(*2), 025004. https://doi.org/10.1088/2043-6262/2/2/025004

(20) Din M.I., Arshad F., Hussain Z. Mukhtar M. (2017). **Green Adeptness in the Synthesis and Stabilization of Copper Nanoparticles: Catalytic, Antibacterial, Cytotoxicity, and Antioxidant Activities.** *Nanoscale Research Letters, 1*2, 638. https://doi.org/10.1186/s11671-017-2399-8

(21) Pereira T.M., Polez V.P., Sousa M.H.,Silva LP. (2020). **Modulating physical, chemical, and biological properties of silver nanoparticles obtained by green synthesis using different parts of the tree Handroanthus heptaphyllus (Vell.) Mattos.** *Colloid Interface Sci. Commun,* 34(100224). https://doi.org/10.1016/j.colcom.2019.100224

(22) S.A.S. (2010). **SAS/ STAT Users Guide for Personal Computers Release 9.1** *SAS. Institute Inc. Cary and N.C, USA.*

(23) Sharma P., Bhatt D., Zaidi M., Saradhi P., Khanna P. Arora S. (2012). **Silver nanoparticle mediated enhancement in growth and antioxidant status of Brassica juncea.** *Applied Biochemistry and Biotechnology,* 167(8), 2225-2233. https://doi.org/10.1007/s12010-012-9759-8

(24) Kerber N. (2008). **As simple As Possible, But Not Simpler- The Case of Dehydroascorbic acid.** *Journal of Chemisry Education*. 85, 1237-1242.

(25) Cheng X., Zhang H., Yin A., Wan XY. (2016). **Modifier effects on Chemical Reduction Synthesis of nanostructured Copper.** *Appllied Surface Sciene, 2*53(5), 2727-2725. https://doi.org/10.1016/j.apsusc.2006.05.125

(26) Kapoor R., Mukherjee T. (2002). **Influence of I-Anions on the Formation and Stabilization of Copper Nanoparticles.** *Chemical Physics Letters, 3*54, 443-448.

(27) Shende S., Ingle A.P., Gade A.Rai M. (2015). **Green synthesis of copper nanoparticles by Citrus medica Linn. (Idilimbu) juice and its antimicrobial activity.** *World J Microbiol Biotechnol,* 31, 865-873. https://doi.org/10.1007/s11274-015-1840-3

(28) Al-Hamdani H., Ahmed S.,| Hameed R., Getan A. (2021). **The Effect of Environmentally safe nanosynthesis with copper particles by using citrus aurantium fruit extract against harmful mosquitoes**. *Asian Journal of Water, Environment and Pollution,* 18(3), 59-67. https://doi.org/10.3233/AJW210029

(29) Pourmortazavi S.M., Taghdiri M., Makari V., Rahimi-Nasrabadi M. (2015). **Procedure optimization for green synthesis of silver nanoparticles by aqueous extract of Eucalyptus oleosa.** *Spectrochim. Acta Part A, 1*36, 1249-1254. https://doi.org/10.1016/j.saa.2014.10.010

(30) Khalida A.S., Aulfat T.Y. (2020). **Investigation of Toxicity of some Plant Extracts on Mosquito Larvae Culex pipiens molestus.** *Al-Rafidain Science Journal,* 29(1), 41-49. https://doi.org/10.33899/rjs.2020.164480

(31) Bazylinski D.A.,Frankel R.B., Konhauser K.O. (2007). **Modes of biomineralization of magnetite by microbes**. *Journal of Geomicrobiology,* 24(6), 465-475. https://doi.org/10.1080/01490450701572259

(32) Dhiraj S. Patil, Dattatray A. Chopade, Manoj A. Kumbhalkar. (2018). **Experimental investigation of effect of cerium oxide nanoparticles as a fuel additive in cottonseed biodiesel blends.** *MAYFEB Journal of Mechanical Engineering*, 1(2018), 1-12.

/14/

3C Tecnología. Glosas de innovación aplicadas a la pyme. ISSN: 2254-4143

Ed.43 | Iss.12 | N.1 January - March 2023

OPTIMIZATION OF SPECIFIC HEATING CONSUMPTION OF COKE OVEN PLANT USING FLOW METER CALIBRATION MODIFICATION

Niranjan Mahato

PhD research schlor, Department of Mechanical Engineering Government Engineering College, Jagdalpur, India (India).

niranjan123mahato@gmail.com - https://orcid.org/0000-0002-2849-8264

Himanshu Agarwal

Professor, Department of Mechanical Engineering, Government Engineering College, Jagdalpur, India

himanshu.jglr@gmail.com

Jainendra Jain

Professor, Department of Applied Mathematics, Government Engineering College, Jagdalpur, India

jj.28481@gmail.com

v

ABSTRACT

Coke oven plant produces coke which acts as a reducing agent in blast furnaces. So, coke is an important material which is also called as a reducing agent. Coke is basically used for manufacturing of steel materials and extraction of metals. In an integrated steel plant coke is a prime material for making high grade of steels. In this present research work, the calibration of flow meter is modified. By this modification of gas flow meter calibration coke oven gas flow reduced from 17100Nm3/hrs to 16900Nm3/hrs, such as 200 Nm3 on hourly basis saving without any extra manpower cost. The proposed method is also cost effective as it saves Rs 6483000 every month for producing coke. This methodology is also helpful for reducing the manufacturing cost of coke in a recovery type of coke plant and stable oven operation and prolongation of coke oven life. Future advancements in this technique will allow us to minimize the need for money, which will revolutionize the nation's economy.

KEYWORDS

Coke, Coke furnaces, heating chambers, heating flues, coke rate

PAPER INDEX

ABBREVIATION

Table 1. Technical type Abbreviation of coke plant.

Serial No.	Code	Full form
01	C.P.D	Coke making duration in hr.
02	N1	No. of ovens
03	N	No. of pushing target / charging target in a day
04	C.W.T	Cross chamber wall temperature
05	V	Gas Flow required in Nm^3/h
06	C.O.G	Coke oven gas
07	C.V	Calorific value of coke oven gas in $kcal/Nm^3$
08	Q	The Specific heat energy consumption in kcal/kg
09	T	Periods of Gas flow in hr
10	W.B.A.D	Weekly basis the average technical data
11	N.P.C.P.D	No. of pushing and charging in a day
12	S.H.C	Specific heating consumption of COG
13	A.S.H.C	Average of specific heating consumption in (kcal/kg)
14	H.W.F.N	Heating chamber wall flue No.
15	P.T	Pause heating time in sec.
16	T.H.W.N	Temperature of the chamber heating wall No.
17	W	dry basis charged coking coal in tones

1. INTRODUCTION

Coke is produced by the proper destructive distillation of coal in coke plant. Specially feeding coal blend comprising of the various different types of blended coals of desired coking parameters is heated in an oxygen-free atmosphere (coked) until the most volatile components in the coal are removed. The process is carried out in battery, which contains twenty or more tall, wide and narrow ovens arranged side by side. In [1] this paper during carbonization coal passes through a softening phase when the coal particles swell and become soft. This soft mass is termed as metaphase and said to be plastic in nature. During this transformational phase coal releases most of its hydrocarbons, heavy oils and tar; the coal particles coalesce and are bound together by the plastic mass. On further heating the plastic mass re-solidifies into a porous mass called semi-coke. On further heating the semi-coke contracts and becomes a structurally stable product which we know as metallurgical coke or simply coke. In [2] the main function of by product plant to purified the raw coke oven gas. The step by step procedure of purification is little complicated. Firstly coke oven gas goes to primary gas cooler then coke oven Gas enters into the electric type tar precipitator from its bottom, via the gas distribution plate gas is uniformly distributed onto the whole section, then flows through high voltage electric field of the

honeycomb upward to leave electric tar precipitator and enters into the exhauster unit. At the upper part of hydrogen sulfide scrubber, hydrogen sulfide in gas is absorbed with enriched ammonia water from ammonia scrubbing and lean solution from de-acidifier and ammonia stripping unit. At the same time of hydrogen sulfide removal in hydrogen sulfide scrubber, also carbon die oxide, hydrocarbons and ammonia are absorbed. Because the absorption process of hydrogen sulfide, CO2, hydrocarbons and ammonia is the process of exothermic reaction, therefore both upper stage and lower stage of hydrogen sulfide scrubber are provided with the coolers for hydrogen sulfide circulating scrubbing solution. In [3] the primary purpose of coke ovens is to transform coal into coke, which is utilized in the blast furnace as a fuel and reducing agent. The entire process of creating coke is fraught with safety risks, such as being hit by or tangled in moving machinery, getting burned, starting a fire or explosion, falling and slipping, being exposed to dust, noise, heat, and gas, etc. The majority of health risks associated with coke production is caused by emissions produced during coal charging, coal carbonization, coke pushing, and coke cooling. Poly nuclear aromatic hydrocarbons, which cause cancer, are present in coke oven emissions along with other hazardous materials. In [4] this article of research developed a new model for the reducing of variation in the burning of coal to coke during the coke making process and to gain the good quality and also to proper develop the energy in coke plant. The total length of the battery is hundred meters, consist of the rectangular type of shaped heating chambers of length sixteen meters, the height is seven meters, and the width 0.41 meters with removal door ends.[5]. In [6] this research paper describes gas pressure in the oven chambers should be positive and higher than pressure at any point of adjacent heating chamber during whole coking period. In [7] a new design of optimum control of temperature of gas coming out of the oven into the stand pipe is about 600-700 °C, and it leaves the hydraulic mains at the temperature of 80-85°C [8].In [9] in this system of ovens, paired vertical flues are envisaged which are interconnected with each other with a provision for recirculation of products of combustion. The heating chamber is divided into pairs of vertical flues. Vertical flues of each pair are connected at the top through a window in the partition wall [10]. In [11] coke oven gas can save 300-400 Nm3/hour by using reversal cycle modification in coke plant [12]. The gas and preheated air are fed to the base of the flues from where they move upwards under the influence of chimney draught.[13]the hot products of combustion cross over to the adjacent flues and pass on the regenerators where the checker-work absorbs most of the sensible heat contained in the product of combustion.[14]. In this paper, the cooled gases from the regenerator move to the waste heat flues and then to the chimney. These two currents of heat flow, i.e. the up-current and down-current are periodically reversed in every 20 minutes to maintain uniform and state temperature condition throughout the whole battery[15]. Readiness of coke at the end of coking period along the length, height and width of coke oven chamber by maintain uniform temperature throughout the length and height of heating wall all along the battery[16].The practical study was to determine in which of the several type alternative toxic air pollution abatement systems which affords the most economical solution to the control of at- morphemic emissions during the charging of coal into the by-product coke plant[17]BF Coke size

is an important factor for blast furnace of operation. The Some type of methodology has been investigated in order to rectify the coke mean size.[18]. this paper, various types of elementary of reaction which having the different steps important for coke formation during thermal-cracking of the hydro- carbons are to be studied[19]. The papers describes, by the petro-graphic specific technique and the semi type coking coals or the non coking of coals to be blended and with coking coals is used to produce BF coke.[20].

However, a there is a requirement to follow a study to reduce the specific heating consumption by rectification of flow meter calibration in coke oven plant oven. Generally in running coke oven plant calibration of flow meter in yearly or half yearly which includes accuracy of flow of coke oven gas is not correct.

The main objective of the present research work is, to reduce the SHC by rectification of flow meter calibration instead of yearly to monthly in own plant lab in coke oven plant. The modification of flow meter is also helpful to reduce the carbon emission which is eco-friendly to the environment.

2. METHODOLOGY OF RESEARCH

The carbon deposits on coke oven walls may not only interrupt the oven operation. But also cause damage to the oven walls, although many studies have been made on the properties of deposited carbons and the mechanism of their formation. There are few on the quantitative emission of carbon formation in an actual coke oven. For the purpose of stable oven operation and prolongation of oven life, it is necessary to remove carbon according to the amount of carbon deposited on coke oven walls. A flow meter is aspecial type of instrument which is used to measure the flow rate of a gas then display the flow-reading to the instrument user via an indicator, digital analogue or the digital type output. The Calibration of the flow meter can be achieved in one of several ways, but generally involves the comparison of the flow meter against a reference standard of higher accuracy. Calibration is an essential part of an instrumentation system to ensure a line of traceability of the measurement system is maintained. To understand the flow meter performance over a period of time, flow meter calibration should always be conducted on "as Found" on the practical basis so meter drift- analysis can be assessed. With the further customer agreement, a further adjustment of the flow meter reading maybe performed to optimize the flow- meter errors.

In this paper, it is introduced that a quantitative emission of carbon formation rate on the wall was developed and new type SOP for regular maintenance, to optimize the SHC by modification of flow meter calibration instead of yearly to monthly in own plant lab in coke oven plant. The modification of flow meter is also helpful to reduce the carbon emission which is eco-friendly to the environment. This method is also helpful for the reducing of coke oven gas flow.

2.1. SEVEN METER TALL BATTERY EXPERIMENTAL DESCRIPTION

The experimental set up for 7-meter-tall coke oven battery required some technical process and operation parameters which are shown in table1 which is given below. There are sixty seven number of heating oven, sixty eight number of heating wall and sixty nine numbers of waste heated boxes for transferring the waste gas tunnel to chimney. There are three number of charging hole for feeding the coking coal into the heating oven. Thirty-two tones of blended dried coal is charge per oven and output coke is around twenty five tones is produced. There are total thirty two number of heating flues out of thirty two sixteen numbers of heating flues in pusher side and sixteen numbers in coke side. The experimental brief description is given below in tabulation form in Table2.

Table 2. Technical parameters for experimental set up.

No. of oven	No. of heating walls	No. of waste heat boxes	Dry charged coal in tones	No. of heating flues in pusher side	No. of heating flues in coke side	No. of heating flues per wall	Output coke per oven	No. of charging hole per oven	Oven height in meter
67	68	69	32	16	16	32	25	03	7

2.2. CPD OF RECOVERY TYPE OF COKE PLANT

2.2 describe mathematical formula for time of coking period

$$CPD = \frac{N_1 \times 24}{N}$$

2.3. NO. OF CHARGING / PUSHING IN A DAY

2.3 describe the advance mathematical expression for determining the No. of production target like pushing and charging schedule.

$$N = \frac{N_1 \times 24}{CPD}$$

2.4. COKE OVEN GAS FLOW REQUIREMENT OF COKE OVEN GAS FLOW ACCORDING TO PUSHING AND CHARGING

2.4 comprise that mathematical equation for calculating the required flow of coke oven gas

$$V = \frac{Q*1000*N*W}{C.V \times T}$$

2.5. CALCULATION FORMULA OF SPECIFIC HEATING CONSUMPTION OF COKE OVEN GAS

2.5 describe the mathematical equation formula for evaluating specific heating gas

$$Q = \frac{V*CV*T}{W*1000*N}$$

This type mathematical expression for calculating in the table 3, table 4 and table 5 respectively.

It was observed that the accuracy of flow of coke oven gas is more on yearly or half yearly calibration of flow meter. Due to this, flow meter is allowing to pass extra gases for producing the combustion process without the recovery of the sensible heat. To establish the reasons for the low efficiency, the calibration method of gas flow meter have suggested. The modification of gas flow meter calibration on monthly basis with respect to pushing and the charging and the possible modification type solution is verified against the Standard Operating Practices and preventive and daily Schedule jobs of Regular Maintenance). Technical data like number of pushing/charging per day is 83 and pause time 20 second is used obtaining values express in table 3.

Table3. S.H.C before modification of flow meter calibration.

S/No.	W.B.A.D	A.S.H.C	N.P.C.P.D	P.T	C.P.D
1	1	670	83	20	19.37
2	2	670	83	20	19.37
3	3	670	83	25	19.37
4	4	670	83	25	19.37
5	5	670	83	20	19.37
6	6	670	83	20	19.37
7	7	670	83	15	18.37
8	8	670	83	15	19.37
9	9	670	83	20	19.37

Table3 describes before modification of gas flow meter calibration coking periods is around 19.37 hours, pause time average is around 20 second at constant production target is 83.The average COG flow required in average pushing/charging 83 is 17100 Nm3/hr at above pushing/charging schedule. The all data is taken as on weekly basis which is mentioned in table 3.

3.   RESULTS WITH FULL DISCUSSION

3.1. MODIFICATION OF GAS FLOW METER CALIBRATION IN RESPECT OF PUSHING/CHARGING

It was observed that the accuracy of flow of coke oven gas is more on yearly or half yearly calibration of flow meter. Due to this, flow meter is allowing to pass extra gases for producing the combustion process without the recovery of the sensible heat. To establish the reasons for the low efficiency, the calibration method of gas flow meter has suggested. The modification of gas flow meter calibration on monthly basis with respect to pushing/charging and the possible rectification solution is verified against the Standard Operating Practices and Schedule jobs of Regular Maintenance). Due to additional gas consumption in coke plant at same pushing charging schedule of 83, the coke oven gas flow is reduced 200 Nm3/hr without affecting the coke quality.

Table 4. S.H.C after modification of flow meter calibration.

S/No.	W.B.A.D	A.S.H.C	N.P.C.P.D	P.T	C.P.D
01	1	660	83	20	19.37
02	2	660	83	20	19.37
03	3	660	83	25	19.37
04	4	660	83	25	19.37
05	5	660	83	20	19.37
06	6	660	83	20	19.37
07	7	660	83	15	18.37
08	8	660	83	15	19.37
09	9	660	83	20	19.37

Table4 describes after modification of gas flow meter calibration coking periods is around 19.37 hours, pause time average is around 20 second at constant production target is 83. The average on the before modification COG flow rate requirement in average pushing and charging 83 is 17100 Nm3/hr as per above pushing and charging target. The all data is taken as on weekly basis which is mentioned in table 3. After the medication of gas flow meter calibration, The average COG flow rate requirement in 83 numbers pushing and charging is 16900 Nm3/hr as per above pushing and charging schedule, which is given in the table 4.Afterthe modification of the COG flow meter calibration, to the thermal regime of coke oven plant at randomly at a time, the temperature of cross wall is taken at 05 numbers of heating walls. The temperature of Cross wall is the all heating wall of the flue (means of the all the 32 no. of heating flues) temperature recorded reading. The temperature of cross-wall data of reading is express in table 4, 16, 17, 18, 19, and 20, respectively.

Table 5. CWT average cross wall reading in a day basis.

HWFN	T.H.W.N (16)	T.H.W.N (17)	T.H.W.N (18)	T.H.W.N (19)	T.H.W.N (20)
01	1170°c	1170°c	1180°c	1180°c	1170°c
02	1170°c	1180°c	1180°c	1180°c	1180°c
03	1180°c	1190°c	1180°c	1190°c	1180°c
04	1190°c	1190°c	1190°c	1200°c	1190°c
05	1210°c	1200°c	1200°c	1200°c	1200°c
06	1210°c	1210°c	1210°c	1210°c	1210°c
07	1220°c	1220°c	1220°c	1220°c	1220°c
08	1230°c	1230°c	1230°c	1230°c	1230°c
09	1220°c	1220°c	1220°c	1220°c	1220°c
10	1220°c	1220°c	1220°c	1220°c	1220°c
11	1230°c	1220°c	1230°c	1220°c	1230°c
12	1220°c	1230°c	1220°c	1220°c	1230°c
13	1230°c	1230°c	1230°c	1230°c	1230°c
14	1230°c	1230°c	1230°c	1230°c	1230°c
15	1230°c	1230°c	1230°c	1230°c	1240°c
16	1220°c	1220°c	1220°c	1220°c	1220°c
17	1220°c	1220°c	1220°c	1220°c	1220°c
18	1220°c	1220°c	1220°c	1220°c	1220°c
19	1240°c	1240°c	1240°c	1240°c	1240°c
20	1250°c	1250°c	1240°c	1250°c	1250°c
21	1240°c	1240°c	1240°c	1230°c	1240°c
22	1250°c	1250°c	1250°c	1250°c	1250°c
23	1240°c	1240°c	1240°c	1240°c	1240°c
24	1250°c	1250°c	1250°c	1250°c	1240°c
25	1250°c	1250°c	1240°c	1240°c	1250°c
26	1240°c	1240°c	1240°c	1230°c	1230°c
27	1230°c	1230°c	1230°c	1220°c	1220°c
28	1220°c	1220°c	1220°c	1200°c	1210°c
29	1210°c	1210°c	1200°c	1210°c	1210°c
30	1200°c	1200°c	1190°c	1200°c	1200°c
31	1190°c	1190°c	1190°c	1190°c	1190°c
32	1180°c	1180°c	1180°c	1190°c	1180°c

The table number 05 describes that the temperature cross wall average data of reading is taken in shift wise such as A, B and C shifts respectively. This represents, after the modification of COG flow, the thermal section of the coke plant is not more affected. The temperature of cross wall is taken in different schedule of shifts like A, B

and C, in different of timing. Comparing the table3 and the table4, it is observed that after modification of the coke oven gas flow meter calibration, 200 Nm3/hr coke oven gas flow is saved. This is beneficial in terms of expenditure.

Figure 1 to 5 shows that the cross-wall temps taken at the different times and different of shifts do not affect the temp of flues. The randomly taken 5 No. ofwall, the cross wall temp is almost same in nature.

Figure 1. Variation of temperature for heating wall/flue number.

Figure1 comprises that the heating wall no. sixteen in x axis flue number and y axis temperature reading is taken. flue number 01 temperature is 1170 °c, flue number 02 temperature is 1170 °c, flue number 03 temperature is 1180 °c, flue number 04temperature is 1190 °c, flue number 05 temperature is 1210 °c, these temperature reading shows that temperature is slowly increases with respect to flue wise, the maximum temperature reading is taken in flue no.20 is 1250 °c. The last five numbers of flues temperature reading such as flue number 28 is 1220 °c, flue number 29 is 1210 °c, flue number 30 is 1200 °c, flue number 31 is 1190 °c, flue number 32 is 1180 °c.

Figure 2. Variation of temperature for heating wall/flue number.

Figure2 comprises that the heating wall no. seventeen, in x axis flue number and y axis temperature reading is taken. flue number 01 temperature is 1170 °c, flue number 02 temperature is 1180 °c, flue number 03 temperature is 1190 °c, flue number 04temperature is 1190 °c, flue number 05 temperature is 1200 °c, these temperature reading shows that temperature is slowly increases with respect to flue wise, the maximum temperature reading is taken in flue no.20 is 1250 °c. The last five numbers of flues temperature reading such as flue number 28 is 1220 °c, flue number 29 is 1210 °c, flue number 30 is 1200 °c, flue number 31 is 1190 °c, flue number 32 is 1180 °c.
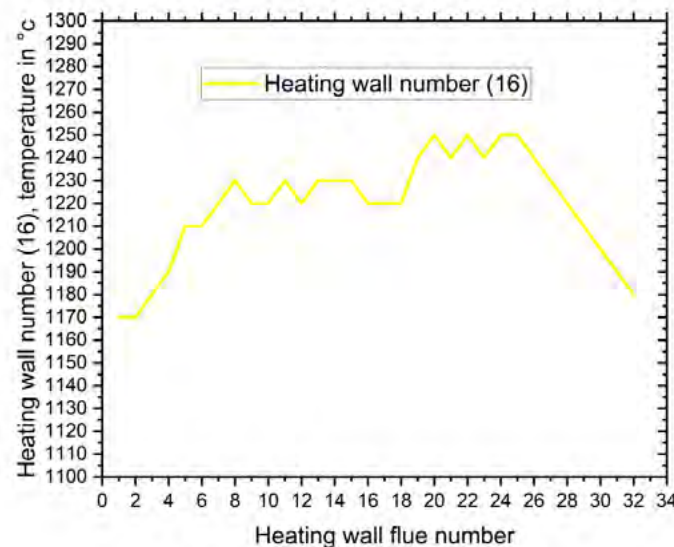

Figure 3. Variation of temperature for heating wall/flue number.

Figure3 comprises that the heating wall no. eighteen, in x axis flue number and y axis temperature reading is taken. flue number 01 temperature is 1180 °c, flue number

02 temperature is 1180 °c, flue number 03 temperature is 1180 °c, flue number 04temperature is 1190 °c, flue number 05 temperature is 1200 °c, these temperature reading shows that temperature is slowly increases with respect to flue wise, the maximum temperature reading is taken in flue no.22 is 1250 °c. The last five numbers of flues temperature reading such as flue number 28 is 1220 °c, flue number 29 is 1200 °c, flue number 30 is 1190 °c, flue number 31 is 1190 °c, flue number 32 is 1180 °c.
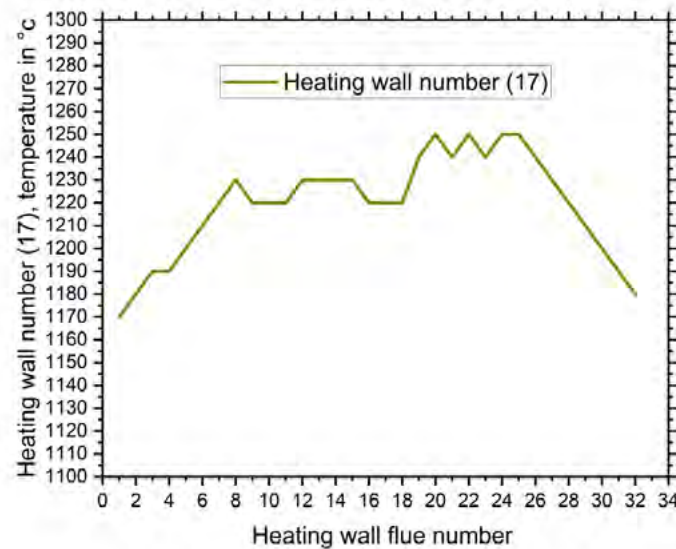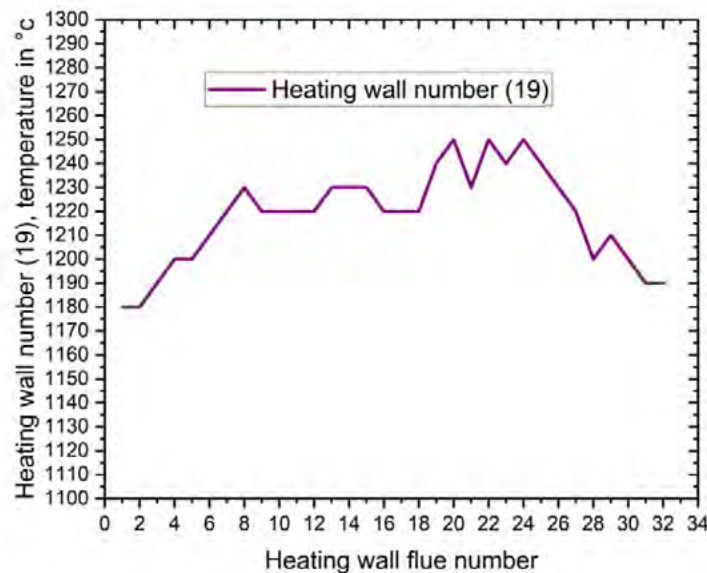

Figure 4. Variation of temperature for heating wall/flue number.

Figure4 comprises that the heating wall no. nineteen, in x axis flue number and y axis temperature reading is taken. flue number 01 temperature is 1180 °c, flue number 02 temperature is 1180 °c, flue number 03 temperature is 1190 °c, flue number 04temperature is 1200 °c, flue number 05 temperature is 1200 °c, these temperature reading shows that temperature is slowly increases with respect to flue wise, the maximum temperature reading is taken in flue no.20 is 1250 °c. The last five numbers of flues temperature reading such as flue number 28 is 1220 °c, flue number 29 is 1210 °c, flue number 30 is 1200 °c, flue number 31 is 1190 °c, flue number 32 is 1190 °c.
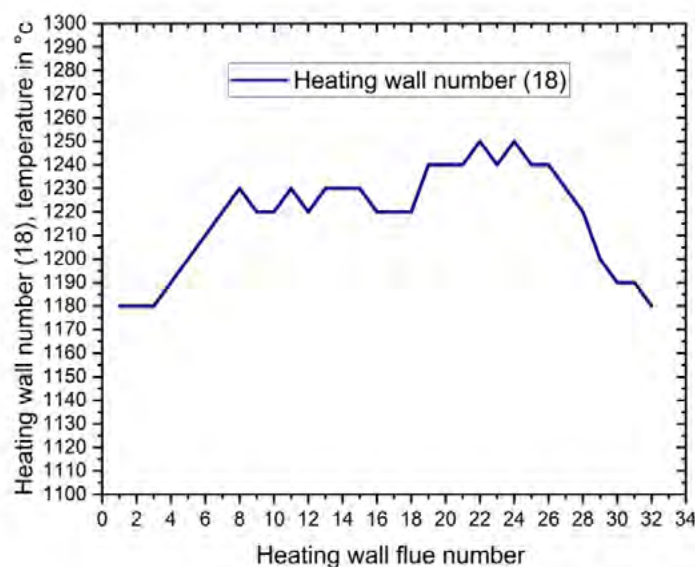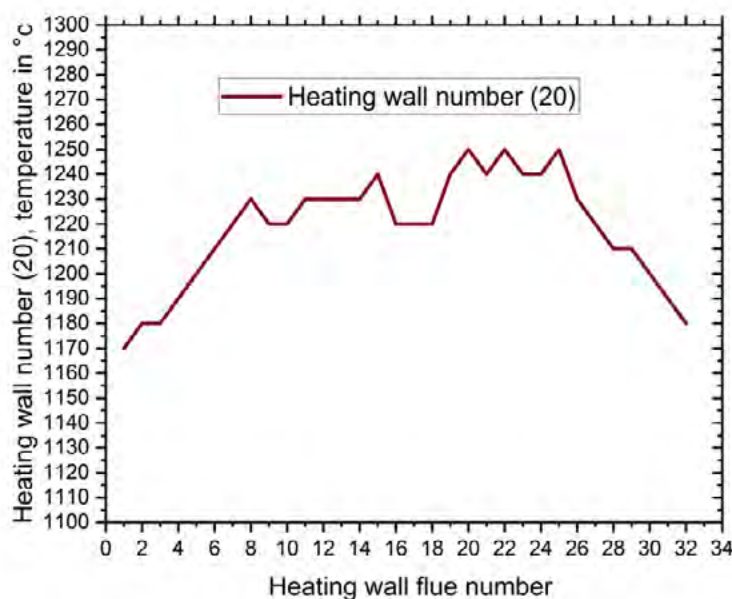
Figure 5. Variation of temperature for heating wall/flue number.

Figure5 comprises that the heating wall no. twenty, in x axis flue number and y axis temperature reading is taken. flue number 01 temperature is 1170 °c, flue number 02 temperature is 1180 °c, flue number 03 temperature is 1180 °c, flue number 04temperature is 1190 °c, flue number 05 temperature is 1200 °c, these temperature reading shows that temperature is slowly increases with respect to flue wise, the maximum temperature reading is taken in flue no.20 is 1250 °c. The last five numbers of flues temperature reading such as flue number 28 is 1210 °c, flue number 29 is 1210 °c, flue number 30 is 1200 °c, flue number 31 is 1190 °c, flue number 32 is 1180 °c.

Table 6. -Comparison analysis of hot strength of coke.

Serial no.	Weekly basis average data	Before modification CSR value	After modification CSR value	Before modification CRI value	After modification CSI value	Before modification gas flow (Nm³/hr)	Before modification gas flow (Nm³/hr)
01	First week	63	63	23	23	17100	16900
02	Second week	63	63	23	23	17100	16900
03	Third week	63	63	23	23	17100	16900
04	4thweek	63	63	23	23	17100	16900
05	5thweek	63	63	23	23	17100	16900
06	6th week	63	63	23	23	17100	16900
07	7th week	63	63	23	23	17100	16900
08	8th week	63	63	23	23	17100	16900
09	9th week	63	63	23	23	17100	16900

Table 6 describes that the hot strength of coke quality, the lab report is taken on daily basis then after it is taken the average value of weekly basis. The lab report is same as on the modification of gas flow meter. Before modification coke strength after reaction(CSR) value is 63 and after modification coke strength after reaction (CSR) value is almost same as 63. Before modification coke reactive index (CRI) value is 23 and after modification coke reactive index (CRI) value is almost same as 23.by the modification of gas flow meter calibration, coke oven gas is saved up to 200 Nm3 onhourly basis.

Figure 6. comparative analysis of CSR and CRI Value before and after modification.

Figure 6 describes that the comparative analysis of hot strength of coke quality like CSR and CRI, the lab report is taken on daily basis then after it is taken the average value of weekly basis. The lab report is same as on the modification of gas flow meter. Before modification coke strength after reaction (CSR) value is 63 and after modification coke strength after reaction (CSR) value is almost same as 63. Before modification coke reactive index (CRI) value is 23 and after modification coke reactive index (CRI) value is almost same as 23.by the modification of gas flow meter calibration, coke oven gas is saved up to 200 Nm3 onhourly basis. The saving of coke oven gas which is shown in figure 7.
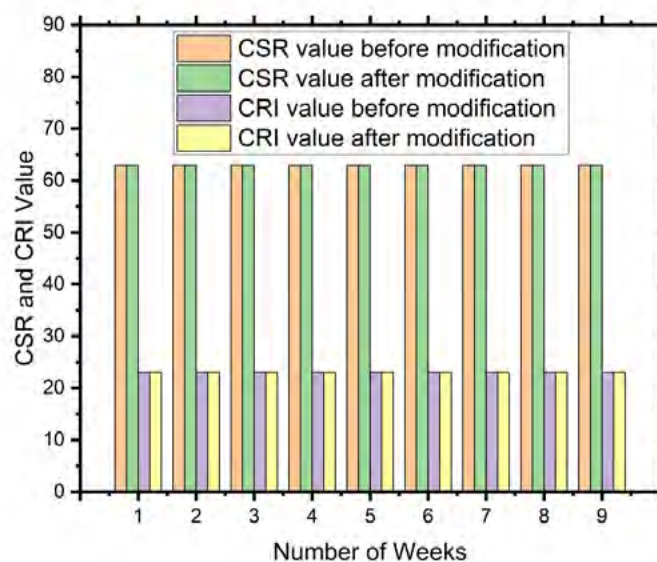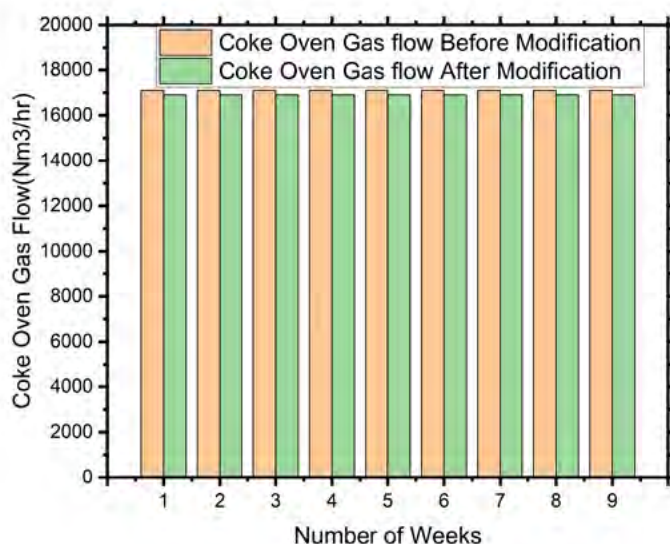
Figure 7. comparative analysis of coke oven gas flow before and after modification

Figure 7 comprises that the comparative analysis of coke oven gas flow before and after modification of gas flow meter. Firstly requirement of coke oven gas flow is about 17100 Nm3/hrs then after rectification gas flow requirement is about 16900 Nm3/hrs. This shows that 200 Nm3/hrs coke oven gas is saving in hourly basis. On the saving of coke oven gas by the modification of gas flow meter calibration the coke quality is not change, quality of coke like CSR and CRI value remains constant.

Table 7. -Comparison analysis tabulation of SHC.

Sr. No.	A.S.H.C (kcal/kg) before rectification	A.S.H.C (kcal/kg) After the rectification	Saving of COG (Nm^3/hr)	COG saving on monthly basis(Nm^3)	Monthly Saving of the COG @ 4.5 rupees/Nm^3
01	670	660	200	144000	648000

Table 7 shows that before and after modification of gas flow meter calibration SHC value reduced from 670 to 660in kcal/kg. The modified COG flow (with the respect of pushing and charging), the average saving in COG is 200 Nm3/hour. This will reduce the production cost of coke.
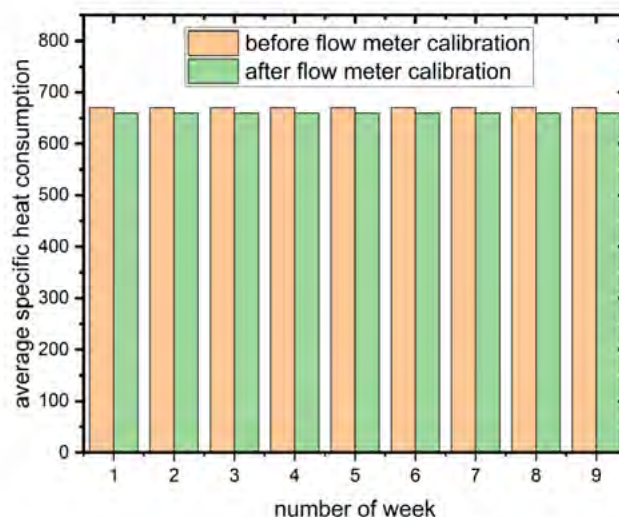
Figure 8. comparative analysis between before and after calibration of flow meter

Figure 8 comprises that the experimental value of specific heat consumption with respect to number of weeks. Specific heat consumption is directly proportional to the gas flow requirement. Firstly requirement of coke oven gas flow is about 17100 Nm3/hrs then after rectification gas flow requirement is about 16900 Nm3/hrs. This shows that 200 Nm3/hrs coke oven gas is saving in hourly basis. After the rectification of smoke pushing specific heat consumption value is reduces from 670kcal/kg to 660kcal/kg which is given in table 6.

4. CONCLUSION

By this modification of gas flow meter calibration coke oven gas flow reduced from 17100Nm3/hrs to 16900Nm3/hrs, such as 200 Nm3 on hourly basis saving without any extra manpower cost. The proposed method is also cost effective as it saves Rs 6483000 every month for producing coke. This methodology is also helpful for reducing the manufacturing cost of coke in a recovery type of coke plant and stable oven operation and prolongation of coke oven life. Future advancements in this technique will allow us to minimize the need for money, which will revolutionize the nation's economy.

ACKNOWLEDGEMENT

REFERENCES

(1)   Bénard C, Berekdar S, Duhamel C, Rosset M-M. (1989). **Input-Output Nonlinear Model of a Coke Oven Battery**. *IFAC Proc,* 22(2), 95-99. https://doi.org/10.1016/b978-0-08-037869-5.50020-0

(2)   Bénard C, Berekdar S, Rosset M-M, Depoux M. (1989). **A Coke Oven Battery Modelization for Transient Operating Conditions**. *IFAC Proc Vol,* 22(4), 451-457. https://doi.org/10.1016/s1474-6670(17)53587-9

(3)   Suzuki G, Mizuno M, Higuchi M, Matsushita T. (1978). **Development of an Automatic Computer Control System for Coke Oven Operation**. *Trans Iron Steel Inst Jp, 18(5)*, 308-316. https://doi.org/10.2355/isijinternational1966.18.308

(4)   Pang S, Lai Y. (2011). **Hybrid intelligent control of coke oven**. *Int Rev Comput Softw,* 6, 1313-9.

(5)   Buczynski R, Weber R, Kim R, Schwöppe P. (2016). **One-dimensional model of heat-recovery, non-recovery coke ovens: Part IV: Numerical simulations of the industrial plant**. *Fuel,* 181(1), 1151-1161. https://doi.org/10.1016/j.fuel.2016.05.033

(6)   Buczynski R, Weber R, Kim R, Schwöppe P. (2016). **One-dimensional model of heat-recovery, non-recovery coke ovens. Part III: Upper-oven, down-comers and sole-flues**. *Fuel,* 181(1), 1132-1150. https://doi.org/10.1016/j.fuel.2016.01.087

(7)   Kostúr K. (2002). **Control system of coking plant. Metalurgija**, *Fuel and Energy abstracts,* 44(2), 93. https://doi.org/10.1016/s0140-6701(03)90704-1

(8)   Razzaq R, Li C, Zhang S. (2013). **Coke oven gas: Availability, properties, purification, and utilization in China**. *Fuel,* 113, 287-299. https://doi.org/10.1016/j.fuel.2013.05.070

(9)   Kertcher LF, Linsky B. (1974). **Economics of Coke Oven Charging Controls**. *J Air Pollut Control Assoc,* 24(8), 765-771. https://doi.org/10.1080/00022470.1974.10469967

(10)   Smolka J, Slupik L, Fic A, Nowak AJ, Kosyrczyk L. (2016). **CFD analysis of the thermal behaviour of heating walls in a coke oven battery**. *Int J Therm Sci,* 104,186-193. https://doi.org/10.1016/j.ijthermalsci.2016.01.010

(11)   Poraj J, Gamrat S, Bodys J, Smolka J, Adamczyk W. (2016). **Numerical study of air staging in a coke oven heating system**. *Clean Technol Environ Policy,* 18, 1815-1825. https://doi.org/10.1007/s10098-016-1234-8

(12)   Nyathi MS, Kruse R, Mastalerz M, Bish DL. (2016). **Nature and origin of coke quality variation in heat-recovery coke making technology**. *Fuel,* 176, 11-19. https://doi.org/10.1016/j.fuel.2016.02.050

(13)   Tiwari HP, Banerjee PK, Saxena VK, Sharma R, Haldar SK, Paul S. (2014). **Effect of heating rate on coke quality and productivity in nonrecovery coke making**. *Int J Coal Prep Util,* 34(6), 306-320. https://doi.org/10.1080/19392699.2014.896349

(14)   Díez MA, Alvarez R, Barriocanal C. (2002). **Coal for metallurgical coke production: Predictions of coke quality and future requirements for cokemaking**. *Int J Coal Geol,* 50(1-4), 389-412. https://doi.org/10.1016/S0166-5162(02)00123-4

(15) Mahato N, Agarwal H, Jain J. (2021). **Reduction of specific heat consumption by modification of reversal cycle period of coke oven battery**. *Mater Today Proc, 6(3), 1149-1153*. https://doi.org/10.1016/j.matpr.2021.12.032

(16) Yang K, Gu Z, Long Y, Lin S, Lu C, Zhu X, et al. (2021). **Hydrogen production via chemical looping reforming of coke oven gas**. *Green Energy Environ, 6(5), 678-692*. https://doi.org/10.1016/j.gee.2020.06.027

(17) Kertcher LF, Linsky B. (1974). **Economics of Coke Oven Charging Controls**. *J Air Pollut Control Assoc,* 24(8), 765-771. https://doi.org/10.1080/00022470.1974.10469967

(18) Nag D, Das B, Banerjee PK, Haldar SK, Saxena VK. (2013). **Methodology to improve the mean size of coke for stamp charge battery**. *Int J Coal Prep Util,* 33(3), 128-136. https://doi.org/10.1080/19392699.2013.769436

(19) Van Speybroeck V, Hemelsoet K, Minner B, Marin GB, Waroquier M. (2007). **The technical achievement which deserves specialmention is the optimization of combustion.** *Mol Simu,* 33(9-10), 879-887. https://doi.org/10.1080/08927020701308315

(20) Sutcu H, Toroglu I, Piskin S. (2009). **Prediction of metallurgical coke strength from the petrographic composition of coal blends**. *Energy Sources, Part A Recover Util Environ Eff,* 31(12), 1047-1055. https://doi.org/10.1080/15567030801909730

/15/

MICRO-ARC OXIDATION ENHANCES MECHANICAL PROPERTIES AND CORROSION RESISTANCE OF TI-6AL-7NB ALLOY

Qabas Khalid Naji

Biomedical Engineering Department, AL-Mustaqbal University Collage, Babil, Iraq.

qabas.khalid@mustaqbal-college.edu.iq

Jassim Mohammed Salman

Department of Metallurgical Engineering, College of Materials Engineering, University of Babylon, Iraq.

mat.jassim.mohammed@uobabylon.edu.iq

Nawal Mohammed Dawood

Department of Metallurgical Engineering, College of Materials Engineering, University of Babylon, Iraq.

nawalmohammed2018@gmail.com

ABSTRACT

Investigation results of micro-arc coating on the (Ti-7Nb-6Al) alloy were presented. It has potential clinical value in applications such as dental implant, knee, and hip prostheses. An electrolyte solution of (Na_2CO_3 + Na_2SiO_3). The micro-arc oxidation (MAO) technique was employed for in situ oxidation of Ti-6Al-7Nb surface. The wettability of a porous TiO_2 covering made up of anatase and rutile phases was investigated. The test findings revealed that the possibility of deposition of ceramics coatings on the surface of Ti-6Al-7Nb alloy by using voltages (400V)at different deposition times (7, 15, and 30) min. The results indicate that ceramics layer of titanium oxide (TiO_2) which is formed during coating porous and homogenous distribution. The bioactive composition of the oxide layers can be suitable for use as advanced biomedical implants. The coatings also revealed an increased surface roughness, porosity, microhardness, surface wettability and corrosion resistance of the Ti-6Al-7Nb substrate reaches to (C_R= 0.1114×10^{-3}mpy) in Ringer's solution and (CR= 1.03×10^{-3}mpy) in Saliva's solution with increased deposition time.

KEYWORDS

MAO; Contact Angle; Clinical Application; Oxidation Time; porosity; and Corrosion Resistance

PAPER INDEX

1. INTRODUCTION

Metallic are the most important technical materials, and because of their great heat conductivity and mechanical properties, they are used as biomaterials [1]. The most important characteristic of a metal as a biomaterial is that it does not cause an adverse reaction when used in service, which is known as biocompatibility [2]. For load-bearing implants and inner fixing systems, metallic materials are the most frequently used. The primary functions of orthopedic implants systems are to restore the load-bearing joints function that undergo to elevate levels of mechanical stress, wear, and fatigue during ordinary activity [3]. Important orthopedic implants are prostheses for ankle, knee, hip, shoulder, elbow joints and also need equipment like cables, screws, plates, pins, etc. that used in the fixation of fracture [4]. Metals are powerful, and most of them are capable to be formed into complicated forms. During or after final formation, the required mechanical characteristics of metals can be accomplished by heat and mechanical processing. In addition, the correct treatment of components produced from chosen metal compositions can achieve a degree of corrosion and wear resistance. The high tensile strength, high yield strength, fatigue resistance and corrosion resistance are some of the features of metallic materials [5]. In medicine, titanium and its alloys have specific advantages over steels, such as low weight, high corrosion resistance, and a wide range of applications,, low density, low thermal conductivity, non-magnetism, processing workability, and other properties that make it a highly appealing material [6]. Because the modulus of elasticity of titanium and its alloys is closer to that of bone than that of stainless steels and cobalt-based alloys, stress shielding is less of a problem [7]. Because of a TiO2 solid oxide layer, Ti alloys are one of the most common choices in biomedical applications due to their main characteristics. On the other hand, have poor tribological characteristics due to their low resistance to plastic shearing, low work hardening, and lack of surface oxide protection [2]. This titanium surface oxide layer, which is generally a few nanometres thick, has high passivity and resistance to chemical attack [8]. Due to the coarse microstructure of cast alloys (as seen by a high coefficient of friction), weak shear strength, low fatigue strength, and restricted elongation compared to wrought alloys, titanium and its alloys have a high price tag as well as a significant sensitivity to friction and wear. As a result, extra microstructural modification is often required to improve mechanical qualities while maintaining the product's form [9]. The surface of biomedical implants is frequently modified to increase corrosion resistance, wear resistance, surface roughness, and biocompatibility [10]. In addition to increasing other desirable features, all revised surfaces should be evaluated for corrosion behavior. In order to get implants that can survive in the human system for longer periods of time, a thorough understanding of the interactions that occur at the atomic level between the surface of the implant, the host, and the biological environment, as well as all types of micromotions of the implants retained inside the human system, should be researched further [11]. The material surface has a significant impact on the biological environment's response to artificial medical devices [12]. Surface modification does more than simply change the appearance of the surface; it also enhances adhesion properties, micro cleaning, functionalization of amine, and biocompatibility [13]. Many types of surfaces may be created using the surface

modification approach to control correct biological response in a specific cell/tissue scenario, with the goal of reducing healing time and limiting harmful reactions [14]. Because titanium and its alloys have poor tribological qualities, such as low wear resistance, they aren't recommended for use in vehicles, the implant's service life is shortened. Surface coatings can help to solve this problem to a considerable extent. Surface engineering can significantly improve the performance of titanium orthopedic devices, allowing them to outperform their inherent capabilities [15]. examples of surface modification processes: physical and chemical method, laser cladding, thermal oxidation, plasma spray, and ion implantation [16].

2. MATERIALS AND METHODS

In the test, Ti-6Al-7Nb alloy with element composition of 6.3Al, 67Nb, 0.47Ta, 0.23Fe, 0.18O, 0.077C, 0.046N,0.0088H, and the balance Ti (wt%) were used as raw materials. The substrate was sliced into 13 mm x 3 mm round wafers and polished using SiC abrasive sheets ranging from 150 to 5000 grit. After that, ultrasonic cleaning with acetone, alcohol, and deionized water was performed. The ceramic coatings were deposited using a DC-AC homemade MAO deposition device with a voltage of (0-500) V and a current of (0-5) A MAO with an impulse frequency of 500 Hz, current density of 20 A/cm2, duty cycle of 10%, and oxidation durations of 7 minutes, 15 minutes, and 30 minutes at voltage 400V. Deionized water and 10 g/L sodium carbonite and 2 g/L sodium silicate were used to make the electrolyte solution. Following the ultrasonic processing of the MAO test sample, the sample was dried and set aside.

3. RESULTS AND DISCUSSION

3.1. CHARACTERIZATION OF OXIDE SURFACE

In Fig.1 (a) The XRD results proved the deposition of titanium oxide layer after MAO on the surface of the Ti-6Al-7Nb alloy substrate at 7min. The formation of TiO_2 layer on the surface of specimen A3 has crystalline phases: rutile (tetragonal) and anatase (tetragonal) phases also the (α-HCP) and (β-BCC) return to the Ti-alloy. The peaks of rutile TiO_2 (200), (211), and (202) at 2Θ° (39.3, 54.2, and 76.0) and those of titania crystals structures (anatase) (101), (103), and (200) at 2Θ° (25.9, 37.9, and 48.3) strength of the Ti-6Al-7Nb alloy peaks reduced compared to the untreated Ti sample. This is due to the crystal structure of both types, the energy gaps for anatase are more than those of rutile, this makes the anatase more pores and it's used in optical application while the rutile is with low energy gape and more stable at high temperatures and more important for medical application [17]. Limiting voltage increased, perhaps due to oxide layer formation as illustrated in Fig.1 (b) at 15min. For the highest deposition time in Fig.1 (c). the presence of anatase indicates that throughout the MAO process, a significant oxidation reaction took place on a titanium surface. As a result, the combination of anatase and rutile crystal phases in the coated

Ti-alloys specimen developed in this work is expected to have a positive influence on Ti-alloy bioactivity by enhancing their osteogenic properties. It is also suggests that predominantly anatase is created at lower forming voltages, however because anatase, as a metastable phase, gradually converts into rutile at higher temperatures as dielectric breakdown processes increase, the mixture of anatase and rutile phases develops at increased deposition time [18].

(a)

(b)
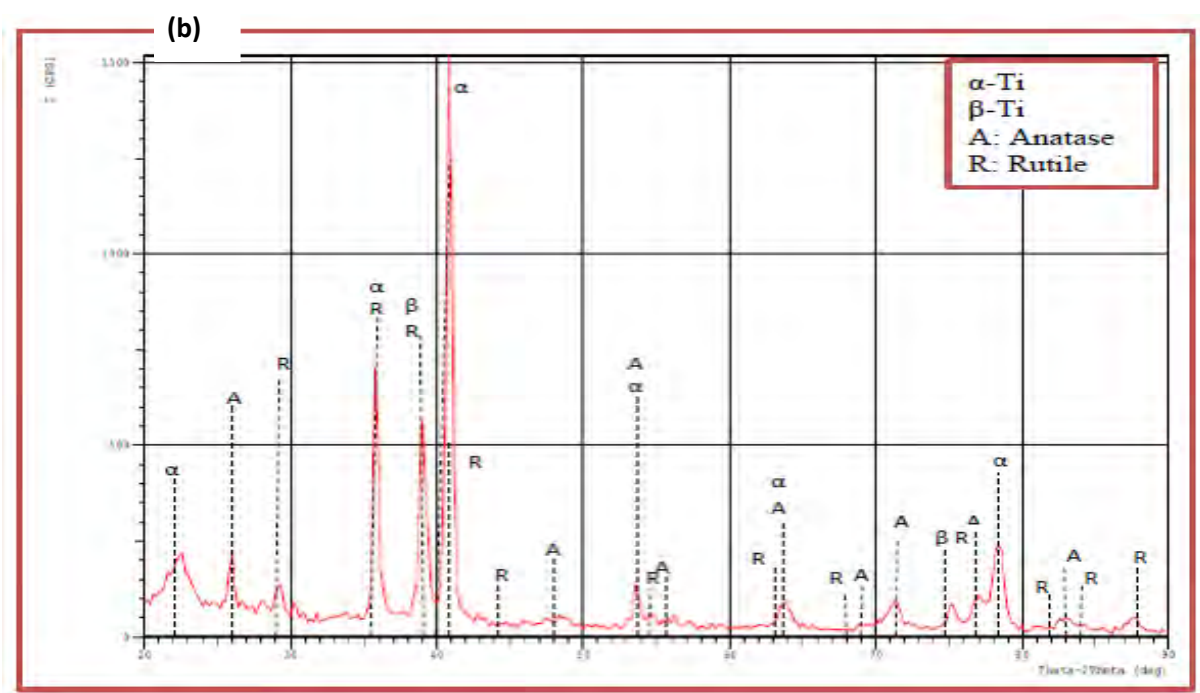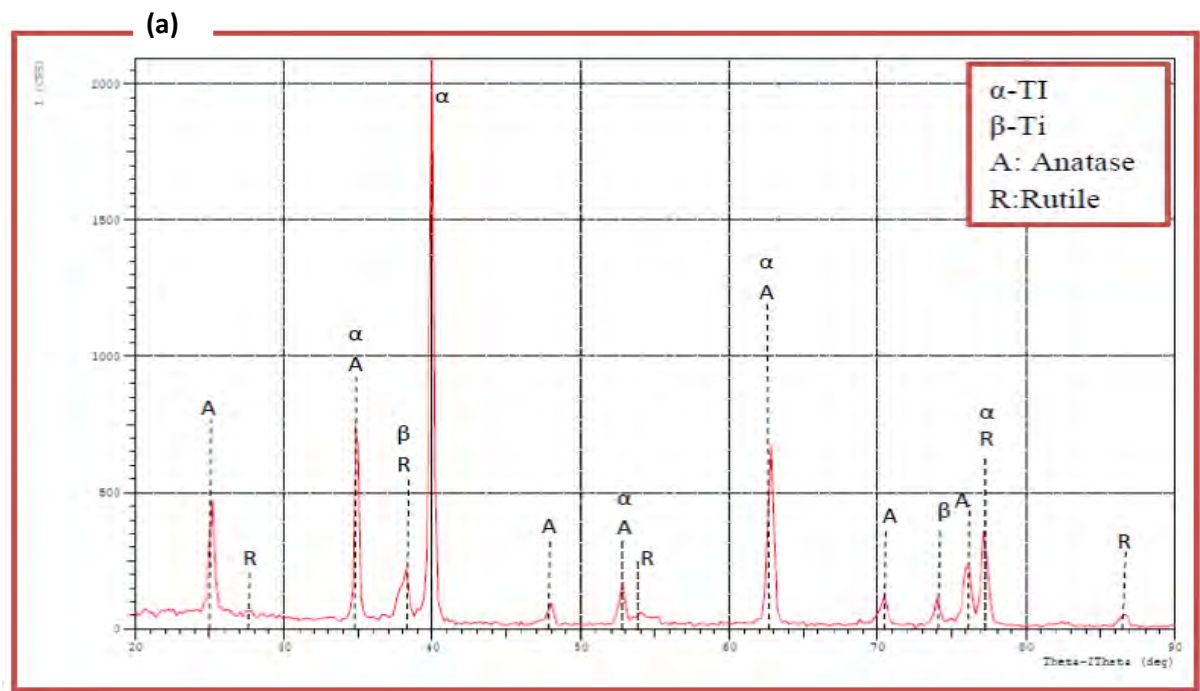
(c)
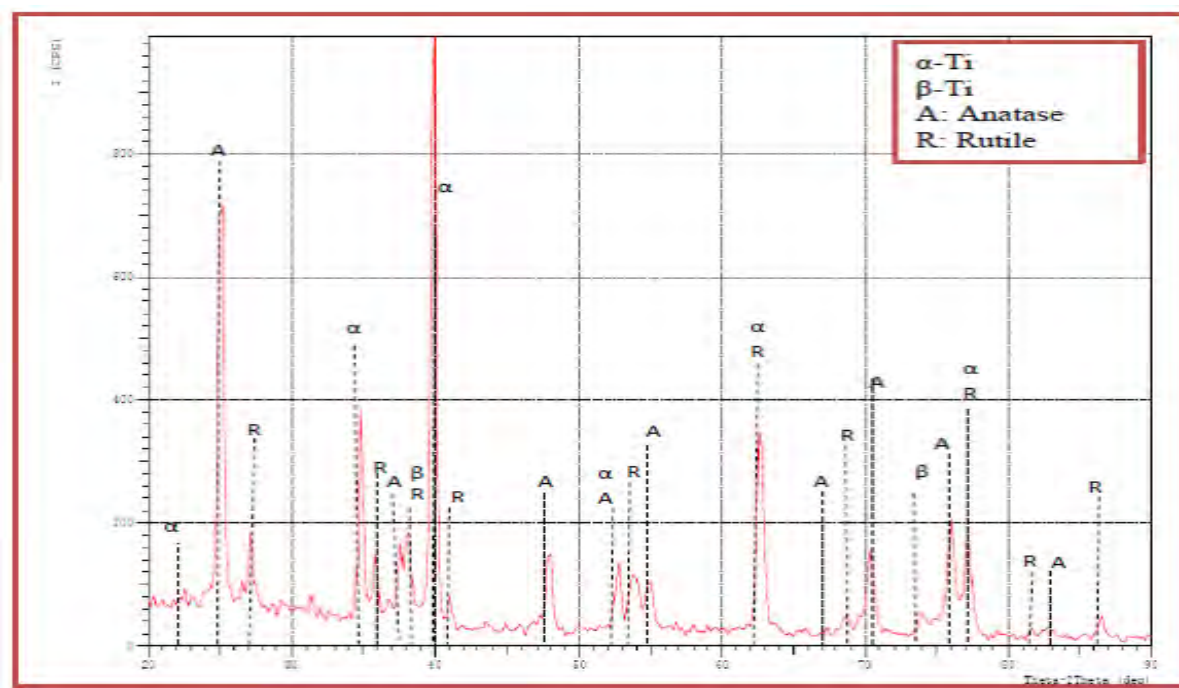
Figure 1. XRD of MAO Process with different time (a) coating at 7min, (c) coating at 15min, and (d) coating at 30min.

The FESEM results of microstructure coated specimen from Fig.2 which show that for surface morphology of the oxide layer TiO2 to the Ti-6Al-7Nb alloys at different magnifications treated by MAO process relatively rougher and exhibited a grainy structure with limited amount of pores with different sizes by the spark discharges. Micro-pores and submicron-pores were visible in the MAO coating, with the micro-pores having a roughly round or elliptical form like a volcanic vent [19].
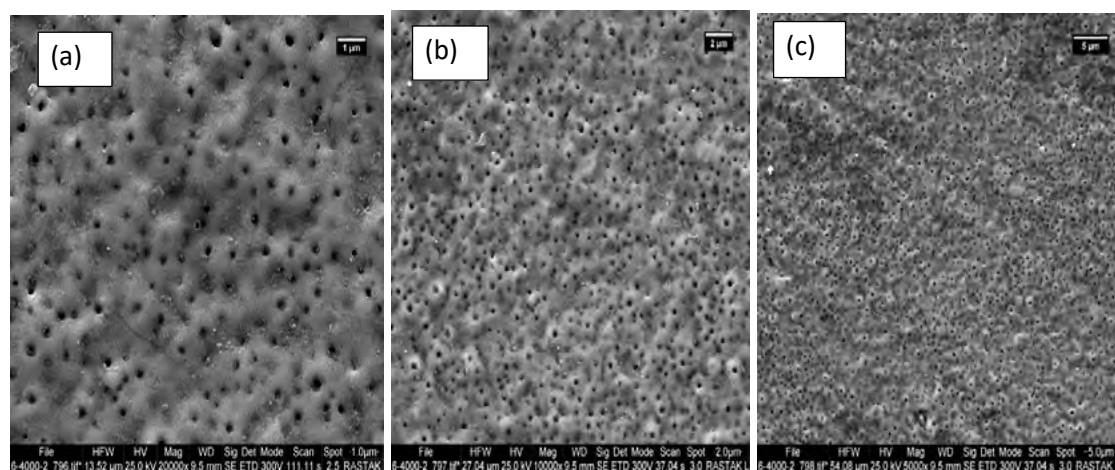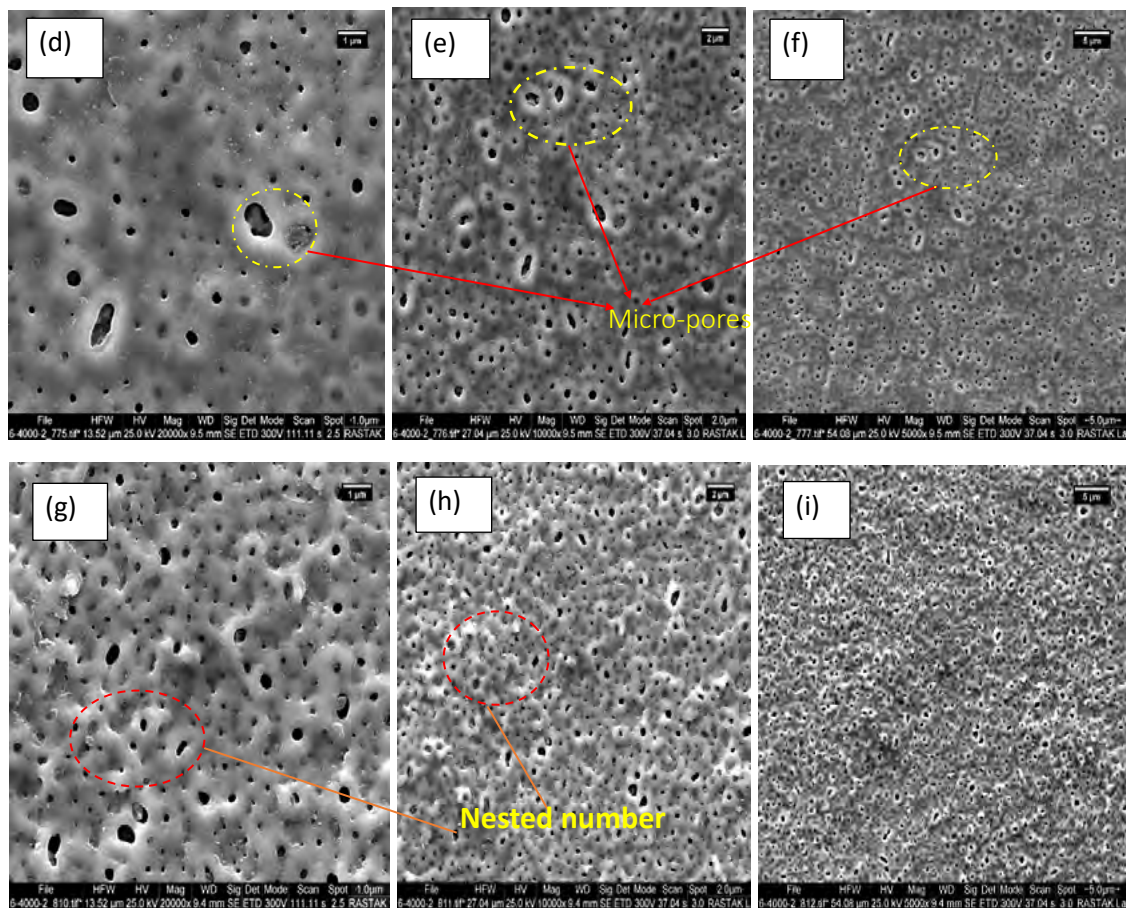
Figure 2. FESEM Micrographs of TiO2 coating MAO process at different magnification and time.

A typical porous structure was also found in coating of sample at 15min. Pores with maximum diameters and homogenous distribution can be observed on the surface of the Ti-alloy. The diameters of the such holes and the surface roughness grew as the voltage rose; after 30 min of treatment, the pores diameters increased, and the coated surface progressively became rough. The oxide layer on both materials is formed by several micro-protrusions with uniformly scattered pores with diameters varying from sub-micron to few microns. When compared to a polished surface that hasn't been covered, the presence of this porosity improves osseointegration because the pores function as sites for bone tissue formation, hence improving anchoring [20]. The FESEM cross-sectional morphology of TiO2 coating layer has a regular thin film structure in thickness with more compact, homogeneity, and full adhesion between the coating and the underlying substrate, as shown in Fig. 3 (a). each sample's coating layer has a compact diffusion layer in contact with the substrate and an external porous conversion zone with discharge channels make up the two sections. The average thickness of the diffusion layer remains constant throughout the procedure. the average thickness of the external porous conversion layer rises as the deposition duration increased, from 1.94µm at 7 min to 5.54µm at 30 min, as shown in Fig.3 (b and c).
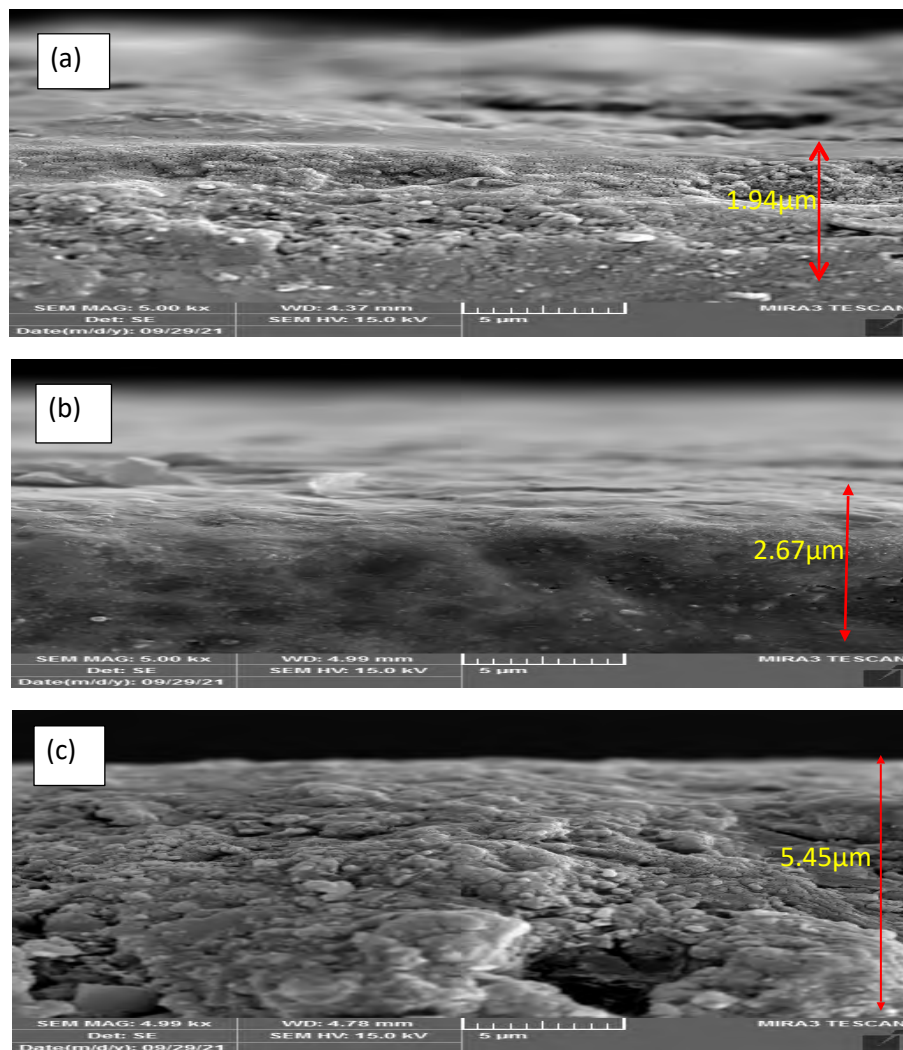
Figure 3. Cross section of MAO coatings: (a) at 7min, (b) 15min, and (c) 30min.

The formation of crossing pores and big pores distributed along the whole thickness. Generally, the coating thickness is increased with increasing deposition time because the voltage on the sample could not reach the sparking threshold, and a thin layer of oxide film quickly formed on the sample surface because of anodic oxidation. When the oxidation time was increased, the sparking voltage was reached and the energy rose; consequently, some discharge channels on the specimens became evident. Oxide film formed on the inner and outer surfaces of the discharge channel as the reaction product erupted along the channel. The oxide coating thickened when the oxidation duration, and energy were increased. Furthermore, the molten oxide spilled over the discharge tube, immediately cooled, and was deposited on the surface. The process was repeated until the end of the oxidation reaction, causing incessant growth of the oxide film [21]. The Presents of schematic data of EDS results for MAO TiO2 coatings with different times on containing Ti, O, Al, and Nb ions. EDS analysis showed that increasing of time up to 30 min had it effects on the content of oxide layer as shown in Fig.4 coated with different times. As a result of the presence of Ti and O2 components in the coatings, TiO2 layers with varied weights of these modification elements.

3C Tecnología. Glosas de innovación aplicadas a la pyme. ISSN: 2254-4143

Ed.43 | Iss.12 | N.1 January - March 2023
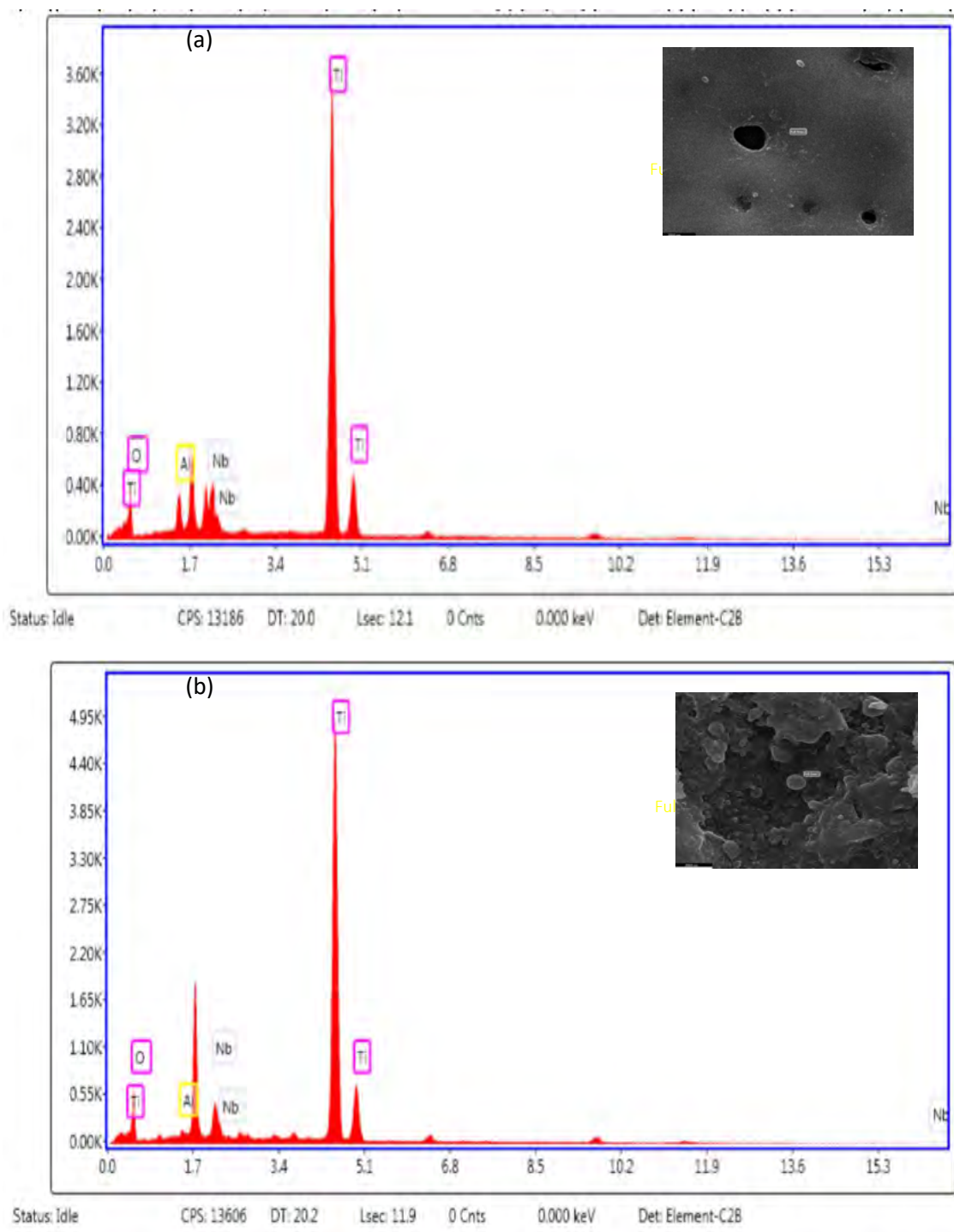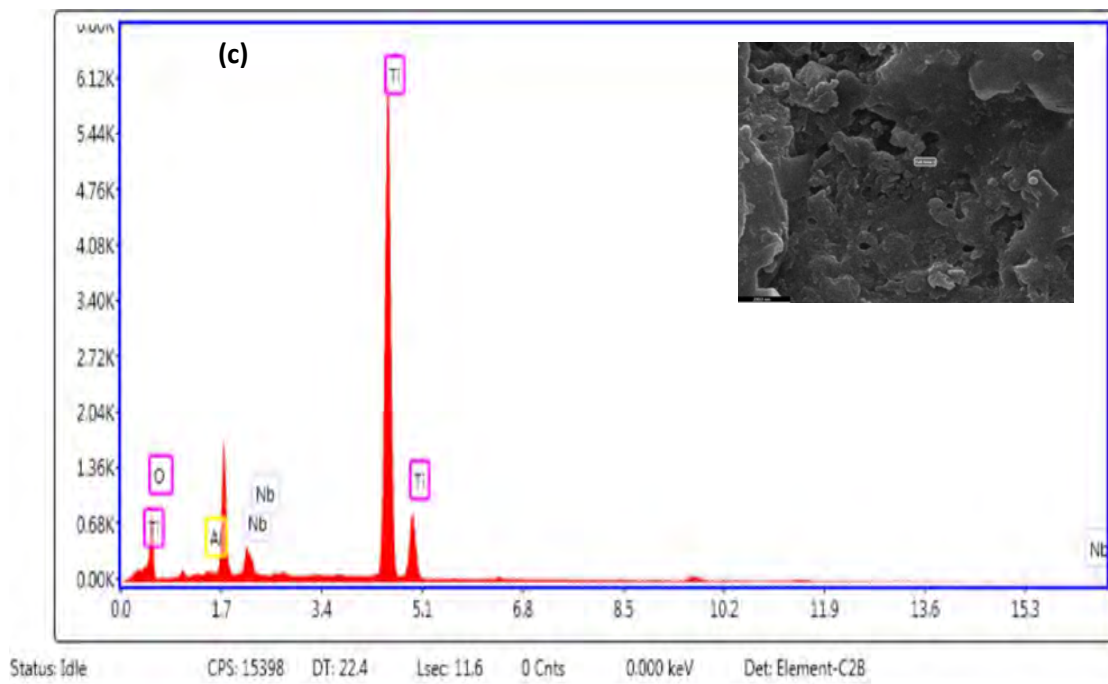
Figure 4. EDS result of (a) coating at 7min, (b) coating at 15min, and (c) coating at 30min.

Results of AFM analysis are given in Fig.5, the differences in surface topography between the substrate and different coatings in 2D and 3D, where observed an increase in the roughness of the TiO2 coatings because of the phenomena of micro-discharge resulting from the nature of the MAO process [22]. The Ra of coatings were more than those of the substrates and increased with time roughness also increased from (7.19nm) for 7min, (12.6nm) for 15min, and (18.8nm) for 30min because increase oxidation time.
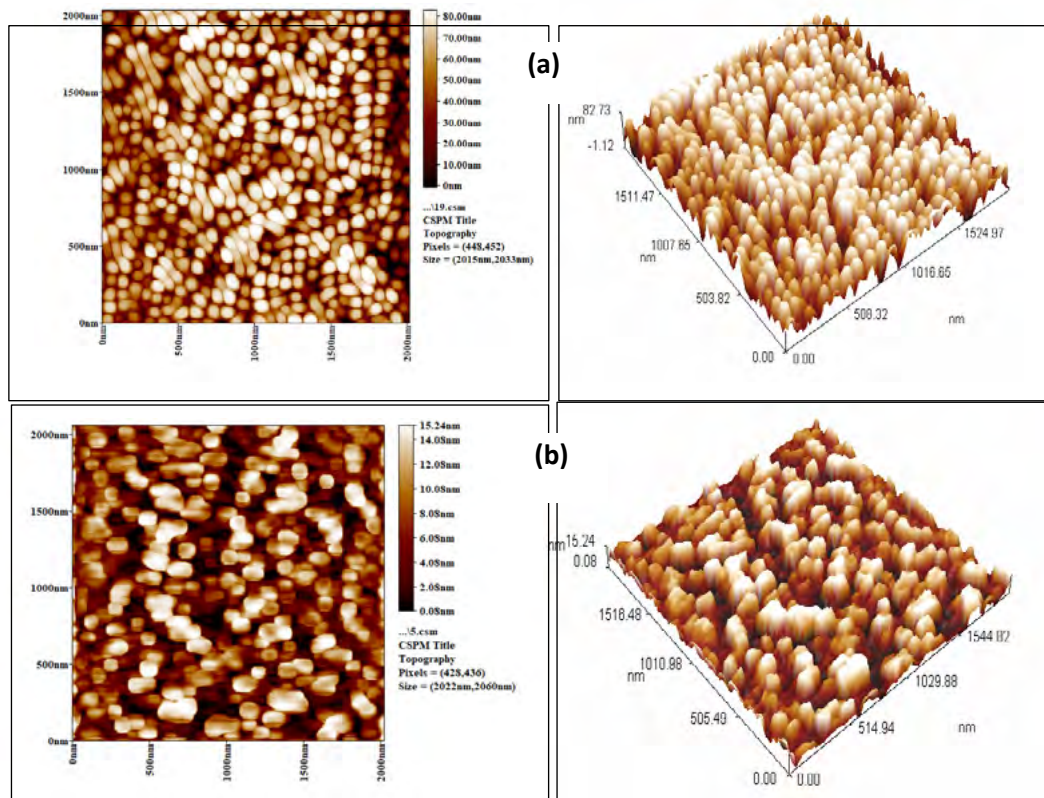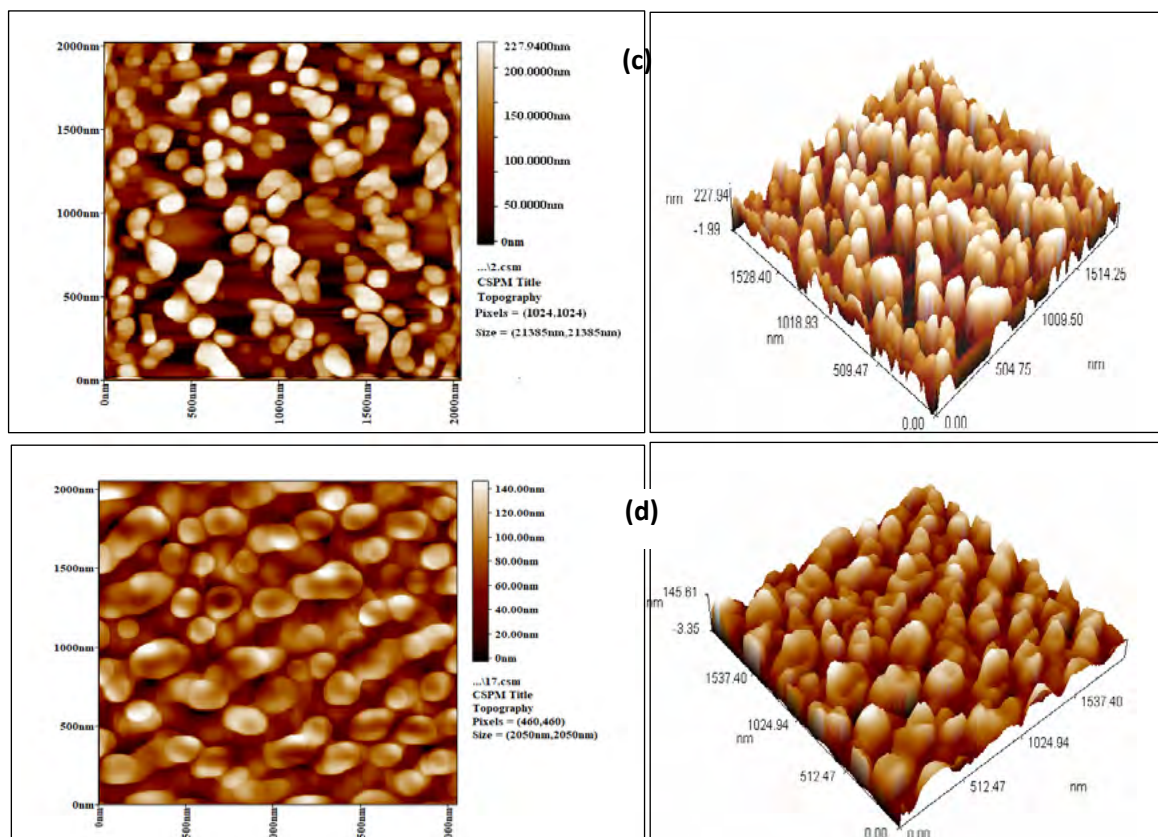
Figure 5. AFM results of samples (a) base, (b) coating at 7min, (c) coating 15min, and (d) coating 30min.

3.2. MECHANICAL PROPERTIES:

Results of micro-hardness at TiO2 of the coated samples at a load of 50gm (0.49N) using a fixed loading duration of (15sec.) in Fig.6. In general, it can be observed that the hardness of coated samples is improved by MAO process. The value of hardness equal to (268.55 HV at 7min) are significantly higher than that of Ti-6Al-7Nb alloy, and the increase hardness value with increase the deposition time to the (311.5 at 15min) because the production of dense oxide layer, which is attributed to formation of thermal micro arcs during MAO and increase thickness of ceramic coating [17]. The MAO treated sample's greater standard deviations might also be attributed to their higher surface porosity. Which resulted in lower leading hardness at the interface (287.3HV at 30min).
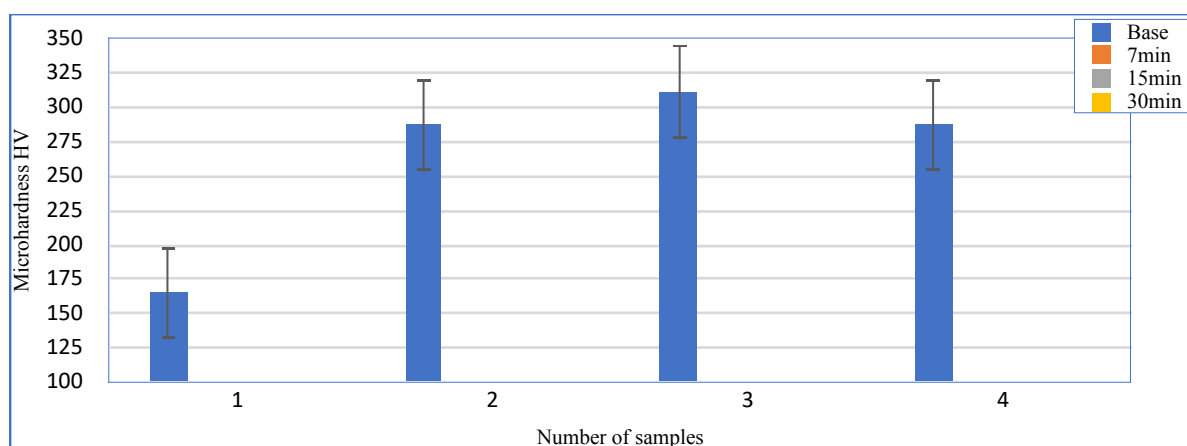
Figure 6. Relationship between the deposition time and the micro-hardness of coatings at TiO2 by MAO process.

Wear resistance is one of the most significant implant mechanical properties that wear failure contributes from all implant's failure reasons. Wear mass loss of test specimens under 10N stress and several times (5, 10, 15, 20, 25, and 30) min were used to evaluate the wear rates produced by pin-on disc sliding wear tests. Generally, it can be observed that the weight loss increased with increasing of loading time. Fig.7 shows that high wear rate of Ti-6Al-7Nb alloy substrate comparison, with coating. The ceramic oxide layers were found to have high wear resistance, resulting in a lower wear rate in the samples. ceramic coatings deposited TiO2 by MAO process, gave the best wear resistance and low wear rate $\left(2.78 \times 10^{-5}\right)$ at 7min. Due to improved hardness by presence of the alpha and beta titanium phases and presence of modified elements could be reduce the friction and increase wear resistance of coating by reduce wear rate. The intensity of micro-discharges rises as the applied duration increases (30min), resulting in an increase in coating porosity owing to a decrease in coating electric resistance. The coating porosity distribution has an impact on both mechanical and tribological properties [23]. This is supported by the current findings, which reveal that the coating has greater wear rates equal $\left(9.46 \times 10^{-6}\right)$ after passing 30min.
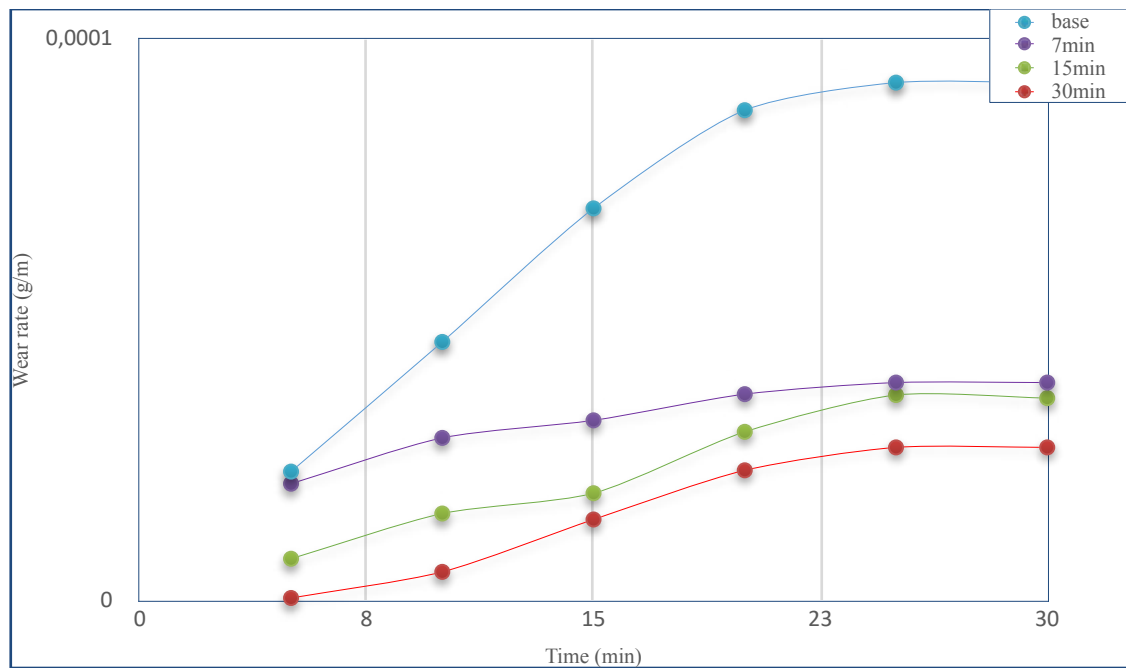
Figure 7. Relationship between wear rate and test time for Ti-6Al-7Nb alloy substrate and MAO process with different deposition time.

3.3. CONTACT ANGLE TEST

The contact angle, which is an essential measuring tool for determining material surface wettability was also discovered to be a key factor in increasing the bioactivity of titanium surfaces. Fig.8 show the contact angles tested of TiO2 by MAO coatings prepared at various deposition times in Ringer's and Saliva's solution. With increased surface roughness and porosity, the specimen's contact angle reduces considerably following MAO treatment. The contact angle reached value to (56.74° at 7min in ringer's solution and 54.7° in saliva's solution) and decreased with increase deposition time reached to (11° at 30min in ringer solution and 13.1° in saliva solution). The MAO treatment resulted in an uneven coating surface, increased roughness, increased absorbability, and decreased contact angles, all of which together affected the surface energy; and the OH and O2 oxygen-containing groups produced on the coated surfboard. These factors combined to increase the wettability of the MAO treated because a large number of micro/nano-pores formed on the oxidation coating surface caused its specific surface area to oxidation coating increase, which benefited water retention [24].
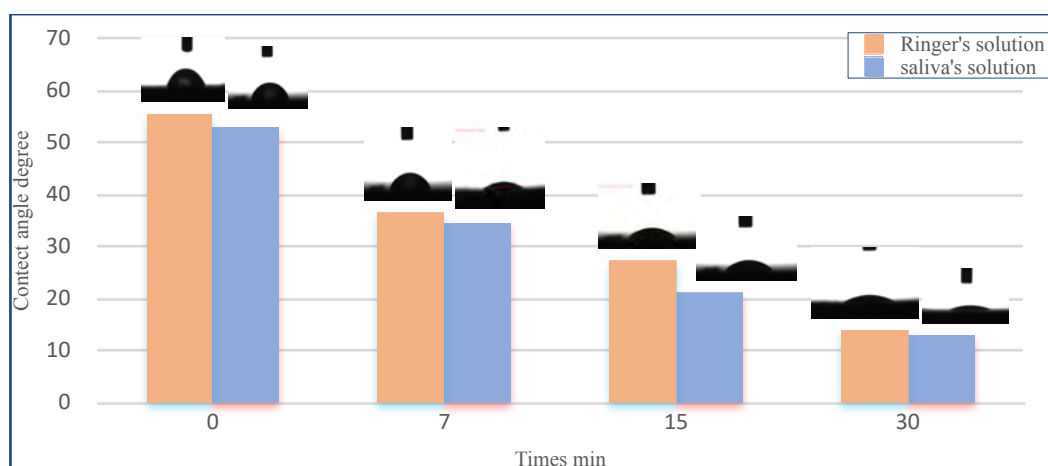
Figure 8. Results of contact angle in TiO2 at 400V in Ringer's and Saliva's solution.

3.4. ELECTROCHEMICAL BEHAVIOR OF THE ALLOY/OXIDE SYSTEMS

The potentiodynamic polarization curves for the Ti-6Al-7Nb alloy substrate and TiO2 coated by MAO process samples in Ringer's solution at 37°C±1 at various times in Fig. 9. Tafel extrapolation is used to calculate the corrosion current densities (icorr.) and corrosion potentials (Ecorr.) using potentiodynamic curves, and corrosion rates (CR) were also included in Table.1. It can be seen from the results obtained in the uncoated substrate has a greater corrosion current density (icorr= 6.8284 A/cm2) of thus lowest corrosion resistance because of the occurrence of metal ions dissolution on the surface of the uncoated substrate. The corrosion current density and corrosion rate of all coated samples by MAO decrease after TiO2 coating, indicating that the TiO2 coating offers a protective layer on the substrate surface that reduces corrosion rate. The lowest corrosion current (icorr. = 2.8161 A/cm2) and increased corrosion potential of the specimens are achieved when coating for 7 min, and this result has a reduced corrosion rate equal to (CR= 3.48×10-3 mpy), indicating that corrosion resistance is improved. Furthermore, the film's surface structure influences the material's corrosive qualities. Materials with denser and thicker oxide layers have a lower corrosion current density and a lower corrosion rate (icorr. = 0.0902A/cm2), and a lower corrosion rate (CR=0.111×10-3 mpy) at (15min).
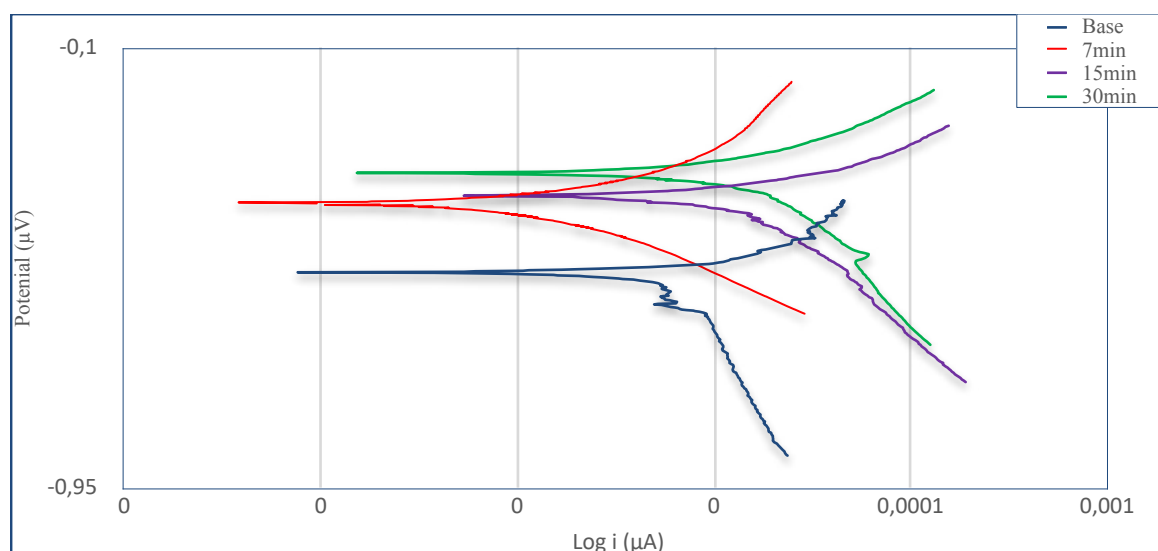
Figure 9. Potentiodynamic polarization curves of TiO2 coated by MAO process and base at different time in Ringer's solution.

The porosity affected the corrosion behavior of highly porous where decreased corrosion resistance because increased (icorr. =1.3643 µA/cm2) and (CR =1.686×10-3mpy). The corrosion behavior of porous metallic materials has in the present work, the oxygen/air entrapped in the most inner pores neither the difficulty of electrolyte penetration into these pores, may result in various passive states on the native oxide surface. The surface area, on the other hand, has minimal influence on the corrosion rate of porous materials. Although Ti is known for its strong resistance to localized corrosion, and localized breakdown of its passive coating occurs at substantially higher potentials, the increased corrosion density with greater porosity level is due to the larger surface area in contact with the electrolyte, but fissures or restrictions to the flow of species into the connected pores can result in corrosion rates that are not proportional to the real contact surface area. Although these challenges may result in faster corrosion rates, good passivation qualities for porous Ti structures have been documented in the literature. On the other hand, increased porosity was also associated with a decreased susceptibility to corrosion (less negative Ecorr.), as interconnected pores encouraged the free flow of ionic species, whereas isolated pores trapped the electrolyte and depleted the oxygen supply, leading to a thinner oxide film. Aside from species free movement, air entrapment, and electrolyte penetration [25].

Table.1. Electrochemical parameters of base and TiO2 coated MAO at different time in Ringer's solution.

Parameters of coating	$i_{corr.}$ (µA/cm²)	$E_{corr.}$ (mV)	Rate of Corrosion (mpy)×10^{-3}	Enhancement percentage (%)
base	6.8284	-533	8.437	/
7min	2.8161	-342	3.480	58.7
15min	0.0902	-341	0.111	98
30min	1.3643	-390	1.686	80

The corrosion behavior in Saliva's solution of the alloy and coated samples TiO2 by MAO process in Fig.10 respectively, and Table.2 it is clear, that the specimen showed relatively similar behavior to that observed in saliva's solution such as MAO process for alloy improved corrosion resistance because of reduction in corrosion current [26,27]].
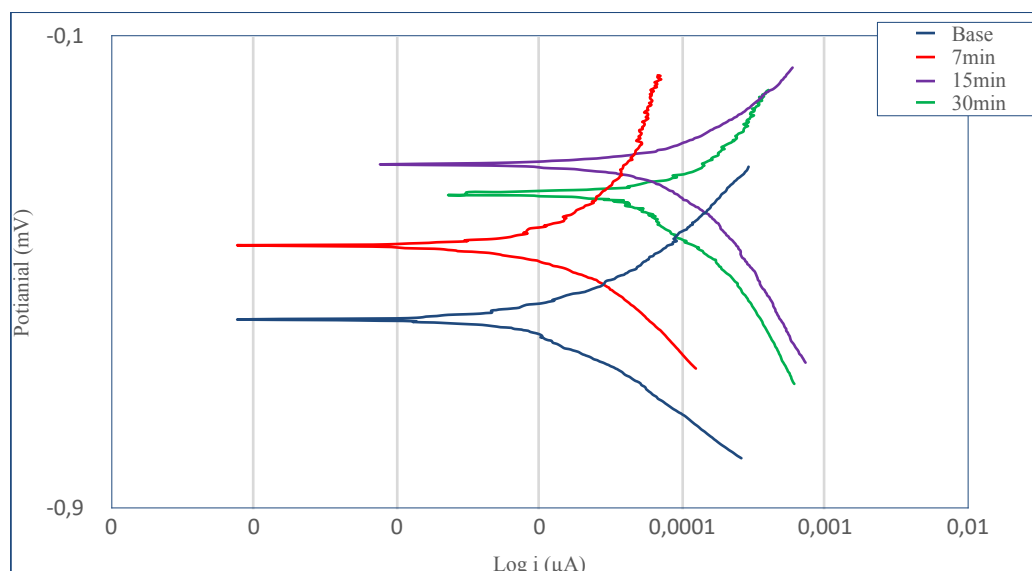
Figure 10. Potentiodynamic polarization curves of TiO2 coating by MAO process and base at different time in Saliva's solution.

Table 2. Electrochemical parameters of base and TiO2 coated MAO at different time in Saliva's solution

Parameters of coating	$i_{corr.}$ (µA/cm²)	$E_{corr.}$ (mV)	Rate of Corrosion (mpy)×10^{-3}	Enhancement percentage (%)
base	7.103	-579	8.777	/
7min	3.479	-491	4.3	51
15min	0.833	-472	1.03	88.26
30min	1.475	-392	1.8	79.5

4. CONCLUSION

In the current study, the TiO2 coating has been deposited on the surface of Ti-6Al-7Nb alloy successfully by using micro-arc oxidation process for biomedical applications.

1. The TiO2 layer formed on Ti-6Al-7Nb alloy substrate material using MAO methods has circular micro holes in rough and volcanic structures because of continuous micro discharges occurring during the process. Rutile TiO2 and anatase TiO2 phases are determined on the material surface following the XRD analysis.

2. The substrate's surface roughness plays has an important role to improving coating-substrate adhesion. AFM topography shows homogeneous and dense at (30 min).

3. EDS results showed that the ratio of Ti/O increased with time at coating.

4. The apparent contact angle somewhat reduces following treatment at various times. The surface morphology and composition of the MAO coatings may be the cause of the MAO coatings' considerable shift in apparent contact angle. Due to its smaller pores, the wettability of the MAO coating created at lower roughness may be underestimated. It's possible that the wettability of the MAO coating generated at reduced roughness is overestimated. The wettability of the MAO coating generated at higher roughness may be overstated since no gas is trapped and the liquid/solid interface is rougher.

5. The potentiodynamic polarization results that Ti-6Al-7Nb base alloy substrate and TiO2 at different times in Ringer's and Saliva's solutions; the best result equal (icorr.=0.0902μA/cm2) in Ringer's solution and (icorr.= 0.833μA/cm2) in Saliva's solution compared to the uncoated sample.

ACKNOWLEDGEMENTS

REFERENCES

(1) L. Thair, U. K. Mudali, N. Bhuvaneswaran, K. G. M. Nair, R. Asokamani, and B. Raj. (2002). **Nitrogen ion implantation and in vitro corrosion behavior of as-cast Ti-6Al-7Nb alloy.** *Corros. Sci.*, 44(11), 2439-2457.

(2) G. Wu, P. Li, H. Feng, X. Zhang, and P. K. Chu. (2015). **Engineering and functionalization of biomaterials via surface modification.** *J. Mater. Chem. B*, 3(10), 2024-2042.

(3) A. T. Sidambe. (2014). **Biocompatibility of advanced manufactured titanium implants-A review.** *Materials (Basel)*, 7(12), 8168-8188.

(4) M. kawano, Y. Takeda, K.Ogasawara. (2015). **Pathological Analysis of Metal Allergy to Metallic Materials,** 305-321.

(5)   G. A. dos Santos. (2017). **The Importance of Metallic Materials as Biomaterials.** *Adv. Tissue Eng. Regen. Med. Open Access*, 3(1), 300-302, 2017.

(6)   L. Mohan and C. Anandan. (2013). **Wear and corrosion behavior of oxygen implanted biomedical titanium alloy Ti-13Nb-13Zr.** *Appl. Surf. Sci.*, 282, 281-290.

(7)   N. Mitsuo. (1998). **Mechanical properties of biomedical titanium alloys.** *Mater. Sci. Eng. A.*, 243(1-2), 231-236.

(8)   S. Shaikh, S. Kedia, D. Singh, M. Subramanian, and S. Sinha. (2019). **Surface texturing of Ti6Al4V alloy using femtosecond laser for superior antibacterial performance.** *J. Laser Appl.*, 31(2), 022011.

(9)   Y. X. Leng, J. Y. Chen, P. Yang, H. Sun, and N. Huang. (2003). **Structure and properties of passivating titanium oxide films fabricated by DC plasma oxidation**. *Surf. Coatings Technol.*, 166(2-3), 176-182.

(10) M. Almasri. (2016). **Introductory Chapter : Dental Implantology, The Challenging Scenarios between Training, Resources, and Patients' Demands.** *Dent. Implantol. Biomater.*

(11) S. V. Dorozhkin. (2015). **Calcium orthophosphate deposits: Preparation, properties and biomedical applications.** *Mater. Sci. Eng. C*, 55 272-326.

(12) A. Prof and A. Prof. (2019). **Surface modification of titanium and titanium alloys: technologies, developments and future interests,** 10, 12-58.

(13) H. Chouirfa, H. Bouloussa, V. Migonney, and C. Falentin-Daudré. (2019). **Review of titanium surface modification techniques and coatings for antibacterial applications.** *Acta Biomater.*, 83, 37-54.

(14) L. C. Zhang and L. Y. Chen. (2019). **A Review on Biomedical Titanium Alloys: Recent Progress and Prospect.** *Adv. Eng. Mater.*, 21(4), 1-29.

(15) [15] Liu, Xuanyong, Chu, Paul K., and Ding, Chuanxian. (2004). **Surface modification of titanium, titanium alloys, and related materials for biomedical applications.** *Materials Science and Engineering R: Reports*, 47(3-4), 49-121.

(16) M. T. Mohammed, Z. A. Khan, and A. N. Siddiquee. (2014). **Surface Modifications of Titanium Materials for developing Corrosion Behavior in Human Body Environment: A Review.** *Procedia Mater. Sci.*, 6(no. Icmpc), 1610-1618.

(17) A. Santos-Coquillat, R. Gonzalez Tenorio, M. Mohedano, E. Martinez-Campos, R. Arrabal, and E. Matykina. (2018). **Tailoring of antibacterial and osteogenic properties of Ti6Al4V by plasma electrolytic oxidation.** *Appl. Surf. Sci.*, 454, 157-172.

(18) V. S. De Viteri et al. (2016). **Structure, tribocorrosion and biocide characterization of Ca, P and I containing TiO 2 coatings developed by plasma electrolytic oxidation.** *Appl. Surf. Sci.*, 367, 1-10.

(19) L. Xu et al. (2018). **Effect of oxidation time on cytocompatibility of ultrafine-grained pure Ti in micro-arc oxidation treatment.** *Surf. Coatings Technol.*, 342, 12-22.

(20) L. C. Campanelli, L. T. Duarte, P. S. C. P. da Silva, and C. Bolfarini. (2014). **Fatigue behavior of modified surface of Ti-6Al-7Nb and CP-Ti by micro-arc oxidation.** *Mater. Des.*, 64, 393-399.

(21) M. Shamsuzzoha, and E.Development. (2014). **TMS2014 Annual Meeting Supplemental Proceedings.** *The Minerals, Metals & Materials Society*, 1, 1057-1062.

(22) D. Quintero et al. (2017). **Anodic films obtained on Ti6Al4V in aluminate solutions by spark anodizing: Effect of OH− and WO4− 2 additions on the tribological properties.** *Surf. Coatings Technol.*, 310, 180-189.

(23) X. Shen, P. Shukla, S. Nath, and J. Lawrence. (2017). **Improvement in mechanical properties of titanium alloy (Ti-6Al-7Nb) subject to multiple laser shock peening.** *Surf. Coatings Technol.*, 327, 101-109.

(24) A. Cunha. (2015). **Multiscale femtosecond laser surface texturing of titanium and titanium alloys for dental and orthopaedic implants**, *University De Bordeaux.*

(25) M. B. Sedelnikova et al. (2020). **Functionalization of pure titanium MAO coatings by surface modifications for biomedical applications.** *Surf. Coatings Technol.*, 394(march), 125812.

(26) A. Khandan, N. Ozada, D. Ogbemudia, and S. Saber-Samandari. (2017). **Novel technology for bone cancer tumor by using hyperthermia treatment via bioceramic mechanism.** *UFGNSM*, 12, 13.

(27) Kumbhalkar, M.A., Rangari, D.T., Pawar, R.D., Phadtare, R.A., Raut, K.R., Nagre, A.N. (2021). **Finite Element Analysis of Knee Joint with Special Emphasis on Patellar Implant**. *Trends in Mechanical and Biomedical Design. Lecture Notes in Mechanical Engineering. Springer*.

/16/

PATHOLOGICAL OUTCOMES OF COVID-19 FOR LUNGS INFECTIONS BASED ON TRANSFER LEARNING TECHNOLOGY

Omar Alsaif

Computer Systems Dept., Northern Technical University, Mosul, Iraq

Mohammed L. Muammer*

mohammed.loay@ntu.edu.iq

ABSTRACT

In 2019 a new Syndrome appear on the Large numbers of people like (High temperature, cough, Loss of sense of smell and taste(forcing a lot of them to enter the critical care unit after while the virus how case this syndrome named (SARS-CoV2).

The aim of this paper is recognize the patient who effected by covid-19 or not using x-ray images. Deep learning techniques utilized to classify these images by using convolutional neural network (CNN). The dataset have been utilized in this work consist of 1000 x-ray images collected from kaggle website and divided it into 80% for training and 20% for validation.

The proposed method using the pertained networks such as (EffienentNet B0, ResNet50) to minimize the training time with high performance, where the EffienentNet B0 network give high accuracy is 98.5%,finaly the model has been implemented on raspberry pi3 successfully for classification task.

KEYWORDS

Covid19; Deep learning; CNN.

PAPER INDEX

1. INTRODUCTION

Since late December 2019, a new coronavirus illness (COVID-19; previously known as 2019-nCoV) epidemic has been detected in Wuhan, China, affecting 26 nations across the world. COVID-19 is a condition that is acutely resolved in most cases, but it can potentially be fatal, with a case fatality rate of 2%. Massive alveolar destruction and gradual respiratory failure may end in mortality if the condition is severe enough[1].
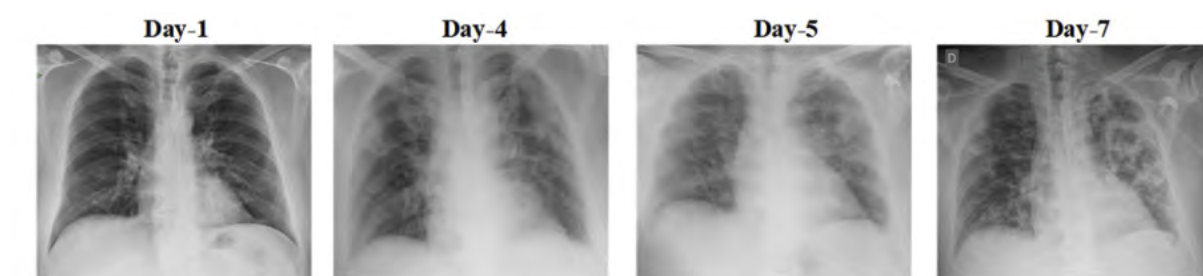
Figure 1. X-ray images for Chest of the patient over 50-year-old COVID-19 with pneumonia [2]

As shows in Fig. 1 the x-ray can appear the development of the lungs disease in seven days, in the first day the lung is clear but in the days-4 the illness patchy appear in the x-ray, while in the days-7 the patient will be in the worst case.

Vruddhi Shah et al in 9dec2020. COVID-19 of CT scan pictures was diagnosed using deep learning. A convolutional neural network is utilized in the deep learning techniques (CNN). The dataset contains There are 738 CT scan images total, 349 of which are for the COVID-19 case and 463 are for a different patient. For the COVID-19 diagnostic, they built a self-made model called CTnet-10, which had an accuracy of 82.1%. Other models used in this study are InceptionV3, ResNet-50, VGG-16, DenseNet-169, and VGG-19; with an accuracy of 94.52%, the VGG-19 model outperformed all other deep learning models. [3][4] Nesreen Alsharman and Ibrahim Jawarneh in 11apr2020, COVID-19 was detected using a transfer learning method. Only GoogleNet CNN has been used. Dataset comprises 349 photos showing COVID-19 medical studies in this investigation. Retraining GoogleNet has a validation accuracy of 82.14 percent[5].

Halgurd S. Maghdid et al. in 12apr2021. From CT and x- ray images, DL was utilized to identify COVID-19 Pneumonia in the chest. The images are processed using a standard convolution neural network (CNN) and a specially designed pre-trained AlexNet model. They used a total of 238 samples (85 x-ray and 153 CT scan images). According to the tests, the models can achieve accuracy rate more than 98 % when using a pre-trained models and 94.1% when using an other CNN[6].

2. MATERIALS AND METHOD

Detecting structural anomalies and disease categorization are two common uses of Deep learning (DL) in radiology. (CNNs) in particular have been found to be very effective at detects anomalies and diseases in chest X-ray imaging[7]. The human nervous system provided inspiration for deep learning models. DL has been shown to improve performance in a variety of fields[8].

2.1. CNN TECHNIQUE

A restricted resource budget is typically used to build CNN, which are subsequently scaled up for greater accuracy when additional resources become available. [9]. Deep CNN is now one of the most popular models, with excellent results on a variety of image categorization challenges. By uncovering robust characteristics (features) in images and reducing the vanishing gradient problem, the notion of sharing weights in DCNN allows for successful image categorization[10].

Convolution, pooling, and fully connected layers make up CNN's three layers. The convolutional layer's primary objective, which is accomplished via the use of filters, is the extraction of characteristics (features) from input pictures. The pooling layer, which comes after the convolutional layer, does down sampling and keeps the most important details from the input pictures. This layer reduces the model's spatial dimension, even the number of parameters, prevents overfitting, and produces a model that is more effective. A soft-max activation function is used by the fully connected layers (final layer) to extract high-level information from the input pictures and classify them into various categories with labels[11].

3. TRANSFER LEARNING

Transfer learning (TL) has demonstrated to be a very smart strategy, especially in sectors with limited data. The model can detect the specific characteristics of a certain classification of images, like shots of the eye, considerably more quickly and often with far less learning samples and computer resources by utilizing a feed-forward technique to adjust the parameters in the network. back propagation is used to retrain the weights of the top layers after the lower layers, which are already tuned to detect the features present in photos in general, have already done so[12].

3.1. EFFICIENT NET B0 TECHNIQUE

Transfer learning is employed in the EfficientNet architecture to save time and processing resources. The EfficientNet model comprises eight versions, spanning from B0 to B7, where each model number corresponds to a version with additional parameters and higher accuracy[13]. Its accuracy values are greater than those of other well-known models as a result[11]. The incredibly effective fundamental compound scaling algorithms form the foundation of the EfficientNet Models, as seen in Fig. 2. This technique enables you to modify a baseline CNN to any resource constraints while maintaining model efficacy, making it helpful for transfer learning

datasets. In terms of accuracy and effectiveness, EfficientNet models typically surpass current CNNs like AlexNet, ImageNet, GoogleNet, and MobileNetV2.[14].

By scaling the baseline network EfficientNet B0 utilizing the same compound model scaling technique as EfficientNet B0, they also produced EfficientNets B1-B7. As a consequence, eight different version of CNN architectures and outcomes are shown using the ImageNet dataset. A 600x600 image can be fed into EfficientNet B7, which has 66 million parameters, whereas a 224x224 image may be input into EfficientNet B0, which has 5.3 million parameters.

CNNs may capture richer and more complex features or characteristics by increasing network depth. The vanishing gradient problem, on the other hand, makes network training more difficult. By increasing the network's width, more fine grained characteristics may be captured. Training is also simple. Networks of various sizes and depths However, they are unable to capture higher characteristics. Finally, high level resolution pictures enable CNN to detect finer patterns. Bigger pictures need more memory and computing power[15].

ConvNets are frequently scaled up to improve accuracy. For example, by adding more layers to ResNet, although it is possible to scale up ConvNets from ResNet-

18 to ResNet200, the process has never been fully understood, and there are presently a number of approaches to achieve so. The most common approach is to make ConvNets deeper or wider[4]. Scaling up models depending on their picture resolution is a different, less frequent, but quickly gaining popularity method[9][16].
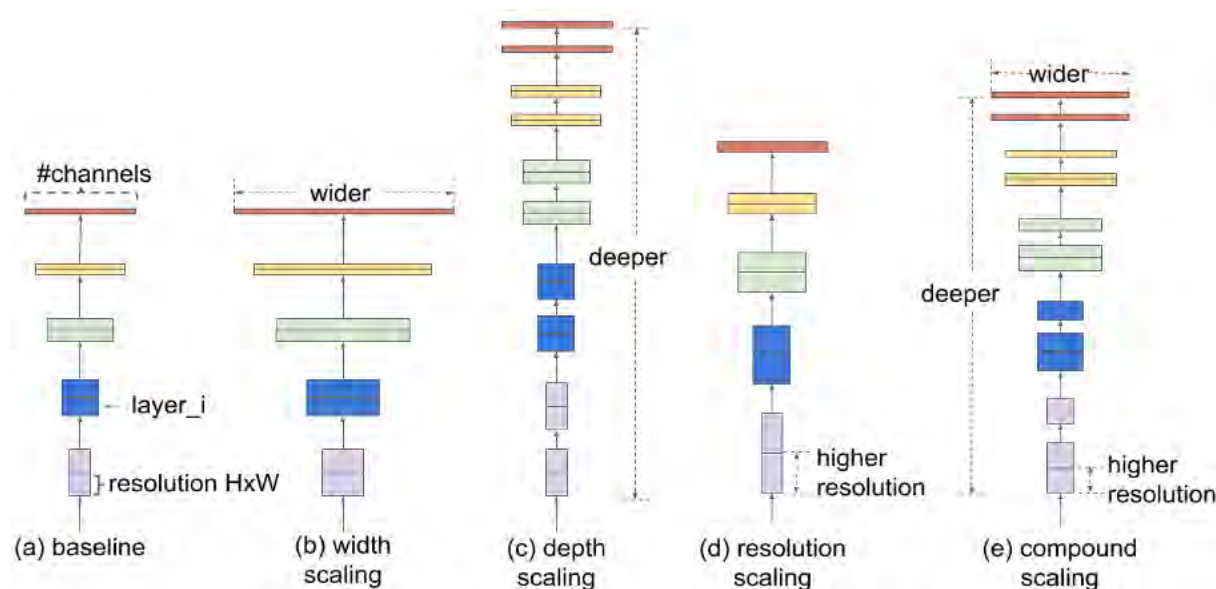
Figure 2. Model Scaling.

3.2. RESNET50 TECHNIQUE

Residual Network is referred to as ResNet, as seen in the Fig. 3. Over time, DL convolutional neural networks have improved picture categorization and identification in a variety of ways. By using deeper network to solve more challenging issues and

improve classification or identification accuracy is getting more and more popular[17]. Deeper neural network training has proven challenging due to problems like the degradation problem and the vanishing gradient problem. The goal of residual process is to resolve both of these problems.
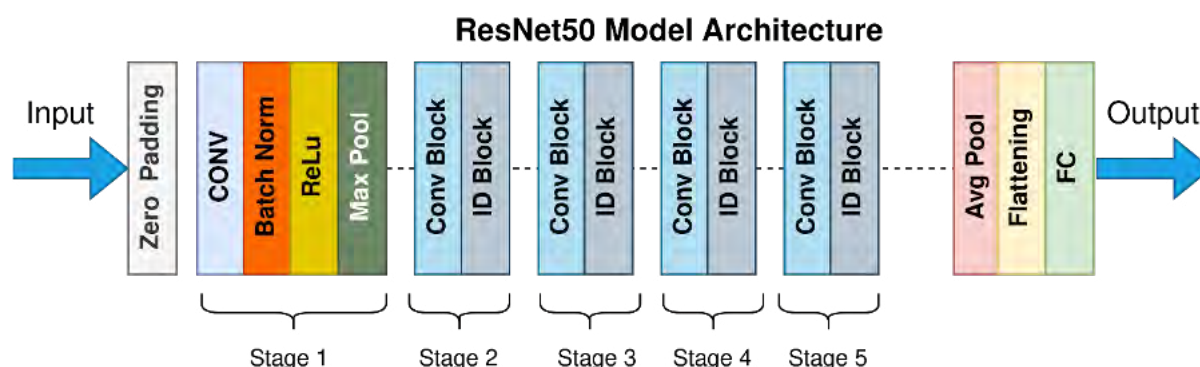
Figure 3. Residual Neural Network.

Each layer tries to learn low or high level properties from images. The method tries to learn some residual in residual process rather than trying to learn more complex features.[8].

In order to overcome these difficulties, residual neural networks (ResNet) include a "Residual block," which includes a "skip or shortcut connection," which transfers the output from the previous layer to the layer ahead, as shown in Fig. 4. If the dimensions of x and F(x) below are not the same, inputs x is multiplied by a corresponding weights W to balance the dimensions of the output layer and the short-cut link [18].
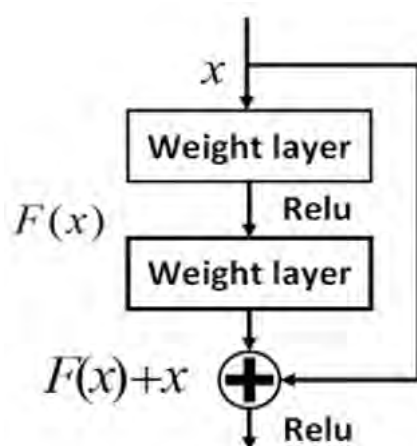
Figure 4. Residual learning: a building block.

4. RASPBERRY PI 3 SYSTEM

Using the Linux operating system, the Raspberry Pi is a tiny computer board that may be connected to a display, keyboard, and mouse. The Raspberry Pi may be used

for electrical structures and network programming. It can also be used as a pc by installing the Apache Webserver and MySQL on the board.[19].

As seen in Fig. 5, the Raspberry Pi 3 (RPI3) module is a low-cost Linux-based small computer. It contains 40 GPIO Pins for managing output components like LEDs, motors, and relays. This section has containing RPI3 hardware specifications [20]:

- SoC: BCM2837

- CPU: quad-core 1.2 GHz, type: ARM, Cortex A53

- GPU: 400 MHz

- Ram: SDRAM 1 GB LPDDR2-900

- Four USB Port • 10/100 Mbps Ethernet.

- 802.11n Wireless LAN and Bluetooth 4.0

Figure 5. Raspberry Pi 3.

5. METHODOLOGY

Fig.6 below shows a block diagram of the whole system design
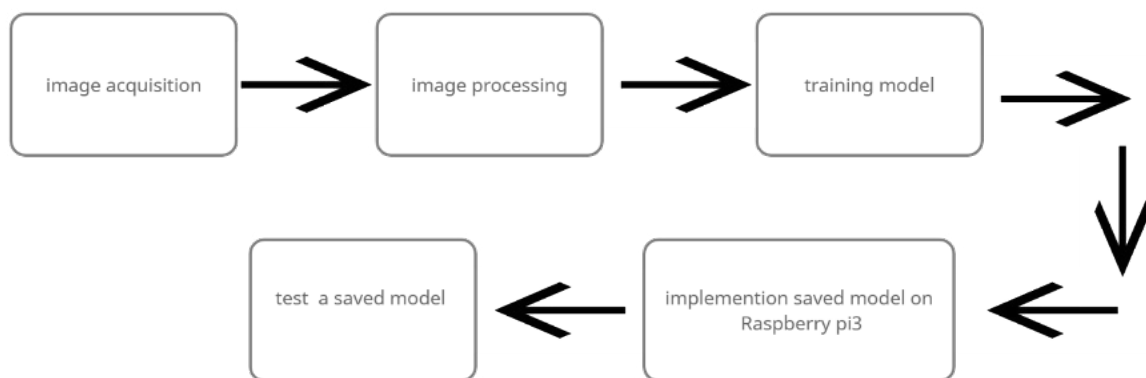
Figure 6. Block Diagram of the whole system.

Image Acquisition: The dataset that has been utilized in this project consists of 1000 images (x-ray) these images are divided into 2 classes each class has 500 x-rays.

Image preprocessing: Two types of preprocessing have been used in our model

1. Image resize: all x-ray images have been resized to 224 widths and 224 heights.

2. Data Augmentation: Data augmentation has been used to reduce overfitting during CNN training and generate more images from the original image. The augmentation processes applied to training datasets are explained below.

- The rotation range is 10 which rotates all training images by 10 degrees.

- The width shift range is 0.2 which increases the width by 2.

- height shift range is 0.2 which increases height by 2.

- The zoom range is 0.2 which zooms in the image by 0.2.

The proposed CNN models using a pre-trained network (Efficient Net B0 and ResNet50) with fine-tuning with data Augmentation to classify covid19 disease. After image preprocessing, a dataset has been divided into 80% for training and 20% for validation.

In transfer learning, the convolution and pooling layers have been stopped and replaced the fully connected layers of the (Efficient Net B0 and ResNet50) with the 2 FC layers. The 2 FC layers contain 512 neurons and 256 neurons respectively and train the network with 80 epochs. The proposed network uses a 32 Batch size and is trained to utilize Adam optimizer with a 1e-4 learning rate. Loss function (categorical_crossentropy) has been used to determine a loss function. The final layer is the output layer with a soft-max activation function, this layer consists of 2 neurons according to the covid19 and normal case. implementation on raspberry pi3

After completing the training of the proposed network and raspberry pi 3 OS has been installed. The saved model has been uploaded to raspberry pi and uses Thonny python IDE to write code x-ray images to classify x-ray COVID-19 diseases. Fig.7 below shows all hardware components that have been used to design the classification system.
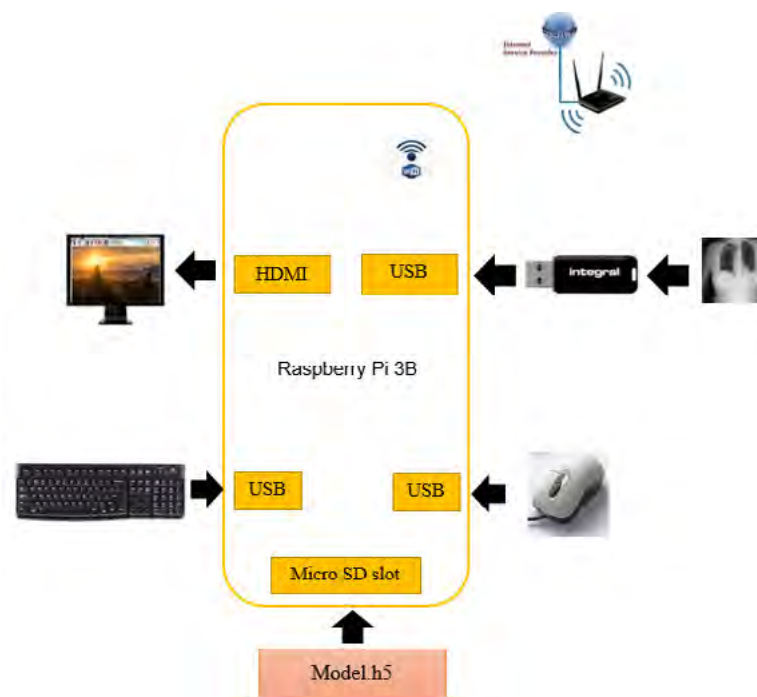
Figure 7. block diagram of the whole system.

After implementation on raspberry pi3 stage need to test the whole system as following

- first step read two images diagnosed as covid-19 and the other normal case
- resize the image to became 224*224 as in the model
- load the model that save on raspberry pi3
- use prediction function
- use smtp library
- enter the email and password of the sender
- enter the email of the doctor how will receive the result and make the decision
- run the systemIf the image was diagnosed as covid-19 the system return (0)
- Else the result will be (1)
- In the same time the doctor will receive the email with the result (normal or covid-19).

6. RESULTS AND DISCUSSION

In the results and discussion part shows the result of the testing the (EffienentNet and ResNet50) networks expressed in figure. (8). The Confusion matrix of the EffienentNet B0 without augmentation, in this cases the model predicted 197 correctly from 200 sample. Figure(9), represent confusion matrix of the EffienentNet B0 with augmentation only 188 samples classified correctly.
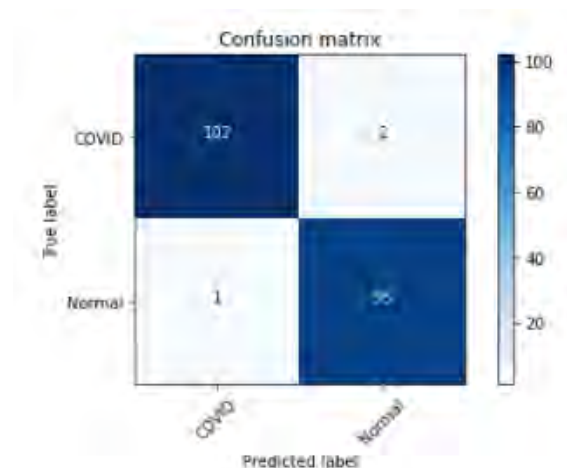
Figure 8. Confusion matrix of the EffienentNet B0 without Augmentation.

3C Tecnología. Glosas de innovación aplicadas a la pyme. ISSN: 2254-4143
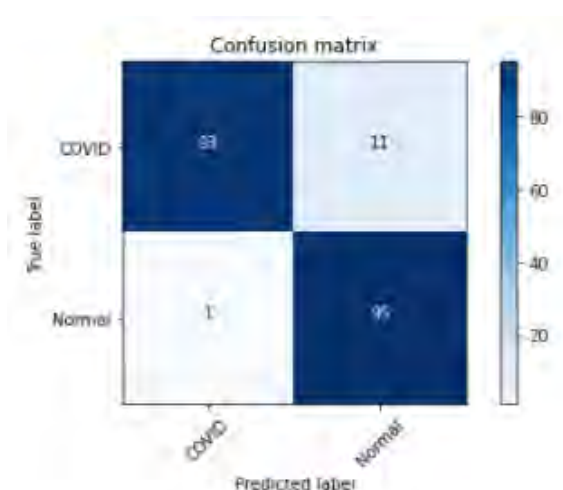
Figure 9. Confusion matrix of the EffienentNet B0 with Augmentation.

Figure (10), represent the Confusion matrix of the ResNet 50 without augmentation, in this cases the model predicted 195 correctly from 200 samples. Figure(11) represent Confusion matrix of the ResNet 50 with augmentation only 192 samples classified correctly.
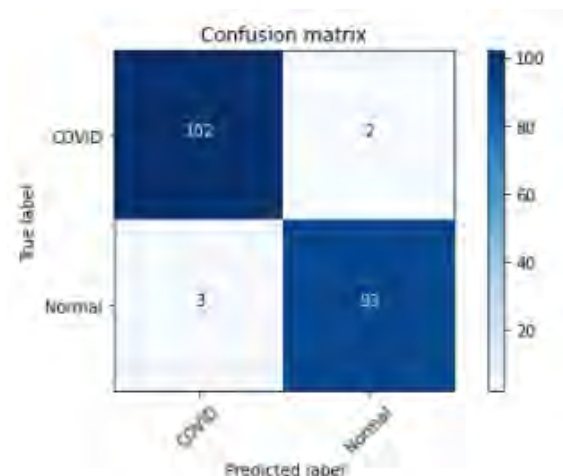
Figure 10. Confusion matrix of the ResNet50 without Augmentation.
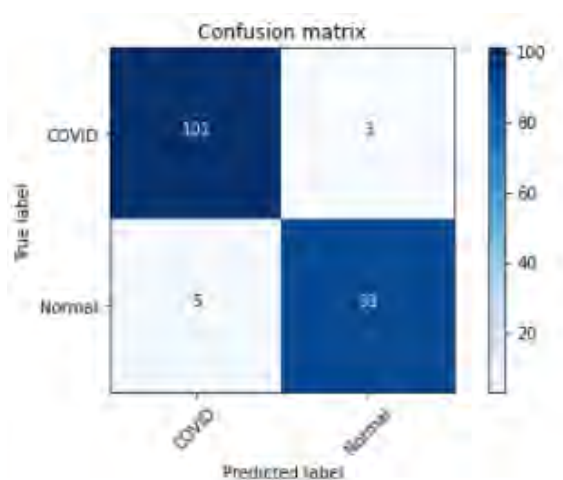
Figure 11 Confusion matrix of the ResNet50 with Augmentation.

After the model has been complete training and implemented on raspberry pi 3. The received email from the raspberry pi 3 after testing two images (covid-19 and normal), Fig. 12 represents the covid-19 case and Fig. 13 represent the normal one.
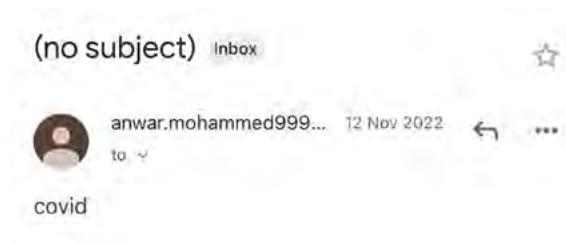
Figure 12. COVID-19 case
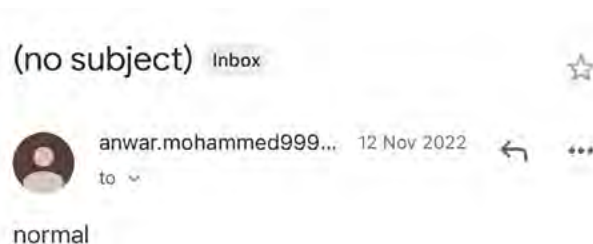
Figure 13. Normal case

7. CONCLUSIONS

In this work, an automatic system for detecting COVID-19 has been constructed successfully to recognize covid-19 case and normal case from x-ray images. For classification, we are successfully used the deep learning methods specially the CNN network with transfer learning like (EffienentNet B0, ResNet50). The obtained result presented by EffienentNet B0 without augmentation is 98.5% for testing accuracy. After the model has been implemented successfully on raspberry pi 3,which give the ability for raspberry pi 3 to distinguish the covid-19 case from normal case from x- ray image. Finally, raspberry pi 3 send email to the doctor represent the situation of the patient.

8. ACKNOWLEDGMENT

REFERENCES

(1)   Z. Xu et al. (2020). **Pathological findings of COVID-19 associated with acute respiratory distress syndrome.** *Lancet Respir. Med.*, 8(4), 420-422. https://doi.org/10.1016/S2213-2600(20)30076-X

(2)   T. Ozturk, M. Talo, E. A. Yildirim, U. B. Baloglu, O. Yildirim, and U. Rajendra Acharya. (2020). **Automated detection of COVID-19 cases using deep neural networks with X-ray images.** *Comput. Biol. Med.*, 121(April), 103792. https://doi.org/10.1016/j.compbiomed.2020.103792

(3)   V. Shah, R. Keniya, A. Shridharani, M. Punjabi, J. Shah, and N. Mehendale. (2021). **Diagnosis of COVID-19 using CT scan images and deep learning techniques.** *Emerg. Radiol.,* 28(3), 497-505. https://doi.org/10.1007/s10140-020-01886-y

(4)   A. H. MARAY, O. I. Alsaif, and K. H. TANOON. (2022). **Design and Implementation of Low-Cost Medical Auditory System of Distortion Otoacoustic Using Microcontroller.** *J. Eng. Sci. Technol.*, 17(2), 1068-1077.

(5)   N. Alsharman and I. Jawarneh. (2020). **GoogleNet CNN neural network towards chest CT-coronavirus medical image classification.** *J. Comput. Sci.*, 16(5), 620-625. https://doi.org/10.3844/JCSSP.2020.620.625

(6)   H. Maghdid, A. T. Asaad, K. Z. G. Ghafoor, A. S. Sadiq, S. Mirjalili, and M. K. K. Khan. (2021). **Diagnosing COVID-19 pneumonia from x-ray and CT images using deep learning and transfer learning algorithms.** *Proc. SPIE 11734, Multimodal Image Exploitation and Learning*, 117340E, https://doi.org/10.1117/12.2588672

(7)   S. Vaid, R. Kalantar, and M. Bhandari. (2020). **Deep learning COVID-19 detection bias: accuracy through artificial intelligence.** *Int. Orthop.*, 44(8), 1539-1542. https://doi.org/10.1007/s00264-020-04609-7

(8)   A. Sai Bharadwaj Reddy and D. Sujitha Juliet. (2019). **Transfer learning with RESNET-50 for malaria cell-image classification.** *Proc. 2019 IEEE Int. Conf. Commun. Signal Process. ICCSP 2019,* 945-949. https://doi.org/10.1109/ICCSP.2019.8697909

(9)   M. Tan and Q. V. Le. (2019). **EfficientNet: Rethinking model scaling for convolutional neural networks.** *36th Int. Conf. Mach. Learn. ICML 2019*, 2019(June), 10691-10700.

(10) I. A. Saleh, O. I. Alsaif, and M. A. Yahya. (2020). **Optimal distributed decision in wireless sensor network using gray wolf optimization.** *IAES Int. J. Artif. Intell.*, 9(4), 646-654. https://doi.org/10.11591/ijai.v9.i4.pp646-654

(11) E. A. Mohammed and H. A. Ahmed. (2022). **Raspberry pi Based Osteoarthritis Disease classification.** 7(2), 3738-3745.

(12) D. S. Kermany et al. (2018). **Identifying Medical Diagnoses and Treatable Diseases by Image-Based Deep Learning.** *Cell*, 172(5), 1122-1131.E9. https://doi.org/10.1016/j.cell.2018.02.010

(13) F. Wu, et al. (2020). **A new coronavirus associated with human respiratory disease in China.** *Nature*, 579(7798), 265-269. https://doi.org/10.1038/s41586-020-2008-3

(14) G. Marques, D. Agarwal, and I. de la Torre Díez. (2020). **Automated medical diagnosis of COVID-19 through EfficientNet convolutional neural network.** *Appl. Soft Comput. J.,* 96, 106691. https://doi.org/10.1016/j.asoc.2020.106691

(15) K. Ali, Z. A. Shaikh, A. A. Khan, and A. A. Laghari. (2022). **Multiclass skin cancer classification using EfficientNets - a first step towards preventing skin cancer.** *Neurosci. Informatics*, 2(4), 100034. https://doi.org/10.1016/j.neuri.2021.100034

(16) S. Q. Alhashmi, K. H. Thanoon, and O. I. Alsaif. (2020). **A Proposed Face Recognition based on Hybrid Algorithm for Features Extraction.** *Proc. 6th*

Int. Eng. Conf. Sustainable Technol. Dev. IEC, 232-236. https://doi.org/10.1109/IEC49899.2020.9122911

(17) M. A. Yahya et al., **Inventions Transmit Diversity Technique**

(18) Q. A. Al-Haija and A. Adebanjo. (2020). **Breast cancer diagnosis in histopathological images using ResNet-50 convolutional neural network.** *IEMTRONICS 2020 - Int. IOT, Electron. Mechatronics Conf. Proc.,* 50. https://doi.org/10.1109/IEMTRONICS51293.2020.9216455

(19) N. A. Hussein. (2017). **International Conference on Computer and Applications, ICCA 2017.** *2017 Int. Conf. Comput. Appl. ICCA 2017,* 395-399.

(20) M. H. Gauswami and K. R. Trivedi. (2018). **Implementation of machine learning for gender detection using CNN on raspberry Pi platform.** *Proc. 2nd Int. Conf. Inven. Syst. Control. ICISC,* 608-613. https://doi.org/10.1109/ICISC.2018.8398872

3C Tecnología. Glosas de innovación aplicadas a la pyme. ISSN: 2254-4143

Ed.43 | Iss.12 | N.1 January - March 2023

/17/

3C Tecnología. Glosas de innovación aplicadas a la pyme. ISSN: 2254-4143

Ed.43 | Iss.12 | N.1 January - March 2023

295

EVALUATION BIOSYNTHESIZED SILVER NANOPARTICLES BY PHOMATROPICA AGAINST SOME MULTIDRUG RESISTANCE BACTERIAL ISOLATES

Thaer Ali Hussein

Department of Biology, College of Education, Quran, University of Basrah, Basrah, Iraq

thbasra2@gmail.com

Ismail J. Abbass

Department of Biology, College of Education, Quran, University of Basrah, Basrah, Iraq

Afrodet A. Salah

Department of Pathological Analysis, College of Science, University of Basrah, Basrah, Iraq

https://doi.org/10.17993/3ctecno.2023.v12n1e43.296-319

ABSTRACT

Researchers describe the extracellular manufacture of silver nanoparticles (AgNPs) from Phomatropica and its effectiveness against certain multidrug-resistant pathogenic bacteria that were obtained from the Central Laboratory of Quran Hospital. These bacteria were pathogenic.

The AgNPs were synthesized and characterized by scan electrons microscopy, Fourier transform infrared spectroscopy, UV-visiblespectrophotometer that established the mostly spherical nanoparticles synthesis with size range between 55-99 nm. The potential antimicrobial activity was reported vs (Staphylococcus aureus, Pseudomonas aeruginosa, Klebsiella pneumonia, and Escherichia coli)by well diffusion method.AgNPs showed different inhibitory areas at different concentrations, the 50µg/mlconcentration of AgNPsappeared inhibition zones varied from(0-21 mm), while at 100 µg/mlofAgNPs varied between (13-25mm) vs the tested pathogenic bacterial strains in this investigation. Nevertheless, the synergetic impact of AgNPs with antibiotics have beendetected in the increasing the inhibitory impact vs the pathogenic bacteria.

In conclusion, Extracellular biosynthesis appears to be a scalable and sustainable process. Because of their biogenic nature, these Ag-NPs might be a better medication candidate and have the potential to completely eliminate the issue of chemical agents.Antibiotic-resistant bacteria are proliferating at an alarming rate. To address this issue, the development of bactericidal agents is critical. AgNPs may provide a solution for drug-resistant bacteria.

KEYWORDS

Phomatropica; Extracellular; AgNPs ; Biosynthesized ;Multidrug resistant MDR

PAPER INDEX

3C Tecnología. Glosas de innovación aplicadas a la pyme. ISSN: 2254-4143

Ed.43 | Iss.12 | N.1 January - March 2023

1.   INTRODUCTION

Nanotechnology, which deals with particles on the microscopic scale ranging in size from 1 to 100 nanometers, is one of the most active study disciplines in current material research (Saif et al., 2016). AgNPs stand out among the many forms of metallic nanoparticles due to the broad-spectrum antibacterial effects they might produce (Prabhu and Poulose, 2012; Rai et al., 2014; Gupta et al., 2017; Loo et al., 2018). These nanoparticles are able to attach themselves to the membranes of bacteria as well as the cell walls, and they might even penetrate the cells themselves. They cause disruptions in the pathways that are used for signal transduction, they cause damage to cellular structures, and they create reactive oxygen species (Kim et al.,2011; Dakal et al., 2016) In the sectors of health and agriculture, AgNPs were utilized to suppress hazardous microbes (Kim et al., 2012; Mishra and Singh, 2015; Burdusel et al., 2018).

The vast majority of the currently available methods for producing nanoparticles have downsides, including the usage of potentially harmful chemicals and the production of waste that is detrimental to the environment (Iravani et al., 2014; Ahmed et al., 2016). Because of this, there was a significant increase in interest in methods of synthesis that are less harmful to the environment in the most recent few years. Microorganisms that are capable of degrading metal salts and producing nanoparticles of the required size and shape are used in the methods. These microbes include bacteria, fungus, and plants (Azmath et al., 2016)

An alternative that is safe, non-toxic, and beneficial to the environment is the biological reduction of metals, which results in the production of nanoparticles (Banu and Balasubramanian, 2014). Since they possess a high tolerance for metallic and are simple to handle, fungi are promising agents for the biogenic production of AgNPs (AgNPs). They also create a significant number of extracellular proteins, which contribute to the nanoparticles' already impressive level of stability (Balaji et al., 2009; Du et al., 2015; Netala et al., 2016). In comparison to bacterial cultures, fungal cultures provide a number of benefits, including a higher rate of biomass production and the elimination of the need for additional steps to obtain the filtrate (Gade et al., 2008).

2.   MATERIALS AND METHODS

2.1. MATERIALS

Potato dextrose and potato dextrose agar (PDA) have been achieved from (Himedia, India) the antibiotics (Chloramphenicol30mg) was obtained from (Himedia, India), (Ampicillin 10mg) was obtained from (Rosteo, Italy). and silver nitrate (AgNO3) have beenbought fromSigma-Aldrich (Germany) and lactophenol cotton blue from Merke (India).

2.2. ISOLATION AND IDENTIFICATION OF FUNGUS

Phomatropica was isolated from soil sample collected different location in Basrah (Southern Iraq) during the year 2022. Soil specimens was taken from approximately (2-5) cm depth.To isolate soil fungus, the serial dilution method was used. To obtain concentrations between one and four, a one-gram soil specimens has been consecutively diluted in sterilized purified water (10-1 to 10-4). Each dilution was transferred aseptically in 0.1 ml increments onto PDA plates. To distribute the sample evenly, a sterilized glass spreader was used. At pH 6.0 and 28 °C, the plates were cultured for 5-6 days. The fungal isolates are sub-cultured on (PDA) plates to produce pure culture. Pure-isolates are kept in a refrigerator at 4 ºC for future research. The isolated fungus was identified using visual characteristics, microscopic structure, and molecular identification.

2.3. COLONY CHARACTERIZATION

2.3.1. MORPHOLOGICAL AND MICROSCOPIC VIEW OF FUNGUS

Phomatropica which is used in the biosynthesis of AgNPs, was isolated from soil and kept alive by maintaining it on PDA medium at 28 degree centigrade and 4 degree centigrade. The colony morphology and micro morphology of the fungus, including the(color, shape, texture of the mycelia, spore formation pattern, etc), were used to identify it. The fungus was also cultured on a PDA medium at 28 degree centigrade for 10 days to analyze its colony morphology. Slide culture was used to investigate the fungus's micro morphological traits. Cultures were grown on PDA slides and cultured there for five days at 28 degree. The slides were then dyed with lactophenol cotton blue and investigated under a microscope light (Dongyanget al,2021). The taxonomic description led to the identification of the isolated fungus (R. Schneid. & Boerema,1975 ;Vaibhar, 2012).

2.3.2. MOLECULAR IDENTIFICATION

2.3.2.1.DNA EXTRACTION

The extraction of DNA from fungi was performed using the method descrybed by (Alshehri and Palanisamy,2020) and following the protocol instructions included in the kit (Presto™ Mini gDNA Yeast Kit/ Genaid/ USA).

2.3.2.2.POLYMERASE CHAIN REACTION (PCR) USING UNIVERSAL PRIMERS

The fungus's internal transcribed spacer region was amplified using PCR. (Schochet al, 2012).the ITS region of 5.8S rDNA genewas amplified by PCR reaction, using universal forward and reverse

Primer ITS1-F :5'-TCCGTAGGTGAACCTGCGG-3'

and

Primer ITS4- R :5'- TCCTCCGCTTATTGATATGC-3'

(Raja et al, 2017).

2.3.2.3. NCBI BLAST

Basic Local Alignment search tool (BLAST) and National Center for Biotechnology Information (NCBI) both provided insurance for Phomatropica.

2.4. PREPARATION OF BIOMASS

For the manufacture of AgNPs, the Phomatropica was the organism of choice. 250 gm of potato and 20 gm of dextrose are to be added for every liter of purified water. To eliminate the medium component from the mycelia biomass, the mycelia were filtered out of the culture broth using Whatman filter paper No. 1 and washed three times in sterile Milli-Q deionized water. This process was done to remove the medium component. Ten days were spent incubating Erlenmeyer flasks on a rotary shaker at a temp of 25 degree centigrade and 120 revolutions per minute. At a temp of 25 degree centigrade, a 250 ml Erlenmeyer flask was agitated continuously for three days using the same method while it contained 10 g of biomass (wet weight) and 100 ml of deionized water. After incubation, the fungal cell filtrate (FCF) was collected by filtering the solution using Whatman filter paper and a Millipore filter with a pore size of 0.45 microns. Filtrate has beenclam and used in order to bring about the desired results of producing AgNPs.

2.5. FUNGAL MEDIATED SYNTHESIS OF AGNPS

For the creation of AgNPs, 100 ml of fungal cell filtrate (FCF) was mixed with 0.017 gm of AgNO3 (Sigma-Aldrich 99.9%, Germany) to achieve a final amount of 1 mM, and the mixture was then left to sit at 28°C in the dark for 72 hours. As a control, flaks with FCF but no AgNO3 were employed. The creation of AgNPswas verified by the color change response after a 72-hour incubation time in dark conditions. The colorless cell filtrate solution with AgNO3 solution turned into a brown color solution. An evaluation of the supernatant using a UV-visible spectrophotometer provided qualitative evidence of the decrease of Ag+.Using a UV-visible spectrophotometer, the absorbance of the sample supernatant was determined between 300 and 900 nm. The reaction mix was then centrifuged three times for 20 minutes at 6000 rpm with distilled water to concentrate the AgNPs. The pellet that was left behind was then dried in a hot air furnace at 40 degree centigrade. After drying, the sample was placed

in a glass vial together with nanoparticles that had been collected by scratching with a sterile spatula. AgNPs were then gathered for additional characterization.

2.6. SILVER NANOPARTICLE DETECTION AND CHARACTERIZATION

By transforming from colorless to light brown, the biosynthesized (AgNPs) in the fungal free-cell filtrate were visually evaluated. They were further validated by a UV-Vis spectrophotometer, scan electrons microscope (SEM), and Fourier transforms infrared spectroscopy (FT-IR).

2.6.1. SONICATION

After it has been cleansed and centrifuged, researchers employ it in our method, which involves using sound energy to agitate particle or discontinuity fibers that are suspended in liquid. In most cases, frequencies higher than 20 kilohertz (kHz) are used. Ultrasonication may be carried out with the assistance of either an ultrasonic bath or an ultrasonic probe (sonicator). For our experiment, we used an ultrasonic bath made by Binder in Germany (Deborah and Chung, 2017)

2.6.2. ASSAY USING UV-VISIBLE SPECTROPHOTOMETRY

The UV-Vis spectrophotometer (CECIL (CE,7200, England)) was used to measure the bio-decrease of Ag+ in aqueous solution after the fungal free-cell filtrate treated with AgNO3 had been incubated for 72 hours. 0.1 ml of the filtrate was obtained during the reduction process, diluted with deionized water, and then placed in a quartz UV-VIS cuvette. 300 to 900 nm was the range of the scanning. Free-cell filtrate that hadn't been altered served as a control. This was handled at the University of Basrah's Polymer Research Center.

2.6.3. FTIR (FOURIER TRANSFORM INFRARED SPECTROSCOPY) ANALYSIS

The free-cell filtrate underwent Fourier Transform Infrared (FTIR) (Bruker Tensor 27, Germany) examination after 72 hours of incubation. To identify the functional groups of the stabilizing and biomolecules capping the AgNPs, FT-IR measurements were conducted. After centrifuging the specimen solution having the nanoparticles at 5,000 rpm for 1200 second, it was filtered. The produced solid material was subsequently crushed with potassium bromide (KBr), and pellets were created. The pellet was examined using FTIR. This was handled at the University of Basrah's Polymer Research Center.

2.6.4. SCAN ELECTRONS MICROSCOPE (SEM)

This electron microscopy unit at Iran's University of Tehran employed a scan electrons microscope (SEM) (TESCAN MIRA3, French) to describe the size and shape of AgNPs(caroling et al., 2013).

2.7. ANTIBACTERIALACTIVITY OF AGNPS

Using the agar well diffusion assay method, the potential of AgNPs was evaluated for their antibacterial effectiveness (Perez et al., 1990). We evaluated four types of multidrug resistant pathogenic bacteria, including Escherichia coli, Klebsiella pneumonia, Staphylococcus aureus and Pseudomonas aeruginosa. Each overnight-grown bacterial culture was streaked with swabs before being placed on sterile Muller-Hinton agar (MHA) plates. Utilizing a sterilized stainless steel Cork borer, wells in agar plates with a diameter of 5 mm were created (local,Iraq). Two concentrations of silver nanoparticle solutions (50 and 100 g/ml) have beenapplied to the wells. After incubation for 1 day at 37 degree centigrade, the wells have beeninvestigated for the existence of inhibitory zones, and the diameters of these placeshave been determined.

2.8. ASSAY FOR DETERMINING SYNERGISTIC EFFECTS.

To assess the bactericidal effectiveness of these nanoparticles both alone and in conjunction with antibiotics, the disk diffusion technique was utilized to measure the synergistic effect of extracellularly generated AgNPs with routinely utilized antibiotics (Ampicillin, Chloramphenicol) (Devi and Joshi, 2012). conventional antibiotic disks (Ampicillin, Chloramphenicol). Standard antibiotic discs (6 mm in diameter) were placed over the MHA medium that had been injected with test organisms after being impregnated with 20 l of freshly made AgNPs. Positive controls were standard antibiotic disks. Filtrate devoid of fungi served as the adverse control. For 24 to 48 hours, these plates were incubated at 37 degree centigrade. The inhibition places of the control and treatment plates have been assessed after incubation. The assays were all carried out in triplicate.

2.9. EVALUATION OF THE INCREASE IN FOLD AREA

The improvement in fold area was determined by comparing the mean contact area of the inhibitory place that was formed by an antibiotic by itself and by an antibiotic in combination with AgNPs. The fold increase area was determined utilizing the formula (B2- A2) / A2, that A represents the inhibition place diameter generated by the activity of antibiotics on their own, and B represents the inhibition place diameter induced by the activity of antibiotics in combination with AgNPs (Birla et al., 2009).

2.10. STATISTICAL ANALYSIS

We utilized the Statistical Package for the Social Sciences (SPSS), version 2020 (Copyright IBM Inc., USA). The least substantial difference (LSD) test was used in the statistical data analysis that was performed utilizing Guide. This test was used to compare the substantial differences that existed between the averages with a probability threshold of p less than 0.01.

3.   RESULTS

3.1. FUNGAL IDENTIFICATION

The discipline of biological science is seeing fast advancements in the use of nanotechnology. In the course of this research, Phomatropica cell filtrate was used to effectively produce AgNPs. The fungus was extracted from the soil and cultivated at a temperature of 28 degrees Celsius on PDA medium. The fungus has been recognized as Phomatium due to the features of its colony morphology (the colonies appeared white, and with regular shape, mycelium pale white color (fig 1a), in the single colony there was a large number of conidia deposit in the middle of the colony) (Fig. 1b) and its micromorphology (Pycnidia, conidia subglobose, flaskshaped with conspicuous dark circumval.
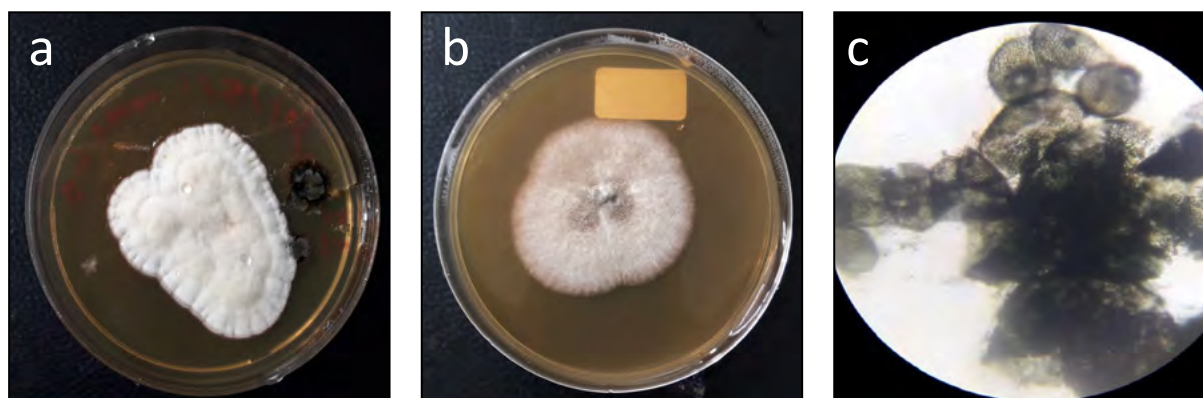
Figure 1. Morphology of Phomatropica

(a,b) Macroscopic morphology (7d and 28 degree centigrade); (c) microscopic morphology (40 x).

3.2. GENETIC IDENTIFICATION OF PHOMATROPICA

3.2.1. GENOMIC DNA EXTRACTION

The technique of electrophoresis for DNA extraction under UV transilluminator showed clear isolated DNA of Phomatropica (Figure2).
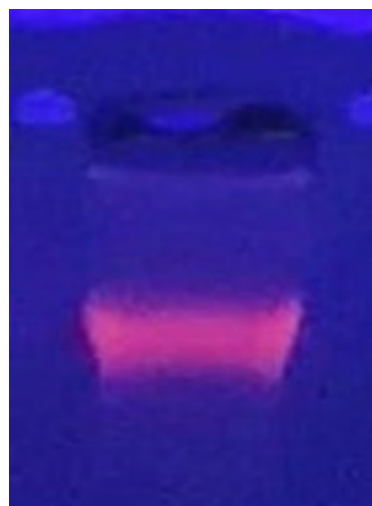
Figure 2. 0.8% of agarose gel Electrophoresis showed total DNA band of Phomatropica.

3.2.2. PCR AMPLIFICATION

The results of the molecular diagnosis of the isolate after electrolysis on agarose gel(1%) showed that the results of the DNA chain reaction using ITS1-ITS4 interfacial primers showed the existence of a

clear bundle resulting from the process of duplication of these genes, and the binding of the primer to its complement sequence in the DNA template ~550 bp (Figure 3).

Figure 3. The electrophoresis of PCR.

3.2.3. SEQUENCING OF ITS GENE

The ITS nucleotidesequence is 100% homology toPhoma tropica (accession number JF 923821.1) as registered in the GenBankdatabase. Based onmolecular and morphological features, the fungal has been determined asPhomatropica.

3.3. SILVER NANOPARTICLE (AGNP) BIOSYNTHESIS

After 24 hours of incubation in the dark condition, P.tropica isolate's extracellular AgNPsbiosynthesis was visually detected to modify the color of the culture

supernatant in comparison to the control. Figures 4 and 5 displayed AgNPs harvest derived from isolation, which ranged in hue from colorless to brown.
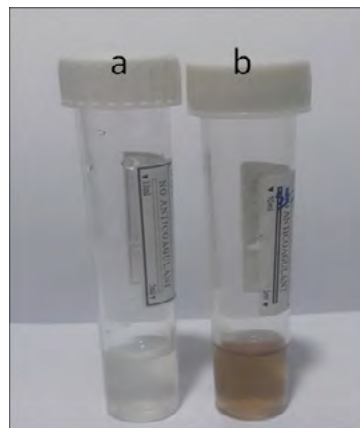
Figure 4. Color change observed in fungal cell filtrate (FCF) of P.tropica after exposure to AgNO3, a- without 1mM AgNO3 b- after 24h treated with AgNO3

Figure 5. Nanoparticles synthesized byP. tropica

3.4. CHARACTERIZATION OFBIOSYNTHESISAGNPS

3.4.1. SONICATION OF AGNPS SOLUTION

Figure 6 shows how 0.001g of AgNPs were blended with 5 ml of purified water and sonicated for 15-20 minutes using an ultrasonic bath.
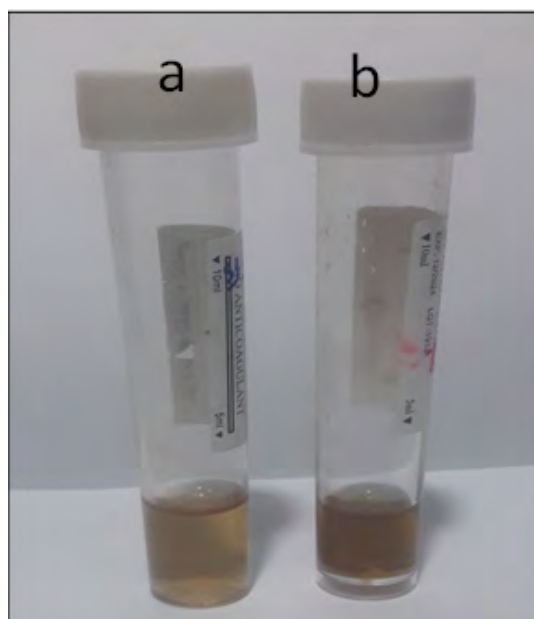
Figure 6. the AgNPs solution, the right(a) one before sonication and the left (b) one after sonication

3.4.2. UV-VISIBLE SPECTROPHOTOMETRY ANALYSIS

By employing a UV-visible spectrophotometer to conduct qualitative testing on the supernatant, the reduction of silver ions was verified. After 24 hours, 1 ml of the sample supernatant was removed, and the absorbance has been determined between 300 and 900 nm utilizing a UV-visible spectrophotometer (fig.7). At 423 nm, the absorbance peak was noted.
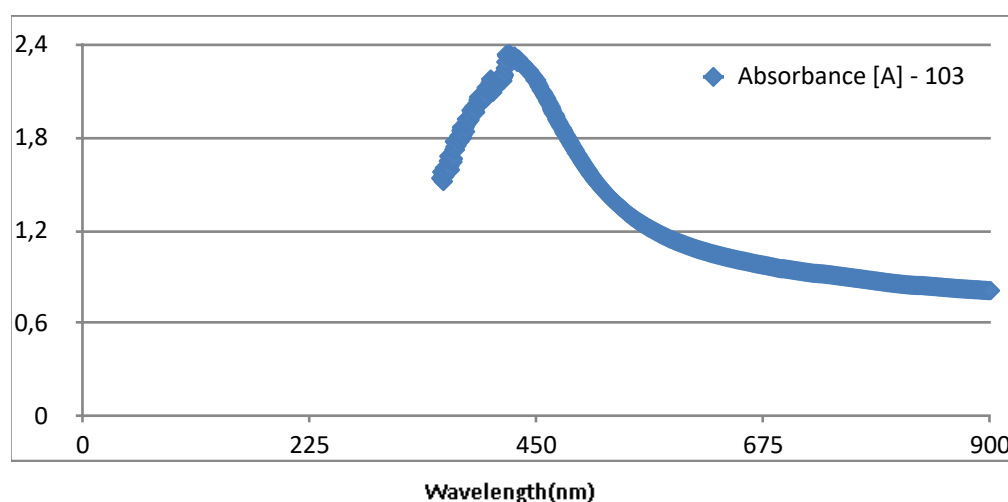
Figure 7. UV-Visible spectra of produced AgNPs by fungi.

3.4.3. SCAN ELECTRONS MICROSCOPE (SEM)

Images collected utilizing SEM with a magnification of 200Kx indicated that the AgNps have been collected and generally spherical in form, with diameters ranging from 55 to 99 nm.
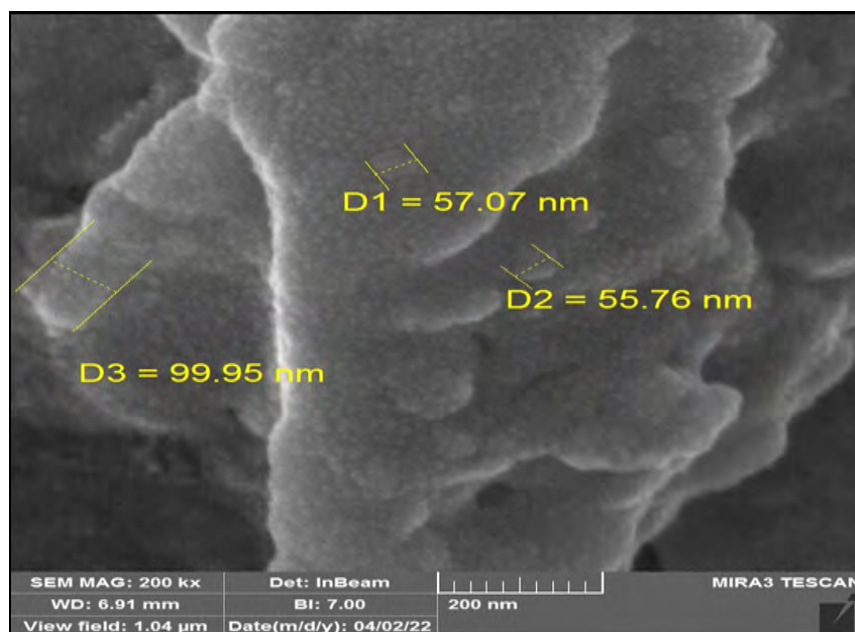
Figure 8. The biosynthesized AgNPs in the fungal free-cell filtrate were depicted in a SEM micrograph as spherical shapes aggregated with size ranges from 55 to 99 nm (magnification 200 K X).

3.4.4. FTIR ANALYSIS

It has been proven that FT-IR experiments have the potential to detect putative biomolecules essential in the bio removal of silver ions and the stability of AgNPs. The FTIR spectrum study indicates that the supernatant of Phomatropica includes biomolecules, which are responsible for the conversion of silver ions into AgNPs (Figure 9). The results of this research also demonstrated the existence of eight distinct stretch bands, and their values are as follows: 3358.43, 2925.48, 2845.13, 1745.26, 1645.62, 1539.88, 1455.99, and 1078.01. (cm-1).
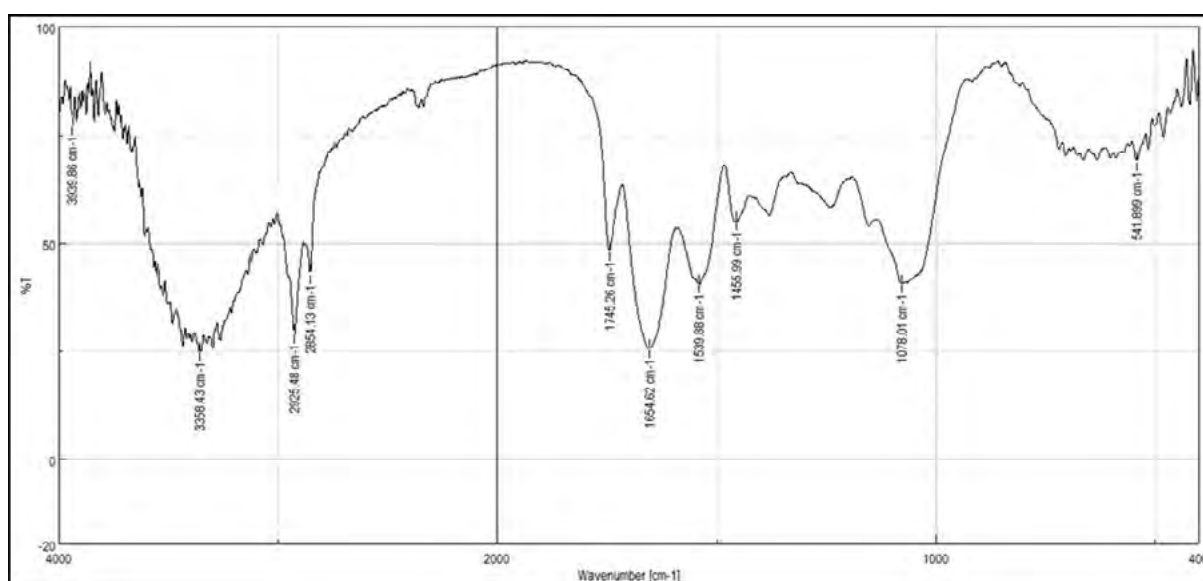
Figure 9. FTIR spectrum of AgNPs biosynthesized by P. tropica with distinct peaks.

3.5. AGNPS HAVE ANTIBACTERIAL ACTIVITIES

The studied strains of Gram negative and Gram positive bacteria were resistant to the biosynthesized AgNPs' antibacterial action. According to the findings, bacterial growth was slightly less inhibited by AgNPs at a 50 g/ml concentration (0-21 mm inhibition zones) than it was by a 100 g/ml concentration (13-25 mm inhibition zones) (Fig.10). AgNPs had the lowest growth inhibitory activity vsK. pneumonia and the highest vsP. aeruginosa. Without AgNPs, no inhibitory zones could be seen in the fungal free cell filtrate (FCF). Similar findings were reported using AgNPs produced by Papulaspora pallidula by Tawfik and Ahmad (2015).
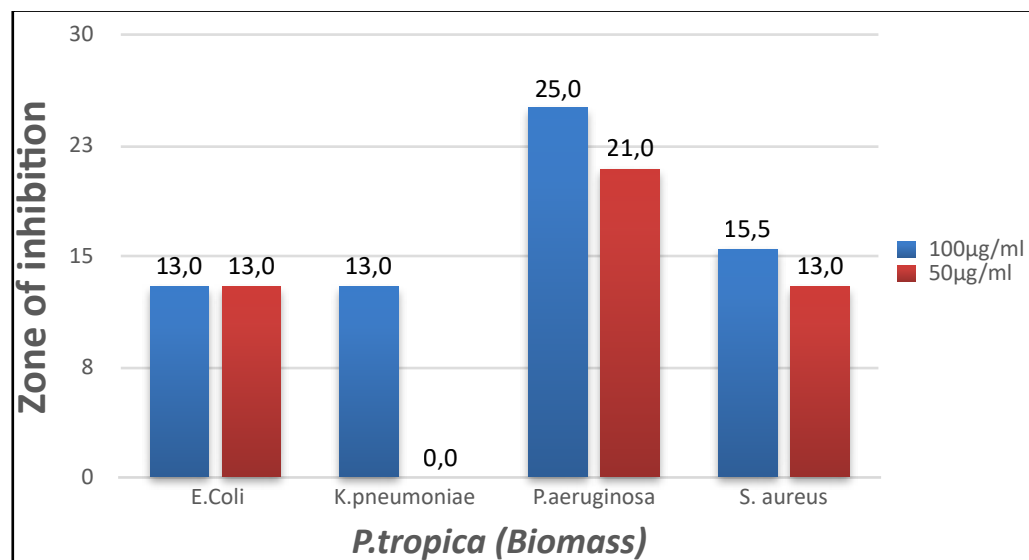
Figure 10. The growth inhibition zones that four strains of human pathogenic bacteria displayed in response to two nanoparticles of silver doses (AgNPs) produced by the fungus P. tropica.

3.6. COMBINATION EFFICACY OF AGNPS WITH AMPICILLINAND CHLORAMPHENICOL

This particular research utilizing the disk diffusion technique, we tested the effectiveness of these AgNPs in conjunction with antibiotics at concentrations of 50 and 100 g/ml versus gram-negative and gram-positive bacteria. The width of the inhibitory zone, measured in millimeters, surrounding antibiotic disks with and without resistance vs test bacteria is illustrated in Fig. 11 and 12. In all of the instances, the inhibition places diameter for antibiotics alone and in conjunction with AgNPs demonstrated a substantial increase in fold area. This was the case with ampicillin and chloramphenicol at concentrations of 50 and 100 µg/ml of AgNPs (Table 1). The synergistic activity of AgNPs at 50 µg/ml concentration with antibiotics were found to be higher vsE. Coli and P. aeruginosa as compared to S.aureusand. K. pneumonia The synergistic activity of AgNPs at 100µg/ml concentration with antibiotics have been detected to be greatervsP. aeruginosa and as E. coli compared to K. pneumonia andS. aureus.

Table 1. Mean inhibition place (mm) brought about by various antibiotics with/withoutAgNPs created utilizing the fungus p tropicavs the test organisms

Bacterial strains	Inhibition Zone (mm)											
	AgNPs 50µg/ml						AgNPs100µg/ml					
	Ampi cillin	Am + AgNPs	Incre ase in fold area	chlor amph enicol	C+ AgNPs	Incre ase in fold area	Ampi cillin	Am + AgNPs	Incre ase in fold area	chlor amph enicol	C+ AgNPs	Incre ase in fold area
E. coli	-	12	3	24	25	0.085	-	12	3	24.5	25.5	0.083
K. pneumonia	-	7.5	0.563	22.5	22.5	0	-	8.5	1.007	23	24.5	0.134
P. aeruginosa	-	10.5	2.063	16	20.5	0.641	-	13.5	4.063	18	25	0.929
S.aureus	15.5	18	0.349	24.5	26	0.126	15.5	18.5	0.425	23	26.5	0.327

The increase in fold area of places of inhibition has been determined by comparing the inhibition place created by antibiotic only with the places of inhibition obtained for antibiotics paired with AgNPs manufactured utilizing the fungal isolate.

* The values represent the averages of three replicates.

differences that are significant at P 0.01.**

-The diameter of the disc, which was measured to be 6 millimeters, was utilized in the lack of the growth of bacteria inhibition places in order to compute the fold increase in columns 1, and 7.
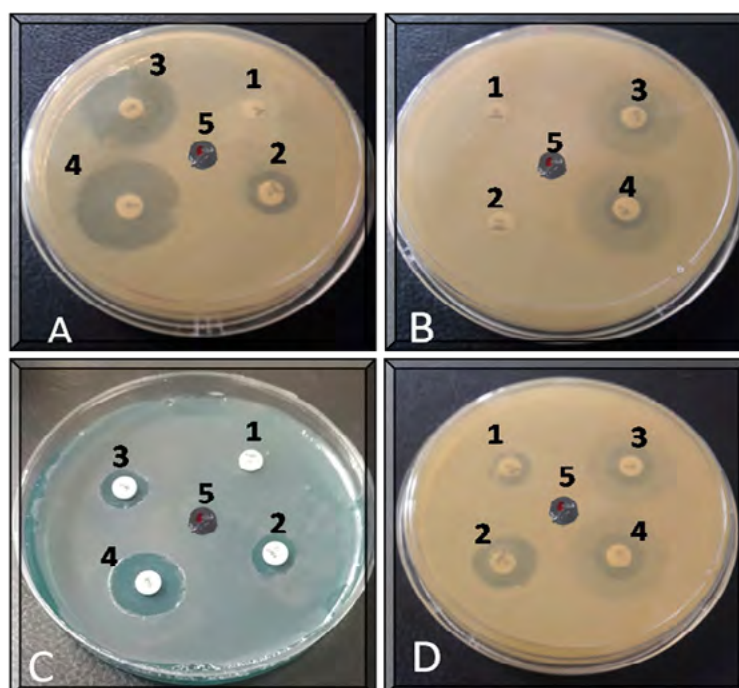
Figure 11. Antibacterial activities of biosynthesized nanoparticles of silver at amount (50 g/ml) vsE. coli (A), K. pneumonia (B), P. aeruginosa (C), S. aureus (D) commercial antibiotic Ampicillin (1) and a combination of AgNPs with Ampicillin (2) commercial antibiotic chloramphenicol (3) and a combination of AgNPs with chloramphenicol (4) Fungal cell-free filtrate (5)
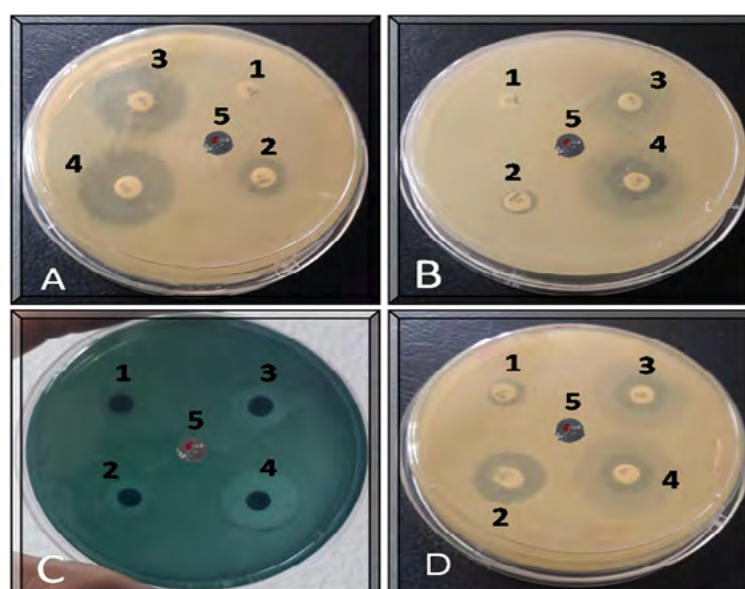
Figure 12. The inhibition places (mm) displayed by biosynthesized nanoparticles of silver at concentrations (100g/ml) vsE. coli (A), Klebsiella pneumonia (B), P. aeruginosa (C), and S. aureus (D) commercial antibiotic Ampicillin (1) and an AgNPs/Ampicillin combination (2) commercial antibiotic chloramphenicol (3) and an AgNPs/Chloramphenicol combination (4) Fungal cell-free filtrate (5).

4. DISCUSSION

4.1. ISOLATION AND IDENTIFICATION OFPHOMATROPICAFROM SOIL

Phomatropica has been chosen for the production of nanoparticles because it is simple to extract from soil, it is straightforward to cultivate on straightforward media such as PDA, and most importantly, it has consistent biochemical properties (Rai et al, 2009). In addition, there is no research done so far on selecting Phomatropica for the production of AgNPs. This is something that has to be done.

(Boerema et al., 2004) conducted research on the Phoma species based on the physical and cultural aspects of each species. The recognition of Phoma depending only on morphological characteristics was relatively inconsistent, which contributed to confusion over its identity. Because of this, molecular-based approaches were used, which turned out to be a superior choice for the detection and investigation of genetic differences amongst fungi (deGruyter et al., 2009; Aveskamp et al., 2010).

Several of the most frequent options for phylogenetic inference at the genus level or lower is bi-parental, nuclear ITS regions. This is because these areas have a greater rate of base replacement than the genes found in most organelles. The phylogenetic connections between Phoma and the groups to which it is closely related were examined in great detail utilizing ITS sequence data (Iryini et al,2009 :Aveskamp et al, 2009).

4.2. BIOSYNTHESIS AND CHARACTERIZATIONOF AGNPS

Since dangerous bacteria have been showing signs of antibiotic resistance during the past ten years, researchers are concentrating on creating new antibacterial substances. Ag-NPs as antibacterial agents have emerged as viable candidates in the current medical landscape (Duran et al. 2007). AgNPs can be produced by microorganisms like fungus, which has significant promise for numerous applications (Alghuthaymiet al., 2015). Due to their capacity to create AgNPs, many Phoma species were shown to be able to synthesis nanoparticles of silver (Aniketet al, 2013 ; Sudhiret al,2016 ; Aniketet al, 2011).This is the first account of the environmentally friendly extracellular production of AgNPs by P. tropica. As evidenced by the color shift from colorless to brownish after 3 days of incubation after being exposed to a solution of 1 mM AgNO3, the current investigation demonstrated that the chosen fungus, P. tropica, displayed a great potential for the AgNPs synthesis in culture medium. These results are consistent with earlier research utilizing several fungi species (Asemet al. 2017;Tejal Barkhade.. 2018 ;Bahimbaet al., 2011: Mohamed et al, 2021).

The addition of AgNO3 to the fungal free-cell filtrate caused a color shift as a result of the excitation of silver's surface plasmon resonance vibration that verified the decrease of silver ions as reported by (Chitra and Annadurai,2013).

4.3. UV-VISIBLE SPECTROPHOTOMETRY ANALYSIS

The current research demonstrated that UV-Vis spectrophotometry examination revealed a maximum with great absorbance at 423 nm, which stated that the investigated fungus had been replicating AgNPs, indicating that the production of AgNPs has been complete after 3 days of incubation with free-cell filtrate. This is in line with a few other pieces of art that have been done (Mohamed et al 2021; Aniket et al, 2013).

When compared to previous studies, it appears that there have been some variances in the features of the AgNPs generated by distinct species of fungus. These variations have been seen in the AgNPs (Birla et al. 2009; Chitra and Annadurai, 2013; Maliszewska et al., 2009; Raheman et al., 2011). These variations might be attributable to the origin of the fungal isolates or strains as well as the environment under which they grew (Marambio-Jones and Hoek, 2012). Based on the findings of Neethu et al. (2018), the amount of fungal mycelium was directly correlated to the amount of AgNP that was synthesized.

4.4. BIOSYNTHESIZED DESCRIPTION AGNPS BY SCAN ELECTRONS MICROSCOPY (SEM)

Different reaction parameters affect the form and size of biosynthesized nanoparticles of silver in solution.

The AgNPsbiosynthesized morphology by the chosen fungus was scattered with size of 55-90 nm, as shown by SEM ostly spherical and pictures.

Numerous studies have noted that different fungus species, pH levels, and temperatures affect the AgNPs shape and size that are generated (Martinez-Castanonet al., 2008; Marambio-Jones and Hoek, 2010; Muhsin and Hachim, 2015 ;Aniketet al, 2013).

4.5. FT-IR ANALYSISA OF THE BIOSYNTHESIZED AGNPS

P. tropica has been shown to contain biomolecules that turn silver ions into AgNPs. These biomolecules occur in 8 different stretching bands, which are: 3358.43, 2925.48, 2845.13, 1745.26, 1645.62, 1539.88, 1455.99, 1078.01, and others (cm-1).

The distinctive hydrogen-linked OH set that could be the result of the formation of nanoparticles in an aqueous phase, is connected to the bending vibrations of the OH alcohol bonds, phenols, and the N-H stretching vibration of main protein amides, all of which make a contribution to the peak at 3358.43cm-1. These vibrations are responsible for the existence of the peak.

The C-H stretching associated with the methylene protein set and the N-H stretching associated with the amine salt are both candidates for the causes of the maxima at 2925.48 and 2845.13 cm-1, respectively. This finding is undeniably linked to the modification of the electric surroundings of the methylene and methane sets that was brought about by the close proximity of the AgNPs and carbonyl. The stretching vibrations of C=O was the source of the experimental group that could be seen at 1745.26 cm-1. In the FTIR spectrum, there are two bands that are visible. These bands have been connected with the stretching vibration of the amide I band and the amide II band of the protein, respectively. The bands have a wavelength of 1645.62 cm-1 and 1539.88 cm-1. (Joshi,2012) suggests that the absorption peak at 1455.99 cm-1 might be related to geometric bending vibration of amino acid residue sets with free protein carboxylate sets -COO- (carboxylate ion), 1078.01 (ethers, esters, and C-O alcohol stretched oxalic acids), and C-N stretched of aliphatic amines.

4.6. AGNPSANTIBACTERIAL ACTIVITY ON PATHOGENIC BACTERIA

At two different doses (100 g/ml and 50 g/ml), the biosynthesized AgNPs were shown to limit the development of human pathogenic bacterial strains, which were examined. This was another finding from the present investigation. In contrast, the effectiveness of AgNPs as an antibacterial agent was inconsistent. Even though the mechanism by which AgNPs prevent bacteria from growing is not extensively established, it is possible that it is linked to the impact of Ag+ by leading to damage of bacterial cell membranes, the damage of enzymes, or the conformational changes of DNA. This is what has been proposed by other study results (Kim et al. 2007; Marambio-Jones and Hoek, 2010).

4.7. COMBINATION EFFICACY OF AGNPS WITH AMPICILLIN AND CHLORAMPHENICOL

According to increased fold area, the biosynthesized AgNPs and the medicines ampicillin and chloramphenicol significantly boosted efficiency vs the chosen human pathogenic bacteria (Birla et al. 2009). These results are consistent with those of earlier research that investigated the synergic impact of AgNPs produced from a variety of fungal species when used in conjunction with a selection of various commercialized antibiotics and put to the test versus Gram-negative and Gram-positive bacteria (Fayaz et al., 2010; Devi and Josh, 2011; Gudikandula et al., 2015; Shareef et al., 2017).

(Fayaz et al. 2010) also showed an increase in the antibacterial activity of chloramphenicol, erythromycin, kanamycin, and ampicillin when used in conjunction with AgNPsvs Salmonella typhi, Escherichia coli, Staphylococcus aureus, and Micrococcus luteus.

(Devi and Joshi, 2011) showed an improvement in the antibacterial activity of ciprofloxacin, chloramphenicol, erythromycin, and methicillin when combined with biosynthesized AgNPs versus Enterococcus faecalis, Salmonella enterica, Streptococcus pyogenes, and Staphylococcus aureus.

5. CONCLUSION

The production of AgNPs using P. tropicawas investigated in the current study this finding is the first for this fungus species in Iraq. The generated AgNPs demonstrated activity versus Gram-positive and Gram-negative human pathogenic bacteria throughout a wide range. This fungus shows potential as a natural source for the synthesis of AgNPs, which have applied in the medical product and pharmaceutical manufacturing industries.

6. ACKNOWLEDGMENT

REFERENCES

(1)   Ahmed, S., Ahmad, M., Swami, B. L., and Ikram, S. (2016). **A review on plants extract mediated synthesis of silver nanoparticles for antimicrobial applications: a green expertise**. *J Adv Res.,* 7, 17-28. https://doi.org/10.1016/j.jare.2015.02.007

(2)   Alshehri, B. and M. Palanisamy. (2020). **Evaluation of molecular identification of *Aspergillus* species causing fungal keratitis**. *Saudi J Biol Sci.,* 27(2), 751-756. https://doi.org/10.1016/j.sjbs.2019.12.030

(3)   Aniket. G*, Swapnil. G*, Nelson.D†andMahendra.R. (2013). **Screening of different species of Phomafor Synthesis of Silver nanoparticles**. 13, 1-33.

(4)   Aniket. G, Mahendra. Rai a &Sulabha.K. (2011). **Phomasorghina, a Phytopathogen Mediated Synthesis of Unique Silver Rods.**

(5)   Asem. A. M1, Saad. EL-Din.H, Amr. F*, Mamdouh S. Eand Salem S. S. (2017). **Extracellular Biosynthesis of Silver Nanoparticles Using Aspergillus sp. and Evaluation of their Antibacterial and Cytotoxicity.** 5, 1-12.

(6)   AveskampMM, deGruyterJ, WoudenbergJHC, VerkleyG J M & Crous P W. (2010). **Highlights of the Didymellaceae: A polyphasic approach to characterise Phoma and related pleosporalean genera**, *Stud Mycol*, 65, 1-60. https://doi.org/10.3114/sim.2010.65.01

(7)   Aveskamp M M, Verkley G J, de Gruyter J, Murace M A,Perelló A et al. (2009). **DNA phylogeny reveals polyphyly of Phoma section Peyronellaea and multiple taxonomic novelties**, Mycologia, 101, 363-382.

(8)   Azmath, P., Baker, S., Rakshith, D., and Satish, S. (2016). **Mycosynthesis of silver nanoparticles bearing antibacterial activity**. *Saudi Pharm. J.,* 24, 140-146. https://doi.org/10.1016/j.jsps.2015.01.008

(9)   Balaji, D. S., Basavaraja, S., Deshpande, R., Mahesh, D. B., Prabhakar, B. K., andVenkataraman, A. (2009). **Extracellular biosynthesis of functionalized silver nanoparticles by strains of Cladosporium cladosporioides fungus**. C*olloids Surf. B: Biointerfaces.* 68, 88-92. https://doi.org/10.1016/j.colsurfb.2008.09.022

(10)   Banu, A. N., and Balasubramanian, C. (2014). **Biosynthesis of silver nanoparticles using Bacillus thuringiensis against dengue vector, Aedes aegypti (Diptera: Culicidae)**. Parasitol. Res. 113, 311-316. https://doi.org/10.1007/s00436-013-3656-0

(11)   Birla, S., Tiwari, V.V., Gade, A.K., Ingle, A.P., Yadav, A.P., & Rai, M.K. (2009). **Fabrication of silver nanoparticles by Phomaglomerata and its combinedeffect against Escherichia coli, Pseudomonas aeruginosa and Staphylococcus aureus.** *Letter of Applied Microbiology*, 48, 173-179. http://dx.doi.org/10.1111/j.1472-765X.2008.02510.x

(12)   Boerema et al. (2004). **PHOMA IDENTIFICATION MANUAL Differentiation of Specific and Infra-specific Taxa in Culture.** 113, 1-470

(13)   (1975). **Phoma tropica R. Schneid. & Boerema.** *Phytopathol. Z*, 83, 361-365.

(14)   Boerema G H, de Gruyter J, Noordeloos M E &Hamers M EC. (2004). **Phoma identification manual: Differentiation of specific and infra-specific taxa in culture,** 475.

(15)   Burdu¸sel, A. C., Gherasim, O., Grumezescu, A. M., Mogoant,ã, L., Ficai, A., and Andronescu, E. (2018). **Biomedical applications of silver nanoparticles: an up-to-date overview**. Nanomaterials, 8(9), 681. https://doi.org/10.3390/nano8090681

(16)   B.V. Bhimba. Navaneetha. N and Priyanka.S. (2011), **Characterization and antibacterial analysis of silver nanoparticles synthesized by the marine fungi Hypocrea lixii MV1 isolated from mangrove sediment soil**. 477-479.

(17)   Caroling G., Tiwari S.K., Ranjitham A.M. and Suja R. (2013). **Biosynthesis of silver anoparticles using aqueous broccoli extract-characterization and study of antimicrobial, cytotoxic effects**. *Asian J Pharm Clin Res*., 6(4), 165-172.

(18) Chitra, K., &Annadurai, G. (2013). **Bioengineered silver nanobowls using Trichoderma viride and its antibacterial activity against Gram-positive and Gram-negative bacteria**. *Journal of Nanostructure Chemistry*, 39, 3-9. http://dx.doi.org/10.1186/2193-8865-3-9

(19) Dakal, T. C., Kumar, A., Majumdar, R. S., and Yadav, V. (2016). **Mechanistic basis of antimicrobial actions of silver nanoparticles**. *Front. Microbiol*., 16, 1831. https://doi.org/10.3389/fmicb.2016.01831

(20) Deborah D.L. Chung, (2017). **Carbon Composites, Composites with carbon fiber, Nanofiber, and Nanotubes, (Second Edition).**

(21) DeGruyter J., Aveskamp M.M.,Woudenberg J.H.,Verkley G.J., Groenewald J.Z. et al. (2009). **Molecular phylogeny of Phoma and allied anamorph genera: Towards a reclassification of the Phoma complex.** *Mycol. Res.*, 113, 508-519.

(22) Dongyang W*, Baiji X, Lin W, Yidi Z, Lijun L* &Yanmin Z*. (2021). **Fungus-mediated green synthesis of nano-silver using Aspergillus sydowii and its antifungal/antiproliferative activities.** Sci. Rep., 11, 10356. https://doi.org/10.1038/s41598-021-89854-5

(23) Du, L., Xu, Q., Huang, M., Xian, L., and Feng, J.-X. (2015). **Synthesis of small silver nanoparticles under light radiation by fungus Penicillium oxalicum and its application for the catalytic reduction of methylene blue**. *Mater. Chem. Phys.,* 160, 40-47. https://doi.org/10.1016/j.matchemphys.2015.04.003

(24) Duran, N., Alves, O.L., De Souza, G.I.H., Esposito, E. and Marcato, P.D. (2007) **Antibacterial effect of silver nanoparticles by fungal process on textile fabrics and their effluent treatment.** *J Biomed Nanotechnol,* 3, 203-208. http://dx.doi.org/10.1080/19430892.2011.628573

(25) Fayaz AM, Balaji K, Girilal M, Yadav R, Kalaichelvan PT, Venketesan R. (2010). **Biogenic synthesis of silver nanoparticles and their synergistic effect with antibiotics: a study against grampositive and gram-negative bacteria**. *Nanomedicine,* 6, 103-109.

(26) Gade, A. K., Bonde, P., Ingle, A. P., Marcato, P. D., Durán, N., and Rai,M. K. (2008). **Exploitation of Aspergillus niger for Synthesis of Silver Nanoparticles**. *J. Biobased Mater. Bioenergy,* 2, 243-247. https://doi.org/10.1166/jbmb.2008.401

(27) Gupta, R. K., Kumar, V., Gundampati, R. K., Malviya, M., Hasan, S. H.,Jagannadham, M. V., et al. (2017). **Biosynthesis of silver nanoparticles from the novel strain of Streptomyces Sp. BHUMBU-80 with highly efficient electroanalytical detection of hydrogen peroxide and antibacterial activity**. *J.Environ. Chem. Eng.,* 5, 5624-5635. https://doi.org/10.1016/j.jece.2017.09.029

(28) Iravani, S., Korbekandi, H., Mirmohammadi, S. V., and Zolfaghari, B. (2014). **Synthesis of silver nanoparticles: chemical, physical and biological methods**. *Res. Pharm. Sci.*, 9, 385-406.

(29) Irinyi L, Kovics G J & Sandor E, (2009). **Taxonomical re-evaluation of Phoma-likesoybean pathogenic fungi.** *MycolRes*, 113, 249-260.

(30) Joshi P. (2012). **The anticancer activity of chloroquine-gold nanoparticles against MCF-7 breast cancer cells**. *Colloids and Surfaces B: Biointerfaces,* 95, 195-200. https://doi.org/10.1016/j.colsurfb.2012.02.039

(31) Kim, S. H., Lee, H. S., Ryu, D. S., Choi, S. J., and Lee, D. S. (2011). **Antibacterial activity of silver-nanoparticles against Staphylococcus aureus and Escherichiacoli**. *Korean J. Microbiol. Biotechnol*. 39, 77-85.

(32) Kim, S. W., Jung, J. H., Lamsal, K., Kim, Y. S., Min, J. S., and Lee, Y. S.(2012). **Antifungal effects of silver nanoparticles (AgNPs) against various plantpathogenic fungi**. *Mycobiology*, 40, 53-58. https://doi.org/10.5941/MYCO.2012.40.1.053

(33) Kim, J.S., Kuk, E., Yu, K.N., Kim, J.H., Park, S.J., Lee, H.J., Kim, S.H., Park, Y.K., Park, Y.H., & Hwang, C.Y. (2007). **Antimicrobial effects of silver nanoparticles**. *Nanomedicine*, 3. 95-101.http://dx.doi.org/10.1016/j.nano.2006.12.001

(34) Kinthokoi, K. J. (2019). **Silver nanoparticles and their antibacterial activity synthesized using selected medicinal plant extracts**. 20, 1-91.

(35) Krishna. G*, Ram.P. M, Samatha.B, Shesha. V.Sathya. S. S. L. (2015). **Fungus-Mediated Synthesis of Silver Nanoparticles and Their Activity against Gram Positive and Gram Negative Bacteria in Combination with Antibiotics**. Health Sciences, 12(7). http://dx.doi.org/10.14456/WJST.2015.67

(36) LamabamSophiya Devi and S. R. Joshi*. (2012). **Antimicrobial and Synergistic Effects of Silver Nanoparticles Synthesized Using Soil Fungi of High Altitudes of Eastern Himalaya**. Mycibiology, 28, 27-34. https://www.tandfonline.com/loi/tmyb20

(37) Loo, Y. Y., Rukayadil, Y., Nor-Khaizura, M. A. R., Kuan, C. H., Chieng, B.W., Nishibuchi, M., et al. (2018). **In vitro antimicrobial activity of green synthesized silver nanoparticles against selected gram-negative foodborne pathogens**. *Front. Microbiol.,* 9:1555. https://doi.org/10.3389/fmicb.2018.01555

(38) Maliszewska, I., Szewezk, K., &Waszak, K. (2009). **Biological synthesis of silver nanoparticles**. *Journal of Physics*, 146, 1-6. http://dx.doi.org/10.1088/1742-6596/146/1/012025

(39) Marambio-Jones, C., & Hoek, E.M.V. (2010). **A review of the antibacterial effects of silver nanomaterilas and potential implications for human health and the environment**. *Journal of Nanoparticles Research*, 12, 1531-1551. http://dx.doi.org/10.1007/s11051-010-9900-y

(40) Matrinez-Castanon GA, Nino-Martinez N, Matinez-Gutierrez F., Martinez-Mendoza, JR, and Ruiz F. (2008). **Synthesis and antibacterial activity of silver nanoparticles with different sizes**. *Journal of Nanoparticles Research*, 10, 1343-1348.

(41) Mishra, S., and Singh, H. B. (2015). **Biosynthesized silver nanoparticles as a nanoweapon against phytopathogens: exploring their scope andpotential in agriculture**. *Appl. Microbiol. Biotechnol,* 99, 1097-1107. https://doi.org/10.1007/s00253-014-6296-0

(42) Mohamed.A. Y, Abdallah M. E, Abd El-Rahim, M.A. El-Samawaty. (2021). **Biosynthesis of silver nanoparticles using Penicilliumverrucosum and analysis of their antifungal activity**. 2125, 2123-2127.

(43) Muhsin TM. and Hachim AK. (2015). **Characterization and antibacterial efficacy of silver nanoparticles biosynthesized by the soil fungus Curvularia tuberculata**. *NanoScience Technology*, 1, 5-11.

(44) Netala, V. R., Bethu, M. S., Pushpalatah, B., Baki, V. B., Aishwarya, S., Rao, J.V., et al. (2016). **Biogenesis of silver nanoparticles using endophytic fungus Pestalotiopsis microspora and evaluation of their antioxidant and anticancer activitie**. *Int. J. Nanomed.* 11, 5683-5696. https://doi.org/10.2147/IJN.S112857

(45) Neethu S. Midhun SJ. Radhakrishnan EK. and Jyothis M. (2018). **Green synthesized silver nanoparticles by marine endophytic fungus Penicillium polonicum and its antibacterial efficacy against biofilm forming, multidrug-resistant Acinetobacter baumanii**, *Microb Pathog*., 116, 263-272.

(46) Perez, C., Paul, M., &Bazerque, P. (1990). **Antibiotic assay by agar well diffusion method**. *Acta Biology and Medical Experiments*, 15, 113-115.

(47) Prabhu, S., and Poulose, E. K. (2012). **Silver nanoparticles: mechanism of antimicrobial action, synthesis, medical applications, and toxicity effects**. *Int. Nano Lett.,* 2, 32. https://doi.org/10.1186/2228-326-2-32

(48) Raheman, F., Deshmukh, S., Ingle, A., Gad, A., & Raj, M. (2011). **Silver nanoparticles: Novel antimicrobial agent synthesized from an endophytic fungus Pestalotia sp. Isolated from leaves of Syzygiumcumini (L)**. *Nanoscience and Biomedical Engineering*, 3, 174-178. http://dx.doi.org/10.5101/nbe.v3i3.p174-178

(49) Rai, M. K. Deshmukh, P. Gade, A. Ingle, A. Kövics, G. J. and Irinyi, L. (2009). **Phoma Saccardo: Distribution, secondary metabolite production and biotechnological applications**. *Critical Reviews in Microbiology*, 35(3), 182-196. https://doi.org/10.1080/10408410902975992

(50) Rai, M., Kon, K., Ingle, A., Duran, N., Galdiero, S., and Galdiero, M. (2014). **Broad-spectrum bioactivities of silver nanoparticles: the emergingtrends and future prospects**. *Appl. Microbiol. Biotechnol*. 98, 1951-1961. https://doi.org/10.1007/s00253-013-5473-x

(51) Raja, H.A., et al. (2017). **Fungal Identification Using Molecular Tools: A Primer for the Natural Products Research Community**. *J Nat Prod.,* 80(3), 756-770.

(52) Saif, S., Tahir, A. and Chen, Y. (2016). **Green Synthesis of Iron Nanoparticles and Their Environmental Applications and Implications**. *Nanomaterials*, 6(11), 209.

(53) Schoch, C.L., et al. (2012). **Nuclear ribosomal internal transcribed spacer (ITS) region as a universal DNA barcode marker for Fungi**. *Proc Natl Acad Sci, 1*09(16), 6241-6246.

(54) Shareef. J. U, Navya R.M, Anand. S, Dinesh.R. (2017). **Synthesis and characterization of silver nanoparticles from Penicillium sps**. 11931, 11923-11932. https://doi.org/10.1016/j.matpr.2017.09.113

(55) (2020). **SPSS - Statistical Package for Social Sciences.** *User's Guide for Statistic,* 26.

(56) Dhiraj S. Patil, Dattatray A. Chopade, Manoj A. Kumbhalkar. (2018). **Experimental investigation of effect of cerium oxide nanoparticles as a fuel**

additive in cottonseed biodiesel blends. *MAYFEB Journal of Mechanical Engineering*, 1, 1-12.

(57) Sudhir. S, Aniket. G and Mahendra. R. (2016). **Large-scale synthesis and antibacterial activity of fungal-derived silver nanoparticles**. *Environmental Chemistry Letters*, 15, 427-434. https://doi.org/10.1007/s10311-016-0599-6

(58) Tejal, B, (2018). **Extracellular Biosynthesis Of Silver Nanoparticles Using Fungus Penicillium Species**. *International Journal of Research-GRANTHAALAYAH*, 6(1), 277–283. https://doi.org/10.29121/granthaalayah.v6.i1.2018.1615

(59) Vaibhar. (2012). **A study of phylogentic variation among Indian phomatropica species by PAPD -PCR and ITS-Rdna sequencing**, 188, 167-194

/18/

3C Tecnología. Glosas de innovación aplicadas a la pyme. ISSN: 2254-4143

Ed.43 | Iss.12 | N.1 January - March 2023

3C Tecnología. Glosas de innovación aplicadas a la pyme. ISSN: 2254-4143

Ed.43 | Iss.12 | N.1 January - March 2023

3C Tecnología. Glosas de innovación aplicadas a la pyme. ISSN: 2254-4143

Ed.43 | Iss.12 | N.1 January - March 2023

RETRACTED PAPER

3C Tecnología. Glosas de innovación aplicadas a la pyme. ISSN: 2254-4143

Ed.43 | Iss.12 | N.1 January - March 2023

RETRACTED PAPER

3C Tecnología. Glosas de innovación aplicadas a la pyme. ISSN: 2254-4143

Ed.43 | Iss.12 | N.1 January - March 2023

3C Tecnología. Glosas de innovación aplicadas a la pyme. ISSN: 2254-4143

Ed.43 | Iss.12 | N.1 January - March 2023

RETRACTED PAPER

3C Tecnología. Glosas de innovación aplicadas a la pyme. ISSN: 2254-4143

Ed.43 | Iss.12 | N.1 January - March 2023

3C Tecnología. Glosas de innovación aplicadas a la pyme. ISSN: 2254-4143

Ed.43 | Iss.12 | N.1 January - March 2023

/19/

3C Tecnología. Glosas de innovación aplicadas a la pyme. ISSN: 2254-4143

Ed.43 | Iss.12 | N.1 January - March 2023

336

COPPER AT SILICA CORE - SHELL NANOPARTICLES AS ANTIBACTERIAL AGENTS BY SOL-GEL CHEMICAL METHODS

Al- Ajeeli, Alaa F. Hashim

Department of Physics, College of Education for Pure Sciences, Tikrit University, Salahuddin, Iraq

alaa.f.hashim@st.tu.edu.iq - https://orcid.org/0000-0003-3688-0663

Razeg, Khalid Hamdi

Department of Physics, College of Education for Pure Sciences, Tikrit University, Salahuddin, Iraq

khalid.hr55@tu.edu.iq

Fuad Tariq Ibrahim

Department of Physics, College of Science, University of Baghdad, Baghdad, Iraq

ABSTRACT

Core-shell Cu@sio2 nanoparticles were created by a chemical reaction in a sol gel, and their ability to inhibit S. aureus and E. coli bacteria was tested, when synthesized and characterized using ultraviolet-visible spectroscopy, a copper band could be seen before and after encapsulation at wavelengths of 625 nanometers and 635 nanometers, which are surface plasmonic resonant frequency bands, respectively. The production of Cu @Sio2 core shell nanoparticles was further confirmed using field emission scanning electron microscope (FESEM) pictures. The core shell nanoparticles have a mean size of 66 nanometers and a spherical shape, as shown in TEM. The X-ray diffraction patterns for the nanoparticles, which show face-centered cubic (FCC) of copper, match the crystal structure of Cu@sio2 we discovered using fourier transform infrared (FT-IR) spectroscopy, the fourier transform infrared interaction between the silica and the synthesized copper NPs was investigated. This revealed the capping of the CuNPs by SiO2. The inhibition zone was evident as a result of the activities of these compounds (14, 14, 16, and 20) and (24, 24, 28, and 30) against Escherichia coli bacteria and Staphylococcus aureus bacteria, respectively.

KEYWORDS

Copper Nanoparticle, Silica, Antibacterial, Inhibition Zone.

PAPER INDEX

1.   INTRODUCTION

The modern concepts for producing nanoparticles with the required size and form are developing as, science and technology grow more quickly, particularly in the fields of nanotechnology and material science. [1-4] Metallic nanoparticles are gaining popularity due to their different physical and chemical characteristics, as well as their wide variety of applications. There is an increase in interest in working with metals, polymer particles, metallic nanoparticles, etc. because of they have several applications in material science due to their tiny size and a huge interaction surface. surrounding medium affects the features of nanoparticles, and the necessary attributes can be introduced by changing the ambiance. The scientific discipline of nanotechnology has enormous promise for use in medicine. Because nanoscience and biology are comparable to nature, their combination will not only help in the battle against harmful microbes, but may also lead to a shift in how infectious disease is treated. [5] [6] Numerous biomedical, and pharmaceutical fields, including diagnostics, genetic engineering, drug delivery, biomarkers, bioimaging, cosmetics, antibacterial, cancer, immunology, cardiology, cancer treatment, bioremediation, water treatments, energy production, and other infectious diseases, can benefit from the use of nanoparticles. [7-9] Paints typically contain different metals and metal oxides as NPs because they have antifungal, anti-algal, and antibacterial effects. Exhibiting water resilience, fewer toxic effects, and antibacterial capabilities through attaching to bacterial cell proteins. [10]

There are generally two ways to synthesize nanoparticles of Sio_2. Since silica has been widely used as an efficient anticorrosive protective material, numerous attempts have been made to coat metal nanoparticles with silica shells of customizable thickness. Due to its excellent compatibility with various materials, great chemical and thermal stability, and huge surface area, silica is a very important material. SiO_2 with copper exhibited excellent corrosion resistance [11] Multi-infectious bacteria can produce antimicrobial resistance by adhering to various substrates like medical equipment or biological surfaces like host organism and forming sticky exopolymeric substances (EPS) called microbial biofilms [12].

Copper nanoparticles are reported to be more efficient than iron oxide and nickel nanoparticles in the attack against pathogenic bacteria that produce biofilms and multidrug resistance. Copper and copper oxide nanoparticles exhibit antibacterial efficacy against the microorganism's Staph aureus, E. coli, Pseudomonas aerugi, and B. subtilis the microorganism's Bacillus nosa that produce biofilms. [13-16].

Copper nanoparticles are useful for a variety of purposes, including medicinal, agricultural, and other industries, and they are inexpensive, these include antifungal, antiviral, antibiotic, anticancer, and photocatalytic uses[17].

In this study, $Cu@Sio_2$ core-shell nanoparticles are fabricated using the chemical sol-gel method [18-19]. Ultrasound is used to disperse copper nanoparticles before mixing them with silica. The final spherical $Cu@Sio_2$ core -shell the spherical shape was observed as well as measuring the antibacterial activities of Escherichia coli and Staphylococcus aureus bacteria.

2.   EXPERIMENTAL PARTS

2.1. SOL-GEL PROCESS

Synthesis of Copper Nanopowder in Chemical Sol Gel (average particle size 30 nanometer ≥99.9%), (TEOS) tetraethylorthosilicate 98%, 0.5 mol (Merck), ethyl alcohol (99.9%), ascorbic acid (99%), cetyltrimethylammonium bromide ≥98%, NH3 ammonium hydrate (25%), also utilized was deionized water.

Experiment was carried out 24C° temperature. Shows the composition of core-shell used in the experiment. The technique of synthesizing core-shell is as follows. First, the copper solution is made up of 180 mg of Cu nanopowder combined with 10 ml of distilled water, (0.004 M) cetyltrimethylammonium bromide (CTAB) diluted in 10 ml of water, and (0.02 M) ascorbic acid mixed in 20 ml of water. and fully dispersed with ultrasound. Then, while stirring, 32.0 ml of ethanol and 0.5 ml of TEOS were combined. 1.5 ml of ammonium hydroxide was combined after stirring for around one hour and the reaction was then completed after another 24 hours of stirring. The core-shell nanoparticles underwent multiple filtering and washing steps using distilled water and ethanol.lastlly,80 °C was used to dry powder to produce Cu@sio2 core-shell.

2.2. CHARACTERIZATION TECHNIQUES

Utilizing X-ray diffraction, Cu@SiO$_2$ core-shell peaks were verified. (XRD; Cu, 30 kV, 15 milliampere); Rigaku Corporation), To make specimens, the sol-gel-fabricated core-shells were disseminated in ethanol. The core-shell shapes were verified using a transmission electron microscope and fesem. Then, measurements using energy dispersive X-ray spectroscopy (EDS) produced to confirm the production of the SiO2 shell and Copper nanopowder core. The following techniques were used to characterize the prepared Cu @Sio$_2$ core shell nanostructures.

2.3. EQUATIONS USED TO ANALYSIS THE XRAY RESULTS.

According to the findings of the XRD examination, the Bragg law Equation (1) was used to compute the d-spacing (the lattice planes distance between the atoms), and the Debye-Scherrer Equation was used to calculate the average crystallite size. (2)

$$2d \ sin\theta = n\lambda \qquad (1)$$

where d is the interplanar distance between atoms, n is an integer (n= 1), and k is an integer (k= 0.15418 nanometer for Cu Ka).

$$D = \frac{K\lambda}{FWHM \ COS\theta} \qquad (2)$$

where K is a constant number factor (0.89), λ= 0.15418 nanometers for Cu Ka, FWHM is the full width at half maximum, θ is the diffraction angle, and (a) is the lattice constant, while D is the average crystallite size. (a) For cubic crystals was calculated by Equation (3) [17]

$$a = d\sqrt{h^2 + k^2 + l^2} \qquad (3)$$

Miller's index (h k l) represents cartesian coordinates for cubic crystals.

2.4. TESTING FOR ANTIMICROBIAL EFFECTIVENESS

The antibacterial capabilities of the composite membrane were tested using the diffusion method against the gram-positive bacterium. Staphylococcus aureus and gram-negative bacteria a kind of bacteria called Escherichia coli. [20]. A disk-shaped test specimen and an untreated control were created with a 10 mm diameter and sterilized in an autoclave for 15 minutes at 120 °C for the disk diffusion procedure. After that, they were placed on individual agar media with E. coli and S. aureus cultures and for 24 hours at 37 °C while the inhibitory zone was monitored.

3.   3. RESULTS AND DISCUSSION

3.1. X-RAY DIFFRACTION

Among the most effective and simple methods for determining out a compound's crystallite properties is X-ray diffraction (XRD). XRD analysis of synthesized copper nanopowder using ascorbic acid and CTAB as stabilizing and reduction agents, confirmed that the finished item is made of metal. The Cu-NPs' XRD patterns are depicted in Fig. 1, and they are very comparable to those seen in JCPDS Copper. 04-0836 (43.6, 50.8, and 74.4) correspond to the metallic Cu planes (111), (200), and (220). The outcome of XRD examination shows that the produced Cu-NPs have a face-centered cubic structure (FCC), in addition to copper peaks, other X-ray diffraction peaks appear after the process of coating the metal with silica figure 2 depicts the Cu@sio2 core shell's XRD pattern. nanostructure as it was created using the sol-gel process. Peaks seen at 2θ values of 21.4, 22.59, 31.8, 45.54, 53.97, 54.55, 56.6, 66.15 and 75.47 correspond to (002), (211), (600), (332), (440),(404), (620),(325)and (435) planes of Cu@Sio_2. These peaks were quite comparable to those of the standard JCPDS Card No. 045-0131 for the sio2 [21].

The JCPDS (Joint Committee on Powder Diffraction Standards) was used to calculate the broadening of the diffraction peaks matching to the strongest reflections, which indicates the mean size of nanocrystals. From the XRD diffraction pattern observed for nanoparticles, the Scherrer equation was applied to calculate the crystallite size.

The results of the XRD examination show that the Cu-NPs that were created had a structure with a face-centered cubic (FCC) with a lattice constant of 0.36 nanometers that matches well with the standard lattice parameter (a = 0.3615 nanometers). JCPDS card no, 04-0836, the average size of copper crystals and cu@sio2 nanoparticles(D) calculated by using equ.1, the Scherrer equation were about 47.08 and 58.9 respectively [21].
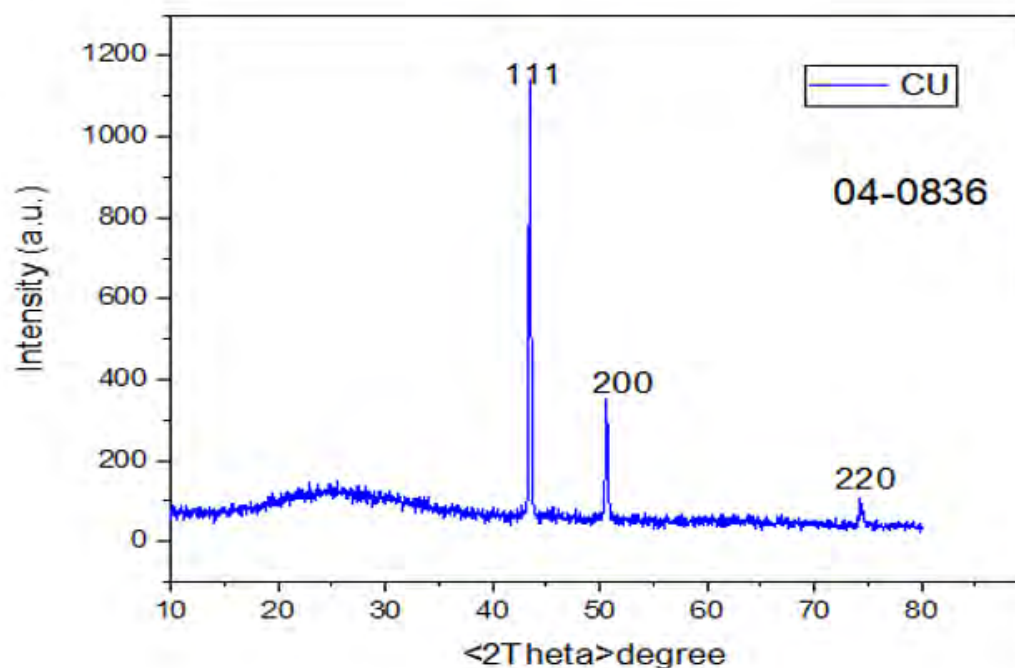
Figure 1. XRD patterns of CuNps
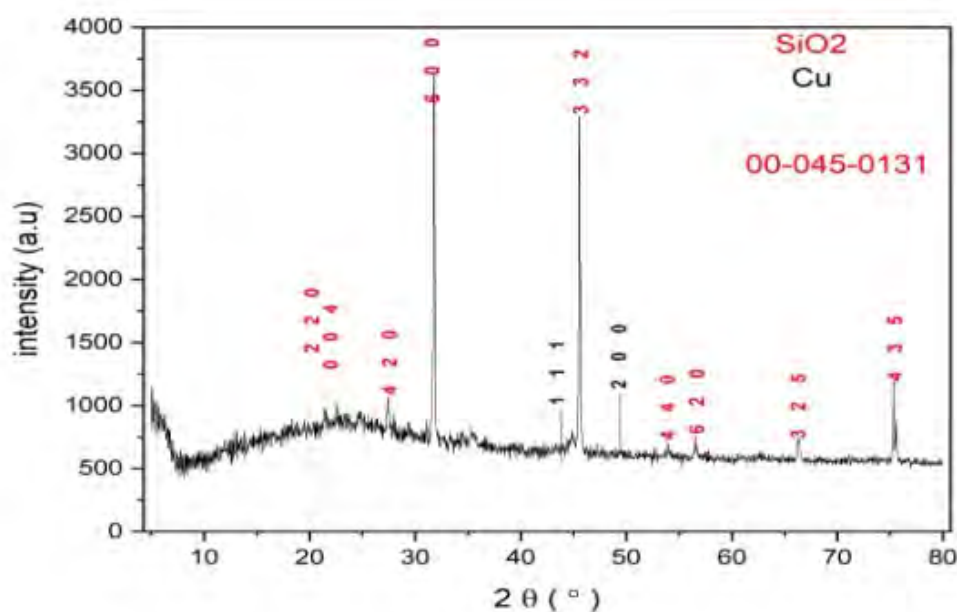
Figure 2. XRD patterns of silica-coated Cu nanoparticles

3.2. UV VISIBLE SPECTROSCOPY

Small metallic nanoparticles exhibit visible electromagnetic wave absorption through surface-based collective conduction electron oscillation [18]. The surface plasmon resonance effect is what's happening here. The advantage of this effect is that it can be used as a tracer for the presence of metallic nanoparticles with a

straightforward UV-visible spectrometer, as demonstrated by the size dependence of the plasmonic resonance of the absorption of copper nanoparticles and core-shell particles of copper / silica prepared by chemical sol-gel method.The results from UV-visible demonstrate a red shift in the absorption spectra caused by the increase in particle size caused by the increased silica coating that the synthesis of $Cu@SiO_2$ nanostructure exhibited in the figure displayed SPR peak at 635 nanometer, when it was at the wavelength of 630 nanometer for cu nanoparticles. Fig:3
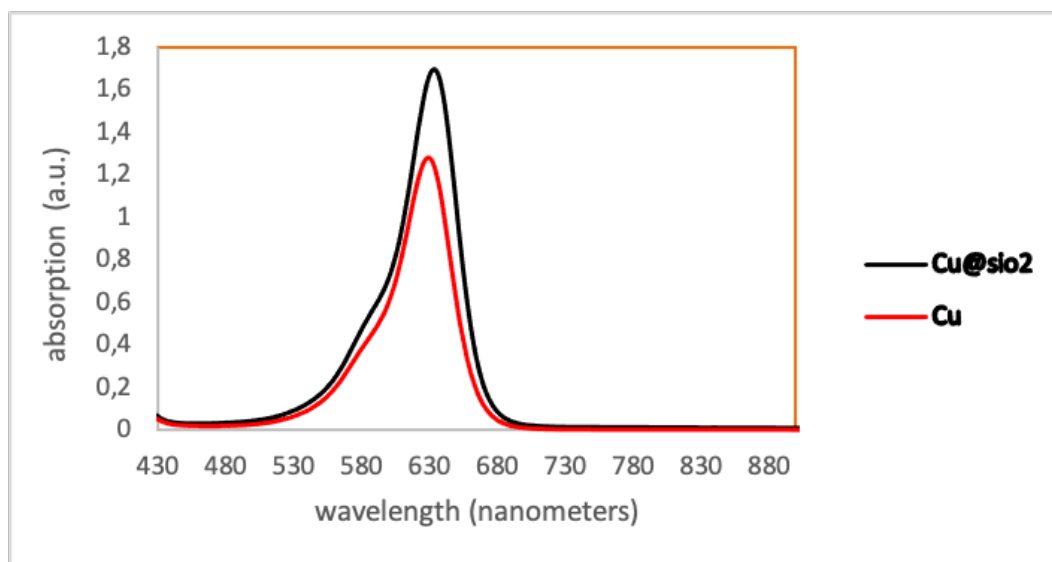
Figure 3. UV-vis absorption spectra for Cu and Cu @Sio2

3.3. FTIR

The FTIR spectra of silica (Sio_2) fig:3a and 3b Cu @ Sio_2 .The wide band at 3356 cm^{-1} in the FTIR of Sio2 corresponds to the O-H stretching vibration. of the condensation of a silanol group (Si-OH) as well as the residual absorbed water in the FTIR spectra of SiO2 and Cu @ Sio2 in Figure. Water molecules' bending and vibrations as they absorbed into the surface of the silica particles caused a small peak at 1666 cm^{-1}. [22].

There were characteristic peaks at 1029 cm-1, 794 cm-1, and 474 cm-1, which represented, respectively, the bending oscillation of O-Si-O, the asymmetrical extending vibration of Si-O-Si, and the symmetric stretching vibration of O-Si-O [23]. The vibrations of the silanol groups stretching are connected with the band at 1029 cm^{-1},while the peak at 1396 cm^{-1} is connected to the stretching of the Si-O bond [22]. Similar to the Sio_2 spectrum, FTIR spectrum of cu @ sio_2 nanoparticles in Figure4b likewise showed typical vibrations, but peaks were displaced to a higher number of waves, such as peaks of 2916 cm^{-1} to 2920 cm^{-1},peaks between 1423 cm^{-1} and 1458 cm^{-1} as well as the peaks between 1639 and 1666 cm^{-1}. This bond can be seen at 1666 cm^{-1} before to the production of nanoparticles and has since migrated to 1639 cm^{-1}.

The results may confirm that the copper nanoparticles were synthesized and encapsulated with silica by the Stober's method; The change in wave numbers was

due to C=C stretching and reveals coordination with Cu nanoparticles. Moreover, FTIR peak in Fig. 4b indicates that a peak of 624 cm $^{-1}$ It may refer to copper nanoparticles [24- 26].
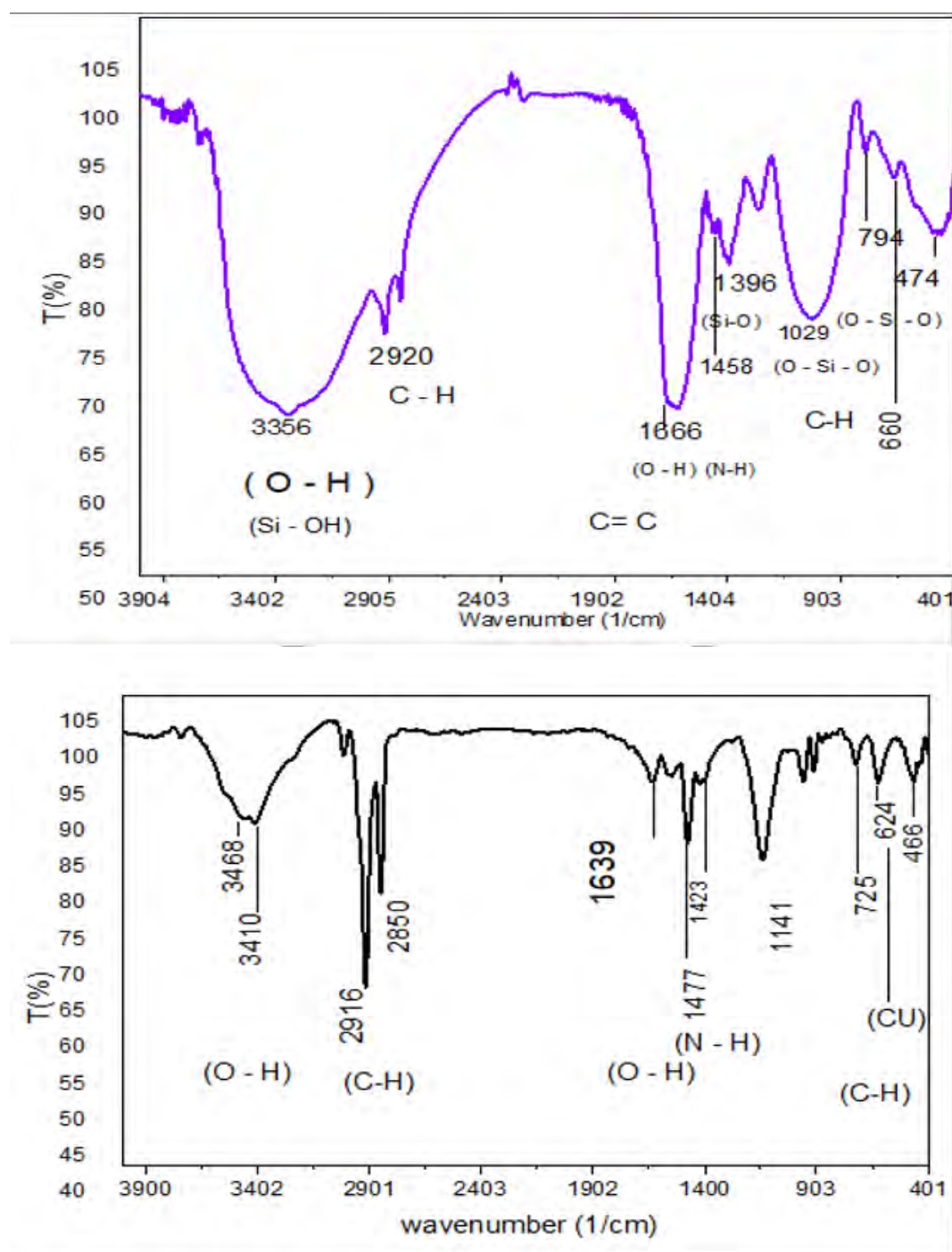
Figure 4. ftir spactra of a- Sio2 b- cu@Sio2

3.4. TEM.

The analyses of the TEM pictures are useful equipment for evaluating the size and form of the prepared nanoparticles. Fig. 4 displays common TEM pictures of cu@Sio2 NPs, their look is spherical in shape with a cover around them, as in Fig. 5, and they also offer a wide range of sizes cu @sio$_2$ core shell dimeter is between (35 and 120) nanometer and rate 66 nanometer as in the fig.6.
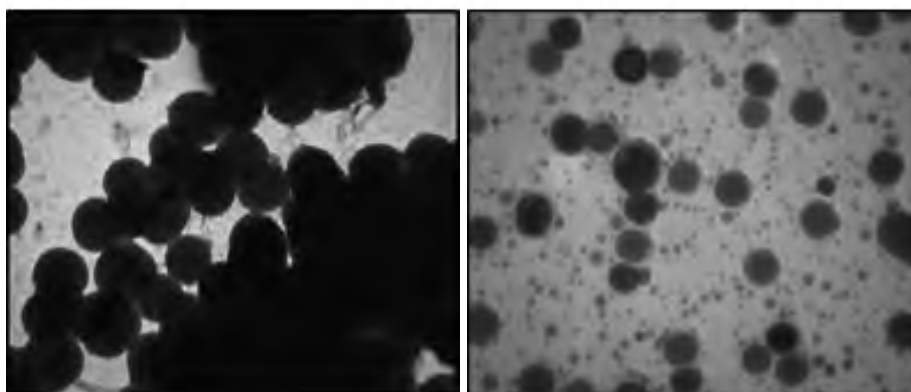
Figure 5. TEM images of Cu@Sio2 core shell NPs
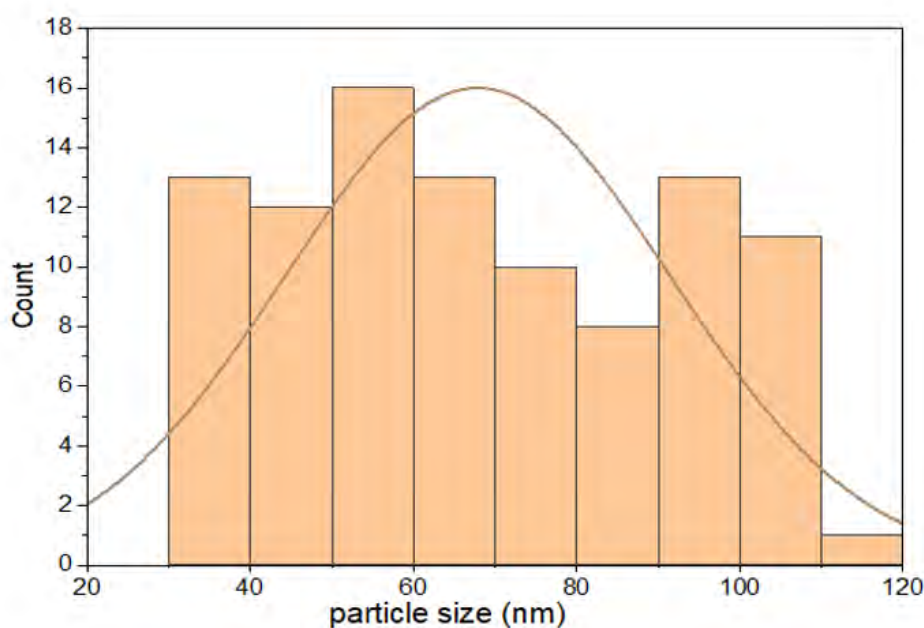
Figure 6. TEM Histograms of Cu@Sio2 core shell NPs

3.5. FESEM-EDX

By using feSEM-EDX analyses, the existence of Cu@sio$_2$ core-shell was established, and the outcome seems to show a spherical agglomeration in the particle size distribution, with diameters ranging from 80 to 184 nanometers. High magnification examination shows more details, though, including the fact that these copper nanoclusters are made up of smaller nanoparticles with good homogeneity, whose average diameter is roughly 152 nanometers (figs. 7 and 8 show this). The copper that was generated and the silica that it was coated in can both be clearly seen in the EDX analysis in Fig. 9. It should be noted that the copper-metal NPs were silicate-coated.
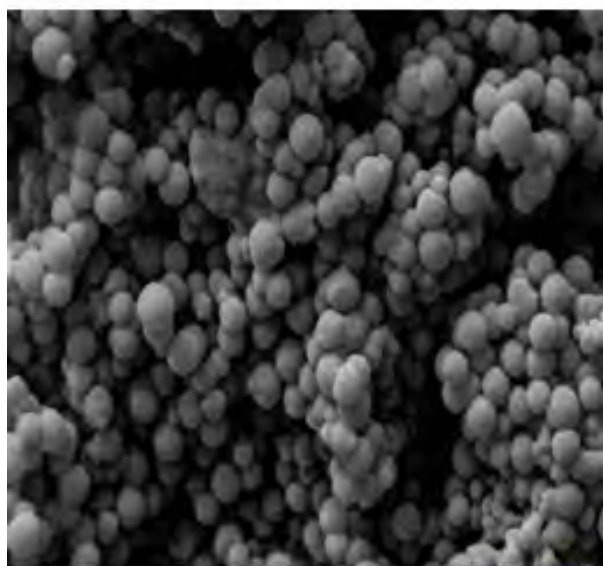
Figure 7. fesem showing the copper nanoparticle capping with silica
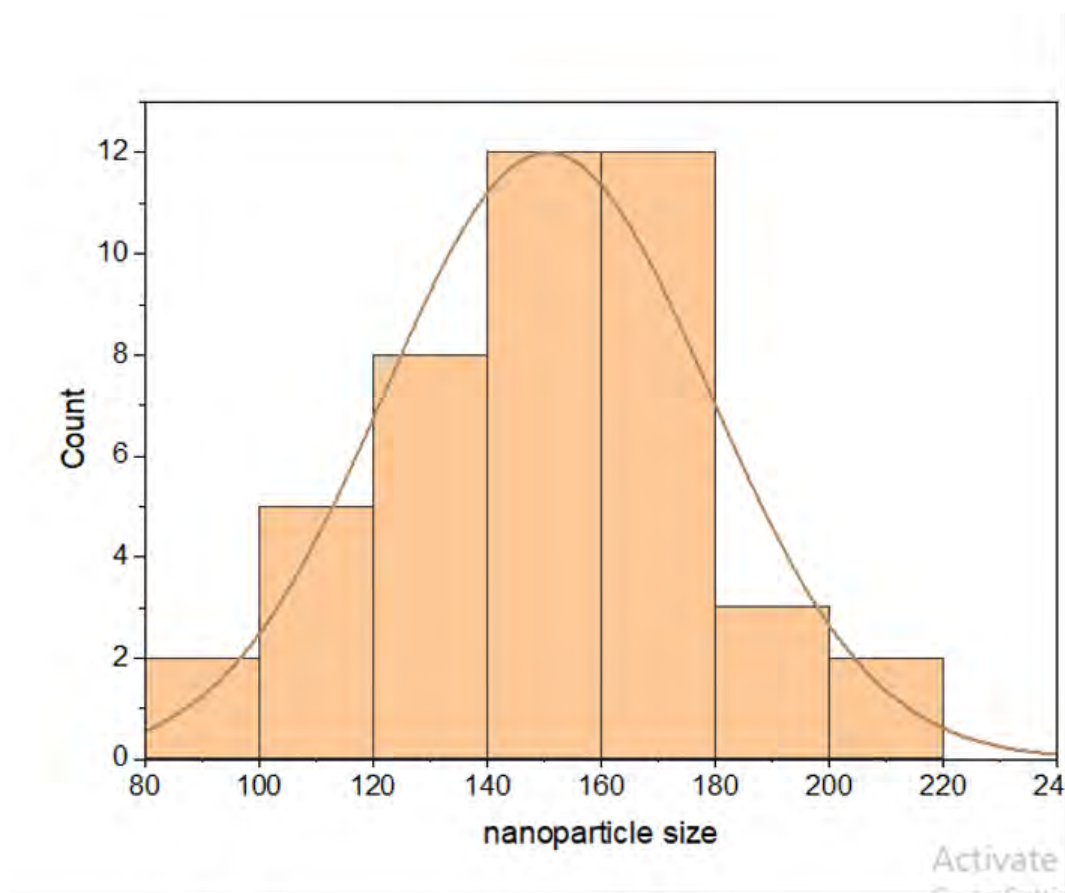
Figure 8. fesem Histograms of Cu@Sio2NPs
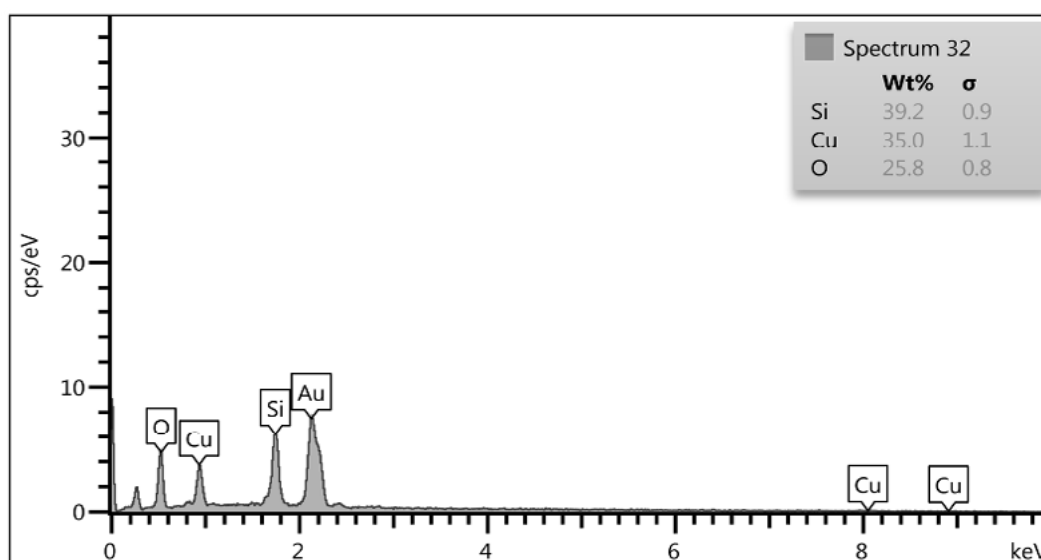
Figure 9. EDS Diagram showing the presence of copper Nps and silica

4. EVALUATION OF ANTIBACTERIAL

4.1. ACTIVITY OF THE CORE-SHELLS

Results of the evaluation of the antibacterial activity of the disc diffusion method prepared from core and shells in Figures (10) and (11) shows the inhibition region where the rate of bacterial reduction was for samples (14, 14, 16 and 20) for Escherichia coli and (24, 24, 28 and 30) for Staphylococcus aureus. Samples were taken with dilute concentrations (12.5, 25, 50, 100) %. They showed a high bacterial reduction rate for each Escherichia coli and Staphylococcus aureus in particular,

cu @sio2core shell, showed greater action against Staphylococcus aureus than their action against Escherichia coli, which was observed from the reduction rate after only 24 hours. The mechanisms by which copper is toxic to bacteria have been identified as the generation of free radicals [27, 28], which leads to the permeabilization of cell membranes, and the degradation of DNA and RNA. In the case of the antibacterial activity of free radicals, interactions with the proteins inside the bacteria in samples containing copper result in the production of hydroxyl radicals (OH) and peroxide anions (O_2). The resultant radicals damage DNA and RNA by degrading intracellular and extracellular components that obstruct the electron transport system. In addition, the eluted copper affects the bacterial outer membrane, creating holes in the outer membrane that are atypically formed. Changes in these membranes alter membrane permeability, leading to a gradual release of lipopolysaccharide molecules and membrane proteins, leading to the death of the bacteria [29].

The size, shape, and concentration of copper nanoparticles, as well as the synthesis procedure, all affect the antibacterial action of cu@sio2 core shell. The presence of the copper nanopowder coated by SiO2 was verified by TEM measurements of core shells made using the sol-gel method.Cu@Sio$_2$ nanoparticles

core - shell displayed sufficient performance as antibacterial agent. Although the presence of the SiO_2 shell prevented direct contact with the Cu nano powder, it still yielded high a reduction rate for bacteria. Thus, it was confirmed that an antibacterial agent capable of overcoming the disadvantages of using nanopowder could be manufactured. In addition, by controlling the thickness of the shell, the elution of Cu can be delayed and antibacterial functions can be maintained for long periods.
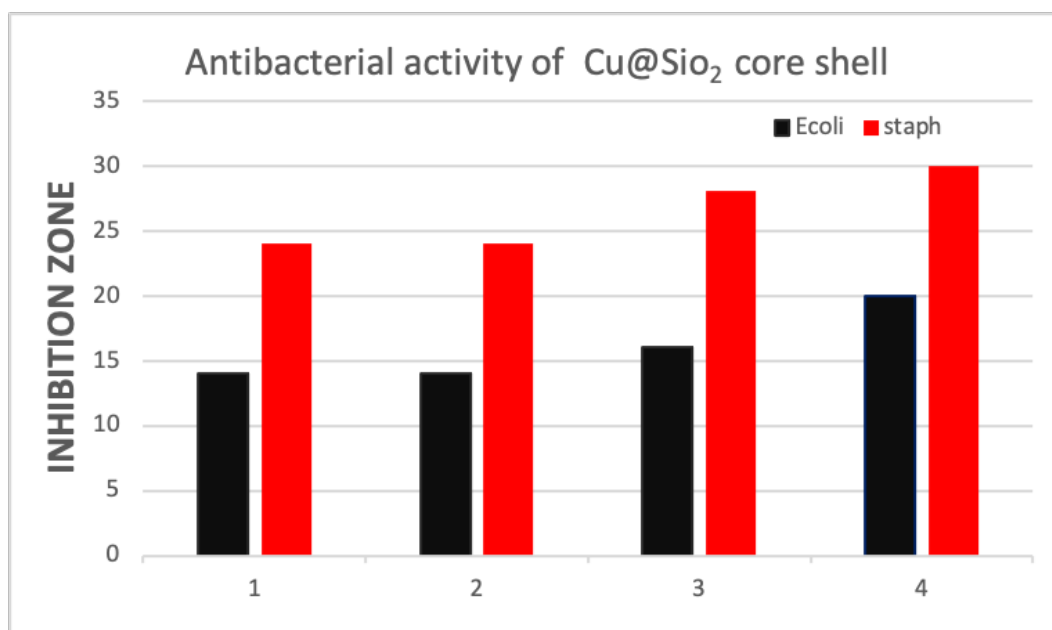
Figure 10. antibacterial activity of copper @sio2 core shell vs E.coli and S. aureus bacteria(the inhibition zone)
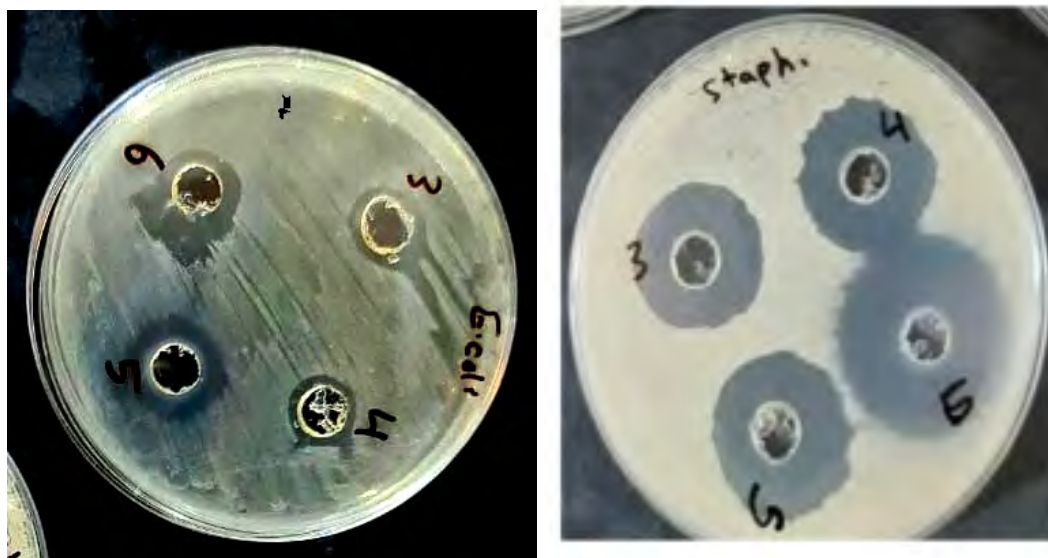
Figure 11. Cu@Sio2 core shell inhibition zone of E. coli and S. aureus bacteria at four diluted concentrations (12.5%, 25%, 50, and 100%)

5. CONCLUSIONS

A chemical sol-gel process was used to create CuSiO2 nanoparticles with a core-shell structure. A spherical sio_2 shell was formed using the sol-gel process, and Cu

nanopowder was present at the center. The presence of ammonia was also confirmed as being essential to the process. Using the shaking flask method, the spectra of xrd confirm the presence of copper nanoparticles, and the Fesem and Tem images confirm the formation of spherical particles. A red shift was observed in the UV-vis absorption spectra, indicating an increase in particle size, and it was confirmed that the core-shells produced through sol-gel method exhibited antibacterial activity. $Cu@sio_2$ core-shell can be used as a futuristic, effective antibacterial agent in biomedical applications.

REFERENCES

(1)   Chauhan, S., Kumar, M., Chhoker, S., & Katyal, S. C. (2016). **A comparative study on structural, vibrational, dielectric and magnetic properties of microcrystalline BiFeO3, nanocrystalline BiFeO3 and core–shell structured BiFeO3@ SiO2 nanoparticles**. *Journal of Alloys and Compounds*, 666, 454-467..

(2)   Fang, L., Wu, W., Huang, X., He, J., & Jiang, P. (2015). **Hydrangea-like zinc oxide superstructures for ferroelectric polymer composites with high thermal conductivity and high dielectric constant**. *Composites Science and Technology*, 107, 67-74.

(3)   Zhou, W., Chen, Q., Sui, X., Dong, L., & Wang, Z. (2015). **Enhanced thermal conductivity and dielectric properties of Al/β-SiCw/PVDF composites**. *Composites Part A: Applied Science and Manufacturing*, 71, 184-191.

(4)   Wen, F., Liu, X., Xu, Z., Tang, H., Bai, W., Zhao, W. S., ... & Wang, G. (2017). L**ow loss and high permittivity composites based on poly (vinylidene fluoride-chlorotrifluoroethylene) and lead lanthanum zirconate titanate**. *Ceramics International*, 43(1), 1504-1508.

(5)   Janardhanan, R., Karuppaiah, M., Hebalkar, N., & Rao, T. N. (2009). **Synthesis and surface chemistry of nano silver particles**. *Polyhedron*, 28(12), 2522-2530.

(6)   Bhattacharyya, S., Kudgus, R. A., Bhattacharya, R., & Mukherjee, P. (2011). **Inorganic nanoparticles in cancer therapy**. Pharmaceutical research, 28, 237-259.

(7)   Tiquia-Arashiro, S., & Rodrigues, D. F. (2016). **Extremophiles: applications in nanotechnology** (p. 193). *New York, NY, USA:: Springer International Publishing*.

(8)   Bhatia, S. (2016). **Natural polymer drug delivery systems: Nanoparticles, plants, and algae**. *Springer*.

(9)   Singh, R., & Nalwa, H. S. (2011). **Medical applications of nanoparticles in biological imaging, cell labeling, antimicrobial agents, and anticancer nanodrugs**. *Journal of biomedical nanotechnology*, 7(4), 489-503. https://doi.org/10.1166/jbn.2011.1324.

(10)   Cuffari B. (2017). Nanotechnology in the Paint Industry. https://www.azonano.com/article.aspx?ArticleID=4710.

(11) Santhoshkumar, J., Agarwal, H., Menon, S., Rajeshkumar, S., & Kumar, S. V. (2019). **A biological synthesis of copper nanoparticles and its potential applications**. *Green Synthesis, Characterization and Applications of Nanoparticles* (pp. 199-221). Elsevier.

(12) Kırmusaoğlu, S. (Ed.). (2019). **Antimicrobials, Antibiotic Resistance, Antibiofilm Strategies and Activity Methods**. BoD–Books on Demand.

(13) Agarwala, M., Choudhury, B., & Yadav, R. N. S. (2014). **Comparative study of antibiofilm activity of copper oxide and iron oxide nanoparticles against multidrug resistant biofilm forming uropathogens**. *Indian journal of microbiology*, 54, 365-368. https://doi.org/10.1007/s12088-014-0462-z.

(14) Chaudhary, J., Tailor, G., Yadav, B. L., & Michael, O. (2019). **Synthesis and biological function of Nickel and Copper nanoparticles**. *Heliyon*, 5(6), e01878. https://doi.org/10.1016/j.heliyon.2019.e01878

(15) Mary, A. A., Ansari, A. T., & Subramanian, R. (2019). **Sugarcane juice mediated synthesis of copper oxide nanoparticles, characterization and their antibacterial activity**. *Journal of King Saud University-Science*, 31(4), 1103-1114. https://doi.org/10.1016/j.jksus.2019.03.003

(16) Ismail, M. I. M. (2020). **Green synthesis and characterizations of copper nanoparticles**. *Materials Chemistry and Physics*, 240, 122283. https://doi.org/10.1016/j.matchemphys.2019.122283

(17) Harishchandra, B. D., Pappuswamy, M., Antony, P. U., Shama, G., Pragatheesh, A., Arumugam, V. A., ... & Sundaram, R. (2020). **Copper nanoparticles: a review on synthesis, characterization and applications**. *Asian Pacific Journal of Cancer Biology*, 5(4), 201-210. ,https://doi.org/10.31557/APJCB.2020.5.4.201

(18) Trapalis, C. C., Kokkoris, M., Perdikakis, G., & Kordas, G. (2003). **Study of antibacterial composite Cu/SiO2 thin coatings**. *Journal of sol-gel science and technology*, 26(1-3), 1213-1218.

(19) Ghosh Chaudhuri, R., & Paria, S. (2012). **Core/shell nanoparticles: classes, properties, synthesis mechanisms, characterization, and applications**. *Chemical reviews*, 112(4), 2373-2433.

(20) Hu, W., Chen, S., Li, X., Shi, S., Shen, W., Zhang, X., & Wang, H. (2009). **In situ synthesis of silver chloride nanoparticles into bacterial cellulose membranes**. *Materials Science and Engineering: C*, 29(4), 1216-1219.

(21) Mishra, G., Verma, S. K., Singh, D., Yadawa, P. K., & Yadav, R. R. (2011). **Synthesis and ultrasonic characterization of Cu/PVP nanoparticles-polymer suspensions**. *Open Journal of Acoustics*, 1(01), 9.

(22) Martınez, J. R., Ruiz, F., Vorobiev, Y. V., Pérez-Robles, F., & González-Hernández, J. (1998). **Infrared spectroscopy analysis of the local atomic structure in silica prepared by sol-gel**. *The Journal of chemical physics*, 109(17), 7511-7514.

(23) Furlan, P. Y., Furlan, A. Y., Kisslinger, K., Melcer, M. E., Shinn, D. W., & Warren, J. B. (2019). **Water as the solvent in the stober process for forming ultrafine silica shells on magnetite nanoparticles**. *ACS Sustainable Chemistry & Engineering*, 7(18), 15578-15584.

(24) Selvaraj, M., Sinha, P. K., Lee, K., Ahn, I., Pandurangan, A., & Lee, T. G. (2005). **Synthesis and characterization of Mn–MCM-41and Zr–Mn-MCM-41**. *Microporous and mesoporous materials*, 78(2-3), 139-149.

(25) Díaz-Visurraga, J., Daza, C., Pozo, C., Becerra, A., von Plessing, C., & García, A. (2012). **Study on antibacterial alginate-stabilized copper nanoparticles by FT-IR and 2D-IR correlation spectroscopy**. *International Journal of Nanomedicine*, 3597-3612.

(26) Ridzuan, R., Maksudur Rahman, K., Najmul Kabir, C., Mohammad Dalour Hossen, B., Rohaya Mohamed, H., Astimar Abdul, A., ... & Nahrul Hayawin, Z. (2013). **Development of Cu nanoparticle loaded oil palm fibre reinforced nanocomposite**. *Advances in Nanoparticles*, 2013.

(27) Sani, A., Cao, C., & Cui, D. (2021). **Toxicity of gold nanoparticles (AuNPs): A review**. *Biochemistry and biophysics reports*, 26, 100991.

(28) Das, S., Debnath, N., Mitra, S., Datta, A., & Goswami, A. (2012). **Comparative analysis of stability and toxicity profile of three differently capped gold nanoparticles for biomedical usage**. *Biometals*, 25, 1009-1022.

(29) Jafari, M., Rokhbakhsh-Zamin, F., Shakibaie, M., Moshafi, M. H., Ameri, A., Rahimi, H. R., & Forootanfar, H. (2018). **Cytotoxic and antibacterial activities of biologically synthesized gold nanoparticles assisted by Micrococcus yunnanensis strain J2**. *Biocatalysis and agricultural biotechnology*, 15, 245-253.

3C Tecnología. Glosas de innovación aplicadas a la pyme. ISSN: 2254-4143

Ed.43 | Iss.12 | N.1 January - March 2023

/20/

3C Tecnología. Glosas de innovación aplicadas a la pyme. ISSN: 2254-4143

Ed.43 | Iss.12 | N.1 January - March 2023

353

BOND STRENGTH OF ACRYLIC SOFT LINER TO ND:YAG LASER-TREATED THERMOPLASTIC ACRYLIC DENTURE BASE MATERIAL

Alkasim A. Alabady

Prosthodontics department / College of Dentistry / University of Baghdad / Iraq

dr.alkasimalabady@gmail.com

Bayan S. Khalaf

Prosthodontics department / College of Dentistry / University of Baghdad / Iraq

bayan.s.khalaf@codental.uobaghdad.edu.iq

https://doi.org/10.17993/3ctecno.2023.v12n1e43.354-364

ABSTRACT

Aim of the study: Using surface roughness and tensile bond strength tests, the objective of this investigation was to ascertain the impact of laser surface modification on the binding strength of injectable thermoplastic acrylic denture base material to acrylic-based soft-liner material.

Materials and methods: Acrylic base soft liner material was bonded to injectable thermoplastic acrylic resin (Deflex). Forty specimens were created (20 disc, 20 dumbbells) 10 of each specimen type as control specimens, and 10 were treated with nano pulse Nd: YAG laser. The data were analyzed using the Kruskal-Wallis test and unpaired t-test (a=.05) and the roughness test was performed utilizing a double column universal test machine.

Results: Compared to the control groups, the laser group had much increased roughness and tensile bond strength.

Conclusions. Following Nd:YAG laser surface treatment, the tensile bonding strength between acrylic soft-liner material and thermoplastic acrylic was increased.

KEYWORDS

Thermoplastic acrylic, Nd:YAG laser, tensile bond strength, surface roughness test

PAPER INDEX

1. BACKGROUND

Following a time of wearing removable dentures, several studies found that patients invariably have badly fitting dentures as a result of bone resorption that caused soft tissue shape changes (1, 2). The use of thermoplastic resins has a number of benefits over traditional powder-liquid systems. With tooth or tissue colored materials, they offer outstanding esthetics and are quite pleasant for the patient. These exhibit excellent wear characteristics, high fatigue endurance, high creep resistance, and solvent resistance in addition to being extremely stable and resisting thermal polymer unzipping. In order to create more uniformly distributed force, minimize localized pressure, and improve retention, the tissue surfaces of removable dentures and maxillofacial prostheses are cushioned with denture lining materials (3, 4).

Studies confirmed the issue of failure between the soft liner and denture foundation owing to many factors that have a negative impact on the bonding strength (5, 6). The binding site should be improved and stronger bonds should result from mechanical locking and increased surface roughness brought about by laser treatment of denture base resin (7). It is quick and easy to determine how well a material or overlay is connected to the substrate beneath using the tensile bond strength (pull-off) test. With the help of this tester, you can decide if surface preparation is necessary, spot relative changes in potential surface strength throughout a treatment region, and assess the effectiveness of surface preparation (8).

2. MATERIALS AND METHODS:

Forty specimens were prepared from injectable thermoplastic dentures base materials and grouped as follows:

1. Group TC: Twenty specimens of injectable thermoplastic acrylic denture base material without laser treatment.

2. Group TT: Twenty specimens of injectable thermoplastic acrylic denture base material subjected to surface treatment with Nd: YAG laser with power: 15 watt, hatch: 0.09, speed: 40 m/s, frequency: 20 Hz, and distance off 12 mm.

According to the tests required for this study the specimens were be divided into two shapes; disc-shaped and dumbbell-shaped.

2.1. PATTERN SHAPES AND DIMENSIONS FOR MOLD PREPARATION

The molds for the disc-shaped specimens were used with dimensions of (25mm x 2mm ± 0.1) diameter and thickness respectively. They were prepared by using high accuracy Computer numerical control (CNC) to make the plastic shapes for the specimens for measuring the surface roughness test. Dumbbell-shaped 3D printed patterns with dimensions of 75 mm in length, 12 mm in diameter at the thick part, and

7 mm at the thin portion were utilized to create the mold for the dumbbell-shaped specimens used for the tensile bond test (9). (figure 1).

A: Overall length of the specimen (75 mm)
B: Distance between shoulders
C: 'Reduced' section
D: Width of grip section (12 mm)
E: Width (7 mm)
F: Gage Length (3 mm)
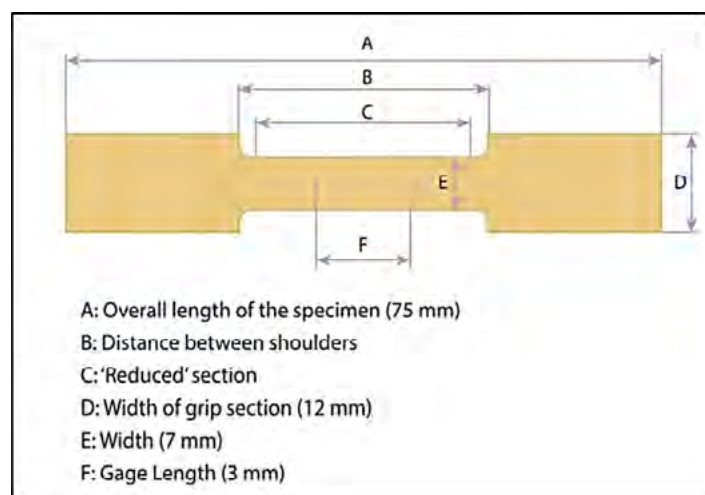
Figure 1. Mold design for dumbbell-shaped specimens

Plastic patterns were invested in silicone putty impression material, the dental stone was proportioned and prepared following the instructions of the manufacturer (W/P ratio: 20ml/100g) and after which it was poured into the aluminum flask's lower half and set over the dental vibrator. Putty and plastic designs were added to the flask's lower half, and then the plastic patterns were cleaned out. Then injectable acrylic cartridges were inserted in the DEFLEX MAD automated programmable device and injected into the flask based on the guidelines provided by the manufacturer, under pressure (5-7Bar) and heat (265° ± 10°) for 10 minutes (15min).

With the use of an acrylic bur and a stone bur, all the surplus and flashes from the acrylic specimens were removed. Next, 600-grit sand paper was used while the water was continuously cooled. All porous specimens from the specimens gathered for the study were discarded. For the finished dumbbell shaped specimens, Before completing, a water-cooled diamond-edged saw was used to remove 3 mm from the thin middle (9) figure 2.

(A)   (B)

Figure 2. (A) disc shaped specimens of thermoplastic acrylic after finishing. (B), dumbbell shaped specimens before cutting from midsection.

20 injectable thermoplastic acrylic test group specimens were handled by Nd: The following settings were used for the surface treatment using a YAG laser (Nano pulse with fiber optic lens): (15 watts of electricity) (Velocity:40 m/s) (hatch 0.09) (20 Hz frequency) (Offset distance: 12 mm). The application for a laser therapy was made at the Institute of Laser for Postgraduate Studies of the University of Baghdad/Iraq, under the direction of a laser specialist. The metal plate was placed underneath the acrylic disc after donning protective eyewear, the laser handpiece was held vertically and at a certain distance from the specimens to continue the laser therapy, as shown in (figure 3, 4).
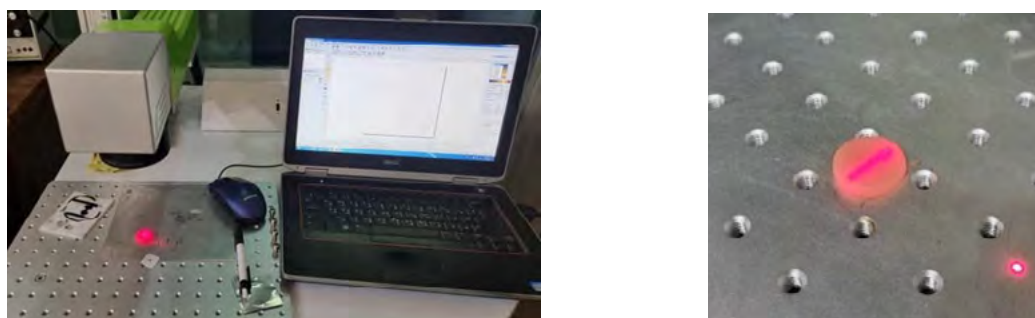
Figure 3. Acrylic (disc shape) specimens during treatment with Nd:YAG laser

Figure 4. Tensile bond strength test specimens before soft liner application (dumbbell-shaped).

For curing the soft liner inside the flask, a digital water bath which is thermostatically controlled was used. Following the instructions of the manufacturer. The flask was removed from the water bath and set aside for bench cooling at room temperature. The flask was opened when it had finished cooling down completely, and the samples were taken out. For deflasking and finishing, before testing, each specimen was immersed for 48 hours in distilled water at 37°C in an incubator. (10).

2.2. SURFACE ROUGHNESS TEST

RA mechanical profilometer was used to analyze roughness. Each specimen had measurements made at several locations for subsequent statistical analysis. The Ra (roughness—arithmetic mean value of all deviations from the midline's roughness profile throughout the measurement length) method is used to examine the data (11).

2.3. TENSILE BOND STRENGTH TEST

The dumbbell-shaped specimens of the current study were used for this test for the acrylic denture base group, including investigation of failure type: cohesive, adhesive, and mixed. The specimens was placed in the same metal grip former, which is fixed at the bottom of the testing machine. The load is applied until failure occurs and the maximum breaking forces are recorded in Newtons.

The outcome of the Nd: YAG laser treatment of the surface on (1) the enhancement of the tensile bond strength of both thermoplastic, and (2) surface roughness. Where the data for this study were gathered, processed, and arranged was evaluated for each of these. The collected data were analyzed statistically.using the SPSS version 19 computer software.

3.   RESULTS

3.1. SURFACE ROUGHNESS TEST

The descriptive statistics for the roughness test are shown in figure (5) and table (1). The injectable thermoplastic acrylic group demonstrated significantly higher roughness values after treatment with the Nd:YAG, while the control groups demonstrated the lowest roughness values.
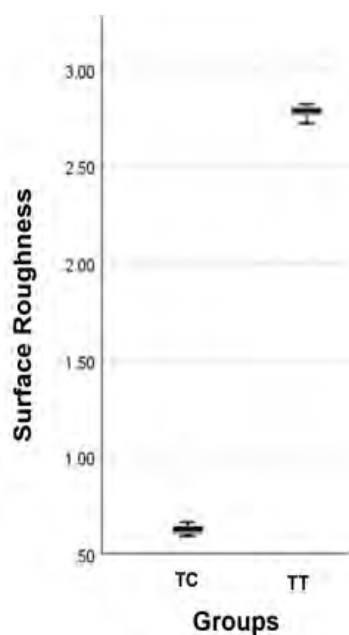
Figure 5. Surface roughness test of the study groups (values in μm)

Table 1. Descriptive statistics and t test of the surface roughness test values of groups with and without laser treatment (μm).

Groups	N	Descriptive statistics				Inferential statistics		
		Mean ± S.E.	S.D.	Min.	Max.	t-test	df	P -Value
Group TC	10	0.62 ± 0.007	0.02	0.59	0.66	148.4306	9	0.0001 HS
Group TT	10	2.78 ± 0.009	0.03	2.72	2.82			

3.2. TENSILE BOND STRENGTH TEST

In figure and table (6), the means of the various test groups for the tensile bond strength test are displayed (2). The group's mean tensile bond value (TT) was greater than the (TC) value for the control groups (no laser surface treatment). The results of the tensile bond strength test in table (4) showed a very significant difference between the groups that received treatment.(27.728, P= 0.0001 HS) when compared. The findings of the pairwise comparisons test for tensile bond strength results between research groups in table (5) revealed a highly significant difference between (Group TC and group TT).
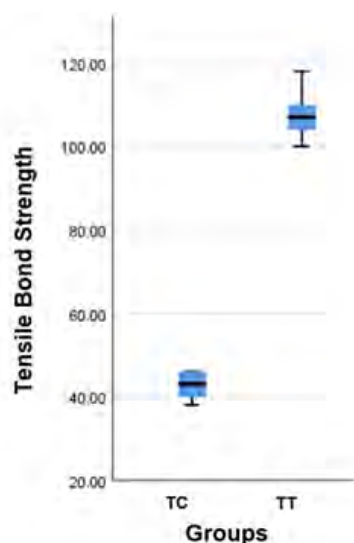
Figure 6. Tensile bond strength of the study groups (values in N).

Table 2. Descriptive statistics data and t test of the tensile bond strength test values of Nd-YAG laser treatment groups and untreated groups (values are in N).

Groups	N	Descriptive statistics				Inferential statistics		
		Mean ± S.E.	S.D.	Min.	Max.	t-test	df	P -Value
Group TC	10	42.80 ± 0.90	2.86	38.00	46.00			
Group TT	10	108.00 ± 1.66	5.25	100.00	118.00	27.728	9	0.0001 HS

Failure modes are described in (table 3). The injectable thermoplastic acrylic group showed mostly cohesive failures 80% with laser treatment and 100% adhesive failure without laser treatment.

Table 3. Modes of failure in each group of specimens

Study Group	Adhesive	Cohesive	Both
Group TC	20	0	0
Group TT	0	16	4

3.3. DISCUSSION

Dental practices have been using thermoplastic acrylic denture base materials for nearly 50 years. Due to these materials' beneficial qualities, their use has expanded in the interim. Their continued advancement has led to the creation of new classes of increasingly cutting-edge materials and technology that enable the creation of dentures that are stronger than standard dentures. The following traits of thermoplastic materials exist: Excellent biocompatibility, no residual monomer, no allergenic or harmful chemicals, ability to keep form. The use of TMs for immediate dentures, post-resection dentures, full and partial dentures, and interim dentures following implantation is increased. because to their excellent flexibility and accuracy as well as their range of hues. (12).

Surface treatment with a laser beam led to preferred surface roughness results, the laser beam produced surface changes by ablation that cause melting and vaporization of the polymer surface and produce that causes some halls, pits and fossa of limited depth which may result in uniform surface roughness. Surface roughness values of treated groups significantly increased when compared to the untreated (control groups), which was caused by the laser's significance as one of the practical uses. This was used in increasing and improving bonding and adhesion between denture base resins material and soft liner. Noticeably, the laser surface treatment produced porous topography with irregular pits and micro-retentive morphological topographical changes. This study agreed with (13) claimed that a different approach to surface treatment to get a stronger bond strength between two materials, the laser, has been suggested. Furthermore, (14) shown that treating the surface of denture base resins with the laser has been said to be a simple and safe process. Additionally, the recent findings support the claims made by (15), who claimed that the PMMA's surface had been modified by lasing in order to expand its surface area and add mechanical locking.

In the present study, we discovered that employing the laser to treat the surface effectively increases the binding strength, resulting in long-term adhesion of denture base materials with acrylic-based denture liners made of soft polymers. Therefore, a strong adherence is required for the long-term use of a soft denture liner. When a soft denture liner is required as the basis for a denture, strong adhesion is required for long-term use. The significant difference in surface roughness between the treated group and the control group was attributed to the effect of laser surface treatment in

increasing the bonding of denture base materials and soft denture liners. Because the laser has an impact on the surface that increases tensile bond strength, the use of modification methods like lasers is required to prevent these issues.

According to the statistical analysis of the current study, applying a laser to a surface to treat it strengthened the tensile bond in the laser-treated groups compared to the control groups. Additionally, the Nd: YAG laser created pits or other abnormalities that the soft lining material was able to penetrate, enhancing the connection in the laser-treated groups. Soft lining materials may therefore pass through any defects or pits left behind by the Nd: YAG laser.

The use of a laser for surface treatment enhanced the tensile bond strength in the groups treated with the laser compared to the control groups, according to the results of the statistical analysis carried out in the current study. Additionally, in the laser-treated groups, the soft lining material was able to infiltrate the abnormalities or pits, strengthening the connection. As a result, soft lining materials may penetrate imperfections or pits created by the Nd: YAG laser. (17) conducted tensile experiments to assess how sandblasting and laser treatments affected the bonding of acrylic resin and robust liners at the interfacial level, consistent with (7) They found that lasing PMMA prior to applying a resillient material led to stronger mean tensile bonds than control specimens. Also, (16) shown that preparing the acrylic resin surface with laser beams at 3 W, 10 Hz, and 300 mJ produced tiny holes the liner could enter, strengthening the binding. The increase in cohesive failures after laser treatment suggests an improvement in the tensile bond strength of the acrylic-based soft lining to the injectable thermoplastic acrylic resin because the adhesion between these materials may be stronger than the intermolecular forces of the relining material. Results that increased the tensile binding strength of the resin-based soft liner to the acrylic resins were similar with the findings of (18,19), which demonstrated cohesive failures. The alternative hypothesis, according to which Nd: YAG laser treatments enhanced the thermoplastic acrylic denture resin's tensile binding strengths to the denture base soft liner, was accepted and the null hypothesis was rejected.

4. CONCLUSION

1. As demonstrated in this work, laser surface treatments change the surface morphology of acrylic resin.

2. Nd: YAG laser treatment of surface injectable thermoplastic acrylic then relined with acrylic-based soft lining resulted in higher mean surface roughness and surface than seen in the untreated control group.

3. Injectable thermoplastic acrylic surface treatment with Nd: YAG laser (power: 15 watt) (speed: 40 m/s) (hatch 0.09) (frequency: 20 Hz) (distance off: 12mm), has shown that when employed as a surface treatment agent, it effectively strengthens the tensile bond between the thermoplastic acrylic denture base material.

REFERENCES

(1) Nakhaei, M., Dashti, H., Ahrari, F., Vasigh, S., Mushtaq, S., & Shetty, R. M. (2016). **Effect of different surface treatments and thermocycling on bond strength of a silicone-based denture liner to a denture base resin**. *J Contemp Dent Pract*, *17*(2), 154-9.

(2) Alkinani, G. A. (2014). **Evaluation of shear bond strength between thermosens as relining material and different denture base materials**. *J Bagh Coll Dentistry*, 26(4), 28-31.

(3) Polyzois, G. L., & Frangou, M. J. (2001). **Influence of curing method, sealer, and water storage on the hardness of a soft lining material over time**. *Journal of Prosthodontics*, 10(1), 42-45.

(4) Dayrell, A., Takahashi, J., Valverde, G., Consani, R., Ambrosano, G., & Mesquita, M. (2012). **Effect of sealer coating on mechanical and physical properties of permanent soft lining materials**. *Gerodontology*, 29(2), e401-e407.

(5) Tugut, F., Akin, H., Mutaf, B., Akin, G. E., & Ozdemir, A. K. (2012). **Strength of the bond between a silicone lining material and denture resin after Er: YAG laser treatments with different pulse durations and levels of energy**. *Lasers in medical science*, 27, 281-285.

(6) Sabah, D. Q., & Khalaf, B. S. (2022). **Effect of thermocycling on surface roughness and shear bond strength of acrylic soft liner to the surface of thermoplastic acrylic treated with Ethyl Acetate**. *Indian Journal of Forensic Medicine & Toxicology*, 16(1), 1353-1360.

(7) Usumez, A., Inan, O., & Aykent, F. (2004). **Bond strength of a silicone lining material to alumina-abraded and lased denture resin**. *Journal of Biomedical Materials Research Part B: Applied Biomaterials: An Official Journal of The Society for Biomaterials, The Japanese Society for Biomaterials, and The Australian Society for Biomaterials and the Korean Society for Biomaterials*, 71(1), 196-200.

(8) Zidan, S., Silikas, N., Haider, J., Alhotan, A., Jahantigh, J., & Yates, J. (2020). **Assessing Tensile bond strength between denture teeth and nano-zirconia impregnated PMMA denture base**. *International journal of nanomedicine*, 9611-9625.

(9) Gorler, O., Dogan, D. O., Ulgey, M., Goze, A., Hubbezoğlu, I., Zan, R., & Ozdemir, A. K. (2015). **The effects of Er: YAG, Nd: YAG, and Ho: YAG laser surface treatments to acrylic resin denture bases on the tensile bond strength of silicone-based resilient liners**. *Photomedicine and laser surgery*, 33(8), 409-414.

(10) Hasan, W. Y., & Ali, M. M. (2018). **Evaluation of thermal conductivity and some other properties of heat cured denture soft liner reinforced by halloysite nanotubes**. *Biomedical and Pharmacology Journal*, 11(3), 1491-1500.

(11) Alves, P. V. M., Lima Filho, R. M., Telles, E., & Bolognese, A. (2007). **Surface roughness of acrylic resins after different curing and polishing techniques**. *The Angle Orthodontist*, 77(3), 528-531.

(12) Chuchulska, B., Yankov, S., Hristov, I., & Aleksandrov, S. (2018). **Thermoplastic materials in the dental practice: a review**. *IJSR*, 6(12), 1074-1076.

(13) Madani, A. S., Astaneh, P. A., Nakhaei, M., Bagheri, H. G., Moosavi, H., Alavi, S., & Najjaran, N. T. (2015). **Effectiveness of Silica-Lasing Method on the Bond Strength of Composite Resin Repair to Ni-Cr Alloy**. *Journal of Prosthodontics*, 24(3), 225-232.

(14) Asadzadeh, N., Ghorbanian, F., Ahrary, F., Rajati Haghi, H., Karamad, R., Yari, A., & Javan, A. (2019). **Bond strength of resin cement and glass ionomer to Nd: YAG laser-treated zirconia ceramics**. *Journal of Prosthodontics*, 28(4), e881-e885.

(15) Aziz, H. K. (2017). **Effect of the CO2 laser as surface treatment on the bond strength of heat cured soft liner to the high impact acrylic denture base material**. *Journal of baghdad college of dentistry*, 325(4203), 1-7.

(16) Tugut, F., Akin, H., Mutaf, B., Akin, G. E., & Ozdemir, A. K. (2012). **Strength of the bond between a silicone lining material and denture resin after Er: YAG laser treatments with different pulse durations and levels of energy**. *Lasers in medical science*, 27, 281-285.

(17) Akin, H., Tugut, F., Guney, U., Kirmali, O., & Akar, T. (2013). **Tensile bond strength of silicone-based soft denture liner to two chemically different denture base resins after various surface treatments**. *Lasers in Medical Science*, 28, 119-123.

(18) M. A. Kumbhalkar, D. V. Bhope and A. V. Vanalkar. (2013). **Enhance Production Rate of Braiding Machine Using Speed Reduction Technique.** *International Journal on Theoretical and Applied Research in Mechanical Engineering (IJTAMRE)*, 2(2) 2319-3182.

(19) Mancuso, D. N., Goiato, M. C., Zuccolotti, B. C. R., Moreno, A., dos Santos, D. M., & Pesqueira, A. A. (2012). **Effect of thermocycling on hardness, absorption, solubility and colour change of soft liners**. *Gerodontology*, 29(2), e215-e219.

3C Tecnología. Glosas de innovación aplicadas a la pyme. ISSN: 2254-4143

Ed.43 | Iss.12 | N.1 January - March 2023

/21/

3C Tecnología. Glosas de innovación aplicadas a la pyme. ISSN: 2254-4143

Ed.43 | Iss.12 | N.1 January - March 2023

365

EXPERIMENTAL ANALYSIS ON POLYPROPYLENE MOULDED PART FOR PERFORMANCE OF LASER PRINTING

Ajay L. Dumanwad

PG Student, Department of Mechanical Engineering, JSPM Narhe Technical Campus, Savitribai Phule Pune University, Pune – 411041, India

ajaydumanwad143@gmail.com

Manoj A. Kumbhalkar

Associate Professor, Department of Mechanical Engineering, JSPM Narhe Technical Campus, Pune, India

manoj.kumbhalkar@rediffmail.com - https://orcid.org/0000-0003-2289-6373

Jaswindar Singh

Director, Ecorea & Kuroda Electric India Pvt. Ltd., Ranjangaon, Pune, India

ABSTRACT

Now a day plastic injection molding is widely used process to manufacture engineering product and consumer goods typically thermoplastic is combined with rubber or another thermoplastic like RM master batch is used to add color to the Molded part also the laser marking on plastic part and their printing cut, faint issue observed. The aim of the study was to Optimize the injection parameters and processing condition for the laser performance on polypropylene part. To achieve enhanced dark laser marking on polypropylene, the process parameter of plastic injection molding and the Raw material master batch mixing parameter successfully prepared this laser–sensitive composite consisted of a high Laser induced carbonization rate.in plastic injection molding use of raw material and mixing of master batch is considerable factor for faint laser marking. Because of laser does not respond well on carbonization added material, it was evident that master batch having the carbon properties is much more responsible for faint laser marking issue on polypropylene material part.

The effect of laser beam interaction (Nd: YVO4) with selected operational parameters on the Quality of graphical features obtained on the surface of polypropylene-molded pieces with different surface Textures (variable parameters of the surface layer). Polypropylene test specimens were injection molded using original injection molds Products with variable end parameters determined by the position of the cavity circle can be identified. The layout of the laser function, the beneficiary texture of the molded piece, the molded color and the support of the marking piece allow the evaluation of the graphic symbol performance by means of laser marking of the type of master back in their rendering relationship. Marked evaluation criteria were adopted for the project.

KEYWORDS

Laser marking, injection moulding, master batch, printing, polypropylene

PAPER INDEX

1.   INTRODUCTION

Plastic injection moulding is the process of heating raw material to its melting point (plastic resin in pellet form in our case), forcing the viscous material into a mould, and allowing it to cool into a hardened shape. In almost every product you encounter, injection moulded parts are used, from electronics to housewares to automotive to food packaging. At its most basic, it's a very simple process, but there's a lot more to it than that—from creating the mould to understanding the chemical and physical properties of the material. Plastic injection moulding arose from metal pressure die casting processes in the late 1800s. Plastics were introduced in the 1920s, but the process was still very crude, with simple two-piece moulds manually clamped together. Since then, the art and science of plastic injection moulding have advanced significantly [1-5].

1.1. INJECTION MOULDING MACHINE TYPE

Injection moulding is a method of transforming thermoplastics or thermosetting materials into a wide range of products. Plasticizing and injection units, clamping and opening units, ejecting or knockout units, and an electric and hydraulic control system comprise an injection machine or injector.

There are four basic types of injection moulding equipment according to the type of screw or plunger. [6]

Four types of injection moulding machines.[6]

1. Conventional injection moulding machine.

2. Piston-type preplastifying machine.

3. Screw-type preplastifying machine.

4. Reciprocating-screw injection machine.
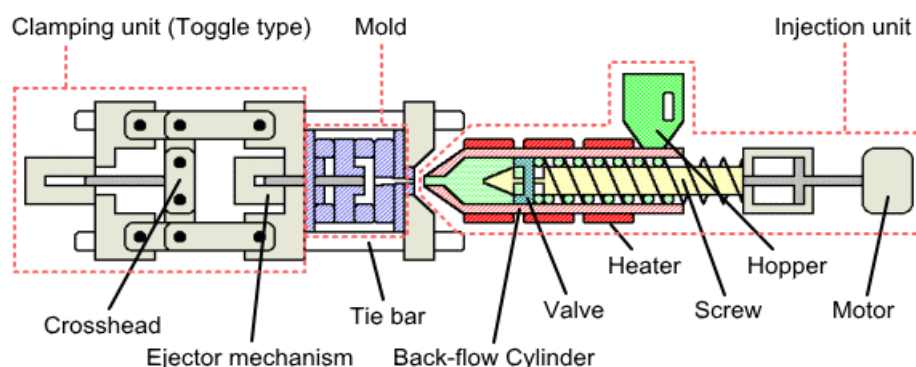
Figure 1. Plastic Injection Moulding machine. [4] (Courtesy: Polypastics Co., Ltd.)

In Conventional injection moulding machine, Plastic granules or pellets are poured into a hopper and fed into the chamber of the heating cylinder in this process. A plunger then compresses the material, forcing it through the heating cylinder's increasingly hotter zones, where it is spread thin by a torpedo. The torpedo is placed in the centre of the cylinder to accelerate the heating of the plastic mass's centre. The

torpedo can also be heated from the inside as well as from the outside. The material flows into the mould from the heating cylinder via a nozzle. The nozzle seals the cylinder and the mould, preventing molten material from leaking. The clamp end of the machine holds the mould closed. Two to three tonnes of pressure are typically applied to polystyrene for each inch of projected area of the work-piece and runner system.[6]

To preplastify the plastic granules, Piston-type preplastifying machine uses a torpedo ram heater. The fluid plastic is pushed into a holding chamber after the melt stage until it is ready to be forced into the mould. Because the moulding chamber is filled to shot capacity during the cooling time of the work-piece, this type of machine produces work-pieces faster than a conventional machine. Because the injection plunger is acting on fluid material, there is no pressure loss when compacting the granules. This enables a larger work-piece with a larger projected area.[6]

Screw- Type preplastifying machine is an extruder that is used to plasticize plastic material. The pellets are fed forward by the turning screw to the heated interior surface of the extruder barrel. The molten, plasticized material exits the extruder and enters a holding chamber before being forced into the mould or die by the injection plunger. The use of a screw provides the following benefits: improved plastic melt mixing and shear action, the ability to run a wider range of stiffer flow heat sensitive materials, colour changes can be handled in less time, and fewer stresses are obtained in the moulded part [6].

A horizontal extruder replaces the heating chamber in a reciprocating-screw injection moulding machine. The rotation of a screw propels the plastic material forward through the extruder barrel. The material changes from granular to plastic molten as it moves through the heated barrel with the screw. As the material advances, the screw returns to a limit switch, which determines the volume of material in front of the extruder barrel. During the shot, the screw advances to displace the material in the barrel. The screw acts as a ram or plunger in this machine.There are several benefits to using reciprocating-screw injection moulding. Because of the screw's mixing cation, it plasticizes heat-sensitive materials more efficiently and blends colours more quickly [6].

The main component of injection moulding machine are clamping unit and injection unit. Clamping unit consist of three main components such as mould, clamping motor drive and Tier bars, the sender is clamped onto the edge of a workbench. Injection Unit consist of three main components viz. Screw motor drive, reciprocating screw & barrel and heaters, thermocouple, ring plunger.

1.2. LASER PRINTERS

Laser printers are another well-known laser-based consumer product, frequently used in conjunction with personal computers. Their operating principle is based on electro photography, also known as xerography, which is the same process used in photocopiers. Figure 2 depicts the electro photographic process. Ions from a corona discharge charge uniformly a photoreceptive surface with a layer of photoconductive material. The surface is frequently that of a rotating drum. The surface is exposed

after charging by scanning the laser beam across it. The intensity of the beam is varied to create a replica of the desired image. The pattern of light intensity replicates the pattern of the to-be-printed text or graphics. In laser-illuminated regions, the photoconductive layer conducts. This allows the electrostatic charge to move and creates an electric charge pattern on the surface [7-12].
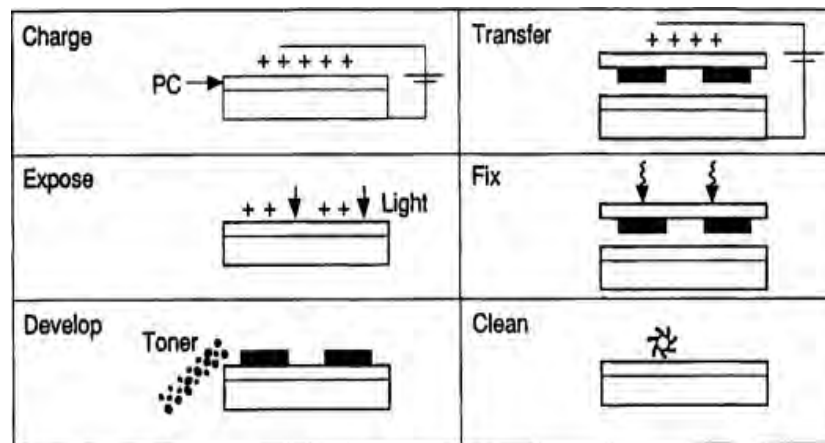
Figure 2. Basic working principle dia. [7]

This sequence is similar to that used in photocopiers, except that the pattern in the exposure step is obtained from projection of an image of the text or graphics to be copied in photocopiers. A computer generates the material and sends it to the laser printer, which stores the data in its memory, composes one page of material at a time, and controls the scanning of the laser beam to produce the desired image. Laser printers produce high-quality prints with sharp images and consistent black levels. [7]

The various type of Lasers is green laser, UV laser, CO2 laser and MOPA laser.

1.3. PROBLEM IDENTIFICATION

As shown in the figure 3, the Engine Room RB Upper Cover has the good laser marking as well as the defective information for the part. In the first stage, the parts are kept in their respective jigs for further laser marking purposes. The part should be properly held and jigged before beginning the laser marking. After that, the inspector should check the part as per inspection and visually check for defects.

As shown in the defect information image below, some alphabetical letters, numeric numbers, or any specific symbol are found cut or faintly printed; because of this, the production team faced too many rejections. The faint marking refers to the cutting or invisible letter found on a part after the laser marking process.
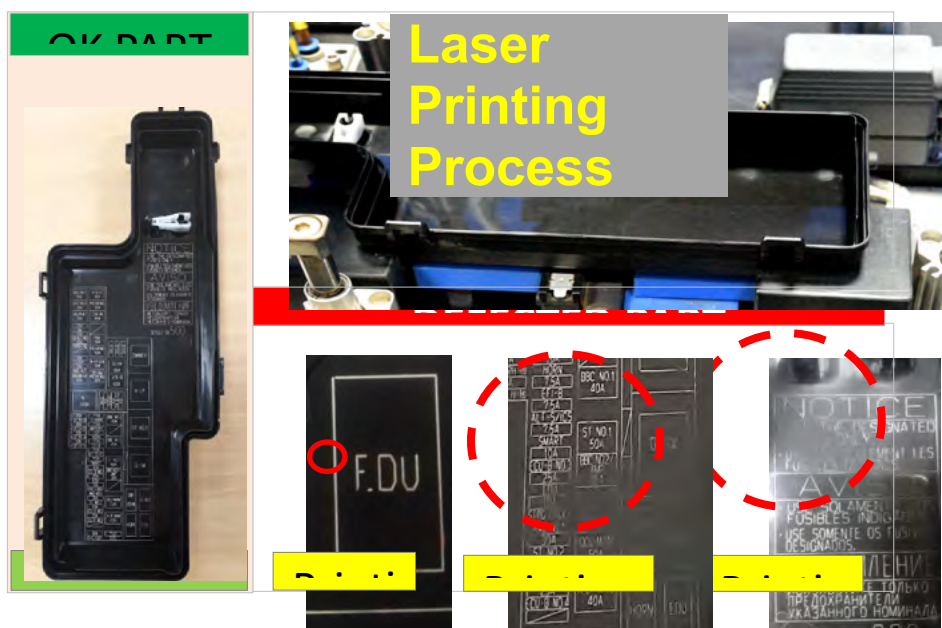
Figure 3. Laser Printing Process on Upper Cover of the moulded part

1.4. DATA COLLECTION

Before experimentation, to investigate the process parameters of the printing problem, it is necessary to have a thorough understanding of the process, which is studied using a process flow chart. The first stage of the work was to collect the rejection data due to faint laser marking. Performance information and performance issues for the evaluation of three steps is done on a numerical scale. They are based on the needs of the high-pressure moulding line of the company or the final product. Priority is given to the cause with the highest rejection part number. After collecting three months of production data from various parts in order to identify the part with the highest rejection ratio. Table 1 displays rejection data for various moulding parts. PPM stands for parts per million. According to the data presented, the highest rejection was observed in the ENG ROOM R/B upper cover.

Table 1. Theme Data (Part wise defect data)

Part name	Feb-22	Mar-22	Apr-22	Prod. Qty.	Rej. Qty	PPM
ENG ROOM R/B UPPER	5,762	8,752	74,58	21,972	1,456	**66,266**
ASSY R/B FRAME FLOOR	12,432	14,235	9,663	36,330	498	**13,708**
COVER FUSE RB NO 2	3,456	2,564	2,657	8,677	250	**28,812**
UPPER RHD PROTECTOR BASE	4,562	4,578	5,060	14,200	39	**2,746**
L TYPE 2P HOUSING FEMALE Grey	6,532	12,452	4,591	23,575	15	636
PROTECTOR COVER L74.4 W269.2 H34 PA66B	7,562	6,423	5,903	19,888	6	302
CONN COWL SIDE RH C/B 2 PP N	6,452	5,423	5,855	17,730	5	282
TOTAL	46,758	54,427	41,187	1,42,372	2,269	15937

By combining the three-month production rejection rate of various moulded parts in a part-by-part pareto chart, it was discovered that the Engine Room RB Assembly upper cover has the highest value as shown in pareto chart (figure 4), indicating the highest total process rejection. Hence, the upper cover was chosen for further drill-down analysis after studying the selected moulded part of the engine room RB assembly.
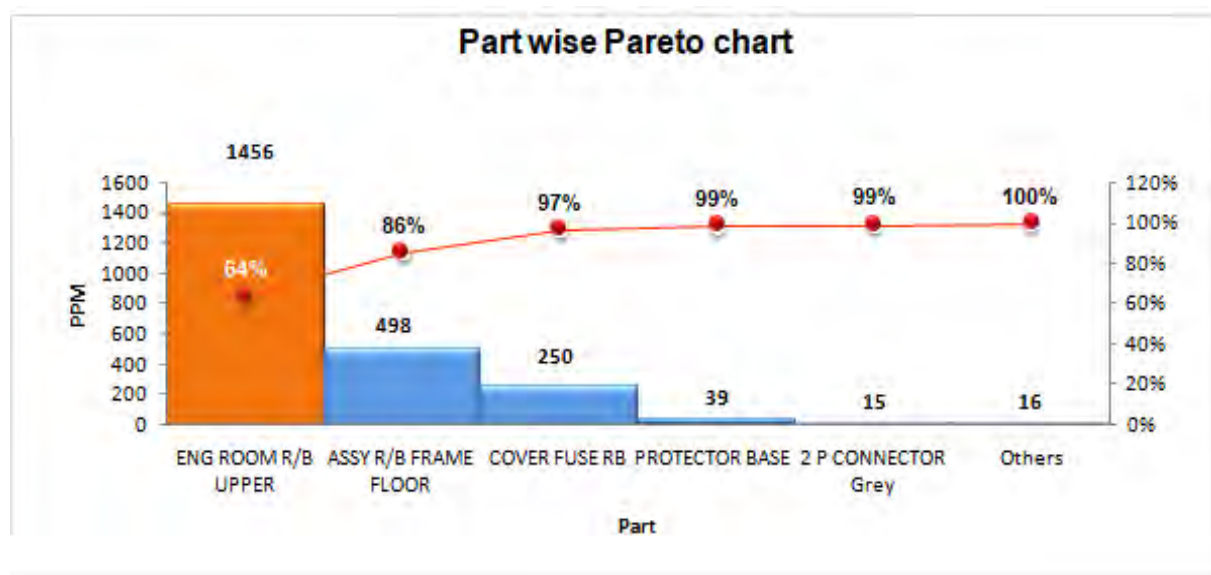
Figure 4. Partwise rejection of the component (Pareto chart)

After selecting the moulded part with the highest rejection ratio for drill-down analysis, it is necessary to investigate which type of rejection occurred as a result of which part was rejected the most frequently. Printing cut issues, printing faint issues,

and other process defects such as short mold, sink mark, flash, flow mark issue, and so on are commonly found in laser-printed parts. Based on the detailed examination of the collected rejection details, it was determined that the majority of the major rejections occurred as a result of the Faint Laser Issue in Engine Room RB Upper Cover, as shown in figure 5.
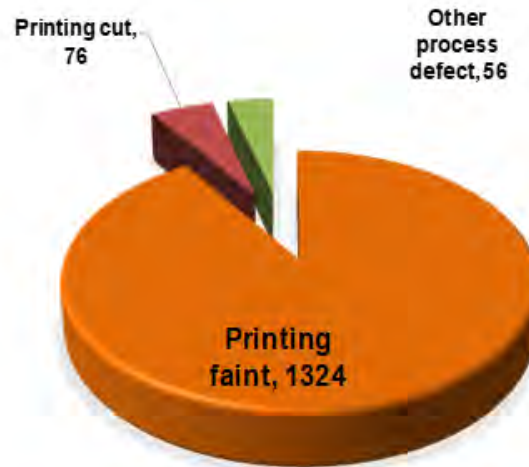
Figure 5. Rejection Detail Analysis (Pie Chart)

After studying part-wise defect data, a part-wise pareto chart, and pie chart data, the part with the highest rejection ratio in three months is chosen for the part-wise pareto chart. And, based on the large number of rejections, it has been determined that the laser faint printing issue in Engine Room RB Upper Cover is a significant factor. So, selecting the above parts and causes for project theme improvement and experiment investigation of process parameters.

The 4M method analysis is a method for evaluating which of the 4M conditions is responsible for a defect mode. The 4M is a method for identifying and grouping causes that have an impact on a specific effect. The 4M categories of man, machine, method, and material are often used in the cause-effect diagram, which is also called a fishbone diagram. We discovered the following significant factors for the same issue shown in Figure 6. In this method, raw material and master batch mixing are considerable factors. In material, the master batch is not suitable for the laser printing issue, and the raw material to master batch ratio is not optimized.
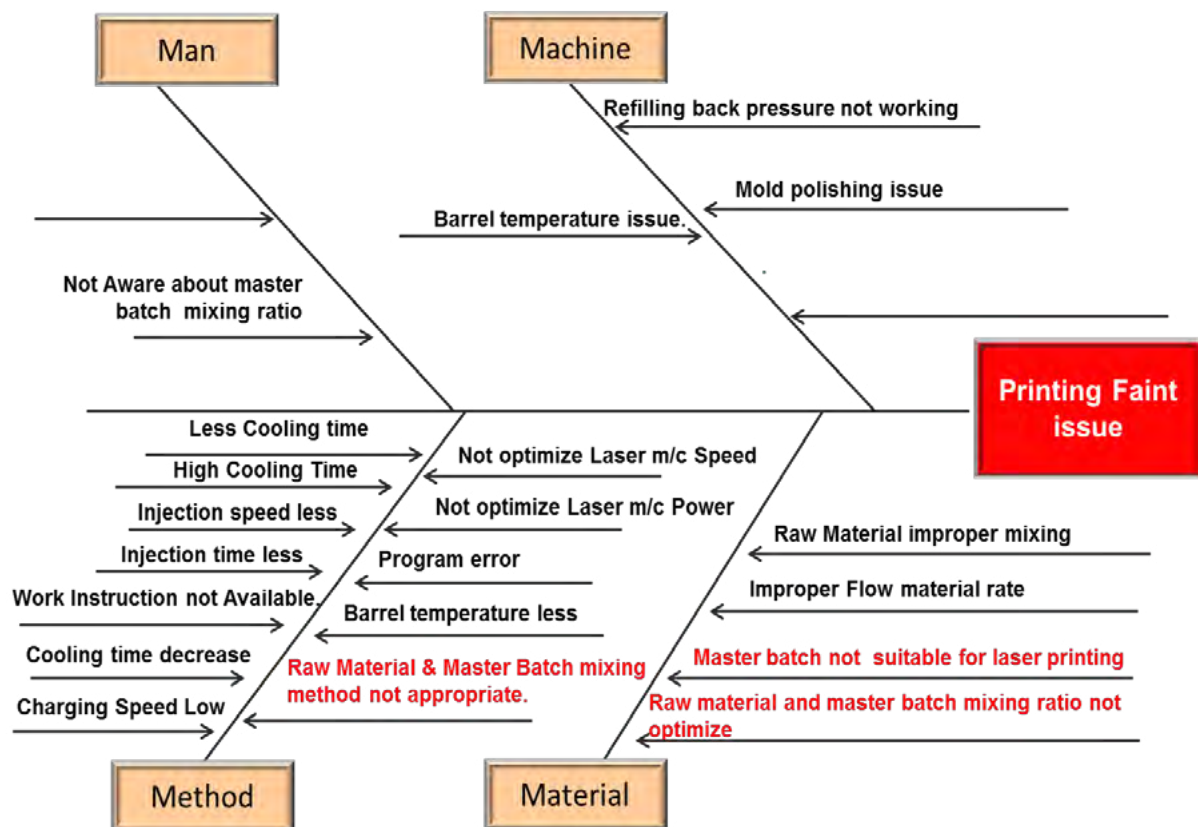
Figure 6. Fish bone dia.

The major problem of printing on the company's moulded part is discussed and resolved with many trials and experiments by changing the different process parameters in this project. The main objective of the work is to find the cause of faint printing. Also, to investigate the problem, an experiment with the existing material using a different batch mixing percentage and time is needed. It is necessary to finalise the percentage of the master batch and the time for mixing MB. The experiments have to be carried out with different batch mixing percentages and times for the suggested material. The final objective of the work is to reduce or eliminate the rejection rate of the laser printing process in Part Engine Room RB Assembly Upper by 100%.

A process flow chart is a diagram that represents the decision-making procedures and the sequential steps of a process. Every step in the chart or visual representation is denoted by a shape. To depict the movement and direction of the process, these forms are joined by an arrow or line. From the initial receipt of raw materials to the final dispatch stage, the following process flow chart is included. Here, the raw material mixing and raw material loading on the hopper are very important stages.
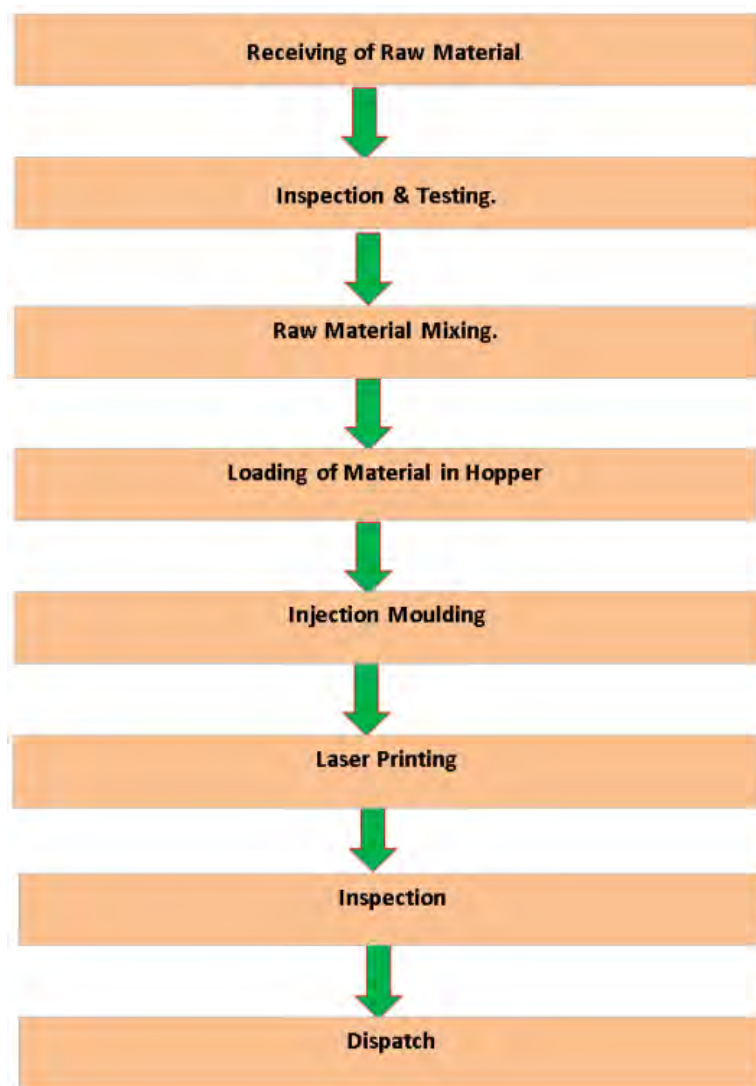
Figure 7. Process Flow chart

2. EXPERIMENTAL TRIAL WITH MASTER BATCH MIXING

2.1. EXPERIMENTAL TRIALS ON EXISTING MATERIAL (340 MASTER BATCH)

To find the exact cause of printing failure on the part, various trials need to be taken with reference to the rejection rate as discussed above. To determine the precise cause of printing on the top cover, various trials for master batch mixing, ranging from 8% to 3%, are considered, and the rejection ratio is calculated. A sample image of raw material with the master batch is given in Figure 8. The existing master batch 340 has a melting point of 1240 °C and a heat stability of 2800C. The upper cover is subjected to five trials with existing material, namely master batch 340, with a MB mixing time of 10 minutes. The total lot for each trial is taken as 50, and it has been observed that the percentage of rejection is reduced with a reduction in the percentage of master

3C Tecnología. Glosas de innovación aplicadas a la pyme. ISSN: 2254-4143

batch mixing. The results obtained on the injection moulding machine for five different trials are given in table 2.
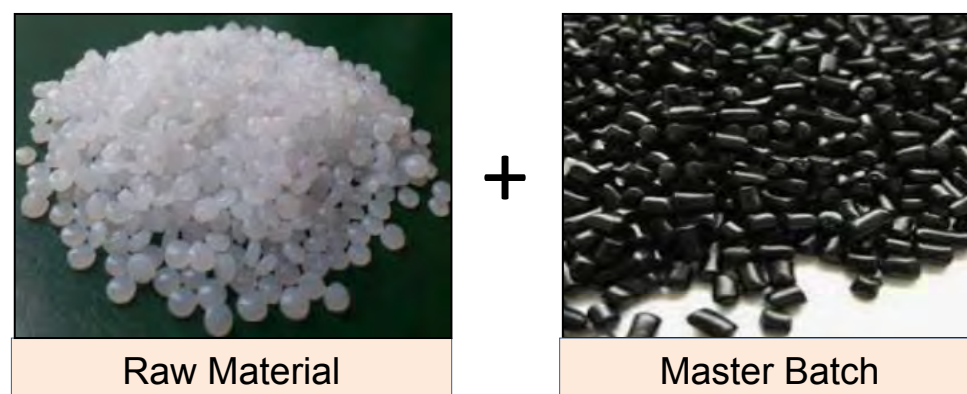
Figure 8. Raw material and master batch mixing

From the above-mentioned analysis, it is evident that master batch percentage and master batch Mixing time is a considerable factor for printing faint lines. Hence, there is a need to improve the master batch mixing as well as change the master batch and check the issue of mixing at the same percentage level. For this purpose, Master Batch 394 is suggested for mixing with a mixing ratio of 2% and a MB mixing time of 10 minutes. The comparison study of the existing master batch and the suggested master batch is given in table 2.

Table 2. Trail on Upper Cover with Existing Material (Master Batch Grade & MB Mixing ratio

Trial	Raw Material PP	% of Master Batch 340	MB Mixing time. In min.	Trial Lot	NG	Rejection %
T1	100%	8%	10	50	7	14%
T2	100%	7%	10	50	7	14%
T3	100%	6%	10	50	6	12%
T4	100%	5%	10	50	5	10%
T5	100%	4%	10	50	5	10%
T6	100%	3%	10	50	2	10%
T7	100%	2%	10	50	1	8%

2.2. COMPARISON STUDY OF EXISTING MASTER BATCH AND SUGGESTED MASTER BATCH

Based on the number of trials taken, the 2% master batch mixing has been finalized for further trials for existing as well as suggested materials for Batch 394. By operating the injection moulding machine for different operating variables and process parameters of the raw material mixing method, we took the rejection of no. part reading from the mixing of RM with master batch.

Existing Master Batch   Suggested Master Batch

Master Batch 340 /TP/P

MFI   :- **0.29**
Gram per 10 min) by ASTM D1238
Melting point (°c) :-124
Heat Stability (°c) :280
Carbon used:-   **Black (WN-96)**

Existing Use **:Master Batch 340 Grade**

Master Batch 394 /TP/P

MFI   :- **25.1**
Gram per 10 min) by ASTM D1238
Melting point (°c) :-126
Heat Stability (°c) :280
Carbon used   :- **Laser Black**

Suggested **:Master Batch 394 Grade**

Following an examination of both the 340 master bath and the 394 master batch, it was determined that the value of the multi-flow index for the 340 master bath is less than required, while the value for the 394 master batch is in the middle of the specifications. As shown in the comparative study above, the carbon used in both master batches is different. It has been concluded that the 394 master batch is a suitable factor; further, there is a need to conduct a trial in an optimized percentage of the master batch with new laser carbon with proper mixing time. Furthermore, a trial in an optimized percentage of the master batch with new laser carbon and proper mixing time is required.

2.2.1. GRADE 340 MASTER BATCH TRIALS

The carbon used in both master batches is different, as shown in the comparative study above.It has been concluded that the 394 master batch is a suitable factor; further, there is a need to conduct a trial in an optimized percentage of the master batch with new laser carbon with proper mixing time. Furthermore, a trial in an optimized percentage of the master batch with the new laser carbon with proper mixing time is required. So, for the next trial, the master batch mixing ratio is set to 2% and the mixing time is set to 10 minutes.

Table 3. Grade 340 Master batch trial Table

Sr/no	Trial	Raw Material PP	% of Master Batch 340	Trial Lot	NG	Rejection %
1	T1	100%	2%	50	3	6%
2	T2	100%	2%	50	4	8%
3	T3	100%	2%	50	3	6%
4	T4	100%	2%	50	3	6%
5	T5	100%	2%	50	4	8%
6	T6	100%	2%	50	4	8%
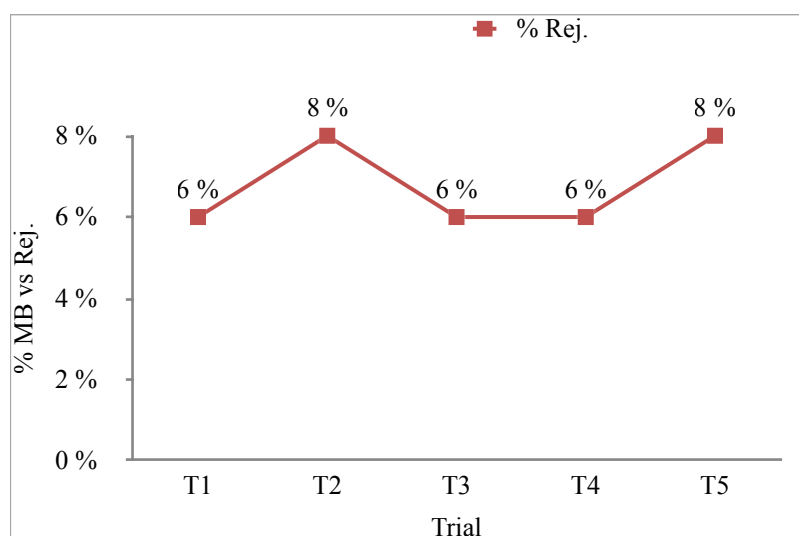
Figure 9. Grade 340 Master batch trial Graph

2.2.2. GRADE 394 MASTER BATCH TRIAL

As per the comparative study, the carbon used in both master batches is different, as shown in the comparative study. It has been concluded that the 394 master batch is a suitable factor; further, there is a need to conduct a trial in an optimized percentage of the master batch with new laser carbon with proper mixing time. Furthermore, a trial in an optimized percentage of the master batch with the new laser carbon with proper mixing time is required. So, for the next trial, the two percentages of the master batch mixing ratio and the mixing time of 10 minutes are fixed.

Table 4. Grade 394 Master batch trial Table

Sr/no	Trial	Raw Material PP	% of Master Batch 394	Trial Lot	NG	% Rej
1	T1	100%	2%	50	2	4%
2	T2	100%	2%	50	2	4%
3	T3	100%	2%	50	1	2%
4	T4	100%	2%	50	2	4%
5	T5	100%	2%	50	1	2%
6	T6	100%	2%	50	1	2%
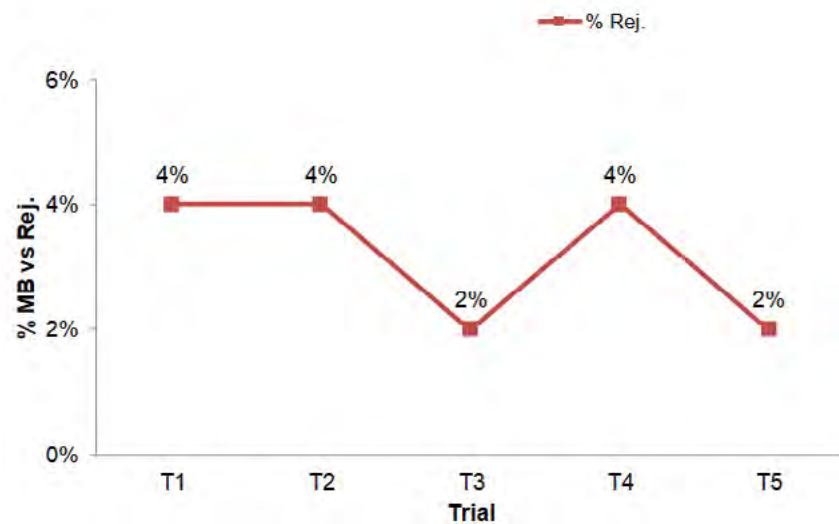
Figure 10. Grade 394 Master batch trial Graph

After taking a constant value of the percentage of master batch mixing and the master batch mixing time mentioned above, it was discovered that the laser printing rejection is lower in the 394 master batch than in the 340 master batch, though the difference is not significant. It has been concluded that the master batch grade change has a positive impact on reducing laser printing rejection.

3. EXPERIMENTAL TRIALS WITH SUGGESTED MATERIAL (394 MB)

3.1.1. CALCULATION OF NEW RPN

After finding the solution for cause, it has been concluded that the main causes, like the first percentage of master batch mixing, the second master batch mixing time, and the third master batch change (394), are now finalized for the further trial calculation as shown in table 5. solution for the causes, let's head towards calculating a new RPN after taking action and a percentage decrease in rejection data.

Table 5. Trial with 394 MB with 2% RM mixing

Sr/no	Trial	Raw Material PP	% of Master Batch 394	Trial Lot	NG	Rejection %
1	T1	100%	2%	50	2	4%
2	T2	100%	2%	50	2	4%
3	T3	100%	2%	50	1	2%
4	T4	100%	2%	50	2	4%
5	T5	100%	2%	50	1	2%
6	T6	100%	2%	50	1	1%

3.1.2. IMPROVED CALCULATION TRIAL

After taking actions, there is a change in the rejection number of the part value that is reduced by almost 50%. It is time to collect data after implementing the RM mixing process parameter and the percentage of RM mixing as shown in the table 6.

Table 6. Trial with 394 MB with 1% RM mixing

Trial	Raw Material PP	% Of Master Batch 394	Trial Lot	NG	% Rejection
T1	100%	3%	50	3	6%
T2	100%	2.5%	50	2	3%
T3	100%	1%	50	1	1%
T4	100%	1%	50	0	0%
T5	100%	1%	50	0	0%

Table 6 shows how lowering the percentage of master batch mixing affects the rejection part number ratio in the laser printing issue. Based on the above-mentioned trials, it has been determined that tumbler mixing for 30 minutes of a new master batch in a 1 percent ratio produces the best laser printing results with the least rejection.

4. RESULT AND DISCUSSION

As per the experimentation carried out to resolve the issue of faint printing on upper cover of the moulded part in the industry, it has been observed that there are no any problems in the process parameters set for moulding and the moulded part in injection moulding is perfect. It means, the faint printing on the moulded upper cover is not an issue of injection moulding and it was the problem due to master batch mixing in the raw material. Based on the several trials by reducing percentage of master batch 394, it has been observed that the 1% mixing of master batch 394 is improved the printing quality and the reduces rejection rate. Based on the analysis carried out the net cost saving of the printing on the moulded part is INR 2,70,812 as shown in table 7 and the reduction in rejection quantity is shown in figure 11.

Table 7. Net cost saving due to reducing rejection quantity

Cost Saving	
➤ Part Cost INR	- 45.95 INR
➤ Rejection Qty (Nov.2018-Jan.2019)	-1456 nos.
➤ Rejection amount Saving Quarterly	-66903 INR
➤ Rejection amount Saving Annually	-2,67,612 INR
➤ Inspection man power saved	-14000 INR
➤ **Net Cost Saving Per Annum**	**- 2,70,812 INR**

Extra Cost	
➤ Old master batch Cost per KG	- 150 INR
➤ New master batch Cost per KG	-200 INR
➤ Annual Master batch Consumption	- 216 Kgs
➤ Extra Cost incurred	- 10800 INR

Other Benefits
➤ Laser Printing machine capacity increased by 8%
➤ Material Mixing operator fatigue improved
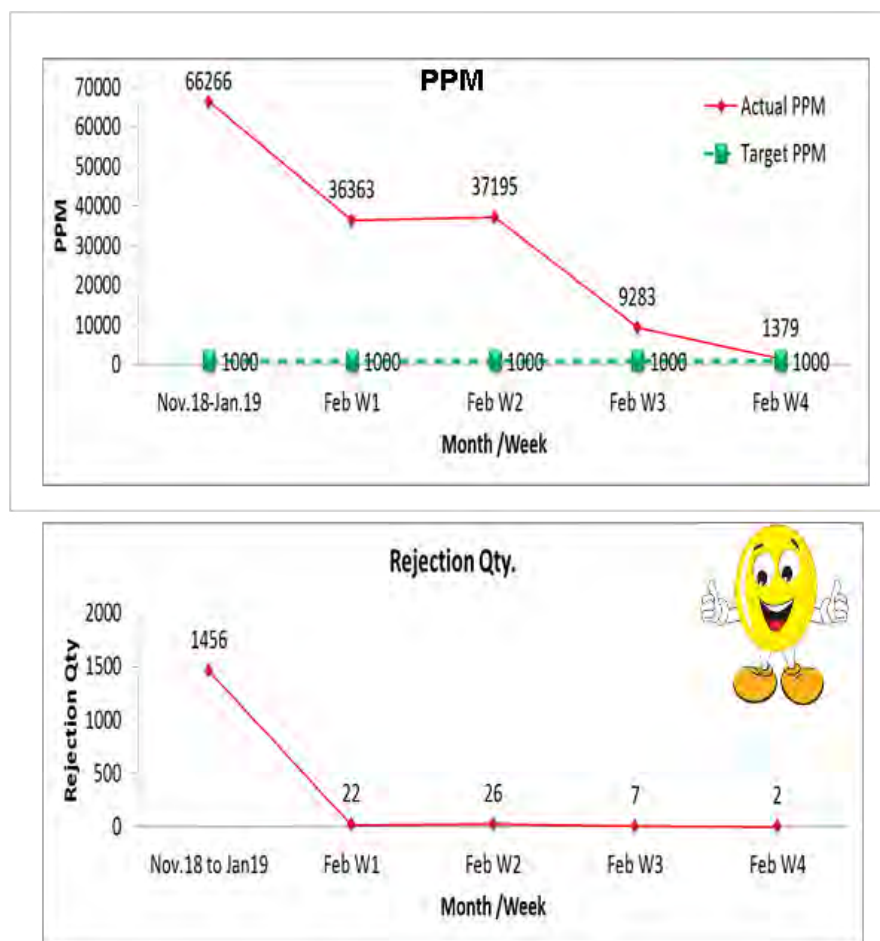
Figure 11. statistics of rejection and reduction in rejection

To reduce the further rejection of printing on any moulded part the standardization in process is very important. The process can be standardized with five quality steps as shown in figure 12. This is the future scope of this research work.
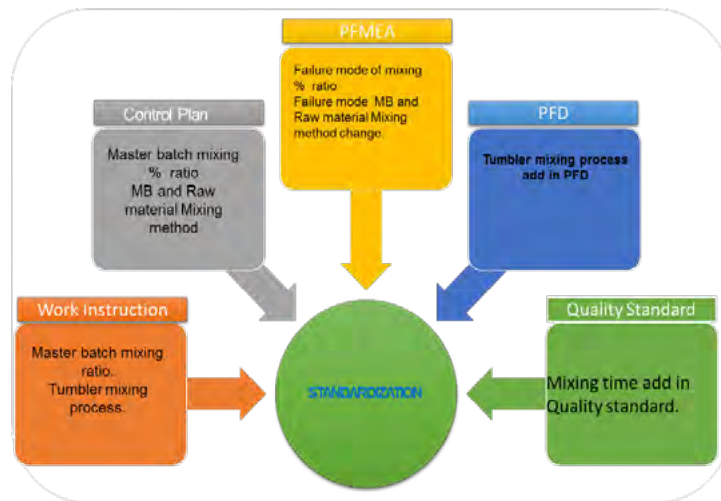
Figure 12. Standardization in process

5. CONCLUSION

• The analysis, investigation methodology is allowed to study and analyze every step of perform making process and to achieve the improvement in product and process quality. The improvements obtained by the implementation of the recommended actions thus reduce the individual rejection of part and risk level associated with each defect is reduced.

• By using 4M methodology it is help to easy recognize the main root cause and improvement.

• After implementation of action the rejection value of faint laser marking is reduced for each of the part, and the total cost saving Detail is as follow.

Cost INR	45.95 INR part
Rejection Qty. (Feb.2022-APR-2022)	456 no's
Rejection amount Saving Annually	2,67,612.0 INR
Inspection man power saved	14000 INR
Net Cost Saving (Per Annum)	2,70,812.0 INR

• By this way laser faint issue, Development time, and cost has been reduced and also there is less chance of occurring same kind of failure in future.

REFERENCES

(1)   Gaikwad, M. U., Krishnamoorthy, A., & Jatti, V. S. (2019). **Investigation and optimization of process parameters in electrical discharge machining (EDM) process for NiTi 60**. *Materials Research Express*, 6(6), 065707.

(2)   Ravikiran, B., Pradhan, D. K., Jeet, S., Bagal, D. K., Barua, A., & Nayak, S. (2022). **Parametric optimization of plastic injection moulding for FMCG**

polymer moulding (PMMA) using hybrid Taguchi-WASPAS-Ant Lion optimization algorithm. *Materials Today: Proceedings*, 56, 2411-2420.

(3)   Huang, C. (2008). **Investigation of injection molding process for high precision polymer lens manufacturing** *(Doctoral dissertation, The Ohio State University)*.

(4)   Czyżewski, P., Sykutera, D., Bieliński, M., & Troszyński, A. (2019). The impact of laser radiation on polypropylene molded pieces depending on their surface conditions. *Polymers*, *11*(10), 1660. https://doi.org/10.3390/polym11101660

(5)   Cheng, J., Zhou, J., Zhang, C., Cao, Z., Wu, D., Liu, C., & Zou, H. (2019). **Enhanced laser marking of polypropylene induced by "core-shell" ATO@ PI laser-sensitive composite**. *Polymer Degradation and Stability,* 167, 77-85.

(6)   Cheng, J., You, X., Li, H., Zhou, J., Lin, Z., Wu, D., ... & Pu, H. (2021). **Laser irradiation method to prepare polyethylene porous fiber membrane with ultrahigh xylene gas filtration capacity**. *Journal of Hazardous Materials*, 407, 124395.

(7)   Yang, J., Xiang, M., Zhu, Y., Yang, Z., & Ou, J. (2022). **Influences of carbon nanotubes/polycarbonate composite on enhanced local laser marking properties of polypropylene**. *Polymer Bulletin*, 1-13.

(8)   Cao, Z., Lu, G., Gao, H., Xue, Z., Luo, K., Wang, K., ... & Luo, M. (2021). **Preparation and laser marking properties of poly (propylene)/molybdenum sulfide composite materials**. *ACS omega*, 6(13), 9129-9140. https://doi.org/10.1021/acsomega.1c00255

(9)   **Injection moulding machine,** *DAICEL Group.*

(10) **AIM processing**

(11) **China plastic moulding**, *Jmoulding*

(12) Ready, J. F. (1997). **Industrial applications of lasers**. *Elsevier*.

(13) Kumbhalkar, M. A., Bhope, D. V., & Vanalkar, A. V. (2015). **Material and stress analysis of railroad vehicle suspension: a failure investigation**. *Procedia Materials Science*, 10, 331-343.

3C Tecnología. Glosas de innovación aplicadas a la pyme. ISSN: 2254-4143

Ed.43 | Iss.12 | N.1 January - March 2023

/22/

3C Tecnología. Glosas de innovación aplicadas a la pyme. ISSN: 2254-4143

Ed.43 | Iss.12 | N.1 January - March 2023

385

Global stability of the Euler-Bernoulli beams excited by multiplicative white noises

Zhenzhen Li

Division of Dynamics and Control, School of Mathematics and Statistics, Shandong University of Technology, ZiBo 255000, China

E-mail: zzlicncn@163.com

Kun Zhao

Beijing Electro-Mechanical Engineering Institute, Beijing 100074, P. R. China

E-mail: zhaokunhit@yeah.net

Hongkui Li

Division of Dynamics and Control, School of Mathematics and Statistics, Shandong University of Technology, ZiBo 255000, China

E-mail: Lhk8068@163.com

Juan L.G. Guirao

Department of Applied Mathematics and Statistics, Technical University of Cartagena, Hospital de Marina, Cartagena 30203, Spain

E-mail: juan.garcia@upct.es

Huatao Chen*

Division of Dynamics and Control, School of Mathematics and Statistics, Shandong University of Technology, ZiBo 255000, China

E-mail: htchencn@sdut.edu.cn

https://doi.org/10.17993/3ctecno.2023.v12n1e43.386-412

ABSTRACT

This paper considers the global stability of the Euler-Bernoulli beam excited by multiplicative white noise. Based on the theory of global random attractors, the Hausdorff dimensions of the global random attractors for the system is obtained. According to the relationship between Hausdorff dimensions and global Lyapunov exponents, the global stability of the stochastic beam is derived.

KEYWORDS

Global stochastic stability, Stochastic Euler-Bernoulli beam, Global Lyapunov exponents

1   INTRODUCTION

The dynamics of the beams are important problem in the elastokinetics [1]. Tajik [2] proposed the stability analysis of motion equations of unbalanced spinning pre-twisted beam. Dai [3] investigated the limit point bifurcations and jump of cantilevered microbeams according to Galerkin method and modal truncation. The bifurcation and chaos for transverse motion of axially accelerating viscoelastic beams was studied by Chen [4]. Pellicano [5] analyzed the linear subcritical behavior, bifurcation analysis and stability of a simply supported beam subjected to an axial transport of mass. Based on the direct method of multiple scales, Mao [6] dealt with problems of stability and saddle-node bifurcations for supercritically moving beam. Using Melnikov method [7], Zhang [8,9] investigated the multi-pulse global bifurcations of a cantilever beam. Zhou [10] studied the chaos and subharmonic bifurcation of a composite laminated buckled beam with a lumped mass. Applying the phase plane and positive position feedback approach, Hamed [11] investigated the stability and bifurcation of the cantilever beam system which carrying an intermediate lumped mass, to name but a few. For more details, one can see refer to Refs [12–15] and the references therein.

Stochastic stability is one of the most important issue in the research areas of stochastic dynamics [16]. It is well known that, when the problem associated with stability are considered, there exists a very useful tool named Lyapunov exponents which can be distinguished as local type and global type [17]. Generally speaking, the solution of system is stability when biggest Lyapunov exponent associated is less than 0. With respect to the investigations on the stability and other dynamics behaviors for the beams by using local Lyapunov exponents, one can refer to the Refs [18–20] and the references therein. Similarly, the global Lyapunov exponents are also the powerful tools in studying the global dynamics for stochastic beams. Unfortunately, calculating the global Lyapunov exponents is not an easy thing, but if we only consider the global stability of the system, we can use the Hausdorff dimension of global attractors associated with system to describe the signs of the biggest global Lyapunov exponent. The method which can be used to get the Hausdorff dimension estimations associated with the global Lyapunov exponents was due to Debussche [21]. Employing this method, together with the support relationship between global random attractors and probability invariant measures proposed by Crauel [22,23]. Chen et al [24] consider the global dynamics of the Euler-Bernoulli beams with additive white noises. With respect to investigation on the global dynamics of the nonautonomous the Euler-Bernoulli beams by global attractors theory, see Chen et al [25].

Let $D = (0, L)$, this paper consider the Euler-Bernoulli beam equation excited multiplicative white noise in the following form

$$u_{tt} + \overline{\alpha}(u_t) - \Delta^2 u + \left[\beta\|\nabla u\|^2 - p\right](-\Delta)u = \sigma u \dot{W}, \tag{1}$$

with the hinged boundary condition

$$x = 0 : u = u_{xx} = 0; x = L : u = u_{xx} = 0, \tag{2}$$

and the initial value

$$t = \tau : u = u_0, u_t = u_1, \tag{3}$$

where $u = t(t, x), x \in D$ is the lateral displacement of the beam, $\overline{\alpha}(u_t)$ denotes the damping, $\beta > 0, \sigma$ are constants, the negative and positive of $p \in \mathbb{R}$ can show the stretch and compress of the beam. $\|\nabla u\|^2$ denotes the geometry of the beam bending for its elongation. W is the one dimensional two-sided real-valued standard Wiener process, $\sigma u \dot{W}$ represents the multiplicative white noise.

Let $\|u\| \equiv \|u\|_{L^2(D)}, \|u\|_s \equiv \|u\|_{H_0^s(D)}, (u, v) \equiv (u, v)_{L^2(D)}, (u, v)_s = (u, v)_{H_0^s(D)}$, where $H^s(D)$, $H_0^s(D)$, $s \in \mathbb{R}$ are the usual Sobolev Spaces,for more detailed, see [26]. $A = \Delta^2$ with boundary condition (2), then $\mathcal{D}(A) = \{u|u \in H^4(D) \bigcap H_0^1(D), \Delta u = 0\}$, and then A is self-adjoint, positive, unbounded linear operators and $A^{-1} \in \mathscr{L}(L^2(D))$ is compact. then, their eigenvalues $\{\lambda_i\}_{i \in \mathbb{N}}$ satisfy $0 < \lambda_1 \le \lambda_2 \le \cdots \to \infty$ and the corresponding eigenvalues $\{e_i\}_{i=1}^{\infty}$ form an orthonormal basis in $L^2(D)$. Following the the mechanism in [27] p55, the power of $(-\Delta)^s, s \in \mathbb{R}$ can also be defined,particularly, $\mathcal{D}(A^{\frac{1}{2}}) = H_0^1(D) \bigcap H^2(D)$. Moreover, for any $s_1, s_2 \in \mathbb{R}, s_1 > s_2, \mathcal{D}(A^{s_1})$ can be compact imbedding in $\mathcal{D}(A^{s_2})$, and the following holds

$$\|u\|_{s_1} \ge \lambda_1^{\frac{s_1 - s_2}{2}} \|u\|_{s_2}, \quad \forall u \in \mathcal{D}(A^{s_1}). \tag{4}$$

Suppose $\overline{\alpha}(u_t) = \alpha A^{\frac{1}{2}} u_t$, here $\alpha > 0$ is a constant, $A^{\frac{1}{2}} u_t$ is called the damping with strongly form, then following abstract form of Euler-Bernoulli beam equation excited multiplicative white noises

$$
\begin{cases}
u_{tt} + \alpha A^{\frac{1}{2}} u_t + Au + \left[\beta\|\nabla u\|^2 - p\right](-\Delta)u = \sigma u \dot{W}, \\
x = 0 : u = u_{xx} = 0; x = L : u = u_{xx} = 0, \\
u(x,\tau) = u_0(x), \partial_t u(x,\tau) = u_1(x).
\end{cases}
\tag{5}
$$

The rest of paper is organized as follows. Preliminaries and main lemmas are listed in Section 2. Section 3 is devoted to derive main results and proof associated. The proofs for the main lemmas are given in Section 4. Finally, the conclusions are presented in section (4).

2   PRELIMINARIES AND MAIN LEMMAS

2.1   PRELIMINARIES

Let $E_1 = \mathcal{D}(A^{\frac{1}{2}}) \times L^2(D), E_2 = \mathcal{D}(A^{\frac{3}{4}}) \times H_0^1(D)$ equipped with Graph norms and the induced inner products, then they are all Hilbert spaces. Let $(X, \|\cdot\|_X)$ be a complete separable metric space with Borel σ-algebra $\mathcal{B}(X)$ and $(\Omega, \mathcal{F}, P)$ be a probability space. We consider $\Omega = \{\omega \mid \omega(\cdot) \in \mathbb{C}(\mathbb{R}, \mathbb{R}), \omega(0) = 0\}, \mathcal{F}$ is the σ-algebra and P is the Wiener measure. Set a family of measure preserving and ergodic transformations $\theta_t \omega(\cdot) = \omega(\cdot + t) - \omega(\cdot), \forall\ t \in \mathbb{R}$, Consider the following system

$$
\begin{cases}
dz + \mu z dt = dW \\
z(-\infty) = 0,
\end{cases}
\tag{6}
$$

and the solution of system (6) is given by

$$
z(\theta_t \omega) := -\mu \int_{-\infty}^0 e^{\mu\tau} (\theta_t \omega)(\tau) d\tau.
\tag{7}
$$

$z(\theta_t \omega)$ is Ornstein-Uhlenbeck process (in Short O-U process). The following results on O-U process belong to Fan [28].

Lemma 1. *The Ornstein-Uhlenbeck process $z(\theta_t \omega)$ defined in system (7) satisfies*

$$
\mathbb{E}\left[|z(\theta_t \omega)|\right] = \frac{1}{\sqrt{\pi\mu}},\ \mathbb{E}\left[|z(\theta_t \omega)|^2\right] = \frac{1}{2\mu},
\tag{8}
$$

and there exists a constant $t_1(\omega) > 0$ satisfying

$$
\int_{-t}^0 |z(\theta_s \omega)|\, ds < \frac{1}{\sqrt{\pi\mu}} t,\ \int_{-t}^0 |z(\theta_e \omega)|^2\, ds < \frac{1}{2\mu} t, \forall\ t \geq t_1,
\tag{9}
$$

and the mapping $t \mapsto z(\theta_t \omega)$ grows sublinearly, i.e.

$$
\lim_{t \to \pm\infty} \frac{z(\theta_t \omega)}{t} = 0.
$$

Moreover If $\mu \geq 2\beta, \beta > 0$, then

$$
\mathbb{E}\left(e^{\beta \int_s^{s+t} |z(\theta_\tau \omega)|^2 d\tau}\right) \leq e^{\frac{\beta t}{\mu}}, \forall\ s \in \mathbb{R}, t \geq 0,
\tag{10}
$$

when $\mu^3 \geq r^2, r \geq 0$, the following holds

$$
\mathbb{E}\left(e^{r \int_s^{s+t} |z(\theta_\tau \omega)| d\tau}\right) \leq e^{\frac{rt}{\sqrt{\mu}}}, \forall\ s \in \mathbb{R}, t \geq 0.
\tag{11}
$$

The following is Random dynamical system which is due to Aronld [29].

Definition 1. *The flow* $\{\theta_t : \Omega \to \Omega, t \in \mathbb{R}\}$ *is a family of measure preserving transformations in probability space, such that* $(t, \omega) \to \theta_t \omega$ *is measurable,* $\theta_0 = id$, $\theta_{t+s} = \theta_t \circ \theta_s$ *for all* $s, t \in \mathbb{R}$. *Then* $\left(\Omega, \mathcal{F}, P, \{\theta_t\}_{t \in \mathbb{R}}\right)$ *is called a metric dynamical system.*

Definition 2. *A random dynamical system (RDS) on Polish space* (X, d) *with Borel* σ *algebra* $\mathcal{B}(X)$ *on* $\left(\Omega, \mathcal{F}, P, \{\theta_t\}_{t \in \mathbb{R}}\right)$ *is a measurable mapping*

$$\phi : \mathbb{R}^+ \times \Omega \times X \to X$$
$$(t, \omega, x) \mapsto \phi(t, \omega)x$$

such that $\mathbb{P} - a.s.$

1. $\phi(0, \omega) = id$ *on* X.

2. $\phi(t + s, \omega) = \phi(t, \theta_s \omega) \circ \phi(s, \omega)$ *for all* $s, t \in \mathbb{R}^+$.

The theory of global random attractors is as following, one can refer to Crauel and Flandoli [22, 30] and Schmalfuss [31].

Definition 3. *A random set* $K(\omega)$ *is said to absorb the set* $B \subset X$ *for a RDS* ϕ, *if* $P - a.s.$ *there exists* $t_B(\omega)$ *such that*

$$\phi(t, \theta_{-t}\omega) B \subset K(\omega), \quad \forall t \geq t_B(\omega).$$

Definition 4. *Let* $\mathcal{B} \subset 2^X$ *is a collection of subsets of* X, *then a closed random set* $\mathcal{A}(\omega)$ *is called random attractor associated with the* RDS ϕ, *if* $\mathbb{P} - a.s.$

1. $\mathcal{A}(\omega)$ *is a random compact set.*

2. $\mathcal{A}(\omega)$ *is invariant i.e.* $\phi(t, \omega), \mathcal{A}(\omega) = \mathcal{A}(\theta_t \omega)$ *for all* $t \geq 0$.

3. *For every* $B \in \mathcal{B}$,
$$\lim_{t \to \infty} \text{dist}(\phi(t, \theta_{-t}\omega) B, \mathcal{A}(\omega)) = 0,$$

where dist $(\cdot, \cdot)$ *denotes the Hausdorff semidistance defined by*

$$\text{dist}(A, B) = \sup_{x \in A} \inf_{y \in B} d(x, y), A, B \subset X.$$

The following random fixed point is important in investigating the global stability.

Definition 5. *[29, 32] Let* $\varphi(t, \omega)$ *be a RDS,* $a(\omega)$ *is a random set and consists of one point* $(\mathbb{P} - a.s.)$. $a(\omega)$ *is called the random fixed point if the following holds*

$$\varphi(t, \omega)a(\omega) = a(\theta_t \omega), \quad \forall t \in \mathbb{R}^+.$$

The coming theorem is very useful to verify the existence of global random attractors in this paper.

Theorem 1. *[24] Suppose* $S_\varepsilon(t, \omega)$ *is a RDS on Polish space* (X, d), *and suppose that* ϕ *possesses an absorbing set in* X *and for any nonrandom bounded set* $B \subset X$, $\lim_{t \to +\infty} S_\varepsilon(t, \theta_{-t}\omega) B$ *is relative compact* *P-a.s. Then* ϕ *possesses uniqueness random attractors defined by the following*

$$\mathscr{A}(\omega) = \overline{\bigcup_{B \in X} \Lambda_B(\omega)},$$

where union is taken over all bounded $B \subset X$, *and* $\Lambda_B(\omega)$ *given by*

$$\Lambda_B(\omega) = \bigcap_{s \geq 0} \overline{\bigcup_{t \geq s} \phi(t, \theta_{-t}\omega) B}.$$

Some powerful transformation on system (5) are derived as following. Set $v_1 = u_t$, we get

$$
\begin{cases}
u_t = v_1, \\
v_{1t} = -\alpha A^{\frac{1}{2}} v_1 - Au - \left[\beta\|\nabla u\|^2 - p\right](-\Delta)u + \sigma u \dot{W}, \\
x = 0 : u = u_x = 0; x = L : u = u_{xx} = 0, \\
u(x,\tau) = u_0(x), v_1(x,\tau) = u_1(x),
\end{cases}
\tag{12}
$$

let $v_2 = v_1 + \varepsilon u$, here $\varepsilon > 0$, we have

$$
\frac{d\boldsymbol{U}}{dt} = \boldsymbol{Q}\boldsymbol{U} + \boldsymbol{X}_1(\omega, \boldsymbol{U}), \ \boldsymbol{U}_\tau = (u_0, u_1 + \varepsilon u_0)^T,
\tag{13}
$$

where

$$
\boldsymbol{U} = \begin{pmatrix} U_1 \\ U_2 \end{pmatrix} = \begin{pmatrix} u \\ v_2 \end{pmatrix}, \ \boldsymbol{Q} = \begin{pmatrix} -\varepsilon I, I \\ -A + \varepsilon\left(\alpha A^{\frac{1}{2}} - \varepsilon\right), -\left(\alpha A^{\frac{1}{2}} - \varepsilon\right) I \end{pmatrix},
$$

$$
\boldsymbol{X}_1(\omega, \boldsymbol{U}) = \begin{pmatrix} X_{11}(\omega, \boldsymbol{U}) \\ X_{12}(\omega, \boldsymbol{U}) \end{pmatrix} = \begin{pmatrix} 0 \\ -\left[\beta\|\nabla u\|^2 - p\right](-\Delta)u + \sigma u \dot{W} \end{pmatrix}.
$$

System (5) and system (13) are equivalent, thus, the dynamical behavior of system (5) can be reflected by system (13).

Set $v = u_t + \varepsilon u - \sigma u z(\theta_t \omega)$, where $z(\theta_t \omega)$ O-U process formulated by (6), it gives that

$$
\frac{d\boldsymbol{V}}{dt} = \boldsymbol{Q}\boldsymbol{V} + \boldsymbol{X}_2(\theta_t \omega) + \boldsymbol{X}_3(V), \ \boldsymbol{V}_\tau = (u_0, u_1 + \varepsilon u_0 - \sigma u_0 z(\theta_t \omega))^T,
\tag{14}
$$

where

$$
\boldsymbol{V} = \begin{pmatrix} V_1 \\ V_2 \end{pmatrix} = \begin{pmatrix} u \\ v \end{pmatrix}, \ \boldsymbol{X}_3(V) = \begin{pmatrix} X_{31}(V) \\ X_{32}(V) \end{pmatrix} = \begin{pmatrix} 0 \\ -\left[\beta\|\nabla u\|^2 - p\right](-\Delta)u \end{pmatrix},
$$

$$
\boldsymbol{X}_2(\theta_t \omega) = \begin{pmatrix} X_{21}(\theta_t \omega) \\ X_{22}(\theta_t \omega) \end{pmatrix} = \begin{pmatrix} \sigma u z(\theta_t \omega) \\ \sigma\left(\mu - \alpha A^{\frac{1}{2}} + 2\varepsilon - \sigma z(\theta_t \omega)\right) u z(\theta_t \omega) - \sigma v z(\theta_t \omega) \end{pmatrix}.
$$

System (14) is a system with random coefficient, which can be studied ω by ω.

2.2   MAIN LEMMAS

In order to obtain the global stochastic stability of the system (13) based on the global random attractors theory, the first step should be utilized to verify the system (13) can induce a RDS.

Lemma 2. *For any $\tau \in \mathbb{R}$ and initial value $\boldsymbol{V}_\tau \in E_1$, system (14) possesses a unique local mild solution $\boldsymbol{V}(t, \tau, \omega; \boldsymbol{V}_\tau) \in C([\tau, \tau + T], E_1), t \in [\tau, \tau + T], \forall T > 0$.*

Let $\varphi(t, \tau, \omega)$ be the solution mapping determined by system (14), which means $\boldsymbol{V}(t, \tau, \omega; \boldsymbol{V}_\tau) = \varphi(t, \tau, \omega)\boldsymbol{V}_\tau$, we have $\varphi(t, 0, \omega) = \varphi(0, -t, \theta_t \omega), \forall t \geq 0, \forall \omega \in \Omega$. Defining

$$
S(t, \omega) := \varphi(t, 0, \omega), \quad \forall t \geq 0, \forall \omega \in \Omega,
$$

gives the RDS associated with system (14), which together with the relationship between $\iota_\varepsilon : (u, v_1)^T \to [y, v_1 - \sigma u z(\theta_t \omega)]^T = (u, v)^T$ implies that system (13) can also generate a RDS $S_\varepsilon(t, \omega)$ with the following from

$$
S_\varepsilon(t, \omega) = \iota^{-1}(\theta_t \omega), S(t, \omega)\iota(\omega) : E_1 \to E_1,
$$

is the RDS induced by system (13). The following are very important in proof for the existence of the global random attractors for the system (14).

Let

$$
p \leq \frac{2}{3}\lambda_1^{\frac{1}{4}}, \ 0 < \varepsilon = \min\left\{1, \frac{\alpha\left(8\lambda_1^{\frac{1}{4}} - 12p\right)}{\lambda_1^{\frac{1}{4}}\left(10\lambda_1^{\frac{1}{4}} - 15p + 4\alpha^2\lambda_1^{\frac{1}{4}}\right)}\right\},
\tag{15}
$$

then

Lemma 3. *For any given $\boldsymbol{U} = [U_1, U_2]^T \in E_1$, the following holds*

$$(\boldsymbol{QU}, \boldsymbol{U})_{E_1} \leq -\frac{\varepsilon}{2}\|\boldsymbol{U}\|_{E_1}^2 - \frac{\varepsilon}{4}\|U_2\|^2 - \frac{3p\varepsilon}{4}\|A^{\frac{1}{4}}U_1\|^2.$$

Based on the Lemma 3, we have

Lemma 4. *For any given bounded set $B \in E_1$, there exists a random variable $r_1(\omega) > 0$ and $T_B(\omega) \geq 0$, for $\forall\, t \geq T_B(\omega)$, the following holds,*

$$\|S_\varepsilon(t, \theta_{-t}\omega)B\|_{E_1} \leq r_1(\omega).$$

Furthermore,

$$\mathbb{E}\left(r_1^2(\omega)\right) < \infty.$$

Lemma 4 shows that $S_\varepsilon(t, \omega)$ has a global absorbing set. In order to obtain the existence of the global random attractors for the system $S_\varepsilon(t, \omega)$, besides the existence of the global absorbing set, we need verify that the $S_\varepsilon(t, \omega)$ is asymptotically compact.

To begin with, we decompose the solution $\boldsymbol{V}$ generated by system (13) with the initial value $\boldsymbol{U}_\tau(\omega) = (u_0, u_1 + \varepsilon u_0)^T$ into two parts $\boldsymbol{U} = \boldsymbol{U}^a + \boldsymbol{U}^b = (u^a, u_t^a + \varepsilon u^a)^T + \left(u^b, u_t^b + \varepsilon u^b\right)^T$, where $\boldsymbol{U}^a$ solves

$$
\begin{cases}
\frac{d\boldsymbol{U}^a}{dt} = \boldsymbol{QU}^a + \left(0, \sigma u^a \dot{W}\right)^T \\[2mm]
\boldsymbol{U}_\tau^a(\omega) = 0,
\end{cases}
\tag{16}
$$

and $\boldsymbol{U}^b$ solves

$$
\begin{cases}
\frac{d\boldsymbol{U}^b}{dt} = \boldsymbol{QU}^b + \left(0, -\left[\beta\|\nabla u\|^2 - p\right](-\Delta)u + \sigma u^b \dot{W}\right)^T \\[2mm]
\boldsymbol{U}_\tau^b = (u_0, u_1 + \varepsilon u_0)^T.
\end{cases}
\tag{17}
$$

Split the solution $\boldsymbol{V}$ of system (14) with the initial value $\boldsymbol{V}_\tau(\omega) = (u_0, u_1 + \varepsilon u_0 - \sigma u_0 z(\theta_{-\tau}\omega))^T$ into two parts $\boldsymbol{V} = \boldsymbol{V}^a + \boldsymbol{V}^b = (u^a, v^a)^T + \left(u^b, v^b\right)^T = (u^a, u_t^a + \varepsilon u^a)^T + \left(u^b, u_t^b + \varepsilon u^b - \sigma u z(\theta_t \omega)\right)^T$, where $\boldsymbol{V}^a$ solves

$$
\begin{cases}
\frac{d\boldsymbol{V}^a}{dt} = \boldsymbol{QV}^a + \left(\sigma u^a z(\theta_t \omega), \sigma\left(\mu - \alpha A^{\frac{1}{2}} + 2\varepsilon - \sigma z(\theta_t \omega)\right) u^a z(\theta_t \omega) - \sigma v^a z(\theta_t \omega)\right)^T \\[2mm]
\boldsymbol{V}_\tau^a(\omega) = 0,
\end{cases}
\tag{18}
$$

and $\boldsymbol{V}^b$ solves

$$
\begin{cases}
\frac{d\boldsymbol{V}^b}{dt} = \boldsymbol{QV}^b + \left(\sigma u^b z(\theta_t \omega), \sigma\left(\mu - \alpha A^{\frac{1}{2}} + 2\varepsilon - \sigma z(\theta_t \omega)\right) u^b z(\theta_t \omega) - \sigma v^b z(\theta_t \omega)\right)^T \\[2mm]
\qquad + \left(0, \left[\beta\|\nabla u\|^2 - p\right]\Delta u\right)^T \\[2mm]
\boldsymbol{V}_\tau^b = (u_0, u_1 + \varepsilon u_0 - \sigma u_0 z(\theta_{-\tau}\omega))^T.
\end{cases}
\tag{19}
$$

For the solutions of system (18) and (19), we have the following priori estimates respectively.

Lemma 5. *The solution $\boldsymbol{U}^a$ of system (16) satisfies*

$$\lim_{t \to +\infty} \left\|A^{\frac{1}{4}}\boldsymbol{U}^a\right\|_{E_1} = 0.$$

Lemma 6. *There exists $r_2(\omega) > \infty, T_2(\omega) \geq 0$, the solutions $\boldsymbol{U}^b$ satisfies*

$$\left\|\boldsymbol{U}^b\right\|_{E_1} \leq r_2(\omega), \quad \forall\, t \geq T_2(\omega).$$

Lemma 7. *There exists $r_3(\omega) > 0, T_3(\omega) \geq 0$, the following holds*

$$\left\|A^{\frac{1}{4}}\boldsymbol{U}^b\right\|_{E_1} \leq r_3(\omega), \quad \forall\, t \geq T_3(\omega).$$

The variation equations of system (13)

$$\frac{d\widehat{U}}{dt} = Q\widehat{U} + \widehat{X}(U)\widehat{U}, \tag{20}$$

where

$$\widehat{X}(U) = \begin{pmatrix} \widehat{X}_1(U), \widehat{X}_3(U) \\ \widehat{X}_2(U), \widehat{X}_4(U) \end{pmatrix}$$

$$= \begin{pmatrix} 0, 0 \\ \left[\beta\|\nabla u\|^2 - p\right](-\Delta)\cdot + 2\beta(\nabla u, \nabla\cdot)(-\Delta)u + \sigma\dot{W}, 0 \end{pmatrix}.$$

On the other hand

$$\frac{d\widehat{V}}{dt} = Q\widehat{V} + \widehat{X}_2(V)\widehat{V} + \widehat{X}_3(V)\widehat{V}, \tag{21}$$

here $\widehat{V} = \{\widehat{V}_1, \widehat{V}_2\}$,

$$\widehat{X}_2((\theta_t\omega)) = \begin{pmatrix} \widehat{X}_{21}((\theta_t\omega)), \widehat{X}_{23}((\theta_t\omega)) \\ \widehat{X}_{22}((\theta_t\omega)), \widehat{X}_{24}((\theta_t\omega)) \end{pmatrix}$$

$$= \begin{pmatrix} \sigma z(\theta_t\omega), 0 \\ \sigma(\mu - \alpha + 2\varepsilon - \sigma z(\theta_t\omega)) z(\theta_t\omega), -\sigma z(\theta_t\omega) \end{pmatrix},$$

$$\widehat{X}_3(V) = \begin{pmatrix} \widehat{X}_{31}(V), \widehat{X}_{33}(V) \\ \widehat{X}_{32}(V), \widehat{X}_{34}(V) \end{pmatrix}$$

$$= \begin{pmatrix} 0, 0 \\ \left[\beta\|\nabla u\|^2 - p\right](-\Delta)\cdot + 2\beta(\nabla u, \nabla\cdot)(-\Delta)u, 0 \end{pmatrix}.$$

Let $\widehat{U} = \left[\widehat{U}_1, \widehat{U}_2\right]$ be the solution of system (20) with initial $t = 0 : \widehat{U}^0 \in E_1$ and $\widehat{V} = \left[\widehat{V}_1, \widehat{V}_2\right]$ be the solution of system (21) with initial value $t = 0 : \widehat{V}_0 = I \in E_1$.

Let $U^{(1)} = \left[U_1^{(1)}, U_2^{(1)}\right], U^{(2)} = \left[U_1^{(2)}, U_2^{(2)}\right]$ are two solutions of system (13), then

$$\frac{dU^{(1)} - U^{(2)}}{dt} = Q\left(U^{(1)} - U^{(2)}\right) + X_1\left(U^{(1)}\right) - X_1\left(U^{(2)}\right), \tag{22}$$

Analogously, let $V^{(1)} = \left[V_1^{(1)}, V_2^{(1)}\right] = [u_1, v_1], V^{(2)} = \left[V_1^{(2)}, V_2^{(2)}\right] = [u_2, v_2]$ are two solutions of system (14) with initial values $V_0^{(1)}, V_0^{(2)}$, where $V_0^{(2)} = V_0^{(1)} + I, I = [I_1, I_2] \in E_1$, then

$$\begin{aligned} \frac{dV^{(1)} - V^{(2)}}{dt} &= Q\left(V^{(1)} - V^{(2)}\right) + X_2\left(V^{(1)}\right) - X_2\left(V^{(2)}\right) \\ &+ X_3\left(V^{(1)}\right) - X_3\left(V^{(2)}\right). \end{aligned} \tag{23}$$

In addition, set $\boldsymbol{\Gamma} = [\Gamma_1, \Gamma_2]^T = U^{(1)} - U^{(2)} - \widehat{U}$, we have the following two Lemmas.

Lemma 8. *For $\forall u_1, u_2 \in \mathcal{D}(A^{\frac{1}{2}})$, there exist constants $c_1(\omega), c_2(\omega)$ in (51), such that*

$$\left\|\widehat{X}_{32}(u_1) - \widehat{X}_{32}(u_2)\right\|_{\mathscr{L}\left(\mathcal{D}(A^{\frac{1}{2}}), L^2(D)\right)} \leq c_1(\omega)\left\|A^{\frac{1}{2}}u_1 - A^{\frac{1}{2}}u_2\right\|,$$

$$\left\|\widehat{X}_{32}(u_1)\right\|_{\mathscr{L}\left(\mathcal{D}(A^{\frac{1}{2}}), L^2(D)\right)} \leq c_2(\omega). \tag{24}$$

Furthemnore,

$$\mathbb{E}(c_1(\omega)) < \infty, \mathbb{E}(c_2(\omega)) < \infty.$$

Lemma 9. *Let $S_\varepsilon(\omega) := S_\varepsilon(t, \omega)$, then $S_\varepsilon(\omega)$ is uniformly quasidifferentiable on $\mathscr{A}(\omega)$.*

The following relationship between Hausdorff dimension and global Lyapunov exponents which will be used to assert the global stochastic stability.

Theorem 2. *[21]Suppose that, for $k = 1, \ldots, d$, $\sup\limits_{u \in A(\omega)} \omega_k(DS_\varepsilon(\omega, u))$ is integrable. Then we can generalize the notion of global Lyapunov exponents introduced in Ref. [17] by setting*

$$\Lambda_k = \mathbb{E}\left(\ln \sup_{u \in A(\omega)} \omega_k(DS_\varepsilon(\omega, u))\right) - \mathbb{E}\left(\ln \sup_{u \in A(\omega)} \omega_{k-1}(DS_\varepsilon(\omega, u))\right),$$

for $k \geq 2$ and

$$\Lambda_1 = \mathbb{E}\left(\ln \sup_{u \in A(\omega)} \omega_1(DS_\varepsilon(\omega, u))\right).$$

And it is easy to see that there exists $\overline{\omega}_d$ satisfying $(26)(27)$ if and only if

$$\Lambda_1 + \ldots + \Lambda_d < 0.$$

3   MAIN RESULTS AND PROOFS

By Lemma 4, we get that $S_\varepsilon(t, \omega)$ has a global absorbing set, which along with Lemma 5, Lemma 6 and Lemma 7 gives that $S_\varepsilon(t, \omega)$ is asymptotically compact. Thus, employing the Theorem 1, it is asserted that there exist global random attractors $\mathscr{A}(\omega), \omega \in \Omega$ for system 13.

Based on the results and the estimations on global random attractors, the Hausdorff dimension of the global random attractors $\mathscr{A}(\omega)$ can be got by the method proposed by Debussche [21]. The outline of this method is as follows.

Firstly, it is verified that $S_\varepsilon(\omega)$ is almost surely *uniformly differentiable* on $A(w)$, i.e. for $\forall u \in A(w)$, there exist a linear operator $DS_\varepsilon(\omega, u)$ in $\mathscr{L}(H)$, the space of continuous linear operator from H to H, such that if u and $u + h$ are in $A(w)$:

$$|S_\varepsilon(\omega)(u + h) - S_\varepsilon(\omega)u - DS_\varepsilon(\omega, u)h| \leq K(\omega)|h|^{1+\alpha}, \tag{25}$$

where $K(w) \geq 1, w \in \Omega$ is a random variable, and $\alpha > 0$ is a constant.

Secondly, there exists an integrable random variable $\overline{\omega}_d$, such that

$$\omega_d(DS_\varepsilon(\omega, u)) \leq \overline{\omega}_d(\omega), \quad \forall u \in \mathscr{A}(\omega), \ \mathbb{P} - a.s, \tag{26}$$

and

$$\mathbb{E}\left(\ln\left(\overline{\omega}_d\right)\right) < 0. \tag{27}$$

Thirdly, there exists a random variable $\overline{\alpha}_1$ such $\mathbb{P}$ almost surely

$$\overline{\alpha}_1 \geq 1, \ \alpha_1(DS_\varepsilon(\omega, u)) \leq \overline{\alpha}_1(\omega), \quad \forall u \in \mathscr{A}(\omega), \ \mathbb{P} - a.s, \tag{28}$$

and

$$\mathbb{E}\left(\ln \overline{\alpha}_1\right) < \infty. \tag{29}$$

Finally,

$$\mathbb{E}(\ln K) < \infty. \tag{30}$$

If the $(26),(27),(28)(29)$ and (30) hold, the Hausdorff dimension of $\mathscr{A}(w)$ is less than d.

The main results in this paper is given in the following Theorem.

Theorem 3. *Let*

$$d = \min\left\{ n \in \mathbb{Z}^+ \mid \frac{1}{n}\sum_{i=1}^{n}\lambda_i^{-\frac{1}{2}} < \frac{\frac{\varepsilon}{2} - \frac{8}{\varepsilon}\left(\beta\bar{r}^2 + |p|\right)^2 - \frac{2M_7}{\sqrt{\pi\mu}} - \frac{2M_8}{2\mu}}{\frac{16\beta^2\bar{r}^4}{\varepsilon\lambda_1^{\frac{1}{4}}}} \right\},$$

when M_7, M_8 are constants described by (56) stated in Section 4, then the Hausdorff dimension of $\mathscr{A}(\omega)$

$$d_H(\mathscr{A}(\omega)) < d.$$

Obviously, employing and Theorem 2, we have that when

$$\lambda_1^{-\frac{1}{2}} \leq \frac{\frac{\varepsilon}{2} - \frac{8}{\varepsilon}\left(\beta\bar{r}^2 + |p|\right)^2 - \frac{2M_7}{\sqrt{\pi\mu}} - \frac{2M_8}{2\mu}}{\frac{16\beta^2\bar{r}^4}{\varepsilon\lambda_1^{\frac{1}{4}}}},$$

the Hausdorff dimension of for system (13) *is 0, which indicates that the global random attractors consists of only one random fixed point which is global stability.*

Proof. The solution mapping of system (20) denoted by $DS_\varepsilon(t, \omega, \boldsymbol{U})$, and $DS(t, \omega, \boldsymbol{V})$ signifies the solution mapping of system (21). Moreover, let $DS_\varepsilon(\omega, \boldsymbol{U}) := DS_\varepsilon(1, \omega, \boldsymbol{U})$. By Lemma 9, we attain $S_\varepsilon(\omega)$ is almost surely uniform differentiable, and the conditions (25) and (30) hold. In the light of (90) and (91) stated in the proof of Lemma 9 in Section 4, the (28) and (29) are satisfied. On the other hand, we have

$$\overline{\omega}_n(DS(\omega, \boldsymbol{V})) = \sup_{\substack{\left\|\overline{U}_0^{(i)}\right\| < 1 \\ i=1,\dots,n}} \exp\left(\frac{1}{t}\int_0^t \mathrm{Tr}(\boldsymbol{Q} + \widehat{\boldsymbol{X}}_2(V) + \widehat{\boldsymbol{X}}_3(V)) \circ Q_n(s)ds\right),$$

where $Q_n(s) = Q_n\left(s, \tau, \boldsymbol{V}_\tau; \widehat{\boldsymbol{V}}_1^0, \dots, \widehat{\boldsymbol{V}}_n^0\right)$ is the orthogonal projector from E_1 onto the space spanned by $\widehat{\boldsymbol{V}}_1(t), \dots, \widehat{\boldsymbol{V}}_n(t)$, here $\boldsymbol{V} = S(t, \tau)\boldsymbol{V}_\tau$ and $\widehat{\boldsymbol{V}}_1, \dots, \widehat{\boldsymbol{V}}_n$ are the solution of system (21) with initial values $\widehat{\boldsymbol{V}}^0 = \widehat{\boldsymbol{V}}_1^0, \dots, \widehat{\boldsymbol{V}}_n^0$ respectively. For any given time s, $\boldsymbol{V}_i(s) = \{\mu_i(s), \nu_i(\tau)\}, i = 1, \dots, n$ is an orthonormal basis of $Q_n(s)E_1$, then

$$\mathrm{Tr}(\boldsymbol{Q} + \widehat{\boldsymbol{X}}_2(V) + \widehat{\boldsymbol{X}}_3(V)) \circ Q_n(s) = \sum_{i=1}^{n}\left((\boldsymbol{Q} + \widehat{\boldsymbol{X}}_2(V) + \widehat{\boldsymbol{X}}_3(V))\boldsymbol{V}_i(s), \boldsymbol{V}_i(s)\right)_{E_1}.$$

In term of Lemma 3, we get

$$(\boldsymbol{Q}\boldsymbol{V}_i, \boldsymbol{V}_i)_{E_1} \leq -\frac{\varepsilon}{2}\|\boldsymbol{V}_i\|_{E_1}^2 - \frac{\varepsilon}{4}\|\nu_i\|^2,$$

and

$$\begin{aligned}
\left(\widehat{\boldsymbol{X}}_3\boldsymbol{V}_i, \boldsymbol{V}_i\right)_{E_1} &= -\left(\left[\beta\|\nabla u\|^2 - p\right](-\Delta)\mu_i, \nu_i\right) - (2\beta(\nabla u, \nabla\mu_i)(-\Delta)u, \nu_i) \\
&\leq \left\|\left[\beta\|\nabla u\|^2 - p\right](-\Delta)\mu_i\right\|\|\nu_i\| + \|2\beta(\nabla u, \nabla\mu_i)(-\Delta)u\|\|\nu_i\| \\
&\leq |\beta\|\nabla u\|^2 - p|\|\Delta\mu_i\|\|\nu_i\| + \frac{2\beta}{\lambda_1^{\frac{1}{8}}}\|\Delta u\|^2\|\nabla\mu_i\|\|\nu_i\| \\
&\leq \frac{8}{\varepsilon}\left(\beta\bar{r}^2 + |p|\right)^2\|\Delta\mu_i\|^2 + \frac{16\beta^2\bar{r}^4}{\varepsilon\lambda_1^{\frac{1}{4}}}\|\nabla\mu_i\|^2 + \frac{\varepsilon}{4}\|\nu_i\|^2,
\end{aligned}\tag{31}$$

moreover, we have

$$\left(\widehat{\boldsymbol{X}}_2\widehat{\boldsymbol{V}}, \widehat{\boldsymbol{V}}\right) \leq \left(M_7\left|z\left(\theta_t\omega\right)\right| + M_8\left|z\left(\theta_t\omega\right)\right|^2\right)\left(\left\|\widehat{V}_1\right\|_{H^2}^2 + \left\|\widehat{V}_2\right\|_{H^2}^2\right),\tag{32}$$

where M_7, M_8 defined by (57) stated in Section 4. Hence, we can obtain

$$\text{Tr}(\boldsymbol{Q} + \widehat{\boldsymbol{X}}_2(\boldsymbol{V}) + \widehat{\boldsymbol{X}}_3(\boldsymbol{V})) \circ Q_n(s)$$

$$\leq -\frac{\varepsilon}{2}\|\boldsymbol{V}_i\|_{E_1}^2 + \frac{8}{\varepsilon}\left(\beta\bar{r}^2 + |p|\right)^2 \|\Delta\mu_i\|^2 + \frac{16\beta^2\bar{r}^4}{\varepsilon\lambda_1^{\frac{1}{4}}}\|\nabla\mu_i\|^2$$

$$+ \left(M_7\,|z\,(\theta_t\omega)| + M_8\,|z\,(\theta_t\omega)|^2\right)\left(\left\|\widehat{V}_1\right\|_{H^2}^2 + \left\|\widehat{V}_2\right\|_{H^2}^2\right)$$

$$\leq -\frac{n\varepsilon}{2} + \frac{8n}{\varepsilon}\left(\beta\bar{r}^2 + |p|\right)^2 + \frac{16\beta^2\bar{r}^4}{\varepsilon\lambda_1^{\frac{1}{4}}}\sum_{i=1}^n\lambda_i^{-\frac{1}{2}}$$

$$+2n\left(M_7\,|z\,(\theta_t\omega)| + M_8\,|z\,(\theta_t\omega)|^2\right).$$

Thus,

$$\overline{\omega}_n(DS_\varepsilon(\omega,\boldsymbol{V})) = \sup_{\substack{\left\|\overline{U}_0^{(i)}\right\|<1 \\ i=1,\dots,n}} \exp\left(\frac{1}{t}\int_0^t \text{Tr}(\boldsymbol{Q} + \widehat{\boldsymbol{X}}_2(V) + \widehat{\boldsymbol{X}}_3(V)) \circ Q_n(s)ds\right)$$

$$= \exp\left(\frac{1}{t}\int_0^t -\frac{n\varepsilon}{2} + \frac{8n}{\varepsilon}\left(\beta\bar{r}^2 + |p|\right)^2 + \frac{16\beta^2\bar{r}^4}{\varepsilon\lambda_1^{\frac{1}{4}}}\sum_{i=1}^n\lambda_i^{-\frac{1}{2}} + 2n\left(M_7\,|z\,(\theta_t\omega)| + M_8\,|z\,(\theta_t\omega)|^2\right)ds\right),$$

which together with (9) gives that $\exists\, T_4(\omega) > 0, \forall\, t \geq T_4$,

$$\overline{\omega}_n(DS_\varepsilon(\omega,\boldsymbol{V}))$$

$$\leq \exp\left(-\frac{n\varepsilon}{2} + \frac{8n}{\varepsilon}\left(\beta\bar{r}^2 + |p|\right)^2 + \frac{2nM_7}{\sqrt{\pi\mu}} + \frac{2nM_8}{2\mu} + \frac{16\beta^2\bar{r}^4}{\varepsilon\lambda_1^{\frac{1}{4}}}\sum_{i=1}^n\lambda_i^{-\frac{1}{2}}\right). \qquad (33)$$

Let

$$T(\theta_t\omega) = \begin{pmatrix} 1 & 0 \\ \sigma z\,(\theta_t\omega) & 1 \end{pmatrix}.$$

Clearly, $T(\theta_t\omega)$ is a linear operator from E_1 to itself, then we have

$$DS_\varepsilon(t,\omega) = T(\theta_t\omega)DS(T,\omega).$$

Let O_n be the space spanned by $e_1,\dots,e_n$ for any $n \in \mathbb{N}$, then the quadratic form $\chi \in O_n \mapsto \|T(\theta_t\omega)\chi\|_{E_1}^2$ is well defined, continuous, and nonnegative on O_n. Let $\alpha_1 \geq \cdots \geq \alpha_n$ be the eigenvalues associated with $\chi_1, \chi_2, \dots, \chi_n \in O_n$ satisfying

$$(T(\theta_t\omega)\chi_i, T(\theta_t\omega)\chi_j)_{E_1} = \alpha_i^2\delta_{ij}.$$

Set $\chi_j = (\xi_j, \eta_j)^T, j = 1, 2, \dots, n$, it can be derived

$$\alpha_i^2 = (T(\theta_t\omega)\chi_i, T(\theta_t\omega)\chi_i)_{E_1}$$

$$\leq (\xi_j, \xi_j)_{H^2} + (\sigma z\,(\theta_t\omega)\,\xi_j + \eta_j, \sigma z\,(\theta_t\omega)\,\xi_j + \eta_j)$$

$$\leq (\xi_j, \xi_j)_{H^2} + (\eta_j, \eta_j) + 2\sigma|z\,(\theta_t\omega)|\,\|\xi_j\|\,\|\eta_j\| + \sigma^2|z\,(\theta_t\omega)|^2\,(\xi_j, \xi_j)$$

$$\leq \|\xi_j\|_{H^2}^2 + \|\eta_j\|^2 + \frac{1}{\lambda_1^{\frac{1}{2}}}\left(\sigma|z\,(\theta_t\omega)| + \sigma^2|z\,(\theta_t\omega)|^2\right)\|\xi_j\|_{H^2}^2 + \sigma|z\,(\theta_t\omega)|\,\|\eta_j\|^2$$

$$\leq 1 + \frac{\sigma}{\lambda_1^{\frac{1}{2}}}|z\,(\theta_t\omega)| + \frac{\sigma^2}{\lambda_1^{\frac{1}{2}}}|z\,(\theta_t\omega)|^2 + \lambda_1^{-1} + \lambda_1^{-1}\sigma|z\,(\theta_t\omega)|.$$

So

$$\ln\alpha_i \leq \ln\left(\frac{\sigma}{2\lambda_1^{\frac{1}{2}}}|z\,(\theta_t\omega)| + \frac{\sigma}{2\lambda_1^{\frac{1}{2}}}|z\,(\theta_t\omega)|^2 + \frac{1}{2\lambda_1} + \frac{\sigma}{2\lambda_1}|z\,(\theta_t\omega)|\right),$$

for any $1 \leq i \leq n$. Since

$$\omega_n(T(\theta_t\omega)) = \alpha_1\alpha_2\ldots\alpha_n,$$

we obtain

$$\ln\omega_n(T(\theta_t\omega)) \leq \ln\left(\frac{n\sigma}{2\lambda_1^{\frac{1}{2}}}|z(\theta_t\omega)| + \frac{n\sigma}{2\lambda_1^{\frac{1}{2}}}|z(\theta_t\omega)|^2 + \frac{n}{2\lambda_1} + \frac{n\sigma}{2\lambda_1}|z(\theta_t\omega)|\right), \tag{34}$$

which combine with Lemma 1 gives that

$$\mathbb{E}\left(\omega_n(T(\theta_t\omega))\right) \leq \mathbb{E}\left(\frac{n\sigma}{2\lambda_1^{\frac{1}{2}}}|z(\theta_t\omega)| + \frac{n\sigma}{2\lambda_1^{\frac{1}{2}}}|z(\theta_t\omega)|^2 + \frac{n}{2\lambda_1} + \frac{n\sigma}{2\lambda_1}|z(\theta_t\omega)|\right)$$

$$\leq M_9, \tag{35}$$

where M_9 given by (58) stated in Section 4. Since (33) and (34), we get that

$$\ln\overline{\omega}_n(DS_\varepsilon(\omega,\boldsymbol{U})) = \ln\overline{\omega}_n(T(\theta_t\omega)) + \ln\overline{\omega}_n(DS(T,\omega))$$

$$\leq \ln\left(\frac{n\sigma}{2\lambda_1^{\frac{1}{2}}}|z(\theta_t\omega)| + \frac{n\sigma}{2\lambda_1^{\frac{1}{2}}}|z(\theta_t\omega)|^2 + \frac{n}{2\lambda_1} + \frac{n\sigma}{2\lambda_1}|z(\theta_t\omega)|\right)$$

$$- \frac{n\varepsilon}{2} + \frac{8n}{\varepsilon}\left(\beta\overline{r}^2 + |p|\right)^2 + \frac{2nM_7}{\sqrt{\pi\mu}} + \frac{2nM_8}{2\mu} + \frac{16\beta^2\overline{r}^4}{\varepsilon\lambda_1^{\frac{1}{4}}}\sum_{i=1}^{n}\lambda_i^{-\frac{1}{2}},$$

then

$$\overline{\omega}_n(DS_\varepsilon(\omega,\boldsymbol{U})) \leq \left(\frac{n\sigma}{2\lambda_1^{\frac{1}{2}}}|z(\theta_t\omega)| + \frac{n\sigma}{2\lambda_1^{\frac{1}{2}}}|z(\theta_t\omega)|^2 + \frac{n}{2\lambda_1} + \frac{n\sigma}{2\lambda_1}|z(\theta_t\omega)|\right)$$

$$\times \exp\left(-\frac{n\varepsilon}{2} + \frac{8n}{\varepsilon}\left(\beta\overline{r}^2 + |p|\right)^2 + \frac{2nM_7}{\sqrt{\pi\mu}} + \frac{2nM_8}{2\mu} + \frac{16\beta^2\overline{r}^4}{\varepsilon\lambda_1^{\frac{1}{4}}}\sum_{i=1}^{n}\lambda_i^{-\frac{1}{2}}\right).$$

Employing (35), we obtain

$$\mathbb{E}\left(\overline{\omega}_n(DS_\varepsilon(\omega,\boldsymbol{U}))\right)$$

$$\leq M_9\mathbb{E}\left(\exp\left(-\frac{n\varepsilon}{2} + \frac{8n}{\varepsilon}\left(\beta\overline{r}^2 + |p|\right)^2 + \frac{2nM_7}{\sqrt{\pi\mu}} + \frac{2nM_8}{2\mu} + \frac{16\beta^2\overline{r}^4}{\varepsilon\lambda_1^{\frac{1}{4}}}\sum_{i=1}^{n}\lambda_i^{-\frac{1}{2}}\right)\right).$$

Let

$$\overline{\omega}_n(\omega) = M_9\exp\left(-\frac{n\varepsilon}{2} + \frac{8n}{\varepsilon}\left(\beta\overline{r}^2 + |p|\right)^2 + \frac{2nM_7}{\sqrt{\pi\mu}} + \frac{2nM_8}{2\mu} + \frac{16\beta^2\overline{r}^4}{\varepsilon\lambda_1^{\frac{1}{4}}}\sum_{i=1}^{n}\lambda_i^{-\frac{1}{2}}\right),$$

then

$$\mathbb{E}\left(\overline{\omega}_n(DS_\varepsilon(\omega,\boldsymbol{U}))\right) \leq \mathbb{E}\left(\overline{\omega}_n(\omega)\right), \tag{36}$$

and

$$\mathbb{E}\left(\ln\overline{\omega}_n(\omega)\right) \leq \ln M_9$$

$$\times \mathbb{E}\left(-\frac{n\varepsilon}{2} + \frac{8n}{\varepsilon}\left(\beta\overline{r}^2 + |p|\right)^2 + \frac{2nM_7}{\sqrt{\pi\mu}} + \frac{2nM_8}{2\mu} + \frac{16\beta^2\overline{r}^4}{\varepsilon\lambda_1^{\frac{1}{4}}}\sum_{i=1}^{n}\lambda_i^{-\frac{1}{2}}\right), \tag{37}$$

together with Lemma 4 we find

$$\ln M_9 \times \mathbb{E}\left(-\frac{n\varepsilon}{2} + \frac{8n}{\varepsilon}\left(\beta\overline{r}^2 + |p|\right)^2 + \frac{2nM_7}{\sqrt{\pi\mu}} + \frac{2nM_8}{2\mu} + \frac{16\beta^2\overline{r}^4}{\varepsilon\lambda_1^{\frac{1}{4}}}\sum_{i=1}^{n}\lambda_i^{-\frac{1}{2}}\right) \leq +\infty.$$

Therefore, we get $d_H(\mathscr{A}(\omega)) < d$. Especially, if

$$
\lambda_1^{-\frac{1}{2}} \leq \frac{\frac{\varepsilon}{2} - \frac{8}{\varepsilon} \left(\beta \overline{r}^2 + |p|\right)^2 - \frac{2M_7}{\sqrt{\pi\mu}} - \frac{2M_8}{2\mu}}{\frac{16\beta^2 \overline{r}^4}{\varepsilon \lambda_1^{\frac{1}{4}}}},
$$

$d_H(\mathscr{A}(\omega)) = 0$, which merges with the Theorem 2 shows that the largest global Lyapunov exponent of $S_\varepsilon(\omega)$ is

$$
\begin{aligned}
\lambda_1 =& \mathbb{E}\left(\ln \overline{\omega}_1(\omega)\right) \\
\leq& \mathbb{E}\left(-\frac{\varepsilon}{2} + \frac{8}{\varepsilon}\left(\beta \overline{r}^2 + |p|\right)^2 + \frac{2M_7}{\sqrt{\pi\mu}} + \frac{2M_8}{2\mu} + \frac{16\beta^2 \overline{r}^4}{\varepsilon \lambda_1^{\frac{1}{4}}} \sum_{i=1}^{n} \lambda_i^{-\frac{1}{2}}\right) < 0,
\end{aligned}
\tag{38}
$$

thus, we can conclude there exists a random fixed point of system (14) which is global stochastic stability.

4　PROOFS FOR LEMMAS

This section is intended to complete the proofs of Lemmas listed in subsection 2.2.

Proof for Lemma 2: Firstly, we display $\boldsymbol{X}_2(\boldsymbol{U}) + \boldsymbol{X}_3(\boldsymbol{U}) : E_1 \rightarrow E_1$ satisfies local Lipschitz condition. Since

$$
\begin{aligned}
&\|\boldsymbol{X}_3(U) - \boldsymbol{X}_3(V) + \boldsymbol{X}_2(U, \theta_t\omega) - \boldsymbol{X}_2(V, \theta_t\omega)\|_{E_1} \\
&\leq \|\boldsymbol{X}_3(U) - \boldsymbol{X}_3(V)\|_{E_1} + \|\boldsymbol{X}_2(U, \theta_t\omega) - \boldsymbol{X}_2(V, \theta_t\omega)\|_{E_1},
\end{aligned}
$$

let $c > 0, \tau \in \mathbb{R}$ are given constant, for $\forall\, \boldsymbol{U}, \boldsymbol{V} \in E_1, \|\boldsymbol{U}\|_{E_1} \leq c, \|\boldsymbol{V}\|_{E_1} \leq c$, combining Lemmas 4 and 7, we get there exists a positive constant $C_1(T, \tau, \omega, c)$ such that

$$
\begin{aligned}
&\|\boldsymbol{X}_3(U) - \boldsymbol{X}_3(V)\|_{E_1} \\
=& \left\|\left(\beta \|\nabla U_1\|^2 - p\right)((-\Delta)U_1 - (-\Delta)V_1) + \left(\beta \|\nabla U_1\|^2 - \beta \|\nabla V_1\|^2\right)(-\Delta)V_1\right\| \\
\leq& \left|\beta \|\nabla U_1\|^2 - p\right| \|\Delta U_1 - \Delta V_1\| + \beta\left(\|\nabla U_1\| + \beta \|\nabla V_1\|\right)\|\Delta V_1\|\|\Delta U_1 - \Delta V_1\| \\
\leq& C_1(T, \tau, \omega, c)\|\mathbf{U} - \mathbf{V}\|_{E_1}.
\end{aligned}
$$

On the other hand, by Lemma 1, there exists a positive constant $C_2(T, \tau, \omega, c)$ which satisfies

$$
\begin{aligned}
&\|\boldsymbol{X}_2(U, \theta_t\omega) - \boldsymbol{X}_2(V, \theta_t\omega)\|_{E_1} \\
=& |\sigma z(\theta_t\omega)| \|U_1 - V_1\|_{H^2} + |\sigma z(\theta_t\omega)| \|V_2 - U_2\| \\
&+ \|\sigma(\mu + 2\varepsilon - \sigma z(\theta_t\omega)) z(\theta_t\omega)(U_1 - V_1)\| + |\sigma\alpha z(\theta_t\omega)| \left\|A^{\frac{1}{2}}V_1 - A^{\frac{1}{2}}U_1\right\| \\
\leq& |\sigma z(\theta_t\omega)| \left\|A^{\frac{1}{2}}V_1 - A^{\frac{1}{2}}U_1\right\| + |\sigma\alpha z(\theta_t\omega)| \left\|A^{\frac{1}{2}}V_1 - A^{\frac{1}{2}}U_1\right\| \\
&+ \frac{|\sigma(\mu + 2\varepsilon - \sigma z(\theta_t\omega)) z(\theta_t\omega)|}{\lambda_1^{\frac{1}{2}}} \left\|A^{\frac{1}{2}}V_1 - A^{\frac{1}{2}}U_1\right\| + |\sigma z(\theta_t\omega)| \|V_2 - U_2\| \\
\leq& C_2(T, \tau, \omega, c)\|\boldsymbol{U} - \boldsymbol{V}\|_{E_1},
\end{aligned}
$$

The indicated above conclude $\boldsymbol{X}_2(\boldsymbol{U}) + \boldsymbol{X}_3(\boldsymbol{U}) : E_1 \rightarrow E_1$ satisfies local Lipschitz condition.

The semigroup method (Theorem 2.5.4 in [33]) is employed to achieve the existence and uniqueness of solution for system (14). Based on Lemma 3.5 in Ref. [24] and Lemma 2.2.3 in Ref. [33], we have $\boldsymbol{Q}$ is m-accretive in $\mathcal{E}_1$, then it can induce a linear semigroup of contractions formulated by $e^{\boldsymbol{Q}t}, t \in \mathbb{R}^+$, which together with the assertion that $\boldsymbol{X}_2(U, \theta_t\omega) + \boldsymbol{X}_3(\boldsymbol{U}) : E_1 \rightarrow E_1$ satisfies local Lipschitz condition can guarantee the system (14) possesses a unique local mild solution with the form

$$
V(t, \tau, \omega; V_\tau) = e^{\boldsymbol{Q}(t-\tau)}V_\tau + \int_\tau^t e^{\boldsymbol{Q}(t-s)}\left(\boldsymbol{X}_2(\theta_s\omega) + \boldsymbol{X}_3(V)(s)\right)ds,
$$

where, $t \geq \tau, t, \tau \in \mathbb{R}$.

Proof for Lemma 3 : Since

$$(\boldsymbol{QU}, \boldsymbol{U})_{E_1}$$

$$\leq -\varepsilon \|U_1\|_{H^2}^2 + \varepsilon \|U_2\|^2 + \varepsilon\alpha \left\|A^{\frac{1}{2}}U_1\right\| \|U_2\| - \varepsilon^2 \|U_1\| \|U_2\| - \alpha \left\|A^{\frac{1}{4}}U_2\right\|^2$$

$$\leq -\varepsilon \|U_1\|_{H^2}^2 + \varepsilon \|U_2\|^2 + \frac{\varepsilon}{2}\left(1 - \frac{3p}{2\lambda_1^{\frac{1}{4}}}\right)\left\|A^{\frac{1}{2}}U_1\right\|^2 + \frac{\varepsilon\alpha^2\lambda_1^{\frac{1}{4}}}{2\lambda_1^{\frac{1}{4}} - 3p}\|U_2\|^2 - \alpha\left\|A^{\frac{1}{4}}U_2\right\|^2$$

$$\leq -\frac{\varepsilon}{2} \|U_1\|_{H^2}^2 + \varepsilon \|U_2\|^2 + \frac{\varepsilon\alpha^2\lambda_1^{\frac{1}{4}}}{2\lambda_1^{\frac{1}{4}} - 3p}\|U_2\|^2 - \alpha\left\|A^{\frac{1}{4}}U_2\right\|^2 - \frac{3p\varepsilon}{4}\|A^{\frac{1}{4}}U_1\|^2$$

$$\leq -\frac{\varepsilon}{2} \|U_1\|_{H^2}^2 + \left(-\frac{\alpha}{\lambda_1^{\frac{1}{4}}} + \varepsilon + \frac{\varepsilon\alpha^2\lambda_1^{\frac{1}{4}}}{2\lambda_1^{\frac{1}{4}} - 3p}\right)\|U_2\|^2 - \frac{3p\varepsilon}{4}\|A^{\frac{1}{4}}U_1\|^2$$

$$\leq -\frac{\varepsilon}{2}\|\boldsymbol{U}\|_{E_1}^2 - \frac{\varepsilon}{4}\|U_2\|^2 - \frac{3p\varepsilon}{4}\|A^{\frac{1}{4}}U_1\|^2,$$

where, p and ε satisfies (15). Thus complete the proof.

Before deriving the other proofs for Lemmas, the following estimations and quantities are introduced

$$2\left(-\left[\beta\left\|A^{\frac{1}{4}}u\right\|^2 - p\right]A^{\frac{1}{2}}u, v\right) \leq -\frac{1}{2\beta}\frac{d}{dt}\left[\beta\|A^{\frac{1}{4}}u\|^2 - p\right]^2$$

$$+ \frac{\varepsilon p^2}{4\beta} + \frac{3p\varepsilon}{2}\|A^{\frac{1}{4}}u\|^2 - \frac{\varepsilon}{4\beta}[\beta\|A^{\frac{1}{4}}u\|^2 - p]^2 \tag{39}$$

$$+ \frac{4\sigma^2|z(\theta_t\omega)|^2}{7\varepsilon\beta}\left[\beta\|A^{\frac{1}{4}}u\|^2 - p\right]^2,$$

$$2\left(\sigma A^{\frac{1}{2}}uz\left(\theta_t\omega\right), A^{\frac{1}{2}}u\right) \leq \frac{\varepsilon}{2}\|A^{\frac{1}{2}}u\|^2 + \frac{2\sigma^2|z(\theta_t\omega)|^2}{\varepsilon}\|A^{\frac{1}{2}}u\|^2,$$

$$2\left(\sigma\left(\mu + 2\varepsilon - \alpha A^{\frac{1}{2}} - \sigma z\left(\theta_t\omega\right)\right)uz\left(\theta_t\omega\right) - \sigma vz\left(\theta_t\omega\right), v\right)$$

$$\leq \frac{2}{\varepsilon}\sigma^2|z\left(\theta_t\omega\right)|^2\|v\|^2 + \frac{\varepsilon}{2}\|v\|^2 + \sigma^2|z\left(\theta_t\omega\right)|^2\left(\frac{4}{\varepsilon}\|u\|^2 + \frac{\varepsilon}{4}\|v\|^2\right) \tag{40}$$

$$+ \frac{\varepsilon}{2}\|v\|^2 + 4\sigma^2|z(\theta_t\omega)|^2\left(\frac{(\mu + 2\varepsilon)^2}{\varepsilon}\|u\|^2 + \frac{\alpha^2}{\varepsilon}\|A^{\frac{1}{2}}u\|^2\right)$$

$$2\left(\sigma A^{\frac{1}{2}}u^a z\left(\theta_t\omega\right), A^{\frac{1}{2}}u^a\right) \leq \frac{\varepsilon}{2}\|A^{\frac{1}{2}}u^a\|^2 + \frac{2\sigma^2|z(\theta_t\omega)|^2}{\varepsilon}\|A^{\frac{1}{2}}u^a\|^2, \tag{41}$$

$$2\left(\sigma(\mu + 2\varepsilon - \alpha A^{\frac{1}{2}} - \sigma z\left(\theta_t\omega\right))u^a z\left(\theta_t\omega\right) - \sigma v^a z\left(\theta_t\omega\right), A^{\frac{1}{2}}v^a\right)$$

$$\leq \frac{2}{\varepsilon}\sigma^2|z\left(\theta_t\omega\right)|^2\|v^a\|^2 + \frac{\varepsilon}{2}\|v^a\|^2 + \sigma^2|z\left(\theta_t\omega\right)|^2\left(\frac{4}{\varepsilon}\|u^a\|^2 + \frac{\varepsilon}{4}\|v^a\|^2\right) \tag{42}$$

$$+ \frac{\varepsilon}{4}\|v^a\|^2 + 8\sigma^2|z(\theta_t\omega)|^2\left(\frac{(\mu + 2\varepsilon)^2}{\varepsilon}\|u^a\|^2 + \frac{\alpha^2}{\varepsilon}\|A^{\frac{1}{2}}u^a\|^2\right),$$

$$(-2\left[\beta\|A^{\frac{1}{4}}u\|^2 - p\right]A^{\frac{1}{2}}u^a, A^{\frac{1}{2}}v^b)$$

$$\leq \frac{3\beta^2}{\lambda_1^{\frac{1}{2}}}\|A^{\frac{1}{2}}u\|^4\left\|A^{\frac{1}{2}}u^a\right\|^2 + 3p^2\|\boldsymbol{V}^a\|_{E_1}^2$$

$$+ 2\frac{d}{dt}\left\|A^{\frac{1}{2}}u^b\right\|^2 + 2\varepsilon^2\left\|A^{\frac{1}{2}}u^b\right\|^2 + 2\sigma^2|z(\theta_t\omega)|^2\left\|A^{\frac{1}{2}}u^b\right\|^2, \tag{43}$$

$$- 2\left[\beta\|A^{\frac{1}{4}}u\|^2 - p\right](A^{\frac{1}{2}}u^b, A^{\frac{1}{2}}v^b)$$

$$= -2\left[\beta\|A^{\frac{1}{4}}u\|^2 - p\right](A^{\frac{1}{2}}u^b, A^{\frac{1}{2}}u_t + \varepsilon u^b - \sigma u z(\theta_t\omega))$$

$$\leq -\frac{d}{dt}\left[\beta\|A^{\frac{1}{4}}u\|^2 - p\right]\|A^{\frac{1}{2}}u^b\|^2 + \frac{\beta}{2}\|A^{\frac{1}{2}}u\|^3\|u_t\|,$$

$$2\left(\sigma\left(\mu + 2\varepsilon - \alpha A^{\frac{1}{2}} - \sigma z(\theta_t\omega)\right)u^b z(\theta_t\omega) - \sigma v z(\theta_t\omega), A^{\frac{1}{2}}v^b\right)$$

$$\leq \frac{\varepsilon}{2}\|A^{\frac{3}{4}}u^b\|^2 + \frac{2\sigma^2|z(\theta_t\omega)|^2}{\varepsilon}\|A^{\frac{1}{4}}u^b\|^2 + \frac{2}{\varepsilon}\sigma^2|z(\theta_t\omega)|^2\|A^{\frac{1}{4}}v^b\|^2 + \frac{\varepsilon}{2}\|A^{\frac{1}{4}}v^b\|^2$$

$$+ \frac{\varepsilon}{2}\|A^{\frac{1}{4}}v^b\|^2 + 4\sigma^2|z(\theta_t\omega)|^2\left(\frac{(\mu + 2\varepsilon)^2}{\varepsilon}\|A^{\frac{1}{4}}u^b\|^2 + \frac{\alpha^2}{\varepsilon}\|A^{\frac{3}{4}}u^b\|^2\right) \tag{44}$$

$$+ \sigma^2|z(\theta_t\omega)|^2\left(\frac{4}{\varepsilon}\|A^{\frac{1}{4}}u^b\|^2 + \frac{\varepsilon}{4}\|A^{\frac{1}{4}}v^b\|^2\right),$$

and

$$\frac{\beta}{2}\|A^{\frac{1}{2}}u\|^3\|u_t\| \leq \frac{\beta}{2}\|\boldsymbol{V}\|_{E_1}^3(\|v\| + \|\varepsilon u\| + \|\sigma u z(\theta_t\omega)\|)$$

$$\leq \frac{\beta}{2}\|\boldsymbol{V}\|_{E_1}^3\left(\|\boldsymbol{V}\|_{E_1} + \varepsilon\|\boldsymbol{V}\|_{E_1} + \sigma|z(\theta_t\omega)|\|\boldsymbol{V}\|_{E_1}\right)$$

$$\leq \left(\frac{\beta + \beta\varepsilon}{2} + \frac{\beta}{2}|\sigma z(\theta_t\omega)|\right)\|\boldsymbol{V}\|_{E_1}^4,$$

By Lemma 4, Lemma 5 and Lemma7, $\widehat{M}(t,\tau,\omega)$ defined as follow is bounded,

$$\widehat{M}(t,\tau,\omega) = \frac{3\beta^2}{\lambda_1^{\frac{1}{2}}}\|A^{\frac{1}{2}}u\|^4\left\|A^{\frac{1}{2}}u^a\right\|^2 + 3p^2\|\boldsymbol{V}^a\|_{E_1}^2 + \frac{\beta}{2}\|A^{\frac{1}{2}}u\|^3\|u_t\|$$

$$+ \left(2\varepsilon^2 + \frac{3p\varepsilon}{2} + 2 - \varepsilon + 2|p|\right)\|A^{\frac{1}{2}}u^b\|^2 < +\infty, \tag{45}$$

$$M_0 = \max\left\{\frac{8\alpha^2 + 2}{\varepsilon} + \frac{8(\mu + 2\varepsilon)^2 + 4}{\varepsilon\lambda_1^{\frac{1}{2}}}, \frac{2}{\varepsilon} + \frac{\varepsilon}{4}\right\}, \tag{46}$$

$$M = \max\left\{\frac{8(\mu + 2\varepsilon)^2 + 6}{\varepsilon\lambda_1^{\frac{1}{2}}} + \frac{8\alpha^2}{\varepsilon}, \frac{\varepsilon^2 + 8}{4\varepsilon}, \frac{8}{7\varepsilon}\right\}, \tag{47}$$

$$M_1 = \frac{4\beta r_1^2(\omega) + 3|p|\lambda_1^{\frac{1}{4}}}{2\lambda_1^{\frac{1}{4}}}, \tag{48}$$

$$M_2 = \frac{3\beta r_1^4(\omega)}{\lambda_1^{\frac{1}{4}}} + 2|p|r_1^2(\omega) + \frac{\varepsilon p^2}{4\beta}, \tag{49}$$

$$M_3 = \max\left\{1, \frac{2}{\varepsilon} + \frac{\varepsilon}{4}, \frac{4(\mu + 2\varepsilon)^2 + 2}{\varepsilon\lambda_1^{\frac{1}{2}}} + \frac{4\alpha^2}{\varepsilon} + \frac{2|p| + 4}{\lambda_1^{\frac{1}{4}}} + \frac{\varepsilon}{4\lambda_1^{\frac{1}{2}}}\right\}, \tag{50}$$

$$c_1(\omega) = \max\left\{1, \frac{6\beta r_1(\omega)}{\lambda_1^{\frac{1}{4}}}\right\}, \quad c_2(\omega) = \max\left\{1, \frac{\overline{r}^2(\omega)}{2} + \frac{2\beta r_1(\omega)}{\lambda_1^{\frac{1}{8}}}\right\}, \tag{51}$$

$$C(p) = \begin{cases} 1, & p \leqslant -2, \\ (1 - \frac{p+2}{\lambda_1^{\frac{1}{4}}}), & -2 < p < \frac{\lambda_1^{\frac{1}{4}} - 2}{2}, \end{cases} \tag{52}$$

$$q = \frac{\sigma\left(\mu + 2\varepsilon + 2\lambda_1^{\frac{1}{2}} + \alpha\lambda_1^{\frac{1}{2}}\right)}{2\lambda_1^{\frac{1}{2}}}, \tag{53}$$

$$-M_4 = -\varepsilon + c_2(\omega), \tag{54}$$

$$M_5 = \frac{\sigma\left(\mu + 2\varepsilon + \alpha\lambda_1^{\frac{1}{4}}\right)}{2\lambda_1^{\frac{1}{4}}} + |\sigma|, \tag{55}$$

$$M_6 = \varepsilon - \frac{16}{\varepsilon}\left(\beta\bar{r}^2 + |p|\right)^2 - \frac{64\beta^2\bar{r}^4}{\varepsilon\lambda_1^{\frac{1}{2}}}, \tag{56}$$

$$M_7 = \sigma + \frac{\sigma}{\lambda_1^{\frac{1}{2}}} + \frac{\sigma\left(\mu + 2\varepsilon + \alpha\lambda_1^{\frac{1}{2}}\right)}{2\lambda_1^{\frac{1}{2}}}, \quad M_8 = \frac{\sigma^2}{2\lambda_1^{\frac{1}{2}}}, \tag{57}$$

$$M_9 = \frac{n\sigma}{2\sqrt{\lambda_1\pi\mu}} + \frac{n\sigma}{2\lambda_1\sqrt{\pi\mu}} + \frac{n\sigma}{4\mu\lambda_1^{\frac{1}{2}}} + \frac{n}{2\lambda_1}. \tag{58}$$

Proof for Lemma 4 : Taking the inner product of V by $\boldsymbol{V} = [u, v]^T$ in E_1, we get that

$$\begin{aligned} \frac{d}{dt}\|\boldsymbol{V}\|_{E_1}^2 &\leq 2(\boldsymbol{QV}, \boldsymbol{V})_{E_1} + 2\left(\sigma A^{\frac{1}{2}}uz\left(\theta_t\omega\right), A^{\frac{1}{2}}u\right) \\ &+ 2\left(-\left[\beta\left\|A^{\frac{1}{2}}u\right\|^2 - p\right]A^{\frac{1}{2}}u, v\right) \\ &+ 2\left(\sigma\left(\mu + 2\varepsilon - \alpha A^{\frac{1}{2}} - \sigma z\left(\theta_t\omega\right)\right)uz\left(\theta_t\omega\right) - \sigma vz\left(\theta_t\omega\right), v\right). \end{aligned} \tag{59}$$

Set

$$\mathcal{H}(t, \tau, \omega) = \overline{\mathcal{H}}(u, v) = \frac{1}{2\beta}\left[\beta\left\|A^{\frac{1}{4}}u\right\|^2 - p\right]^2 + \left\|A^{\frac{1}{2}}u\right\|^2 + \|v\|^2.$$

By (40) and Lemma 3, we find that

$$\begin{aligned} \frac{d}{dt}\overline{\mathcal{H}}(u, v) &\leq -\frac{\varepsilon}{2}\overline{\mathcal{H}}(u, v) + \frac{\varepsilon p^2}{4\beta} + \frac{4\sigma^2|z(\theta_t\omega)|^2}{7\varepsilon\beta}\left[\beta\|A^{\frac{1}{4}}u\|^2 - p\right]^2 \\ &+ \left(\frac{\alpha^2 + 2}{\varepsilon} + \frac{(\mu + 2\varepsilon)^2 + 4}{\varepsilon\lambda_1^{\frac{1}{2}}}\right)\sigma^2|z(\theta_t\omega)|^2\|A^{\frac{1}{2}}u\|^2 \\ &+ \left(\frac{2}{\varepsilon} + \frac{\varepsilon}{4}\right)\sigma^2|z\left(\theta_t\omega\right)|^2\|v\|^2 \\ &\leq -\frac{\varepsilon}{2}\overline{\mathcal{H}}(u, v) + M\sigma^2|z(\theta_t\omega)|^2\overline{\mathcal{H}}(u, v) + \frac{\varepsilon p^2}{4\beta}, \end{aligned} \tag{60}$$

where M is formulated by (47). Then, for any $t > 0$, the following holds

$$\mathcal{H}(0, -t, \omega) \leq e^{-\frac{\varepsilon}{2}t + \int_{-t}^0 M\sigma^2|z(\theta_s\omega)|^2 ds}\mathcal{H}(-t, -t, \omega) + \frac{\varepsilon p^2}{4\beta}\int_{-t}^0 e^{-\frac{\varepsilon}{2}s + \int_s^0 M\sigma^2|z(\theta_k\omega)|^2 dk}ds.$$

Since $v = u_t + \varepsilon u - \sigma u z\left(\theta_t \omega\right)$, we get

$$
\begin{aligned}
\|\boldsymbol{U}\|_{E_1}^2 \leq & 2\left\|A^{\frac{1}{2}} u\right\|^2 + 2\left\|u_t + \varepsilon u - \sigma u z\left(\theta_t \omega\right)\right\|^2 + 2\left\|\sigma u z\left(\theta_t \omega\right)\right\|^2 \\
\leq & 2\left(1 + \frac{\sigma^2}{\lambda_1^{\frac{1}{4}}}|z(\theta_t \omega)|^2\right)\|\boldsymbol{V}\|_{E_1}^2.
\end{aligned}
\tag{61}
$$

Thus, we have

$$
\begin{aligned}
\|\boldsymbol{U}\left(0, -t, \omega\right)\|_{E_1}^2 \leq & 2\left(1 + \frac{\sigma^2}{\lambda_1^{\frac{1}{4}}}|z(\theta_t \omega)|^2\right)\|\boldsymbol{V}\left(0, -t, \omega\right)\|_{E_1}^2 \\
\leq & 2\left(1 + \frac{\sigma^2}{\lambda_1^{\frac{1}{4}}}|z(\theta_t \omega)|^2\right)e^{-\frac{\varepsilon}{2}t + \int_{-t}^0 M\sigma^2|z(\theta_s \omega)|^2 ds}\mathcal{H}(-t, -t, \omega) \\
& + \left(1 + \frac{\sigma^2}{\lambda_1^{\frac{1}{4}}}|z(\theta_t \omega)|^2\right)\frac{\varepsilon p^2}{2\beta}\int_{-t}^0 e^{-\frac{\varepsilon}{2}s + \int_s^0 M\sigma^2|z(\theta_k \omega)|^2 dk} ds.
\end{aligned}
\tag{62}
$$

Since the random variable $z(\theta_t \omega)$ is tempered, along with Lemma 1, we can infer that

$$
\frac{2\sigma^2}{\lambda_1^{\frac{1}{4}}}|z(\theta_t \omega)|^2 e^{-\frac{\varepsilon}{2}t + \int_{-t}^0 M\sigma^2|z(\theta_s \omega)|^2 ds}\mathcal{H}(-t, -t, \omega) \to 0, t \to +\infty,
$$

and

$$
\frac{2\sigma^2}{\lambda_1^{\frac{1}{4}}}|z(\theta_t \omega)|^2 \frac{\varepsilon p^2}{4\beta}\int_{-t}^0 e^{-\frac{\varepsilon}{2}s + \int_s^0 M\sigma^2|z(\theta_k \omega)|^2 dk} ds \to 0, t \to +\infty,
$$

similarly

$$
2e^{-\frac{\varepsilon}{2}t + \int_{-t}^0 M\sigma^2|z(\theta_s \omega)|^2 ds}\mathcal{H}(-t, -t, \omega) \to 0, t \to +\infty,
$$

and

$$
\frac{\varepsilon p^2}{2\beta}\int_{-t}^0 e^{-\frac{\varepsilon}{2}s + \int_s^0 M\sigma^2|z(\theta_k \omega)|^2 dk} ds < \infty.
$$

Let

$$
\rho_1(\omega) = \frac{\varepsilon p^2}{2\beta}\int_{-t}^0 e^{-\frac{\varepsilon}{2}s + \int_s^0 M\sigma^2|z(\theta_k \omega)|^2 dk} ds.
\tag{63}
$$

According to (59) - (63), we obtain that there exists $T_1(\omega) > 0$, such that

$$
\|\boldsymbol{U}(t, \theta_{-t}\omega)\|_{E_1} = \|\boldsymbol{U}\left(0, -t, \omega\right)\|_{E_1} \leq r_1(\omega), \quad \forall t \geq T_1(\omega),
\tag{64}
$$

where $r_1(\omega) = \sqrt{\rho_1(\omega)}$.

On the other hand, utilizing (10), we obtain

$$
\begin{aligned}
\mathbb{E}\left(\rho_1(\omega)\right) = & \frac{\varepsilon p^2}{2\beta}\int_{-\infty}^0 e^{-\frac{\varepsilon}{2}s}\mathbb{E}\left(e^{M\sigma^2 \int_s^0 |z(\theta_k \omega)|^2 dk}\right) ds \\
\leq & \frac{\varepsilon p^2}{2\beta}\int_{-\infty}^0 e^{-\frac{\varepsilon}{2}s - \frac{sM\sigma^2}{\mu}} ds \\
= & \frac{\varepsilon p^2}{2\beta}\int_{\overline{T}}^0 e^{-\frac{\varepsilon}{2}s - \frac{sM\sigma^2}{\mu}} ds - \frac{\varepsilon p^2}{2\beta}\int_{-\infty}^{\overline{T}} e^{\left(\overline{\varepsilon} + \frac{M\sigma^2}{\mu}\right)s} ds \\
= & \frac{\varepsilon p^2}{2\beta}\int_{\overline{T}}^0 e^{-\frac{\varepsilon}{2}s - \frac{sM\sigma^2}{\mu}} ds - \frac{\varepsilon p^2 e^{\overline{\varepsilon} + \frac{M\sigma^2}{\mu}\overline{T}}}{2\beta\left(\overline{\varepsilon} + \frac{M\sigma^2}{\mu}\right)} \\
< & +\infty.
\end{aligned}
\tag{65}
$$

Proof for Lemma 5 : Taking the inner product $(\cdot, \cdot)_{E_1}$ of (18) with $A^{\frac{1}{2}}\boldsymbol{V}^a$ gives

$$
\begin{aligned}
\frac{d}{dt}\|A^{\frac{1}{4}}\boldsymbol{V}^a\|_{E_1}^2 =& 2(\boldsymbol{Q}\boldsymbol{V}^a, A^{\frac{1}{2}}\boldsymbol{V}^a)_{E_1} + 2(\sigma A^{\frac{1}{2}}u^a z\,(\theta_t\omega)\,, Au^a) \\
&+ 2\left(\sigma(\mu + 2\varepsilon - \alpha A^{\frac{1}{2}} - \sigma z\,(\theta_t\omega))u^a z\,(\theta_t\omega) - \sigma v^a z\,(\theta_t\omega)\,, A^{\frac{1}{2}}v^a\right).
\end{aligned}
\tag{66}
$$

Substituting (41) and (42) into (66),, we infer the following by combining with Lemma 3

$$
\begin{aligned}
\frac{d}{dt}\|A^{\frac{1}{4}}\boldsymbol{V}^a\|_{E_1}^2 \leq& -\frac{\varepsilon}{2}\|A^{\frac{1}{4}}\boldsymbol{V}^a\|_{E_1}^2 + \left(\frac{4}{\varepsilon} + \frac{\varepsilon}{4}\right)\sigma^2|z\,(\theta_t\omega)\,|^2\|A^{\frac{1}{4}}v^a\|^2 \\
&+ \left(\frac{8(\mu + 2\varepsilon)^2}{\varepsilon\lambda_1^{\frac{1}{2}}} + \frac{8\alpha^2}{\varepsilon} + \frac{4}{\varepsilon\lambda_1^{\frac{1}{2}}} + \frac{2}{\varepsilon\lambda_1^{\frac{1}{2}}}\right)\sigma^2|z(\theta_t\omega)|^2\|A^{\frac{3}{4}}u^a\|^2,
\end{aligned}
$$

hence

$$
\frac{d}{dt}\|A^{\frac{1}{4}}\boldsymbol{V}^a\|_{E_1}^2 \leq \left(-\frac{\varepsilon}{2} + \sigma^2|z(\theta_t\omega)|^2 M_0\right)\|A^{\frac{1}{4}}\boldsymbol{V}^a\|_{E_1}^2,
$$

where M_0 is given by (46). Thus, we have

$$
\|A^{\frac{1}{4}}\boldsymbol{V}^a\|_{E_1}^2 \leq e^{\int_{-t}^0 -\frac{\varepsilon}{2}t + \sigma^2|z(\theta_s\omega)|^2 M_0 ds}\|A^{\frac{1}{4}}\boldsymbol{V}^a(-t, -t, \omega)\|_{E_1}^2.
$$

Since the random variable $z(\theta_t\omega)$ is tempered, along with Lemma 1 states

$$
e^{\int_{-t}^0 -\frac{\varepsilon}{2}t + \sigma^2|z(\theta_s\omega)|^2 M_0 ds}\|A^{\frac{1}{4}}\boldsymbol{V}^a(-t, -t, \omega)\|_{E_1}^2 \to 0, t \to +\infty,
$$

Thus, it can be obtained that

$$
\lim_{t \to +\infty}\left\|A^{\frac{1}{4}}\boldsymbol{U}^a\right\|(t, \theta_{-t}\omega)_{E_1} = 0.
$$

Proof for Lemma 6 : Taking the inner product $(\cdot, \cdot)_{E_1}$ of (19) with $\boldsymbol{V}^b$ gives

$$
\frac{d}{dt}\|\boldsymbol{V}^b\|_{E_1}^2 \leq \Upsilon^{(1)} + \Upsilon^{(2)},
\tag{67}
$$

here

$$
\begin{aligned}
\Upsilon^{(1)} =& 2(\boldsymbol{Q}\boldsymbol{V}^b, \boldsymbol{V}^b) + 2\left(\sigma A^{\frac{1}{2}}u^b z\,(\theta_t\omega)\,, A^{\frac{1}{2}}u^b\right) + 2\left(-\left[\beta\left\|A^{\frac{1}{4}}u^b\right\|^2 - p\right]A^{\frac{1}{2}}u^b, v^b\right) \\
&+ 2\left(\sigma\left(\mu + 2\varepsilon - \alpha A^{\frac{1}{2}} - \sigma z\,(\theta_t\omega)\right)u^b z\,(\theta_t\omega) - \sigma v z\,(\theta_t\omega)\,, v^b\right), \\
\Upsilon^{(2)} =& 2\left(\left[\beta\left\|A^{\frac{1}{4}}u^b\right\|^2 - p\right]A^{\frac{1}{2}}u^b, v^b\right) + 2\left(-\left[\beta\left\|A^{\frac{1}{4}}u\right\|^2 - p\right]A^{\frac{1}{2}}u, v^b\right),
\end{aligned}
\tag{68}
$$

in which $\Upsilon^{(1)}$ is bounded. On the other hand

$$
\begin{aligned}
\Upsilon^{(2)} =& 2\left[\beta\left\|A^{\frac{1}{4}}u - A^{\frac{1}{4}}u^a\right\|^2 - p\right]\left(A^{\frac{1}{2}}u, \frac{1}{2}v^b\right) + 2\left[\beta\left\|A^{\frac{1}{4}}u - A^{\frac{1}{4}}u^a\right\|^2 - p\right]\left(-A^{\frac{1}{2}}u^a, \frac{1}{2}v^b\right) \\
&+ 2\left(-\left[\beta\left\|A^{\frac{1}{4}}u\right\|^2 - p\right]A^{\frac{1}{2}}u, v^b\right) \\
\leq& \frac{\beta}{\lambda_1^{\frac{1}{4}}}\left(2\left\|\boldsymbol{V}\right\|^2 + 2\left\|\boldsymbol{V}^a\right\|^2 + \frac{|p|\lambda_1^{\frac{1}{4}}}{\beta}\right)(\left\|\boldsymbol{V}\right\|^2 + \left\|\boldsymbol{V}^a\right\|^2) + \left(\frac{\beta}{\lambda_1^{\frac{1}{4}}}\left\|\boldsymbol{V}\right\|^2 + |p|\right)\left\|\boldsymbol{V}\right\|^2 \\
&+ \frac{\beta}{2\lambda_1^{\frac{1}{4}}}\left(4\left\|\boldsymbol{V}\right\|^2 + 2\left\|\boldsymbol{V}^a\right\|^2 + \frac{3|p|\lambda_1^{\frac{1}{4}}}{\beta}\right)\overline{\mathcal{H}}(u^b, v^b).
\end{aligned}
\tag{69}
$$

Set

$$\mathcal{H}^{'}(t, \tau, \omega) = \overline{\mathcal{H}}(u^b, v^b) = \frac{1}{2\beta} \left[\beta \left\| A^{\frac{1}{4}} u^b \right\|^2 - p \right]^2 + \left\| A^{\frac{1}{2}} u^b \right\|^2 + \|v^b\|^2,$$

taking account into (67), (68) and (69), we can get

$$\frac{d}{dt}\overline{\mathcal{H}}(u^b, v^b) \leq - \frac{\varepsilon}{2}\overline{\mathcal{H}}(u^b, v^b) + \left(\frac{\beta}{\lambda_1^{\frac{1}{4}}} \|\boldsymbol{V}\|^2 + |p| \right) \|\boldsymbol{V}\|^2 + \frac{\varepsilon p^2}{4\beta}$$

$$+ \left(M\sigma^2 |z(\theta_t\omega)|^2 + \frac{2\beta}{\lambda_1^{\frac{1}{4}}} \|\boldsymbol{V}\|^2 + \frac{\beta}{\lambda_1^{\frac{1}{4}}} \|\boldsymbol{V}^a\|^2 + 3|p| \right) \overline{\mathcal{H}}(u^b, v^b) \qquad (70)$$

$$+ \frac{2\beta \|\boldsymbol{V}\|^2 + 2\beta \|\boldsymbol{V}^a\|^2 + |p|\lambda_1^{\frac{1}{4}}}{\lambda_1^{\frac{1}{4}}}(\|\boldsymbol{V}\|^2 + \|\boldsymbol{V}^a\|^2).$$

Thus,

$$\mathcal{H}^{'}(0, -t, \omega) \leq e^{-\frac{\varepsilon}{2}t + \int_{-t}^{0} M\sigma^2|z(\theta_s\omega)|^2 + \frac{\beta}{2\lambda_1^{\frac{1}{4}}} \left(4\|\boldsymbol{V}\|^2 + 2\|\boldsymbol{V}^a\|^2 + \frac{3|p|\lambda_1^{\frac{1}{4}}}{\beta} \right) ds} \mathcal{H}^{'}(-t, -t, \omega)$$

$$+ \int_{-t}^{0} e^{-\frac{\varepsilon}{2}s + \int_{s}^{0} M\sigma^2|z(\theta_k\omega)|^2 + \frac{\beta}{2\lambda_1^{\frac{1}{4}}} \left(4\|\boldsymbol{V}\|^2 + 2\|\boldsymbol{V}^a\|^2 + \frac{3|p|\lambda_1^{\frac{1}{4}}}{\beta} \right) dk}$$

$$\times \left(\frac{2\beta \|\boldsymbol{V}\|^2 + 2\beta \|\boldsymbol{V}^a\|^2 + |p|\lambda_1^{\frac{1}{4}}}{\lambda_1^{\frac{1}{4}}}(\|\boldsymbol{V}\|^2 + \|\boldsymbol{V}^a\|^2) + \frac{\beta \|\boldsymbol{V}\|^4}{\lambda_1^{\frac{1}{4}}} + |p| \|\boldsymbol{V}\|^2 + \frac{\varepsilon p^2}{4\beta} \right) ds.$$

Applying Lemma 4 and Lemma 5, we obtain

$$\mathcal{H}^{'}(0, -t, \omega) \leq e^{-\frac{\varepsilon}{2}t + \int_{-t}^{0} M\sigma^2|z(\theta_s\omega)|^2 + M_1 ds} \mathcal{H}^{'}(-t, -t, \omega)$$

$$+ M_2 \int_{-t}^{0} e^{-\frac{\varepsilon}{2}s + \int_{s}^{0} M\sigma^2|z(\theta_k\omega)|^2 + M_1 dk} ds,$$

where M_1, M_2 are defined by (48) and (49) correspondingly. Since the random variable $z(\theta_t\omega)$ is tempered, together with Lemma 1, we find

$$e^{-\frac{\varepsilon}{2}t + \int_{-t}^{0} M\sigma^2|z(\theta_s\omega)|^2 + M_1 ds} \mathcal{H}^{'}(-t, -t, \omega) \to 0, t \to +\infty,$$

and

$$M_2 \int_{-t}^{0} e^{-\frac{\varepsilon}{2}s + \int_{s}^{0} M\sigma^2|z(\theta_k\omega)|^2 + M_1 dk} ds < \infty.$$

Let

$$\rho_2(\omega) = M_2 \int_{-t}^{0} e^{-\frac{\varepsilon}{2}s + \int_{s}^{0} M\sigma^2|z(\theta_k\omega)|^2 + M_1 dk} ds. \qquad (71)$$

As indicated above, we obtain that there exists $T_2(\omega) > 0$ such that

$$\|\boldsymbol{U}\|_{E_1}(t, \theta_{-t}\omega) = \|\boldsymbol{U}\|_{E_1}(0, -t, \omega) \leq r_2(\omega), \quad \forall t \geq T_2(\omega),$$

where $r_2(\omega) = \sqrt{\rho_2(\omega)}$.

Proof for Lemma 7 : Taking the inner product $(\cdot, \cdot)_{E_1}$ of (19) with $A^{\frac{1}{2}}\boldsymbol{V}^b$ gives

$$\frac{d}{dt}\|A^{\frac{1}{4}}\boldsymbol{V}^b\|_{E_1}^2 \leq 2(\boldsymbol{Q}\boldsymbol{V}^b, A^{\frac{1}{2}}\boldsymbol{V}^b) + 2\left(\sigma A^{\frac{1}{2}} u^b z\left(\theta_t\omega\right), Au^b \right)$$

$$+ 2\left(-\left[\beta \left\| A^{\frac{1}{4}} u \right\|^2 - p \right] A^{\frac{1}{2}} u, A^{\frac{1}{2}} v^b \right) \qquad (72)$$

$$+ 2\left(\sigma \left(\mu + 2\varepsilon - \alpha A^{\frac{1}{2}} - \sigma z\left(\theta_t\omega\right) \right) u^b z\left(\theta_t\omega\right) - \sigma v z\left(\theta_t\omega\right), A^{\frac{1}{2}} v^b \right).$$

Set

$$\mathcal{H}_1(t,\tau,\omega) = \overline{\mathcal{H}}_1(u,v) = \left[\beta\|A^{\frac{1}{4}}u\|^2 - p - 2\right]\|A^{\frac{1}{2}}u^b\|^2 + \|A^{\frac{1}{4}}\boldsymbol{V}^b\|_{E_1}^2, \tag{73}$$

we find

$$\mathcal{H}_1(t,\tau,\omega) = \|A^{\frac{1}{4}}\boldsymbol{V}^b\|_{E_1}^2 + \beta\|A^{\frac{1}{2}}u^b\|^2\|A^{\frac{1}{4}}u\|^2 - p\|A^{\frac{1}{2}}u^b\|^2 - 2\|A^{\frac{1}{2}}u^b\|^2$$

$$\geq \|A^{\frac{1}{4}}u^b\|^2 + \beta\|A^{\frac{1}{2}}u^b\|^2\|A^{\frac{1}{4}}u\|^2 + (1 - \frac{p+2}{\lambda_1^{\frac{1}{4}}})\|A^{\frac{3}{4}}u^b\|^2$$

$$\geq \|A^{\frac{1}{4}}u^b\|^2 + \beta\|A^{\frac{1}{2}}u^b\|^2\|A^{\frac{1}{4}}u\|^2 + C(p)\|A^{\frac{3}{4}}u^b\|^2$$

$$\geq 0,$$

where $C(p)$ is given by (52), which along with (43), (44) and (72) states that

$$\frac{d}{dt}\overline{\mathcal{H}}_1(u,v) \leq -\frac{\varepsilon}{2}\overline{\mathcal{H}}_1(u,v) + \overline{\mathcal{H}}_1(u,v) + \widehat{M}(t,\tau,\omega)$$

$$+ \sigma^2|z(\theta_t\omega)|^2\left[\beta\|A^{\frac{1}{4}}u\|^2 - p - 2\right]\|A^{\frac{1}{2}}u^b\|^2$$

$$+ \left(\frac{4(\mu+2\varepsilon)^2 + 2}{\varepsilon\lambda_1^{\frac{1}{2}}} + \frac{4\alpha^2}{\varepsilon} + \frac{2|p|+4}{\lambda_1^{\frac{1}{4}}} + \frac{\varepsilon}{4\lambda_1^{\frac{1}{2}}}\right)\sigma^2|z(\theta_t\omega)|^2\|A^{\frac{3}{4}}u^b\|^2$$

$$+ \left(\frac{2}{\varepsilon} + \frac{\varepsilon}{4}\right)\sigma^2|z(\theta_t\omega)|^2\|A^{\frac{1}{4}}v^b\|^2$$

$$\leq -\frac{\varepsilon}{2}\overline{\mathcal{H}}_1(u,v) + \left(1 + M_3\sigma^2|z(\theta_t\omega)|^2\right)\overline{\mathcal{H}}_1(u,v) + \widehat{M}(t,\tau,\omega),$$

where $\widehat{M}(t,\tau,\omega)$ and M_3 are defined by (45) and (50) respectively. Then by Lemma 4, Lemma 5 and Lemma7, the following holds

$$\mathcal{H}_1(0,-t,\omega) \leq e^{-\frac{\varepsilon}{2}t + \int_{-t}^0\left(1 + M_3\sigma^2|z(\theta_s\omega)|^2\right)ds}\mathcal{H}_1(-t,-t,\omega)$$

$$+ r\int_{-t}^0 e^{-\frac{\varepsilon}{2}s + \int_s^0(1 + M_3\sigma^2|z(\theta_k\omega)|^2)dk}ds.$$

Since the random variable $z(\theta_t\omega)$ is tempered, applying Lemma 1, we find

$$e^{-\frac{\varepsilon}{2}t + \int_{-t}^0\left(1 + M_3\sigma^2|z(\theta_s\omega)|^2\right)ds}\mathcal{H}_1(-t,-t,\omega) \to 0, t \to +\infty,$$

$$r\int_{-t}^0 e^{-\frac{\varepsilon}{2}s + \int_s^0(1 + M_3\sigma^2|z(\theta_k\omega)|^2)dk}ds < \infty.$$

then we get

$$\mathcal{H}_1(0,-t,\omega) \leq \rho_{30}(\omega),$$

where $\rho_{30}(\omega) = r\int_{-t}^0 e^{-\frac{\varepsilon}{2}s + \int_s^0(1 + M_3\sigma^2|z(\theta_k\omega)|^2)dk}ds$.
Exploiting (61) and (73), we can obtain

$$\|A^{\frac{1}{4}}\boldsymbol{V}^b\|_{E_1}^2(0,-t) + \beta\|A^{\frac{1}{2}}u^b\|^2(0,-t)\|A^{\frac{1}{4}}u\|^2(0,-t)$$

$$\leq \rho_{30}(\omega) + \frac{p+2}{\lambda_1^{\frac{1}{4}}}\|A^{\frac{3}{4}}u^b\|^2(0-t)$$

$$\leq \rho_{30}(\omega) + \frac{p+2}{\lambda_1^{\frac{1}{4}}}\|A^{\frac{1}{4}}\boldsymbol{V}^b\|_{E_1}^2(0,-t),$$

then

$$(1 - \frac{p+2}{\lambda_1^{\frac{1}{4}}})\|A^{\frac{1}{4}}\boldsymbol{V}^b\|_{E_1}^2(0,-t) \leq \rho_{30}(\omega),$$

utilizing (52), we get

$$\|A^{\frac{1}{4}}\boldsymbol{V}^b\|_{E_1}^2(0,-t) \leq \frac{\lambda_1^{\frac{1}{4}}}{\lambda_1^{\frac{1}{4}} - p - 2}\rho_{30}(\omega). \tag{74}$$

By (72)-(74), we obtain that there exists $T_{30}(\omega) > 0$, such that

$$\|A^{\frac{1}{4}} \boldsymbol{V}^b\|_{E_1}^2(0, -t) \leq \rho_3(\omega), \quad \forall\, t \geq T_{30}(\omega), \tag{75}$$

where, $\rho_3(\omega) = \dfrac{\lambda_1^{\frac{1}{4}}}{\lambda_1^{\frac{1}{4}} - p + 2} \rho_{30}(\omega)$. Since the relation between $\|A^{\frac{1}{4}} \boldsymbol{U}^b\|_{E_1}$ and $\|A^{\frac{1}{4}} \boldsymbol{V}^b\|_{E_1}$,

$$
\begin{aligned}
&\|A^{\frac{1}{4}} \boldsymbol{U}^b\|_{E_1}^2 (0, -t, \omega) \\
&\leq 2 \left(1 + \frac{\sigma^2}{\lambda_1^{\frac{1}{4}}} |z(\theta_t \omega)|^2 \right) \|A^{\frac{1}{4}} \boldsymbol{V}^b (0, -t, \omega)\|_{E_1}^2 \\
&\leq \frac{2r\lambda_1^{\frac{1}{4}}}{\lambda_1^{\frac{1}{4}} - p + 2} \left(1 + \frac{\sigma^2}{\lambda_1^{\frac{1}{4}}} |z(\theta_t \omega)|^2 \right) \int_{-t}^{0} e^{-\frac{\varepsilon}{2}s + \int_s^0 (1 + M_3 \sigma^2 |z(\theta_k \omega)|^2) dk} ds.
\end{aligned}
\tag{76}
$$

Since the random variable $z(\theta_t \omega)$ is tempered, we get the following holds by Lemma 1,

$$\frac{2r\sigma^2}{\lambda_1^{\frac{1}{4}} - p + 2} |z(\theta_t \omega)|^2 \int_{-t}^{0} e^{-\frac{\varepsilon}{2}s + \int_s^0 (1 + M_3 \sigma^2 |z(\theta_k \omega)|^2) dk} ds \to 0, t \to +\infty,$$

and

$$\frac{2r\lambda_1^{\frac{1}{4}}}{\lambda_1^{\frac{1}{4}} - p + 2} \int_{-t}^{0} e^{-\frac{\varepsilon}{2}s + \int_s^0 (1 + M_3 \sigma^2 |z(\theta_k \omega)|^2) dk} ds < \infty.$$

Thus, there exists a constant $T_3(\omega) > 0$ such that

$$\left\| A^{\frac{1}{4}} \boldsymbol{U}^b \right\|_{E_1} (t, \theta_{-t}\omega) = \left\| A^{\frac{1}{4}} \boldsymbol{U}^b \right\|_{E_1} (0, -t, \omega) \leq r_3(\omega), \ \forall\, t > T_3(\omega),$$

Proof for Lemma 8 : For $\forall\, \kappa \in \mathcal{D}(A^{\frac{1}{2}})$, we find that

$$
\begin{aligned}
&\left\| \left(\widehat{X}_{32}(u_1) - \widehat{X}_{32}(u_2) \right) \kappa \right\| \\
&\leq \left\| \left(\beta \|\nabla u_1\|^2 - \beta \|\nabla u_2\|^2 \right) (-\Delta)\kappa \right\| + \|2\beta(\nabla u_1, \nabla \kappa)(-\Delta)u_1 - 2\beta(\nabla u_2, \nabla \kappa)(-\Delta)u_2\| \\
&\leq \beta \left(\|\nabla u_1\| - \|\nabla u_2\| \right) \left(\|\nabla u_1\| + \|\nabla u_2\| \right) \|(-\Delta)\kappa\| \\
&\quad + 2\beta \|(\nabla u_1, \nabla \kappa)\| \|(-\Delta)u_1 - (-\Delta)u_2\| + 2\beta \,|\, (\nabla u_1 - \nabla u_2, \nabla \kappa) \,|\,\|(-\Delta)u_2\| \\
&\leq \beta \left(\|\nabla u_1\| - \|\nabla u_2\| \right) \left(\|\nabla u_1\| + \|\nabla u_2\| \right) \|(-\Delta)\kappa\| \\
&\quad + 2\beta \|\nabla u_1\| \|\nabla \kappa\| \|(-\Delta)u_1 - (-\Delta)u_2\| + 2\beta \|\nabla u_1 - \nabla u_2\| \|\nabla \kappa\| \|(-\Delta)u_2\|,
\end{aligned}
$$

Merging Lemma 4 with (51), we find

$$
\begin{aligned}
&\left\| \left(\widehat{X}_{32}(u_1) - \widehat{X}_{32}(u_2) \right) \kappa \right\| \\
&\leq \beta \left(\|\nabla u_1\| - \|\nabla u_2\| \right) \left(\|\nabla u_1\| + \|\nabla u_2\| \right) \|(-\Delta)\kappa\| \\
&\leq \frac{\beta}{\lambda_1^{\frac{1}{4}}} \left(\|\Delta u_1\| - \|\Delta u_2\| \right) 2r_1(\omega) \|(-\Delta)\kappa\| \\
&\quad + \frac{2\beta}{\lambda_1^{\frac{1}{4}}} r_1(\omega) \|\Delta \kappa\| \|(-\Delta)u_1 + \Delta u_2\| + \frac{2\beta}{\lambda_1^{\frac{1}{4}}} \|\Delta u_1 - \Delta u_2\| \|\Delta \kappa\| r_1(\omega) \\
&\leq c_1(\omega) \|\Delta u_1 - \Delta u_2\| \|\Delta \kappa\|, \quad \forall u_1, u_2 \in \mathcal{D}(A^{\frac{1}{2}}),
\end{aligned}
$$

along with Lemma 4 demonstrates $\mathbb{E}\,(c_1(\omega)) \leq \infty$, hence

$$
\begin{aligned}
\left\| \widehat{X}_{32}(u_1) - \widehat{X}_{32}(u_2) \right\|_{\mathscr{L}\left(\mathcal{D}(A^{\frac{1}{2}}), L^2(D) \right)} &= \sup_{\kappa \in \mathcal{D}(A^{\frac{1}{2}})} \frac{\| \left(\widehat{X}_{32}(u_1) - \widehat{X}_{32}(u_2) \right) \kappa \|}{\|\kappa\|_{\mathcal{D}(A^{\frac{1}{2}})}} \\
&\leq c_1(\omega) \left\| A^{\frac{1}{2}} u_1 - A^{\frac{1}{2}} u_2 \right\|.
\end{aligned}
$$

On the other hand, since

$$
\begin{aligned}
\left\| \widehat{X}_{32}\left(u \right) \right\|_{\mathscr{L}\left(\mathcal{D}(A^{\frac{1}{2}}), L^2(D) \right)} &= \sup_{\kappa \in \mathcal{D}(A^{\frac{1}{2}})} \frac{\left\| \widehat{X}_{32}\left(u \right) \kappa \right\|}{\left\| \kappa \right\|_{\mathcal{D}(A^{\frac{1}{2}})}} \\
&= \frac{\left\| \left[\beta \|\nabla u\|^2 - p \right](-\Delta)\kappa + 2\beta(\nabla u, \nabla\kappa)(-\Delta)u \right\|}{\|\Delta\kappa\|} \\
&\leq \frac{\left\| \left[\beta \|\nabla u\|^2 - p \right](-\Delta)\kappa \right\| + \left\| 2\beta(\nabla u, \nabla\kappa)(-\Delta)u \right\|}{\|\Delta\kappa\|} \\
&\leq [\beta\|\nabla u\|^2 - p]^2 + \frac{2\beta}{\lambda_1^{\frac{1}{8}}}\|\Delta u\|^2.
\end{aligned}
$$

In term of Lemma 4 and (51), we find

$$
\left\| \widehat{X}_{32}(u) \right\|_{\mathscr{L}\left(\mathcal{D}(A^{\frac{1}{2}}), L^2(D) \right)} \leq \frac{\overline{r}^2(\omega)}{2} + \frac{2\beta}{\lambda_1^{\frac{1}{8}}} r_1(\omega) = c_2(\omega),
$$

and

$$
\mathbb{E}\left(c_2(\omega) \right) \leq \infty.
$$

Proof for Lemma 9 : Taking the inner product of (23) by $\boldsymbol{V}^{(1)} - \boldsymbol{V}^{(2)}$ in E_1 illustrates

$$
\begin{aligned}
\frac{1}{2}\frac{d\left\| \boldsymbol{V}^{(1)} - \boldsymbol{V}^{(2)} \right\|_{E_1}^2}{dt} &= \left(\boldsymbol{Q}\left(\boldsymbol{V}^{(1)} - \boldsymbol{V}^{(2)} \right), \boldsymbol{V}^{(1)} - \boldsymbol{V}^{(2)} \right)_{E_1} \\
&+ \left(\boldsymbol{X}_2\left(\boldsymbol{V}^{(1)} \right) - \boldsymbol{X}_2\left(\boldsymbol{V}^{(2)} \right), \boldsymbol{V}^{(1)} - \boldsymbol{V}^{(2)} \right)_{E_1} \\
&+ \left(X_{32}\left(\omega, u_1 \right) - X_{32}\left(\omega, u_2 \right), v_1 - v_2 \right),
\end{aligned} \tag{77}
$$

Merging with (24), we have

$$
\left\| X_{32}\left(\omega, u_1 \right) - X_{32}\left(\omega, u_2 \right) \right\| \leq c_2 \left\| A^{\frac{1}{2}}\left(u_1 - u_2 \right) \right\|. \tag{78}
$$

Furthermore, we get

$$
\begin{aligned}
\left(X_{32}\left(\omega, u_1 \right) - X_{32}\left(\omega, u_2 \right), v_1 - v_2 \right) &\leq \left\| X_{32}\left(\omega, u_1 \right) - X_{32}\left(\omega, u_2 \right) \right\| \|v_1 - v_2\| \\
&\leq c_2(\omega)\left\| A^{\frac{1}{2}}\left(u_1 - u_2 \right) \right\| \|v_1 - v_2\| \\
&\leq \frac{c_2(\omega)}{2}\left\| \boldsymbol{V}^{(1)} - \boldsymbol{V}^{(2)} \right\|_{E_1}^2,
\end{aligned} \tag{79}
$$

and

$$
\begin{aligned}
&\left(\boldsymbol{X}_2\left(\boldsymbol{V}^{(1)} \right) - \boldsymbol{X}_2\left(\boldsymbol{V}^{(2)} \right), \boldsymbol{V}^{(1)} - \boldsymbol{V}^{(2)} \right)_{E_1} \\
&\leq \frac{|\sigma z\left(\theta_t\omega \right)\left(\mu + 2\varepsilon - \sigma z\left(\theta_t\omega \right) \right)| + 2\lambda_1^{\frac{1}{2}}|\sigma z\left(\theta_t\omega \right)|}{2\lambda_1^{\frac{1}{2}}}\left(\|u^n - u^m\|_{H^2}^2 + \|v^n - v^m\|^2 \right) \\
&+ \frac{|\alpha\sigma z\left(\theta_t\omega \right)|}{2}\left(\left\| A^{\frac{1}{2}}(u^n - u^m) \right\|^2 + \|v^n - v^m\|^2 \right) \\
&\leq \frac{|\sigma z\left(\theta_t\omega \right)\left(q - \sigma z\left(\theta_t\omega \right) \right)| + 2\lambda_1^{\frac{1}{2}}|\sigma z\left(\theta_t\omega \right)|}{2\lambda_1^{\frac{1}{2}}}\|\boldsymbol{V}_n - \boldsymbol{V}_m\|_{E_1}^2 \\
&\leq \left(q|z\left(\theta_t\omega \right)| + \frac{\sigma^2\left| z\left(\theta_t\omega \right) \right|^2}{2\lambda_1^{\frac{1}{2}}} \right)\|\boldsymbol{V}_n - \widehat{\boldsymbol{V}}_m\|_{E_1}^2,
\end{aligned} \tag{80}
$$

here q is defined by (53), and

$$\left(\boldsymbol{Q}\left(\boldsymbol{V}^{(1)} - \boldsymbol{V}^{(2)} \right), \boldsymbol{V}^{(1)} - \boldsymbol{V}^{(2)} \right) \leq -\frac{\varepsilon}{2}\|\boldsymbol{V}^{(1)} - \boldsymbol{V}^{(2)}\|_{E_1}^2 - \frac{\varepsilon}{4}\|v_1 - v_2\|^2. \tag{81}$$

Substituting (79), (80) and (81) into (77), we get

$$\frac{d\left\|\boldsymbol{V}^{(1)} - \boldsymbol{V}^{(2)}\right\|_{E_1}^2}{dt} \leq \left(-\varepsilon + c_2(\omega) + 2q|z\left(\theta_t\omega\right)| + \frac{\sigma^2}{\lambda_1^{\frac{1}{2}}}\left|z\left(\theta_t\omega\right)\right|^2 \right) \left\|\boldsymbol{V}^{(1)} - \boldsymbol{V}^{(2)}\right\|_{E_1}^2.$$

thus, we have

$$\left\|\boldsymbol{V}^{(1)} - \boldsymbol{V}^{(2)}\right\|_{E_1}^2 (0, -t, \omega) \leq e^{\int_{-t}^0 -M_4 + 2q|z(\theta_s\omega)| + \frac{\sigma^2}{\lambda_1^{\frac{1}{2}}}|z(\theta_s\omega)|^2 ds} \|\boldsymbol{I}\|_{E_1}^2, \tag{82}$$

taking into account the between $\left\|\widehat{\boldsymbol{V}}\right\|_{E_1}^2$ and $\left\|\widehat{\boldsymbol{U}}\right\|_{E_1}^2$,

$$\left\|\boldsymbol{U}^{(1)} - \boldsymbol{U}^{(2)}\right\|_{E_1}^2 \leq 2\left(1 + \frac{\sigma^2}{\lambda_1^{\frac{1}{4}}}|z(\theta_t\omega)|^2 \right) e^{\int_{-t}^0 -M_4 + 2q|z(\theta_s\omega)| + \frac{\sigma^2}{\lambda_1^{\frac{1}{2}}}|z(\theta_s\omega)|^2 ds} \|\boldsymbol{I}\|_{E_1}^2,$$

here $M_4 > 0$ is formulated by (54). Combine assertion that random variable $z(\theta_t\omega)$ is tempered with Lemma 1, we find

$$\frac{2\sigma^2}{\lambda_1^{\frac{1}{4}}}|z(\theta_t\omega)|^2 e^{\int_{-t}^0 -M_4 + 2q|z(\theta_s\omega)| + \frac{\sigma^2}{\lambda_1^{\frac{1}{2}}}|z(\theta_s\omega)|^2 ds} \to 0, t \to +\infty,$$

and

$$2e^{\int_{-t}^0 -M_4 + 2q|z(\theta_s\omega)| + \frac{\sigma^2}{\lambda_1^{\frac{1}{2}}}|z(\theta_s\omega)|^2 ds} < \infty,$$

then, $\exists\, t_0', \forall\, t \geq t_0', \left\|\boldsymbol{U}^{(1)} - \boldsymbol{U}^{(2)}\right\|_{E_1}^2 \leq p_1'$, set $p_1 = \max\{1, p_1'\}$, we obtain

$$\left\|\boldsymbol{U}^{(1)} - \boldsymbol{U}^{(2)}\right\|_{E_1}^2 (0, -t, \omega) = \left\|\boldsymbol{U}^{(1)} - \boldsymbol{U}^{(2)}\right\|_{E_1}^2 (t, \theta_{-t}\omega) \leq p_1\|\boldsymbol{I}\|_{E_1}.$$

and

$$p_1(\omega) \geq 1, \mathbb{E}(p_1(\omega)) < \infty, \mathbb{E}\left(\ln\left(p_1(\omega)\right)\right) < \infty. \tag{83}$$

On the other hand, taking the inner product of (21) by $\widehat{\boldsymbol{V}}$ in E_1, which together with Lemma 3 shows

$$(\boldsymbol{Q}\widehat{\boldsymbol{V}}, \widehat{\boldsymbol{V}})_{E_1} \leq -\frac{\varepsilon}{2}\|\widehat{\boldsymbol{V}}\|_{E_1}^2 - \frac{\varepsilon}{4}\left\|\widehat{V}_2\right\|^2, \tag{84}$$

and

$$\left(\widehat{\boldsymbol{X}}_3\widehat{\boldsymbol{V}}, \widehat{\boldsymbol{V}} \right)_{E_1}$$
$$= -\left(\left[\beta\|\nabla u\|^2 - p \right](-\Delta)\widehat{V}_1, \widehat{V}_2 \right) - \left(2\beta\left(\nabla u, \nabla\widehat{V}_1\right)(-\Delta)u, \widehat{V}_2 \right)$$
$$\leq |\beta\|\nabla u\|^2 - p| \left\|\Delta\widehat{V}_1\right\| \left\|\widehat{V}_2\right\| + \frac{2\beta}{\lambda_1^{\frac{1}{4}}}\|\Delta u\|^2 \left\|\Delta\widehat{V}_1\right\| \left\|\widehat{V}_2\right\| \tag{85}$$
$$\leq \frac{8}{\varepsilon}\left(|\beta\|\nabla u\|^2 - p| \left\|\Delta\widehat{V}_1\right\| \right)^2 + \frac{8}{\varepsilon}\left(\frac{2\beta}{\lambda_1^{\frac{1}{4}}}\|\Delta u\|^2 \left\|\Delta\widehat{V}_1\right\| \right)^2 + \frac{\varepsilon}{4}\left\|\widehat{V}_2\right\|^2$$
$$\leq \frac{8}{\varepsilon}\left(\beta\overline{r}^2 + |p| \right)^2 \left\|\Delta\widehat{V}_1\right\|^2 + \frac{64\beta^2\overline{r}^4}{\varepsilon\lambda_1^{\frac{1}{2}}}\left\|\Delta\widehat{V}_1\right\|^2 + \frac{\varepsilon}{4}\left\|\widehat{V}_2\right\|^2,$$

with the similar calculation of (80), we have

$$\left(\widehat{\boldsymbol{X}}_2\widehat{\boldsymbol{V}}, \widehat{\boldsymbol{V}}\right) \leq \left(M_5|z\left(\theta_t\omega\right)| + \frac{\sigma^2}{2\lambda_1^{\frac{1}{4}}}|z\left(\theta_t\omega\right)|^2\right)\left\|\widehat{\boldsymbol{V}}\right\|_{E_1}^2,\tag{86}$$

where M_5 is given by (55). From (84), (85) and (86), we get

$$\begin{aligned}\frac{d\|\widehat{\boldsymbol{V}}\|_{E_1}^2}{dt} &\leq -\varepsilon\|\widehat{\boldsymbol{V}}\|_{E_1}^2 + 2\left(\left(M_5|z\left(\theta_t\omega\right)| + \frac{\sigma^2}{2\lambda_1^{\frac{1}{4}}}|z\left(\theta_t\omega\right)|^2\right)\left\|\widehat{\boldsymbol{V}}\right\|_{E_1}^2\right)\\ &\quad + 2\left(\frac{8}{\varepsilon}\left(\beta\overline{r}^2 + |p|\right)^2\left\|\Delta\widehat{V}_1\right\|^2 + \frac{64\beta^2\overline{r}^4}{\varepsilon\lambda_1^{\frac{1}{2}}}\left\|\Delta\widehat{V}_1\right\|^2\right)\\ &\leq \left(-M_6 + 2M_5|z\left(\theta_t\omega\right)| + \frac{\sigma^2}{\lambda_1^{\frac{1}{4}}}|z\left(\theta_t\omega\right)|^2\right)\left\|\widehat{\boldsymbol{V}}\right\|_{E_1}^2,\end{aligned}\tag{87}$$

where $M_6 > 0$ is defined by (56). Thus

$$\|\widehat{\boldsymbol{V}}\|_{E_1} \leq e^{\int_{-t}^0 -M_6 + 2M_5|z(\theta_s\omega)| + \frac{\sigma^2}{\lambda_1^{\frac{1}{4}}}|z(\theta_s\omega)|^2 ds}\|\boldsymbol{I}\|_{E_1},$$

by the relation between $\left\|\widehat{\boldsymbol{V}}\right\|_{E_1}^2$ and $\left\|\widehat{\boldsymbol{U}}\right\|_{E_1}^2$, we have

$$\begin{aligned}\left\|\widehat{\boldsymbol{U}}\right\|_{E_1}^2 &\leq 2\left(1 + \frac{\sigma^2}{\lambda_1^{\frac{1}{4}}}|z(\theta_t\omega)|^2\right)\|\widehat{\boldsymbol{V}}\|_{E_1}^2\\ &\leq 2\left(1 + \frac{\sigma^2}{\lambda_1^{\frac{1}{4}}}|z(\theta_t\omega)|^2\right)e^{\int_{-t}^0 -M_6 + 2M_5|z(\theta_s\omega)| + \frac{\sigma^2}{\lambda_1^{\frac{1}{4}}}|z(\theta_s\omega)|^2 ds}\|\boldsymbol{I}\|_{E_1}.\end{aligned}$$

The random variable $z(\theta_t\omega)$ is tempered, which together with Lemma 1 gives that

$$\frac{2\sigma^2}{\lambda_1^{\frac{1}{4}}}|z(\theta_t\omega)|^2 e^{\int_{-t}^0 -M_6 + 2M_5|z(\theta_s\omega)| + \frac{\sigma^2}{\lambda_1^{\frac{1}{4}}}|z(\theta_s\omega)|^2 ds} \to 0, t \to +\infty,$$

and

$$2e^{\int_{-t}^0 -M_6 + 2M_5|z(\theta_s\omega)| + \frac{\sigma^2}{\lambda_1^{\frac{1}{4}}}|z(\theta_s\omega)|^2 ds} < \infty,$$

then, $\exists\, t_2',\ \forall\, t \geq t_2',\ \left\|\widehat{\boldsymbol{U}}\right\|_{E_1}^2 \leq p_2'$, set $p_2 = \max\{1, p_2'\}$, we obtain

$$\left\|\widehat{\boldsymbol{U}}\right\|_{E_1}^2(0, -t, \omega) = \left\|\widehat{\boldsymbol{U}}\right\|_{E_1}^2(t, 0, \theta_{-t}\omega) \leq p_2\|\boldsymbol{I}\|_{E_1},\tag{88}$$

then we can get

$$\mathbb{E}(p_2(\omega)) < \infty.\tag{89}$$

In the rest paper, the value of $\widehat{\boldsymbol{U}}$ at $t = 1$ is still denoted by $\widehat{\boldsymbol{U}}$, and $\widehat{\boldsymbol{U}}(1) = \widehat{DS}_\varepsilon\left(\omega, \boldsymbol{U}^{(1)}\right)\boldsymbol{I}$, where $\widehat{DS}_\varepsilon\left(\omega, \boldsymbol{U}^{(1)}\right)$ is the linear solution mapping of system (20).

According to (84) and (89), we get that

$$\left\|\widehat{DS}_\varepsilon\left(\omega, \boldsymbol{U}^{(1)}\right)\right\|_{\mathscr{L}(E_1, E_1)} = \sup_{I \in E_1}\frac{\|\widehat{DS}_\varepsilon\left(\omega, \boldsymbol{U}^{(1)}\right)\boldsymbol{I}\|_{E_1}}{\|\boldsymbol{I}\|_{E_1}} \leq p_2(\omega),\tag{90}$$

and

$$p_2(\omega) \geq 1, \mathbb{E}\left(\ln\left(p_2(\omega)\right)\right) < \infty. \tag{91}$$

On the other hand, Γ satisfies

$$
\begin{aligned}
\|\Gamma(\omega)\|_{E_1} &\leq \|\boldsymbol{U}^{(1)} - \boldsymbol{U}^{(2)}\|_{E_1} + \| - \widehat{\boldsymbol{U}}\|_{E_1} \\
&\leq (p_1 + p_2)\|\boldsymbol{I}\|_{E_1} \\
&\leq c(\omega)\|\boldsymbol{I}\|_{E_1},
\end{aligned}
$$

where $c(\omega) = \max\{1, p_1 + p_2\}$. Obviously, when $t = 1$

$$\|\Gamma(1, \omega)\|_{E_1} \leq c(\omega)\|\boldsymbol{I}\|_{E_1}.$$

Combining (91) with (89), we have

$$\mathbb{E}\left(\ln c(\omega)\right) < \infty, \mathbb{E}\left(c(\omega)\right) < \infty.$$

Since $S_\varepsilon(\omega) := S_\varepsilon(1, \omega)$, merging with (88) and (25), we can conclude that $S_\varepsilon(\omega)$ is almost surly uniform differentiable on $\mathscr{A}(\omega)$.

CONCLUSIONS

This paper consider global stochastic stability of the Euler-Bernoulli beam equations excited by multiplicative white noise. The system can induce a RDS which owns global random attractors, moreover, Hausdorff dimension of the attractor is finite. Specially, when $\lambda_1^{-\frac{1}{2}} \leq \frac{\frac{\varepsilon}{2} - \frac{8}{\varepsilon}\left(\beta\overline{r}^2 + |p|\right)^2 - \frac{2M_7}{\sqrt{\pi\mu}} - \frac{2M_8}{2\mu}}{\frac{16\beta^2\overline{r}^4}{\varepsilon\lambda_1^{\frac{1}{4}}}}$,

the Hausdorff dimension is 0, which indicates that the stochastic Euler-Bernoulli beam possesses a random fixed point which is global stochastic stability.

ACKNOWLEDGEMENT

REFERENCES

[1]   Crespo da Silva M, Glynn C. Nonlinear flexural-flexural-torsional dynamics of inextensional beams. i. equations of motion. *Journal of Structural Mechanics* 1978; **6**(4):437–448.

[2]   Tajik M, Karami Mohammadi A. Nonlinear vibration, stability, and bifurcation analysis of unbalanced spinning pre-twisted beam. *Mathematics and Mechanics of Solids* 2019; **24**(11):3514–3536.

[3]   Dai H, Wang Y, Wang L. Nonlinear dynamics of cantilevered microbeams based on modified couple stress theory. *International Journal of Engineering Science* 2015; **94**:103–112.

[4]   Chen LQ, Yang XD. Transverse nonlinear dynamics of axially accelerating viscoelastic beams based on 4-term galerkin truncation. *Chaos, Solitons & Fractals* 2006; **27**(3):748–757.

[5]   Pellicano F, Vestroni F. Nonlinear dynamics and bifurcations of an axially moving beam. *Journal of Vibration and Acoustics* 2000; **122**(1):21–30.

[6]   Mao XY, Ding H, Chen LQ. Internal resonance of a supercritically axially moving beam subjected to the pulsating speed. *Nonlinear Dynamics* 2019; **95**(1):631–651.

[7]   Wiggins S. *Global bifurcations and chaos: analytical methods*, vol. 73. Springer Science & Business Media: Heidenburg, 2013.

[8]   Zhang W, Yao M, Zhang J. Using the extended melnikov method to study the multi-pulse global bifurcations and chaos of a cantilever beam. *Journal of Sound and Vibration* 2009; **319**(1-2):541–569.

[9]   ZHANG W, Yao M. Theories of multi-pulse global bifurcations for high-dimensional systems and application to cantilever beam. *International Journal of Modern Physics B* 2008; **22**(24):4089–4141.

[10] Zhou L, Ji P, Chen F. Chaos and subharmonic bifurcation of a composite laminated buckled beam with a lumped mass. *Chaos, Solitons & Fractals* 2021; **147**:110 933.

[11] Hamed Y, El Shehry A, Sayed M. Nonlinear modified positive position feedback control of cantilever beam system carrying an intermediate lumped mass. *Alexandria Engineering Journal* 2020; **59**(5):3847–3862.

[12] Emam SA, Nayfeh AH. On the nonlinear dynamics of a buckled beam subjected to a primary-resonance excitation. *Nonlinear Dynamics* 2004; **35**(1):1–17.

[13] Ghayesh MH. Nonlinear forced dynamics of an axially moving viscoelastic beam with an internal resonance. *International Journal of Mechanical Sciences* 2011; **53**(11):1022–1037.

[14] Ghayesh MH. Subharmonic dynamics of an axially accelerating beam. *Archive of Applied Mechanics* 2012; **82**(9):1169–1181.

[15] Zhang W. Global and chaotic dynamics for a parametrically excited thin plate. *Journal of Sound and vibration* 2001; **239**(5):1013–1036.

[16] Mao X. *Stochastic differential equations and applications*. Elsevier, 2007.

[17] Constantin P, Foiaş C, Temam R. *Attractors representing turbulent flows*, vol. 314. American Mathematical Soc., 1985.

[18] Pezeshki C, Dowell EH. Generation and analysis of lyapunov exponents for the buckled beam. *International journal of non-linear mechanics* 1989; **24**(2):79–97.

[19] Wedig WV. Dynamic stability of beams under axial forces–lyapunov exponents for general fluctuating loads. *Structural Dynamics*. Routledge, 2022; 141–148.

[20] Janevski G, Kozić P, Pavlović R. Moment lyapunov exponents and stochastic stability of a thin-walled beam subjected to eccentric axial loads. *Journal of Theoretical and Applied Mechanics* 2012; **50**(1):61–83.

[21] Debussche A. Hausdorff dimension of a random invariant set. *Journal de mathématiques pures et appliquées* 1998; **77**(10):967–988.

[22] Crauel H. Random point attractors versus random set attractors. *Journal of the London Mathematical Society* 2001; **63**(2):413–427.

[23] Crauel H. Global random attractors are uniquely determined by attracting deterministic compact sets. *Annali di Matematica pura ed applicata* 1999; **176**(1):57–72.

[24] Chen H, Guirao JLG, Cao D, Jiang J, Fan X. Stochastic euler–bernoulli beam driven by additive white noise: global random attractors and global dynamics. *Nonlinear Analysis* 2019; **185**:216–246.

[25] Chen H, Guirao JL, Jiang J, Cao D, Fan X. Kernel sections and global dynamics of nonautonomous euler–bernoulli beam equations. *The European Physical Journal Plus* 2020; **135**(1):1–36.

[26] Chueshov I, Lasiecka I. *Von Karman Evolution Equations: Well-posedness and Long Time Dynamics*. Springer Science & Business Media, 2010.

[27] Temam R. *Infinite-dimensional dynamical systems in mechanics and physics.* Springer-Verlag: New York, 1997.

[28] Fan X. Attractors for a damped stochastic wave equation of sine–gordon type with sublinear multiplicative noise. *Stochastic Analysis and Applications* 2006; **24**(4):767–793.

[29] Arnold L. *Random dynamical systems.* Springer-Verlag, 1998.

[30] Crauel H, Flandoli F. Attractors for random dynamical systems. *Probability Theory and Related Fields* 1994; **100**(3):365–393.

[31] Schmalfuss B. Measure attractors and stochastic attractors, institut for dynamische systeme. *Technical Report*, Bermen University 1995.

[32] Crauel H, Imkeller P, Steinkamp M. Bifurcations of one-dimensional stochastic differential equations. *Stochastic dynamics* 1999; :27–47.

[33] Zheng S. *Nonlinear evolution equations.* CRC Press: Florida, 2004.

3C Tecnología. Glosas de innovación aplicadas a la pyme. ISSN: 2254-4143

Ed.43 | Iss.12 | N.1 January - March 2023